Springer Series in Surface Sciences 65

Sascha Sadewasser
Thilo Glatzel *Editors*

Kelvin Probe Force Microscopy

From Single Charge Detection to Device Characterization

Springer

Springer Series in Surface Sciences

Volume 65

This series covers the whole spectrum of surface sciences, including structure and dynamics of clean and adsorbate-covered surfaces, thin films, basic surface effects, analytical methods and also the physics and chemistry of interfaces. Written by leading researchers in the field, the books are intended primarily for researchers in academia and industry and for graduate students.

More information about this series at http://www.springer.com/series/409

Sascha Sadewasser · Thilo Glatzel
Editors

Kelvin Probe Force Microscopy

From Single Charge Detection to Device Characterization

Springer

Editors
Sascha Sadewasser
International Iberian
Nanotechnology Laboratory
Braga
Portugal

Thilo Glatzel
Department of Physics
University of Basel
Basel
Switzerland

ISSN 0931-5195 ISSN 2198-4743 (electronic)
Springer Series in Surface Sciences
ISBN 978-3-319-75686-8 ISBN 978-3-319-75687-5 (eBook)
https://doi.org/10.1007/978-3-319-75687-5

Library of Congress Control Number: 2018931494

Printed on acid-free paper

This Springer imprint is published by the registered company Springer International Publishing AG part of Springer Nature
The registered company address is: Gewerbestrasse 11, 6330 Cham, Switzerland

Foreword

Atomic Force Microscopy AFM and its Off-springs: The Ultimate Toolkits for Nanoscience and Technology

Nature is the best example of a system functioning on the nanometer scale, where the involved materials, energy consumption, and data handling are optimized. The emergence of Atomic Force Microscopy (AFM) 31 years ago in the then-fledgling field of nanotechnology led to a shift of paradigm in the understanding and perception of matter at its most fundamental level. It undoubtedly has opened new avenues in physics, chemistry, biology, and medicine and still is inspiring researchers around the world testified so far by more than 350'000 scientific articles in peer-reviewed journals (according to the web of science). The high flexibility of AFM to image, probe, and manipulate materials with unprecedented resolution and to be combined with other technologies made it the most powerful and versatile toolkit in nanoscience and technology of today. As a consequence, new revolutionary concepts stimulated a number of new technologies.

Kelvin probe force microscopy emerged quite early in the history of AFM and showed the enormous potential of the method impacting surface science on the atomic scale to a great extent ever since. The new edition "Kelvin Probe Force Microscopy—From Single Charge Detection to Device Characterization" gives the reader an overview of the dramatic developments in the last decade taking the technique into diverse fields of applications and beyond.

Basel, Switzerland
July 2017

Christoph Gerber

Preface

Seven years have passed since the first volume "Kelvin probe force microscopy—Measuring and compensating electrostatic forces" has been published in 2011. It presented the first book dedicated solely to Kelvin probe force microscopy (KPFM), about 20 years after the invention of KPFM in 1991 by Nonnenmacher et al. The book gave an overview and good starting point for newcomers to the field, provided in-depth descriptions of the underlying techniques, and presented a variety of examples for applications. Since then we have seen a strongly increased development of KPFM techniques, an improved understanding of the involved physical principles, and a multitude of new applications in numerous fields. Therefore, we feel it is a good time to summarize the recent advances into a second volume of the book, which is entitled "Kelvin Probe Force Microscopy—From Single Charge Detection to Device Characterization". The subtitle reflects the remarkable development that KPFM has seen in the recent 5 to 10 years. Several new techniques have been developed providing measurements of the surface potential that are faster, free of capacitive cross-talk, and with better resolution and noise level. KPFM in liquid environments, improved theoretical understanding, and time-resolved KPFM are other major steps that have given new impulses to the field. Another important development is the imaging of electrostatic forces at atomic and intramolecular scale, providing fundamental insights into organic and inorganic matter. All these advances have paved the ground for the characterization and the progress of knowledge in material science and device applications.

Motivated by these developments and opportunities, KPFM and electrostatic force microscopy (EFM) have received increasing attention in the scientific literature and at scientific conferences and workshops. Large conferences on materials science (e.g., the annual spring and fall meetings of the (European) Materials Research Society) have hosted several dedicated symposia where KPFM and EFM played a significant role. Conferences specialized to certain types of device concepts (e.g., solar cells, nanowires, nanoelectronis, etc.) typically have dedicated sessions for scanning probe microscopy where KPFM and EFM have a large impact. In addition, specialized conferences (e.g., the annual nc-AFM conference)

and numerous smaller workshops typically hold sessions devoted to these techniques.

In view of these advances and interest in the local characterization of electrical surface properties by KPFM, we feel that it is a good time to provide a review of the state-of-the-art of the field in the form of the present book. We aim at summarizing and describing the advances and recent applications in this second volume, again providing a first contact for newcomers into the field and also an overview with in-depth discussions of specific techniques or applications for the specialist. Volume 2 contains 15 completely new chapters and starts with a fully revised chapter giving an introduction to the principles of the technique. The book is structured into four parts, covering "Experimental Methods and Technical Aspects", "Data Interpretation and Theoretical Aspects", "Application to Device Characterization", and "Atomic Scale Experiments". We could win the leading scientists and researchers to contribute their expertise in the various chapters and we thank them for their efforts and contributions.

We hope that the reader finds the book a useful resource in the daily work, an inspiration to try out new techniques and applications, and to go beyond the current state-of-the-art in the field of electrostatic and Kelvin probe force microscopy.

Braga, Portugal — Sascha Sadewasser
Basel, Switzerland — Thilo Glatzel

Contents

Contributors

Mahshid Ahmadi Department of Materials Science and Engineering, University of Tennessee, Knoxville, TN, USA

Ralf Bechstein Institut für Physikalische Chemie, Johannes Gutenberg-Universität Mainz, Mainz, Germany

Liam Collins Center for Nanophase Materials Sciences and Institute for Functional Imaging of Materials, Oak Ridge National Laboratory, Oak Ridge, TN, USA

Michael Ellner SPM Theory & Nanomechanics Group, Departamento de Física Teórica de la Materia Condensada and Condensed Matter Physics Center (IFIMAC), Universidad Autónoma de Madrid, Madrid, Spain

Thilo Glatzel Department of Physics, University of Basel, Basel, Switzerland

Benjamin Grévin National Center for Scientific Research – CNRS, UMR5819 CEA-CNRS-UGA, CEA-INAC/SYMMES, Grenoble Cedex 9, France

Peter Grütter Department of Physics, McGill University, Montreal, Canada

Prokop Hapala Institute of Physics of the Czech Academy of Sciences, Prague 6, Czech Republic

Alex Henning Department of Materials Science and Engineering, Northwestern University, Evanston, IL, USA

Pavel Jelínek Institute of Physics of the Czech Academy of Sciences, Prague 6, Czech Republic

Stephen Jesse Oak Ridge National Laboratory, The Institute for Functional Imaging of Materials and The Center for Nanophase Materials Sciences, Oak Ridge, TN, USA

Sergei V. Kalinin Oak Ridge National Laboratory, The Institute for Functional Imaging of Materials and The Center for Nanophase Materials Sciences, Oak Ridge, TN, USA

Kei Kobayashi Kyoto University, Kyoto, Japan

Lili Kou Department of Applied Physics, Graduate School of Engineering, Osaka University, Suita, Osaka, Japan

Angelika Kühnle Institut für Physikalische Chemie, Johannes Gutenberg-Universität Mainz, Mainz, Germany; Physical Chemistry I, Bielefeld University, Bielefeld, Germany

Yan Jun Li Department of Applied Physics, Graduate School of Engineering, Osaka University, Suita, Osaka, Japan; National Key Laboratory for Electronic Measurement and Technology, North University of China, Taiyuan, Shan Xi, China

Zong Min Ma National Key Laboratory for Electronic Measurement and Technology, North University of China, Taiyuan, Shan Xi, China

Yoichi Miyahara Department of Physics, McGill University, Montreal, Canada

Yoshitaka Naitoh Department of Applied Physics, Graduate School of Engineering, Osaka University, Suita, Osaka, Japan

Sabine Neumayer School of Physics, University College Dublin, Belfield, Dublin, Ireland

Nicoleta Nicoara International Iberian Nanotechnology Laboratory, Braga, Portugal

Martin Ondráček Institute of Physics of the Czech Academy of Sciences, Prague 6, Czech Republic

Ruben Perez SPM Theory & Nanomechanics Group, Departamento de Física Teórica de la Materia Condensada and Condensed Matter Physics Center (IFIMAC), Universidad Autónoma de Madrid, Madrid, Spain

Leo Polak Department of Physics and Astronomy, Vrije Universiteit Amsterdam, Amsterdam, The Netherlands

Pablo Pou SPM Theory & Nanomechanics Group, Departamento de Física Teórica de la Materia Condensada and Condensed Matter Physics Center (IFIMAC), Universidad Autónoma de Madrid, Madrid, Spain

Philipp Rahe Fachbereich Physik, Universität Osnabrück, Osnabrück, Germany

Brian J. Rodriguez School of Physics and Conway Institute of Biomedical and Biomolecular Research, University College Dublin, Dublin, Ireland

Yossi Rosenwaks Faculty of Engineering, Department of Physical Electronics, Tel Aviv University, Tel Aviv, Israel

Ali Sadeghi Department of Physics, Shahid Beheshti University, G. C., Tehran, Iran

Sascha Sadewasser International Iberian Nanotechnology Laboratory, Braga, Portugal

Suhas Somnath Oak Ridge National Laboratory, The Institute for Functional Imaging of Materials and The Center for Nanophase Materials Sciences, Oak Ridge, TN, USA

Hagen Söngen Institut für Physikalische Chemie, Johannes Gutenberg-Universität Mainz, Mainz, Germany; Graduate School Materials Science in Mainz, Mainz, Germany; Physical Chemistry I, Bielefeld University, Bielefeld, Germany

Evgheni Strelcov Institute for Research in Electronics and Applied Physics, University of Maryland, College Park, MD, USA

Yasuhiro Sugawara Department of Applied Physics, Graduate School of Engineering, Osaka University, Suita, Osaka, Japan

Martin Švec Institute of Physics of the Czech Academy of Sciences, Prague 6, Czech Republic

Stefan A. L. Weber Max Planck Institute for Polymer Research, Mainz, Germany

Haunfei Wen Department of Applied Physics, Graduate School of Engineering, Osaka University, Suita, Osaka, Japan

Rinke J. Wijngaarden Department of Physics and Astronomy, Vrije Universiteit Amsterdam, Amsterdam, The Netherlands

Hirofumi Yamada Kyoto University, Kyoto, Japan

Abbreviations

A	Acceptor
AC	Alternating current
AFM	Atomic force microscopy
AM	Amplitude modulation
BE	Band excitation
BEM	Boundary element method
BHJ	Bulk heterojunction
BM	Bias modulated
BP	Black phosphorus
CITS	Continuous imaging current spectroscopy
cKPFM	Contact-mode Kelvin probe force microscopy
CL	Closed loop
CMOS	Complementary metal–oxide–semiconductor
CNT	Carbon nanotube
CP	Colloidal probe
CPD	Contact potential difference
CT	Charge transfer
D	Donor
DC	Direct current
DFT	Density functional theory
DH	Dual harmonic
D-KPFM	Dissipation Kelvin probe force microscopy
DLTS	Deep level transient spectroscopy
DOS	Density of states
DOSS	Density of surface states
DSSC	Dye-sensitized solar cell
EcFM	Electrochemical force microscopy
ECM	Equivalent charge model
EDL	Electric double layer
EFM	Electrostatic force microscopy

EIS	Electrochemical impedance spectroscopy
ES	Electrostatic
ESM	Electrochemical strain microscopy
ETL	Electron transport layer
FDA	Fast data acquisition
FDM	Finite difference method
FEM	Finite element method
FET	Field-effect transistor
FFT	Fast Fourier transform
FF-trEFM	Fast free time-resolved electrostatic force microscopy
FIB	Focused ion beam
finFET	Fin field-effect transistor
FM-AFM	Frequency modulation atomic force microscopy
FM	Frequency modulation
FV	Force volume
GB	Grain boundary
GCS	Gouy–Chapman–Stern
GDM	General dynamic mode
GF	Green's function
GICM	Generalized image charge method
G-mode	General mode
HAM	Heterodyne amplitude modulation
HH	Half harmonic
H-KPFM	Heterodyne Kelvin probe force microscopy
HOMO	Highest occupied molecular orbital
HOPG	Highly oriented pyrolytic graphite
HR	High resolution
HTL	Hole transport layer
IETS	Inelastic electron tunneling spectroscopy
iFFT	Inverse fast Fourier transform
IM	Intensity modulated
ISFET	Ion-sensitive field-effect transistor
ITO	Indium tin oxide
jCPD	Junction contact potential difference
KPFM	Kelvin probe force microscopy
KPFS	Kelvin probe force spectroscopy
LCPD	Local contact potential difference
LIA	Lock-in amplifier
LPTV	Large perturbation transient photovoltage
LSA	Linear superposition approximation
LUMO	Lowest unoccupied molecular orbital
MFM	Magnetic force microscopy
MF	Multifrequency
MOSFET	Metal-oxide-semiconductor field-effect transistor
MSSC	Meso-superstructured solar cell

nc-AFM	Non-contact atomic force microscopy
NGR	Non-geminate recombination
NIM	Nanoimpedance microscopy
NL	Non-linear
NW	Nanowire
OFET	Organic field-effect transistor
OHP	Outer Helmholtz plane
OLBS	Open-loop bias spectroscopy
OLEP	Open-loop electrical potential
OL	Open loop
OM	Optical microscopy
OPV	Organic photovoltaics
PCA	Principal component analysis
PCE	Power conversion efficiency
PFM	Piezoresponse force microscopy
PI controller	Proportional–integral controller
PLL	Phase-locked loop
PP	Pump-probe
PSC	Perovskite solar cell
PthBE	Photothermal band excitation
PTIR	Photothermal-induced resonance
PV	Photovoltaic
QD	Quantum dot
RMS	Root mean square
SAM	Self-assembled monolayer
SCL	Space-charge limited
SCM	Scanning capacitance microscopy
SCR	Space-charge region
SFMM	Scanning frequency mixing microscopy
SF	Single frequency
SGM	Scanning gate microscopy
SGS	Scanning gate spectroscopy
SHO	Simple harmonic oscillator
SIM	Scanning impedance microscopy
SIMS	Secondary ion mass spectrometry
SOFC	Solid oxide fuel cell
SOI	Silicon-on-insulator
SPM	Scanning probe microscopy
SP	Surface potential
SPV	Surface photovoltage
SQDM	Scanning quantum dot microscopy
SRH	Shockley–Read–Hall
SR	Short range
SSRM	Scanning spreading resistance microscopy
STHM	Scanning tunneling hydrogen microscopy

STM	Scanning tunneling microscopy
STP	Scanning tunneling potentiometry
STS	Scanning tunneling spectroscopy
SWCNT	Single-wall carbon nanotube
TCO	Transparent conductive oxide
TD	Time domain
TPV	Transient photovoltage
Tr	Time-resolved
UHV	Ultra-high vacuum
UV	Ultraviolet
vdW	Van der Waals
VL	Vacuum level
VM	Voltage modulated
XC	Exchange–correlation
XPS	X-ray photoelectron spectroscopy

Part I
Experimental Methods and Technical Aspects

Chapter 1
Experimental Technique and Working Modes

Sascha Sadewasser and Thilo Glatzel

Abstract Kelvin probe force microscopy (KPFM) is a scanning probe microscopy technique providing the capability to image the surface potential of a sample with high spatial and energy resolution. It is based on non-contact atomic force microscopy (nc-AFM) and continuously minimizes the electrostatic interaction between the scanning tip and the surface. Compared to electrostatic force microscopy (EFM) which also measures the electrostatic properties KPFM compensates these force contributions. The two main working modes are the amplitude modulation and the frequency modulation technique, in which the electrostatic force or the electrostatic force gradient are minimized by the application of an appropriate dc-bias voltage, respectively. For metals and semiconductors, the contact potential difference is determined, which is related to the sample's work function, while for insulators information about local charges and dipoles is obtained. This chapter provides a brief introduction to nc-AFM, EFM, and various KPFM techniques.

1.1 Introduction

Surface science was revolutionized in 1982 by the invention of the scanning tunneling microscope (STM) by Binnig and Rohrer [1]. In 1986 the invention of the atomic force microscope (AFM) widened the range of samples from conductive to non-conductive ones [2]. Further development lead to the non-contact (or dynamic) mode of the AFM [3], where a cantilever supporting a sharp tip at its end is vibrated close to its resonance frequency and changes in the vibration due to tip-sample interaction are used to maintain a constant distance to the sample surface while

S. Sadewasser (✉)
International Iberian Nanotechnology Laboratory, Avenida Mestre Jos Veiga s/n, 4715-330 Braga, Portugal
e-mail: sascha.sadewasser@inl.int

T. Glatzel
Department of Physics, University of Basel, Klingelbergstr. 82, 4056 Basel, Switzerland
e-mail: thilo.glatzel@unibas.ch

S. Sadewasser and T. Glatzel (eds.), *Kelvin Probe Force Microscopy*,
Springer Series in Surface Sciences 65, https://doi.org/10.1007/978-3-319-75687-5_1

scanning across the sample. Forces exerted by the tip on the sample are minimal in non-contact mode.

A wide field of applications has been opened by the combination of the AFM with other measurement methods, thus providing additional sample properties on a lateral scale in the nanometer range. The electrostatic interaction between tip and sample is measured by two AFM variations, the electrostatic force microscope (EFM) and the Kelvin probe force microscope (KPFM). In EFM, the electrostatic forces are measured qualitatively, while in KPFM a dc-bias voltage is applied between tip and sample to compensate the electrostatic forces. The KPFM was first developed by Nonnenmacher et al. [4] and it allows to image surface electronic properties, namely the contact potential difference (CPD). The name "Kelvin probe force microscope" originates from the macroscopic method developed by Lord Kelvin in 1898 using a vibrating parallel plate capacitor arrangement, where a voltage applied to one vibrating plate is controlled such that no current is induced by the vibration [5]. The reduction of this exact principle to the microscopic scale, however, results in a poor sensitivity, since the size of the capacitor plates is too small to generate a sufficient current. Therefore, in KPFM the electrostatic force is measured instead. The cantilever in an AFM is a very sensitive force sensor allowing to measure forces down to the pN range, thus the CPD can be measured with high spatial and energy sensitivity. A dc bias applied to the sample (or the tip) is controlled in such a way that the electrostatic forces between tip and sample are minimized.

This chapter will initially describe the working principle of non-contact atomic force microscopy (nc-AFM) and then explain the EFM and KPFM techniques. Two main working modes of KPFM will be described which are both widely applied in research laboratories. At the end of the chapter some notes on other working modes are given.

1.2 Non-contact Atomic Force Microscopy

An AFM consists of a sharp tip supported at the end of a cantilever serving as a force sensor [2]. The sample's topography is imaged by scanning the tip across a sample surface while maintaining a constant force or force gradient by a feedback loop. Different modes for AFM operation can be used. In contact mode the tip is brought into contact with the sample, and repulsive tip-sample interaction is measured. In non-contact mode (also called dynamic mode) the tip is oscillated at or near its fundamental resonance frequency [3]. The oscillation is mechanically excited using a piezoelectric element on which the cantilever-chip is mounted. Interaction forces between tip and sample cause a shift in the resonance frequency. A third mode uses an oscillating cantilever, however, the regime of repulsive tip-sample interaction is reached in the lower turn-around point of the oscillation cycle, while in the rest of the oscillation cycle attractive forces dominate the interaction. In this tapping or intermittent contact mode and in the non-contact mode the forces exerted by the scanning tip on the sample are considerably reduced with respect to the contact mode.

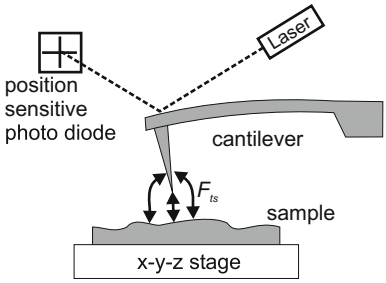

Fig. 1.1 Working principle of an AFM consisting of the beam deflection detection system with laser and position sensitive photodiode and the sample on a piezo-driven xyz-stage

In nc-AFM or dynamic AFM (DFM) the cantilever is oscillated at or near its resonance frequency and the change in the oscillation is monitored in dependence of the tip-sample interaction. Figure 1.1 shows the basic AFM experimental setup consisting of the cantilever and tip, the sample on a xyz-stage with piezo control, and the detection system with a laser and a position sensitive photodiode. Alternatively to the displayed beam-deflection detection an interferometric technique or a piezoelectric and piezoresistive detection can be used [6].

The oscillation of the cantilever can be described by its equation of motion, which in general is a three dimensional problem. By considering the tip as a point-mass spring the equation of motion for the tip can be represented as [7]:

$$m\ddot{z} + \frac{m\omega_0}{Q}\dot{z} + kz = F_{ts} + F_0 \cos(\omega_d t), \tag{1.1}$$

where k denotes the spring constant, Q the quality factor, F_{ts} the tip-surface interaction, F_0 and ω_d the amplitude and angular frequency of the driving force, respectively. The free resonance frequency f_0 (without tip-surface interaction, $F_{ts} = 0$) is a function of the spring constant k and the effective mass m^*, which also accounts for the specific geometry of the cantilever:

$$\omega_0 = 2\pi f_0 = \sqrt{\frac{k}{m^*}}. \tag{1.2}$$

When the tip is approached to the surface, forces act between tip and sample. This tip-surface interaction may consist of various contributions, short range repulsive and chemical binding forces, the van der Waals force F_{vdW}, and the long-range electrostatic and magnetic forces, F_{el} and F_{mag}, respectively. The short-range interaction is usually described by the empirical Lennard-Jones type interaction potential, which is illustrated in Fig. 1.2 [8]. The repulsive force in a distance r can be described by a power law interaction potential:

$$U_{rep} = \left(\frac{\sigma_0}{r}\right)^n, \tag{1.3}$$

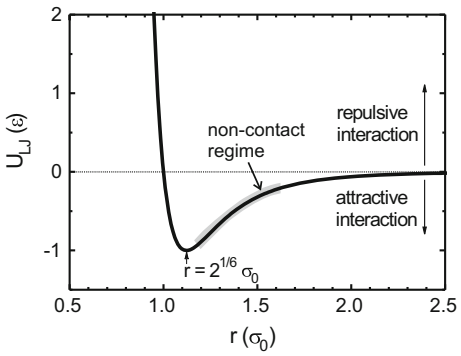

Fig. 1.2 Lennard-Jones type interaction potential describing the typical interaction of an AFM tip and the sample surface at small tip-sample distances

where the exponent is usually set to $n = 12$. Frequently, this repulsive part is also described by an exponential dependence:

$$U_{rep} = c \cdot \mathrm{e}^{-r/\sigma'}. \tag{1.4}$$

Here σ_0 and σ' are characteristic lengths, where σ' is on the order of 0.02 nm.

At larger distance, the interaction potential becomes attractive, goes through a minimum and then approaches zero towards large tip-sample distances. The total short-range interatomic interaction potential comprising the repulsive and attractive part can thus be described by a Lennard-Jones potential [8]:

$$U_{LJ} = -4\epsilon \left[\left(\frac{\sigma_0}{r} \right)^6 - \left(\frac{\sigma_0}{r} \right)^{12} \right], \tag{1.5}$$

as illustrated in Fig. 1.2.

The repulsive force at very small tip-sample distances results from the Pauli exclusion principle for the overlapping electron clouds of the tip and sample atoms. The chemical forces are due to the bonding state of a quantum mechanical overlap of the electron wave functions of tip and sample. These chemical interactions obey an exponential distance dependence and are only relevant at distances below ~5 Å [9].

An additional contribution to the attractive part of the short-range interaction force is the van der Waals force. It is an always present interaction between atoms and molecules due to the interaction between induced electrostatic dipoles, i.e. as a result of electromagnetic field fluctuations. For the case of AFM, it can be approximated by considering a sphere of radius R in front of an infinite plane, representing the sample surface and is usually expressed as [7, 8]:

$$F_{vdW} = -\frac{HR}{6r^2}, \tag{1.6}$$

where H is the Hamaker constant, and r the closest distance between the sphere and the plane (the tip and the sample). For tip-sample distances smaller than an intermolecular distance a_0, F_{vdW} is replaced by the adhesion force F_{adh}. For the case of a stiff contact and a small tip radius the adhesion force can be described by $F_{adh} = -4\pi R\gamma$, where γ is the surface energy [7, 10, 11]. As indicated by the gray area of the interaction potential in Fig. 1.2, nc-AFM is typically operated in the attractive region of the interaction.

The relevant force for EFM and KPFM is the electrostatic force F_{el}. It can be expressed by considering the tip-sample system as a capacitor. Thus, with the energy of a capacitor, $U_{el} = 1/2CV^2$, the force can be written as:

$$F_{el} = -\nabla U_{el} = \frac{1}{2}\frac{\partial C}{\partial r}V^2 + CV\frac{\partial V}{\partial r}, \tag{1.7}$$

where C is the capacitance and V the total voltage. For simplicity, a metallic tip and sample can be considered. In the case of AFM, the most significant contribution is due to the forces perpendicular to the sample surface (denominated z-direction), therefore (1.7) simplifies to:

$$F_{el} = \frac{1}{2}\frac{\partial C}{\partial z}V^2, \tag{1.8}$$

which is always attractive because $\partial C/\partial z < 0$ [12], see also Chap. 8.3.3. A detailed discussion of the electrostatic force will follow in the next section. The magnetic forces are only relevant if tip and/or sample material are magnetic. Generally, for KPFM this is not the case and therefore these forces will not be considered here.

When approaching the tip to the sample, the interaction forces will cause a shift of the resonance curve of the cantilever. For small oscillation amplitudes the system can be regarded as a weakly perturbed harmonic oscillator. In this case the shift of the resonance curve can be approximated by introducing an effective spring constant k_{eff} [7]:

$$k_{eff} = k - \frac{\partial F_{ts}}{\partial z}. \tag{1.9}$$

The spring constant is lowered by the force gradient. For small force gradients this shifts the resonance curve, in the case of attractive forces to lower frequencies and vice versa. The frequency shift can be approximated by [7, 13]:

$$\Delta f_0 = -\frac{f_0}{2k}\frac{\partial F_{ts}}{\partial z}. \tag{1.10}$$

Equations (1.9) and (1.10) are approximations to the solution of the equation of motion (1.1) for small oscillation amplitudes and small force gradients. In many situations they provide a quick and easy way to interpret the experiments. However, in many practical cases of KPFM, large oscillation amplitudes are used, and thus throughout the oscillation cycle the tip-sample interaction continuously varies. The above approximations are no longer valid in this case and more elaborate methods

have to be used. In classical first-order perturbation theory the solution to the equation of motion gives the frequency shift Δf_0 as a function of the tip-sample distance d, the oscillation amplitude A_0, the spring constant k and the free resonance frequency f_0 as [7, 14]:

$$\Delta f_0 = -\frac{f_0}{kA_0^2}\frac{1}{T_0}\int_0^{T_0} F_{ts}\left(d + A_0 + A_0\cos(2\pi f_0 t)\right) A_0\cos(2\pi f_0 t)\,\mathrm{d}t. \tag{1.11}$$

Two different detection modes can be applied in AFM. Mainly in the intermittent contact mode the amplitude modulation technique is used [3] where the cantilever is excited at a constant frequency slightly off resonance. A change in the tip-sample distance leads to a change of the force gradient, which results in a shift of the resonance peak; thus, the oscillation amplitude at the fixed driving frequency changes. A feedback loop adjusts the tip-sample distance to maintain a constant amplitude. This detection method is usually applied in air, where the quality factor Q of the cantilever is on the order of 1–10^3. When operating an AFM in vacuum, the quality factor increases by several orders of magnitude (typically above 10^5) due to the reduced damping and the nc-AFM mode can be used. This results in a reduced bandwidth in the amplitude detection mode and a very slow response time of the system is the consequence [13]. Albrecht et al. [13] have introduced the frequency modulation technique (FM-mode) for tracking the resonance frequency in these cases. In this mode, the change of the resonance curve is detected by directly measuring the frequency shift of the resonance peak. The cantilever serves as the frequency determining element and is always excited at its resonance frequency using a feedback loop. Through an additional controller the oscillation amplitude is kept constant as well allowing to directly distinguish conservative and dissipative force contributions. The resonance frequency is measured using a frequency demodulator, or a phase locked loop (PLL), for example. For a change of the tip-sample distance during the scan the resonance frequency changes and the z-controller adjusts the tip-sample distance to maintain a constant frequency shift Δf_0 with respect to the free resonance of the cantilever. The experimental set-up of this FM-mode is illustrated in Fig. 1.5 in Sect. 1.4.3 below. For both modes, according to (1.10), the measured surface topography approximately corresponds to a surface of constant force gradient.

1.3 Electrostatic Force Microscopy

The electrostatic forces (1.7 and 1.8) contributing to the total force between cantilever and sample surface can be measured by electrostatic force microscopy (EFM). The most elegant way to separate the electrostatic from other force contributions is to modulate the force field by an ac-voltage $V_{ac}sin(\omega_{ac}t)$ at the frequency ω_{ac} inducing an electrostatically driven oscillation of the cantilever at the frequency ω_{ac}. This approach will also be valid for all major KPFM modes discussed later and will

therefore be introduced in more detail. Considering the tip-sample system as a capacitor, the electrostatic force in (1.8) can now be expressed as:

$$F_{el} = \frac{1}{2}\frac{\partial C}{\partial z}[V_{dc} - V_{CPD} + V_{ac}\sin(\omega_{ac}t)]^2, \tag{1.12}$$

where $\partial C/\partial z$ is the capacitance gradient of the tip-sample system and the CPD is the difference in work function $\boldsymbol{\Phi}$ between sample and tip:

$$V_{CPD} = \boldsymbol{\Delta\Phi}/e = (\boldsymbol{\Phi}_{sample} - \boldsymbol{\Phi}_{tip})/e, \tag{1.13}$$

where e is the elementary charge.[1] Equation (1.12) can be written as $F_{el} = F_{dc} + F_{\omega_{ac}} + F_{2\omega_{ac}}$, where the spectral components are:

$$F_{dc} = \frac{\partial C}{\partial z}\left[\frac{1}{2}(V_{dc} - V_{CPD})^2 + \frac{V_{ac}^2}{4}\right], \tag{1.14}$$

$$F_{\omega_{ac}} = \frac{\partial C}{\partial z}(V_{dc} - V_{CPD})V_{ac}\sin(\omega_{ac}t), \tag{1.15}$$

$$F_{2\omega_{ac}} = -\frac{\partial C}{\partial z}\frac{V_{ac}^2}{4}\cos(2\omega_{ac}t). \tag{1.16}$$

Here, F_{dc} induces an additional static force contribution influencing the topography signal, $F_{\omega_{ac}}$ modulated at the ac-frequency is used to measure the CPD in KPFM mode, and $F_{2\omega_{ac}}$ can be used for capacitance microscopy (see Sect. 1.4.4) [15]. The amplitude at the frequency ω_{ac} which can be detected by lock-in technique is therefore directly related to the magnitude of the electrostatic forces induced by the applied ac-voltage. By recording the magnitude of the lock-in signal variations of the electrostatic force can be measured. Typically EFM is performed in a two pass mode, measuring in the first pass the topography (typically including influences of the uncompensated electrostatic forces) and in the second pass lifting the cantilever typically several 10 nm up exciting the cantilever electrically or mechanically and measuring the electrostatic force while following the recorded topography trace with an applied dc-bias voltage offset [16]. A simultaneous measurement of the the topography and the electrostatic force signal is also possible by using different frequencies or even resonances for both channels. The acquired signal always contains influences from the capacitance gradient as well as the CPD and can therefore not easily be

[1] In principle, the definition of the CPD could also be selected as $V_{CPD} = (\boldsymbol{\Phi}_{tip} - \boldsymbol{\Phi}_{sample})/e$, which corresponds to $-V_{CPD}$ of (1.13). Typically the definition of (1.13) is selected such that the changes in V_{CPD} directly correspond to changes in the work function. Thus, images of V_{CPD} represent the same contrast as images of the sample's work function $\boldsymbol{\Phi}_{sample}$, just with a constant absolute offset, which is equal to the work function of the tip. In the experimental realization this would correspond to a situation, where the voltage is applied to the sample and the tip is grounded (see Sect. 1.4.3).

related with absolute work function values. Another clear disadvantage of the EFM beside the lack of a quantitative measurement of the CPD are the influences of the uncompensated electrostatic force on the topography [17, 18]. Nevertheless, the literature reports many EFM studies, likely motivated by the fact, that experimentally the EFM technique is simpler to handle and requires less equipment, namely it does not require an additional feedback loop, as does KPFM.

1.4 Kelvin Probe Force Microscopy

KPFM combines nc-AFM and EFM with the Kelvin probe technique. The macroscopic Kelvin technique was developed in 1898 by Kelvin [5] for the measurement of surface potentials: the sample constitutes one plate of a parallel plate capacitor, with a known metal forming the other plate, which is vibrated at frequency ω. Due to the changing distance between the plates, the capacitance changes, resulting in an alternating current in the circuit connecting the plates. This current is reduced to zero by applying a dc-voltage to one of the plates. This voltage corresponds to the contact potential difference of the two materials.

The KPFM employs the same principle, applying a dc-voltage to compensate the CPD between the AFM tip and the sample [19]. However, instead of the current as the controlling parameter, the electrostatic force is used as described above for the EFM. As the cantilever of an AFM is a very sensitive force probe, this technique results in a high sensitivity of the CPD measurement, even for the very reduced size of the capacitor formed by the tip and the sample. Compared to EFM, in KPFM an additional dc-voltage (V_{dc}) between tip and sample is applied to minimize the electrostatic forces resulting in a zero amplitude at the frequency ω, see (1.15). For that purpose an additional feedback loop is required.

While the KPFM measurement results in the determination of the CPD, which is the work function of the sample relative to that of the tip, (1.13) can be used to deduce the sample's work function on an absolute scale. Using a calibrated tip with a known work function, the work function of the sample can be calculated from the CPD measurement according to (1.13). However, for absolute work function measurements, operation under ultra-high vacuum (UHV) conditions is mandatory [20], as it is well known that the work function is highly sensitive to the surface cleanness [4].

As in the case of the topography measurement, also for the CPD measurement two different modes can be distinguished. The amplitude modulation technique (AM-mode) controls the applied dc-bias by reducing the amplitude of the induced oscillation at the ac-frequency to zero, and the frequency modulation technique (FM-mode) minimizes the variation in the frequency shift Δf_0 at the ac-frequency.

1.4.1 AM-KPFM

In the AM-mode, the amplitude of the cantilever oscillation at the ac-frequency ω_{ac} is measured; it is induced by the electrostatic force and is proportional to it. The amplitude is detected using the beam deflection signal and a lock-in amplifier tuned to the frequency of the ac-bias (see also Sect. 1.4.3). As can be seen from (1.15), this signal is minimized by controlling V_{dc} to match the contact potential difference V_{CPD}. Recording V_{dc} while scanning the topography, an image of the CPD is obtained. Some KPFM systems use this technique with ac-frequencies of several kHz to several tens of kHz. To get sufficient sensitivity, ac-voltages of 1–3 V are typically used [21, 22].

An improvement to this technique is obtained by tuning the ac-frequency to an eigenmode of the cantilever. In this way a resonance-enhanced detection is achieved, providing the possibility to lower the ac-voltage maintaining a high sensitivity to the electrostatic force. An elegant way to use resonance-enhanced KPFM is to tune the ac-frequency to the second eigenmode of the cantilever [23, 24]. While the fundamental resonance is mechanically excited and used for topography detection, the ac-voltage simultaneously excites electrostatically a cantilever oscillation, for example of the second eigenmode, which is used for the CPD detection. Then the oscillation at ω_{ac} is amplified by the quality factor Q of the respective eigenmode. This enhances the sensitivity and permits to use lower ac-voltages, down to the order of 100 mV. Working with the resonance-enhanced detection, also the response time of the system is determined by the quality factor. This can be quantitatively expressed in a similar way as for the fundamental resonance used for the topography detection [13]. The system reacts to a change (for example a change in the CPD upon scanning the tip) with a response time τ until a new stable state is reached, where [13, 25]:

$$\tau = \frac{Q}{\pi f_2}. \tag{1.17}$$

Using typical values of $Q = 5000 - 15000$ and $f_2 = 450 - 1200\,kHz$ the response time results to a view ms. This means that scanning is easily possible with scan speeds on the order of SI1s/line.

The limiting factor in this mode is the bandwidth of the photodiode used for the detection of the cantilever oscillation. This bandwidth depends on the specific type and manufacturer of the AFM system. In many commercial systems a photodiode with a bandwidth of ~500 kHz is used; therefore, the stiffest cantilevers used for detection on the second oscillation mode have the fundamental resonance frequency in the range of 70–80 kHz, and the second resonance around 400–470 kHz ($f_2 \sim 6.3 f_0$, due to the geometry of the cantilever [26]). Typical resonance curves for the fundamental and second oscillation mode are shown in Fig. 1.3. The amplitude of the second resonance mode is smaller by about a factor of 10 when the same excitation amplitude is used for the mechanical excitation of the dither-piezo.

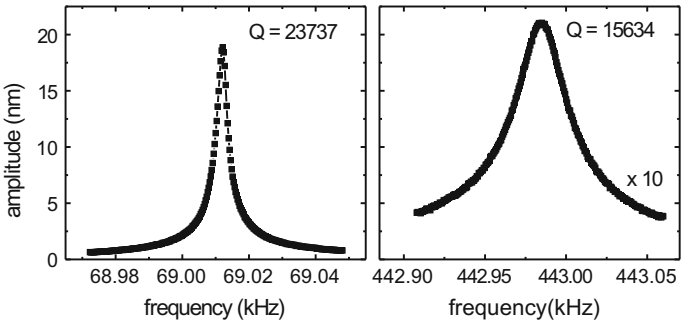

Fig. 1.3 Resonance peaks of the fundamental and second eigenmode of a typical cantilever for force modulation AFM (Nanosensors PPP-EFM). The Q-factors for the two resonances are also given

Thus, the resonance-enhanced AM-mode KPFM has two advantages: (i) a simultaneous measurement of topography and CPD is possible due to the use of two independent resonance modes and (ii) the resonance enhancement provides a higher sensitivity to the electrostatic force and therefore allows to use smaller ac-voltages. This in turn has two additional advantages. First, the ac-amplitude affects the topography image by inducing a constant electrostatic background, as can be seen by the $V_{ac}^2/4$-term in (1.14). Second, large ac-voltages possibly induce band bending at the surface of semiconductors [27], which would cause an incorrect determination of the work function.

1.4.2 FM-KPFM

In the frequency modulation mode, the applied ac-bias voltage induces a modulation of the electrostatic force, which results in an oscillation of the frequency shift Δf_0 at the frequency f_{ac} of the ac-bias. This oscillation is detected by a lock-in amplifier tuned to the frequency of the ac-bias. The measured signal is approximately proportional to the force gradient, as can be concluded from (1.10) and (1.15):

$$\Delta f_0(\omega_{ac}) \propto \frac{\partial F_{\omega_{ac}}}{\partial z} = \frac{\partial^2 C}{\partial z^2}(V_{dc} - V_{CPD})V_{ac}\sin(\omega_{ac}t). \tag{1.18}$$

As was shown in [28], the frequency ω_{ac} has to be chosen in an appropriate range. The lower limit is dictated by an increasing crosstalk to the topography signal: if the frequency is too low, the tip-sample distance control follows the additional electrostatic force and the tip-sample distance starts to oscillate at the frequency ω_{ac}. The higher the frequency the lower the coupling to the topography. On the other hand, the bandwidth of the frequency demodulator or the PLL determines the upper limit

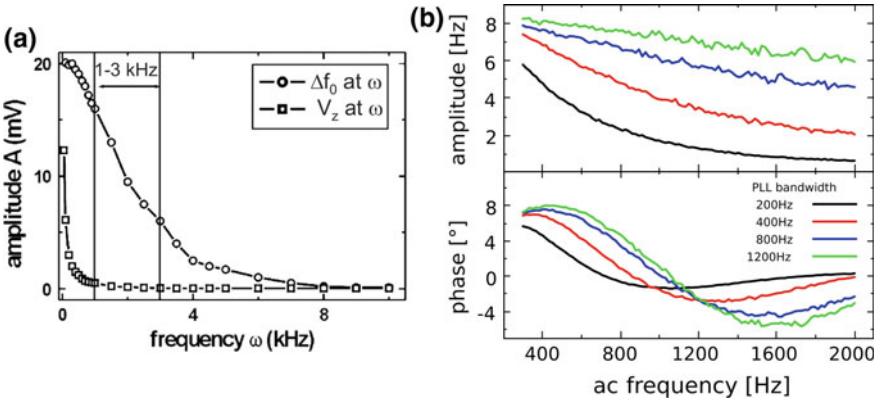

Fig. 1.4 **a** Dependence of the amplitude of the frequency shift Δf_0 and the height control signal of the topography, V_z, at the frequency ω of the ac voltage. The measurements were obtained on a HOPG sample with a bias slightly above the CPD using a room temperature UHV-AFM system by Omicron Nanotechnology, reprinted from Publication Appl. Surf. Sci. 210, 84, (2003), with permission from Elsevier [28]. **b** Amplitude and phase dependence of the frequency shift Δf_0 at the ac frequency ω_{ac} from the PLL bandwidth of the phase controller experimentally obtained with a metal-coated cantilever on a Cu(111) sample with a Nanonis Control System (RC 4.5)

of the frequency range. Figure 1.4a shows the amplitudes at ω_{ac} of the oscillation of Δf_0 and of the oscillation of the piezo voltage V_z, which controls the tip-sample distance as well as the dependence of the signal on the demodulator bandwidth. With increasing frequency ω_{ac} the crosstalk to the topography signal decreases but also the signal intensity of the electrostatic force decreases due to the restricted bandwidth of the frequency demodulator. Also in this mode, higher V_{ac} results in higher sensitivity at the cost of an influence on the topography and a possibly induced band bending on semiconductor samples (see above). Typical values for $f_{ac} = \omega_{ac}/2\pi$ and V_{ac} are in the range of 1–3 kHz and 1–3 V, respectively. Increasing the bandwidth of the PLL by tuning the phase controller time constant to higher frequencies allows to use higher ac frequencies f_{ac} as presented for four different values in Fig. 1.4b. The data have been measured with a metal coated cantilever on a Cu(111) surface with a UHV-AFM at room temperature by a Nanonis Control System (RC 4.5). A typical bandwidth for high resolution measurements is 200 Hz which allows still fast enough measurements by rejecting high frequency noise.

1.4.3 Technical Realization

Figure 1.5 shows a typical setup of the electronic system of a KPFM. The cantilever oscillation is detected by a beam deflection method using a laser, reflected from the backside of the cantilever onto a position sensitive photodiode. The signal is fed

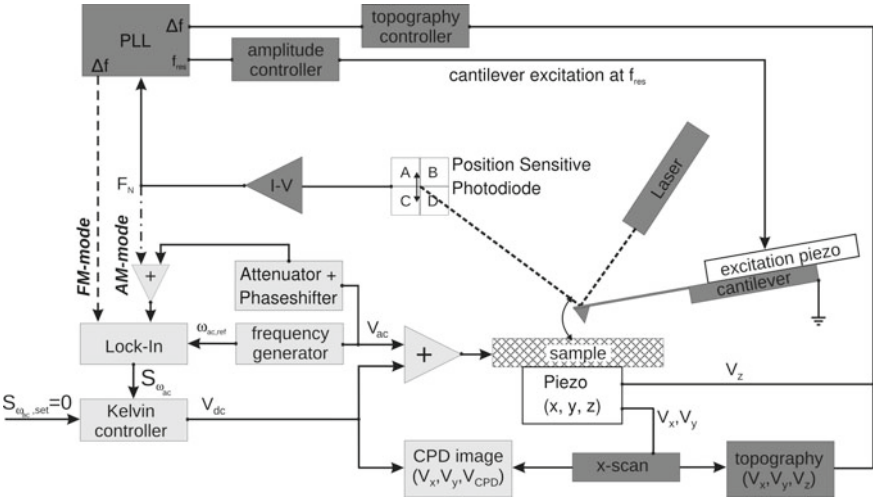

Fig. 1.5 Block diagram of the electronic realization of a KPFM. The dashed line indicates the FM-mode and the dashed-dotted line the AM-mode setup. Dark grey boxes are the regular non-contact AFM topography part and the light gray boxes are the KPFM part of the setup. In the AM-KPFM part an additional attenuator combined with a phase shifter can be used to compensate for capacitive crosstalk. See text for details

into a frequency detector, as for example a phase locked loop (PLL) or a frequency demodulator, which mechanically excites the cantilever oscillation on the fundamental resonance frequency f_{res}. For the detection of the electrostatic forces a frequency generator feeds the desired ac-voltage into an adder element, and at the same time provides the reference frequency for the lock-in amplifier. Depending on the used lock-in amplifier, also the reference output voltage can be used directly as the ac bias for the sample. In FM-mode KPFM, the Δf_0 signal from the PLL is directly fed into the lock-in amplifier (see dashed arrow in Fig. 1.5), which then detects the magnitude of the frequency shift at the ac frequency, induced by the electrostatic forces. The lock-in output, the x-component or the in-phase signal after appropriate phase adjustment, serves as input to the Kelvin controller, which adjusts a dc voltage such that the input signal ($S_{\omega_{ac}}$) goes towards zero. This dc voltage V_{dc} is the second input to the adder, which provides then the complete voltage to the sample, consisting of the sum of ac- and dc-bias. On the other hand, as was shown above, the dc-bias matches the CPD and thus the dc-bias is recorded with the scan to provide the spatially resolved CPD image.

Figure 1.5 shows also the setup for the AM-mode KPFM. In this case, the output signal from the position sensitive photodiode is connected to the input of the lock-in amplifier, as shown by the dashed-dotted line in Fig. 1.5. The rest of the setup is identical to the FM-mode setup. Thus, in the AM-mode, the amplitude of the induced oscillation of the cantilever is measured directly, as described above in Sect. 1.4.1. For a better separation of the fundamental resonance frequency from the

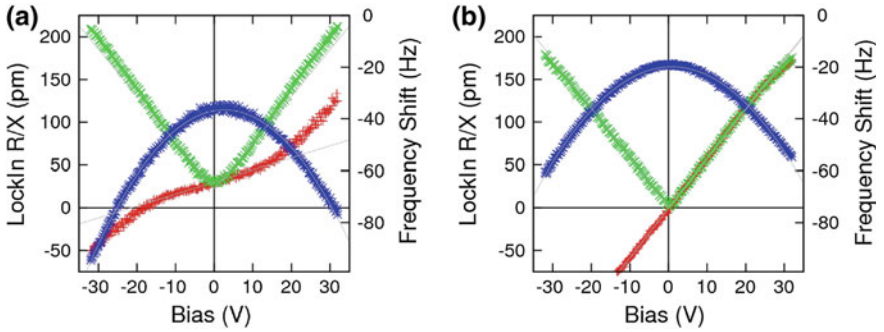

Fig. 1.6 Frequency shift (blue) and lock-in signals (amplitude (green) and x-component or in-phase signal (red)) used for KPFM. The in-phase signal is used as in input for the Kelvin controller. **a** A capacitive crosstalk might induce an offset in the amplitude and in-phase signal, leading to a false CPD value. A phase change or inappropriate adjusted phase might even enhance this effect. **b** This error can and should be compensated by an appropriate circuit if necessary, see Fig. 1.5, since already small offsets can induce severe changes and artefacts in the measured CPD

ac-frequency signal from the photodiode a high and/or low-pass filter might optionally by used. AM-KPFM measurements can be influenced by capacitive crosstalk between the ac-bias voltage and the deflection output signal of the photodiode or the z-piezo signal [27, 29, 30]. As depicted in Fig. 1.6a this kind of crosstalk results in an offset of the detected KPFM signal. The main KPFM signal is the measured amplitude R (green) which is shifted up to positive values inducing also a shift of the x-component used as the input for the Kelvin controller. As can be seen in the red curve in Fig. 1.6a this will result in a false CPD value which can even be enhanced by an inappropriate phase adjustment. The best way to reduce this capacitive coupling is an appropriate shielding of the signal lines inside the UHV chamber as well as different feedthroughs for signal and bias lines [27, 31]. As shown by Diesinger et al. [30] an additional active compensation of the crosstalk by an externally applied ac-bias reduces the crosstalk down to the noise level [29]. This ac-bias crosstalk compensation needs to have exactly the same frequency ω_{ac} as the ac-bias excitation and its phase and amplitude are fitted to the capacitive crosstalk measured between the photodiode and the Kelvin signal. However, for well-shielded AFM systems such crosstalk influences are negligible especially for measurements on metallic or semiconducting samples since the strength of the elctrostatic forces (slope of the lock-in amplitude in Fig. 1.6) is strongly enhanced compared to insulating surfaces like KBr used for the measurements in Fig. 1.6, which might induce CPD-offsets of several V.

1.4.4 Other Modes and Additional Experimental Options

The capability of KPFM to acquire images of the CPD relies on (1.15), as discussed above. A closer examination of (1.15) shows that the electrostatic force component at the ac frequency ω_{ac} not only exhibits the dependence on the voltage difference $(V_{dc} - V_{CPD})$, but also a possible contribution of the capacitance gradient $\partial C/\partial z$ has to be considered. Local variations of this contribution possibly affect measurements. This effect should be severe for EFM imaging, where the CPD is not compensated and therefore variations in the EFM signal obtained from the lock-in amplifier might erroneously be attributed to CPD variations. However, the effect on KPFM images should be much smaller or even negligible, as the Kelvin controller reduces the $(V_{dc} - V_{CPD})$ part of (1.15) to zero. Therefore, the $\partial C/\partial z$ contribution should not affect AM or FM-KPFM imaging. Moreover, considering (1.16), it is seen that by monitoring the induced oscillation of the cantilever at the frequency $2\omega_{ac}$ it becomes possible to aquire an image of $\partial C/\partial z$ [32, 33]. In the case of applying the FM-mode imaging, the corresponding second derivative would be imaged: $\partial C^2/\partial^2 z$. As (1.16) is independent of the applied dc-bias V_{dc} and V_{CPD}, the only dependence of this force component stems from variations in the capacitance gradient. In the experimental set-up, such a measurement can be realized by using an additional lock-in amplifier with the reference tuned to $2\omega_{ac}$, which then as an output signal provides the capacitance gradient [15].

Hochwitz et al. [15] have used this capacitance imaging to study complementary metal-oxide-semiconductor (CMOS) gates. Comparing individual devices in a CMOS chip, the monitored CPD did not show a clear distinction between properly functioning gates and gates that failed in operation. However, the capacitance gradient provided a clear signal difference between functional and non-functional CMOS gates. The authors concluded therefore, that the mechanism for the failure is beneath the surface. While the KPFM imaging is highly surface sensitive, the capacitance gradient provides also information from a region below the surface.

The subsurface sensitivity of the capacitance imaging is explained by the fact that for semiconductors the application of the ac-bias V_{ac} affects the charge distribution at the surface and subsurface region below the tip. Depending on the doping type of the sample and whether the ac-bias is in the positive or negative half of the oscillation cycle, the surface will undergo accumulation or depletion, respectively. The magnitude of the resulting change in the capacitance gradient depends on the charge carrier concentration [16, 34], similar to the way scanning capacitance microscopy works [35].

Recently several publications appeared using the so called Kelvin probe force spectroscopy (KPFS) method based on the fact that dynamic compensation during measurement is hindered by strong electrical coupling of the used tuning fork sensors [36–47]. This method can also be beneficial for cantilever based systems as for example presented on a Si(111) surface by Sadewasser et al. [48]. Figure 1.7 shows the basic principle of these measurements. First an area of interest is located and a grid of specific measurement points is defined. In between every single measurement

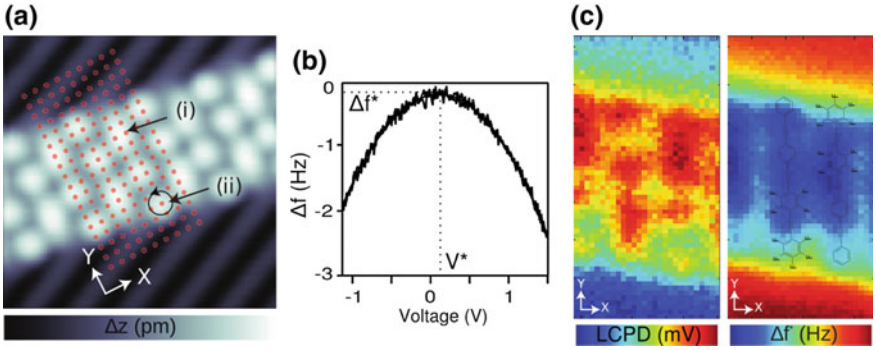

Fig. 1.7 Kelvin probe force spectroscopy. **a** The area of interest is selected and a grid of measurement points (i) is defined. To avoid thermal drift the relative tip-sample position can be adjusted by atom tracking (e.g. at position (ii)). **b** Example of a single bias-voltage dependent curve of the frequency shift. **c** Two dimensional maps of the extracted local contact potential difference (V^*) and the frequency shift at the CPD (Δf^*) calculated with a parabolic fit. Adapted with permission from ACS Nano 7, 9098 (2013) [36]. Copyright (2013) American Chemical Society

(i) an atom-tracking step (ii) [49] might be used to avoid thermal drift artefacts even at temperatures as low as 5K. In every point a dc-bias spectroscopy will be performed at constant height and the resulting frequency shift curve as shown in Fig. 1.7b will be fitted by a parabolic function to extract the coordinates V^* and Δf^* of the maximum. V^* corresponds to the LCPD while Δf^* is the frequency shift corresponding to the electronically uninfluenced interaction force. The results for such a measurement on a molecular assembly of donor-acceptor molecules arranged on a Au(111) surface are presented in Fig. 1.7c [36].

Another interesting new KPFM mode is the so called dissipation KPFM (D-KPFM) presented recently by Miyahara et al. [50, 51] and also discussed in detail in Chap. 2. This technique enables force and force-gradient sensitive KPFM by using the dissipation signal of standard nc-AFM for the dc-bias voltage feedback. It avoids low ac-voltage frequency oscillation and the need of an additional lock-in detection circuit enabling faster scanning and a straight-forward implementation. However, specific attention has to be paid to the correct adjustment of the excitation phase and occurring dissipation due to inelastic tip-sample interactions. The resulting CPD values are comparable to the ones obtained by the AM- or FM-KPFM techniques.

One way to avoid completely the compensation or even application of a dc-bias voltage is the so called open-loop KPFM approach. This technique was presented by N. Kobayashi et al. in 2010 focusing on the need to measure surface potentials in liquid environments [52, 53]. It is based on the measurement of the two electrostatically excited components ω_{ac} and $2\omega_{ac}$ and the calculation of the CPD by eliminating the influence of the capacitance gradient. Therefore, this approach is not only limited to the application to liquids but can also be applied to sensitive samples like insulators or low-doped semiconductors to avoid dc-bias induced effects. Many details and different approaches for the accurate detection can be found in several chapters

of this book: band excitation and G-mode KPFM in Chap. 3 by S. Jesse et al., an introduction to liquid KPFM in Chap. 4 by K. Kobayashi et al., and the application of liquid KPFM in Chap. 13 by L. Collins et al.

1.5 Additional Remarks

Due to the extremely short-range nature of the tunneling current, the scanning tunneling microscope provides a high sensitivity to the sample topography; the tunneling current passes almost exclusively through the outer-most tip atom. In contrast to this, in KPFM the electrostatic forces are relevant for the imaging process. Since those have a long-range character, it is not anymore the outer-most tip atom, but the whole tip, which determines the interaction between tip and sample, possibly also the cantilever itself. Therefore, the tip shape plays a role in KPFM imaging and several authors have studied the influences. Colchero et al. [54] have analytically investigated the influence of the tip and the cantilever in electrostatic force microscopy. Based on their analysis, the cantilever plays an important role in EFM and AM-KPFM imaging, despite the fact that the distance between cantilever and sample is $\sim 10^4$ times larger than the distance between the tip apex and the sample. However, due to the much larger surface area of the cantilever with respect to the tip apex, its role remains important. Their suggestion to avoid a reduction in spatial resolution due to interaction with the cantilever is to use FM-KPFM. Due to the shorter interaction range of the force gradient, the influence of the cantilever is considerably reduced, providing a better spatial resolution. This was later confirmed quantitatively by Zerweck et al. [55], who performed finite element simulations to describe the electrostatic interaction between the tip and a sample and extract the spatial resolution from scan lines of model structures. Basically, the resolution in FM-mode imaging is limited by the tip radius [56, 57]. However, both studies did not consider the resonance-enhanced AM-mode KPFM, which in many experimental studies has also provided very high resolution on the order of the tip radius [31, 58], even down to the submolecular and atomic scale [59–62].

The influence of the cantilever on EFM and KPFM imaging was also studied by investigating the dependence of the relative contribution of the capacitance derivative for the tip and the cantilever. Hochwitz et al. [63] numerically simulated the influence of the tip-to-cantilever area and the relative tip-to-cantilever distance to the sample on the ratio $\left(\partial C_{tip}/\partial z\right) / \left(\partial C_{cantilever}/\partial z\right)$. The relative area of the cantilever to the tip was varied between 10^1 and 10^9 and the ratio between the tip-sample distance and the cantilever-sample distance was varied between 10^{-1} and 10^{-4}. As is shown in Fig. 1.8a, the ratio of tip to cantilever capacitance gradient varies in form of a relative sharp step function. The authors find an optimal working region for KPFM or EFM with the cantilever to tip area in the range between 10^3 and 10^6 and the tip-sample distance to cantilever-sample distance to be less than 10^{-3}. This last criterion means that for a typical tip height of ~ 10 μm a tip-sample distance of 10 nm or less

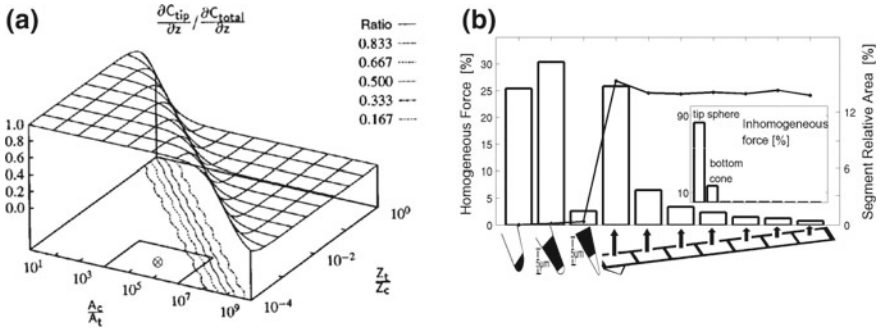

Fig. 1.8 **a** Surface plot showing the relative contribution of the tip/sample capacitance compared to the total probe/sample capacitance as functions of the area and sample spacing over a topographically flat surface. A_c/A_t is the ratio of the cantilever area to the tip area and Z_t/Z_c is the ratio of the tip-sample distance to the cantilever-sample distance. Reprinted with permission from J. Vac. Sci. Technol. B 14, 457, (1996) [63]. Copyright 1996, American Vacuum Society. **b** Role of the cantilever in quantitative Kelvin probe force microscopy (KPFM) using the boundary element method to calculate the point spread function of the entire probe. The figure shows that the cantilever has a very strong effect on the absolute value of the measured contact potential difference but the spatial resolution is mainly restricted by the front most part of the tip. Reprinted with permission from Beilstein Journal of Nanotechnology 2, 252,(2011) [64]

should be maintained. On the other hand, the first criterion leads to the conclusion, that the intuitive guess that a finer tip results in a finer resolution only applies to a certain limit. If the tip gets too sharp, a decrease in resolution results, since the ratio of cantilever area to tip area increases. Thus, long, slender, and slightly blunt tips should provide better resolution [63].

An experimental study confirming the simulations of Hochwitz et al. [63] was presented by Glatzel et al. [28]. Different cantilever types were comparatively used for the imaging of gold islands on a HOPG substrate. For the nominally same tip radius, short tips provide less potential contrast between Au and HOPG as compared to measurements with tips with a 3–5 times larger tip height. For the latter tips, the cantilever is further away from the sample and therefore the averaging due to the long-range electrostatic force is reduced. Experimentally, the CPD contrast between gold and graphite was about twice as large for the longer tips. Furthermore, as shown in Fig. 1.8b, it was shown by Elias et al. [64] that different parts of the cantilever beam and the tip cone have weighted contributions to the spatial and energy resolution. While the spatial resolution is mainly influenced by the tip apex size the energy resolution is also influenced by the cantilever beam.

Sadewasser and Lux-Steiner [17] showed the impact of the electrostatic forces on the topography imaging with regular nc-AFM imaging at fixed sample bias. For a fixed sample bias the electrostatic force acting on the tip is different depending on the local CPD under the present tip position, as can be seen from (1.12). Thus, these uncompensated electrostatic forces contribute to the topography contrast, in addition to the van-der-Waals forces. For a sample consisting of only two materials

with different CPD, correct topography imaging is possible, when the sample bias is selected to correspond to the average CPD of the two materials. However, for more than two materials, it is not possible to apply a fixed bias and maintain a correct imaging of the topography in nc-AFM [17]. In such a case, KPFM has to be used to provide a local compensation of the electrostatic forces and allow imaging of the topography based on purely van der Waals forces. These conclusions apply to KPFM imaging in the AM- as well as in the FM-mode. Thus, KPFM not only allows imaging the CPD structure of a sample, but also provides for a topography imaging free from the influence of electrostatic forces. The relevance of electrostatic forces for topography imaging in nc-AFM was also addressed by Dianoux et al. [65].

References

1. G. Binnig, H. Rohrer, C. Gerber, E. Weibel, Phys. Rev. Lett. **49**(1), 57 (1982)
2. G. Binnig, C. Quate, C. Gerber, Phys. Rev. Lett. **56**(9), 930 (1986)
3. Y. Martin, C. Williams, H. Wickramasinghe, J. Appl. Phys. **61**(10), 4723 (1987)
4. M. Nonnenmacher, M.P. O'Boyle, H.K. Wickramasinghe, Appl. Phys. Lett. **58**(25), 2921 (1991)
5. L. Kelvin, Phil. Mag. **46**, 82 (1898)
6. S. Morita, F.J. Giessibl, E. Meyer, R. Wiesendanger (eds.), *Noncontact Atomic Force Microscopy* (Springer International Publishing, 2015). https://doi.org/10.1007/978-3-319-15588-3
7. R. García, R. Pérez, Surf. Sci. Rep. **47**, 197 (2002)
8. J.N. Israelachvili, *Intermolecular and Surface Forces* (Elsevier LTD, Oxford, 2011)
9. R. Pérez, M. Payne, I. Stich, K. Terukura, Phys. Rev. Lett. **78**, 678 (1997)
10. L. Zitzler, S. Herminghaus, F. Mugele, Phys. Rev. B **66**, 155436 (2002). https://doi.org/10.1103/PhysRevB.66.155436
11. B. Derjaguin, V. Muller, Y. Toporov, J. Colloid Interface Sci. **53**(2), 314 (1975). https://doi.org/10.1016/0021-9797(75)90018-1
12. A. Sadeghi, A. Baratoff, S.A. Ghasemi, S. Goedecker, T. Glatzel, S. Kawai, E. Meyer, Phys. Rev. B **86**, 075407 (2012). https://doi.org/10.1103/PhysRevB.86.075407
13. T. Albrecht, P. Grütter, D. Horne, D. Rugar, J. Appl. Phys. **69**(2), 668 (1991)
14. F. Giessibl, Phys. Rev. B **56**(24), 16010 (1997)
15. T. Hochwitz, A. Henning, C. Levey, C. Daghlian, J. Slinkman, J. Never, P. Kaszuba, R. Gluck, R. Wells, J. Pekarik, R. Finch, J. Vac. Sci. Technol. B **14**(1), 440 (1996)
16. P.A. Rosenthal, E.T. Yu, R.L. Pierson, P.J. Zampardi, J. Appl. Phys. **87**(4), 1937 (1999)
17. S. Sadewasser, M. Lux-Steiner, Phys. Rev. Lett. **91**, 266101 (2003)
18. M. Yan, G.H. Bernstein, Ultramicroscopy **106**(7), 582 (2006). https://doi.org/10.1016/j.ultramic.2006.02.002
19. J. Weaver, D. Abraham, J. Vac. Sci. Technol. B **9**(3), 1559 (1991)
20. A. Kikukawa, S. Hosaka, R. Imura. Appl. Phys. Lett. **66**(25), 3510 (1995)
21. R. Shikler, T. Meoded, N. Fried, B. Mishori, Y. Rosenwaks, J. Appl. Phys. **86**(1), 107 (1999)
22. R. Shikler, T. Meoded, N. Fried, Y. Rosenwaks, Appl. Phys. Lett. **74**(20), 2972 (1999)
23. C. Sommerhalter, *Kelvinsondenkraftmikroskopie im Ultrahochvakuum zur Charakterisierung von Halbleiter-Heterodioden auf der Basis von Chalkopyriten* (Dissertation, Freie Universitt Berlin, 1999)
24. A. Kikukawa, S. Hosaka, R. Imura, Rev. Sci. Instrum. **67**(4), 1463 (1996)
25. S. Kawai, H. Kawakatsu, Appl. Phys. Lett. **89**, 013108 (2006). https://doi.org/10.1063/1.2219415

26. H.J. Butt, M. Jaschke, Nanotechnology **6**, 1 (1995)
27. C. Sommerhalter, T. Glatzel, T. Matthes, A. Jäger-Waldau, M. Lux-Steiner, Appl. Surf. Sci. **157**, 263 (2000)
28. T. Glatzel, S. Sadewasser, M. Lux-Steiner, Appl. Sur. Sci. **210**, 84 (2003)
29. T. Glatzel, Kelvin probe force microscopy for solar cell applications. Scanning Probe Microscopy for Energy Research, vol. 7 (World Scientific Pub Co, 2013)
30. H. Diesinger, D. Deresmes, J.P. Nys, T. Melin, Ultramicroscopy **108**, 773 (2008). https://doi.org/10.1016/j.ultramic.2008.01.003
31. C. Sommerhalter, T.W. Matthes, T. Glatzel, A. Jäger-Waldau, M.C. Lux-Steiner, Appl. Phys. Lett. **75**(2), 286 (1999)
32. Y. Martin, D. Abraham, H. Wickramasinghe, Appl. Phys. Lett. **52**(13), 1103 (1988)
33. D. Abraham, C. Williams, J. Slinkman, H. Wickramasinghe, J. Vac. Sci. Technol. B **9**(2), 703 (1991)
34. F. Müller, A.D. Müller, M. Hietschold, S. Kämmer, Meas. Sci. Technol. **9**, 734 (1998)
35. C. Williams, Annu. Rev. Mater. Sci. **29**, 471 (1999). https://doi.org/10.1146/annurev.matsci.29.1.471
36. S. Kawai, A. Sadeghi, X. Feng, P. Lifen, R. Pawlak, T. Glatzel, A. Willand, A. Orita, J. Otera, S. Goedecker, E. Meyer, ACS Nano **7**(10), 9098 (2013). https://doi.org/10.1021/nn403672m
37. L. Gross, F. Mohn, P. Liljeroth, J. Repp, F.J. Giessibl, G. Meyer, Science **324**(5933), 1428 (2009). https://doi.org/10.1126/science.1172273
38. T. Knig, G.H. Simon, H.P. Rust, G. Pacchioni, M. Heyde, H.J. Freund, J. Am. Chem. Soc. **131**, 17544 (2009). https://doi.org/10.1021/ja908049n
39. F. Mohn, L. Gross, N. Moll, G. Meyer, Nat. Nano **7**(4), 227 (2012)
40. L. Gross, B. Schuler, F. Mohn, N. Moll, N. Pavliček, W. Steurer, I. Scivetti, K. Kotsis, M. Persson, G. Meyer, Phys. Rev. B **90**, 155455 (2014). https://doi.org/10.1103/PhysRevB.90.155455
41. B. Schuler, S.X. Liu, Y. Geng, S. Decurtins, G. Meyer, L. Gross, Nano Lett. **14**(6), 3342 (2014). https://doi.org/10.1021/nl500805x
42. W. Steurer, J. Repp, L. Gross, I. Scivetti, M. Persson, G. Meyer, Phys. Rev. Lett. **114**, 036801 (2015). https://doi.org/10.1103/PhysRevLett.114.036801
43. R. Pawlak, T. Glatzel, V. Pichot, L. Schmidlin, S. Kawai, S. Fremy, D. Spitzer, E. Meyer, Nano Lett. **13**(12), 58035807 (2013). https://doi.org/10.1021/nl402243s
44. R. Pawlak, A. Sadeghi, R. Jöhr, A. Hinaut, T. Meier, S. Kawai, Ł. Zajac, P. Olszowski, S. Godlewski, B. Such, T. Glatzel, S. Goedecker, M. Szymoński, E. Meyer, J. Phys. Chem. C **121**(6), 3607 (2017). https://doi.org/10.1021/acs.jpcc.6b11873
45. P. Hapala, M. Švec, O. Stetsovych, N.J. van der Heijden, M. Ondráček, J. van der Lit, P. Mutombo, I. Swart, P. Jelnek, Nat. Commun. **7**, 11560 (2016). https://doi.org/10.1038/ncomms11560
46. F. Albrecht, J. Repp, M. Fleischmann, M. Scheer, M. Ondráĉek, P. Jelínek, Phys. Rev. Lett. **115**(7) (2015). https://doi.org/10.1103/physrevlett.115.076101
47. F. Albrecht, M. Fleischmann, M. Scheer, L. Gross, J. Repp, Phys. Rev. B **92**, 235443 (2015). https://doi.org/10.1103/PhysRevB.92.235443
48. S. Sadewasser, C. Leendertz, F. Streicher, M.C. Lux-Steiner, Nanotechnology **20**, 505503, (2009). https://doi.org/10.1088/0957-4484/20/50/505503
49. D.W. Pohl, R. Möller, Rev. Sci. Instrum. **59**(6), 840 (1988). https://doi.org/10.1063/1.1139790
50. Y. Miyahara, J. Topple, Z. Schumacher, P. Grutter, Phys. Rev. Appl. **4**(5) (2015). https://doi.org/10.1103/physrevapplied.4.054011
51. Y. Miyahara, P. Grutter, Appl. Phys. Lett. **110**(16), 163103 (2017). https://doi.org/10.1063/1.4981937
52. N. Kobayashi, H. Asakawa, T. Fukuma, Rev. Sci. Instrum. **81**(12), 123705 (2010). https://doi.org/10.1063/1.3514148
53. N. Kobayashi, H. Asakawa, T. Fukuma, J. Appl. Phys. **110**(4), 044315 (2011). https://doi.org/10.1063/1.3625230
54. J. Colchero, A. Gil, A. Baró, Phys. Rev. B **64**, 245403 (2001)

55. U. Zerweck, C. Loppacher, T. Otto, S. Grafström, L. Eng, Phys. Rev. B **71**, 125424 (2005). https://doi.org/10.1103/PhysRevB.71.125424
56. F. Krok, K. Sajewicz, J. Konior, M. Goryl, P. Piatkowski, M. Szymonski, Phys. Rev. B **77**, 235427 (2008). https://doi.org/10.1103/PhysRevB.77.235427
57. K. Sajewicz, F. Krok, J. Konior, Jpn. J. Appl. Phys. **49**(2), 025201 (2010). https://doi.org/10.1143/JJAP.49.025201
58. Y. Rosenwaks, R. Shikler, T. Glatzel, S. Sadewasser, Phys. Rev. B **70**, 085320 (2004)
59. G. Enevoldsen, T. Glatzel, M. Christensen, J. Lauritsen, F. Besenbacher, Phys. Rev. Lett. **100**, 236104 (2008). https://doi.org/10.1103/PhysRevLett.100.236104
60. R. Jöhr, A. Hinaut, R. Pawlak, A. Sadeghi, S. Saha, S. Goedecker, B. Such, M. Szymoski, E. Meyer, T. Glatzel, J. Chem. Phys. **143**(9), 094202 (2015). https://doi.org/10.1063/1.4929608
61. S. Kawai, T. Glatzel, H.J. Hug, E. Meyer, Nanotechnology **21**(24), 245704 (2010)
62. F. Bocquet, L. Nony, C. Loppacher, T. Glatzel, Phys. Rev. B **78**, 035410 (2008). https://doi.org/10.1103/PhysRevB.78.035410
63. T. Hochwitz, A. Henning, C. Levey, C. Daghlian, J. Slinkman, J. Vac. Sci. Technol. B **14**(1), 457 (1996)
64. G. Elias, T. Glatzel, E. Meyer, A. Schwarzman, A. Boag, Y. Rosenwaks, Beilstein J. Nanotechnol. **2**, 252 (2011). https://doi.org/10.3762/bjnano.2.29
65. R. Dianoux, F. Martins, F. Marchi, C. Alandi, F. Comin, J. Chevrier, Phys. Rev. B **68**, 045403 (2003). https://doi.org/10.1103/PhysRevB.68.045403

Chapter 2
Dissipation Modulated Kelvin Probe Force Microscopy Method

Yoichi Miyahara and Peter Grütter

Abstract We review a new experimental implementation of Kelvin probe force microscopy (KPFM) in which the dissipation signal of frequency modulation atomic force microscopy (FM-AFM) is used for dc bias voltage feedback (D-KPFM). The dissipation arises from an oscillating electrostatic force that is coherent with the tip oscillation, which is caused by applying the ac voltage between the tip and sample. The magnitude of the externally induced dissipation is found to be proportional to the effective dc bias voltage, which is the difference between the applied dc voltage and the contact potential difference. Two different implementations of D-KPFM are presented. In the first implementation, the frequency of the applied ac voltage, f_{el}, is chosen to be the same as the tip oscillation ($f_{el} = f_m$: 1ωD-KPFM). In the second one, the ac voltage frequency, f_{el}, is chosen to be twice the tip oscillation frequency ($f_{el} = 2f_m$: 2ωD-KPFM). In 1ωD-KPFM, the dissipation is proportional to the electrostatic force, which enables the use of a small ac voltage amplitude even down to ≈10 mV. In 2ωD-KPFM, the dissipation is proportional to the electrostatic force gradient, which results in the same potential contrast as that obtained by FM-KPFM. D-KPFM features a simple implementation with no lock-in amplifier and faster scanning as it requires no low frequency modulation. The use of a small ac voltage amplitude in 1ωD-KPFM is of great importance in characterizing of technically relevant materials in which their electrical properties can be disturbed by the applied electric field. 2ωD-KPFM is useful when more accurate potential measurement is required. The operations in 1ω and 2ωD-KPFM can be switched easily to take advantage of both features at the same location on a sample.

Y. Miyahara (✉) · P. Grütter
Department of Physics, McGill University, 3600 rue University,
Montreal H3A 2T8, Canada
e-mail: yoichi.miyahara@mcgill.ca

P. Grütter
e-mail: grutter@physics.mcgill.ca

S. Sadewasser and T. Glatzel (eds.), *Kelvin Probe Force Microscopy*,
Springer Series in Surface Sciences 65, https://doi.org/10.1007/978-3-319-75687-5_2

2.1 Introduction

Kelvin probe force microscopy (KPFM), a variant of atomic force microscopy (AFM) has become one of the most widely used tools to investigate electronic properties of nanoscale material as well as nanoscale devices. In KPFM, a contact potential difference (CPD) between the AFM tip and sample surface is measured by probing a capacitive electrostatic force, F_{el}, that is a function of the CPD, V_{cpd}, and applied dc bias voltage, V_{bias} as expressed in $F_{el} \propto (V_{bias} - V_{cpd})^2$. To separate the electrostatic force component from other force components such as chemical bonding force, van der Waals force, and magnetic force, the capacitive electrostatic force is modulated by applying an ac voltage. The resulting modulated component of the measured observable which is typically the resonant frequency shift or the change in amplitude of an oscillating AFM cantilever is detected by lock-in detection [1].

KPFM has been implemented in several different ways that can be classified mainly into two distinct categories, amplitude modulation (AM-) KPFM [1–4] and frequency modulation (FM-) KPFM [4, 5].

In AM-KPFM, one of the cantilever resonance modes is excited by applying an ac voltage and the resulting oscillation amplitude is detected as a measure of the capacitive electrostatic force, which is used for controlling the dc bias voltage to nullify the oscillation amplitude. This implementation benefits from enhanced electrostatic force detection sensitivity by tuning the modulation frequency to one of the resonance frequencies of the AFM cantilever, leading to an enhanced detection sensitivity of the electrostatic force by its quality (Q) factor that can reach over 10,000 in vacuum environment [6]. In single-pass implementation in which the topography and CPD images are taken simultaneously, the second flexural mode is usually chosen for detecting the electrostatic force while the first flexural mode is used for detecting short-range interaction which is used for the topography imaging.

In FM-KPFM, a low frequency (typically several hundred Hz) ac voltage is superposed with the dc bias voltage, resulting in the modulation in the resonance frequency shift. The amplitude of the modulated resonance frequency shift is demodulated by a lock-in amplifier and then used for the dc bias voltage feedback. Although this method requires a much higher ac voltage amplitude than AM-KPFM, it is known to offer higher spatial resolution because the resonance frequency shift is determined by the electrostatic force gradient with respect to the tip-sample distance rather than the electrostatic force itself [3, 4, 7].

In this chapter, we report two alternative KPFM implementations (1ωD-KPFM and 2ωD-KPFM) in which the dissipation signal of a frequency modulation atomic force microscopy (FM-AFM) is used for detecting the capacitive electrostatic force or electrostatic force gradient [8, 9]. The dissipation is induced by applying a coherent sinusoidal ac voltage which is 90° out of phase with respect to the tip oscillation. The externally induced dissipation signal can be used for the dc bias voltage feedback as it is proportional to the effective dc potential difference, $V_{dc} \equiv (V_{bias} - V_{cpd})$.

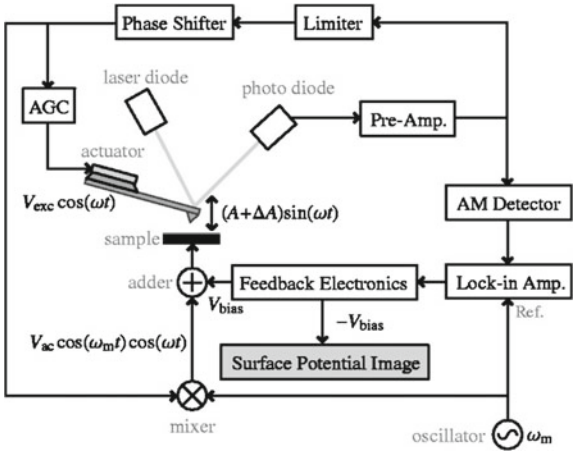

Fig. 2.1 Block diagram of dissipation modulated Kelvin probe force microscopy technique proposed by Fukuma et al. [10]. The induced dissipation is detected by measuring the change in the amplitude of tip oscillation. Reprinted from [10], with the permission of AIP Publishing

In 1ωD-KPFM, the angular frequency of the applied ac voltage, ω_{el}, is chosen to be the same as the tip oscillation ($\omega_{el} = \omega_m$). In 2ωD-KPFM, ω_{el} is chosen to be twice ω_m ($\omega_{el} = 2\omega_m$). We will show that, in 1ωD-KPFM, the induced dissipation is proportional to the electrostatic force, which enables the use of a small ac voltage amplitude down to $\approx$10 mV whereas, in 2ωD-KPFM, the dissipation is proportional to the electrostatic force gradient, which results in the same potential contrast as that obtained by FM-KPFM.

The idea of using induced dissipation for KPFM was first reported by Fukuma et al. [10] which they named DM-KPFM. In their implementation, the dissipation is measured through the change in tip oscillation amplitude rather than the dissipation signal (Fig. 2.1). Despite the demonstrated higher sensitivity of DM-KPFM (Fig. 2.2), the technique has not been widely adopted, probably because of its rather complex implementation and limited detection bandwidth due to the amplitude detection [10]. The use of the ac voltage with twice the frequency of the tip oscillation was proposed by Nomura et al. [11] for DM-KPFM to be sensitive to electrostatic force gradient rather than electrostatic force itself.

Our implementation of D-KPFM features a simple implementation with no lock-in amplifier, enabling faster scanning as it requires no low frequency modulation. The use of a small ac voltage amplitude in 1ωD-KPFM is of great importance in characterizing technically relevant materials in which their electrical properties can be disturbed by the applied electric field (e.g. resulting in band-bending effects at interfaces). 2ωD-KPFM is useful when more accurate potential measurements are required. The operations in 1ω and 2ωD-KPFM can be switched easily to take advantage of both features at the same location on a sample.

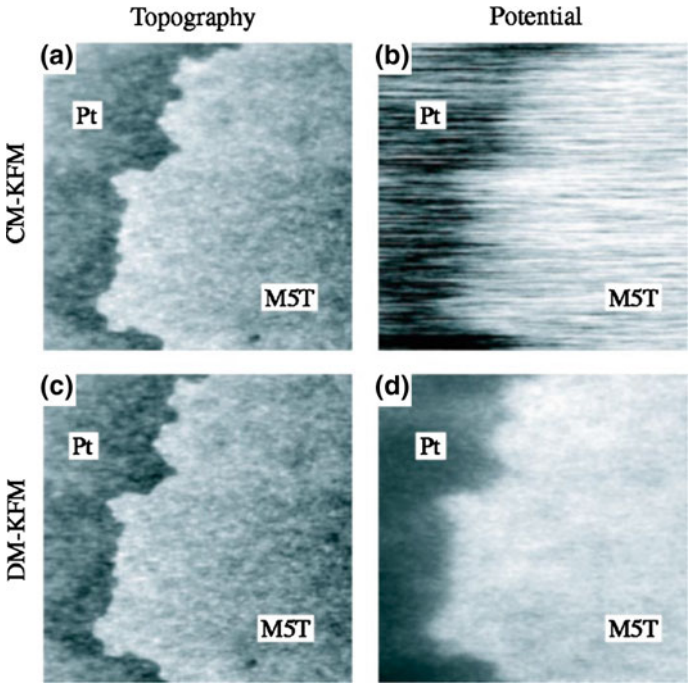

Fig. 2.2 Topography and CPD images of dimethylquinquethiophene monolayer formed on a Pt surface. **a** Topography and **b** CPD images taken by FM-KPFM. **c** Topography and **d** CPD images taken by DM-KPFM. From [10]. Reprinted from [10], with the permission of AIP Publishing

2.2 Theory

To understand the principle of operation of the D-KPFM technique, we will first review the theory of FM-AFM and the effect of a periodic applied force on the in-phase and quadrature signal (commonly known as frequency shift and dissipation) of the FM-AFM system. We will then discuss the detailed analysis of the electrostatic force in the presence of the applied coherent ac voltage and how its effect appears in the resonant frequency shift and dissipation.

2.2.1 Review of Theory of Frequency Modulation Atomic Force Microscopy

Frequency shift and dissipation in frequency modulation atomic force microscopy

We consider the following equation of motion of the AFM cantilever to model FM-AFM.

$$m\ddot{z}(t) + m\frac{\omega_0}{Q}\dot{z}(t) + k \times (z(t) - z_0) = F_{\mathrm{ts}}(t) + F_{\mathrm{exc}}(t) \tag{2.1}$$

where m, ω_0, Q, k are the effective mass, angular resonance frequency, mechanical quality factor, and effective spring constant of the AFM cantilever, respectively. z_0 is the mean distance of the tip measured from the sample surface. $F_{\mathrm{ts}}(t)$ and $F_{\mathrm{exc}}(t)$ are the force acting on the tip caused by tip-sample interaction and an external drive force that is used to excite the cantilever oscillation, respectively. In FM-AFM, the AFM cantilever is used as a mechanical resonator with a high Q (typically >1000) which acts as a frequency determining component of a self-driven oscillator [12]. Such a self-driven oscillator is realized by a positive feedback circuit equipped with an amplitude controller that keeps the cantilever oscillation amplitude constant [12, 13]. In this case, the external driving force, $F_{\mathrm{exc}}(t)$, is generated by a time-delayed (phase-shifted) cantilever deflection signal such as $F_{\mathrm{exc}}(t) = gkz(t - t_0)$ which is commonly transduced by piezoacoustic or photothermal excitation scheme [14] through a phase shifter electronics. Here g represents the gain of the positive feedback circuit and is called *dissipation signal*, and t_0 is the time delay set by the phase shifter.[1] For the typical cantilever with a high Q factor and high spring constant used for FM-AFM, we can assume a harmonic oscillation of the cantilever such as $z(t) = z_0 + A\cos(\omega_{\mathrm{m}}t)$. When t_0 is set to be $\frac{1}{4}T_0, \frac{3}{4}T_0, \frac{5}{4}T_0, \cdots$ ($T_0 \equiv 2\pi/\omega_0$), the oscillation frequency, $f_{\mathrm{m}} = \omega_{\mathrm{m}}/2\pi$, tracks its mechanical resonance frequency such that $f_{\mathrm{m}} = f_0 (\equiv \omega_0/2\pi)$. In this condition, the frequency shift, Δf, and dissipation signal, g, are expressed as follows [16–18]:

$$\Delta f \approx -\frac{f_0^2}{kA}\int_0^{T_0} F_{\mathrm{ts}}(t)\cos(\omega_{\mathrm{m}}t)dt \tag{2.2}$$

$$g \approx \frac{1}{Q} + \frac{2f_0}{kA}\int_0^{T_0} F_{\mathrm{ts}}(t)\sin(\omega_{\mathrm{m}}t)dt. \tag{2.3}$$

It is important to notice that in general, the force acting on the tip, $F_{\mathrm{ts}}(t)$, can have an explicit time dependence in addition to the time dependence due to the time-varying tip position which is expressed as $F_{\mathrm{ts}}(z(t))$ [17]. The explicit time dependence can originate from various tip-induced processes such as dynamic structural relaxation of either tip or/and sample [17] and single-electron tunneling [19]. In the case of electrostatic force, $F_{\mathrm{ts}}(t)$ is determined by the applied voltage as well as the tip position. It is thus essential to take into account both dependencies explicitly. Before going into further detail of the electrostatic force, we will look at the effect of time-varying periodic force on frequency shift and damping (dissipation) of the cantilever.

[1] In general, g takes a complex value if the transfer function of the excitation system is to be taken into account. We neglect the effect of the transfer function here. See [15] for more detail.

Effect of coherent periodic force on frequency shift and dissipation

In general, the periodically oscillating force, $F_{\mathrm{ts}}(t)$, can be represented by a Fourier series:

$$F_{\mathrm{ts}}(t) = F_0 + \sum_{n=1}^{\infty} \{F_{\mathrm{in}}^{(n)} \cos(n\omega_{\mathrm{m}} t) + F_{\mathrm{quad}}^{(n)} \sin(n\omega_{\mathrm{m}} t)\} \tag{2.4}$$

The cosine terms represent the force component which is in-phase (even) with the tip oscillation, which is conservative and the sine terms represent 90° out-of-phase (quadrature, odd) component which is dissipative [18]. Substituting (2.4) into (2.2) and (2.3) yields the following results[2]:

$$\Delta f = -\frac{1}{2}\frac{f_0}{kA} F_{\mathrm{in}}^{(1)} \tag{2.5}$$

$$g = g_0 \left(1 + \frac{Q}{kA} F_{\mathrm{quad}}^{(1)}\right) \tag{2.6}$$

where $g_0 \equiv 1/Q$ is the dissipation signal in the absence of $F_{\mathrm{ts}}(t)$, which is determined by the intrinsic damping of the cantilever. Equations (2.5) and (2.6) indicate that Δf and g are proportional to the Fourier in-phase (even), $F_{\mathrm{in}}(\equiv F_{\mathrm{in}}^{(1)})$, and quadrature (odd), $F_{\mathrm{quad}}(\equiv F_{\mathrm{quad}}^{(1)})$, coefficients of the fundamental harmonic component (in this case ω_{m}) of $F_{\mathrm{ts}}(t)$, respectively. We can understand this result intuitively with the schematics shown in Fig. 2.3. Figure 2.3a shows the tip position, z, restoring force, $-kz$, the in-phase fundamental Fourier component, $F_{\mathrm{in}} \cos(\omega_{\mathrm{m}} t)$, and the total force acting on the cantilever. Similarly, Fig. 2.3b shows the tip position, z, intrinsic damping force, $m\gamma_0 \dot{z}$, the quadrature fundamental Fourier component, $F_{\mathrm{quad}} \sin(\omega_{\mathrm{m}} t)$, and the instantaneous power delivered from the tip-sample interaction. As can be seen from these figures, while the in-phase component just influences the restoring force, resulting in the resonance frequency shift, the quadrature component can change the damping force, resulting in a signal in the dissipation channel. This can also be understood by non-zero average power delivered by the quadrature tip-sample interaction as shown in the power-time plot (Fig. 2.3b).

2.2.2 Analysis of Electrostatic Force with AC Bias Voltage

The capacitive electrostatic force between two conductors connected to an ac and dc voltage source is described as follows:

[2] We use the identities, $\int_0^{T_0} \cos(n\omega_{\mathrm{m}} t)\cos(\omega_{\mathrm{m}} t) = 0$, and $\int_0^{T_0} \sin(n\omega_{\mathrm{m}} t)\sin(\omega_{\mathrm{m}} t) = 0$ for $n \neq 1$.

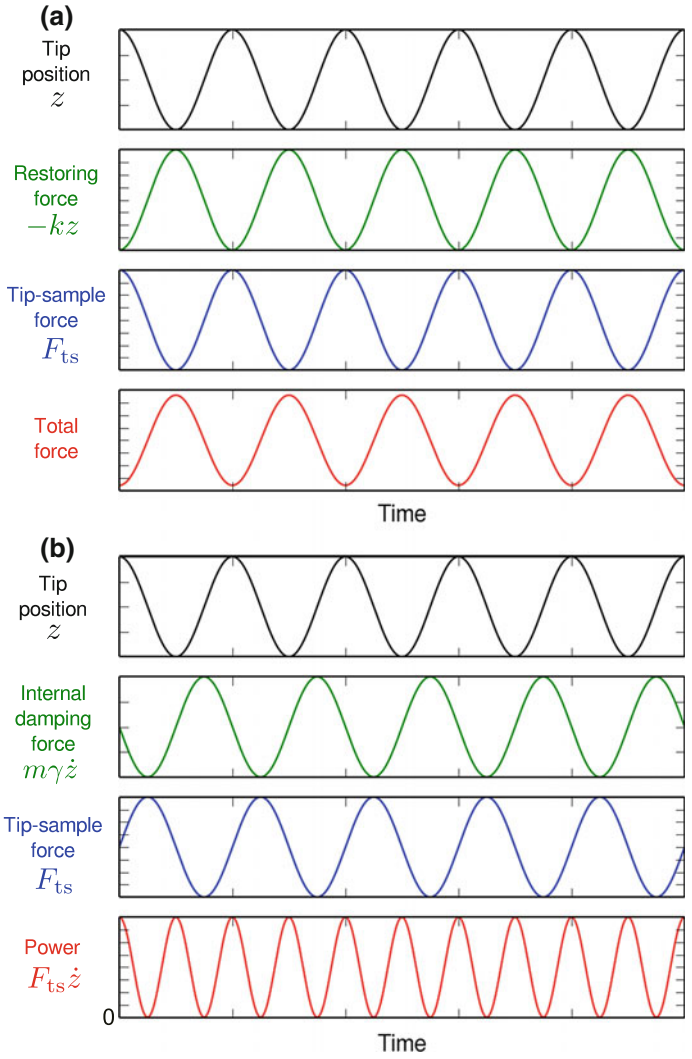

Fig. 2.3 **a** Schematic representation of tip position, z, restoring force, $-kz$, the in-phase fundamental Fourier component, $F_{\mathrm{in}}\cos(\omega_{\mathrm{m}}t)$, and the total force. **b** Schematic representation of tip position, z, internal damping force, $m\gamma_0\dot{z}$, the quadrature fundamental Fourier component, $F_{\mathrm{quad}}\sin(\omega_{\mathrm{m}}t)$, and the instantaneous power delivered from the tip-sample interaction

$$F_{\mathrm{el}}(t) = \frac{1}{2}\frac{\partial C}{\partial z}\{V_{\mathrm{bias}} + V_{\mathrm{ac}}\cos(\omega_{\mathrm{el}}t + \phi) - V_{\mathrm{cpd}}\}^2 \tag{2.7}$$

$$= F_0 + F_\omega + F_{2\omega}$$

$$F_0 = \frac{1}{2}\frac{\partial C}{\partial z}\left[(V_{\mathrm{bias}} - V_{\mathrm{cpd}})^2 + \frac{V_{\mathrm{ac}}^2}{2}\right] = \alpha\left(V_{\mathrm{dc}}^2 + \frac{V_{\mathrm{ac}}^2}{2}\right) \tag{2.8}$$

$$F_\omega = \frac{\partial C}{\partial z}(V_{\mathrm{bias}} - V_{\mathrm{cpd}})V_{\mathrm{ac}}\cos(\omega_{\mathrm{el}}t + \phi)$$

$$= 2\alpha V_{\mathrm{dc}}V_{\mathrm{ac}}\cos(\omega_{\mathrm{el}}t + \phi) \tag{2.9}$$

$$F_{2\omega} = \frac{1}{4}\frac{\partial C}{\partial z}V_{\mathrm{ac}}^2\cos\{2(\omega_{\mathrm{el}}t + \phi)\} = \frac{1}{2}\alpha V_{\mathrm{ac}}^2\cos\{2(\omega_{\mathrm{el}}t + \phi)\} \tag{2.10}$$

where C denotes the tip-sample capacitance, V_{bias} and V_{cpd} denote the applied dc voltage and the contact potential difference (CPD), and V_{ac}, ω_{el}, ϕ denote the amplitude, angular frequency, and phase of the applied ac bias voltage, respectively. $V_{\mathrm{dc}} \equiv V_{\mathrm{bias}} - V_{\mathrm{cpd}}$ is the effective dc bias voltage. It is important to notice that although the three force component terms, F_0, F_ω, $F_{2\omega}$, are grouped by the frequency of ω_{el} harmonic component such as 0, ω, 2ω, they do not represent the frequency of harmonic components of the actual oscillating electrostatic force in the presence of the mechanical tip oscillation because $\alpha \equiv \frac{1}{2}\frac{\partial C}{\partial z}(z(t))$ is also a function of time through the time-dependent tip position $z(t) = z_0 + A\cos(\omega_{\mathrm{m}}t)$. It is the interaction of the oscillating electric field and mechanical tip oscillation that results in an "electromechanical heterodyning" effect as we will see below.

By Taylor expanding $\alpha(z)$ around the mean tip position z_0,

$$\alpha(z) = \alpha(z_0) + \alpha'(z - z_0) + \frac{1}{2}\alpha''(z - z_0)^2 + \cdots.$$

$$= \alpha_0 + \alpha' A\cos(\omega_{\mathrm{m}}t) + \frac{1}{2}\alpha'' A^2\cos^2(\omega_{\mathrm{m}}t) + \cdots. \tag{2.11}$$

Taking the first order yields,

$$\alpha(z) \approx \alpha_0 + \alpha'(z - z_0) = \alpha_0 + \alpha' A\cos(\omega_{\mathrm{m}}t). \tag{2.12}$$

Substituting $\alpha(z)$ into (2.8) yields

$$F_0(t) = \{\alpha_0 + \alpha' A\cos(\omega_{\mathrm{m}}t)\}\left(V_{\mathrm{dc}}^2 + \frac{V_{\mathrm{ac}}^2}{2}\right)$$

$$= \alpha_0\left(V_{\mathrm{dc}}^2 + \frac{V_{\mathrm{ac}}^2}{2}\right) + \alpha' A\left(V_{\mathrm{dc}}^2 + \frac{V_{\mathrm{ac}}^2}{2}\right)\cos(\omega_{\mathrm{m}}t). \tag{2.13}$$

The first term in (2.13) represents a time-invariant force which causes the static deflection of the cantilever whereas the second term represents an oscillating force with a frequency of $\omega_m/2\pi$. As this oscillating force is in phase with $z(t)$, it causes the resonance frequency shift.

Next, we look at F_ω and $F_{2\omega}$ terms ((2.9) and (2.10)) in the same way:

$$\begin{aligned} F_\omega(t) &= 2\{\alpha_0 + \alpha' A\cos(\omega_m t)\}V_{dc}V_{ac}\cos(\omega_{el}t + \phi) \\ &= 2\alpha_0 V_{dc}V_{ac}\{\cos(\omega_{el}t)\cos\phi - \sin(\omega_{el}t)\sin\phi\} \\ &+ \alpha' A V_{dc}V_{ac}[\cos\{(\omega_{el}+\omega_m)t+\phi\} + \cos\{(\omega_{el}-\omega_m)t+\phi\}] \end{aligned} \tag{2.14}$$

$$\begin{aligned} F_{2\omega}(t) &= \frac{1}{2}\{\alpha_0 + \alpha' A\cos(\omega_m t)\}V_{ac}^2\cos\{2(\omega_{el}t+\phi)\} \\ &= \frac{1}{2}\alpha_0 V_{ac}^2\cos\{2(\omega_{el}t+\phi)\} \\ &+ \frac{1}{4}\alpha' A V_{ac}^2[\cos\{(2\omega_{el}-\omega_m)t+2\phi\} + \cos\{(2\omega_{el}+\omega_m)t+2\phi\}]. \end{aligned} \tag{2.15}$$

Here, we notice that the electro-mechanical heterodyning produces other spectral components ($\omega_{el}+\omega_m$, $\omega_{el}-\omega_m$, $2\omega_{el}-\omega_m$, $2\omega_{el}+\omega_m$) than ω_{el} and $2\omega_{el}$ which are usually considered in most KPFM literature. To calculate the frequency shift and dissipation, these additional spectral components need to be included. In the following, we consider two interesting cases (1) $\omega_{el}=\omega_m$, and (2) $\omega_{el}=2\omega_m$ which corresponds to 1ωD-KPFM and 2ωD-KPFM, respectively.

Case I, $\omega_{el}=\omega_m$: *1ωD-KPFM*
In the case of $\omega_{el}=\omega_m$, gathering the time invariant terms found in F_0 (2.13) and F_ω (2.14), the actual dc term, $F_{dc}(t)$ can be found to be:

$$F_{dc}^{1\omega}(t) = \alpha_0\left(V_{dc}^2 + \frac{V_{ac}^2}{2}\right) + \alpha' A V_{dc}V_{ac}\cos\phi. \tag{2.16}$$

The terms with ω_m are found in F_0 (2.13), F_ω (2.14) and $F_{2\omega}$ (2.15) and gathering them yields the following result:

$$\begin{aligned} F_{\omega_m}^{1\omega}(t) &= 2\alpha_0 V_{dc}V_{ac}\cos(\omega_m t+\phi) \\ &+ \alpha' A\left\{\left(V_{dc}^2+\frac{V_{ac}^2}{2}\right)\cos(\omega_m t) + \frac{1}{4}V_{ac}^2\cos(\omega_m t+2\phi)\right\} \\ &= 2\alpha_0 V_{dc}V_{ac}\{\cos(\omega_m t)\cos\phi - \sin(\omega_m t)\sin\phi\} \\ &+ \alpha' A\left(V_{dc}^2+\frac{V_{ac}^2}{2}\right)\cos(\omega_m t) \\ &+ \frac{1}{4}\alpha' A V_{ac}^2\{\cos(\omega_m t)\cos(2\phi) - \sin(\omega_m t)\sin(2\phi)\} \end{aligned}$$

$$
\begin{aligned}
&= \left\{ \alpha' A V_{\mathrm{dc}}^2 + 2\alpha_0 V_{\mathrm{dc}} V_{\mathrm{ac}} \cos\phi + \frac{\alpha' A}{2} \left(1 + \frac{1}{2} \cos(2\phi) \right) V_{\mathrm{ac}}^2 \right\} \cos(\omega_{\mathrm{m}} t) \\
&\quad - 2V_{\mathrm{ac}} \left\{ \alpha_0 V_{\mathrm{dc}} \sin\phi + \frac{1}{4} \alpha' A V_{\mathrm{ac}} \sin(2\phi) \right\} \sin(\omega_{\mathrm{m}} t) \\
&= F_{\mathrm{in}}^{1\omega} \cos(\omega_{\mathrm{m}} t) + F_{\mathrm{quad}}^{1\omega} \sin(\omega_{\mathrm{m}} t)
\end{aligned} \tag{2.17}
$$

As we have seen in Sect. 2.2.1, the amplitude of $\cos(\omega_{\mathrm{m}} t)$ and $\sin(\omega_{\mathrm{m}} t)$ terms, $F_{\mathrm{in}}^{1\omega}$ and $F_{\mathrm{quad}}^{1\omega}$, determine the frequency shift, Δf, and dissipation, g, respectively. Here the superscript, 1ω, refers to the case of $\omega_{\mathrm{el}} = \omega_{\mathrm{m}}$ and thus 1ωD-KPFM.

$F_{\mathrm{in}}^{1\omega}$ and $F_{\mathrm{quad}}^{1\omega}$ are expressed as follows:

$$
\begin{aligned}
F_{\mathrm{in}}^{1\omega} &= \alpha' A V_{\mathrm{dc}}^2 + 2\alpha_0 V_{\mathrm{dc}} V_{\mathrm{ac}} \cos\phi + \frac{\alpha' A}{2} \left(1 + \frac{\cos(2\phi)}{2} \right) V_{\mathrm{ac}}^2 \\
&= \alpha' A \left(V_{\mathrm{dc}} + \frac{\alpha_0 \cos\phi}{\alpha' A} V_{\mathrm{ac}} \right)^2 - \left[\frac{\alpha_0^2 \cos^2\phi}{\alpha' A} - \frac{\alpha' A}{2} \left(1 + \frac{\cos(2\phi)}{2} \right) \right] V_{\mathrm{ac}}^2
\end{aligned} \tag{2.18}
$$

$$
\begin{aligned}
F_{\mathrm{quad}}^{1\omega} &= -2V_{\mathrm{ac}} \left\{ \alpha_0 V_{\mathrm{dc}} \sin\phi + \frac{1}{4} \alpha' A V_{\mathrm{ac}} \sin(2\phi) \right\} \\
&= -2\alpha_0 V_{\mathrm{ac}} \sin\phi \left(V_{\mathrm{dc}} + \frac{1}{2} \frac{\alpha' A \cos\phi}{\alpha_0} V_{\mathrm{ac}} \right)
\end{aligned} \tag{2.19}
$$

Equation (2.18) shows that a $\Delta f - V_{\mathrm{bias}}$ curve is a parabola whose vertex is located at $V_{\mathrm{bias}} = V_{\mathrm{cpd}} - \dfrac{\alpha_0}{\alpha' A} V_{\mathrm{ac}} \cos\phi$ and (2.19) shows that a $g - V_{\mathrm{bias}}$ curve is a straight line which intersects $F_{\mathrm{quad}} = 0$ line at $V_{\mathrm{bias}} = V_{\mathrm{cpd}} - \dfrac{1}{2} \dfrac{\alpha' A}{\alpha_0} V_{\mathrm{ac}} \cos\phi$.

When $\phi = 90°$ is chosen, we find

$$
F_{\mathrm{in}}^{1\omega} = \alpha' A \left(V_{\mathrm{dc}}^2 + \frac{V_{\mathrm{ac}}^2}{4} \right) \tag{2.20}
$$

$$
F_{\mathrm{quad}}^{1\omega} = -2\alpha_0 (V_{\mathrm{bias}} - V_{\mathrm{cpd}}) V_{\mathrm{ac}} \tag{2.21}
$$

Substituting (2.20) and (2.21) into (2.5) and (2.6) yields

$$
\Delta f = -\frac{1}{2} \frac{f_0}{k} \frac{F_{\mathrm{in}}}{A} = -\frac{1}{2} \frac{f_0}{k} \alpha' \left\{ (V_{\mathrm{bias}} - V_{\mathrm{cpd}})^2 + \frac{V_{\mathrm{ac}}^2}{4} \right\} \tag{2.22}
$$

$$
g = g_0 \left(1 - \frac{Q}{kA} F_{\mathrm{quad}} \right) = g_0 \left\{ 1 + 2 \frac{Q}{kA} \alpha_0 (V_{\mathrm{bias}} - V_{\mathrm{cpd}}) V_{\mathrm{ac}} \right\} \tag{2.23}
$$

In this case, the dissipation, g, is proportional to $V_{dc} = V_{bias} - V_{cpd}$. It is therefore possible to use the dissipation signal, g, as the input for the KPFM bias voltage feedback controller if g_0 is chosen as its control setpoint value. It is important to notice that Δf is proportional to electrostatic force gradient whereas g is proportional to *electrostatic force*.

Case II, $\omega_{el} = 2\omega_m$: 2ω*D-KPFM*
In this case, $\omega_{el} + \omega_m = 3\omega_m$ and $\omega_{el} - \omega_m = \omega_m$. The actual dc term, F_{dc}, becomes:

$$F_{dc}^{2\omega}(t) = \alpha_0 \left(V_{dc}^2 + \frac{V_{ac}^2}{2} \right) \tag{2.24}$$

The terms with ω_m are found in F_0 ((2.13)) and F_ω ((2.14)) in this case and result in

$$\begin{aligned} F_{\omega_m}^{2\omega}(t) &= \alpha' A \left\{ \left(V_{dc}^2 + \frac{V_{ac}^2}{2} \right) \cos(\omega_m t) + V_{dc} V_{ac} \cos(\omega_m t + \phi) \right\} \\ &= \left\{ V_{dc}^2 + V_{dc} V_{ac} \cos\phi + \frac{V_{ac}^2}{2} \right\} \cos(\omega_m t) \\ &\quad - \alpha' A V_{dc} V_{ac} \sin\phi \sin(\omega_m t) \\ &= F_{in}^{2\omega} \cos(\omega_m t) + F_{quad}^{2\omega} \sin(\omega_m t) \end{aligned} \tag{2.25}$$

where

$$F_{in}^{2\omega} = \alpha' A \left(V_{dc} + \frac{V_{ac}}{2} \cos\phi \right)^2 + \frac{\alpha' A}{2} \left(1 - \frac{\cos^2\phi}{2} \right) V_{ac}^2 \tag{2.26}$$

$$F_{quad}^{2\omega} = -\alpha' A V_{dc} V_{ac} \sin\phi \tag{2.27}$$

When $\phi = 90°$,

$$F_{in}^{2\omega} = \alpha' A \left(V_{dc}^2 + \frac{V_{ac}^2}{2} \right) \tag{2.28}$$

$$F_{quad}^{2\omega} = -\alpha' A V_{dc} V_{ac} \tag{2.29}$$

In contrast to $\omega_{el} = \omega_m$ (1ωD-KPFM) case ((2.19)), F_{quad} is proportional to α' rather than α, indicating g is sensitive to *electrostatic force gradient*. Substituting (2.28) and (2.29) into (2.5) and (2.6) yields:

$$\Delta f = -\frac{1}{2}\frac{f_0}{k}\frac{F_{\text{in}}}{A} = -\frac{1}{2}\frac{f_0}{k}\alpha' \left\{ (V_{\text{bias}} - V_{\text{cpd}})^2 + \frac{V_{\text{ac}}^2}{2} \right\} \tag{2.30}$$

$$g = g_0 \left(1 - \frac{Q}{kA} F_{\text{quad}} \right) = g_0 \left\{ 1 + \frac{Q}{k}\alpha'(V_{\text{bias}} - V_{\text{cpd}})V_{\text{ac}} \right\}. \tag{2.31}$$

Here we notice the following two important points: (1) the apparent shift of V_{cpd} appearing in $\Delta f - V_{\text{bias}}$ curves does not depend on α and is just determined by ϕ and V_{ac}, (2) there is no apparent shift of V_{cpd} in a $g - V_{\text{bias}}$ curve. The point (2) indicates an important advantage of 2ωD-KPFM over 1ωD-KPFM as there is no need for carefully adjusting the phase, ϕ, for accurate V_{cpd} measurements.

2.3 Experimental

Figure 2.4 depicts the block diagram of the experimental setup used for both 1ω and 2ωD-KPFM measurements. The setup is based on the self-oscillation mode FM-AFM system[3] [12]. While two additional components, a phase shifter and a proportional-integrator (PI) controller, are required for both 1ω and 2ωD-KPFM operation, a frequency doubler that generates an ac voltage with the frequency of $2\omega_{\text{m}}$ from the cantilever deflection signal is also required for 2ωD-KPFM operation. The amplitude controller that consists of a root-mean-square (RMS) amplitude detector and a PI controller (NanoSurf easyPLLplus oscillator controller) is used to keep the amplitude of tip oscillation constant. The detection bandwidth of the RMS amplitude detector is extended to about 3 kHz by replacing the integration capacitor in the original RMS detector circuit. The output of the amplitude controller is the dissipation signal.

The cantilever deflection signal is fed into another phase shifter (Phase shifter 2), which adjust the relative phase, ϕ, of the ac voltage to produce the coherent ac voltage that is 90° out of phase with respect to the cantilever deflection oscillation. The frequency doubler is used to produce a sinusoidal ac voltage with two times the tip oscillation frequency. The dissipation signal is fed into the input of the PI controller, which regulates V_{bias} to maintain a constant dissipation equal to the value without V_{ac} applied, g_0. Although in the following experiments we used a digital lock-in amplifier (HF2LI, Zurich Instruments) operated in the external reference mode as a phase shifter as well as a frequency doubler for convenience, other simpler phase shifter circuits such as an all-pass filter can also be used for the D-KPFM measurements.

We used a JEOL JSPM-5200 atomic force microscope with the modifications described below. The original laser diode that was located in the vacuum chamber was replaced by a fiber-optic collimator with a focusing lens that is connected to a fiber-coupled laser diode module (OZ Optics) that is located outside the vacuum

[3] D-KPFM will also work with the phase-locked loop tracking oscillator method in which the cantilever oscillation is excited by an external oscillator [13].

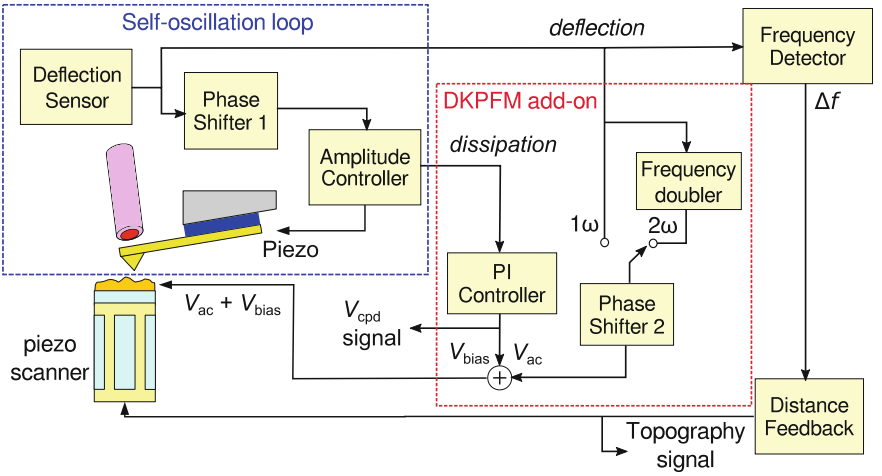

Fig. 2.4 Block diagram of the experimental setup for force sensitive (1ωD-KPFM) and force-gradient sensitive (2ωD-KPFM) dissipation modulated KPFM techniques. Reprinted from [9], with the permission of AIP Publishing

chamber. The laser diode was mounted on a temperature controlled fixture and its driving current was modulated with a radio frequency signal with a RF bias-Tee (Mini-Circuits: PBTC-1GW) to reduce the deflection detection noise mainly caused by mode-hopping and optical feedback [20]. A deflection noise density floor as low as $13\,\mathrm{fm}/\sqrt{\mathrm{Hz}}$ was achieved. The open source scanning probe microscopy control software GXSM was used for the control and data acquisition [21]. A commercial silicon AFM cantilever (NSC15, MikroMasch) with a typical spring constant of about 20 N/m and resonance frequency of ~300 kHz was used in high-vacuum environment with the pressure of 1×10^{-7} mbar. The ac and dc voltages were applied to the sample with respect to the grounded tip to minimize the capacitive crosstalk [22] to the piezoelectric plate used for driving cantilever oscillation that is located beneath the cantilever support.

2.4 Results and Discussion

2.4.1 Validation of D-KPFM Theory

To validate the analysis described in the previous Sect. 2.2.2, Δf-V_{bias} and g-V_{bias} curves are measured with the coherent ac voltage with different phases applied.

1ωD-KPFM case

Figure 2.5 shows simultaneously measured Δf and g versus V_{bias} curves with a coherent sinusoidal ac voltage with the amplitude, $V_{\mathrm{ac}} = 100\,\mathrm{mV_{p-p}}$ and various

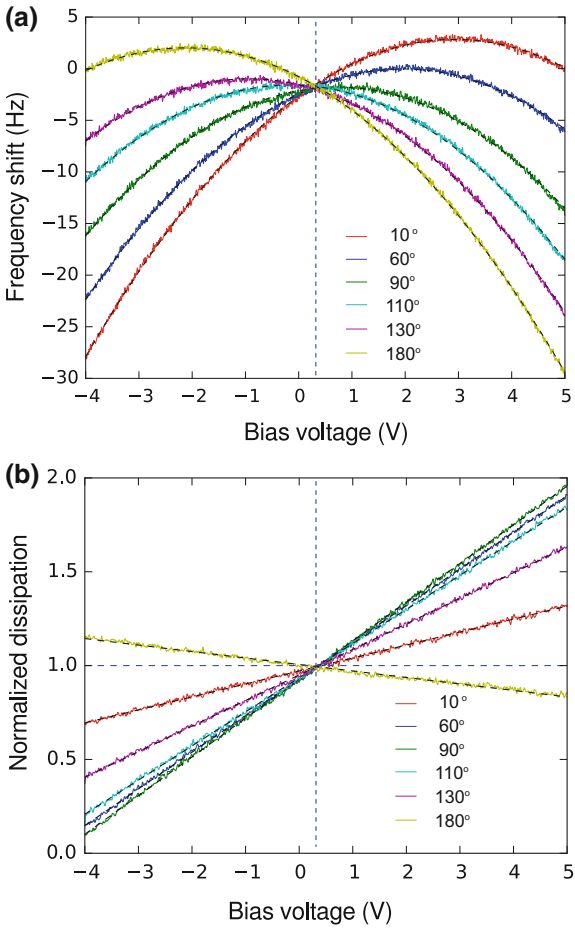

Fig. 2.5 Validation of 1ωD-KPFM theory. **a** Frequency shift, Δf, and **b** dissipation signal, g, versus dc bias voltage, V_{bias}, curves taken with a coherent sinusoidally oscillating voltage with the amplitude, $V_{\text{ac}} = 100\,\text{mV}_{\text{p-p}}$ and various phases, ϕ, applied to a 200 nm thick SiO_2 on Si substrate. The dissipation signal is normalized with the value without the ac bias voltage (indicated with the horizontal blue dashed line). In both figures, dashed lines represent fitted curves assuming a parabola for Δf and a linear line for g as indicated in (2.18) and (2.19), respectively. The oscillation amplitude of the tip was $7.2\,\text{nm}_{\text{p-p}}$ and the quality factor of the cantilever was 9046. Reprinted with permission from [8]. Copyright 2016 by the American Physical Society

phases, ϕ applied. The curves were taken on a Si substrate with 200 nm thick SiO_2. A fitted curve with a parabola for each Δf-V_{bias} curve (2.18) or a linear line for each g-V_{bias} curve (2.19) is overlaid on each experimental curve, indicating a very good agreement between the theory and experiments. As can be seen in Fig. 2.5a, b, the position of the parabola vertex shifts and the slope of g-V_{bias} curve changes systematically with varying phase.

To further validate the theoretical analysis, the voltage coordinate for the vertices (parabola maximum voltage) of Δf-V_{bias} curves and the slope of g-V_{bias} lines (dissipation slope) are plotted against the phase, ϕ, as shown in Fig. 2.6. Each plot is overlaid with a fitted curve (solid curve) with the cosine function (2.18) for the parabola maximum voltage and with the sine function (2.19) for the dissipation slope, showing an excellent agreement between the experiment and theory. The parabola maximum voltage versus phase curve intersects that for the parabola without ac voltage

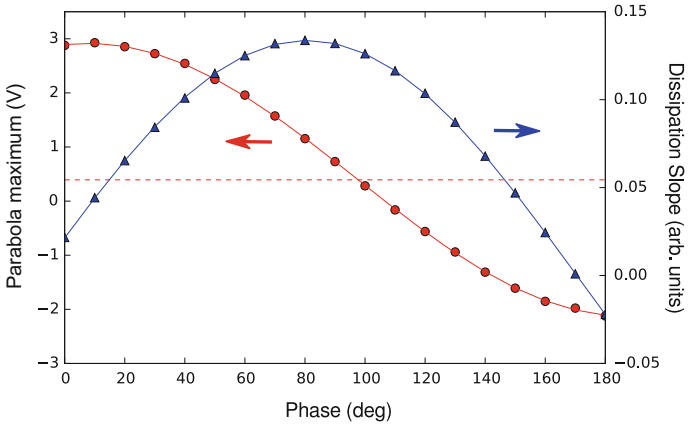

Fig. 2.6 Parabola maximum voltage of the measured Δf-V_{bias} curves (red circles) (Fig. 2.5a) and the dissipation slope of g-V_{bias} curves (blue circles) (Fig. 2.5b). Each solid line represents the fitted curve with the cosine function (2.18) for the parabola maximum voltage and with the sine function (2.19) for the dissipation slope. The horizontal dashed line indicates the voltage for parabola maximum voltage without the ac bias voltage. Reprinted with permission from [8]. Copyright 2016 by the American Physical Society

at the phase of 97° as opposed to 90° which is predicted by the theory. This deviation arises mainly from the phase delay in the photodiode preamplifer electronics. The dissipation slope takes its maximum value at around 81°, again deviating from the theoretical value of 90°. This deviation is probably due to the residual capacitive crosstalk to the excitation piezo [22, 23].

2ωD-KPFM case

To validate (2.26) and (2.27), Δf-V_{bias} and g-V_{bias} curves were measured while a coherent sinusoidally oscillating voltage with $\omega_{\text{el}} = 2\omega_{\text{m}}$, $V_{\text{ac}} = 1$ V (2 $V_{\text{p–p}}$) and various phases, ϕ, is superposed with V_{bias}.

Figure 2.7a, b show the simultaneously measured Δf and g versus V_{bias} curves, respectively. The curves are taken on a template stripped gold surface. A fitted curve with a parabola for each of the Δf-V_{bias} curves (2.26) or with a linear line for each of the g-V_{bias} curves (2.27) is overlaid on each experimental curve, indicating a very good agreement between the theory and experiments. As is shown in Fig. 2.7a, b, the position of the parabola vertex shifts both in V_{bias} and Δf axes and the slope of g-V_{bias} curve changes systematically with the varied phase, ϕ. For further validating the theory, the voltage coordinate of the parabola vertex (parabola maximum voltage) of each Δf-V_{bias} curve and the slope of each g-V_{bias} curve are plotted against ϕ in Fig. 2.8. Each plot is overlaid with a fitted curve (solid curve) with the cosine function (see (2.26)) for the parabola maximum voltage and with the sine function (2.27) for the dissipation slope, demonstrating an excellent agreement between the experiment and theory. The V_{bias} dependence of the frequency shift coordinate of the parabola vertices (frequency shift offset) also shows a very good agreement with the

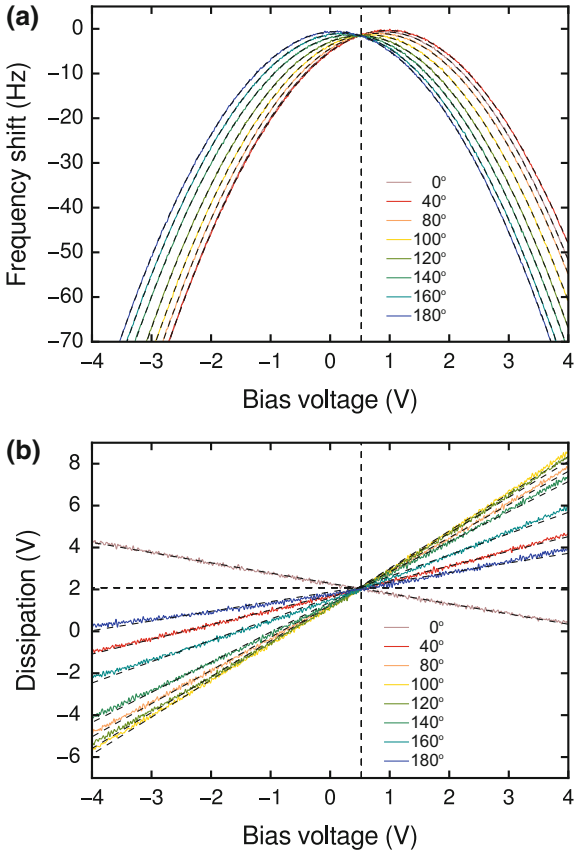

Fig. 2.7 **a** Frequency shift, Δf, and **b** dissipation signal, g, versus dc bias voltage, V_{bias}, curves taken with a coherent sinusoidally oscillating voltage with $\omega_{\text{el}} = 2\omega_{\text{m}}$, $V_{\text{ac}} = 1$ V and various ϕ, applied to a template stripped gold substrate. The vertical dashed line in (**a**) and (**b**) indicates V_{cpd} which is measured as the voltage coordinate of the parabola vertex without V_{ac}. The horizontal dashed line in (**b**) indicates the dissipation without V_{ac}. In both figures, the dashed lines represent fitted curves assuming a parabola for Δf and a linear line for g as indicated in (2.26) and (2.27), respectively. The oscillation amplitude of the tip was 10 $\text{nm}_{\text{p-p}}$ and the quality factor of the cantilever was 25,000

theory (second term of (2.26)) as shown in Fig. 2.8b. The parabola maximum voltage versus phase curve intersects that of $\Delta f - V_{\text{bias}}$ without ac bias voltage at $\phi = 121°$. The deviation from the theoretically predicted value of 90° is due to the phase delay in the detection electronics. We also notice that the amplitude of parabola maximum voltage versus phase curve is 0.472 V which is in good agreement with 0.5 V predicted by the theory ($V_{\text{ac}}/2$ as seen in (2.26)).

2.4.2 Illustrative Example of D-KPFM Imaging

Figure 2.9 shows an example to illustrate how this technique works. Figure 2.9a, b show the topography and dissipation images of a CCD image sensor taken with FM mode without applying ac voltage at a constant dc voltage of 50 mV. The topography contrast in Fig. 2.9a is a convolution of the true topography and the electrostatic contrast except for black slits which are actual recesses. This 'apparent topography'

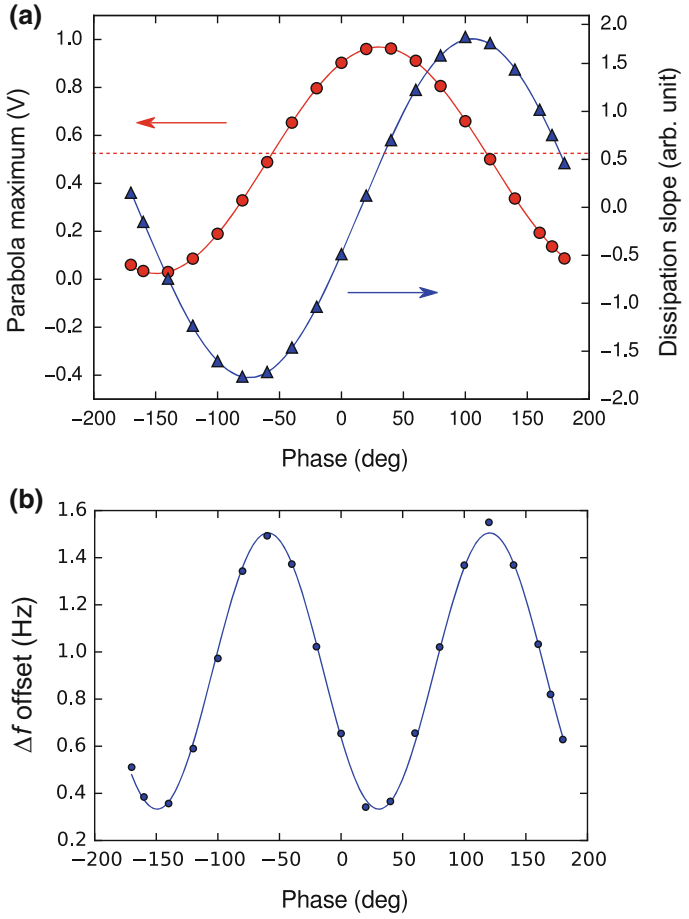

Fig. 2.8 **a** Voltage coordinate of the vertices of the measured Δf-V_{bias} curves (parabola maximum voltage) (red circles) extracted from the results Fig. 2.7a and the slope of dissipation-V_{bias} curves (blue triangles) extracted from Fig. 2.7b as a function of phase. Each solid line represents the fitted curve with the cosine function (2.26) for the parabola maximum voltage and with the sine function (2.27) for the dissipation slope. The horizontal dashed line indicates the voltage coordinate of the parabola measured without the ac bias voltage. **b** Δf offset as a function of phase. The solid line represents the fitted curve with the second term of (2.26). Reprinted from [9], with the permission of AIP Publishing

contrast is caused by the different electrostatic force on the differently doped regions (bright: n-doped, dark: p-doped) [24, 25]. The dissipation image taken with no ac voltage applied (Fig. 2.9b) shows no contrast, indicating no observable Joule dissipation due to the mismatch of the tip oscillation frequency and the dielectric relaxation time of the sample under these imaging condition [26]. It is important to notice that the dissipation signal in FM-AFM is sensitive only to the tip-sample interaction

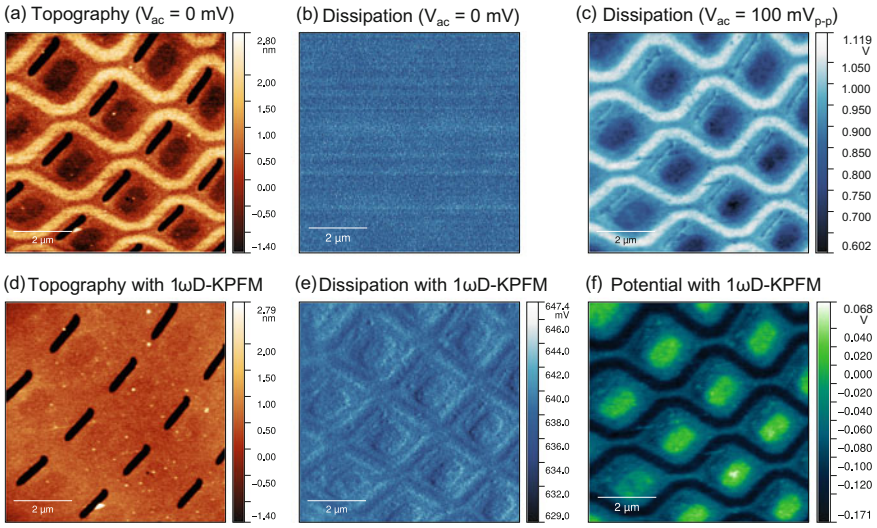

Fig. 2.9 **a** Topography and **b** dissipation images of a CCD image sensor with FM mode with no ac voltage and a constant $V_{bias} = 50$ mV applied. $\Delta f = -0.3$ Hz. No contrast is observed in (**b**). **c** Dissipation image taken with FM mode with a coherent ac voltage with its amplitude, $V_{ac} = 100\ mV_{p-p}$ ($\omega_{el} = \omega_m$) applied. The similar contrast to the topography (**a**) is observed. **e** Topography, **f** dissipation, **g** potential images taken with 1ωD-KPFM technique with $V_{ac} = 100\ mV_{p-p}$, $\omega_{el} = \omega_m$

force with the time (phase) delay comparable to the tip oscillation period as demonstrated in the previous sections (Sect. 2.4.1). Figure 2.9c shows the very similar contrast to the apparent topography (a). Figure 2.9d–f show the simultaneously taken topography, dissipation, and CPD images with the 1ωD-KPFM technique. While the apparent topography in (a) disappears in (d), the similar contrast instead appears in the CPD image (f). Here, the dissipation image (e) is now the input for the KPFM bias feedback controller (e.g. error signal for PI controller in Fig. 2.4) and the CPD image is the output of the PI controller. The electrostatic contrast which appears as the apparent topography contrast is thus transferred to the CPD contrast through the induced dissipation.

2.4.3 Comparison of Different KPFM Techniques

In this section, we compare the KPFM images taken with FM-KPFM, AM-KPFM, 1ωD-KPFM and 2ωD-KPFM to evaluate the performance of each technique. We used a patterned MoS_2 flake for the comparison. The several ten μm scale size of the sample together with the etched stripe pattern with 2 μm pitch enables to find the same region of the sample even in the separate experimental runs. Flakes of

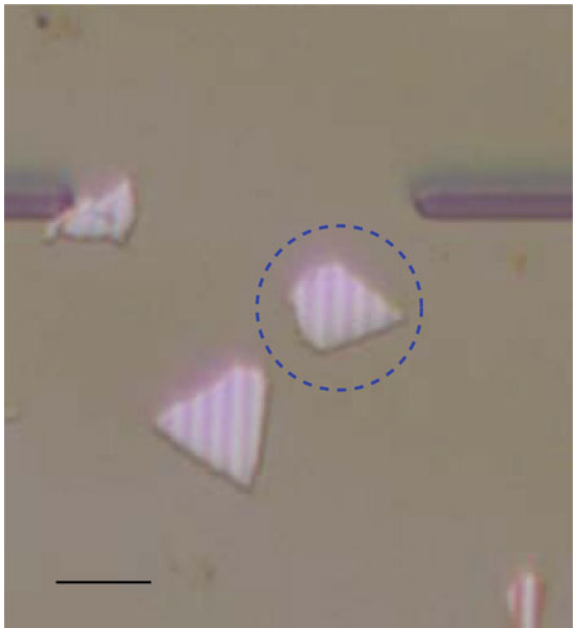

Fig. 2.10 Optical micrograph of the patterned MoS_2 flakes exfoliated on SiO_2/Si substrate. The flake in the circle is the one imaged by the KPFM imaging experiments. Scale bar is 20 μm

MoS_2 were deposited onto a SiO_2/Si substrate by mechanical exfoliation and a stripe pattern was created by electron beam lithography and the subsequent reactive ion etching on top of the flakes. Figure 2.10 shows the optical micrograph of the MoS_2 flake used for the KPFM imaging experiments.

Figure 2.11 shows topography and CPD images of the patterned MoS_2 flake by (a) 1ωD-KPFM, (b) AM-KPFM, (c) 2ωD-KPFM and (d) FM-KPFM techniques. The 1ωD-KPFM, 2ωD-KPFM and FM-KPFM images were taken with the identical cantilever tip ($f_0 = 306,553$ Hz, $k = 20.8$ N/m, $Q = 14,963$) and the AM-KPFM image was taken with a different one ($f_0 = 298,044$ Hz, $k = 27.2$ N/m, $Q = 14,700$). These two cantilevers were of the same type (NSC15, MikroMasch) and taken from the same batch. In 1ωD-KPFM imaging, a sinusoidal ac voltage with an amplitude of $V_{ac} = 100\,mV_{p-p}$ coherent with the tip oscillation was applied to the sample. In AM-KPFM imaging, a sinusoidal ac voltage with the amplitude of $V_{ac} = 8\,V_{p-p}$ whose frequency was tuned to the second flexural resonance peak (resonance frequency: 1,903,500 Hz, quality factor: 2400) was applied to the sample. The resulting oscillation amplitude was detected by a high-speed digital lock-in amplifier (HF2LI, Zurich Instruments) and the detected amplitude was used for the dc bias voltage feedback [2, 3]. In FM-KPFM imaging, a sinusoidal ac voltage with the amplitude of $V_{ac} = 2.0\,V_{p-p}$ and frequency of 300 Hz was applied to the sample [5]. The number of pixels in the images is 512 × 512. The scanning time for 1ωD-KPFM, 2ωD-KPFM and FM-KPFM imaging was 512 s/frame (1 s/line). The scanning time for AM-KPFM was for 1024 s/frame (2 s/line). In all the imaging modes, the frequency shift signal was used for the tip-sample distance control (topography) feedback.

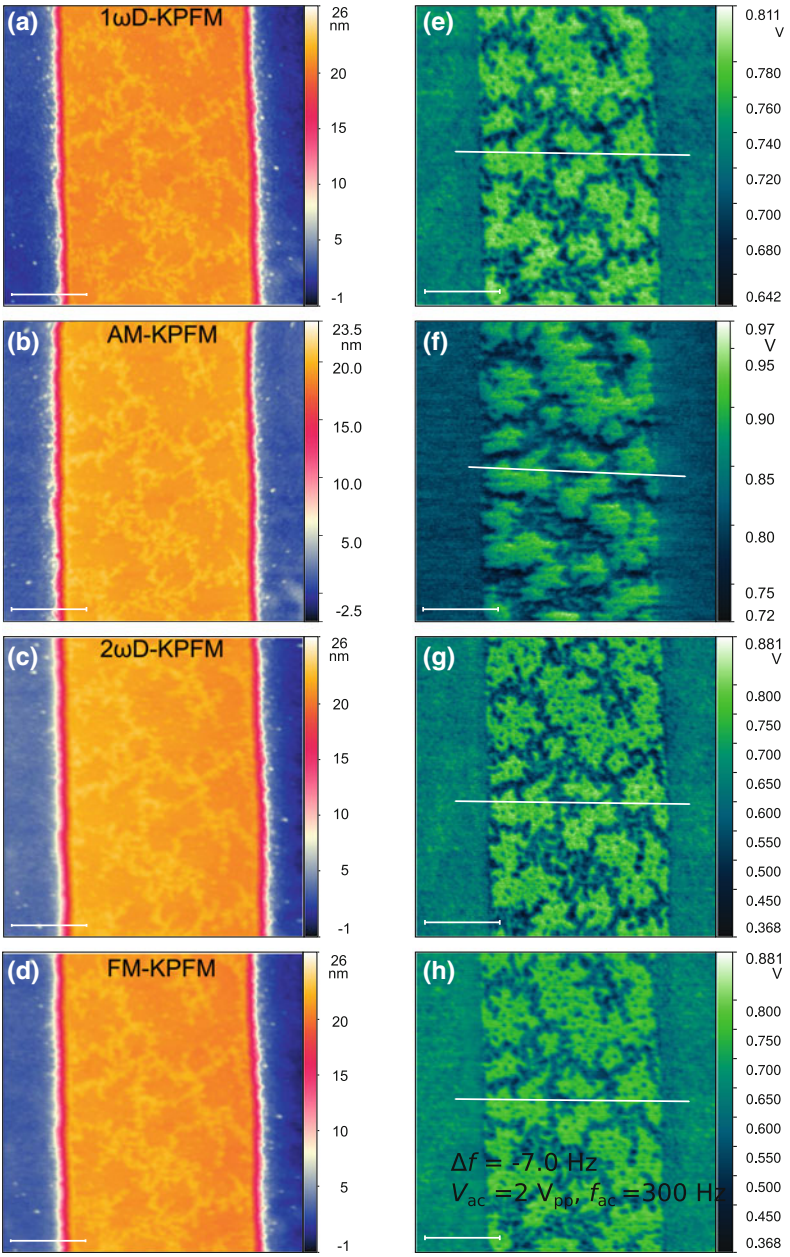

Fig. 2.11 Topography and CPD images of the patterned MoS_2 flake. Topography images taken by **a** 1ωD-KPFM, **b** AM-KPFM, **c** 2ωD-KPFM and **d** FM-KPFM techniques. CPD images taken by **e** 1ωD-KPFM, **f** AM-KPFM, **g** 2ωD-KPFM and **h** FM-KPFM techniques. **i** Profiles of the CPD images by **e** 1ωD-KPFM and **f** AM-KPFM techniques. **j** Profiles of the CPD images by **g** 2ωD-KPFM and **h** FM-KPFM techniques

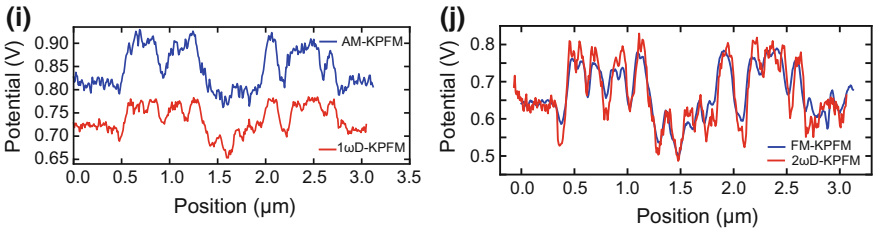

Fig. 2.11 (continued)

The topography images (Fig. 2.11a–d) show an unetched terrace located between the etched regions. The height of the terrace is approximately 20 nm with respect to the etched regions. A clear fractal-like pattern can be seen on the terrace in all the CPD images. The observed pattern in the CPD images can be ascribed to the residue of the etch resist (PMMA) as the topography images show a similar contrast with a thickness of about 1 nm.

Comparison between 1ω*D-KPFM and AM-KPFM*

First, we compare the CPD images taken by 1ωD-KPFM (Fig. 2.11e) and AM-KPFM (Fig. 2.11f). The CPD image by 1ωD-KPFM shows better clarity than that by AM-KPFM. The difference is due to the lower signal-to-noise ratio of the amplitude signal of the second flexural mode oscillation despite that a much higher $V_{ac} = 8\,V_{p-p}$ was applied in AM-KPFM. The higher effective spring constant of the second flexural mode oscillation ($k_{2nd} \sim 40 \times k \approx 800\,N/m$) compared to the first mode [2, 27] and lower observed quality factor ($Q_{2nd} = 2400$ compared with 14,700 for the first mode) account for the difference as the signal in both operating modes is proportional to Q/k. Notice that the cantilevers with lower effective spring constant ($k \approx 2 \sim 3\,N/m$) have been used in the most reported AM-KPFM measurements in which V_{ac} of the order of 100 mV is employed [2–4, 7, 28]. Figure 2.11i shows the line profiles of potential on the same location indicated as a white line in the CPD images Fig. 2.11e, f. Two profiles are in a very good agreement except the constant offset. This observed similarity can be understood by the fact that both 1ωD-KPFM and AM-KPFM are sensitive to the electrostatic force. The constant offset between two profiles is probably due to the different tips used in the two separate experiments.

Comparison between 2ω*D-KPFM and FM-KPFM*

Now we turn to the comparison between 2ωD-KPFM (Fig. 2.11g) and FM-KPFM (Fig. 2.11h). The CPD images taken by 2ωD-KPFM and FM-KPFM look very similar and the line profiles of two images taken on the same location indicated as a white line show a good agreement. A closer inspection reveals slightly larger potential contrast in the 2ωD-KPFM image compared with the FM-KPFM image, which is due to the faster KPFM feedback response of 2ωD-KPFM by virtue of the absence of low frequency modulation which is required for FM-AFM.

Comparison between 1ω*D-KPFM and* 2ω*D-KPFM*

Although both potential images taken by 1ωD-KPFM (Fig. 2.11e) and 2ωD-KPFM (Fig. 2.11g) show almost identical patterns on the terrace with nearly the same signal-to-noise ratio, we notice lower contrast in the CPD image taken by 1ωD-KPFM than that by 2ωD-KPFM from the inspection of the line profiles, Fig. 2.11i, j. The peak-to-peak value of the potential variation in the 1ωD-KPFM image is ∼0.12 V, about one half that in the 2ωD-KPFM image (∼0.3 V). A similar difference in the potential contrast taken by FM-KPFM and AM-KPFM has also been reported in the literature and is ascribed to the fact that the AM-KPFM is sensitive to electrostatic force whereas FM-KPFM uses the modulation in the resonance frequency shift which is sensitive to the electrostatic force gradient [4, 28]. As we have already discussed, the same argument applies to 1ωD-KPFM and 2ωD-KPFM. The smaller CPD contrast observed in 1ωD-KPFM than in 2ωD-KPFM can be explained by larger spatial average due to the stray capacitance including the body of the tip and the cantilever [29–32]. We noticed that an ac voltage amplitude (2 V) much larger than that required for 1ωD-KPFM (100 mV) was necessary for 2ωD-KPFM. This indicates $\alpha > \alpha' A$ which is determined by the distance dependence of the tip-sample capacitance. This condition could be changed by engineering the tip shape.

In spite of lower potential contrast, 1ωD-KPFM has a clear advantage in that it requires much smaller $V_{ac} = 100\,\mathrm{mV_{p-p}}$ compared with $2\,\mathrm{V_{p-p}}$ for 2ωD-KPFM. This advantage is important for electrical characterizations of technically relevant materials whose electrical properties are influenced by the externally applied electric field as is the case in semiconductors where the influence of a large V_{ac} can induce band-bending effects.

2.4.4 Dynamic Response of D-KPFM

The detection bandwidth of D-KPFM is determined by the bandwidth of the cantilever amplitude control feedback loop used in FM-KPFM. In fact, we notice that applying the coherent V_{ac} causing dissipative force can be used to measure the dynamics of the cantilever amplitude control feedback system.

In FM-KPFM, the AFM cantilever serves as the frequency determining element of a self-driven oscillator so that the oscillation frequency keeps track of the resonance frequency of the cantilever. In this way, the conservative force has no influence on the drive amplitude (dissipation signal) when the time delay set by the phase shifter is properly adjusted as already discussed in Sect. 2.2.1 whereas the amplitude controller compensates for the effective Q factor change caused by dissipative force. Therefore, by modulating V_{bias} at a low frequency (<a few kHz) in addition to applying the coherent V_{ac}, the amplitude of the dissipative force can be modulated as can been seen in (2.21) and (2.29). The frequency response of the amplitude feedback loop can thus be measured by demodulating the dissipation signal with a lock-in amplifier. The measured −3 dB bandwidth of the cantilever amplitude feedback loop

is as high as 1 kHz, which is wider than that of the typical PLL frequency detector (400 Hz in this experiment).

Notice that in contrast to the settling time of the oscillation amplitude of a cantilever subject to a change in conservative force which is known to be $\tau \sim Q/f_0$ [12], the response time of the dissipation signal is not limited by Q and can be faster because of the active damping mechanism built in the cantilever amplitude control feedback loop [13] as well as the induced energy dissipation which is given by $\pi F_{\text{quad}} A$ in addition to the internal dissipation of the cantilever, $\pi k A^2/Q$. The active damping behavior of the cantilever amplitude controller indeed manifests itself in the effective negative dissipation shown in g-V_{bias} curves (Figs. 2.5 and 2.7). This explains the observed fast response of the cantilever amplitude feedback loop, resulting in the wider bandwidth of the voltage feedback loop in D-KPFM than that in FM-KPFM which is limited by bias modulation frequency. The typical PLL frequency detector has the detection bandwidth of <1 kHz which sets the upper limit of the bias modulation frequency to several hundred Hz.

The low frequency V_{bias} modulation can also be used for D-KPFM imaging in the case where other dissipative interactions such as the Joule dissipation [26] and single-electron tunneling [19, 33] or the dissipation artifact caused by the crosstalk to the frequency shift [15] contribute to the dissipation signal. It is possible to separate the induced electrostatic dissipation just as is done in FM-KPFM with Δf and in DM-KPFM with the tip oscillation amplitude [10]. The modulated dissipation signal due to the modulation of V_{bias} can be demodulated with a lock-in amplifier which can then be used for the KPFM bias feedback.

2.5 Conclusion

We reviewed D-KPFM, a new experimental technique for KPFM in which the dissipation signal of FM-AFM is used for KPFM bias-voltage feedback. We show that D-KPFM can be operated in two different modes, 1ωD-KPFM and 2ωD-KPFM which are sensitive to electrostatic force and electrostatic force gradient, respectively. The technique features a simpler implementation and faster scanning than the most commonly used FM-KPFM technique as it requires no low frequency modulation.

We provided the theory of D-KPFM by combining two key aspects: (1) the effect of the periodically oscillating force on the resonant frequency shift and dissipation signal in FM-AFM and (2) the detailed analysis of the electrostatic force by explicitly taking into account the effect of the tip oscillation.

We validated the theory by fitting with the experimental Δf-V_{bias} and g-V_{bias} curves in both 1ω and 2ωD-KPFM cases. We experimentally showed the equivalence of 1ωD-KPFM and AM-KPFM and that of 2ωD-KPFM and FM-KPFM in terms of their sensitivity to electrostatic force and electrostatic force gradient, respectively. We demonstrated that 1ωD-KPFM requires a significantly smaller ac voltage amplitude (a few tens of mV) than 2ωD-KPFM and FM-KPFM. Even though the potential contrast obtained by 1ωD-KPFM is about two times smaller than that by

2ωD-KPFM, the use of the small ac voltage is of great advantage for characterizing materials whose properties are sensitive to the externally applied electric field such as semiconductors. The operations in 1ω and 2ωD-KPFM can be switched easily to take advantage of both features at the same location on a sample.

References

1. M. Nonnenmacher, M.P. OBoyle, H.K. Wickramasinghe. Appl. Phys. Lett. **58**(25), 2921 (1991), http://aip.scitation.org/doi/10.1063/1.105227. https://doi.org/10.1063/1.105227
2. A. Kikukawa, S. Hosaka, R. Imura, Rev. Sci. Instrum. **67**(4), 1463 (1996), http://aip.scitation.org/doi/10.1063/1.1146874. https://doi.org/10.1063/1.1146874
3. C. Sommerhalter, T.W. Matthes, T. Glatzel, A. Jäger-Waldau, M.C. Lux-Steiner, Appl. Phys. Lett. **75**(2), 286 (1999), http://aip.scitation.org/doi/abs/10.1063/1.124357
4. U. Zerweck, C. Loppacher, T. Otto, S. Grafstrom, L.M. Eng, Phys. Rev. B **71**(12), 125424 (2005), https://link.aps.org/doi/10.1103/PhysRevB.71.125424
5. S. Kitamura, M. Iwatsuki, Appl. Phys. Lett. **72**(24), 3154 (1998), http://aip.scitation.org/doi/10.1063/1.121577. https://doi.org/10.1063/1.121577
6. Z. Schumacher, Y. Miyahara, L. Aeschimann, P. Grütter, Beilstein J. Nanotechnol. **6**, 1450 (2015), http://www.beilstein-journals.org/bjnano/content/6/1/150. https://doi.org/10.3762/bjnano.6.150
7. S.A. Burke, J.M. LeDue, Y. Miyahara, J.M. Topple, S. Fostner, P. Grutter, Nanotechnology **20**(26), 264012 (2009), http://iopscience.iop.org/0957-4484/20/26/264012. https://doi.org/10.1088/0957-4484/20/26/264012
8. Y. Miyahara, J. Topple, Z. Schumacher, P. Grutter, Phys. Rev. Appl. **4**(5), 054011 (2015), http://link.aps.org/doi/10.1103/PhysRevApplied.4.054011. https://doi.org/10.1103/PhysRevApplied.4.054011
9. Y. Miyahara, P. Grutter, Appl. Phys. Lett. **110**(16), 163103 (2017), http://aip.scitation.org/doi/10.1063/1.4981937. https://doi.org/10.1063/1.4981937
10. T. Fukuma, K. Kobayashi, H. Yamada, K. Matsushige, Rev. Sci. Instrum. **75**(11), 4589 (2004), http://aip.scitation.org/doi/10.1063/1.1805291
11. H. Nomura, K. Kawasaki, T. Chikamoto, Y.J. Li, Y. Naitoh, M. Kageshima, Y. Sugawara, Appl. Phys. Lett. **90**(3), 033118 (2007), http://aip.scitation.org/doi/10.1063/1.2432281. https://doi.org/10.1063/1.2432281
12. T.R. Albrecht, P. Grutter, D. Horne, D. Rugar, J. Appl. Phys. **69**(2), 668 (1991), http://aip.scitation.org/doi/10.1063/1.347347. https://doi.org/10.1063/1.347347
13. U. Dürig, H.R. Steinauer, N. Blanc, Journal of Applied Physics **82**(1997), 3641 (1997), http://aip.scitation.org/doi/10.1063/1.365726. https://doi.org/10.1063/1.365726
14. A. Labuda, K. Kobayashi, Y. Miyahara, P. Grütter, Rev. Sci. Instrum. **83**(May), 053703 (2012), http://dx.doi.org/10.1063/1.4712286. https://doi.org/10.1063/1.4712286
15. A. Labuda, Y. Miyahara, L. Cockins, P. Grütter, Phys. Rev. B **84**(12), 125433 (2011), http://link.aps.org/doi/10.1103/PhysRevB.84.125433. https://doi.org/10.1103/PhysRevB.84.125433
16. H. Hölscher, B. Gotsmann, W. Allers, U. Schwarz, H. Fuchs, R. Wiesendanger, Phys. Rev. B **64**(7), 075402 (2001), http://link.aps.org/doi/10.1103/PhysRevB.64.075402. https://doi.org/10.1103/PhysRevB.64.075402
17. L.N. Kantorovich, T. Trevethan, Phys. Rev. Lett. **93**(23), 236102 (2004), http://link.aps.org/doi/10.1103/PhysRevLett.93.236102. https://doi.org/10.1103/PhysRevLett.93.236102
18. J.E. Sader, T. Uchihashi, M.J. Higgins, A. Farrell, Y. Nakayama, S.P. Jarvis, Nanotechnology **16**(3), S94 (2005), http://iopscience.iop.org/article/10.1088/0957-4484/16/3/018
19. Y. Miyahara, A. Roy-Gobeil, P. Grutter, Nanotechnology **28**(6), 064001 (2017), http://doi.org/10.1088/1361-6528/aa5261. https://doi.org/10.1088/1361-6528/aa5261

20. T. Fukuma, M. Kimura, K. Kobayashi, K. Matsushige, H. Yamada, Rev. Sci. Instrum. **76**(5), 53704 (2005), http://aip.scitation.org/doi/10.1063/1.1896938
21. P. Zahl, T. Wagner, R. Möller, A. Klust, J. Vac. Sci. Technol. B Nanotechnol. Microelectron. **28**(3), C4E39 (2010), http://avs.scitation.org/doi/10.1116/1.3374719. https://doi.org/10.1116/1.3374719
22. H. Diesinger, D. Deresmes, J.P. Nys, T. Mélin, Ultramicroscopy **108**(8), 773 (2008), http://linkinghub.elsevier.com/retrieve/pii/S0304399108000132. https://doi.org/10.1016/j.ultramic.2008.01.003
23. T. Mélin, S. Barbet, H. Diesinger, D. Théron, D. Deresmes, Rev. Sci. Instrum. **82**(3), 036101 (2011), http://aip.scitation.org/doi/10.1063/1.3516046. https://doi.org/10.1063/1.3516046
24. S. Sadewasser, M. Lux-Steiner, Phys. Rev. Lett. **91**(26), 1 (2003), http://link.aps.org/doi/10.1103/PhysRevLett.91.266101. https://doi.org/10.1103/PhysRevLett.91.266101
25. Y. Miyahara, L. Cockins, P. Grutter, in *Kelvin Probe Force Microscopy*, ed. by S. Sadewasser, T. Glatzel (Springer Berlin Heidelberg, 2012), chap. 9, pp. 175–199, http://www.springer.com/materials/surfaces+interfaces/book/978-3-642-22565-9?changeHeader. https://doi.org/10.1007/978-3-642-22566-6-9
26. W. Denk, D.W. Pohl, Appl. Phys. Lett. **59**(17), 2171 (1991), http://scitation.aip.org/content/aip/journal/apl/59/17/10.1063/1.106088. https://doi.org/10.1063/1.106088
27. J. Melcher, S. Hu, A. Raman, Appl. Phys. Lett. **91**(5), 53101 (2007), http://aip.scitation.org/doi/10.1063/1.2767173
28. T. Glatzel, S. Sadewasser, M. Lux-Steiner, Appl. Surf. Sci. **210**(1–2), 84 (2003), http://linkinghub.elsevier.com/retrieve/pii/S0169433202014848. https://doi.org/10.1016/S0169-4332(02)01484-8
29. T. Hochwitz, A.K. Henning, C. Levey, C. Daghlian, J. Vac. Sci. Technol. B Nanotechnol. Microelectron. **14**(1), 457 (1996), http://scitation.aip.org/content/avs/journal/jvstb/14/1/10.1116/1.588494. https://doi.org/10.1116/1.588494
30. H.O. Jacobs, H.F. Knapp, A. Stemmer, Rev. Sci. Instrum. **70**(3), 1756 (1999), http://aip.scitation.org/doi/10.1063/1.1149664. https://doi.org/10.1063/1.1149664
31. E. Strassburg, A. Boag, Y. Rosenwaks, Rev. Sci. Instrum. **76**(8), 083705 (2005), http://scitation.aip.org/content/aip/journal/rsi/76/8/10.1063/1.1988089. https://doi.org/10.1063/1.1988089
32. G. Cohen, E. Halpern, S.U. Nanayakkara, J.M. Luther, C. Held, R. Bennewitz, A. Boag, Y. Rosenwaks, Nanotechnology **24**(29), 295702 (2013), http://iopscience.iop.org/article/10.1088/0957-4484/24/29/295702. https://doi.org/10.1088/0957-4484/24/29/295702
33. L. Cockins, Y. Miyahara, S.D. Bennett, A.a. Clerk, S. Studenikin, P. Poole, A. Sachrajda, P. Grutter, Proc. Natl. Acad. Sci. USA. **107**(21), 9496 (2010), http://www.pnas.org/content/107/21/9496. https://doi.org/10.1073/pnas.0912716107

Chapter 3
Dynamic Modes in Kelvin Probe Force Microscopy: Band Excitation and G-Mode

Stephen Jesse, Liam Collins, Sabine Neumayer, Suhas Somnath and Sergei V. Kalinin

Abstract Since its invention in 1991, Kelvin Probe Force Microscopy (KPFM) has developed into the primary tool used to characterize electrical phenomena on the nanometer scale, with multiple applications for transport, ferroelectric, biological, organic and inorganic photovoltaics, amongst a myriad of other materials. At the same time, this multitude of applications is underpinned by a relatively simple detection scheme utilizing the classical lock-in signal detection combined with tip bias feedback. It has been widely recognized that this detection scheme has several limitations, including influences of the experimental parameters (e.g. driving amplitude, feedback gains, phase offset) as well as loss of information on other material properties (e.g. capacitance and its bias dependence and time-dependent responses). In this chapter, we review the operational principles of KPFM, briefly overview the existing excitation schemes beyond the classical lock-in—feedback principle, and discuss at length the implementations and applications of KPFM based on band excitation and the full information capture embodied in general mode (G-Mode). The future potential pathways for development of detection in KPFM are discussed.

S. Jesse · L. Collins · S. Somnath · S. V. Kalinin (✉)
Oak Ridge National Laboratory, The Institute for Functional Imaging of Materials and The Center for Nanophase Materials Sciences, Oak Ridge, TN 37831, USA
e-mail: sergei2@ornl.gov

S. Jesse
e-mail: sjesse@ornl.gov

L. Collins
e-mail: collinslf@ornl.gov

S. Somnath
e-mail: somnaths@ornl.gov

S. Neumayer
School of Physics, University College Dublin, Belfield, Dublin 4, Ireland
e-mail: sabine.neumayer@ucd.ie

S. Sadewasser and T. Glatzel (eds.), *Kelvin Probe Force Microscopy*,
Springer Series in Surface Sciences 65, https://doi.org/10.1007/978-3-319-75687-5_3

3.1 Introduction

The invention of Scanning Probe Microscopy (SPM) in the last quarter of the XX century [1, 2] opened the door for the systematic exploration of the nanoscale world [3]. Immediately after the first spectacular demonstration of atomic resolution on semiconductor and insulator surfaces [4], it was realized that the sensitivity of SPM to probe minute forces could be extended to applications for probing long range magnetic and electrostatic forces. These latter applications embodied in Electrostatic Force Microscopy (EFM) [5, 6] and Kelvin Probe Force Microscopy (KPFM) [7] have in turn enabled studies of the broad set of materials and phenomena associated with the changes in charge state of surfaces and interfaces.

Some of the earliest applications of KPFM, and related techniques, dealt with investigating contact electrification phenomena [8]. In general, the fact that contact between dissimilar materials resulted in local charging was known since the dawn of science, however both the nature of the process, and spatial distribution of the resultant charge patterns, remained virtually unknown. KPFM provided insight into these mechanisms [9] and hence an understanding into fundamental mechanisms of meteorological phenomena, industrial safety, and applications such as piezotronic nanogenerators [10–12].

Another broad set of KPFM applications is related to studies of electronic and transport phenomena in semiconductors. In static semiconductor materials, the surface work function is directly related to the local carrier concentrations [13], enabling the applications of KPFM to dopant profiling. These applications, however, suffer from the potential effects of the water layers and surface states [14] which often reduce these studies to semi-quantitative or qualitative investigations. However, since the early work by Tanimoto and Vatel [15, 16] it has been shown that KPFM can be used to map transport in laterally biased devices. In these experiments, the KPFM probe acts as moving voltage electrode, providing a map of the internal potential distribution across active devices from which corresponding resistances can be reconstructed [17–20]. These approaches were further extended to map frequency-dependent transport phenomena [19, 21–30], and are discussed at length in the Chapter by Strelcov et al.

Beyond semiconductor materials and devices, KPFM was broadly used for the characterization of ferroelectrics. In these materials, the presence of the spontaneous polarization results in polarization bound charge at surfaces and interfaces. Under ambient conditions, these charges are compensated by environmental charges (external screening) or band bending (internal screening), giving rise to a broad set of static and dynamic phenomena ranging from domain-specific potentials [25] to spurious potential behavior on phase transitions [25, 31–33] as well as temperature induced domain potential inversion [34]. These observations led to the emergence of ionic screening model of ferroelectrics [35, 36] establishing the role of chemical factors in ferroelectric behavior [37–40], and prediction of novel ferro-ionic states [41, 42].

In addition, a broad spectrum of biological applications emerged, including the detection of surface potential changes induced by specific adsorption or binding [43]. Similarly, KPFM provides high- resolution and -potential sensitivity enabling direct measurement of surface potential variation across individual biomolecules [44], optoelectronic properties of photovoltaic biosystems [45], or cholesterol induced electrostatic microscopic domains in complex lipid domain structures [46, 47]. It should be noted however that KPFM of biological system necessitates development of liquid KPFM modes [48–53], as is summarized in Chapter by Collins et al. Similar developments are necessitated for KPFM studies of corrosion, batteries and fuel cells, as well as other liquid-based electrochemically active systems.

Of a broad interest are applications of photovoltaic materials and devices [54, 55]. In this case, imaging of static surface potentials provides insight into local terminations, surface composition, and presence of serendipitous phases. However, it is the evolution of the surface potential upon changes of light illumination conditions that elucidates local photovoltage phenomena, intrinsically related to photovoltaic mechanisms. These applications in turn stimulate the development of the time-resolved and ultrafast KPFM modes [56–58].

The applications highlighted above illustrate a broad spectrum of KPFM applications and related techniques. However, the vast majority of published research utilizes the simple lock-in based version of KPFM, which combines heterodyne detection of the electrostatic forces and simple feedback to establish nulling potential conditions. This implementation originally stemmed from intrinsic instrumentation limitations, in addition to offering an easy way to record and interpret spatial maps of the surface potential, and hence ensuring the broad acceptance of KPFM. However, in the last decade the emergence of fast flexible electronics has enabled rapid progress in the development of more complex detection and signal processing schemes for KPFM. In this chapter, we begin by briefly reviewing the basic principles of KPFM operation and underpinning signal processing. We then discuss in detail KPFM modes based on band excitation (BE) and the opportunities offered by the full information collection modes (G-mode) [59–62].

3.2 Principles of EFM and KPFM

The classical implementations of KPFM [7] and EFM [6] are both based on the dual-pass method. The surface topography is first acquired by the grounded tip in standard intermittent contact atomic force microscopy (AFM). Subsequently, electrostatic data is collected at a predefined height above the surface. In EFM, the cantilever is driven mechanically or electrically. The electrostatic force, F, acting between the dc biased conductive tip and the sample surface causes a change of the cantilever resonance frequency that is proportional to the force gradient

$$\Delta\omega = \frac{\omega_0}{2k}\frac{dF(z)}{dz}, \tag{3.1}$$

where k is the spring constant and ω_0 is the resonance frequency of the cantilever. To maintain resonant excitation, the driving frequency ω_p is adjusted and the frequency shift $\Delta\omega$ is recorded as the EFM image.

In KPFM, the cantilever is driven electrically with a tip bias $V_{tip} = V_{dc} + V_{ac}\cos(\omega t)$, where V_{ac} is referred to as the driving voltage, with simultaneous mechanical excitation in some cases. The electrostatic force, $F_{el}(z)$, between the tip and the contact potential difference (CPD) V_{CPD} is:

$$F_{el}(z) = \frac{1}{2}\left(V_{tip} - V_{CPD}\right)^2\frac{\partial C(z)}{\partial z}, \tag{3.2}$$

where $C(z)$ is the tip-surface capacitance, which depends on tip geometry, surface topography as well as tip surface separation, z. The first harmonic component of the electrostatic force is

$$F_{1\omega}^{el}(z) = \frac{\partial C(z)}{\partial z}\left(V_{dc} - V_{CPD}\right)V_{ac}\sin(\omega t). \tag{3.3}$$

Feedback is used to nullify this term by adjusting the constant component of the tip bias, V_{dc}, which is fulfilled when V_{dc} is equal to the CPD (V_{CPD}). Thus, a surface potential map can be obtained by mapping the nulling potential V_{dc} at which the condition $F_{1\omega}^{el} = 0$ is met.

Note, that KPFM operation is only valid if this implicit assumption of a precise nulling of the first harmonic force is achieved. This, however, is rarely experimentally verified as it can be difficult to do so under closed loop operation. In practice, the interpretation of the measured CPD necessitates careful consideration of the influence of the instrumentation, and in particular the bias feedback loop as well as parasitic signals [25]. The effect of incorrect feedback operation have been studied originally by Kalinin et al. [25] and is covered in detail by Melin et al. [63] in the first edition of this book, as well as elsewhere [64, 65].

A number of factors can prevent the recorded amplitude from converging to precisely zero when $V_{dc} = V_{CPD}$, comprising the non-ideality of the feedback loop, electronic offsets of the instrumentation as well as parasitic signals due to capacitive coupling between ac excitation voltage and deflection output signal. Moreover, experimental limitations like thermo-mechanical and electrical noise, have to be taken into account. Experimental parameters such as excitation amplitude and frequency, phase projection and feedback gains can further influence the measurements. Due to the strong dependence of CPD values on feedback effects in closed loop KPFM, absolute values for the CPD can vary within a ~1 V range, dependent on the instrument [65]. Although some forms of parasitic signal components can be minimized [64, 66], careful calibration of all electronic equipment is

required, combined with the use of shielded electronic cabling or active feedback compensation [63].

In addition to the feedback effect, non-local capacitive interactions should be considered when interpreting KPFM measurements. For example, a tip positioned above a certain location of interest does not only interact with the sample location directly beneath the tip, but also with adjacent sample areas. With this consideration in mind, the first harmonic of the electrostatic force between the tip/cantilever and the sample surface can be described as:

$$F_{1\omega}(z) = F_t + F_c = V_{ac}(V_{dc} - V_{CPD})\frac{\partial C_t(z)}{\partial z} + V_{ac}(V_{dc} - V_{av})\frac{\partial C_c(z)}{\partial z} \tag{3.4}$$

where F_t and F_c are forces acting on tip and cantilever, respectively, C_t and C_c are tip-surface and cantilever-surface capacitance, z is the distance from the surface, V_{dc} is tip dc bias, V_{ac} is the periodic bias applied to the tip, V_{CPD} is the CPD below the tip, and V_{av} is the average CPD detected by the cantilever. The operation of KPFM implies that the measured nulling bias is

$$V_{dc} = \frac{V_{CPD}F_t + V_{av}F_c}{F_t + F_c} + \frac{\delta}{V_{ac}(F_t + F_c)}, \tag{3.5}$$

where δ is a constant dependent on feedback loop parameters. The average image potential, V_{dc}^{av}, and the relative potential difference between features of different potential (with the size larger than the measurement resolution but smaller than the cantilever size), ΔV_{dc}, can be defined as:

$$V_{dc}^{av} = V_{av} + \frac{\delta}{V_{ac}(F_t + F_c)}. \tag{3.6}$$

and

$$\Delta V_{dc} = (V_1 - V_2)\frac{F_t}{F_t + F_c}. \tag{3.7}$$

Hence, image contrast in the first approximation is independent of feedback operation, whereas absolute CPD measurements can often be difficult to obtain as de-convolution of real physical values from the measurement is not easy [25]. Note that long range averaging, or stray capacitance effects, are features of all voltage modulated AFM techniques and not solely confined to KPFM. Furthermore, the resolution theory of KPFM [67–70] presents the generalization of (3.6) and (3.7) to the distributed model of the probe.

Adopting a frequency modulated (FM) detection scheme [71, 72], which is sensitive to electrostatic force gradients rather than forces, allows to minimize the impact of stray cantilever capacitance. Consequently, FM-KPFM is only sensitive to electrostatic forces confined to the tip apex. Amplitude-modulated (AM)-KPFM

Table 3.1 Comparison of advanced modes of KPFM

Mode	Excitation	Drive Scheme	Detection	Interaction	Feedback	Output	References
AM-KPFM (dual pass)	*SF*	E	*LIA*	F_{el}	✓	*CPD*	[75]
AM-KPFM (single pass)	*MF*	E + P	*LIA*	F_{el}	✓	*CPD*	[7, 76, 77]
FM-KPFM	*MF*	E + P	*PLL & LIA*	F'_{el}	✓	*CPD*	[73]
HAM-KPFM	*MF*	E + P	*LIA or PLL*	F_{el} or F'_{el}	✓	*CPD*	[78–82]
DH-KPFM	*SF*	E	*LIA or PLL*	F_{el} or F'_{el}	×	*CPD* + *C′*	[62, 83, 84]
D-KPFM	*SF*	E + P	*LIA or PLL*	F_{el} or F'_{el}	✓	*CPD*	[76, 77]
BE-KPFM	*MF*	E	*FDA*	F_{el} and F'_{el}	×	*CPD* + *C′*	[85]
PthBE-KPFM	*MF*	E + P	*FDA*	F'_{el}	×	*CPD* + *C′*	[86]
IM-KPFM	*MF*	E + P	*FDA*	F'_{el}	×	*CPD* + *C′*	[87, 88]
tr-KPFM	*SF*	E	*LIA*	F_{el}	×	*CPD* + *tr-F*$_{el}$	[89–91]
tr-EFM	*SF*	E + P	*LIA*	F_{el}	×	*Charge dynamics*	[56–58, 92]
pp-KFPM	*SF*	E + P	*LIA*	F_{el} or F'_{el}	✓	*Fast CPD*	[93, 94]
G-mode-KPFM	*SF*	E	*FDA*	F'_{el}	×	*Fast CPD* + *C′*	[60–62]

Acronyms used: Amplitude modulation (AM); frequency modulation (FM); heterodyne amplitude modulation (HAM); dual harmonic (DH); dissipation (D); band excitation (BE); photothermal excitation band excitation (PthBE); intermodulation (IM); time resolved (tr); pump-probe (pp), general acquisition (G); single frequency (SF); multifrequency (MF); electrical (E); mechanical actuation (P); lockin amplifier (LIA); phase locked loop (PLL); fast data acquisition (FDA)

is thought to have spatial resolution on the order of 10 s of nm whereas FM-KPFM has been demonstrated for atomic resolution imaging [71–73], although the sample resolution of any KPFM mode is strongly dependent on experimental parameters such as operational mode, imaging environment, tip shape, tip-sample distance.

Beyond AM- or FM-KPFM, there has been a rapid rise in the number of KPFM modes within the last 10 years. A table summarizing the most widely used KPFM techniques now available is given in Table 3.1. These modes generally aimed to (i) eliminate measurement artifacts, (ii) improve sensitivity and resolution, (iii) capture more channels of information (e.g., polarization forces, dielectric properties), and/or (iv) capture system dynamics or kinetics. The various approaches can be distinguished based on their excitation waveform, either single frequency (SF) or multi-frequency (MF). In SF methods, the system is perturbed using a single frequency sinusoidal excitation waveform and corresponding amplitude and phase of the fundamental (and/or harmonic) response. SF detection methods, however, do not capture all information about tip-sample interactions, which led to the development of MF SPM techniques. In MF modes, the system is excited at two or more frequencies, which is often used for simultaneous topography imaging. The MF methods were recently reviewed by Garcia [74]. We further distinguish techniques in terms of detection methods used, be that heterodyne detection (e.g., LIA or PLL) or using other forms of data acquisition, as well as the drive scheme chosen (i.e., purely electrostatic excitation as in lift mode/dual pass AM-KPFM, or mechanical and electrical excitation as in single pass AM- or FM-KPFM). A description of the sensitivity to either the electrostatic force, force gradient or both is also provided in Table 3.1. Finally, these advanced modes of KPFM can be further distinguished by the requirement of dc bias regulation for the determination of the CPD. In regards to the latter, we refer to techniques which require bias feedback as closed loop (CL) approaches, whereas modes which negate the requirement for bias feedback are regarded as open loop (OL) approaches.

3.3 Classic KPFM Methods

Since the inception of dynamic AFM techniques, detection techniques including lock-in amplifier (LIA) and phase locked loop (PLL) have been used to attenuate unwanted noise and amplify the signal of interest.

The LIA [95] is one of the most popular detection methods used in KPFM measurements to extract the cantilever response signal at a specific frequency from a noisy photodetector background. The LIA operates by mixing the input signal, the vertical deflection signal from the photodetector, with a reference signal which is also used to electrically excite the cantilever. For an input waveform, $U_{in}(s)$, and the sinusoidal excitation signal used in LIA-based KPFM measurements, the output from the LIA can be calculated as:

$$U_{out}(t) = \frac{1}{T}\int_{t-T}^{t} \sin(2\pi f_{ref} + \varphi)\ U_{in}(s)\ ds. \tag{3.8}$$

Here, f_{ref} is the frequency of the electrical excitation/reference signal, φ is the phase offset that can be chosen in LIA settings, and T is the duration over which the signals are mixed. Since, U_{out} is 0 for all frequencies besides f_{ref}, the LIA only returns the signal from the f_{ref} frequency of U_{in}. Modern LIA are commonly two-phase detectors and perform the above calculation for φ set to 0 and 90° to obtain in-phase and out-of-phase response, which in turn provides the amplitude and phase information from U_{in} for f_{ref}. While the LIA simplifies the extraction of the desired signal with high signal-to-noise, LIAs also have many disadvantages. The intrinsic nature of the LIA detection results in irretrievable loss of information relating to response at other frequencies, as well as transient and spurious signals. In the case of complex and non-linear dynamic systems such as an AFM cantilever, information from only one eigenmode can be recorded from a single LIA, whereas response at other modes and correspondingly relevant information remain undetected. Furthermore, the change in resonance frequency of the tip-sample system and hence change in response magnitude (indirect cross-talk [96, 97]) can result in significant misinterpretation of information. Finally, all LIAs suffer from a compromise between the bandwidth and the temporal resolution since they require a finite time period (~100 μs–4 ms) to mix the reference and input signals. This precludes the detection of high-speed transients in the signal.

Another popular detection scheme uses phase-locked loops (PLL) [98]. PLLs use a feedback system to ensure a constant phase difference between input signal and the reference signal thereby enabling direct detection of the frequency difference between the input and reference signals. This allows tracking the changes in resonance frequency of the cantilever as it interacts with the surface, providing information on the force gradient. PLLs can be based on LIAs or a more complex setup leading to a substantial increase in complexity of the governing equations [99]. This approach is directly implemented in EFM. PLL based KPFM measurements typically employ an additional feedback loop that uses the measured changes in cantilever resonance frequencies to match the electrical excitation frequency with the cantilever resonance frequency [100, 101].

3.4 Dynamic KPFM Without DC Bias Feedback

As described above, classical KPFM approaches rely on CL bias feedback for compensating the electrostatic force and hence determination of the CPD. However, in certain cases, such as liquid KPFM or non-invasive measurements on voltage sensitive materials, techniques which can accurately measure the CPD while obviating the application of dc bias is preferable. This latter limitation is related to the potential of the probe bias to induce electrochemical processes in polar and

reactive media [50, 51]. KPFM without dc bias also presents an opportunity to circumvent CL operation, overcoming problems associated with the feedback effect as well as increasing the imaging bandwidth which is often limited by the bias feedback loop. Finally, open loop (OL) approaches can often access additional information relating to the tip-sample capacitance which is nullified in classical KPFM.

An OL-KPFM imaging technique used to map the CPD of semiconductor materials in ultrahigh vacuum (UHV) was first demonstrated by Takeuchi et al. [102]. Here we refer to the technique as dual harmonic (DH)-KPFM as it relies on the detection of the harmonic responses of a voltage modulated probe. In DH-KPFM, an ac voltage at a single drive frequency, ω is used for cantilever excitation, which does not require the application of a dc bias between tip and sample (i.e. $V_{dc} = 0$). A schematic describing the expected cantilever response for an off resonance excitation is shown in Fig. 3.1a. The electrostatic force acting on the tip causes harmonic cantilever responses at ω and 2ω, described by (3.9) and (3.10):

$$A_\omega = G(\omega)\frac{|F_\omega|}{k} = G(\omega)\left|C_z'(V_{CPD})\right|\frac{V_{ac}}{k}, \tag{3.9}$$

$$A_{2\omega} = G(2\omega)\frac{|F_{2\omega}|}{k} = G(2\omega)\left|C_z'\right|\frac{V_{ac}^2}{4k}, \tag{3.10}$$

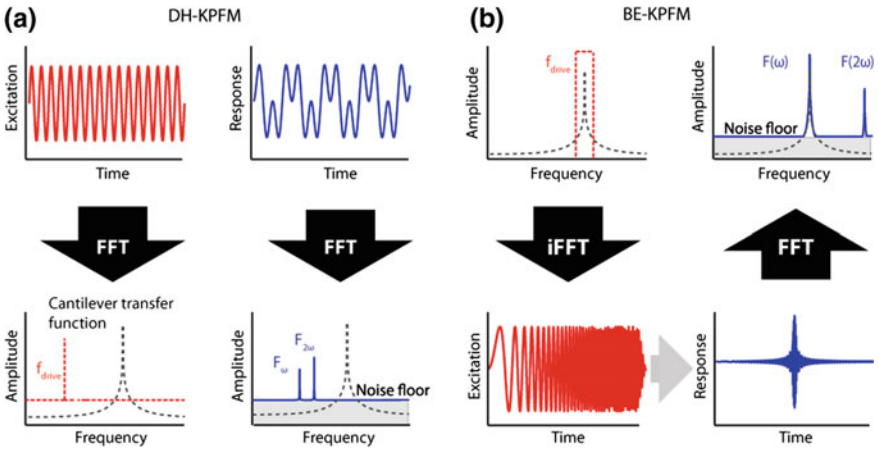

Fig. 3.1 Scheme of **a** single frequency and **b** BE excitation and response. **a** The cantilever is excited with a sinusoidal function at one fixed frequency and has a dynamic response at the fundamental drive as well as a frequency doubled response. **b** In BE, a drive signal of a predefined amplitude density in a frequency band around the resonance is chosen for excitation and applied to the tip as inverse Fourier transformed signal in the time domain. The resulting response is Fourier transformed into the frequency domain and used to obtain the cantilever transfer function (© IOP Publishing. Reproduced with permission. All rights reserved) [104]

where $G(\omega)$ and $G(2\omega)$ are the gains due to the cantilever transfer function at ω and 2ω respectively. Considering that the first harmonic response contains information on the V_{CPD} coupled with $C_z^{'}$, and the second harmonic contains a $C_z^{'}$ specific response, the ratio of the harmonics yields V_{CPD} as described by (3.11):

$$V_{CPD} = \frac{V_{ac} X_{gain}}{4} \frac{A_\omega \cos(\varphi_\omega)}{A_{2\omega}}, \tag{3.11}$$

at a certain excitation voltage V_{ac} and upon knowing the cantilever transfer function gain, $X_{gain} = G(\omega)/G(2\omega)$. The phase (φ_ω) of the cantilever response at ω provides information on the polarity of V_{CPD}. It should be noted that in its initial implementation, DH-KPFM was performed using FM detection in UHV during FM-AFM imaging [102]. Building on this work, Kuo et al. [103], have recently achieved atomic resolution surface potential imaging using DH-KPFM in UHV in dual pass mode. This study was the first to realize atomic resolution imaging of Si (111)7 × 7 by dual pass mode and did so without the requirement for bias voltage regulation. Interestingly the authors further concluded that DH-KPFM is stable and suitable for high speed KPFM, as it avoids instability related to the bias feedback loop [103].

In general, DH-KPFM garnered little attention until several years after its first realization, when it was implemented under both ambient [105, 104] and liquid [49, 52, 53] environments. Indeed, the application of DH-KPFM in liquid was an exciting breakthrough which highlighted the opportunity for OL-KPFM approach for liquid measurements, an area discussed elsewhere in this book. Collins et al. [105] first extended this approach to ambient, by demonstrating simultaneously mapping of changes in surface potential and dielectric properties resulting from surface modification of ferroelectric thin films after poling by applying a dc bias to the tip in contact with the sample [105]. It was noted that both DH- and conventional KPFM measured similar relative surface potentials between positively and negatively poled domains on bismuth ferrite, however agreement between the techniques faltered when comparing absolute surface potentials [105]. This result was later corroborated in a separate study which found a similar offset when comparing work function measurements of graphene using DH and standard KPFM, discussed later in Fig. 3.7 [104]. It was suggested that these discrepancies in absolute surface potentials were due to the feedback effect, explaining why agreement between relative values was realized as described by (3.7). Recently, Polak et al. [66], demonstrated that, after careful calibration of parasitic signals for both cases, CPD measured by KPFM and DH-KPFM can be made independent of both frequency and amplitude of the excitation signal.

In a different, albeit related approach, Borgani et al. [87] configured multifrequency intermodulation (IM) AFM for measuring surface potentials. Intermodulation IM-EFM is operated during single pass imaging and consists of driving the cantilever with two pure drive tones, one drive used to mechanically actuate the cantilever and another to modulate the electrostatic force. A significant advantage of this method over DH-KPFM is its applicability to resonance excitation,

precluded in single frequency DH-KPFM due to complications in determining X_{gain} when the harmonics are positioned on the cantilever resonance frequency itself (i.e., indirect cross talk due to changes in the resonance peak). IM-EFM has been applied to spatially resolve photogeneration of charge in a photovoltaic thin film, and to investigate local charge injection and extraction on surface-modified Al_2O_3 nanoparticles in a low-density polyethylene matrix [88]. Since the responses of interest all lie close to the resonance frequency, this approach leads to increased signal to noise ratios over off resonance DH-KPFM and is expected to allow for higher spatial resolution as the tip is closer to the sample when operated in single pass.

3.5 Band Excitation KPFM

In recent years, many in the SPM community have shifted towards the capture of multidimensional datasets, which include additional information in either space, voltage and/or time dimensions (e.g. force volume imaging AFM [106–108], conductive AFM IV spectroscopy [109], switching [110] and relaxation [111] spectroscopy Piezoresponse Force Microscopy (PFM)). For many systems, conventional KPFM measurements only provide a snapshot of the system parameters, and often additional dynamic [89] or spatial [11] information on charge, voltage, and capacitive behavior is required. In particular, for electroactive systems or devices, capturing electrodynamics (e.g., charge migration, ion diffusion) requires multidimensional bias and time-resolved KPFM approaches [89, 93].

In addition, several obstacles have to be overcome for truly quantitative KPFM, including; (i) elimination of the influence of instrumentation on the measurement, especially the feedback effect, and (ii) overcoming the long range capacitive interactions between the probe (comprising tip apex, cone, cantilever) and the sample surface [112]. The former originates from non-idealities of the feedback or nulling approach adopted in KPFM, which is known to introduce artefacts into the measurement and even topographical crosstalk. The latter is a direct consequence of the long range nature of the electrostatic force, which results in contribution to the measured CPD not only by interactions at the tip apex, but also at the cone and cantilever beam [113]. Hence, the measured CPD is averaged over the entire probe and sample surface and therefore dependent on tip–sample separation [112].

The band excitation (BE) [114, 115] method is a generalization of traditional LIA-based techniques which allows parallel detection at multiple frequencies simultaneously. A comparison between single frequency (DH-KPFM) and BE in EFM/KPFM is shown in Fig. 3.1.

Unlike in single frequency techniques, in BE modes the excitation voltage of an amplitude, V_{ac}, is applied in a band of frequencies centered around the cantilever resonance frequency, ω_0. The signal in the time domain that is used to excite the cantilever is generated via inverse Fast Fourier Transformation (iFFT) from a digital

signal with predefined amplitude and phase content across a chosen range of frequencies. Simultaneously, the response within that frequency band is recorded using high-speed data acquisition techniques. The cantilever transfer function, i.e., the segment of the response–frequency curve around $\omega_{0,}$ can be obtained from the ratio of the Fourier transform (FFT) of the response and excitation signals. This curve is then collected at each spatial point (or each point of parameter space for complex spectroscopic imaging methods), at the rate comparable to classical lock-in detection.

For analysis of BE data, the response curve is transformed into classical physical observables. As a simplest version of such analysis, the cantilever response is fitted using a simple harmonic oscillator (SHO) model and can therefore be described by the three parameters: the resonance frequency, ω_0, the amplitude at the resonance, $A(\omega_0) = A_0$, and the quality factor, Q, as given by (3.12) and (3.13):

$$A(\omega) = \frac{A_{\max}\omega_0^2}{\sqrt{\left(\omega^2 - \omega_0^2\right)^2 + \left(\omega\omega_0/Q\right)^2}}, \tag{3.12}$$

$$\varphi(\omega) = \tan^{-1}\left(\frac{\omega\omega_0/Q}{\omega^2 - \omega_0^2}\right). \tag{3.13}$$

Maps of ω_0, A_0, φ and Q can be de-convoluted from the acquired response data and stored as images.

KPFM in BE mode has previously been performed by Guo et al. who demonstrated two different configurations. First, OL BE-KPFM [85], which is a bias spectroscopy measurement that results in 4D data set comprising amplitude response of the cantilever versus frequency, bias and XY positions and was used to quantify electronic properties. Secondly, half harmonic BE (HHBE)-KPFM [116], in which two 3D BE data sets, corresponding to the first and second harmonic amplitudes versus frequency and XY positions at fixed dc tip biases are collected. Subsequently, Collins et al. [112], extended the OLBE-KPFM approach to allow force volume mode enabling the capture of the 3D spatial variation in the long range interactions as well as separating conservative and dissipative electrostatic interactions simultaneously. Later the OLBE-KPFM approach was further improved by adopting photothermal excitation of the cantilever leading to higher sensitivity to the force gradient as in FM-KPFM and improved spatial resolution compared to force detection [86].

3.5.1 Open Loop BE-KPFM

In OLBE-KPFM [85], a sequence of BE pulses with varying dc voltage offset is applied to probe the first harmonic response (Fig. 3.2a). Using high speed data acquisition techniques, the full cantilever response is collected as the tip scans

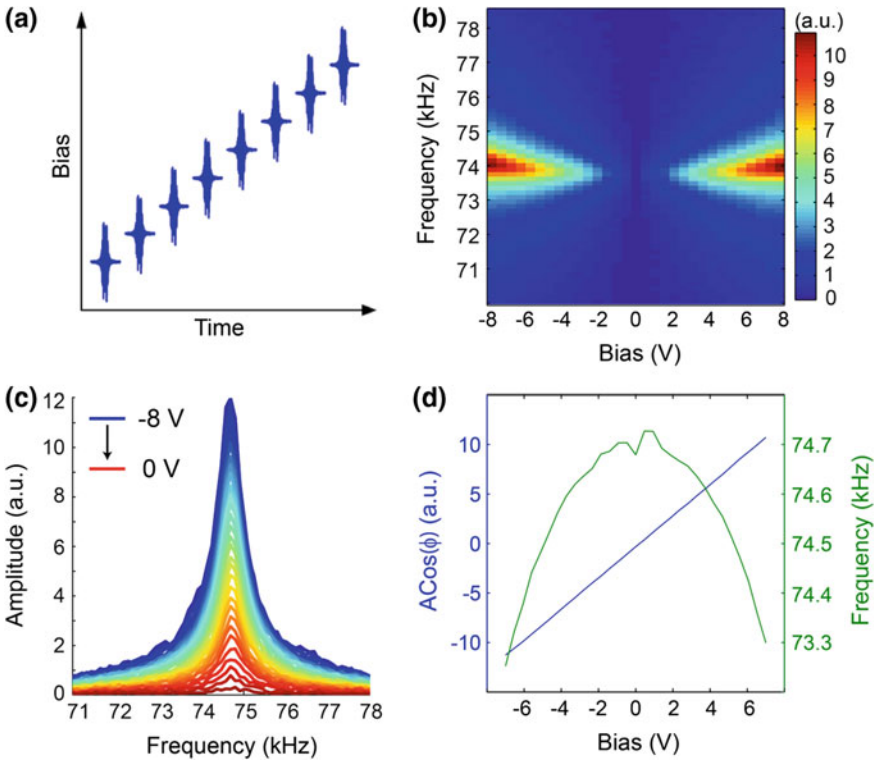

Fig. 3.2 BE-KPFM operating principle. **a** Sequence of band excitation pulses with linearly increasing dc voltage offset. **b** Cantilever response amplitude as a function of frequency and bias. **c** Cantilever response amplitude as a function of frequency at negative dc voltage values. **d** Mixed amplitude response (left y-axis) and resonance frequency (right y-axis) versus applied bias [112]

across the sample in lift mode and stored as amplitude and phase data versus frequency and bias at each XY position. The amplitude response as a function of frequency and bias is shown in Fig. 3.2b, c for a single point measurement acquired 10 nm above the surface of a freshly cleaved highly ordered pyrolytic graphite (HOPG) surface. This 2D data provides information on the cantilever transfer function near the mechanical resonance frequency as well as on the electrostatic forces acting between tip and sample surface.

Figure 3.2c shows a strong bias dependence of the recorded response amplitude versus frequency for negative bias values. The values for $A_0\ cos(\varphi)$ and ω_0 obtained from SHO fitting are shown in Fig. 3.2d as a function of bias [112], where $A_0\ cos(\varphi)$ is a linear function of bias, while ω_0 exhibits a parabolic bias dependence. Therefore, BE-KPFM is sensitive to the electrostatic force and the force gradient simultaneously, combining the advantages inherent in both AM- and FM-KPFM [112]. Note that the relative noise in $\omega_0(V)$ is larger in the vicinity of the nulling potential, as a result of smaller response amplitudes.

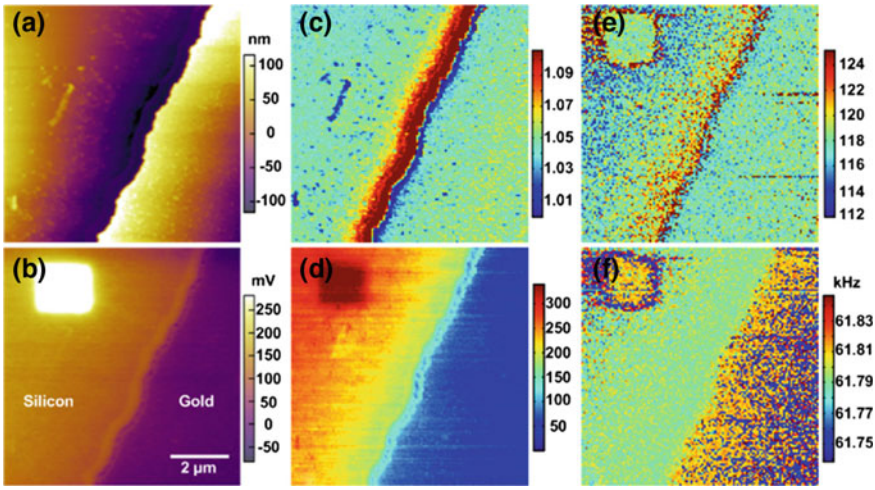

Fig. 3.3 **a** Topography and **b** KPFM image (zero-order flattened) of charge-written Au/Si surface. OL-BE-KPFM images of **c** slope and **d** nulling potential. Maps of **e** Q factor and **f** resonance frequency upon averaging for all biases (© IOP Publishing. Reproduced with permission. All rights reserved) [85]

OLBE-KPFM imaging of an Au/Si sample with a charge-written pattern on Si containing contrast in topography (step edge), work function (Au vs. Si) and charge, is shown in Fig. 3.3. The topography and corresponding classical AM-KPFM images are provided in Fig. 3.3a, b. An advantage of capturing the bias dependence at each location is that the capacitance gradient channel can be assessed, as shown in Fig. 3.3c, clearly illustrating changes in tip-sample capacitance gradient at the step edge due to the interactions between the tip and the side wall. The nulling potential of the amplitude response, Fig. 3.3d, demonstrates similar contrast and CPD values as AM-KPFM, however, an absolute offset is observed between the two approaches, in agreement with several other studies comparing KPFM approaches [105, 104].

In a different study, OLBE-KPFM was combined with switching spectroscopy (SS)-PFM by Li et al. [117], yielding quantitative information about the surface charge state during polarization switching. In this way, OLBE-KPFM was used as a complementary measurement to the electromechanical characteristics studied with SS-PFM. As a proof of principle, correlations between switching properties and surface potentials of two samples, a single crystal Pb-based relaxor material (PIMNT) and a $BiFeO_3$ ferroelectric thin film were demonstrated, as shown in Fig. 3.4.

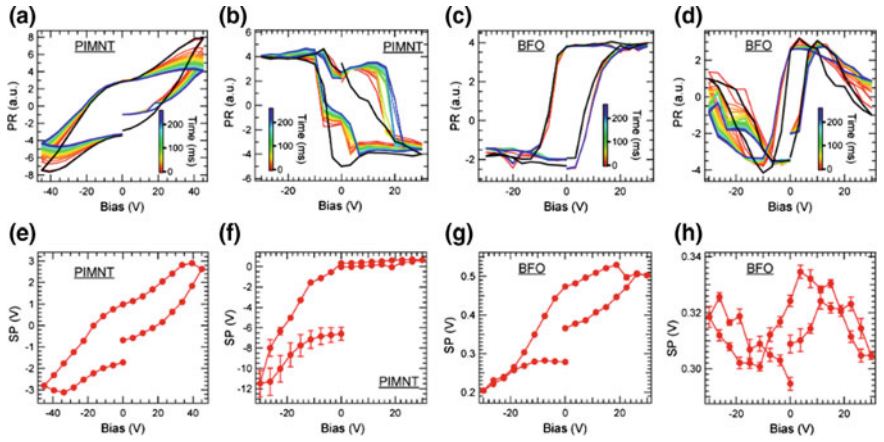

Fig. 3.4 **a–d** Dynamic switching spectroscopy and **e–h** Surface potential loops for [111]-PIMNT single crystals and BFO thin films. The switching and surface potential loops were measured at the sample locations (tip height ~200 nm for surface potential measurement). Reprinted from Li et al. [117], with the permission of AIP Publishing

3.5.2 Half Harmonic BE-KPFM

In HHBE-KPFM [116] the BE method is applied in a dc bias free, or constant bias approach to KPFM. The idea is similar to dual harmonic-KPFM [104], but in a multifrequency embodiment. In comparison to single frequency DH-KPFM, HHBE has many advantages including resonance enhancement as well as direct transfer function correction [116]. The basic principles are illustrated in Fig. 3.5. In previously discussed BE techniques, cantilever excitation and response acquisition are performed within the same frequency band centered around the resonance, ω_0. Therefore, the second harmonic response centered at $2\omega_0$ is not detected. In order to measure the second harmonic response, an electrical BE drive centered at half the resonance frequency $\omega_0/2$ is applied to the cantilever. Consequently, the second harmonic response lies in the frequency band around the first harmonic resonance (referred to as half BE (HBE)). For each image pixel, BE and HBE excitation pulses are applied sequentially. In this way, first and second harmonic response components fall within the frequency band of the cantilever transfer function and $X_{gain} = 1$, which allows for direct comparison. From the ratio of measured BE and HBE signals, the CPD image can be obtained as $V_{CPD} = V_{dc} - V_{ac}/4 \cdot A_{BE}(\omega)/A_{HBE}(\omega)$, where all parameters are now known from the experiment.

Aside from quantification of CPD without application of dc bias, as well as obviating the requirement for correction of the cantilever transfer function, access to the full SHO parameters can provide an additional level of information unavailable in standard KPFM. For example, it is known that the presence of a capacitive force in AM-KPFM will result in resonance frequency shifts due to electrostatic tip-surface interactions, as employed in FM-KPFM. Furthermore, the Q-factor of

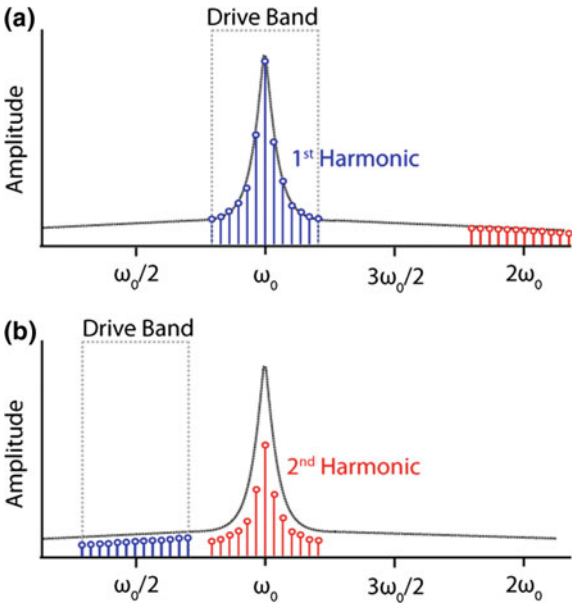

Fig. 3.5 Operation principle of HHBE-KPFM. **a** Electrical drive in BE comprises a band of frequencies around a center ω_0, the first harmonic response is acquired within the same band whereas the second harmonic response at $2\omega_0$ does not fall within the detected bandwidth. **b** HBE excitation at $\omega_0/2$ is applied sequentially upon recording the response at the second harmonic frequency in the frequency (doubled) band centered around ω_0. Consequently, response signals at first and second harmonic frequencies fall within the same frequency band (© IOP Publishing. Reproduced with permission. All rights reserved) [104]

the cantilever response contains information on the dissipation processes in the tip-surface system. Voltage spectroscopy in BE and HBE-KPFM modes are demonstrated as a method to uncover hidden bias dependent material properties. In Fig. 3.6, HBE amplitude, resonance frequency, and Q-factor images at $V_{dc} = 7$ V are shown. Note that the resonance frequency image shows clear topographic and charge contrast. The bias dependence of the resonance frequency is further illustrated in Fig. 3.6d and exhibits a parabolic dependence for small biases. Deviations from this quadratic dependence were assigned to parasitic static electrostatic forces and associated changes in tip-surface separation.

As a further development of this approach, Collins et al. [104], performed a quantitative analysis of work function measurements recorded using open loop (DH-KPFM and HHBE-KPFM) and closed loop (AM-KPFM) KPFM techniques. All measurements were conducted on the sample location over Al_2O_3-coated single layer graphene, which exhibited a large defect across the width of the hexagon structure, on a copper electrode [104]. While the values for the CPD measured in DH-KPFM and HHBE-KPFM were shown to agree, an offset of 55 mV was observed between OL and CL techniques. Meanwhile, all techniques showed a

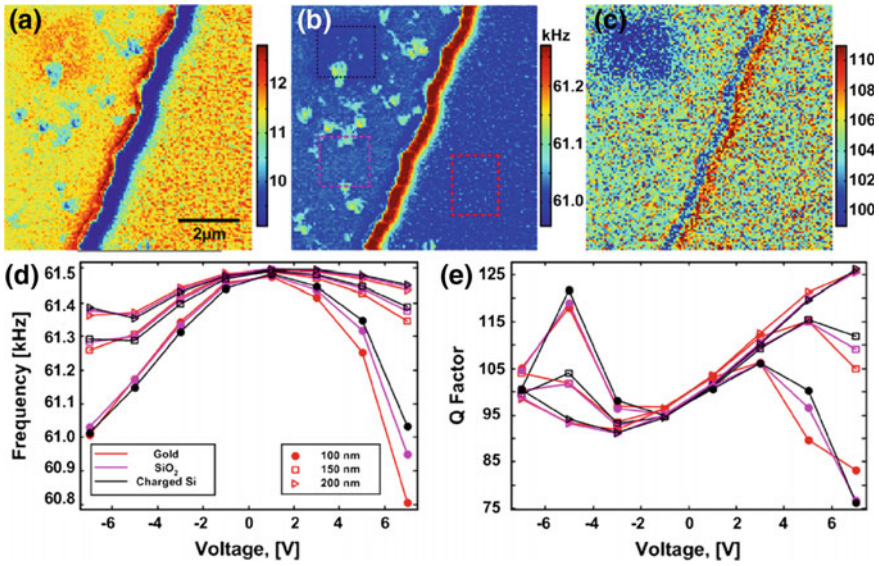

Fig. 3.6 **a** HBE amplitude (arbitrary unit), **b** frequency, and **c** Q-factor at static tip bias of 7 V_{dc} and 100 nm lift height. **d** Frequency dependence on static tip biases and lift heights. **e** Q-factor dependence on static tip biases and lift heights. Reprinted from Guo et al., with the permission of AIP Publishing [116]

CPD difference of ~120 mV between the Al_2O_3-coated graphene and the Al_2O_3-coated Cu substrate (see Fig. 3.7d). The offset between techniques was attributed to feedback effects, as described previously [104].

3.5.3 Photothermal BE-KPFM

Attempting to improve the bias sensitivity to the electrostatic force gradient, photothermal BE (PthBE)-KPFM was developed [86]. Figure 3.8 shows a schematic illustrating the differences between OLBE and PthBE-KPFM setups. Common to both is dc bias pulses applied to the conductive cantilever. BE waveforms are used to detect the resultant changes in the dynamic cantilever response by recording the resonance peak of the oscillating cantilever. The difference between OLBE-KPFM and PthBE-KPFM is the excitation mode, i.e., where the BE signal is supplied for excitation. In OLBE-KPFM, the BE excitation waveform is applied as a voltage directly to the conductive probe, as shown in Fig. 3.8a. Conversely, in PthBE-KPFM, the BE waveform is used to modulate the laser focused on the cantilever base, resulting in actuation of the cantilever due to the photothermal effect.

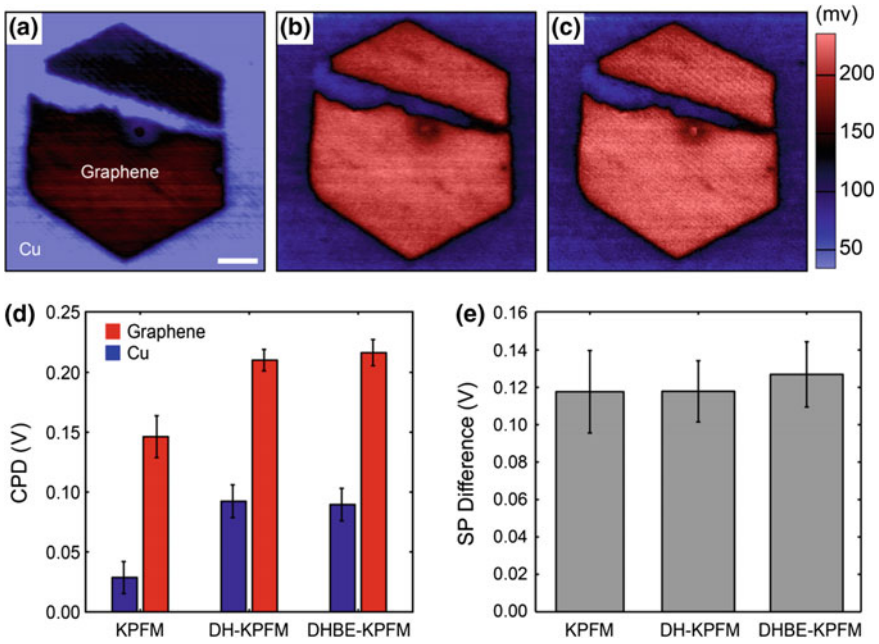

Fig. 3.7 CPD maps of a single hexagonal graphene layer obtained with **a** KPFM, **b** DH-KPFM, and **c** HHBE-KPFM (vertical scale = 200 mV, offset = +135 mV for all images). Bar chart for **d** CPD (mean ± std. dev.) for graphene and Cu and **e** the SP difference (mean ± std. dev.) for measurements using CL-KFPM, DH-KPFM, and HHBE-KPFM (© IOP Publishing. Reproduced with permission. All rights reserved) [104]

When relying on capacitive actuation of the cantilever, the response becomes increasingly smaller approaching the CPD, eventually vanishing at V_{CPD} as shown in Fig. 3.8b. The small amplitude at bias values close to zero can decrease the accuracy of the SHO fitting procedure used to determine the resonance frequency which is why large deviations in frequency can be observed. On the contrary, photothermal actuation is very sensitive to the electrostatic force gradient, and capable of detecting small changes in resonance frequency at bias values close to the CPD in comparison to OLBE-KPFM. PthBE-KPFM imaging was demonstrated on a model sample combining topographic, material, and charge contrast, as shown in Fig. 3.9. A region of positive charge is written on the SiOx surface using bias lithography by scanning a tip biased with 9 V in contact mode at a scan rate of 0.5 Hz within an area of 1.5 μm [2] indicated in Fig. 3.9a. PthBE-KPFM was shown to allow for a more localized probing of the true CPD compared to AM-KPFM as well as having the added benefit of containing information related to local dielectric properties and electronic dissipation between tip and sample accessible through subtle changes in amplitude and Q maps [86].

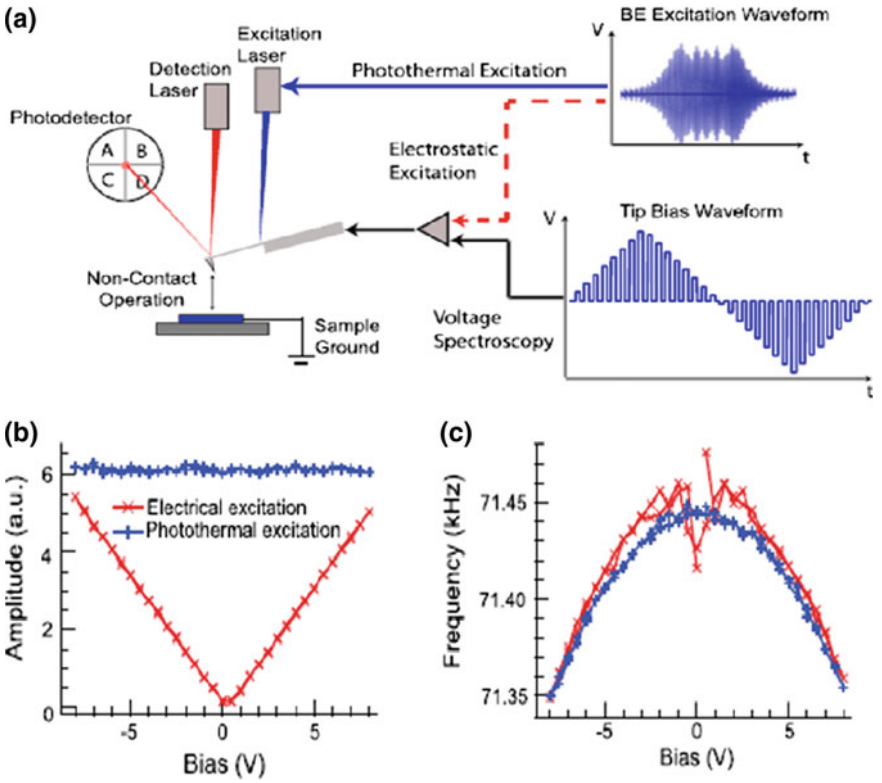

Fig. 3.8 **a** Schematic of the working principle of OLBE (red dashed line) and PthBE (blue line)—KPFM utilizing electrostatic and photothermal excitation of the cantilever, respectively. In this case, voltage spectroscopy is performed using a dc bipolar square wave applied between a conductive probe and sample. Bias dependence of **b** cantilever response amplitude and **c** resonance frequency for OLBE (red line) and PthBE (blue line)—KPFM, respectively. Reprinted from Collins et al. [86], with the permission of AIP Publishing

3.5.4 Force Volume BE-KPFM

A major consideration when studying electrostatic forces is the long-range nature of the interaction. This poses a complication regarding the interpretation of KPFM measurements, and ultimately limits the maximum achievable resolution of the technique. The dependence of tip-sample interactions on the distance has prompted research into the development of 3D mapping techniques where apart from variations in the XY plane also the influence of the tip-sample distance is captured. Wang et al. [117] first developed 3D-KPFM to characterize the in-plane piezoelectric potential of ZnO nanowires that were laterally deflected. This technique was developed to eliminate artifacts imposed by the high topographical variations that occur along the edges of micro/nanowires, which made characterization by

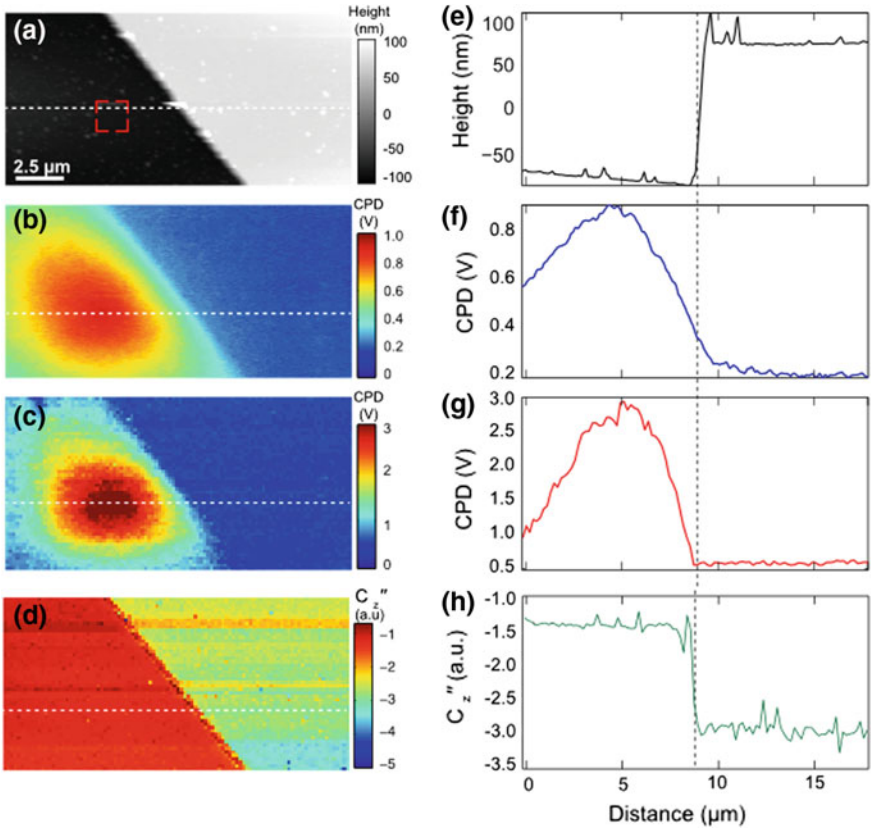

Fig. 3.9 **a** AFM tapping mode topography image of a SiO_x/Au boundary collected after charging a 1.5 µm area of SiOx as indicated with the dashed red box. KPFM maps of the CPD collected using **b** standard AM-KPFM (lift height = 50 nm) and **c** PthBE-KPFM (lift height = 50 nm) and **d** C_z'' obtained from PthBE-KPFM data. **e**–**h** Cross sections taken from areas indicated by dashed white lines in (**a**)–(**d**), respectively. Reprinted from Collins et al. [86], with the permission of AIP Publishing

conventional KPFM inappropriate or impossible. However, since their setup relied on bias feedback, parasitic contributions to the measured tip-sample profile can be expected as a result of the feedback effect [85, 112].

This limitation was overcome through the development of force volume (FV) BE-KPFM [112], where instead of raster scanning in the surface plane, the measurement is performed as a function of distance for each position on a dense grid of points. In FVBE-KPFM a 5D data set is captured, which contains response versus frequency, bias, and position (X, Y, Z). An example of a bias versus distance spectroscopy measurement showing both amplitude and frequency is given in Fig. 3.10a and b respectively for a single location on the Si substrate as indicated by the star symbol in Fig. 3.10c. The resulting multidimensional data can be

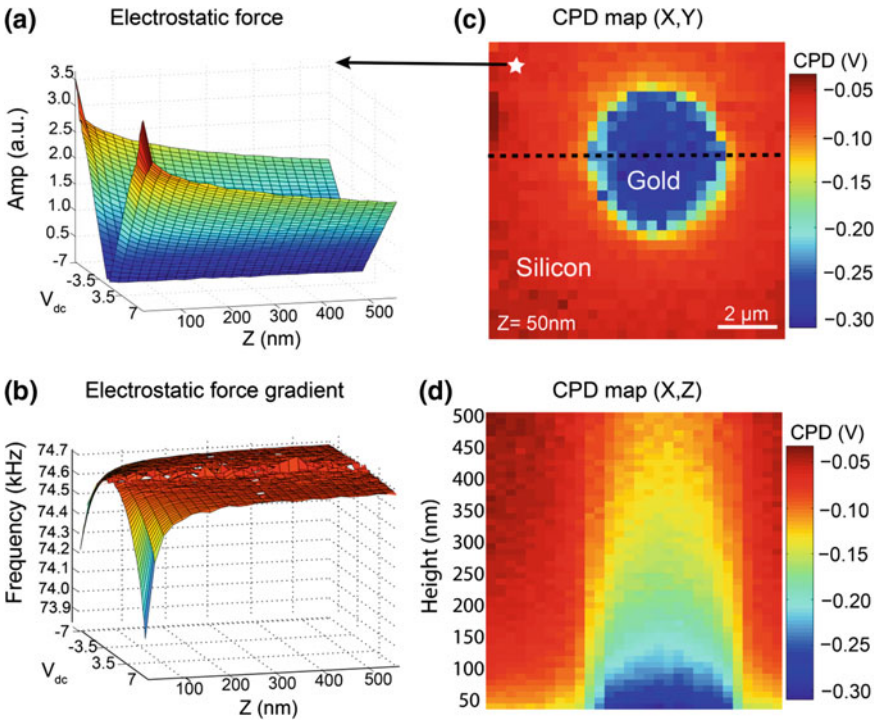

Fig. 3.10 Force volume BE-KPFM 3D CPD mapping. Single point **a** electrostatic force and **b** electrostatic force gradient measurement as a function of tip sample distance (Z). Spatial mapping of the CPD in the **c** X-Y plane (Z = 50 nm) and the **d** X-Z plane (X plane indicated by a dashed black line in image (**c**)) determined from fitting to the electrostatic force of a 45 × 45 × 50 (X, Y, Z) grid recorded on a gold/silicon test structure [112]

compressed by fitting the bias dependence of the electrostatic force (linear) and the electrostatic force gradient (parabolic). The set of fitting parameters allows to obtain the 3D CPD and the capacitance gradient from the electrostatic force and force gradient, respectively. Notably, these measurements also provide two independent methods to determine the capacitance gradient through evaluation of either the distance or bias dependence. Figure 3.10c, d depict maps of the CPD for a single XY plane from a 45 × 45 × 50 grid, allowing to access a plethora of information on the overall interactions between tip and sample present in KPFM measurements. In this regard, FVBE-KPFM can provide useful insight between KPFM experiments and modelling and potentially be used to completely de-convolute the effect of the probe geometry.

3.6 Time Resolved KPFM

While classical KPFM methods have seen extraordinary success in the characterization of static or quasi-static processes, the measured potential is averaged over the pixel measurement time, and hence mask much of the relevant information on dynamic processes taking place below these timescales. The importance of probing system kinetics for understanding material and device functionality has recently been highlighted by the KPFM community. The result of which is the sharp rise in novel modes of KPFM, or related techniques, to achieve local time-resolved analysis of the surface potential, charge or ionic transport phenomena. Such methods offer insight beyond the time averaged CPD, on fast local charging, or ion dynamics and have demonstrated their usefulness in measuring time dependent ionic transport in lateral devices [118], surface photo-voltage and charge carrier generation [56, 92], as well as charge screening and ion dynamics at the solid-liquid interface [49, 51].

Sadewasser et al. [119] and the group of Ginger [56] made the first great strides in the development of time resolved SPM measurements for studying optoelectronic properties of thin film solar cells. In tr-EFM, upon illumination of the sample, charge carriers in the photovoltaic material are generated by the photoelectric effect. The resulting accumulation of charge, changes the electrostatic force gradient. In the first implementation of tr-EFM, the force gradient was indirectly detected by continuous capture of changes in the resonance frequency shift using a PLL and home built detection platform. This approach allowed measurements of transient events on spatial/time resolution of ~100 nm/~100 μs [56, 92]. tr-EFM has been demonstrated to be particular useful towards obtaining local quantum efficiency maps as a function of material properties and preparation [56], degradation [92, 120], and excitation wavelength [120].

In more recent work by the same group [57, 58], the time resolution was pushed to sub microsecond achieved by adopting an open loop approach. In fast free (FF) tr-EFM [58] the cantilever oscillation is digitized while triggering a light pulse that initiates local dynamics of interest. Instead of heterodyne detection, the cantilever motion is analyzed by demodulating the digitized cantilever signal numerically and the instantaneous phase (and instantaneous frequency) is extracted via a Hilbert transform of the cantilever position versus time. This approach was shown to be capable of discerning local dynamics with short transient rise times of ~100–200 ns and in certain implementations, sub cycle detection of dynamic events was achieved. Unfortunately, tr-EFM, as the name suggests, cannot be used for quantification of the surface potential or surface photovoltage, as this parameter is lost in favor of information on recombination rates for postulated physical mechanisms [58].

Strelcov et al., developed a time resolved (tr)-KPFM which allows detection of surface potential with submicron spatial resolution, on modest timescales between ten milliseconds to tens of seconds [89]. This approach allows separation of surface versus bulk ionic activity on insulating surfaces, where current flow is well below

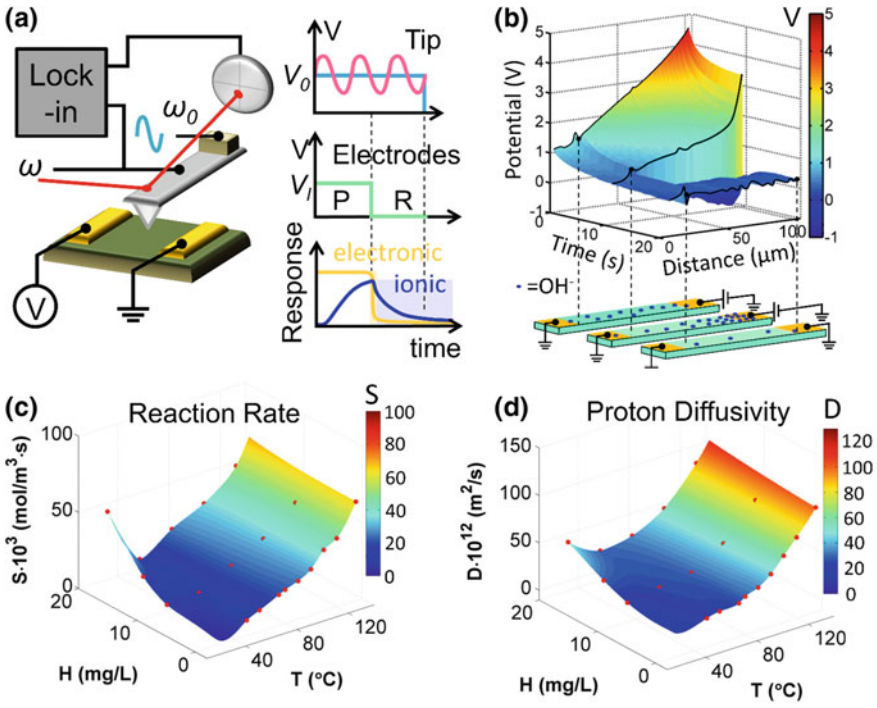

Fig. 3.11 Time-resolved KPFM: **a** A schematic of tr-KPFM method showing a sample with two lateral electrodes. Oscillations of the AFM tip are influenced by local CPD and monitored via a lock-in amplifier. Graphs on the right display voltages applied to the tip and electrodes during the polarization (P) and relaxation (R) periods. Separation of electronic and ionic responses is possible due to the difference in their time constants. **b** An example of tr-KPFM response in a Ca-doped $BiFeO_3$ sample. CPD (averaged over dimension parallel to electrodes) as a function of interelectrode distance and time changes as negative surface ions (presumably, adsorbed OH-groups) are re-distributed in response to applied lateral electric field. **c**, **d** Modeling the measured tr-KPFM response allows separation of different contributing mechanisms. Here, phase diagrams show how water splitting reaction rate and proton diffusivity in nanostructured ceria thin film change as a function of temperature and air humidity. ((**b**) with permission from Strelcov et al. [89] Copyright 2013 American Chemical Society. (**c**, **d**) Adapted from © IOP Publishing. Reproduced with permission. All rights reserved) [121]

the detection limit of modern current amplifiers (Fig. 3.11a, b). tr-KPFM has been demonstrated on memristive and ferroelectric samples revealing the details of polarization switching [89, 90]. More recently, it has been proven useful in probing electrochemical reactions on platforms consisting of nanostructured ceria where the surface potential change over time could be attributed to the transport of protons and hydroxyl groups [91]. Modeling of tr-KPFM responses in this system allowed determination [121] of different contributing mechanisms and extraction of relevant electrochemical parameters (such as water splitting reaction rate and proton diffusivity on ceria surfaces) from the tr-KPFM data (Fig. 3.11c, d).

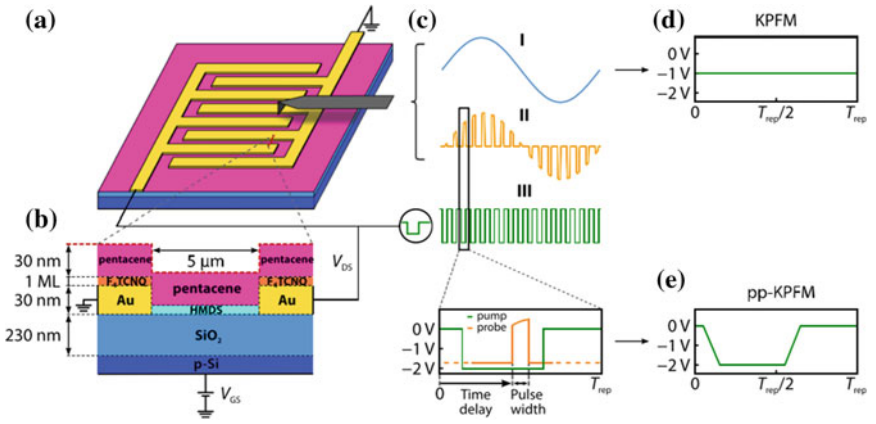

Fig. 3.12 **a** Schematic describing the operation of PP-KPFM on a pentacene-based bottom-gate organic field effect transistor (OFET). **b** Cross-sectional view across the OFET transport channel displaying the different fabrication layers. **c** In pp-KPFM fast electrical pulses with a slower sinusoidal envelope (signal II) is used. The electrical pump pulses (signal III) are synced with the pp-KPFM tip excitation and applied to the device in order to measure surface potential dynamics. **d** Standard KPFM does not resolve the dynamics providing only the time averaged surface potential, whereas **e** the dynamics can be resolved by pp-KPFM. Reprinted from Murawski et al. [94], with the permission of AIP Publishing

In a different, albeit related approach, Murawski et al. developed Pump-probe (pp)-KPFM [93] to simultaneously measure the time averaged CPD with nanosecond changes in surface charge. As shown in Fig. 3.12, short probing pulses are modulated by a slower sinusoidal envelope, and synchronized to electric pump pulses applied to the device under investigation. This scheme allows tracking charge carriers injected into the transport channel where the achievable time resolution is determined by the width of the probe pulses. A second KPFM loop is used to minimize the average electrostatic force, at the same time, providing a measure of the time-averaged potential distribution as in classical KPFM. This method allows for spatial mapping of "speed bumps" in organic field-effect transition devices [94].

Sugawara et al. [78] developed Heterodyne (H)-KPFM. This method is based on the heterodyne (i.e., frequency conversion) and AM detection of the electrostatic force, where mixing products are generated by excitation at the first cantilever resonance and some other driving frequency far from resonance. This approach retains the potential sensitivity of AM-KPFM but having the improved spatial resolution normally afforded by FM-KPFM [78, 80]. Furthermore, Garrett et al., demonstrated that H-KPFM enables much faster measurements compared to conventional KPFM [79], allowing capture of several frames per minute in air. The fast scanning capability was harnessed to quantify voltage dynamics of perovskite solar cells using H-KPFM under illumination and post illumination conditions, Fig. 3.13. In this way H-KPFM was used to quantify local variation in the nanoscale surface

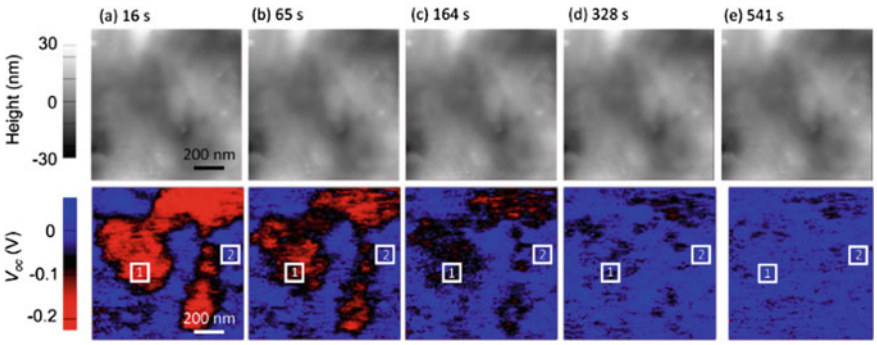

Fig. 3.13 Spatial and temporal variation of the residual photogenerated voltage within perovskite solar cells consisting of a $CH_3NH_3PbI_3$ and a [6,6]-phenyl C61-butyric acid methyl ester layer. Topography and V_{oc} scans recorded after the solar cell is illuminated and brought back to dark conditions after **a** 16, **b** 65, **c** 164, **d** 328, and **e** 541 s. Reprinted with permission from Garrett et al. [122]. Copyright 2017 American Chemical Society

photovoltage as well as capturing its time dependent evolution, providing information on light induced ion migration [122]. Chapter 5 by Sadewasser et al. in this book provides a further detailed description of time-resolved EFM and KPFM techniques.

3.7 G-Mode KPFM

The traditional KPFM techniques rely on either LIA or PLL detection, which has the effect of limiting both the information captured (i.e., attenuation of all response outside detection frequency) as well as imposing bandwidth limitations (i.e., LIA time constant). The BE methods simultaneously detects responses at multiple harmonics, enabling fast response function methods. However, both single frequency and BE ignore non-harmonic response such as electrical transients, intermodulation products, and spurious topographic changes.

In 2015, general acquisition mode (G-Mode) SPM was developed [59]. G-Mode is based on rapid capture of the full data stream from the photodetector, allowing to explore the full cantilever deflection spectrum with extremely high time resolution. In the short time since its inception, the G-Mode approach has been shown to have advantages for tapping mode AFM [59], PFM [123, 124], magnetic force microscopy (MFM) [60] and KPFM [60–62, 125].

In G-Mode KPFM, as depicted in Fig. 3.14, the AFM photodetector signal is captured, stored, and compressed at the sampling rate limit (~4–10 MHz). Combining full data acquisition with adaptive filtering and statistical cleaning methods (e.g., principal component analysis [126, 127]) has been shown to be an effective method for recovering densely sampled acquisitions of the dynamic cantilever

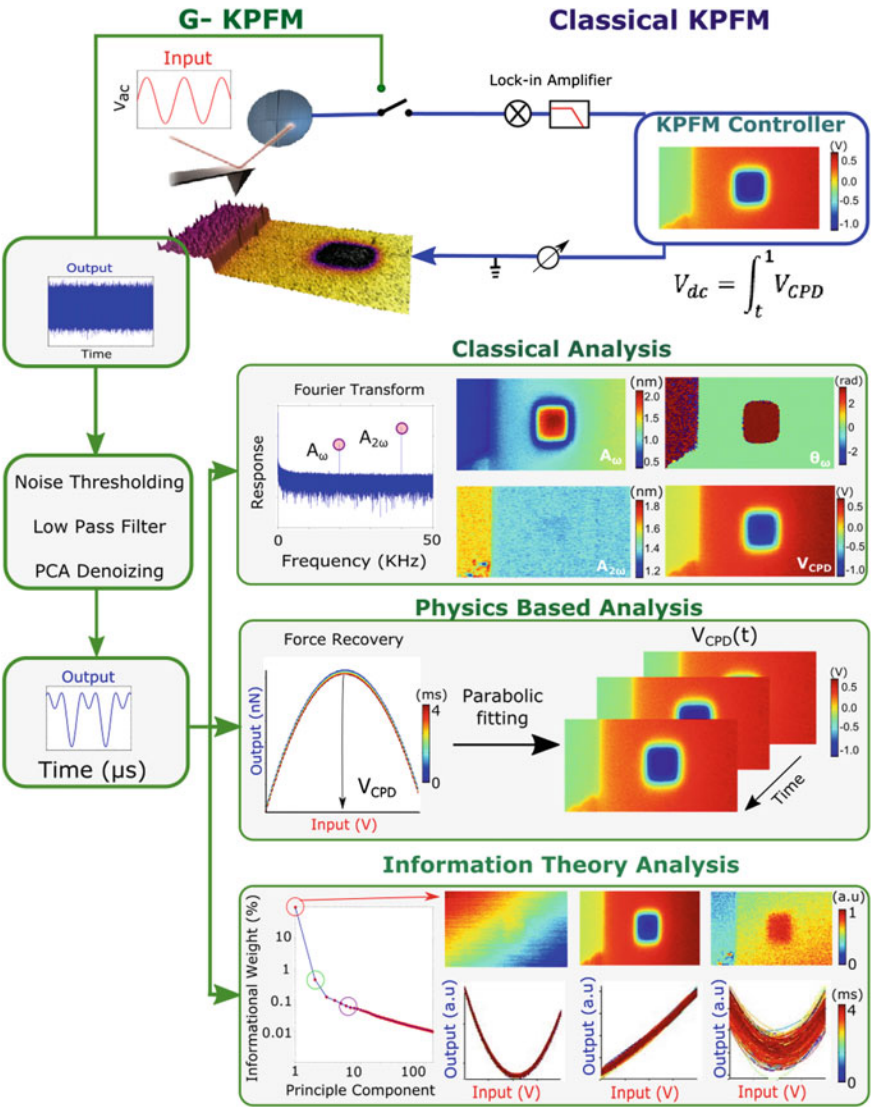

Fig. 3.14 Principles of G-Mode SPM. G-mode captures the complete raw signal from the photodetector thereby adding the time dimension for each spatial pixel. After compression and storing the data it can be analysed by several different approaches including classical analysis using digital demodulation, physics based analysis by recovery of the force in real space, or data mining using information theory analysis

trajectory. Already several analysis methods have been implemented, including emulation of conventional LIA methods using software based approaches [60, 61], as well as physics- [125] and information-based [128] analysis. All of which have

been used to extract quantitative measurements of electronic properties (i.e. surface potential and capacitance gradient) as well as data mining the cantilever response for additional hidden information.

3.7.1 Classical Analysis Approach: Digital Heterodyne Detection

G-Mode KPFM is based on complete information recovery in a wide frequency band comprising all present harmonics. Figure 3.15a shows the response measured above a single spatial location upon modulating the applied dc sample bias with a triangular waveform captured in G-Mode KPFM. While in Fig. 3.15a, only response for a frequency range between 0 and 120 kHz is shown for illustration purposes, the response spectra are stored up to 4 MHz (or even 100 MHz). Measuring and storing entire spectrograms at each pixel allows examination of the cantilever response separately for each frequency, without the requirement of multiple LIA or the need to repeat measurements with different LIA settings. The ratio of the response FFT to the FFT input signal at a given frequency yields the cantilever response amplitude and phase like conventional LIA techniques described in (3.8). The amplitude (and phase) responses of the electrostatic components at dc (A_{dc}), the drive frequency (A_{ω}) and twice the drive frequency ($A_{2\omega}$) are captured using G-Mode as a function of V_{dc} (and V_{ac}) as shown in Fig. 3.15b–d. The A_{dc} component exhibits a parabolic bias dependence and the local maximum coincides with the CPD. The first harmonic response (A_{ω}) is a linear function of the applied bias and the local minimum corresponds to the CPD (Fig. 3.15c). The second harmonic response ($A_{2\omega}$) does not show any bias dependence (Fig. 3.15d).

In comparison to traditional KPFM, the G-Mode KPFM data (i.e. by digital LIA detection) was shown to have significant advantages in terms of increased flexibility in data exploration across frequency, time, space, and noise domains [62]. The capabilities of G-Mode KPFM are highlighted in Fig. 3.16, on a Si sample with a top oxide layer and Au (100 nm) and Pt (20 nm) electrodes. In Fig. 3.16a, b, topography and CPD obtained with conventional closed loop KPFM is shown. Figure 3.16c, d depicts maps of capacitance gradient signal and CPD extracted using G-Mode KPFM. As stated, the second harmonic amplitude channel, Fig. 3.16c, is related only to the capacitance gradient, affected by topography as well as dielectric properties. In this instance, this information channel yields the ability to clearly separate metal electrodes and silicon oxide substrate, however, no difference between Au and Pt are observed. It has been demonstrated that by using this response, in combination with finite element modelling of the cantilever tip shape, allows for precise quantification of the dielectric properties [129]. The G-KPFM CPD image, determined using (3.11), is shown in Fig. 3.16d. Gaussian fitting of the data from a 2 μm^2 area was used to show that the mean and standard deviations for Au and Si were within error for both KPFM techniques,

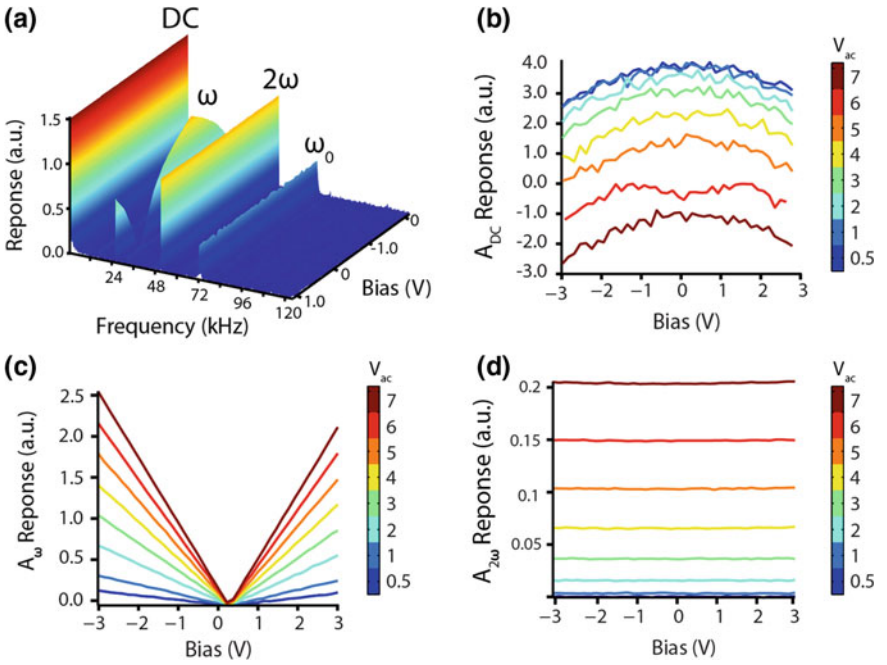

Fig. 3.15 Response as a function of bias in point spectroscopy G-Mode KPFM. **a** Response spectrogram versus bias measured at a single spatial location. Bias dependence of **b** dc, **c** first and **d** second harmonic response as a function of V_{ac} obtained with a digital LIA procedure. (© IOP Publishing. Reproduced with permission. All rights reserved) [62]

Au (385 ± 6 mV, 398 ± 6 mV) and Si (503 ± 8 mV and 509 ± 7 mV) respectively. Figure 3.16e, f demonstrates the additional flexibility provided by G-Mode KPFM regarding optimization of measurement noise. As shown in Fig. 3.16e, f, permanently recording the data stream in G-KPFM allows for systematic adjustment of filtering parameters until optimal noise levels have been achieved, without risking loss of information or reductions in spatial resolution. This de-noising advantage of G-Mode KPFM can even be further extended at the post processing stage using multivariate statistical methods for removal of unwanted noise.

Collins et al. [62] also highlighted increased flexibility and greater control over the frequency/time and spatial domains achieved using G-KPFM, as shown in Fig. 3.17. In G-Mode, each pixel is associated with a response spectrogram whose length is determined by the pixel time and the sampling rate. Therefore, the signal-to-noise ratio and/or frequency resolution of the frequency response vector can be traded off for a higher spatial resolution in the fast scan axis. However, in the slow scanning direction there is no additional response sampling and therefore flexible resolution cannot be obtained in that dimension. Figure 3.17a shows, an image of the capacitance gradient and a zoomed inset displaying a particle that exhibits differences in dielectric properties compared to the background.

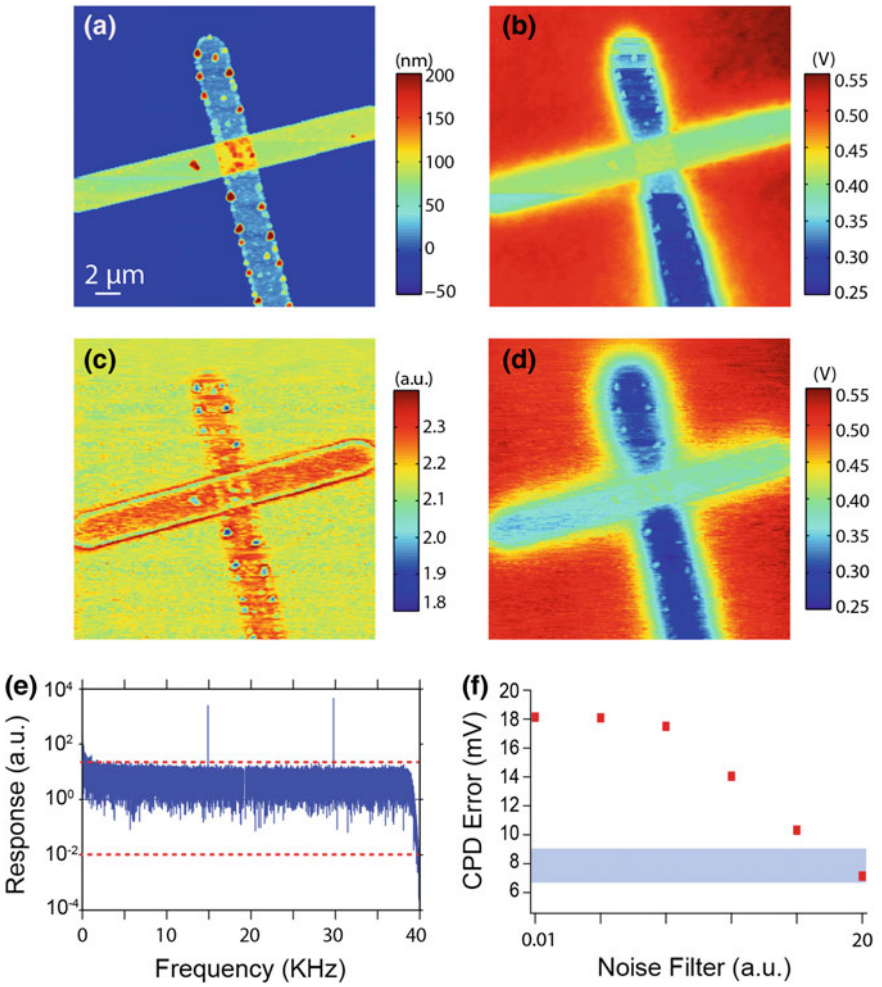

Fig. 3.16 G-Mode KPFM measurements on Au/Pt/Si sample. Conventional closed loop KPFM **a** topography and **b** CPD images. G-Mode KPFM maps of **c** second harmonic response and **d** CPD determined from (3.11). **e** Single pixel power spectrum with red dashed lines indicating the range of noise threshold. **f** CPD error values using varying noise thresholds for (**c**), blue band represents comparison with conventional KPFM (© IOP Publishing. Reproduced with permission. All rights reserved) [62]

Figure 3.17b–d illustrates an example of multiresolution imaging showing the same particle at 256 × 512, 256 × 1024 and 256 × 2048 pixel resolution, respectively. In the original low pixel density image, a single pixel defines the particle boundary whereas in the higher resolution images a varying gradient across several pixels is observed across the boundary. This flexible type of data exploration is only possible through access to a stored photodetector data stream and notably this

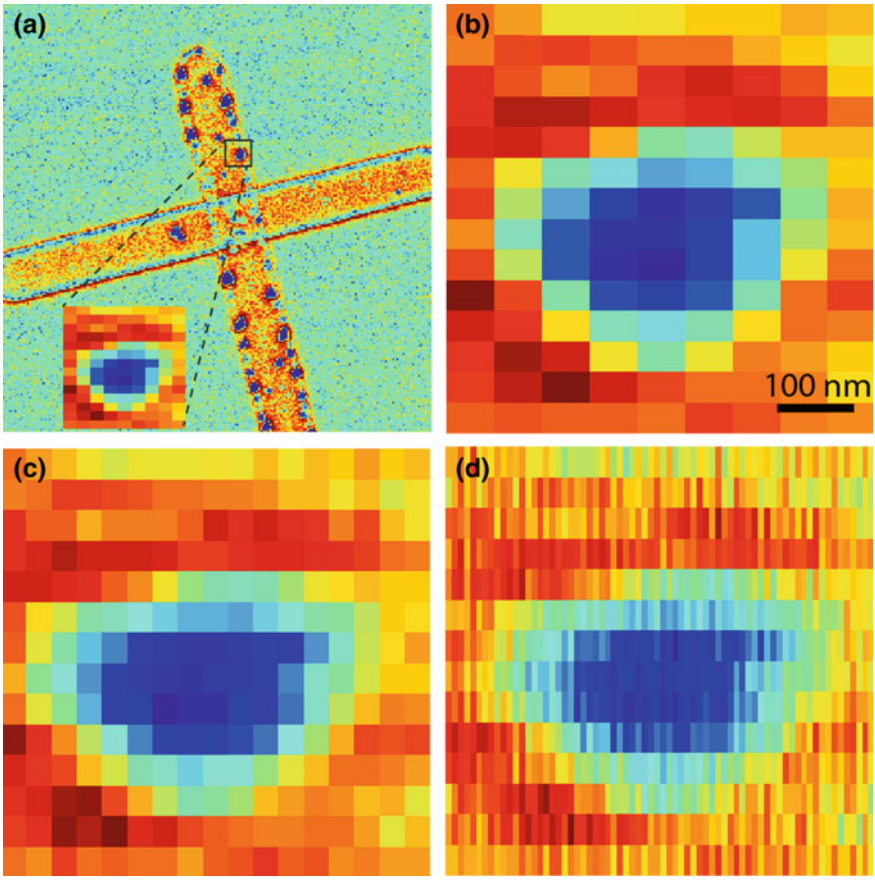

Fig. 3.17 Multiresolution G-Mode KPFM. **a** A 256 × 256 map of the obtained capacitance gradient, particle exhibiting variation in dielectric properties shown in inset. Area of interest depicted in (**a**) shown at different resolutions of **b** 256, **c** 1024, and **d** 2048 pixels along the fast scan axis (© IOP Publishing. Reproduced with permission. All rights reserved) [62]

analysis can be performed without ever changing the original data set. In conventional KPFM several measurements would be necessary to obtain different resolutions.

The additional information channels afforded by G-Mode have been further leveraged to simultaneously probe magnetic and electrostatic properties of the high entropy (HEA) alloy CoFeMnNiSn [62]. Traditionally, dual investigation of local electric and magnetic response would demand subsequent MFM and KPFM measurements, as shown in Fig. 3.18 [62]. In contrast, G-Mode KPFM can be configured to capture both channels of information simultaneously. To do this G-Mode was operated in dual pass mode using a magnetic AFM tip, where the topography of the HEA is shown in Fig. 3.18a. During the lift portion of the image,

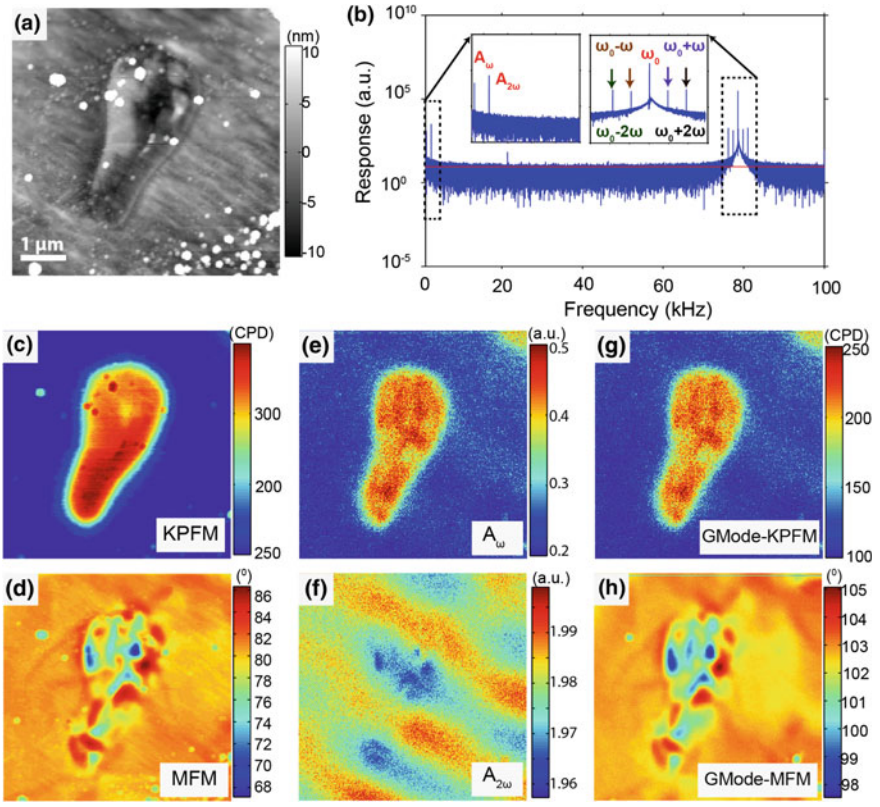

Fig. 3.18 **a** AFM topography image of a CoFeMnNiSn high entropy alloy (HEA). **b** Single pixel photodetector response, as translating into frequency domain using Fourier transform, demonstrating complex tip-sample interaction with multiple harmonics and sidebands evident. Variation in **c** CPD and **d** magnetic domains determined using conventional KPFM and MFM consecutively. Digital LIA analysis of G-Mode data showing **e** A_ω and **f** $A_{2\omega}$ used to determine the open loop **g** calculated CPD. **h** The simultaneously recorded magnetic domain response from LIA analysis of the mechanical excitation at fundamental resonance (ω_0). Reprinted from Collins et al. [60], with the permission of AIP Publishing

the magnetic AFM tip is photothermally excited at its fundamental resonance frequency (ω_0) while a low frequency electrical excitation (few kHz) is applied directly to the probe. The result is a multifrequency response of the cantilever, as seen from the G-Mode FFT response spectra showing multiple low frequency harmonics as well as side bands around the resonance frequency, Fig. 3.18b. The magnetic response is determined by the phase shift of the mechanical drive on resonance (Fig. 3.18h), whereas the CPD (Fig. 3.18g) is determined from the low frequency harmonics (Fig. 3.18e, f). In addition, similar to IM-EFM, the sidebands generated around the resonance frequency could be used for quantification of the CPD [87].

3.7.2 *Physics Based Analysis: Recovery of Force-Voltage Dependence*

Alternatively, the G-Mode allows reconstruction of the force-voltage dynamics directly from the measured cantilever trajectory [61] (Fig. 3.20). G-mode KPFM imaging capabilities have been demonstrated on a sample of freshly cleaved HOPG containing exposed graphene layers due to partial delamination, which are not electronically coupled to the graphite surface. As shown in Fig. 3.19b, the measured response is plotted as a function of the applied ac voltage to recover the parabolic bias dependence of the electrostatic force. While this bias spectroscopy approach has been used in single point mode or in combination with force mapping, G-KPFM is the first technique that permits this level of information to be acquired at standard imaging speeds and in the absence of a dc bias applied to the tip. Fitting the bias dependence to a second order polynomial allows extraction of relevant CPD and capacitance gradient channels for the entire image, Fig. 3.19c–e. After fitting the 4 GB dataset (for a 128 × 128 image), maps of V_{CPD} (x, y, t) and $C'z$(x, y, t) are obtained.

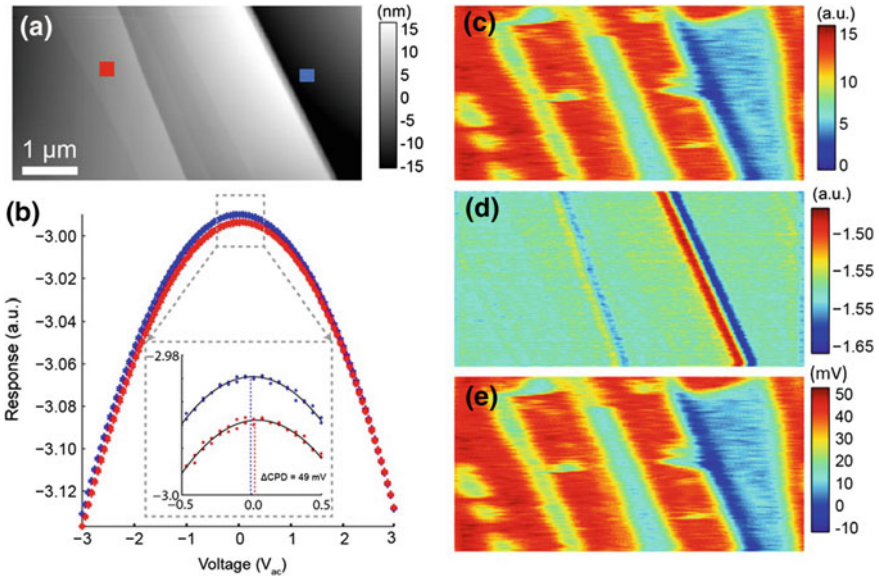

Fig. 3.19 G-KPFM imaging on a partially delaminated HOPG sample. **a** Topography, **b** parabolas averaged over the 4 ms pixel time for two single points at different locations (as indicated on (**a**) by squares) showing an CPD offset of 49 mV. Coefficients of **c** second and **d** first order fits determined from fitting the parabolas for the first period of oscillation at each spatial location of the map. **e** Map of CPD values obtained from the fitting parameters. Reprinted from Collins et al. [61]

Notice, fitting of the data can be performed over a partial, full, or many periods of the ac voltage modulation depending on the required temporal component. In this way, G-KPFM is much faster than conventional methods, where demodulation of the response is typically performed over hundreds of periods of oscillation. As such, G-KPFM provides the opportunity to quantify significant information relating to fast charge dynamics beyond a time averaged values for the CPD (as in classical KPFM). Notice that for low frequency excitation, as shown in this example, the force inversion can be performed directly. For high frequency operation, in which one or more of the dynamic responses lie close to a mechanical resonance of the cantilever, an additional correction of the transfer function needs to be performed [125].

3.7.3 *Information Based Analysis: Data Mining*

Besides using a physics-based approach, G-Mode KPFM data can also be analyzed via information theory. Indeed, methods for quick evaluation of sample properties that do not require computationally expensive fitting procedures will be important going forward in the era of big data. One approach is to use principal component analysis (PCA), which is a multivariate statistical method in which data is separated into orthonormal components sorted in descending order of their statistical significance according to the variance within the data set [126, 127, 130 131 132 133 134]. PCA outputs an eigenvalue loading map as well as an eigenvector for each principal component. For G-KPFM, the raw deflection signal can be effectively de-correlated into electrostatic interactions solely by statistical means using PCA [61]. Moreover, PCA is also capable of separating more exotic behavior while also providing a good assessment of the quality of data.

In Fig. 3.21, PCA analysis of the raw data from Fig. 3.20 is presented. More than 98.6% of the statistically relevant information is contained in the first five components, whereas higher order principle components were found to be dominated by noise. The loading map of the first principle component corresponds to the average response while third and fifth component loading maps represent variation in charge density distribution (voltage shift of parabola maximum) and capacitance (amplitude shift of parabola) as shown in the previous section. In this case, de-correlation of the raw data stream into electrostatic interactions using PCA is in good agreement with physics based approaches. Notice, the 2nd and 4th eigenvectors, Fig. 3.21d, h, have smooth variation in time, but lack spatial correlations in the loading maps (Fig. 3.21c, g). This type of behavior suggests that instead of material characteristics, these components are dominated by experimental noise/error. Furthermore, once noise can be identified in a particular component, the data can be easily re-derived from the remaining principle components, effectively denoising the signal.

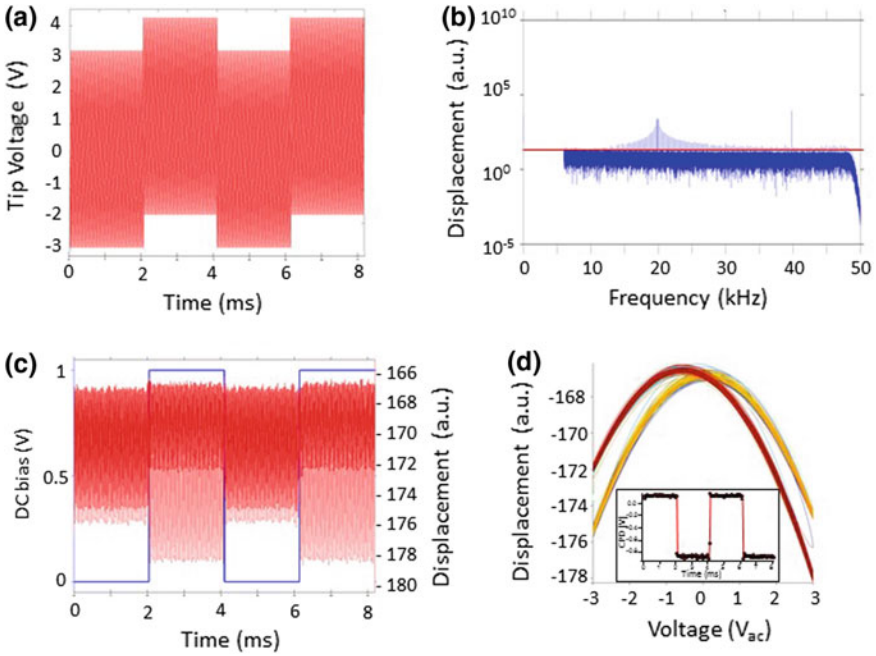

Fig. 3.20 **a** Tip voltage waveform (V_{ac} = 6 $V_{p\text{-}p}$ at 20 kHz, V_{dc} = +1 V with 4.096 ms pulse width). G-Mode KPFM data in the **b** frequency domain and **c** time domain after noise thresholding (red line in **b**) and low pass (50 kHz) and band pass filters (0.1–6 kHz) were applied to the raw data. The excitation voltage consisted of a single frequency V_{ac} superimposed on a square wave modulation (blue line indicates dc bias applied to the tip) resulting in many harmonics across a broad frequency range. **d** Recovered parabolas and inset show the measured CPD determined from parabolic fitting of the parabolas corresponding to a time resolved measurement of the applied dc bias. Adapted from Collins et al. [61]

3.7.4 General Dynamic Mode

G-mode can be further extended for complete characterization of the dynamic behavior of systems in a technique called General Dynamic Mode (GDM) [128]. Figure 3.22a shows the general principle of GDM KPFM, where the complete response from the photodetector is recorded for a sequence of sinusoidal waveforms with increasing frequencies. A Fourier transform of the measured response results in the basic measurement unit of GDM, which is a two dimensional spectrogram with the excitation frequency on one axis and the measurement frequency on the other. The example GDM spectrogram in Fig. 3.22a shows the dispersion of energy from the excitation frequencies to other frequencies. In the case of KPFM, the energy disperses to harmonics of the cantilever resonance frequencies. Performing GDM KPFM on a spatially resolved grid of points gives rise to 4D data which can be analyzed using multivariate statistical analysis techniques such as PCA [126,

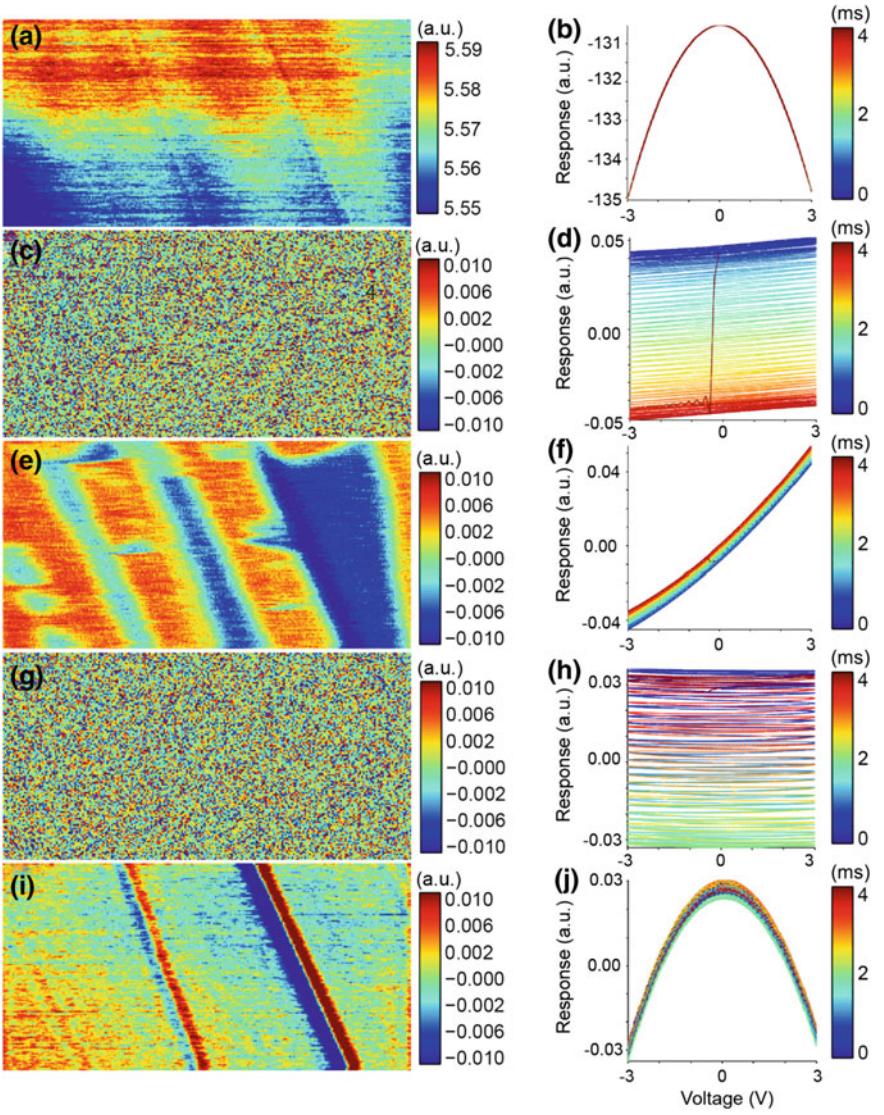

Fig. 3.21 Electrostatic interactions separated using information theory analysis. The left column **a**, **c**, **e**, **g**, **i** shows the first five principle components from PC 1 (top) to PC 5 (bottom). The right column **b**, **d**, **f**, **h**, **j** depicts the corresponding eigenvalues with the response plotted versus the applied voltage. Colors indicate variations over time (time per pixel = 4 ms). While the PCA components generally do not have well-defined physical meaning, in this case the first component is average strength of capacitive interactions, third is effective potential, and fifth is the capacitance change due to surface topography. The second and fourth are the signal transients (linear and parabolic) due to tip motion. Generally, such agreement between physically-expected behavior and PCA results is common in the systems where the contributing parameters are uncorrelated [127]. Reprinted from Collins et al. [61]

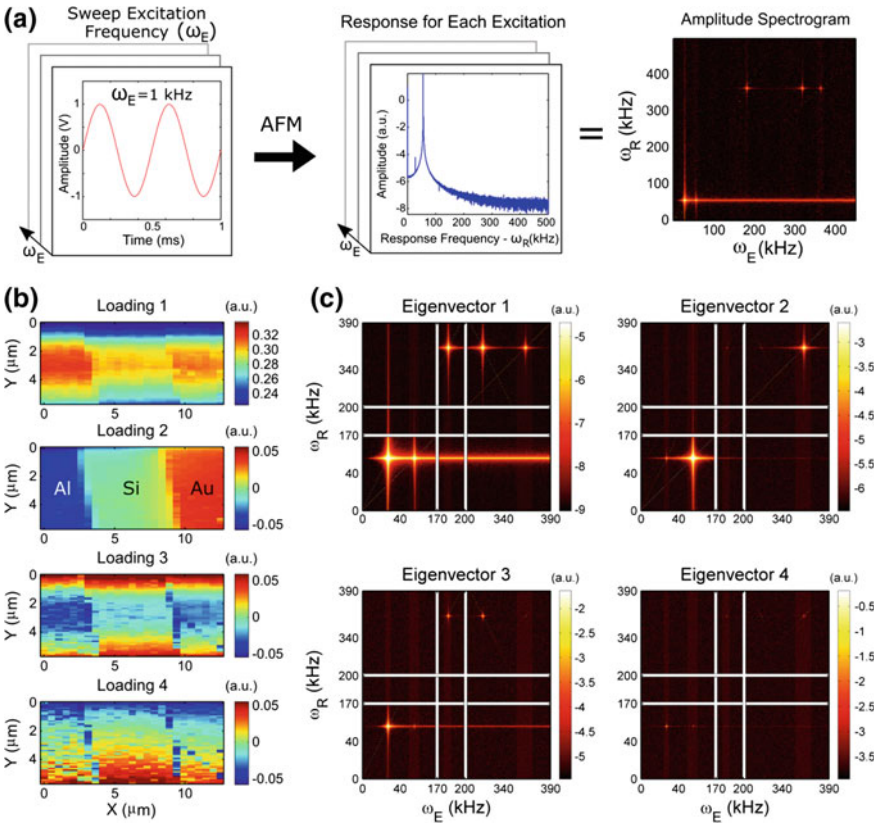

Fig. 3.22 General dynamic mode (GDM) and application to KPFM. **a** In GDM, the complete response from the AFM is acquired for a sequence of excitation waveforms of increasing frequency. The fundamental GDM result is a 2D spectrogram with the excitation frequency on one axis and the response frequency on the other. **b**, **c** Results of PCA applied to a dataset where KPFM GDM experiments were performed on a 2D spatial grid of points. The first four (**b**) PCA loading maps and (**c**) corresponding eigenvectors, which are GDM spectrograms ((**b**, **c**) © IOP Publishing. Reproduced with permission. All rights reserved) [128]

127, 130 131 132 133 134]. Figure 3.22b, c shows the results for PCA on a GDM KPFM measurement on a silicon substrate with aluminum and gold electrodes. Among the major statistical trends that it identifies, PCA clearly separates the response from the three materials in the sample, and it also extracts information that is very similar to the capacitance gradient. In many cases, the sheer volume of data generated by GDM KPFM can be overwhelming to analyze as-is on desktop computers. However, the sparsity of the spectrograms can be leveraged to construct condensed datasets that can be analyzed on desktop computers using the aforementioned methods.

3.8 KPFM Spectroscopies

In addition to the broad number of driving modes in KPFM, several groups have developed a number of spectroscopic modes of KPFM. Generally, spectroscopic imaging refers to the imaging modalities where the local response is measured as a function of local stimulus. In SPM, most celebrated examples of spectroscopic measurements are continuous imaging current spectroscopy (CITS) in STM, and I (V) and force-volume mapping measurements in AFM. In voltage modulated SPMs, a broad spectrum of spectroscopic imaging modes has been developed in the context of PFM [135] where bias- and time- dependence of electromechanical response [110, 136–139] is used to analyze domain nucleation and growth [140–142], distribution of nucleation centers [143, 144], domain wall dynamics [145–147], ferroelectric nonlinearities [148, 149], Preisach densities [148, 150–152], and many other phenomena [153, 154]. Similar techniques have evolved in the context of the Electrochemical Strain Microscopy [155–157] (ESM) used for probing electrochemical processes in batteries [158–162], fuel cell [163–166], and electroresistive materials [118, 167, 168].

The preponderance of spectroscopic imaging modes in PFM and ESM is enabled by the fact that the measurement is performed while the tip is in contact with the surface during the modification or detection stage. In comparison, in KPFM the surface modification can be performed with the tip in contact with the surface, whereas detection is typically performed when above the surface, necessitating complicated tip trajectory. Given the mismatch between the size of the modified region (e.g. tip-induced charged patch or induced reaction region) and spatial resolution of KPFM, this has severely limited the interest to the KPFM spectroscopies. In most cases, the surface potential established on the surface after scanning a square or rectangular region with a biased tip was studied.

Kim et al. [169] used this approach to explore ionically induced ferroelectric behavior in titanium dioxide (TiO_2) thin films. Scanning pristine as well as positively and negatively pre-poled samples while applying stepwise varying biases between −13 V and +13 V caused changes in surface potentials that were measured in subsequent KPFM scans. As depicted in Fig. 3.23, resulting KPFM images showed areas of modified surface potentials dependent on polarity and amplitude of the previously applied dc voltage. Surface potential values extracted from these different areas as a function of bias exhibit offsets along the x-axis for pre-poled TiO_2 films analog to hysteretic behavior. The observed phenomena were ascribed to bulk charge injection and could be detected because dissipation was slow compared to scan time.

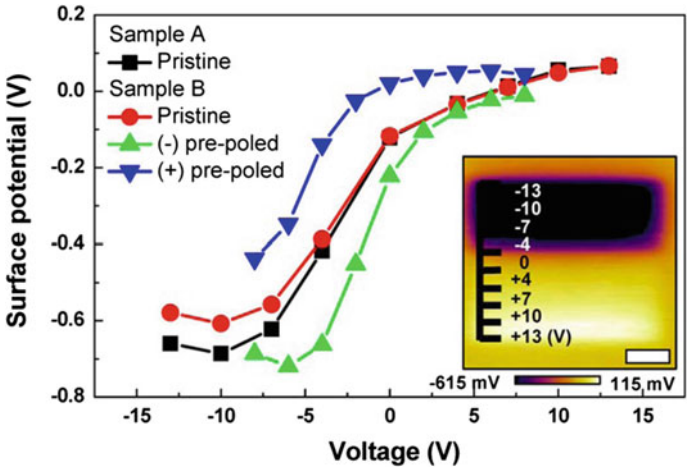

Fig. 3.23 Surface potential in dependence of bias applied during contact mode scanning prior to KPFM imaging. The values were extracted and averaged from KPFM images of pristine, positively and negatively pre-poled TiO_2 thin films. The inset shows a KPFM surface potential image after bias scanning of a pristine sample, scale bar is 1.5 μm. Adapted with permission from Kim et al. [170]. Copyright 2012 American Chemical Society

3.8.1 Contact KPFM

The EFM and KPFM techniques discussed so far are based on measuring electrostatic interactions above the sample surface or in tapping mode. However, electrostatic forces also act on the tip when it is in contact with the sample, which can result in cantilever displacement up to several pm. While electrostatic contributions to functional response measured in voltage modulated contact mode techniques such as PFM [171] and ESM [161] can lead to artefacts, contact mode KPFM [172, 173] (cKPFM) harnesses these forces to gain insight into the tip-sample junction charge phenomena. Electrostatic interactions between sample and a tip in contact with the surface can be used to realize information on the local junction contact potential difference (jCPD), capacitance gradients and junction electrochemical effects. While jCPD and CPD can be quantitatively the same in some cases, e.g. for metal-metal junctions, significant differences arise if the contact is formed by materials that interact chemically or in the presence of charge transport processes such as electrochemical reactions, ionic motion, and charge injection. Therefore, studying the jCPD necessitates contact mode techniques, which additionally provide the opportunity to probe electrochemical phenomena at the tip-surface junction and to explore triboelectric effects. As discussed for non-contact KPFM modes, the first harmonic of the electrostatic force $F_{1\omega}$ acting on the tip is a linear function of the capacitance gradient $\partial C/\partial z \equiv C'$, the applied ac voltage V_{ac} and a dc term $(V_{dc} - V_{jCPD})$ comprising applied bias and junction potential (see (3.2) in Sect. 3.2). If the tip is in contact with the sample, C' is

undefined and treated as proportionality coefficient between the electrostatic force $F_{1\omega}$ and voltages. The displacement $D_{1\omega}$ of the tip caused by $F_{1\omega}$ acting against the contact stiffness k* can be obtained from $D_{1\omega} = F_{1\omega}/k^*$, which yields (3.14):

$$D_{1\omega} = \frac{C'}{k^*} V_{ac}\left(V_{dc} - V_{jCPD}\right) \tag{3.14}$$

The measured displacement is therefore a linear function of $(V_{dc} - V_{jCPD})$ with capacitance gradient and tip-sample contact stiffness determining the slope.

In cKPFM, dc write pulses induce local changes in the jCPD, which are monitored by detecting the first harmonic electrostatic response to an ac voltage while simultaneously applying a dc voltage in an open loop technique. The absence of a bias feedback loop precludes associated artefacts and bandwidth limitations as outlined in Sect. 3.2. Dependent on experimental demands, two different methods can be used. In the first approach, small-amplitude dc voltage sweeps are performed after each dc write pulse, similar to other bias spectroscopy techniques (Fig. 3.24a). The reading bias is of low magnitude so that surface charge states are not modified during readout. The multiple bias steps required for sweeping the dc voltage result in high acquisition times, precluding detection of fast potential changes. Significantly faster readout can be achieved by applying multiple cycles of dc write pulses with single pulse dc read steps that vary with each cycle, as outlined in Fig. 3.24b. In this method, the readout can be much faster compared to the first method, enabling tracking of dissipation and charge injection processes at small time scales. However, this approach can only be used under the premise that voltage induced phenomena are independent from measurement history through fast relaxation times and complete reversibility.

The principle of cKPFM and its capabilities were demonstrated by Balke et al. [173] by measuring electrostatic interactions between an AFM tip in contact with an amorphous hafnium oxide (HfO_2) thin film. Scanning the HfO_2 surface while

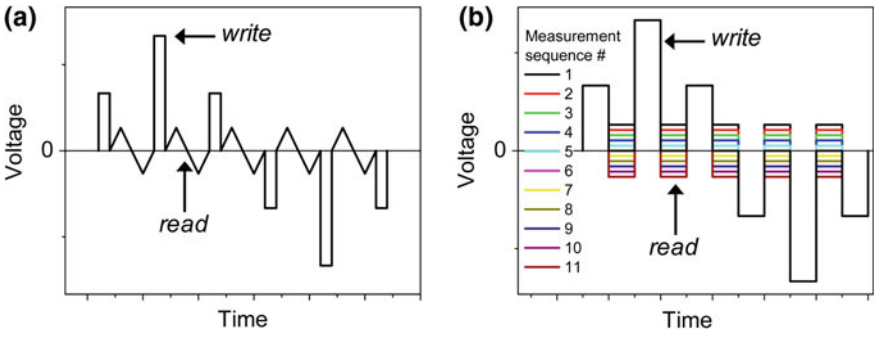

Fig. 3.24 DC voltage waveforms applied in the two cKPFM methods: **a** full dc sweeps during read steps, **b** application of multiple cycles upon sequential variation of dc bias during read steps. ac voltages are superimposed on the depicted waveforms. Reprinted with permission from Balke et al. [173]. Copyright 2014 American Chemical Society

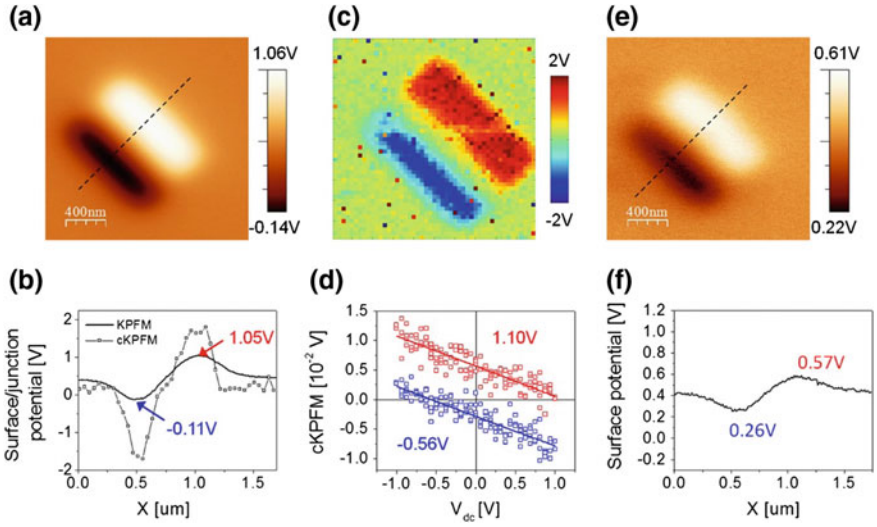

Fig. 3.25 **a** KPFM surface potential image of a HfO_2 surface after charge patterning by applying ±5 V to the tip during scanning. **b** Cross sections of surface potential obtained with KPFM (as indicated in (**a**)) and cKPFM. **c** jCPD map extracted from the x-intercept of the linear fit of bias dependent electrostatic response as displayed in **d** for averaged cKPFM curves from the two different areas. **e** KPFM scan after cKPFM spectroscopy and **f** cross section as indicated by dashed line in (**e**). Reprinted with permission from Balke et al. [173]. Copyright 2014 American Chemical Society

applying dc biases of ±5 V resulted in a charge pattern that was investigated with BE-cKPFM spectroscopy upon using the bias sweep read method that is depicted in Fig. 3.24a, as well as classical closed-loop KPFM for comparison. KPFM mapping above the surface shows a decrease in CPD at sample areas where a negative voltage was applied and an increase in CPD at regions scanned with a positive voltage (Fig. 3.25a, b). The local jCPD can be obtained from the x-intercept of the linear fit through the measured cKPFM signal versus dc read voltage and composited into maps. The jCPD map and averaged cKPFM curves showed pronounced changes in junction potential within the charge patterned areas (Fig. 3.25c, d). Compared to classical KPFM, potential values measured in contact mode exhibit higher magnitude and charge patterned areas are better defined, corresponding to narrower peaks in the depicted cross section in Fig. 3.25b. Since lateral resolution scales with cantilever dimensions and lift height, these differences can be ascribed to the higher resolution achieved in contact mode. KPFM imaging after cKPFM spectroscopy revealed relaxation of surface potentials (Fig. 3.25e, f).

Charge dissipation was further explored by taking multiple consecutive KPFM and cKPFM scans after writing a charge pattern. cKPFM scanning was conducted in the absence of a dc bias, equivalent to contact EFM [174], ESM, and PFM where the measured response corresponds to the y-intercept of cKPFM curves. In KPFM images and corresponding cross sections (Fig. 3.26a, c) no change in CPD is

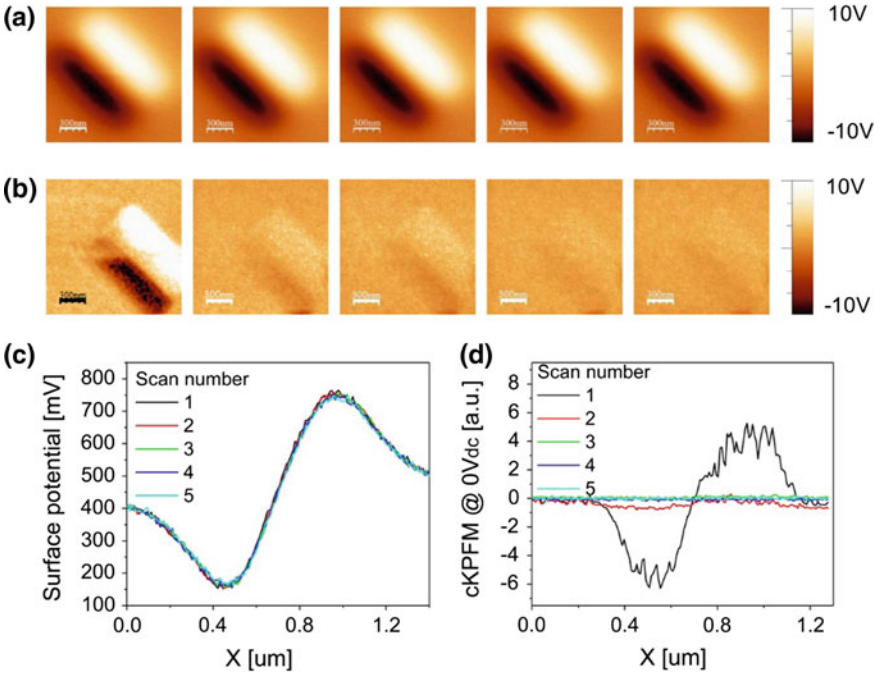

Fig. 3.26 Five consecutively scanned **a** KPFM and **b** cKPFM images of a charge patterned area on HfO_2 (scan time 6 and 3 min/image, respectively). **c**, **d** Corresponding cross sections of KPFM and cKPFM images, respectively. Reprinted with permission from Balke et al. [173]. Copyright 2014 American Chemical Society

observed within the 30 min during which the depicted 5 images were acquired. However, in cKPFM scans and cross sections, nearly complete dissipation is apparent after 3 min, which corresponds to the scan time of one image (Fig. 3.26b, d). These observations highlight the strong impact of the tip on charge detrapping.

To study the change in jCPD in response to dc write pulses at smaller time scales, the method outlined in Fig. 3.24b was implemented as the observed electrostatic phenomena fulfilled independence from bias history. The measured cKPFM signal after each write step is depicted in Fig. 3.27a as a function of dc voltages applied during read steps. In agreement with (3.14), the obtained curves exhibit linear behavior with varying *y*-offsets dependent on dc write pulses and corresponding jCPD. Moreover, slopes of the cKPFM curves, which are proportional to tip-sample contact stiffness and capacitance gradient show variations. The jCPD values extracted from x-intercepts of these curves, change hysteretically with dc write voltages (Fig. 3.27b), which was attributed to dynamic changes in physical, chemical or electrochemical surface charge. Electrostatic forces emanating from these voltage-induced charges did not affect the contact resonance frequency as determined from atomic force acoustic microscopy measurements where ac voltages induce mechanical sample oscillations and only the dc pulses are applied

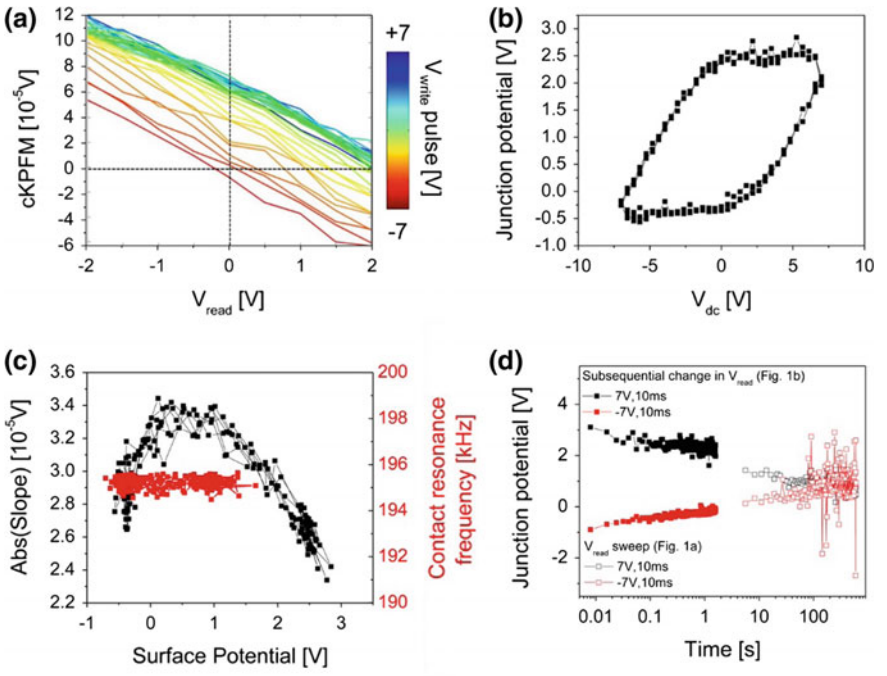

Fig. 3.27 **a** cKPFM curves a function of reading voltage for each dc write pulse measured on HfO_2. **b** jCPD extracted from the x-intercept of linear fits through cKPFM curves. **c** Slope of cKPFM signal and contact resonance frequency as obtained from atomic force acoustic microscopy measurements as function of potential. **d** Junction potential showing charge dissipation after application of single ±7 V pulses at different time scales. Data at times <1 s were measured using the method outlined in Fig. 3.21b while long term measurements were conducted using the method from Fig. 3.22a. Reprinted with permission from Balke et al. [173]. Copyright 2014 American Chemical Society

to the tip. The diagram in Fig. 3.27c shows that the obtained values for the resonance frequency are nearly constant over a potential range of ~2.5 V, in contrast to the cKPFM slopes that are strongly dependent on the jCPD. As the contact resonance which directly relates to the contact stiffness is constant, the observed changes in slopes are attributed to variations in capacitance gradients, which are correlated with the presence of surface charge. Furthermore, the change in slopes indicate that measuring only the y-intercept in scanning cKPFM at 0 V or conducting closed-loop KPFM does not provide complete information on junction charge effects. Charge dissipation after dc write pulses can be studied over a large time scale ranging from 4 ms to several hundred seconds by combining both methods depicted in Fig. 3.24. Single pulse read steps allow to access charge dynamics at temporal resolutions of several ms whereas complimentary information on long-term behavior up to hundreds of seconds can be obtained using full dc sweeps during readout (Fig. 3.27d).

Apart from providing a path to study junction charge phenomena at high lateral resolution, cKPFM also reveals the strong electrostatic interactions present in dynamic contact mode techniques such as ESM and PFM. While electromechanical and electrochemical strains are related to sample deformation [175–178], electrostatic contributions originate from forces acting on the tip. Increasing the contact stiffness by using higher force setpoints or cantilevers with higher force constants can reduce electrostatic interactions that obfuscate genuine PFM or ESM response. However, in standard experiments electrostatic contributions are often non-negligible even if tips of several N/m stiffness are used. Artefacts can particularly arise in PFM switching experiments, where high dc-voltage pulses are applied to induce ferroelectric polarization switching but can also cause charge injection or activate chemical processes. Hysteresis loops obtained in these PFM switching experiments in conjunction with contrast in PFM images are often treated as evidence for ferroelectricity. However, both observations can also be made on clearly non-ferroelectric materials [179, 180]. As depicted in Fig. 3.23b, areas of different contrast in PFM-like images can arise solely from spatial variations in jCPD due to surfaces charges in the absence of ferroelectric domains. Similarly, the hysteresis shape of jCPD versus dc write voltages (Fig. 3.23c) originates from charge injection, which is subject to occupation and liberation of available electronic traps at the surface and therefore associated with electron barriers that have to be overcome [180]. Moreover, slow redistribution of adsorbates and ionic motion can contribute to the hysteretic behavior as they further govern the ability of the material surface to retain and compensate injected charges within the duration of the measurement. Band formation in cKPFM curves corresponding to offsets in *y*-direction is related to these changes in junction potential upon application of dc write pulses. As a result, the *y*-intercept that reflects the off-field PFM signal exhibits hysteretic behavior similar to the bias dependence of the jCPD. It is therefore difficult to determine signal origin in PFM experiments where amplitude and phase loops obtained on amorphous HfO_2 have been shown to strongly resemble those obtained on ferroelectric lead zirconate titanate (PZT). Monitoring relaxation of the measured response after applying dc write pulses can provide insight into dissipation of injected charges and detrapping as well as stability of nanosized ferroelectric domains, albeit these phenomena are indistinguishable in the observed response and can therefore not elucidate signal origin. However, ferroelectric behavior can be identified from the hysteresis shaped cKPFM curves depicted for PZT in Fig. 3.28, which show remanent offsets at 0 V that arise from the presence of permanent dipoles in the material, whereas the observed band formation was ascribed to injection of charges occurring in addition to polarization switching. The width of the two bands of different offsets can therefore provide information on charge injection properties of the sample surface. The ability to distinguish between electromechanical response and electrostatic interactions is particularly important to study materials whose functional properties are unclear. For example, cKPFM measurements on strontium titanate ($SrTiO_3$/(Sr,Ca)RuO_3/$NdGaO_3$) revealed characteristics similar to PZT, however the polarization induced remanence was much weaker. In combination with PFM studies, the sample could

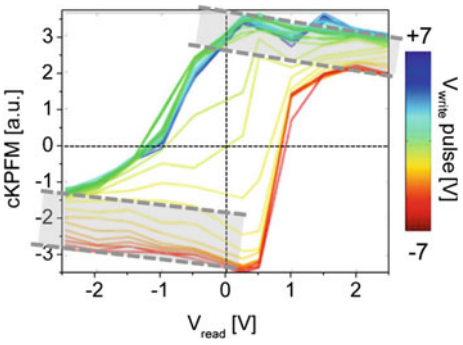

Fig. 3.28 Hysteresis shaped cKPFM curves versus dc read voltage measured on ferroelectric PZT. Adapted with permission from Balke et al. [172]. Copyright 2015 American Chemical Society

be classified to exhibit relaxor-like material behavior at room temperature [22]. Furthermore, the ability of cKPFM to obtain clear information on the number of polarization states provides a path to investigate coupled electrochemical-ferroelectric states that cannot be separated in classical hysteresis measurements [181].

Since electrostatic interactions can play a major role in contact mode AFM techniques, cKPFM was used to quantify electrostatic forces emanating from charge injection in HfO_2 by Balke et al. [180]. Moreover, the electric field strength in the tip-sample junction that governs field induced phenomena like nanoscale melting, water condensation and dissociation as well as ionic conduction was obtained in combination with finite element modeling. Electrostatic forces caused by locally modified junction potentials through charge injection predominantly act on the tip apex whereas contributions of tip cone and cantilever are negligible, facilitating high lateral resolution in cKPFM measurements. The electrostatic interactions are dependent on local sample permittivity and conductivity as well as surface topography. Upon considering only forces at the tip apex and setting $V_{dc} = 0$, the relationship $D_{1\omega} = -C'_{apex}/k^* \; V_{ac} \; V_{jCPD}$ can be derived from (3.14). Independent determination of k^* and V_{jCPD} in combination with measurements of $D_{1\omega}$ allows to quantitatively assess local electrostatic force and capacitance gradient C'_{apex}. In order to obtain quantitative apex displacement, static calibration of the cantilever sensitivity was used in conjunction with a correction factor that takes the shape of the contact resonance mode into account [182]. The contact stiffness k* was derived from the resonance frequency of the SHO fitted BE response and determines the amount of tip displacement, which was found to be of several pm. The hysteretic junction potential in dependence of dc write pulses was obtained from cKPFM spectroscopy measurements. Capacitance gradient and jCPD were used to numerically model the electric field distribution which is dependent on microstructure, local material properties and tip geometry. A field strength of 1 V/nm was estimated in the tip-sample junction, which is expected to lead to charge and mass transport processes in tip vicinity.

3.9 Outlook

In 25 years since its invention, Kelvin probe force microscopy has become the preeminent tool for probing electronic and transport phenomena in nanoscale systems. This progress was largely related to the ease of implementation via classical lock-in—feedback circuit electronics viable in late 80s, and also by the fact that KPFM yielded the 2D maps of materials parameters open for immediate physical interpretation. Despite this progress, the applicability of KPFM was largely limited to ambient and UHV environments, and relatively low imaging rates. These in turn have been limited by the physics of the imaging process, i.e. the time- and voltage dependence of bias-induced forces, and data processing limitations.

The XXI century has seen the rapid increase of the advanced big data technologies, which, among other things, allows information-theory and physics based analysis of large data streams as illustrated in Fig. 3.29 [183]. This removes traditional limitations on the KPFM imaging, and enables a broad spectrum of signal processing based on parallel frequency band excitation detection and full information capture G-Mode method. This allows imaging in liquid environment, fast KPFM, and variable resolution KPFM among others.

In the future, combination of the on-the fly data analytics and theory-assisted experiment will allow further progress in KPFM, bringing it to the information

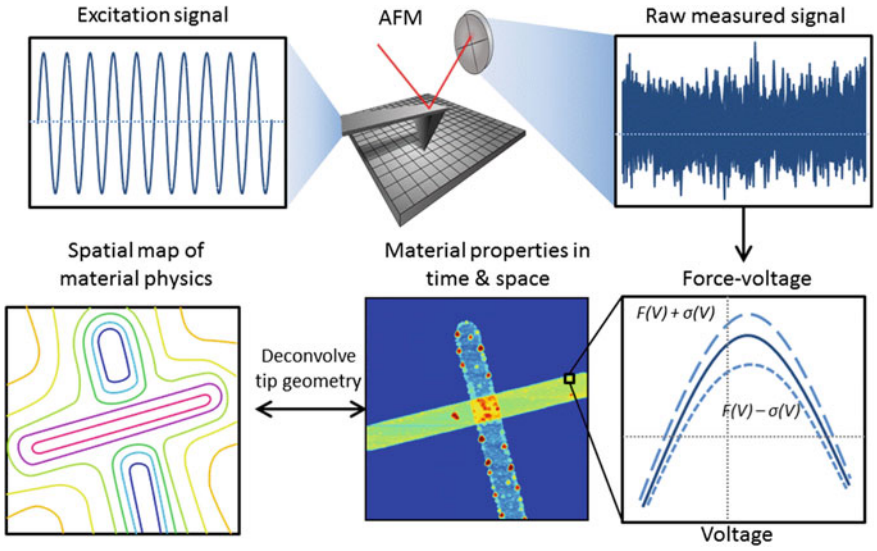

Fig. 3.29 Bayesian paradigm for KPFM measurements. The knowledge of measured signal and excitation signal will allow Bayesian inference to reconstruct F(V) curve with associated uncertainty intervals for each spatio-temporal pixel. These represent the maximum amount of information that can be derived from measurement. From these, the knowledge of tip properties (e.g. available via calibration) can be used to deconvolute relevant materials properties

limits of measurement speed. Equally important is the development of Bayesian inference based methods for analysis of resultant data, establishing both inversion of information flow into physically relevant parameters and establishments of limitations and confidence intervals associated with this inversion. Once available, this data can be combined with reconstruction theory for tip-surface interaction analysis to extract relevant materials physics.

Acknowledgement This research was conducted at and supported by the Center for Nanophase Materials Sciences, which is a DOE Office of Science User Facility.

References

1. G. Binnig, H. Rohrer, C. Gerber, E. Weibel, Phys. Rev. Lett. **50**(2), 120–123 (1983)
2. G. Binnig, H. Rohrer, Helv. Phys. Acta **55**(6), 726–735 (1982)
3. C. Gerber, H.P. Lang, Nat. Nanotechnol. **1**(1), 3–5 (2006)
4. F.J. Giessibl, Mater. Today **8**(5), 32–41 (2005)
5. J. Weaver, D.W. Abraham, J. Vac. Sci. Technol. B: Microelectron. Nanometer Struct. Process. Meas. Phenom. **9**(3), 1559–1561 (1991)
6. Y. Martin, D.W. Abraham, H.K. Wickramasinghe, Appl. Phys. Lett. **52**(13), 1103–1105 (1988)
7. M. Nonnenmacher, M.P. O'Boyle, H.K. Wickramasinghe, Appl. Phys. Lett. **58**(25), 2921–2923 (1991)
8. B.D. Terris, J.E. Stern, D. Rugar, H.J. Mamin, Phys. Rev. Lett. **63**(24), 2669–2672 (1989)
9. H. Baytekin, A. Patashinski, M. Branicki, B. Baytekin, S. Soh, B.A. Grzybowski, Science **333**(6040), 308–312 (2011)
10. Z.L. Wang, MRS Bull. **37**(09), 814–827 (2012)
11. D.J. Bayerl, X. Wang, Adv. Func. Mater. **22**, 652–660 (2012)
12. S. Lu, Q. Liao, J. Qi, S. Liu, Y. Liu, Q. Liang, G. Zhang, Y. Zhang, Nano Res. **9**, 372–379 (2016)
13. S.M. Sze, *Physics of Semiconductor Devices*, 2nd edn. (Wiley-Interscience, New York, 1981)
14. H. Sugimura, Y. Ishida, K. Hayashi, O. Takai, N. Nakagiri, Appl. Phys. Lett. **80**(8), 1459–1461 (2002)
15. M. Tanimoto, O. Vatel, J. Vac. Sci. Technol. B **14**(2), 1547–1551 (1996)
16. O. Vatel, M. Tanimoto, J. Appl. Phys. **77**(6), 2358–2362 (1995)
17. B.D. Huey, D.A. Bonnell, Appl. Phys. Lett. **76**(8), 1012–1014 (2000)
18. D.A. Bonnell, B. Huey, D. Carroll, Solid State Ionics **75**, 35–42 (1995)
19. M. Freitag, A.T. Johnson, S.V. Kalinin, D.A. Bonnell, Phys. Rev. Lett. **89**(21) (2002)
20. S.V. Kalinin, J. Shin, S. Jesse, D. Geohegan, A.P. Baddorf, Y. Lilach, M. Moskovits, A. Kolmakov, J. Appl. Phys. **98**(4), 044503 (2005)
21. S.V. Kalinin, M.R. Suchomel, P.K. Davies, D.A. Bonnell, J. Am. Ceram. Soc. **85**(12), 3011–3017 (2002)
22. S.V. Kalinin, D.A. Bonnell, J. Appl. Phys. **91**(2), 832–839 (2002)
23. S.V. Kalinin, D.A. Bonnell, M. Freitag, A.T. Johnson, Appl. Phys. Lett. **81**(27), 5219–5221 (2002)
24. S.V. Kalinin, D.A. Bonnell, Phys. Rev. B **65**(12), 125408 (2002)
25. S.V. Kalinin, D.A. Bonnell, Phys. Rev. B **63**(12), 125411 (2001)
26. J. Shin, V. Meunier, A.P. Baddorf, S.V. Kalinin, Appl. Phys. Lett. **85**(18), 4240–4242 (2004)

27. S.V. Kalinin, J. Shin, G.M. Veith, A.P. Baddorf, M.V. Lobanov, H. Runge, M. Greenblatt, Appl. Phys. Lett. **86**(10) (2005)
28. S.V. Kalinin, D.A. Bonnell, Phys. Rev. B **70**(23) (2004)
29. S.V. Kalinin, S. Jesse, J. Shin, A.P. Baddorf, M.A. Guillorn, D.B. Geohegan, Nanotechnology **15**(8), 907–912 (2004)
30. B.J. Rodriguez, S. Jesse, V. Meunier, S.V. Kalinin, Appl. Phys. Lett. **88**(14), 143128 (2006)
31. S.V. Kalinin, D.A. Bonnell, in *Ferroelectric Thin Films Viii*, vol. 596, ed. by R.W. Schwartz, P.C. McIntyre, Y. Miyasaka, S.R. Summerfelt, D. Wouters (2000), pp. 327–332
32. S.V. Kalinin, D.A. Bonnell, Zeitschrift Fur Metallkunde **90**(12), 983–989 (1999)
33. S.V. Kalinin, D.A. Bonnell, J. Appl. Phys. **87**(8), 3950–3957 (2000)
34. S.V. Kalinin, C.Y. Johnson, D.A. Bonnell, J. Appl. Phys. **91**(6), 3816–3823 (2002)
35. D.D. Fong, A.M. Kolpak, J.A. Eastman, S.K. Streiffer, P.H. Fuoss, G.B. Stephenson, C. Thompson, D.M. Kim, K.J. Choi, C.B. Eom, I. Grinberg, A.M. Rappe, Phys. Rev. Lett. **96** (12) (2006)
36. S.K. Streiffer, J.A. Eastman, D.D. Fong, C. Thompson, A. Munkholm, M.V.R. Murty, O. Auciello, G.R. Bai, G.B. Stephenson, Phys. Rev. Lett. **89**(6), 067601 (2002)
37. M.J. Highland, T.T. Fister, D.D. Fong, P.H. Fuoss, C. Thompson, J.A. Eastman, S.K. Streiffer, G.B. Stephenson, Phys. Rev. Lett. **107**(18), 187602 (2011)
38. M.J. Highland, T.T. Fister, M.I. Richard, D.D. Fong, P.H. Fuoss, C. Thompson, J.A. Eastman, S.K. Streiffer, G.B. Stephenson, Phys. Rev. Lett. **105**(16), 167601 (2010)
39. R.V. Wang, D.D. Fong, F. Jiang, M.J. Highland, P.H. Fuoss, C. Thompson, A.M. Kolpak, J. A. Eastman, S.K. Streiffer, A.M. Rappe, G.B. Stephenson, Phys. Rev. Lett. **102**(4), 047601 (2009)
40. G.B. Stephenson, M.J. Highland, Phys. Rev. B **84**(6), 064107 (2011)
41. A.V. Ievlev, A.N. Morozovska, E.A. Eliseev, V.Y. Shur, S.V. Kalinin, Nat. Commun. **5** (2014)
42. A. Ievlev, S. Jesse, A. Morozovska, E. Strelcov, E. Eliseev, Y. Pershin, A. Kumar, V.Y. Shur, S. Kalinin, Nat. Phys. **10**(1), 59–66 (2014)
43. A.K. Sinensky, A.M. Belcher, Nat. Nanotechnol. **2**(10), 653–659 (2007)
44. C. Leung, H. Kinns, B.W. Hoogenboom, S. Howorka, P. Mesquida, Nano Lett. **9**(7), 2769–2773 (2009)
45. H.F. Knapp, P. Mesquida, A. Stemmer, Surf. Interface Anal. **33**(2), 108–112 (2002)
46. E. Finot, Y. Leonenko, B. Moores, L. Eng, M. Amrein, Z. Leonenko, Langmuir **26**(3), 1929–1935 (2010)
47. B. Moores, F. Hane, L. Eng, Z. Leonenko, Ultramicroscopy **110**(6), 708–711 (2010)
48. L. Collins, J. Kilpatrick, S.V. Kalinin, B.J. Rodriguez, arXiv:1701.06633 (2017)
49. L. Collins, J.I. Kilpatrick, I.V. Vlassiouk, A. Tselev, S.A. Weber, S. Jesse, S.V. Kalinin, B. J. Rodriguez, Appl. Phys. Lett. **104**(13), 133103 (2014)
50. L. Collins, S. Jesse, J.I. Kilpatrick, A. Tselev, O. Varenyk, M.B. Okatan, S.A. Weber, A. Kumar, N. Balke, S.V. Kalinin, Nat. Commun. **5** (2014)
51. L. Collins, S. Jesse, J.I. Kilpatrick, A. Tselev, M.B. Okatan, S.V. Kalinin, B.J. Rodriguez, Beilstein J. Nanotechnol. **6**(1), 201–214 (2015)
52. N. Kobayashi, H. Asakawa, T. Fukuma, Rev. Sci. Instrum. **81**(12), 123705 (2010)
53. N. Kobayashi, H. Asakawa, T. Fukuma, J. Appl. Phys. **110**(4), 044315 (2011)
54. R. Berger, A.L. Domanski, S.A. Weber, Eur. Polym. J. **49**(8), 1907–1915 (2013)
55. A. Liscio, G. De Luca, F. Nolde, V. Palermo, K. Müllen, P. Samorì, J. Am. Chem. Soc. **130** (3), 780–781 (2008)
56. D.C. Coffey, D.S. Ginger, Nat. Mater. **5**(9), 735–740 (2006)
57. R. Giridharagopal, G.E. Rayermann, G. Shao, D.T. Moore, O.G. Reid, A.F. Tillack, D. J. Masiello, D.S. Ginger, Nano Lett. **12**(2), 893–898 (2012)
58. D.U. Karatay, J.S. Harrison, M.S. Glaz, R. Giridharagopal, D.S. Ginger, Rev. Sci. Instrum. **87**(5), 053702 (2016)
59. A. Belianinov, S.V. Kalinin, S. Jesse, Nat. Commun. **6** (2015)

60. L. Collins, A. Belianinov, R. Proksch, T. Zuo, Y. Zhang, P.K. Liaw, S.V. Kalinin, S. Jesse, Appl. Phys. Lett. **108**(19), 193103 (2016)
61. L. Collins, A. Belianinov, S. Somnath, N. Balke, S.V. Kalinin, S. Jesse, Sci. Rep. **6** (2016)
62. L. Collins, A. Belianinov, S. Somnath, B.J. Rodriguez, N. Balke, S.V. Kalinin, S. Jesse, Nanotechnology **27**(10), 105706 (2016)
63. H. Diesinger, D. Deresmes, T. Mélin, *Kelvin Probe Force Microscopy* (Springer, 2012), pp. 25–44
64. T. Mélin, S. Barbet, H. Diesinger, D. Théron, D. Deresmes, Rev. Sci. Instrum. **82**(3), 036101 (2011)
65. S. Barbet, M. Popoff, H. Diesinger, D. Deresmes, D. Théron, T. Mélin, J. Appl. Phys. **115** (14), 144313 (2014)
66. L. Polak, S. de Man, R.J. Wijngaarden, Rev. Sci. Instrum. **85**(4), 046111 (2014)
67. E. Strassburg, A. Boag, Y. Rosenwaks, Rev. Sci. Instrum. **76**(8), 083705 (2005)
68. S. Sadewasser, T. Glatzel, R. Shikler, Y. Rosenwaks, M.C. Lux-Steiner, Appl. Surf. Sci. **210** (1–2), 32–36 (2003)
69. A. Blumel, H. Plank, A. Klug, E. Fisslthaler, M. Sezen, W. Grogger, E.J.W. List, Rev. Sci. Instrum. **81**(5), 056107 (2010)
70. T. Glatzel, L. Zimmerli, S. Koch, B. Such, S. Kawai, E. Meyer, Nanotechnology **20**(26) (2009)
71. F. Bocquet, L. Nony, C. Loppacher, T. Glatzel, Phys. Rev. B **78**(3), 035410 (2008)
72. G.H. Enevoldsen, T. Glatzel, M.C. Christensen, J.V. Lauritsen, F. Besenbacher, Phys. Rev. Lett. **100**(23), 236104 (2008)
73. S. Kitamura, K. Suzuki, M. Iwatsuki, Appl. Surf. Sci. **140**(3–4), 265–270 (1999)
74. R. Garcia, E.T. Herruzo, Nat. Nanotechnol. **7**(4), 217–226 (2012)
75. H.O. Jacobs, H.F. Knapp, A. Stemmer, Rev. Sci. Instrum. **70**(3), 1756–1760 (1999)
76. Y. Miyahara, P. Grutter, Appl. Phys. Lett. **110** (2017)
77. Y. Miyahara, J. Topple, Z. Schumacher, P. Grutter, Phys. Rev. Appl. **4**(5) (2015)
78. Y. Sugawara, L. Kou, Z. Ma, T. Kamijo, Y. Naitoh, Y.J. Li, Appl. Phys. Lett. **100**(22), 223104 (2012)
79. J.L. Garrett, J.N. Munday, Nanotechnology **27**(24), 245705 (2016)
80. Z.M. Ma, J.L. Mu, J. Tang, H. Xue, H. Zhang, C.Y. Xue, J. Liu, Y.J. Li, Nanoscale Res. Lett. **8**(1), 532 (2013)
81. J.L. Garrett, D. Somers, J.N. Munday, J. Phys.: Condens. Matter **27**(21), 214012 (2015)
82. Z.M. Ma, L. Kou, Y. Naitoh, Y.J. Li, Y. Sugawara, Nanotechnology **24**(22), 225701 (2013)
83. O. Takeuchi, Y. Ohrai, S. Yoshida, H. Shigekawa, Jpn. J. Appl. Phys. Part 1 Regul. Pap. Short Notes Rev. Pap. **46**(8B), 5626 (2007)
84. L. Collins, J. Kilpatrick, M. Bhaskaran, S. Sriram, S.A. Weber, S. Jarvis, B.J. Rodriguez, Presented at the Proceedings of ISAF-ECAPD-PFM 2012 (2012) (unpublished)
85. S. Guo, S.V. Kalinin, S. Jesse, Nanotechnology **23**(12), 125704–125704 (2012)
86. L. Collins, S. Jesse, N. Balke, B.J. Rodriguez, S. Kalinin, Q. Li, Appl. Phys. Lett. **106**(10) (2015)
87. R. Borgani, D. Forchheimer, J. Bergqvist, P.-A. Thorén, O. Inganäs, D.B. Haviland, Appl. Phys. Lett. **105**(14), 143113 (2014)
88. R. Borgani, L.K. Pallon, M.S. Hedenqvist, U.W. Gedde, D.B. Haviland, Nano Lett. **16**(9), 5934–5937 (2016)
89. E. Strelcov, S. Jesse, Y.-L. Huang, Y.-C. Teng, I.I. Kravchenko, Y.-H. Chu, S.V. Kalinin, ACS Nano **7**(8), 6806–6815 (2013)
90. E. Strelcov, A.V. Ievlev, S. Jesse, I.I. Kravchenko, V.Y. Shur, S.V. Kalinin, Adv. Mater. **26** (6), 958–963 (2014)
91. J. Ding, E. Strelcov, S.V. Kalinin, N. Bassiri-Gharb, Nano Lett. **15**(6), 3669–3676 (2015)
92. O.G. Reid, G.E. Rayermann, D.C. Coffey, D.S. Ginger, J. Phys. Chem. C **114**(48), 20672–20677 (2010)
93. J. Murawski, T. Graupner, P. Milde, R. Raupach, U. Zerweck-Trogisch, L. Eng, J. Appl. Phys. **118**(15), 154302 (2015)

94. J. Murawski, T. Mönch, P. Milde, M. Hein, S. Nicht, U. Zerweck-Trogisch, L. Eng, J. Appl. Phys. **118**(24), 244502 (2015)
95. P.A. Remillard, M.C. Amorelli, Google Patents (1993)
96. R. Proksch, S.V. Kalinin, Nanotechnology **21**(45) (2010)
97. S. Jesse, S. Guo, A. Kumar, B.J. Rodriguez, R. Proksch, S.V. Kalinin, Nanotechnology **21** (40), 405703 (2010)
98. J. Klapper, J.T. Frankle, P. Atkinson, IEEE Trans. Syst. Man Cybern. **9**(7), 402–403 (1979)
99. D. Banerjee, *PLL Performance, Simulation and Design*, 5 ed. (National Semiconductor, 2017)
100. T. Albrecht, P. Grütter, D. Horne, D. Rugar, J. Appl. Phys. **69**(2), 668–673 (1991)
101. Y. Martin, C.C. Williams, H.K. Wickramasinghe, J. Appl. Phys. **61**(10), 4723–4729 (1987)
102. O. Takeuchi, Y. Ohrai, S. Yoshida, H. Shigekawa, Jpn. J. Appl. Phys. **46**(8S), 5626 (2007)
103. L. Kou, Z. Ma, Y.J. Li, Y. Naitoh, M. Komiyama, Y. Sugawara, Nanotechnology **26**(19), 195701 (2015)
104. L. Collins, J. Kilpatrick, S.A. Weber, A. Tselev, I.V. Vlassiouk, I.N. Ivanov, S. Jesse, S. Kalinin, B. Rodriguez, Nanotechnology **24**(47), 475702 (2013)
105. L. Collins, J. Kilpatrick, M. Bhaskaran, S. Sriram, S.A. Weber, S. Jarvis, B.J. Rodriguez, Presented at the Applications of Ferroelectrics Held Jointly with 2012 European Conference on the Applications of Polar Dielectrics and 2012 International Symposium on Piezoresponse Force Microscopy and Nanoscale Phenomena in Polar Materials (ISAF/ECAPD/PFM), 2012 International Symposium (2012) (unpublished)
106. H. Söngen, M. Nalbach, H. Adam, A. Kühnle, Rev. Sci. Instrum. **87**(6), 063704 (2016)
107. V. Parpura, P.G. Haydon, E. Henderson, J. Cell Sci. **104**(2), 427–432 (1993)
108. T. Fukuma, Y. Ueda, S. Yoshioka, H. Asakawa, Phys. Rev. Lett. **104**(1), 016101 (2010)
109. W. Frammelsberger, G. Benstetter, J. Kiely, R. Stamp, Appl. Surf. Sci. **252**(6), 2375–2388 (2006)
110. S. Jesse, A.P. Baddorf, S.V. Kalinin, Appl. Phys. Lett. **88**(6), 062908 (2006)
111. R.K. Vasudevan, S. Zhang, M. Baris Okatan, S. Jesse, S.V. Kalinin, N. Bassiri-Gharb, J. Appl. Phys. **118**(7), 072003 (2015)
112. L. Collins, M.B. Okatan, Q. Li, I.I. Kravenchenko, N.V. Lavrik, S.V. Kalinin, B. J. Rodriguez, S. Jesse, Nanotechnology **26**(17) (2015)
113. S. Hudlet, M. Saint Jean, C. Guthmann, J. Berger, Eur. Phys. J. B-Condensed Matter Complex Syst. **2**(1), 5–10 (1998)
114. S. Jesse, R. Vasudevan, L. Collins, E. Strelcov, M.B. Okatan, A. Belianinov, A.P. Baddorf, R. Proksch, S.V. Kalinin, Annu. Rev. Phys. Chem. **65**, 519–536 (2014)
115. S. Jesse, S.V. Kalinin, R. Proksch, A. Baddorf, B. Rodriguez, Nanotechnology **18**(43), 435503 (2007)
116. S. Guo, S.V. Kalinin, S. Jesse, Appl. Phys. Lett. **100**(6), 063118 (2012)
117. Q. Li, Y. Liu, D. Wang, R.L. Withers, Z. Li, H. Luo, Z. Xu, Appl. Phys. Lett. **101**(24), 242906 (2012)
118. E. Strelcov, Y. Kim, S. Jesse, Y. Cao, I.N. Ivanov, I.I. Kravchenko, C.-H. Wang, Y.-C. Teng, L.-Q. Chen, Y.H. Chu, S.V. Kalinin, Nano Lett. **13**(8), 3455–3462 (2013)
119. S. Sadewasser, T. Glatzel, M. Rusu, A. Meeder, D. Fuertes Marrón, A. Jäger-Waldau, M. Lux-Steiner, MRS Proc. **668**, H5.4.1 (2001)
120. G. Shao, G.E. Rayermann, E.M. Smith, D.S. Ginger, J. Phys. Chem. B **117**(16), 4654–4660 (2013)
121. J. Ding, E. Strelcov, V.S. Kalinin, N. Bassiri-Gharb, Nanotechnology **27**(34), 345401–345411 (2016)
122. J.L. Garrett, E.M. Tennyson, M. Hu, J. Huang, J.N. Munday, M.S. Leite, Nano Lett. (2017)
123. S. Somnath, A. Belianinov, S.V. Kalinin, S. Jesse, Appl. Phys. Lett. **107**(26), 263102 (2015)
124. S. Somnath, A. Belianinov, S.V. Kalinin, S. Jesse, Nat. Commun. **7** (2016)
125. L. Collins, M. Ahmadi, T. Wu, B. Hu, S. Kalinin, S. Jesse, ACS Nano **11**(9), 8717–8729 (2017)
126. I. Jolliffe, *Principal Component Analysis* (Wiley Online Library, 2002)

127. S. Jesse, S.V. Kalinin, Nanotechnology **20**(8), 085714 (2009)
128. S. Somnath, L. Collins, M.A. Matheson, S.R. Sukumar, S.V. Kalinin, S. Jesse, Nanotechnology **27**(41), 414003 (2016)
129. G. Gramse, G. Gomila, L. Fumagalli, Nanotechnology **23**(20), 205703 (2012)
130. N. Bonnet, J. Microsc.-Oxf. **190**, 2–18 (1998)
131. M. Bosman, M. Watanabe, D.T.L. Alexander, V.J. Keast, Ultramicroscopy **106**(11–12), 1024–1032 (2006)
132. F. Woolfe, E. Liberty, V. Rokhlin, M. Tygert, Appl. Comput. Harmon. Anal. **25**(3), 335–366 (2008)
133. T. Elgamal, M. Yabandeh, A. Aboulnaga, W. Mustafa, M. Hefeeda, Presented at the Proceedings of the 2015 ACM SIGMOD International Conference on Management of Data (2015) (unpublished)
134. I. Mitliagkas, C. Caramanis, P. Jain, Presented at the Advances in Neural Information Processing Systems (2013) (unpublished)
135. N. Balke, I. Bdikin, S.V. Kalinin, A.L. Kholkin, J. Am. Ceram. Soc. **92**, 1629–1647 (2009)
136. Y. Liu, H.-L. Cai, M. Zelisko, Y. Wang, J. Sun, F. Yan, F. Ma, P. Wang, Q.N. Chen, H. Zheng, X. Meng, P. Sharma, Y. Zhang, J. Li, Proc. Natl. Acad. Sci. U.S.A. **111**, E2780–E2786 (2014)
137. P. Bintachitt, S. Trolier-McKinstry, K. Seal, S. Jesse, S.V. Kalinin, Appl. Phys. Lett. **94**(4), 042906 (2009)
138. W. Sun, Q. Yu, J. Li, J.-F. Li, J. Phys. Chem. C **119**, 19891–19896 (2015)
139. P. Wang, J. Zhao, L. Wei, Q. Zhu, S. Xie, J. Liu, X. Meng, J. Li, Nanoscale, 3806–3817 (2017)
140. A.L. Kholkin, I.K. Bdikin, V.V. Shvartsman, N.A. Pertsev, Nanotechnology **18**, 095502 (2007)
141. N. Balke, S. Choudhury, S. Jesse, M. Huijben, Y.H. Chu, A.P. Baddorf, L.Q. Chen, R. Ramesh, S.V. Kalinin, Nat. Nanotechnol. **4**, 868–875 (2009)
142. S.M. Neumayer, E. Strelcov, M. Manzo, K. Gallo, I.I. Kravchenko, A.L. Kholkin, S.V. Kalinin, B.J. Rodriguez, J. Appl. Phys. **118**, 244103 (2015)
143. S. Jesse, B.J. Rodriguez, S. Choudhury, A.P. Baddorf, I. Vrejoiu, D. Hesse, M. Alexe, E.A. Eliseev, A.N. Morozovska, J. Zhang, L.Q. Chen, S.V. Kalinin, Nat. Mater. **7**(3), 209–215 (2008)
144. J. Xiao, T.S. Herng, J. Ding, K. Zeng, Acta Mater. **123**, 394–403 (2017)
145. V.R. Aravind, A.N. Morozovska, S. Bhattacharyya, D. Lee, S. Jesse, I. Grinberg, Y.L. Li, S. Choudhury, P. Wu, K. Seal, A.M. Rappe, S.V. Svechnikov, E.A. Eliseev, S.R. Phillpot, L.Q. Chen, V. Gopalan, S.V. Kalinin, Phys. Rev. B **82**(2) (2010)
146. V. Anbusathaiah, S. Jesse, M.A. Arredondo, F.C. Kartawidjaja, O.S. Ovchinnikov, J. Wang, S.V. Kalinin, V. Nagarajan, Acta Mater. **58**, 5316–5325 (2010)
147. E.A. Eliseev, A.N. Morozovska, G.S. Svechnikov, E.L. Rumyantsev, E.I. Shishkin, V.Y. Shur, S.V. Kalinin, Phys. Rev. B—Condens. Matter Mater. Phys. **78**, 1–10 (2008)
148. P. Bintachitt, S. Jesse, D. Damjanovic, Y. Han, I.M. Reaney, S. Trolier-McKinstry, S.V. Kalinin, Proc. Natl. Acad. Sci. U.S.A. **107**(16), 7219–7224 (2010)
149. F. Griggio, S. Jesse, A. Kumar, O. Ovchinnikov, H. Kim, T.N. Jackson, D. Damjanovic, S. V. Kalinin, S. Trolier-Mckinstry, Phys. Rev. Lett. **108**, 1–5 (2012)
150. S. Guo, O.S. Ovchinnikov, M.E. Curtis, M.B. Johnson, S. Jesse, S.V. Kalinin, J. Appl. Phys. **108**(8), 084103 (2010)
151. O. Ovchinnikov, S. Jesse, S. Guo, K. Seal, P. Bintachitt, I. Fujii, S. Trolier-McKinstry, S.V. Kalinin, Appl. Phys. Lett. **96**(11), 112906 (2010)
152. Y. Kim, A. Kumar, O. Ovchinnikov, S. Jesse, H. Han, D. Pantel, I. Vrejoiu, W. Lee, D. Hesse, M. Alexe, S.V. Kalinin, ACS Nano **6**, 491–500 (2012)
153. A. Kumar, Y. Ehara, A. Wada, H. Funakubo, F. Griggio, S. Trolier-McKinstry, S. Jesse, S. V. Kalinin, J. Appl. Phys. **112**(5), 052021 (2012)
154. A. Kholkin, A. Morozovska, D. Kiselev, I. Bdikin, B. Rodriguez, P. Wu, A. Bokov, Z.G. Ye, B. Dkhil, L.Q. Chen, M. Kosec, S.V. Kalinin, Adv. Func. Mater. **21**, 1977–1987 (2011)
155. T.M. Arruda, A. Kumar, S.V. Kalinin, S. Jesse, Nano Lett. **11**, 4161–4167 (2011)

156. N. Balke, S. Jesse, P. Yu, B. Carmichael, S.V. Kalinin, A. Tselev, Nanotechnology **27**, 425707 (2016)
157. R. Proksch, J. Appl. Phys. **116**, 066804 (2014)
158. N. Balke, S. Jesse, A.N. Morozovska, E. Eliseev, D.W. Chung, Y. Kim, L. Adamczyk, R.E. Garcia, N. Dudney, S.V. Kalinin, Nat. Nanotechnol. **5**(10), 749–754 (2010)
159. S. Kalinin, N. Balke, S. Jesse, A. Tselev, A. Kumar, T.M. Arruda, S.L. Guo, R. Proksch, Mater. Today **14**(11), 548–558 (2011)
160. S. Jesse, N. Balke, E. Eliseev, A. Tselev, N.J. Dudney, A.N. Morozovska, S.V. Kalinin, ACS Nano **5**(12), 9682–9695 (2011)
161. N. Balke, S. Jesse, Y. Kim, L. Adamczyk, A. Tselev, I.N. Ivanov, N.J. Dudney, S.V. Kalinin, Nano Lett. **10**(9), 3420–3425 (2010)
162. S.Y. Luchkin, K. Romanyuk, M. Ivanov, A.L. Kholkin, J. Appl. Phys. **118**, 072016 (2015)
163. A. Kumar, S. Jesse, A.N. Morozovska, E. Eliseev, A. Tebano, N. Yang, S.V. Kalinin, Nanotechnology **24**(14), 145401 (2013)
164. A. Kumar, D. Leonard, S. Jesse, F. Ciucci, E.A. Eliseev, A.N. Morozovska, M.D. Biegalski, H.M. Christen, A. Tselev, E. Mutoro, E.J. Crumlin, D. Morgan, Y. Shao-Horn, A. Borisevich, S.V. Kalinin, ACS Nano **7**(5), 3808–3814 (2013)
165. D.N. Leonard, A. Kumar, S. Jesse, M.D. Biegalski, H.M. Christen, E. Mutoro, E.J. Crumlin, Y. Shao-Horn, S.V. Kalinin, A.Y. Borisevich, Adv. Energy Mater. **3**(6), 788–797 (2013)
166. S. Doria, N. Yang, A. Kumar, S. Jesse, A. Tebano, C. Aruta, E. Di Bartolomeo, T.M. Arruda, S.V. Kalinin, S. Licoccia, G. Balestrino, Appl. Phys. Lett. **103**(17), 171605 (2013)
167. Y. Kim, E. Strelcov, I.R. Hwang, T. Choi, B.H. Park, S. Jesse, S.V. Kalinin, Sci. Rep. **3**, 2924 (2013)
168. I. Sugiyama, Y. Kim, S. Jesse, E. Strelcov, A. Kumar, A. Tselev, E.K. Rahani, V.B. Shenoy, T. Yamamoto, N. Shibata, Y. Ikuhara, S.V. Kalinin, Sci. Rep. **4**, 6725 (2014)
169. Y. Kim, A.N. Morozovska, A. Kumar, S. Jesse, E.A. Eliseev, F. Alibart, D. Strukov, S.V. Kalinin, ACS Nano **6**(8), 7026–7033 (2012)
170. Y. Kim, A.N. Morozovska, A. Kumar, S. Jesse, E.A. Eliseev, F. Alibart, D. Strukov, S.V. Kalinin, Ionically-mediated electromechanical hysteresis in transition metal oxides. ACS Nano **6**(8), 7026–7033 (2012)
171. N. Balke, I. Bdikin, S.V. Kalinin, A.L. Kholkin, J. Am. Ceram. Soc. **92**(8), 1629–1647 (2009)
172. N. Balke, P. Maksymovych, S. Jesse, A. Herklotz, A. Tselev, C.-B. Eom, I.I. Kravchenko, P. Yu, S.V. Kalinin, ACS Nano **9**, 6484–6492 (2015)
173. N. Balke, P. Maksymovych, S. Jesse, I.I. Kravchenko, Q. Li, S.V. Kalinin, ACS Nano **8**, 10229–10236 (2014)
174. J. Hong, S.-I. Park, Z. Khim, Rev. Sci. Instrum. **70**(3), 1735–1739 (1999)
175. A.N. Morozovska, E.A. Eliseev, A.K. Tagantsev, S.L. Bravina, L.Q. Chen, S.V. Kalinin, Phys. Rev. B **83**(19) (2011)
176. A.N. Morozovska, E.A. Eliseev, S.V. Kalinin, J. Appl. Phys. **111**(1) (2012)
177. B.J. Rodriguez, S. Jesse, A.N. Morozovska, S.V. Svechnikov, D.A. Kiselev, A.L. Kholkin, A.A. Bokov, Z.G. Ye, S.V. Kalinin, J. Appl. Phys. **108**(4), 042006 (2010)
178. A.N. Morozovska, E.A. Eliseev, N. Balke, S.V. Kalinin, J. Appl. Phys. **108**(5), 053712 (2010)
179. N. Balke, P. Maksymovych, S. Jesse, A. Herklotz, A. Tselev, C.-B. Eom, I.I. Kravchenko, P. Yu, S.V. Kalinin, ACS Nano **9**(6), 6484–6492 (2015)
180. N. Balke, S. Jesse, B. Carmichael, M.B. Okatan, I.I. Kravchenko, S.V. Kalinin, A. Tselev, Nanotechnology **28**(6), 065704 (2017)
181. S.M. Yang, A.N. Morozovska, R. Kumar, E.A. Eliseev, Y. Cao, L. Mazet, N. Balke, S. Jesse, R.K. Vasudevan, C. Dubourdieu, S.V. Kalinin, Nat. Phys. (2017)
182. N. Balke, S. Jesse, P. Yu, B. Carmichael, S.V. Kalinin, A. Tselev, Nanotechnology **27**(42), 425707 (2016)
183. S.V. Kalinin, E. Strelcov, A. Belianinov, S. Somnath, R.K. Vasudevan, E.J. Lingerfelt, R.K. Archibald, C. Chen, R. Proksch, N. Laanait, (ACS Publications, 2016)

Chapter 4
Practical Aspects of Kelvin Probe Force Microscopy in Liquids

Kei Kobayashi and Hirofumi Yamada

Abstract There has been a strong demand for the development of scanning probe techniques that can map the distribution of surface charge and surface potential at nanometer scale in liquid media. While electrostatic force microscopy (EFM) and Kelvin probe force microscopy (KPFM) have routinely been used in vacuum and ambient conditions, they are not readily applicable in polar liquid media. In this chapter, we review the practical aspects of electrostatic and capacitive force detection in liquids and discuss the feasibility of measuring the surface charge or potential distribution in polar liquid media.

4.1 Introduction

Electrostatic force microscopy (EFM) and Kelvin probe force microscopy (KPFM) are scanning probe techniques for mapping local surface charge and potential. These methods utilize the detection of the electrostatic forces induced by an alternating modulation voltage that is applied between the tip and sample surface. These methods have been commonly used under ambient conditions as well as in vacuum environments. Recently, there has been a strong demand for local surface charge and potential measurements in polar liquids, especially in aqueous solutions containing electrolytes (ions). However, since the surface charges are screened by the surrounding counter ions in aqueous solutions, forming an electric double layer (EDL), the electrostatic interaction between tip and surface is not as simple as that in vacuum or air.

The spatial resolution of the scanning probe techniques stems from the strong distance dependence of the tip-sample interaction. We first review the potential profile of the EDL and analyze the electrostatic force as well as the capacitive force acting between the tip and sample in terms of the tip-sample distance dependence, that is critical for obtaining high spatial resolution in the local surface charge and

K. Kobayashi (✉) · H. Yamada
Kyoto University, Kyoto, Japan
e-mail: keicoba@iic.kyoto-u.ac.jp

S. Sadewasser and T. Glatzel (eds.), *Kelvin Probe Force Microscopy*,
Springer Series in Surface Sciences 65, https://doi.org/10.1007/978-3-319-75687-5_4

potential measurements. We then discuss the possibility of the local surface charge and potential measurements in liquid media using voltage modulation techniques in detail and present some criteria for achieving nanometer-scale surface charge and potential measurements. Finally, we also demonstrate the surface charge measurement on a biological sample using the three-dimensional (3D) force mapping technique, as an alternative method to map the local surface charge and potential in liquid media.

4.2 Electric Double Layer

In this section, we review the basic properties of the EDL [1]. When a charged surface is exposed to an aqueous solution containing ions, counter ions having the charge opposite to the surface charge in the solution are attracted to the charged surface, which causes a density gradient toward the charged surface. The distribution of the ion of any species i in the solution follows the Boltzmann distribution, given by

$$n_i = n_i^{\infty} \exp\left(- \frac{z_i e \phi}{k_B T} \right), \tag{4.1}$$

where ϕ is the potential measured with respect to the bulk solution, e and z_i are the elementary charge and the ion valence, n_i^{∞} is the ion concentration in the bulk solution, and k_B and T are the Boltzmann constant and temperature. The total charge density is thus given by

$$\rho = \sum_i z_i e n_i = e \sum_i z_i n_i. \tag{4.2}$$

Since the charge density is related to the potential by the Poisson's equation as

$$\rho = - \varepsilon_r \varepsilon_0 \nabla^2 \phi, \tag{4.3}$$

we obtain the Poisson-Boltzmann equation by combining (4.1) and (4.3), which is given by

$$\nabla^2 \phi = - \frac{e}{\varepsilon_r \varepsilon_0} \sum_i z_i n_i^{\infty} \exp\left(- \frac{z_i e \phi}{k_B T} \right). \tag{4.4}$$

Here we consider the one-dimensional (1D) capacitor model, in which a pair of planar metallic electrodes are facing each other in an aqueous solution, as shown in Fig. 4.1a. The Poisson-Boltzmann equation for the 1D capacitor model is given by

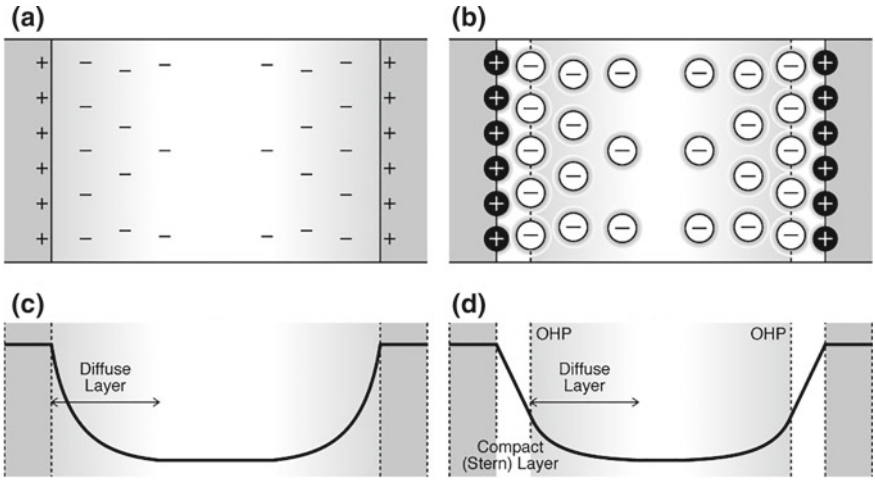

Fig. 4.1 Schematic model of equally charged electrodes in electrolyte. **a** Gouy-Chapman model. **b** Potential profile in Gouy-Chapman model. **c** Gouy-Chapman-Stern (GCS) model. **d** Potential profile in GCS model. OHP stands for the outer Helmholtz plane, which is defined as the surface of the compact layer

$$\frac{\mathrm{d}^2}{\mathrm{d}x^2}\phi(x) = -\frac{e}{\varepsilon_\mathrm{r}\varepsilon_0}\sum_i z_i n_i^\infty \exp\left(-\frac{z_i e\,\phi}{k_\mathrm{B}T}\right), \tag{4.5}$$

where x is a coordinate. In order to further simplify the equation, we consider the case where only monovalent ions exist in the solution (a 1:1 electrolyte). In this case, the equation is simplified as

$$\frac{\mathrm{d}^2}{\mathrm{d}x^2}\phi(x) = \frac{en^\infty}{\varepsilon_\mathrm{r}\varepsilon_0}\sinh\left(\frac{e\phi}{k_\mathrm{B}T}\right), \tag{4.6}$$

where n^∞ is the concentration of the monovalent ions. By solving (4.6) with a boundary condition of the surface potential at the charged surface, $\phi(0) = \phi_\mathrm{D}$, we obtain

$$\frac{\tanh[e\phi/(4k_\mathrm{B}T)]}{\tanh[e\phi_\mathrm{D}/(4k_\mathrm{B}T)]} = e^{-\kappa_\mathrm{D}x}, \tag{4.7}$$

where κ_D is given by

$$\kappa_\mathrm{D} = \sqrt{\frac{2\,e^2 n^\infty}{\varepsilon_\mathrm{r}\varepsilon_0 k_\mathrm{B}T}}. \tag{4.8}$$

κ_D^{-1} is the so-called the Debye screening length (L_D) corresponding to the thickness of the diffuse layer, in which the concentration of the counter ions is higher than in the bulk. Figure 4.1b shows a potential profile of a pair of equally charged electrodes. The left-hand side of (4.7) can be simplified as

$$\frac{\phi(x)}{\phi_D} = \exp(-\kappa_D x), \tag{4.9}$$

when the surface potential is low and the condition

$$e\phi_D/(4\,k_B T) < 0.5, \tag{4.10}$$

is met, namely for $\phi_D < 50\,\mathrm{mV}$. Note that (4.9) is the solution of the linearized version of the 1D Poisson-Boltzmann equation, which is given by

$$\frac{d^2\phi(x)}{dx^2} = \kappa_D^2 \phi(x). \tag{4.11}$$

Since the relationship between the surface potential and the surface charge density is determined by Gauss's law, the surface charge on the electrode with the potential ϕ_D is given by

$$\sigma_s = -\varepsilon_r \varepsilon_0 \left.\frac{d\phi(x)}{dx}\right|_{x=0} = \sqrt{8k_B T \varepsilon_r \varepsilon_0 n^\infty}\,\sinh\left(\frac{e\phi_D}{2k_B T}\right), \tag{4.12}$$

and the capacitance of the diffuse layer per unit area is defined by

$$C_D = \frac{d\sigma_s}{d\phi_D} = \sqrt{\frac{2e^2 \varepsilon_r \varepsilon_0 n^\infty}{k_B T}}\cosh\left(\frac{e\phi_D}{2k_B T}\right) = \kappa_D \varepsilon_r \varepsilon_0 \cosh\left(\frac{e\phi_D}{2k_B T}\right). \tag{4.13}$$

This simple interface model is referred to as the Gouy-Chapman model. Since the model fails to explain the experimentally measured capacitance versus voltage characteristics, Stern modified the Gouy-Chapman model by taking into account the finite size of the ions and introduced an idea of a thin layer (compact layer or Stern layer) on the surface where even the bound counter ions cannot reach, as shown schematically in Fig. 4.1c. Since the charge density in the compact layer is zero, the capacitance of the compact layer per unit area is simply given by

$$C_S = \frac{\varepsilon_r \varepsilon_0}{t_c}, \tag{4.14}$$

where t_c is the thickness of the compact layer. Now the surface potential of the electrode is modified to

$$\phi_0 = \phi_D + \sqrt{\frac{8k_B T n^\infty}{\varepsilon_r \varepsilon_0}} \sinh\left(\frac{e\phi_D}{2k_B T}\right) t_c. \tag{4.15}$$

This interface model is referred to as the Gouy-Chapman-Stern (GCS) model, in which the EDL is composed of two layers; i.e., the diffuse layer and the compact layer. Figure 4.1d shows a potential profile of a pair of equally charged electrodes in the GCS model.

4.3 Capacitive Force

The electrostatic force acting between tip and sample in EFM or KPFM (F_{el}) is generally described as

$$F_{el} = \frac{1}{2}\frac{dC_{ts}}{dz} V_{ts}^2, \tag{4.16}$$

where C_{ts} is the capacitance between tip and sample, V_{ts} is the voltage between tip and sample, and z is the tip-sample distance. When a modulation voltage of an amplitude V_{ac} at an angular frequency ω_m (frequency: f_m) with a dc offset voltage V_{dc}, namely $V_m = V_{dc} + V_{ac}\cos(\omega_m t)$, is applied between tip and sample, the electrostatic force becomes

$$F_{el} = \frac{1}{2}\frac{dC_{ts}}{dz}\left[(V_{dc} + V_{SP})^2 + \frac{1}{2}V_{ac}^2 + 2(V_{dc} + V_{SP})V_{ac}\cos(\omega_m t) + \frac{1}{2}V_{ac}^2\cos(2\,\omega_m t)\right] \tag{4.17}$$

where V_{SP} is the surface potential difference between tip and sample. The last term in the equation ($2\omega_m$ component) is often referred to as the capacitive force.

In order to analyze the electrostatic force acting between tip and sample that is induced by the modulation voltage, it is important to understand the voltage drop of the modulation voltage between a pair of electrodes which are facing each other [2]. The equivalent circuit for a pair of facing electrodes in electrolyte can be depicted as shown in Fig. 4.2a. Note that the circuit is valid only when the EDLs of the surfaces do not overlap with each other. In this model, the EDL capacitance C_{EDL} is comprised of a series of the compact (Stern) layer capacitance C_S and the diffuse layer capacitance C_D. The impedance of the bulk solution is expressed by a parallel circuit of the bulk solution resistance per unit area, R_B, and capacitance per unit area, C_B. R_B is described as

$$R_B = d\rho_B, \tag{4.18}$$

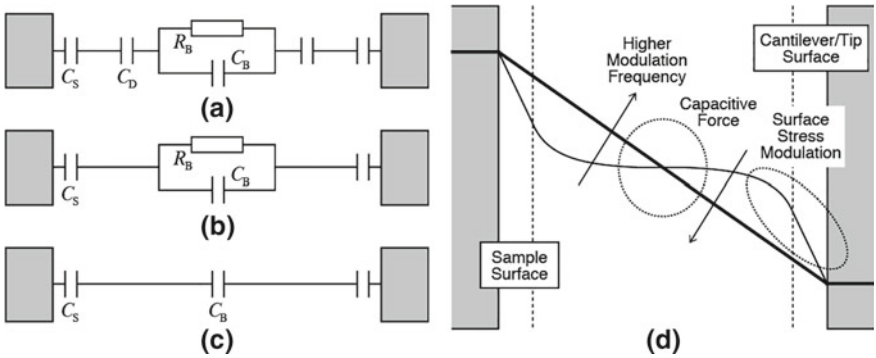

Fig. 4.2 Equivalent circuits for a pair of facing electrodes in aqueous solutions for a modulation frequency (f_m) in the ranges of **a** $f_m < f_D$, **b** $f_D < f_m < f_c$, and **c** $f_c < f_m$. **d** Snapshot of the potential profile when the voltage of the sample is positive with respect to the cantilever and tip. In the low modulation frequency regime ($f_m < f_D$), only the potential gradient (electric field) at the interface is modulated, and the cantilever deflection is predominantly caused by the surface stress variation. In the high modulation frequency regime ($f_c < f_m$), the electric field in the bulk solution is effectively modulated, and the cantilever deflection is predominantly caused by the capacitive force

where d and ρ_B are the distance between the electrodes and the resistivity of the electrolyte, respectively.

When f_m is very low, the modulation voltage is effectively applied to the electrode/electrolyte interface, and charge and discharge of the diffuse layer occur with an ionic current flow in the bulk solution. This happens when f_m is lower than a threshold frequency (f_D), which is defined as the frequency at which the impedance of C_D becomes smaller than R_B, i.e.,

$$f_D = \frac{1}{2\pi R_B (C_D/2)} = \frac{1}{\pi d \kappa_D \varepsilon_r \varepsilon_0 \rho_B \cosh\left(\frac{eV_{ac}^D}{2k_B T}\right)} \propto \frac{\sqrt{n^\infty}}{\varepsilon_r}, \tag{4.19}$$

where V_{ac}^D is the magnitude of the modulation voltage applied to the diffuse layer, which roughly corresponds to $V_{ac}/2$ because V_{ac} is effectively applied to the two diffuse layers and divided by the two. In this case, the impedance of the bulk solution is dominated by the bulk solution resistance R_B, and most of the modulation voltage is effectively applied to C_D, which does not depend on the tip-sample distance. This causes a modulation in the cantilever deflection induced by the surface stress variation [3, 4]. Therefore, f_m should be higher than f_D for EFM or KPFM in aqueous solutions.

Even though this criterion is met; i.e. f_m is higher than f_D, ionic current flow still occurs in the bulk solution; the equivalent circuit in this regime is depicted in Fig. 4.2b. Therefore, f_m should be even higher than another threshold frequency, namely the characteristic relaxation frequency of the ionic current flow (f_c), which is dependent only on the physical property of the solution, defined as

$$f_c = \frac{1}{2\pi\varepsilon_r\varepsilon_0\rho_B} \propto \frac{n_\infty}{\varepsilon_r}. \tag{4.20}$$

If this criterion is met, the impedance of C_B becomes smaller than R_B, and thus a further simplified equivalent circuit, shown in Fig. 4.2c, can be used.

Figure 4.2d illustrates a potential profile between tip and sample for an alternating modulation voltage [2, 5]. The figure depicts a snapshot of the potential profile when the voltage of the sample is positive with respect to the cantilever with a tip. The thin voltage potential curve corresponds to the profile for a lower modulation frequency ($f_m < f_D$: Fig. 4.2a), while the thick voltage potential curve corresponds to that for a higher modulation frequency ($f_m > f_c$: Fig. 4.2c). In the former case the cantilever deflection induced by the surface stress variation is prominent, while in the latter case the modulation voltage is effectively applied in C_B and the cantilever deflection induced by the capacitive force is expected.

We can calculate the capacitive force in aqueous solutions as a function of the tip-sample distance. The total capacitive force acting on a cantilever with a tip is considered as a sum of the force components acting on a spherical tip apex, a conical tip body, and a cantilever part [6, 7]. Each component can be calculated by integrating the force acting on a unit area by taking the voltage division ratio between C_B and C_S into account for each component [2]. It should be noted that the capacitive force as well as the electrostatic force at the tip-sample distance of less than a few tens of nanometers is affected by the dielectric saturation, i.e. the reduction of the dielectric constant in the EDL in the case of a high electric field [8, 9]. The Booth equation is generally used for the dielectric saturation, which is given by

$$\varepsilon_r(E) = n_w^2 + \frac{3\left(\varepsilon_r^\infty - n_w^2\right)}{\beta E}\left[\coth(\beta E) - \frac{1}{\beta E}\right], \tag{4.21}$$

where n_w is the refractive index of water, and β is given by

$$\beta = \frac{5\mu_w\left(n_w^2 + 2\right)}{2k_B T}, \tag{4.22}$$

where μ_w is the electric dipole moment of a water molecule. Although the dielectric constant is a nonlinear function of the electric field, it can be approximated to a parabolic form when the electric field is less than 0.1 V/nm as

$$\varepsilon_r(E) \approx \varepsilon_r^\infty - \nu E^2, \tag{4.23}$$

using a constant ν.

4.4 Electrostatic Force

Here, we consider the variation in the potential profile when the tip-sample distance is reduced. Figure 4.3a shows a schematic of ac potential profiles for a large and a short distance with f_m higher than f_c. As the tip-sample distance decreases, the alternating electric field in the bulk solution is increased. However, because of the increase in C_B, the voltage division ratio between C_B and C_S also changes. In other words, the potential drop in C_S also increases by the reduction of the tip-sample distance. This phenomenon deteriorates the spatial resolution of the electrostatic force as well as the capacitive force measurements [2].

We also calculated the electric field induced by an externally applied dc voltage (V_{dc}), as shown in Fig. 4.3b. In the GCS model, when the distance between the electrodes is large and there is no overlap of the EDLs ($d > 2L_D$), the potential gradient at the midpoint is almost zero. As the two surfaces come close to each other, an increase in the potential gradient at the midpoint is expected due to the charge regulation [10, 11].

We can calculate the electrostatic force per unit area, namely the Maxwell stress (T_{el}) using the dc electric field $\left(E_{dc}^{m}\right)$ and ac electric field $\left(E_{dc}^{m}\right)$ at the midpoint ($x = d/2$) as

$$T_{el}(\omega_m) = \frac{1}{2}\varepsilon_r\varepsilon_0 E^2 = \frac{1}{2}\varepsilon_r\varepsilon_0\left[E_{dc}^{m} + E_{ac}^{m}\cos(\omega_m t)\right]^2$$
$$= \frac{1}{2}\varepsilon_0\varepsilon_r\left[\left(E_{dc}^{m}\right)^2 + \frac{1}{2}\left(E_{ac}^{m}\right)^2 + 2E_{dc}^{m}E_{ac}^{m}\cos(\omega_m t) + \frac{1}{2}\left(E_{ac}^{m}\right)^2\cos(2\omega_m t)\right]. \tag{4.24}$$

The dc electric field at the midpoint can be calculated from the dc potential profile between the electrodes. The potential of the electrode surface can be

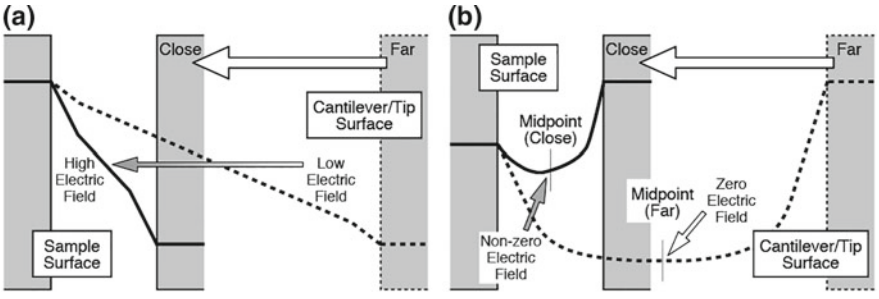

Fig. 4.3 **a** Schematic of ac potential profiles between a pair of facing electrodes in aqueous solution for two tip-sample distances. The ac potential profiles depict an instantaneous maximum voltage for the case when V_{ac} is applied to the left electrode (sample) with respect to the right electrode (cantilever with a tip). **b** Schematic of dc potential profiles between a pair of facing electrodes for two tip-sample distances

considered as constant in weak electrolyte solutions such as pure water [11]. For the calculation of the dc potential profile between the two electrodes, an analytical solution expressing the relationship of d, ϕ_0, and E is required. However, the analytical solution of the Poisson-Boltzmann equation can be obtained only in the case when ϕ_d is less than 50 mV and the distance between the surfaces is larger than L_D [12]. Therefore, we used an approximate equation, which is valid for arbitrary potential, by the linear superposition approximation (LSA) [13]. The dc electric field at the midpoint between the surfaces is expressed as

$$E_{dc}^{m} = -\left.\frac{d\phi_{dc}}{dx}\right|_{x=d/2} = \frac{2k_BT}{de}\left\{-\ln\left[\frac{1+\gamma_1 e^{-\frac{\kappa_D d}{2}}}{1-\gamma_1 e^{-\frac{\kappa_D d}{2}}}\right] + \ln\left[\frac{1+\gamma_2 e^{-\frac{\kappa_D d}{2}}}{1-\gamma_2 e^{-\frac{\kappa_D d}{2}}}\right]\right\} + \frac{4\kappa_D k_B T}{de}(-\gamma_1+\gamma_2)e^{-\frac{\kappa_D d}{2}}, \tag{4.25}$$

where γ_i is given by

$$\gamma_i = \tanh\left(\frac{e\phi_i}{4k_BT}\right). \tag{4.26}$$

The first and second terms in (4.25) are the dc electric field at the midpoint when the EDLs of the surfaces are not overlapping, and that when they are overlapping, respectively. On the other hand, the ac electric field at the midpoint between the surfaces is expressed as

$$E_{ac}^{m} = -\left.\frac{d\phi_{ac}}{dx}\right|_{x=d/2} = \frac{V_{ac}}{d}\frac{1+2\frac{C_B}{C_S}}{\left(2\frac{C_B}{C_S}\frac{f_c}{f_m}\right)^2 + \left(1+2\frac{C_B}{C_S}\right)^2}\cos(\omega_m t) \tag{4.27}$$

taking the voltage division ratio into account. Furthermore, we took into account the dielectric saturation [8, 9].

We measured the electrostatic and capacitive forces induced on a conductive cantilever with a tip when an alternating voltage is applied between the cantilever and a sample surface in aqueous solutions [14]. We found that the electrostatic force contribution to the cantilever deflection becomes dominant when a high modulation frequency was used. However, we could not observe the steep increase in the electrostatic force that should be expected for the electrostatic force acting on the tip apex. On the contrary, we observed the electrostatic force even when the cantilever was far from the sample surface, despite that the potential gradient at the midpoint is expected to be almost zero in the GCS model (see Fig. 4.3b) and thereby negligible electrostatic force since there is no overlap of the EDLs ($d > 2L_D$). We consider that this is due to the alternating electric field being directly applied to C_B between the cantilever part and sample surface with a high modulation frequency

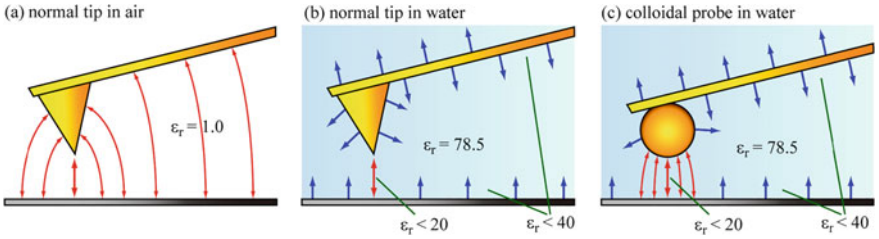

Fig. 4.4 Schematics of the electric field distributions in the experimental conditions with a metal-coated regular cantilever with a tip in **a** air, **b** water, and **c** a metal-coated colloidal probe (CP) cantilever in water. The red arrows show the electric field between the tip and the sample, and the blue arrows show the electric field in the EDLs. Reprinted from J. Appl. Phys. 116, 134307 (2014) with the permission of AIP Publishing

(large E_{ac}^{m}) and thus an unexpected voltage drop in the bulk solution (nonzero E_{dc}^{m}) could cause a significant electrostatic force on the cantilever part since it is proportional to the product of E_{ac}^{m} and E_{dc}^{m}. Therefore, we consider that we need to reduce the long-range parasitic electrostatic force acting on the cantilever.

We measured the capacitive and electrostatic force in an aqueous solution using a colloidal probe (CP) cantilever to demonstrate the effect of the reduction of the long-range parasitic electrostatic force. Figure 4.4a shows the schematics of the dc electric field distribution between a cantilever with a regular sharp tip and the sample in air. The electric field exists between the entire cantilever and the sample. On the other hand, Fig. 4.4b shows the dc electric field distribution between a regular cantilever and a sample in water. Since the dc electric field is screened by the EDLs, there should be no dc electric field at the midpoint between the cantilever part and sample. However, we indeed observed the long-range parasitic electrostatic force acting on the cantilever part. Figure 4.4c shows the dc electric field distribution between a CP cantilever and a sample in water. Since the effective interaction area of the CP is much larger than that of the regular cantilever, it is expected that we could detect the electrostatic force acting on the CP that overwhelms the parasitic electrostatic force acting on the cantilever part by using the CP cantilever.

We used the second resonance mode of the CP cantilever, which was around 855 kHz, in order to excite the cantilever at a high frequency. The spring constant and quality factor at the second resonance were determined as 1,350 N/m and 12, respectively. Figure 4.5a shows the amplitude of the ω_m component as a function of V_{dc} obtained when the tip-sample distance was kept at about 10 nm in pure water. V_{dc} and V_{ac} were set at 0 V and 2.8 V peak-to-peak, respectively. The result shows that the hysteresis caused by the surface stress effect is negligible, but no minimum point was observed in this measurement range. This fact means that the KPFM bias voltage feedback cannot be used even using the CP cantilever. As explained in Fig. 4.3b, V_{dc} mainly drops at C_S, while the electric field in C_B matters the measured electrostatic force. Depending on the combination of the materials of tip and sample and the electrolyte, the force minimum might be observed in the

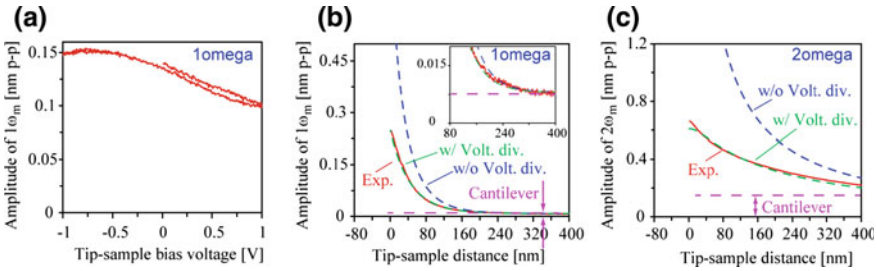

Fig. 4.5 **a** Amplitude of ω_m as a function of V_{dc} in water. Amplitudes of **b** ω_m component ($f_m = f_2 = 855$ kHz) and **c** $2\omega_m$ component ($f_m = f_2/2 = 378$ kHz) of the cantilever deflection signal as a function of the tip-sample distance in water. The inset in **b** shows the magnified data at large distance. The red, blue, and green curves show the experimental curve, theoretically fitted curve without taking into account the voltage division ratio, and with it, respectively. The purple broken line shows the offset in the oscillation amplitude caused by the electrostatic/capacitive force acting on the cantilever other than the colloid. Reprinted from J. Appl. Phys. 116, 134307 (2014) with the permission of AIP Publishing

measurement range, but it is difficult to estimate the surface potential difference anyway.

Figure 4.5b, c show plots of the amplitudes of the ω_m and $2\omega_m$ components as a function of the tip-sample distance, respectively. In both results, as the tip-sample distance was decreased, the magnitude of both components increased due to the increase in C_B. The purple broken line shows the offset caused by the electrostatic force acting on the cantilever, which has almost no dependence on the tip-sample distance. The increase in the $2\omega_m$ component was almost double the offset at the closest distance, while the ω_m component showed a steep increase. The blue and green broken curves shown in Fig. 4.5b, c are the fitting curves calculated by the theoretical equation, (4.24), without and with taking into account the voltage division by C_S in (4.27), respectively. From the best fitted parameters, the local surface potential difference under the CP was estimated to be 0.25 V. We also obtained the parameters such as $L_D = 30$ nm and $C_S = 0.011$ F/m^2 by the fitting. L_D was shorter than that expected from (4.8) probably because of the dissolved CO_2 from the ambient, while C_S was smaller than the literature value of 0.2–0.3 F/m^2 [15] probably because of the surface roughness, adsorbates or contaminants.

Finally, we discuss the criteria for the geometry of the cantilever and tip required for the local surface potential measurements. Reduction of the cantilever dimensions and increase of the tip height both would lead to the reduction of the parasitic long-range electrostatic force. In particular, the reduction of the cantilever dimensions is preferred because it increases the resonance frequency, which is favorable for sensitive force detection. Note that even if such a dedicated force sensor is available, the Stern layer capacitance and the dielectric constant that is typically lower than the liquid media attenuate the voltage division ratio in the bulk solution and thereby attenuate the local electrostatic force. Therefore, great care should be taken to estimate the local surface potential using the voltage modulation techniques.

4.5 Surface Charge Measurement by Force Mapping

We have shown that the detection of the capacitive and electrostatic force induced by the modulation voltage application are fairly complicated. It is rather straightforward to directly measure the electrostatic force acting on the cantilever with a tip as a function of the tip-sample distance by a force distance curve measurement, and then analyze it to deduce the surface charge and/or surface potential [16–20]. In this section, we demonstrate the local charge density measurement of plasmid DNA molecules using frequency modulation AFM (FM-AFM). For small-amplitude FM-AFM, the frequency shift (Δf) signal is approximately proportional to the force gradient. Hence, an increase in the electrolyte concentration leads to an increase in the observed Δf signal as well as in the spatial resolution because of the decrease in L_D despite the weakening of the F_{el} itself.

We used plasmid pUC18 (2686 base pairs) DNA molecules (Takara Bio) on a muscovite mica (Furuuchi Chemical) as a model sample. We coated the mica substrate with a positively charged poly-L-lysine (PL) layer. A water solution of the DNA (2–3 mg/L) was dropped onto the PL-coated mica surface. After 5–10 min, the sample was rinsed with a KCl solution, and imaged by FM-AFM without drying.

We used a home-built FM-AFM setup with an ultra-low noise deflection sensor [21] and a photothermal excitation setup [22]. We used a cantilever with a spring constant of about 30 N/m. The resonance frequency of the cantilever in the solution was about 150 kHz. The oscillation amplitude was set to 0.4 and 0.8 nm peak-to-peak in the 100 mM and 10 mM KCl solutions which were slightly smaller than L_D (0.97 and 3.07 nm at 298 K), respectively, to obtain a better spatial resolution. We obtained 3D Δf maps in a volume of $60 \times 40 \times 8.8$ nm^3 ($128 \times 64 \times 200$ pixels) in XYZ by consecutively collecting Δf maps in 2D(ZX) planes, which were collected by recording the Δf data while approaching the tip to the sample surface with a velocity of about 300 nm/s (corresponding to a triangular waveform of about 17 Hz) until Δf reached a predetermined threshold value [23].

For calculation of the surface charge from the measured frequency shift map, we employed the DLVO (Derjaguin, Landau, Verwey and Overbeek) force model [24], which assumes the total interaction force as the sum of F_{el} and van der Waals force (F_{vdW}). For a 1:1 symmetric electrolyte, the EDL force vector acting between two surfaces is calculated by

$$\overrightarrow{\mathbf{F}}_{el} = \iint_S \left\{ 2n^{\infty} k_B T \left[\cosh\left(\frac{e\phi}{k_B T} \right) - 1 \right] \mathbf{I} - \frac{\varepsilon_r \varepsilon_0}{2} (\nabla \phi)^2 \right\} \cdot \hat{\mathbf{n}} \, dS, \tag{4.28}$$

where the z component of $\overrightarrow{\mathbf{F}}_{el}$ gives F_{el}. The first term is the osmotic pressure tensor term, which is always repulsive, and the second term is the Maxwell stress tensor term, which is always attractive, both of which can be calculated once the distribution of the potential is determined [25, 26]. $\mathbf{I}$ and $\hat{\mathbf{n}}$ are the unit tensor and

the unit normal vector, respectively. We calculated the potential distribution by solving the Poisson-Boltzmann equation [27, 28]. While the constant charge or constant potential condition is commonly known, the surface conditions in the electrolytes are always somewhere between these extremes (charge regulation) [11, 29]. We calculated the potential distribution with the LSA [13, 30]. Namely, we first calculated the surface potential and charge densities of the two surfaces under the condition that the EDLs do not overlap. Secondly, the potential distribution between the two surfaces was determined by linearly superposing the effective potential distributions calculated for the two surfaces using the potential formulae. Finally, F_{el} acting between the surfaces was calculated using (4.28) from the potential and the electric field [24, 30]. Then we calculated the theoretical Δf_{el} curves from the theoretical F_{el} curves using the experimental parameters. The DNA molecule was modeled as a cylinder with a radius of 1.3 nm considering the hydration layers on the DNA, and the tip radius was set to 12 nm as it gave the best fit of the theoretical Δf curves to the experimental Δf curves.

For calculation of F_{vdW}, we employed the surface element integration (SEI) method using the Derjaguin construction [25], as

$$F_{vdW}(z+z_0) = \iiint_{V_t} \iiint_{V_s} F_{atom-atom}(r)\mathrm{d}V_s\mathrm{d}V_t \approx \iint_{S_{ts}} P_{vdW}\,\mathrm{d}S_{ts}, \tag{4.29}$$

where z_0 is an offset parameter used to correct the difference in the onset position of the F_{vdW}. P_{vdW} is F_{vdW} per unit area given by

$$P_{vdW}(z) = -\left[A_H^{\nu=0}\exp(-2z/\lambda_D) + A_H^{\nu>0}\right]\frac{1}{6\pi z^3}, \tag{4.30}$$

where $A_H^{\nu=0}$ and $A_H^{\nu>0}$ are the Hamaker constants representing the zero-frequency and dispersion contributions, respectively. The radius of the DNA was set to 1.0 nm for the calculation of F_{vdW}.

Figure 4.6a, b show the topography images reconstructed from the 3D Δf maps. The helical structures of the DNA molecules are visible in both images, as indicated by the arrows in the images. The helical structures are less clear than our previous result [31] mainly due to the larger roughness of the PL layer surface. Figure 4.6c, d show the 2D(XY) Δf maps obtained at a distance of around 0.4 nm above the DNA molecules in the 100 mM and 10 mM solutions, respectively. Figure 4.6e, f show the 2D(ZX) Δf maps obtained in the XY planes including lines A–B and C–D that cross the DNA molecules in the 100 mM and 10 mM solutions, respectively. The yellow pixels in each map represent the points without data because the tip was retracted. The interface of the regions with and without data in each map represents the topographic line profile, from which the heights of the DNA molecules are estimated to be about 1.8 and 1.6 nm in the 100 mM and 10 mM solutions, respectively.

In principle, repulsive and attractive F_{el} are expected on the DNA molecules and the PL layer, respectively. Since L_D is half the height of the DNA molecules in the

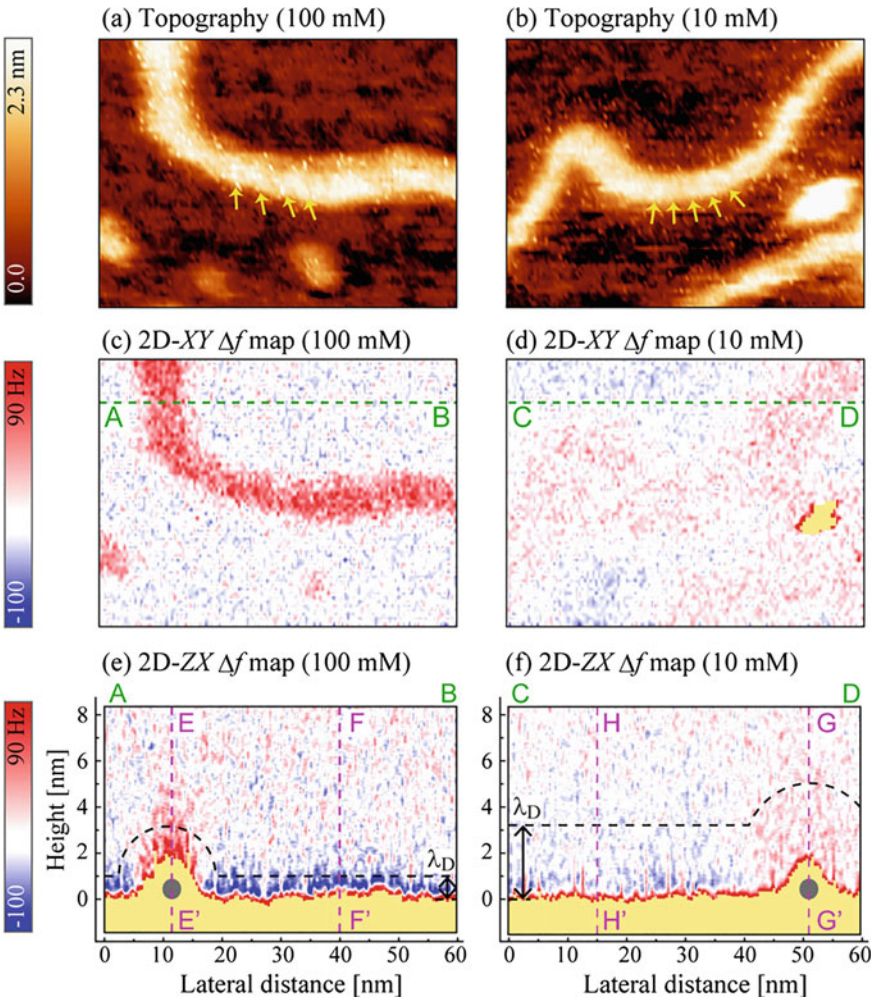

Fig. 4.6 **a** and **b** are topography images of plasmid DNA molecules on mica coated with a poly-L-lysine layer at constant Δf of +100 Hz reconstructed from 3D Δf data in 100 mM and 10 mM KCl solutions, respectively. The arrows indicate the helical periodicity of the DNA molecules, which is about 3.6 nm. **c** and **d** are 2D(XY) Δf maps obtained at the surface of 0.4 nm from DNA in 100 mM and 10 mM KCl solutions, respectively. **e** and **f** are 2D(ZX) Δf maps of the plasmid DNA molecules extracted from the 3D Δf data in a ZX plane crossing DNA in 100 mM and 10 mM KCl solutions, respectively. The black dotted curves schematically indicate L_D in each solution. Reprinted from [19], © IOP Publishing. Reproduced with permission. All rights reserved

100 mM KCl solution, the EDL of the PL layer (blue area) is not overlapped with that of the DNA molecule (red area). On the other hand, in the 10 mM KCl solution, L_D is 1.5 times larger than the height of the DNA molecule. Hence the EDL of the PL substrate (blue) is overlapped with that of the DNA molecule (red).

Therefore, F_{el} on the DNA molecule is not solely reflected by the EDL of the DNA molecule, but also reflected by the EDL on the PL layer in 10 mM solution.

We then constructed theoretical 2D Δf_{el} maps to determine if they are consistent with the experimental 2D(XY) Δf_{el} maps. Figure 4.7a, b show the theoretical 2D Δf_{el} maps for 100 mM and 10 mM KCl solutions, respectively. The lateral size of the DNA molecule was set to about 7 times larger than the actual size considering the tip convolution effect. Note that Δf_{el} caused by F_{el} spreads out to the distance of L_D in each map.

Figure 4.7c shows the averaged Δf versus distance curves measured on the DNA molecule and the PL layer in the 100 mM solution at the locations indicated by the E–E′ and F–F′ lines, respectively, in Fig. 4.6e. The red and blue solid curves are obtained on the DNA molecule and PL layer, respectively. On both surfaces, the exponential F_{el} is dominant at distances larger than 0.5 nm, while F_{vdW} and Pauli repulsion force are dominant at distances less than 0.5 nm. Since Fig. 4.6e showed that the EDL of the PL substrate (blue area) was not overlapped with that of the

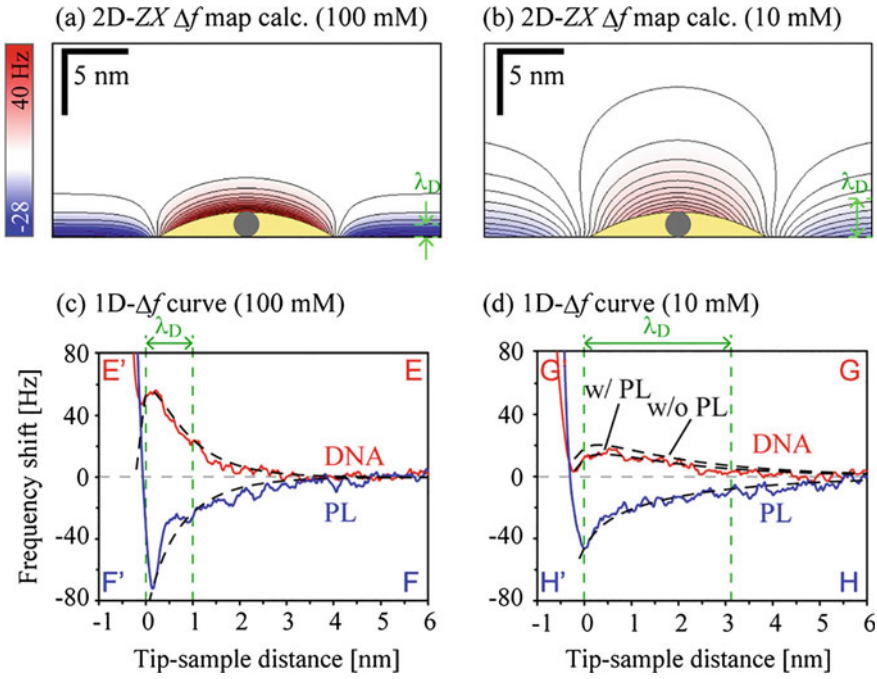

Fig. 4.7 **a** and **b** are theoretically calculated 2D(ZX) Δf_{el} maps (30 × 15 nm^2) in 100 mM and 10 mM KCl solutions, respectively. The gray circles indicate the positions of the DNA molecules. **c** and **d** are 1D Δf curves extracted from the 2D(ZX) Δf maps in 100 mM and 10 mM KCl solutions. The red and blue curves show the experimental data obtained on the DNA molecules and the PL substrate, respectively, and the black dotted curves show the theoretical curves that gave the best fit. Reprinted from [19], © IOP Publishing. Reproduced with permission. All rights reserved

DNA molecule (red area) in the 100 mM solution, we calculated the theoretical force curve on the DNA molecule by setting n^{∞} = 130 mM and pH = 6.0 of the solutions as the fitting parameters. Note that the PL layer was not taken into account in this case, and we set the charge density of the DNA (σ_{DNA}) as −150 mC/m^2. The theoretical Δf_{el} curve that gave the best fit to the experimental Δf curve on the DNA is shown as the dotted curve in Fig. 4.7c. For these conditions ϕ_{silica} and σ_{silica} were determined to be −6 mV and −17 mC/m^2, respectively. This result suggests that the charge density of the molecule can be quantitatively evaluated using FM-AFM in a strong electrolyte.

In the case of the 10 mM solution, we found from Fig. 4.6f that the EDL of the PL substrate (blue area) was overlapped with that of the DNA molecule (red area). In such a case, the PL substrate should be taken into account to estimate the charge density on the DNA molecule because F_{el} measured on the DNA molecule was influenced by the positive charges on the PL substrate. We plotted the theoretical Δf_{el} curves on the DNA molecule that gave the best fit to the experimental Δf curve using the models with and without the PL layer in the 10 mM solution in Fig. 4.7d, using the parameters n^{∞} = 15 mM and pH = 5.7. We found that the theoretical Δf_{el} for the model with the PL layer was about 30% larger than that calculated for the model without the PL layer. The result suggests that it is difficult to estimate the charge density in an electrolyte of such a low concentration with a nanometer-scale resolution. Therefore, the charge density measurement by FM-AFM in a strong electrolyte is preferred.

4.6 Summary

This chapter reviews the practical aspects of the surface potential and charge measurement based on the electrostatic force detection in liquid environment. We first reviewed the basic properties of the EDL, and then analyzed the capacitive force and electrostatic force induced by the alternating modulation voltage. We presented the criteria for the modulation frequency for obtaining high spatial resolution in local surface charge and potential measurements, namely $f_m > f_D$ and $f_m > f_c$. Several researchers have also demonstrated the electrostatic force detection based on the voltage modulation technique with a modulation frequency that meets the criteria [5, 32–35].

We observed a long-range parasitic electrostatic force even when a high-frequency modulation voltage that meets the criteria was used, and suggested the use of a cantilever with a small surface area and/or a tip with a high aspect ratio. We then demonstrated a local surface potential and charge measurement using a CP cantilever. Even if the local information on the surface charge or surface potential under the tip can be detected, the KPFM bias feedback may not be used since the dependence of the electrostatic force on the applied dc voltage was not straightforward.

Finally, we also demonstrated a surface charge measurement on a biological sample using the 3D force mapping technique, which is an alternative method to map the local surface charge and potential in liquid media. Since the lateral resolution is determined by the overlap of the EDLs, the charge density measurement with a nanometer-scale resolution is only feasible in a strong electrolyte.

References

1. A.J. Bard, L.R. Faulkner, *Electrochemical Methods, Fundamentals and Applications,* 2nd edn. (Wiley, 2001)
2. K. Umeda, K. Kobayashi, N. Oyabu, Y. Hirata, K. Matsushige, H. Yamada, J. Appl. Phys. **113**, 154311 (2013)
3. T.L. Sounart, T.A. Michalske, K.R. Zavadil, J. Microelectromech. Syst. **14**, 125 (2005)
4. V. Mukundan, P. Ponce, H.E. Butterfield, B.L. Pruitt, J. Micromech. Microeng. **19**, 065008 (2009)
5. L. Collins, S. Jesse, J.I. Kilpatrick, A. Tselev, O. Varenyk, M.B. Okatan, S.A.L. Weber, A. Kumar, N. Balke, S.V. Kalinin, B.J. Rodriguez, Nat. Commun. **5**, 3871 (2014)
6. S. Hudlet, M. Saint Jean, C. Guthmann, J. Berger, Eur. Phys. J. B **2**, 5 (1998)
7. J. Colchero, A. Gil, A.M. Baró, Phys. Rev. B **64**, 245403 (2001)
8. F. Booth, J. Chem. Phys. **19**, 391 (1951)
9. L. Yang, B.H. Fishbine, A. Migliori, L.R. Pratt, J. Chem. Phys. **132**, 044701 (2010)
10. D.Y.C. Chan, D.J. Mitchell, J. Colloid Interface Sci. **95**, 193 (1983)
11. R. Pericet-Camara, G. Papastavrou, S.H. Behrens, M. Borkovec, J. Phys. Chem. B **108**, 19467 (2004)
12. R. Hogg, T.W. Healy, D.W. Fuersten, Trans. Faraday Soc. **62**, 1638 (1966)
13. H. Ohshima, *Biophysical Chemistry of Biointerfaces*. (Wiley, 2010)
14. K. Umeda, K. Kobayashi, N. Oyabu, Y. Hirata, K. Matsushige, H. Yamada, J. Appl. Phys. **116**, 134307 (2014)
15. D.C. Grahame, Chem. Rev. **41**, 441 (1947)
16. J. Sotres, A.M. Baró, Appl. Phys. Lett. **93**, 103903 (2008)
17. J. Sotres, A.M. Baró, Biophys. J. **98**, 1995 (2010)
18. I. Siretanu, D. Ebeling, M.P. Andersson, S.L.S. Stipp, A. Philipse, M.C. Stuart, D. van den Ende, F. Mugele, Sci. Rep. **4**, 4956 (2014)
19. K. Umeda, K. Kobayashi, N. Oyabu, K. Matsushige, H. Yamada, Nanotechnology **26**, 285103 (2015)
20. C. Zhao, D. Ebeling, I. Siretanu, D. van den Ende, F. Mugele, Nanoscale **7**, 16298 (2015)
21. T. Fukuma, M. Kimura, K. Kobayashi, K. Matsushige, H. Yamada, Rev. Sci. Instrum. **76**, 053704 (2005)
22. K. Kobayashi, H. Yamada, K. Matsushige, Rev. Sci. Instrum. **82**, 033702 (2011)
23. K. Kobayashi, N. Oyabu, K. Kimura, S. Ido, K. Suzuki, T. Imai, K. Tagami, M. Tsukada, H. Yamada, J. Chem. Phys. **138**, 184704 (2013)
24. J.N. Israelachvili, *Intermolecular and Surface Forces*, 3rd edn. (Academic Press, 2010)
25. S. Bhattacharjee, M. Elimelech, J. Colloid Interface Sci. **193**, 273 (1997)
26. V.A. Parsegian, D. Gingell, Biophys. J. **12**, 1192 (1972)
27. D.Y.C. Chan, R.M. Pashley, L.R. White, J. Colloid Interface Sci. **77**, 283 (1980)
28. D. McCormack, S.L. Carnie, D.Y.C. Chan, J. Colloid Interface Sci. **169**, 177 (1995)
29. I. Popa, P. Sinha, M. Finessi, P. Maroni, G. Papastavrou, M. Borkovec, Phys. Rev. Lett. **104**, 228301 (2010)
30. S. Lin, M.R. Wiesner, Langmuir **26**, 16638 (2010)

31. S. Ido, K. Kimura, N. Oyabu, K. Kobayashi, M. Tsukada, K. Matsushige, H. Yamada, ACS Nano **7**, 1817 (2013)
32. N. Kobayashi, H. Asakawa, T. Fukuma, Rev. Sci. Instrum. **81**, 123705 (2010)
33. N. Kobayashi, H. Asakawa, T. Fukuma, Rev. Sci. Instrum. **83**, 033709 (2012)
34. K. Honbo, S. Ogata, T. Kitagawa, T. Okamoto, N. Kobayashi, I. Sugimoto, S. Shima, A. Fukunaga, C. Takatoh, T. Fukuma, ACS Nano **10**, 2575 (2016)
35. L. Collins, S. Jesse, J.I. Kilpatrick, A. Tselev, M.B. Okatan, S.V. Kalinin, B.J. Rodriguez, Beilstein J. Nanotechnol. **6**, 201 (2015)

Chapter 5
Time-Resolved Electrostatic and Kelvin Probe Force Microscopy

Sascha Sadewasser and Nicoleta Nicoara

Abstract Electrostatic (EFM) and Kelvin probe force microscopy (KPFM) have contributed significantly to the understanding of nanoscale electronic properties and the structure-property relationship in numerous electronic and optoelectronic materials and device systems. In many applications, knowledge about the dynamics of electronic processes is of high importance to understand limitations and improve device performance. Both EFM and KPFM typically measure on time scales of milliseconds to tens of milliseconds, which provides access to dynamic processes on that time scale. Nevertheless, only a limited number of studies have made use of this time resolution and investigated dynamic effects. In addition, more recently several methods have been presented that extend the time resolution to even faster processes. The different methods are presented in detail and some relevant results obtained for a variety of materials and device systems are reviewed.

5.1 Introduction

Electrostatic (EFM) and Kelvin probe force microscopy (KPFM) are commonly used to image spatial variations of the contact potential difference (CPD), which results from the electrostatic forces between tip and sample and is defined as the difference in work function of the tip and the sample [1]. Variations in CPD images can have different origins. (i) The CPD can reflect spatial variations in the charge density [2–4], individual localized charges [5], or even partial charge densities within a single molecule [6, 7]. (ii) Variations in the local surface structure or chemistry can affect the CPD by means of a change in the surface dipole or the electron affinity [8, 9]. (iii) A change in the material under the tip will affect the local work function and thereby the CPD [10]. Finally, (iv) doping type and charge-carrier concentration in semiconductors will control the position of the

S. Sadewasser (✉) · N. Nicoara
International Iberian Nanotechnology Laboratory, Av. Mestre José Veiga S/N, 4715-330 Braga, Portugal
e-mail: Sascha.Sadewasser@inl.int

S. Sadewasser and T. Glatzel (eds.), *Kelvin Probe Force Microscopy*,
Springer Series in Surface Sciences 65, https://doi.org/10.1007/978-3-319-75687-5_5

Fermi level, affecting the work function, which is defined as the energy difference between the local vacuum level and the Fermi level [11]. In most applications of EFM and KPFM, spatial variations are imaged in a static fashion, meaning that variations of the CPD with time are not present, not considered, or not measureable.

In fact, KPFM in the most wide-spread realization is inherently a slow technique due to a feedback circuit which applies a dc voltage to the tip (or the sample) to compensate the electrostatic forces between tip and sample. The time constant of the KPFM controller is typically in the range of milliseconds (see also Chap. 1). For EFM, the electrostatic forces directly represent the signal of interest and a controller is not used. Therefore, measurements are somewhat faster, but still limited by the atomic force microscopy (AFM) circuitry and cantilever response times (see Chap. 1). Nevertheless, especially in view of points (i) and (iv) above, the dynamics of charges are of high interest in materials and device characterization and knowledge of the nanoscale charge-carrier dynamics can provide valuable insight into device functionality and limitations in device performance.

The first study of dynamical effects by KPFM was presented by Sadewasser et al. [12]. The authors studied light-induced changes in a $CuGaSe_2$ semiconductor used in photovoltaic applications. The surface photovoltage (SPV), defined as the difference between the CPD under illumination and that in the dark was monitored in single-point measurements after switching on and off a laser light source. The CPD change was monitored in real time over the course of several minutes. Similar experiments were also performed using EFM on organic photovoltaic blends [13–15]. Instead of light, changes in the charge-carrier distribution can also be induced by applying a bias step, a technique which in combination with EFM has been used on glasses to study ion transport in solid electrolytes [16] already in 2004, and later also on organic field-effect transistors (OFETs) [17–19]. Bürgi et al. [20] characterized the charge transport in polymer transistors after bias changes using KPFM and Strelcov et al. used a similar technique on ionic materials and devices [21].

A better time resolution in EFM measurements was achieved by the group of Ginger in 2012 by digitizing the full cantilever oscillation and extracting the instantaneous oscillation frequency in a post-processing analysis, leading to a time resolution down to 100 μs [22, 23]. Also in KPFM, techniques for assessing faster dynamic processes were presented. The first report of light intensity-modulated (IM) KPFM by Takihara et al. in 2008 [24] measured minority carrier lifetimes at grain boundaries in a polycrystalline Si solar cell down to 100 μs. The same technique was used by various groups for the characterization of organic devices [25–28]. In a similar approach using a bias-modulation Narchi et al. measured the minority carrier lifetime in epitaxial Si solar cell materials [29]. Using a pump-probe approach (pp-KPFM), Murawski et al. [30, 31] have measured pentacene-based OFETs determining charge-carrier dynamics with a time resolution of 2 μs using bias pulses applied to the drain electrode of the OFET devices. Schumacher et al. [32] have introduced a light-based pump probe approach for KPFM and measured the charge carrier lifetime in low-temperature grown GaAs of ~1 ps, currently the best time-resolution that has been demonstrated experimentally.

Table 5.1 Overview of the techniques used for time-resolved EFM and KPFM and their properties

Abbreviation	Name	Measurement signal	Demonstrated time resolution	Excitation signal	Sections
trEFM	Time-resolved EFM	EFM signal measured in real time, tip height	~100 µs	Light, bias	5.2.1, 5.2.2
trKPFM	Time-resolved KPFM	KPFM signal measured in real time	~1–4 s[a]	Light, bias	5.3.1, 5.3.2
FF-trEFM	Fast-free time-resolved EFM	Analysis of full cantilever oscillation to extract instan-taneous frequency shift	~10 ns	Bias	5.2.3
IM-KPFM	Intensity-modulated KPFM	Averaged SPV	~20 ns[b]	Light	5.3.3
BM-KPFM	Bias-modulated KPFM	Averaged CPD	~0.2 µs[b]	Bias	5.3.4
pp-KPFM	Pump-probe KPFM	Averaged SPV/ CPD by synchronizing controller to pump pulse	~1 ps[b]	Light, bias	5.3.5

[a]The best time resolution is determined by the KPFM controller time constant (typically 1–30 ms)
[b]The best time resolution is determined by the thermal noise level [32]

In this chapter, we present the various techniques used for time-resolved EFM and KPFM experiments in detail and provide representative examples for applications. Section 5.2 reviews the various techniques used for time-resolved EFM, including real-time measurements and the detailed analysis of the full cantilever oscillation to achieve better time resolution. Section 5.3 reviews KPFM methods, separated in sub sections dedicated to real-time measurements, intensity-modulated, bias-modulated, and finally pump-probe KPFM. Section 5.4 concludes and provides an outlook. An overview of the various techniques is given in Table 5.1.

5.2 Time-Resolved Electrostatic Force Microscopy

5.2.1 Real-Time Measurements After Bias Pulsing

The measurement of time-dependent phenomena using EFM can be performed directly if the time scales of the processes of interest are sufficiently slow. As detailed in Chap. 1, in EFM the effect of the electrostatic forces resulting from the

modulation of the applied bias are measured either in the oscillation amplitude signal (amplitude modulation mode, AM-mode) or in the frequency shift Δf (frequency modulation mode, FM-mode). In both cases, the time resolution is limited by the time constants of the AFM measurement setup. The cantilever oscillation reacts to an external change with a response time τ given by $\tau = Q/(\pi f)$ [33], where Q is the quality factor and f is the frequency. For typical implementations the response time is on the order of milliseconds to tens of milliseconds. Therefore, upon a change in applied bias, e.g. a bias pulse, any reaction of the sample electronic structure leading to a change in CPD occurring on a time scale slower than the response time of the EFM setup can be observed in real time, simply by continuously measuring the EFM signal as a function of time. This can be effectively done in a point measurement, leading to a time-spectroscopy data set showing directly the time-dependent evolution of the EFM signal. If the sample's processes are sufficiently slow, also a line- or image-scanning mode can be applied. It is important to note that for the implementation of this time-resolved EFM mode no special circuitry or setup is required.

Ng and Marohn showed a first application of time-resolved EFM to measure the kinetics of trap formation and release in organic field-effect transistors (OFETs) [17]. For the measurement, a bias stress (−10 V) is applied to the bottom gate of a poly-(9-9´-dioctyl-fluorene-co-bithiophene) (F8T2) transistor on a Si/SiO_2 substrate. After release of the bias stress, the temporal development of the EFM signal is observed. At the same time EFM scanning was used to locate the trapped charges. Figure 5.1 shows images of the relative frequency shift before, immediately after the bias stress, and after a longer time period of 30 min after the bias stress, which shows that the device gradually returns to the initial state as the charges are released from the trap states. Performing bias-spectroscopy measurements in a single point in the center of the transistor channel, the CPD was determined by fitting the resulting Δf(V) parabola. The time dependence of the obtained CPD reflects the release of trapped charges, which was compared for an

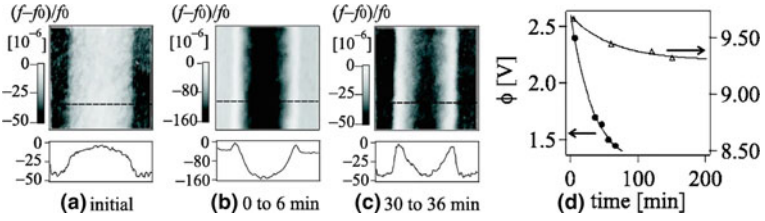

Fig. 5.1 Relative frequency shift images (10 × 10 μm^2) of an annealed F8T2-OTS organic field effect transistor device. The tip bias was $V_{tip} = 1$ V, while the transistor itself was grounded, $V_g = V_{sd} = 0$ V. **a** Image before applying a gate bias stress of $V_g = -10$ V, **b** and **c** after releasing the bias stress at the times stated below the image. The position of the line profiles are indicated by the dashed lines. **d** Decay curves of the CPD obtained from bias-spectroscopy measurements in a point in the center of the transistor channel for a F8T2-oxide (open triangles) and a F8T2-OTS (solid circles) OFET device. Reprinted from J. Appl. Phys. 100, 084505 (2006), with the permission of AIP Publishing

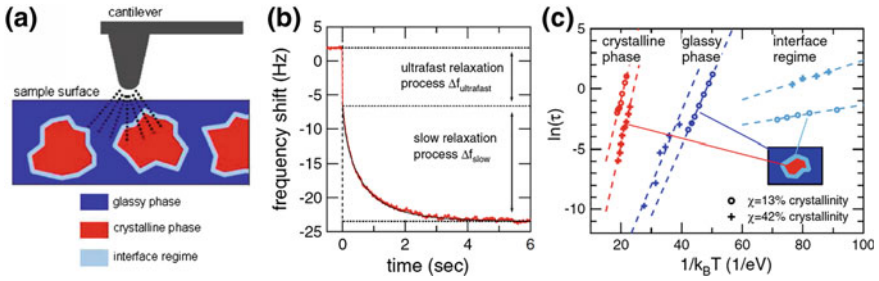

Fig. 5.2 **a** Illustration of the measurement setup for the characterization of ion dynamics in partially crystallized $LiAlSiO_4$ glass ceramics. **b** Typical relaxation curve after the bias pulse with a fast relaxation that cannot be resolved by the measurement technique and a subsequent slow relaxation process, which is ascribed to the ion dynamics. **c** Arrhenius plot of the relaxation measurements in different positions (illustrated in the inset) as a function of temperature for a $LiAlSiO_4$ glass ceramic with 13% (circles) and 42% (crosses) crystallinity. Reprinted with permission from Phys. Rev. Lett. 98, 225901 (2007). Copyright 2007 by the American Physical Society

OFET with F8T2 deposited on oxide and on a modified oxide using a cross-linked monolayer of octadecyl-trichlorosilane (OTS), as shown in Fig. 5.1d. The time constant for the two setups were found to be 33 min (for F8T2-OTS) and 63 min for F8T2-oxide. The authors also recognized that the measurement of charge release from trap states is only possible, if the trapped charges are not shielded by mobile charges (e.g. due to a high carrier concentration).

In the previous example, the bias pulse was applied to or across a device structure and the tip was used to observe the effects of the bias pulse on the charge carriers in the device. In a series of studies on glassy materials, Schirmeisen et al. [16, 34–36] induced changes in the sample electronic structure by directly applying a bias pulse to the AFM tip and thereby determined ion dynamics in these materials. To illustrate this technique, Fig. 5.2a shows the measurement setup for the characterization of partially crystallized $LiAlSiO_4$ glass ceramics [35]. Figure 5.2b shows a typical relaxation curve after the bias pulse is finished. It is composed of two parts, a fast initial part which cannot be resolved by the used method and a subsequent slower relaxation process. The authors studied samples with different levels of crystallinity and separated measurements in glassy regions and crystalline regions, which were performed as a function of temperature in the range from 127 to 620 K. The corresponding Arrhenius plots are shown in Fig. 5.2c from which activation energies of 0.58 and 1.03 eV were obtained. Comparison to literature values for macroscopically determined activation energies of pure glassy and crystalline samples led to the identification of the glassy (0.58 eV) and the crystalline phase (1.03 eV). Right at the interface, the authors determined a significantly lower activation energy of only 0.04 eV, which they assume to be due to the motion of very few ions in the thin (few nanometers) interface layer. These studies nicely demonstrate the huge potential of time-resolved EFM measurements to determine the physical processes at the nanometer scale and obtain quantitative measurements of e.g. activation energies.

5.2.2 Real-Time Measurements After Light Pulses

Similar to the time-dependent change upon a bias pulse, also that upon a light pulse can be measured. In an illuminated semiconductor sample electron-hole pairs are generated. If the pairs are spatially separated, a photovoltage builds up, which can be sensed by EFM. The separation of charges can be induced by a built-in electric field, for example in a pn-junction or due to a surface band bending, by charge selective contacts, and/or by capture of charge carriers in trap states [37, 38]. After the light pulse is finished, the sample in the dark relaxes back into its original equilibrium state. Charge generation and separation are typically fast processes and not detectable by the real-time EFM method. Nevertheless, the release of trapped charges can be significantly slower and take up to hours depending on the materials system and the characteristics of the trap state.

Several groups have used time-resolved EFM (trEFM) measuring the change in EFM signal in real-time after a light pulse. Most of these works investigate the release of charges from trap states in organic materials used in photovoltaic applications. Coffey and Ginger presented a seminal study on blended films of organic polymers used for photovoltaics [13]. Specifically, they investigated the nanostructured donor/acceptor interfaces of 50:50 blend films of poly-(9,9´-dioctylfluorene-co-benzothiadiazole) (F8BT) and poly-(9,9´-dioctylfluorene-co-bis-N,N´-(4-butylphenyl)-bis-N,N´-phenyl-1,4-phenylenediamine (PFB). Figure 5.3a shows the experimental setup with the blend film deposited on a transparent ITO contact, which was illuminated by a light emitting diode (wavelength = 405 nm, which excited both components of the blend) through the ITO contact, while the EFM tip measures on the free side of the blend film. When the sample is illuminated, the EFM signal (Δf) gradually drops to a new equilibrium value corresponding to the generated charges being separated in the potential well created by the tip (biased at +10 V), illustrated in Fig. 5.3b. The charging curves show a single exponential dependence which depends on the light intensity, as shown in Fig. 5.3c. The charging rates are attributed to the charge dissociation in the tip-sample capacitor forming a potential well created by the tip bias. The local photo-induced charging rates are faster by an order of magnitude in the blend compared with the individual pure polymers, as seen in Fig. 5.3d. Additionally, it was shown that blend films exhibit faster charging rates when cast from chloroform compared with those cast from xylenes. Using a point-by-point mapping, complete images of the charging rates were obtained, which provided for the surprising observation that the charging rate at the donor/acceptor interface is reduced by 30–50%. The authors also showed that for a variation in the blend composition, the determined microscopic charging rates correlate well with the macroscopic external quantum efficiencies of the films. For their technique, Coffey and Ginger [13] stated a spatial and time resolution of 100 nm and 100 μs, respectively.

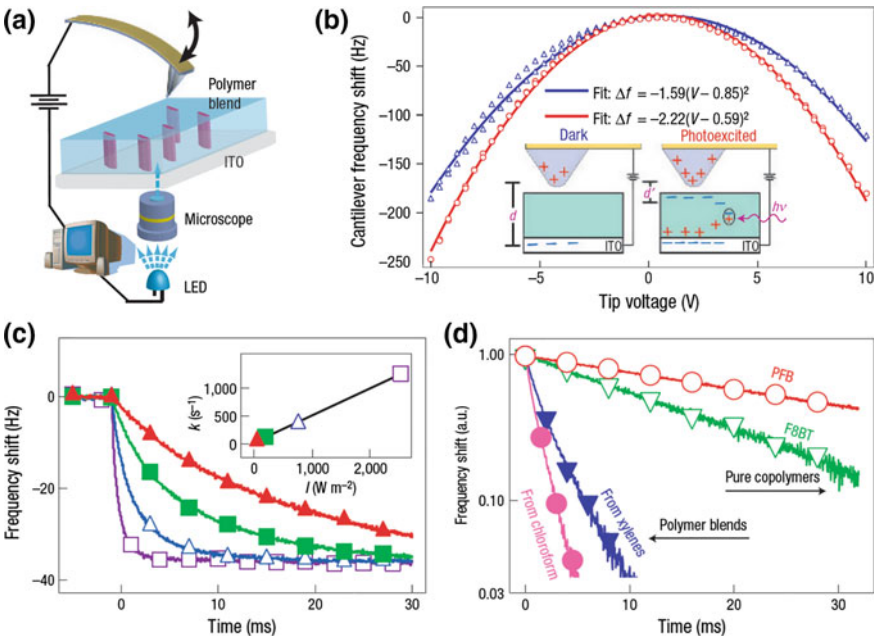

Fig. 5.3 **a** Schematic diagram of the measurement setup with a polymer blend sample illuminated by a pulsed light emitting diode (LED). The EFM tip measures charge accumulation by a change in the frequency shift Δf. **b** Bias spectroscopy curves of a 50:50 blend film of F8BT/PFB in dark (triangles) and under illumination (circles) with 405 nm LED. The parabola maximum shifts by 260 mV due to the charge separation under illumination, as illustrated in the inset. **c** Normalized charge build-up during illumination of the F8BT/PFB film with different light intensities leading to a linear dependence of the charging rate on the light intensity (inset). **d** Normalized charge build-up as a function of time for different polymer films (pure F8BT, pure PFB, and 50:50 blends of F8BT/PFB) prepared by spin-casting using chloroform and xylenes under illumination intensity of 760 W/m^2. The blend films exhibit a significantly increased rate. Reproduced from Nature Materials 5, 735 (2006) with permission from the Nature Publishing Group

Using the same technique, the group of Ginger also analyzed the photooxidation behavior of F8BT and PFB blends [39, 40]. Using localized photon doses between 0.1 and 25 J/cm^2 with a blue laser (405 nm wavelength), they found a significant decrease of the charging rate for the higher photon doses [39]. It was also found that the trEFM charging rate images allowed the identification of the local photooxidation and trap formation with higher sensitivity compared with KPFM images. Using charging rate images under illumination with different wavelength, further insight was gained about the effects of photooxidation on the nanoscale properties of the donor/acceptor blend [40]. In these experiments, the blend film was imaged initially in the pristine state at three different wavelength, 365, 405, and 455 nm in a N_2 atmosphere using a flow cell setup. Then, photooxidation was performed in ambient air for 20 min using a blue laser at 405 nm. Subsequently, the charging rate images were repeated under illumination with the same three wavelength

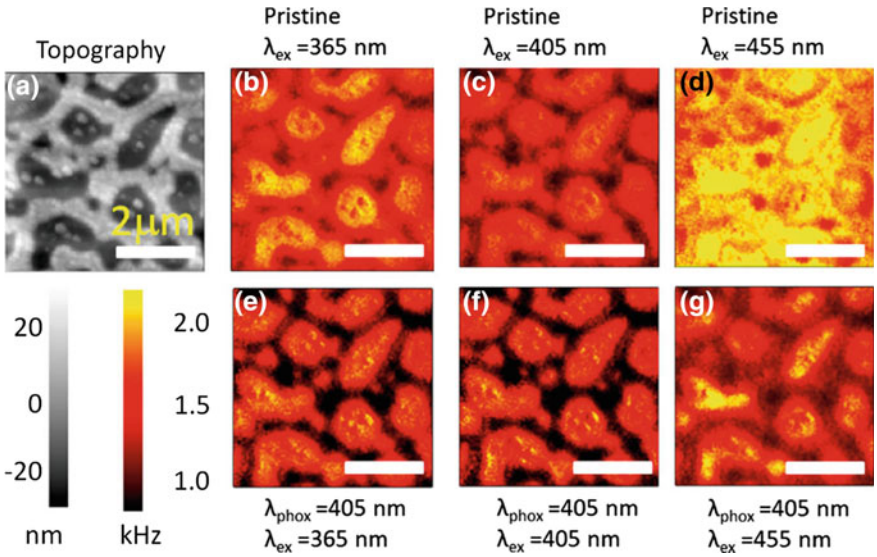

Fig. 5.4 **a** Topography image of a F8BT/PFB all-polymer bulk heterojunction photovoltaic blend. **b–d** trEFM images of the charging rate obtained under illumination with 365 nm, 405 nm, and 455 nm wavelength, respectively, for the pristine sample before photooxidation. **e–g** trEFM charging rate images at 365 nm, 405 nm, and 455 nm illumination, respectively, after photo oxidized by a 405 nm laser illumination. Reprinted with permission from J. Phys. Chem. B 117, 4654–4660 (2013). Copyright 2013 American Chemical Society

(Fig. 5.4). A faster degradation due to the photooxidation was observed in the regions of higher topography, which were attributed to F8BT-rich domains. At the device level, the authors observe a stronger degradation in the photoresponse due to photooxidation with wavelength in the range where the F8BT absorbs. The trEFM results suggest that the explanation for the device degradation is due to the local photooxidation of the F8BT-rich domains.

5.2.3 *Improved Time Resolution by Analysis of the Cantilever Oscillation*

In the examples presented in the previous two sections, time-resolved EFM was performed by measuring the EFM signal in real time after a bias or light pulse. The time resolution in this case is limited by the time constant of the AFM controller and values down to 100 μs were reported [13]. To reach a better time resolution and measure faster processes, other methods have to be used. Giridharagopal et al. [22] have presented a novel method for time-resolved EFM measurements which

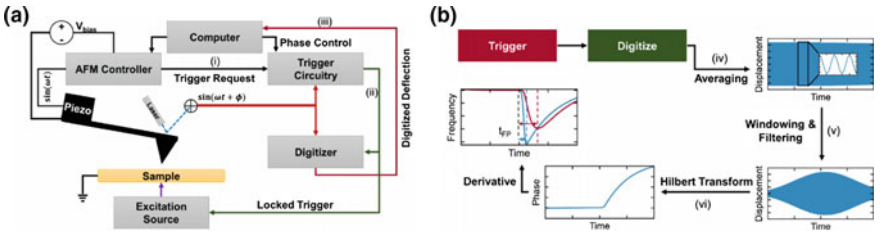

Fig. 5.5 **a** Schematic diagram of the experimental setup for fast free trEFM. A trigger signal, requested by the AFM controller with a defined phase to the cantilever oscillation, (i) starts the digitizer and is applied to the sample. (ii) The cantilever oscillation is digitized with a high sampling rate (up to 50 MHz) and read by a computer. (iii) The cantilever oscillation contains the response of the cantilever to the trigger signal. **b** Representation of the flow diagram of the measurement procedure. The digitized cantilever oscillation is averaged (iv) over many repetitions, extracted in the window of interest and filtered, (v) and subsequently Hilbert transformed (vi) to extract the instantaneous frequency of the cantilever. Reprinted from Rev. Sci. Instrum. 87, 053702 (2016) with the permission of AIP Publishing

reaches time resolution down to ~10 ns [23]. The method relies on the acquisition of the full data set of the cantilever oscillation by digitizing the oscillation signal with up to 50 MHz. A bias or light pulse is used to excite the charge dynamics to be measured in the sample. This trigger pulse is applied with a defined phase relation to the cantilever oscillation. Thus, averaging over many repetitions is possible thereby increasing the signal-to-noise ratio.

The setup for this fast free time-resolved electrostatic force microscopy (FF-trEFM) measurement mode is shown in Fig. 5.5a [23]. A trigger signal with a defined phase to the cantilever oscillation is requested by the AFM controller. (i) The trigger signal is used to excite the process of interest in the sample, e.g. a light or a bias pulse, and at the same time starts the digitizer. (ii) The cantilever oscillation is then digitized with a high sampling rate and the full oscillation trajectory is stored by a computer. (iii) This cantilever oscillation contains the response of the cantilever to the trigger signal, which perturbs it from the sinusoidal motion. Since the trigger has a defined phase relation to the cantilever oscillation, the measurement can be repeated many times (15–30 times per pixel for images and 1500 times for point measurements) to allow for data averaging and noise-level reduction, (iv) illustrated in Fig. 5.5b. The averaged signal is then filtered (v) and a Hilbert transformation (vi) is used to extract the instantaneous phase, of which subsequently the derivative with respect to time is taken to obtain the instantaneous frequency of the cantilever [23]. As characteristic time of the transient response of the sample to the perturbation the authors use the "time to first peak" (t_{FP}), which is the time from the trigger signal to the minimum in the instantaneous frequency curve, illustrated in Fig. 5.5b. Measuring a full image takes about one hour and post-processing the data an additional 90 min, which might be reduced by optimized software and dedicated computers [22].

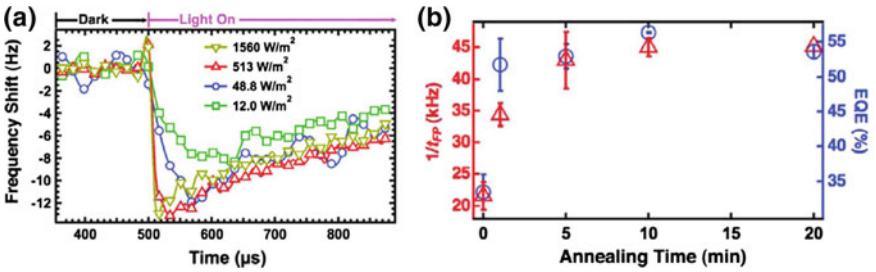

Fig. 5.6 **a** Instantaneous frequency shift curves of a P3HT:PCBM film for various light intensities, from which the t_{FP} value is extracted at the minimum. **b** Development of the spatially averaged $1/t_{FP}$ values (red triangles) and EQE (blue circles) with annealing of a P3HT:PCBM organic photovoltaic device, showing a good agreement between the microscopically determined t_{FP} values and the macroscopically determined EQE. Reprinted with permission from Nano Lett. 12, 893 (2012). Copyright 2012 American Chemical Society

Karatay et al. [23] provide a detailed analysis of the FF-trEFM technique comparing model experiments with simulations. Various experimental conditions and parameter settings are analyzed comparatively. On the other hand, Giridharagopal et al. [22] measured the photo-induced charge generation in the donor/acceptor polymer:fullerene blend poly-(3-hexylthiophene):phenyl-C_{61}-butyric acid methyl ester (P3HT:PCBM), which is widely used in organic photovoltaics [41]. Figure 5.6 shows instantaneous frequency shift curves of the P3HT:PCBM film for various light intensities, obtained by FF-trEFM. From the minimum of the curves the characteristic time t_{FP} is extracted. The authors averaged these times over an image and find a good agreement with the dependence of the spatially-averaged $1/t_{FP}$ values after various annealing steps for different durations at 110 °C with the macroscopically determined external quantum efficiency (EQE) values of complete devices.

5.3 Time-Resolved Kelvin Probe Force Microscopy

5.3.1 Real-Time Measurements After Light Pulsing

Also for KPFM, time-resolved measurements in real time have been reported. In difference to the EFM case described above, KPFM usually relies on a feedback circuit that compensates the CPD. The Kelvin controller typically operates with a time constant of milliseconds to tens of milliseconds, thus imposing a minimum for the time resolution. The absence of a controller in the EFM case allows a somewhat better time resolution down to 100 µs, as described above [13].

The first report of time-resolved KPFM dates to 2001, when Sadewasser et al. [12] reported a study of the time dependence of the surface photovoltage (SPV) of chalcopyrite solar cell materials. The surface photovoltage (SPV) is the difference

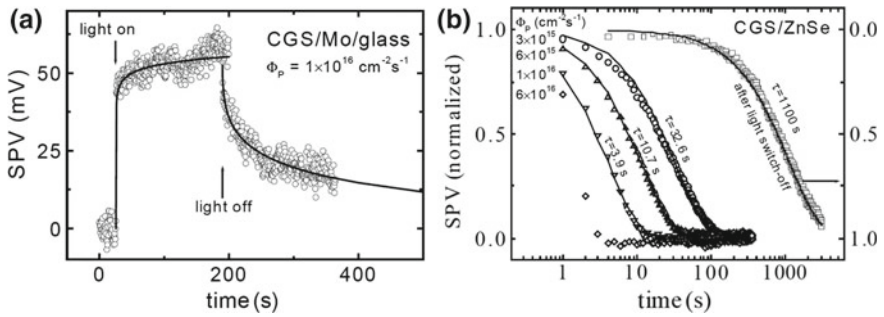

Fig. 5.7 **a** SPV transients measured on a $CuGaSe_2$ film on a Mo/glass substrate. Upon switching on the light (red laser, 675 nm) the SPV increases initially abruptly followed by a small and slower further increase. After light switch-off the SPV gradually relaxes back to zero. The data (open circles) can be fitted by a stretched exponential behavior (solid line). **b** Various SPV transients measured for different light intensities (photon flux is given in the legend) for a $CuGaSe_2$ film deposited on a ZnSe substrate. The transients can be well described by a simple exponential dependence for which the relaxation time is given. The transient after switching the light off is much slower (right inverted axis). Figure reproduced from [12] with permission

between the CPD under illumination and in the dark and thus represents the change of the CPD under illumination. $CuGaSe_2$ (CGS) was studied on two different substrates, a Mo/glass substrate, typically used in thin-film solar cells, and a ZnSe substrate resembling the interface with a potential n-type contact layer. The SPV transients measured on the free CGS surface are shown in Fig. 5.7a after switching on illumination by a red laser (675 nm) and after switching it off. Upon illumination a sharp increase in SPV is seen followed by a further small and gradual increase. After light switch-off, the SPV decays gradually back to zero. For photovoltaic applications, the interface between the p-type CGS and the n-type ZnSe is relevant. In this case, the SPV transients, Fig. 5.7b, show the opposite sign, due to the pn junction between CGS and ZnSe. The transients can be described well by a simple exponential dependence with a time constant in the range of a few to tens of seconds and which depends on the light intensity. For the relaxation process in the dark, the time constant is significantly larger, about 18 min. Using a typical attempt frequency, the authors estimated a thermally activated trap-release process with a trap energy of 0.86 eV at mid-gap of the CGS material.

Measurements of charge carrier dynamics in real time were demonstrated for various solar cell materials upon and after illumination if the samples, including dye-sensitized solar cells [42, 43] and ZnO [43]. For perovskite solar cell materials, Garrett et al. [44] used a heterodyne technique for fast imaging in KPFM. This technique allows fast scanning during KPFM imaging with an acquisition time of 16 s for one image [45] and thus provides great advantages for imaging dynamic processes on time scales of a few seconds or slower. The authors studied a ($CH_3NH_3PbI_3$) perovskite layer with a [6,6]-phenyl C_{61}-butyric acid methyl ester (PCBM) layer as electron transport material, both deposited by spin-coating, leading to perovskite films with grain size on the order of ~1 μm. Figure 5.8 shows

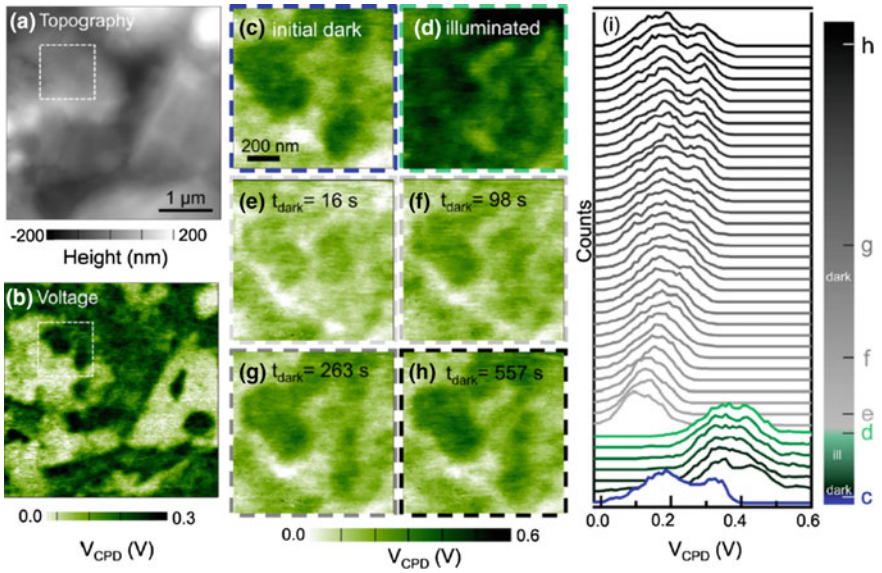

Fig. 5.8 **a** KPFM topography image of a $CH_3NH_3PbI_3$ perovskite/PCBM layer and, **b** corresponding CPD image in the dark. **c** CPD in dark taken within the white highlighted area in **b** and **d** the corresponding area imaged under illumination with a 54 µW laser at 500 nm. **e**–**h** Representative CPD images taken after illumination was switched of at the times indicated in the image. Only after about 9 min the material has returned to its initial dark state. **i** Histograms of CPD images taken over time, including measurements initially in the dark (blue line), under illumination (green lines), and after light switch off (grey lines). The evolution of the CPD distribution can be well seen. Reprinted with permission from Nano Lett. 17, 2554 (2017). Copyright 2017 American Chemical Society

the topography and CPD in the initial dark conditions. Upon illumination with a 500 nm laser, the CPD increases by about 0.2 V with some local variations. After the light is switched off again, an interesting time-dependent CPD evolution starts with an initial reduction by ~0.3 V with a clearly narrower distribution of the CPD values, as seen in the time evolution of the histograms in Fig. 5.8. (i) Gradually, the CPD distribution evolved back to the initial (broader) dark distribution over the course of about 9 min. Similar behavior is found after illumination with various light intensities up to 4.3 mW. The authors attribute the observed dynamic behavior in the local electronic response to intragrain ion migration [46, 47]. Under illumination, charge accumulation occurs and when the cell is in the dark again, charge migration occurs.

This photo-induced ion migration is attributed to the ions moving to depleted regions, in agreement with photoluminescence experiments [46]. The behavior was found to be reversible at low illumination intensities without any permanent material damage. The imaging revealed that some areas show stronger changes while others do not show any significant CPD change with light or after light switch-off,

highlighting the importance of spatially-resolved materials characterization to improve understanding of the underlying processes. From an exponential fit to the data a time constant of 185 s was obtained.

5.3.2 *Real-Time Measurements After Bias Pulsing*

As in the case of EFM, also for KPFM the real-time dynamic effects after bias pulse s can be useful to bring upon additional insight into materials and device properties and functionality. For the case of OFETs, Bürgi et al. [20] have presented an early study observing the dynamic charging and discharging processes in the polymers upon gate voltage changes and under illumination. For a gate voltage change from −50 to −53 V, Fig. 5.9a shows the charging behavior of an OFET based on P3HT, with source and drain at 0 V. The charge density reaches its final distribution within a few seconds in an exponential dependence, which is independent of the position in the channel, but does depend on the applied gate voltage and on the temperature. The process could be well described by a drift model analysis with only the field-effect mobility as a free parameter, as seen in Fig. 5.9b. The same authors also analyzed the light-induced release of charge carriers from trap states for OFETs

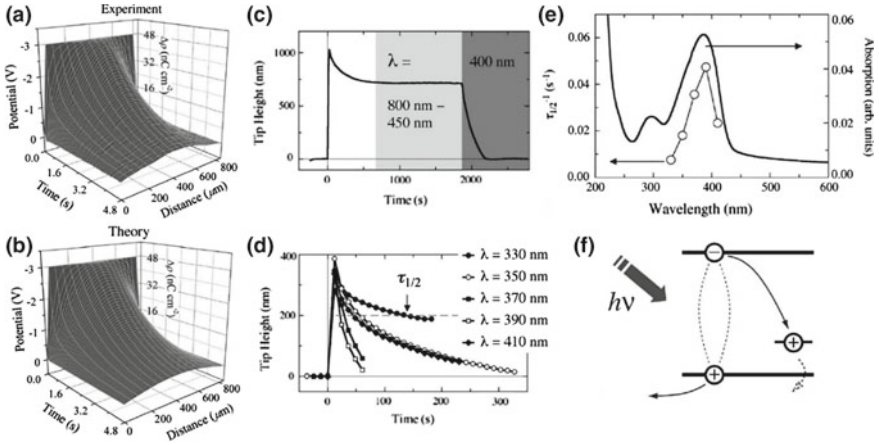

Fig. 5.9 **a** Charging process of a P3HT OFET upon a step-like change in gate-voltage from −50 to −53 V (at time 0) measured by KPFM at 180 K in line-profiling mode between the source (at <0 nm) and drain (>840 nm) contacts as a function of time. **b** Drift-model analytical result obtained by only adjusting the field-effect mobility, giving a good description of the experimental data. **c** The photon-assisted release of trapped charges in a TFB transistor is observed as a change in the topography height for wavelengths smaller than 450 nm and, **d** the time constant of the trap release depends on the illuminating wavelength. **e** The trap-release time constant for a TFB/SiO_2 transistor shows a similar spectral dependence as the absorption spectrum. **f** Schematic illustration of the mechanism for the photo-induced trap release. Reprinted from Synthetic Metals 146, 297 (2004) with permission from Elsevier

based on poly[(9,9-dioctylfluorene-2,7-diyl)-alt-phenylene-(N-(p-2-butylphenyl) imino-phenylene)] (TFB) [20]. Here the topography signal was used as a measure of changes in the electrostatic forces due to electronic changes in the sample upon illumination with different wavelength. Figure 5.9c shows how the tip height evolves with time after filling the trap states by stressing the OFET with a gate voltage of −60 V, which was released at time 0 to −25 V. After an initial decrease, due to charge release from shallow traps with a release rate of the order of a few $(100\ \mathrm{s})^{-1}$ at room temperature, the trapped charge stays constant. Subsequently, the sample is illuminated monochromatically with decreasing wavelength. It is observed that only for wavelength smaller than 450 nm are charge carriers released from the trap states. The charge-release time $\tau_{1/2}$ (defined as the time at which the tip height has recovered to half of its initial height) depends strongly on the wavelength of the illuminating light, as seen in Fig. 5.9d. At the same time, $\tau_{1/2}$ shows a similar spectral dependence as the absorption of the polymer (Fig. 5.9e), relating microscopically determined characteristic time scales to a macroscopic property. From this relation, the authors conclude that the trap states are located in the conjugated polymer, close to or at the insulator interface, rather than in the SiO_2 dielectric [48]. The mechanism for the trap release is illustrated in Fig. 5.9f, suggesting that photo-induced excitons recombine with trapped holes, leaving behind a high energy hole which is more mobile.

Melzer et al. [49] studied the charge reversal of a pentacene-based OFET using time-dependent KPFM in real time, scanning a full line profile across the channel from source to drain. They performed a point-by-point measurement applying a bias sweep from +20 to −30 V and back to +20 V across the channel and measured the surface potential in the charge-reversal point from an electron to a hole rich device. The procedure is repeated in 70 points (separated by 120 nm) across the channel. Analyzing the time required for the carrier front to reach the center of the channel, the authors extracted carrier mobility values for the device, leading to an electric field and areal hole density dependent mobility. The obtained values are in agreement with predictions from a transmission-line approximation.

5.3.3 *Intensity-Modulated KPFM*

The above examples measured the time-dependent processes by KPFM in real time. However, due to the KPFM controller used in many experimental setups, the time resolution is limited to the millisecond range. Faster processes can still be measured with KPFM using techniques based on modulated light or bias, as will be introduced in the following sections.

The first report of fast KPFM measurements was presented by Takihara et al. [24] in 2008. The authors used intensity-modulated light to determine the minority-carrier lifetime in polycrystalline silicon solar cells. In this technique, later coined intensity-modulated KPFM (IM-KPFM), the KPFM circuit measures the average CPD upon modulated excitation. The concept is illustrated in Fig. 5.10a.

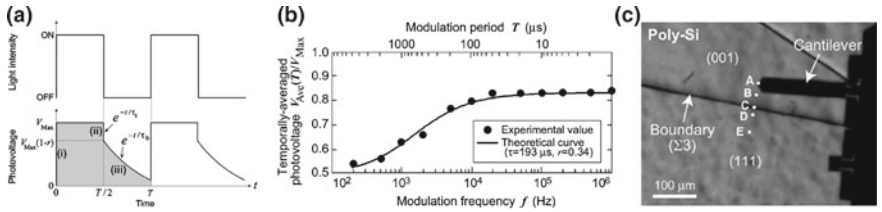

Fig. 5.10 **a** Schematic illustration of the modulated light intensity and the corresponding photovoltage response as a function of time. The photovoltage relaxes initially very fast due to a surface photovoltage related part and subsequently slower due to a bulk effect. **b** Temporally-averaged and normalized photovoltage spectrum as a function of the modulation frequency of the illumination. **c** Optical image indicating the measurement points of the photovoltage spectra across a grain boundary in poly-crystalline silicon solar cell material. Reprinted from Appl. Phys. Lett. 93, 021902 (2008) with the permission of AIP Publishing

When the light is switched on, the photovoltage builds up very fast and is constant during illumination. When the light switches off, the photovoltage drops sharply due to recombination of photo-excited charge carriers in the surface layer with the surface recombination rate $1/\tau_s$, which is assumed to be much faster than the modulation rate of the light. Subsequently, the photovoltage further decays gradually with the bulk recombination rate, which is determined by the minority carrier lifetime τ_b. This whole cycle is much faster than the Kelvin controller, which therefore measures an average value of the photovoltage. By measuring the average photovoltage upon variation of the modulation frequency of the light, a spectrum is obtained, as shown in Fig. 5.10b. The authors present an analytical expression for the analysis of the frequency spectra, which is used to describe the data and extract the relaxation times. For the experiments a Ti:Al_2O_3 laser at 910 nm was used, with an acousto-optic light modulator. Measuring such photovoltage spectra across a grain boundary in a polycrystalline Si solar cell (see Fig. 5.10c), the authors find a decrease in the bulk minority carrier lifetime by a factor of about 2 right at the Σ3 grain boundary.

Later, Fernández Garillo et al. [27] used the same technique for the characterization of organic donor/acceptor blends for solar cells. The authors provided an in-depth analysis of the technique and extended it from a point measurement approach to measuring full images in a point-by-point spectroscopy approach with sub-10 nm resolution and subsequent automated data analysis. The measurement procedure is illustrated in Fig. 5.11. As introduced by Takihara et al. [24], a frequency spectrum is recorded in a point measurement, where the average SPV depends on the specific built-up and decay process time scales of the sample and on the modulation frequency. These point measurements are repeated on a predefined grid covering a specific sample area. Numerical fitting of the frequency spectra as a post-processing analysis leads to the time constants of the SPV built-up (from the high frequency regime) and decay (from the low frequency regime). The automated fitting procedure leads to images of the two time constants. The authors note that the frequency spectra depend on both, the kinetics of the recombination mechanism

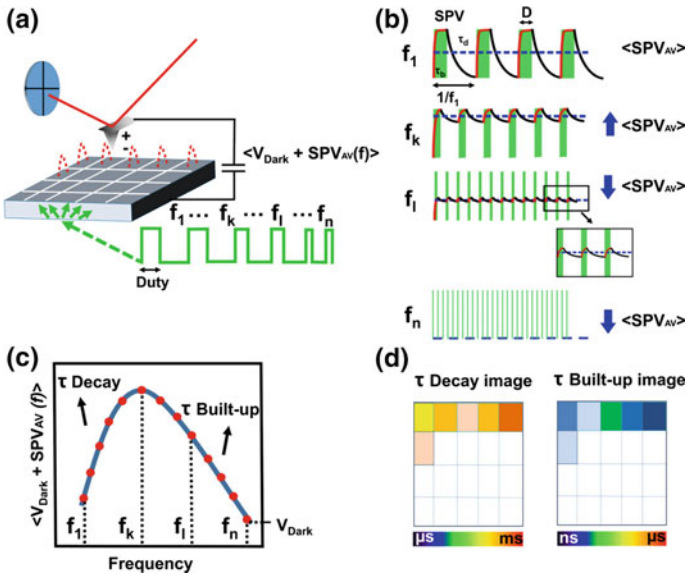

Fig. 5.11 Detailed illustration of the IM-KPFM technique. **a** Point spectra are taken on a grid in the sample surface area of interest, measuring an averaged photovoltage spectrum as a function of modulation frequency. **b** Surface potential for increasing modulation frequencies of the modulated illumination. The measured average surface potential is determined by the interplay between built-up and decay of the photovoltage and the respective time constants of these processes, τ_b and τ_d. **c** Schematic frequency spectrum of the average SPV. **d** An automated fitting is used to calculate pixel-by-pixel images of the time constants for decay and built-up processes. Reprinted from ACS Appl. Mater. Interfaces 8, 31460–31468 (2016) with permission from the American Chemical Society

as well as on the effective photocharging rate of the sample. Considering a SPV built-up which is much faster than the modulation the built-up can be considered instantaneous and with increasing modulation frequency the average SPV increases as a smaller part of the decay occurs and finally saturates when the modulation is faster than the decay time constant τ_d. On the other hand, when the illumination pulse duration becomes comparable to the SPV built-up time constant τ_b, the average SPV starts to decrease again.

This imaging technique was applied for the characterization of bulk heterojunction photovoltaic materials system consisting of a PDBS-TQx network with $PC_{71}BM$ aggregates (Fig. 5.12). The frequency dependent average SPV spectrum, shown in Fig. 5.12c, exhibits a strong increase for small frequencies, followed by a smaller decrease and subsequently, for high frequencies, another slight increase [27]. Therefore, two decay processes are observed (SPV increases) and one build-up process (SPV decrease). A second built-up process is identified to be too fast for the experimental setup and the time constant of this very fast build-up process is estimated to ~10 ns. For the observable time-dependent SPV processes the spatial variation of the respective time constants is shown in Fig. 5.12d–f.

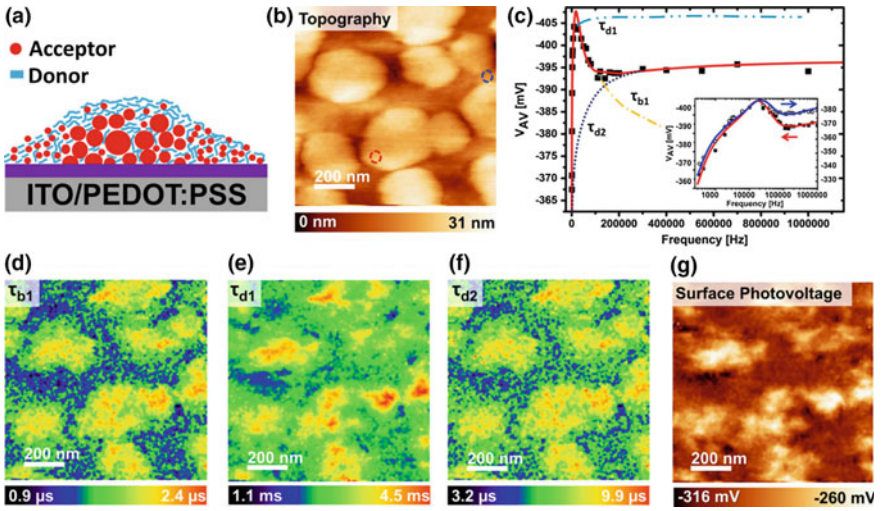

Fig. 5.12 **a** Schematic illustration of a bulk heterojunction solar cell consisting of a PDBS-TQx network (blue) and $PC_{71}BM$ aggregates (red). **b** Topography image acquired during 2D spectroscopy imaging. **c** Frequency spectrum in a single point showing the data (squares) and a numerical fit (red line). The contributions of different processes are illustrated by the dashed and dotted lines. The inset shows two spectra acquired at the red and blue circled points in **b**. Images of the spatially-resolved time constants for the **d** slow build-up, **e** slow decay, and **f** fast decay process, extracted from the frequency spectra taken with modulated illumination at 515 nm and 9.48 mW/mm^2. **g** Surface photovoltage image. Reprinted from ACS Appl. Mater. Interfaces 8, 31460–31468 (2016) with permission from the American Chemical Society

The spatially resolved SPV can be summed from the individual SPV values of the different processes and is shown in Fig. 5.12g. In all four images a clear contrast is seen, where higher time constants for the three processes and higher SPV values are related to the mesoscopic islands. Additional experiments were performed for different light intensities to gain more understanding of the SPV dynamics. It was observed that the fast decay time constant (τ_{d2}) decreases by 1.5 orders of magnitude when increasing the optical power four-fold to ~3.8 mW/mm^2, whereas the slow decay time constant (τ_{d1}) remains nearly constant. Carrier-concentration dependent nongeminate recombination processes [50, 51] and a trap-delayed mechanism with a recombination rate proportional to the trap density [50, 52–54] would be consistent with these observations.

5.3.4 Bias-Modulated KPFM

Similar to the above described IM-KPFM with a light-intensity modulation, also a bias-modulated KPFM (BM-KPFM) mode has been described to measure charge carrier dynamics at time scales faster than the KPFM feedback electronics.

Narchi et al. [29] applied this method for the characterization of the minority carrier lifetime in epitaxial Si solar cells in cross-sectional measurements. The sample consisted of a heavily p-doped (100) Si wafer with a non-intentionally doped epitaxially-grown silicon layer of 5 μm thickness, followed by a n^{++} amorphous Si layer of 15 nm thickness.

The bias modulation results in similar effects as light modulation, under forward bias, an excess of minority carriers occurs at the junction (corresponding to the illuminated case), while for reverse bias a lack of minority carriers prevails (corresponding to the sample in the dark). The recombination of excess minority carriers is much slower than their injection [55], which means that the changes observed in the sample when the bias goes from forward to reverse (reverse recovery time) are slower than when the bias goes from reverse to forward (forward recovery time). These recovery times are closely related to the minority carrier lifetime τ [56–58].

Narchi et al. [29] measured across the crystalline/epitaxial Si junction at different frequencies of the bias modulation. The signal is a square wave centered on 0 V, with an amplitude of 0.6 V and a duty cycle of 50%. For high modulation frequencies above 1 MHz, the potential image is very similar to that under constant bias (0 V), showing that the modulation is too fast and no significant recombination occurs. Defects at the interface are responsible for a related decrease in the surface potential at modulation frequencies of 0.5 and 1 MHz. This decrease is caused by shorter carrier lifetime (in the range of 0.2–1 μs) due to recombination at interface defects. Below 500 kHz, the interface region remains constant, but a surface potential increase is observed within the bulk region of the epitaxial layer. At these lower frequencies, corresponding to lifetimes in the range between 2 and 20 μs, recombination occurs in the epitaxial layer. Both observed lifetimes are in agreement with macroscopic time-resolved microwave conductivity measurements performed on the same sample, which however did not provide information about the origin of the two related processes. Thus, BM-KPFM provided valuable additional insight and allowed to assign the shorter lifetime limiting the device performance to the defective interface between the crystalline and epitaxial Si.

5.3.5 Pump-Probe KPFM

A slightly different approach to measuring fast dynamic processes by KPFM has been presented by Murawski et al. [30, 31]. This approach is based on a pump-probe scheme and therefore called pump-probe KPFM (pp-KPFM). The basic idea in this technique is to only detect the Kelvin voltage during short selected times and then move this "time window" with respect to a bias pump pulse applied to the sample. Figure 5.13 shows a schematic illustration of the working principle and the respective measurement circuit. As in regular KPFM, an ac bias is applied to the sample to allow the detection of the CPD by means of a modulation of the electrostatic force. This modulated force becomes zero when the modulation

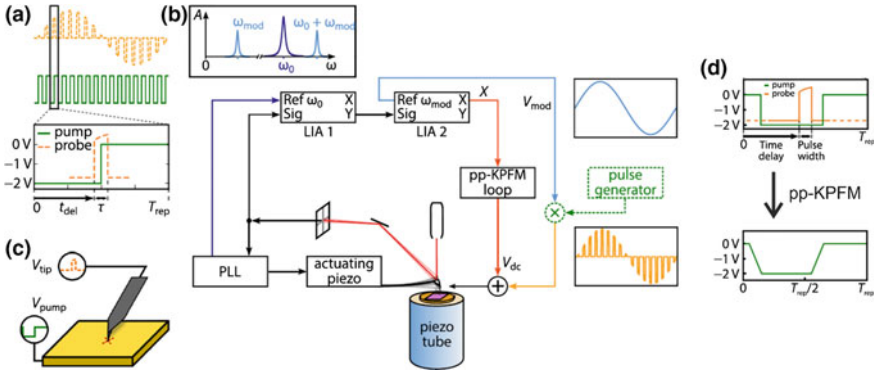

Fig. 5.13 **a** Schematic illustration of the measurement principle of pump-probe KPFM. A square wave pump pulse signal (green line) is applied to the sample. The probe pulse signal has a sinusoidal envelope (yellow dashed line) and a controlled time delay with respect to the pump pulse (see zoom-in showing a single cycle). **b** Schematic illustration of the signal path used for the pp-KPFM set-up. The sinusoidal ac-detection voltage as used in regular KPFM is mixed with the square wave pump pulse signal, which is also applied to the sample. The probe pulse signal is added to the pp-KPFM feedback voltage from the controller and applied to the tip. A frequency spectrum of the cantilever motion is depicted in the inset on the top left. **c** The schematic of the tip-sample system shows the probe pulse applied to the tip and the pump pulse to the sample. **d** This pump-probe approach allows the measurement of dynamic processes in the surface potential by shifting the probe pulse with respect to the pump pulse, giving a time resolution (slope in the bottom plot) corresponding to the probe pulse width. Reprinted and adapted from J. Appl. Phys. 118, 154302 (2015) and J. Appl. Phys. 118, 244502 (2015) with permission of AIP Publishing

voltage is zero, which is achieved by mixing the sinusoidal modulation voltage (ac bias) with a square wave signal. The resulting probe signal is a probe pulse with a sinusoidal envelope. As a consequence, changes in the surface potential are only detectable in the short time window when the ac voltage is applied. This probe signal applied to the tip is synchronized with a controllable time delay to a pump signal consisting of a square wave signal. This detection scheme allows a time resolution which corresponds to the width of the probe pulse, as seen in Fig. 5.13d.

In a detailed analysis of the pp-KPFM technique, the authors realized that the continuous application of the Kelvin compensation voltage leads to topography artifacts during the on-time of the pp-KPFM [30]. To minimize these topography artifacts, a second control loop is introduced that compensates the time-averaged CPD and thus separates the time-averaged from the time-dependent CPD. The authors note that the two control loops should be operated at separate modulation frequencies. Performing test measurements, a time resolution of 4 ns was demonstrated [30].

The application of this pp-KPFM approach was demonstrated for a pentacene OFET structure [30], the experimental setup and results are shown in Fig. 5.14. The bottom gate in this structure is kept at a constant voltage to generate a fixed background charge carrier concentration. The square wave pump probe is applied to the drain electrode with an amplitude of −2 V and a frequency of 50 kHz,

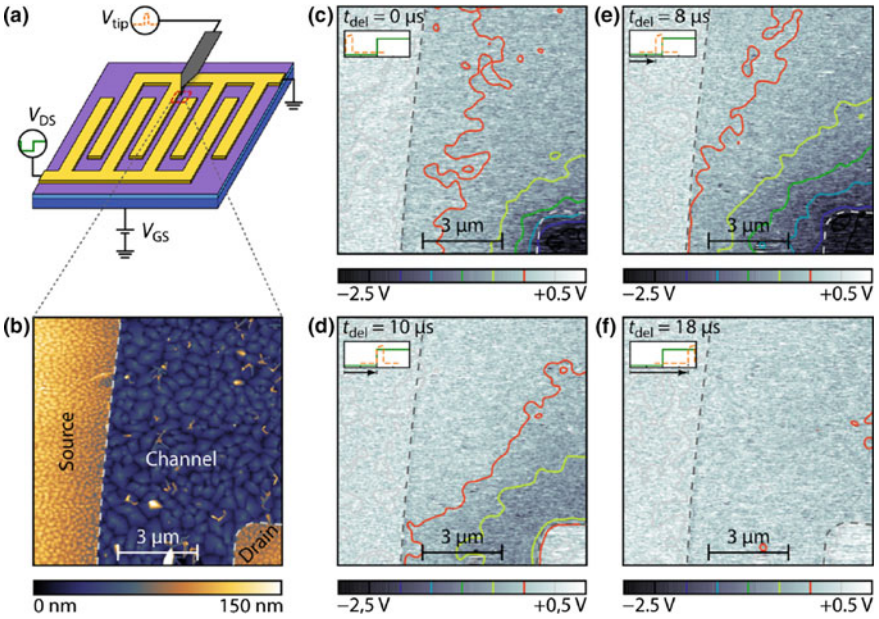

Fig. 5.14 **a** Schematic illustration of the measurement setup of the pentacene OFET sample with a bottom gate used in the pp-KPFM experiments, with interdigitated gold contacts. The red dashed line illustrates the measured area for which the topography is shown in **b**. The gold electrodes are covered by a 30 nm thick pentacene film. **c–f** pp-KPFM images at specific time delays of the probe pulse with respect to pump pulse, which has a repetition frequency of 50 kHz (corresponding to a cycle time of 20 µs). The probe-to-pump pulse relation is illustrated in the top left corner of each image. Isopotential lines are indicated by the colored solid lines showing the evolution of the CPD in the transistor channel. The dashed lines indicate the position of the electrodes. Reprinted from J. Appl. Phys. 118, 154302 (2015) with permission of AIP Publishing

keeping the source electrode grounded. The probe pulse width was adjusted to 2 µs (setting thereby the time resolution of the measurement) and the time delay was scanned through the whole repetition cycle. In the beginning of the cycle the drain electrode is at −2 V with respect to the source electrode. The surface potential drops along the channel between the two electrodes reflecting the charge-carrier distribution. A stronger drop is observed close to the drain electrode, indicating a space charge limited transport. The potential drop then becomes more distributed with longer time delays. Just after the drain electrode is grounded again, the charge distribution in the channel is in a non-equilibrium situation, which then relaxes over the next 8 µs.

Schumacher et al. [32] presented a similar pump-probe approach using light to excite a potential change in the sample, as is done in macroscopic optical pump-probe techniques [59]. The advantage of this approach is that it is not required to have a device structure as a sample with contacts to apply a bias, but basic materials dynamic properties can be studied that occur upon light illumination.

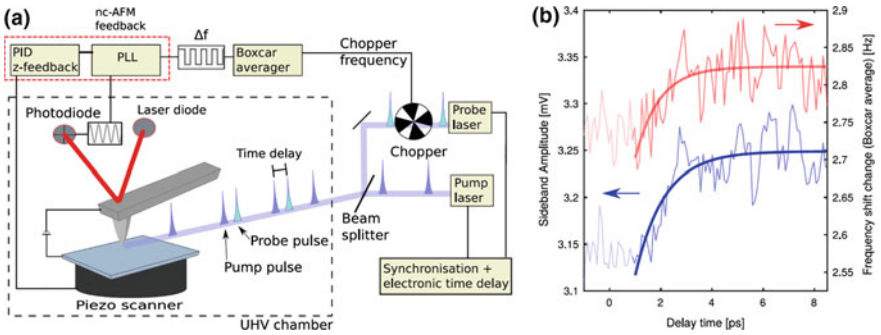

Fig. 5.15 **a** Schematic illustration for a pump-probe KPFM setup using light pulses. The time delay between pump and probe pulse is controllable and provides the time resolution. A chopper modulates the probe pulse to achieve a better signal-to-noise ratio. The frequency shift is sensitive to the probe pulses and the selected time delay. **b** Experimental time-resolved pp-KPFM spectra as a function of time delay obtained on low-temperature grown GaAs at a lift height of 1 nm and a bias voltage of 950 mV. The pump pulse is provided by a 780 nm laser and the probe pulse by a 610 nm laser. Two measurement methods are compared, direct sideband detection (blue thin line) and boxcar averaging of the frequency shift signal (red thin line). The thick lines represent fits with an exponential decay with time constants of (1.1 ± 0.4) ps for the sideband detection and (0.9 ± 0.6) ps for the boxcar detection. Reprinted from Appl. Phys. Lett. 110, 053111 (2017), with the permission of AIP Publishing

The setup is similar to the above presented setup for a bias-based pump-probe, however pulsed laser illumination is used, as shown in Fig. 5.15a. The pump pulse excites the sample resulting in a change in the electrostatic force detected by the cantilever. The following probe pulse excites the sample starting from a state where the effect of the pump probe has partially decayed already. Varying the time delay between pump and probe pulse the decay behavior can be measured. As in the other fast KPFM techniques described above, the measured signal is an average CPD value which reflects the time dependent behavior. The authors show that the minimal time resolution of the technique is determined by the thermal noise of the cantilever [33, 60], which determines if the electrostatic force difference between two different time delays can be distinguished or not.

The authors demonstrate the application of the technique on a low-temperature grown GaAs (LT-GaAs), which is known to have carrier lifetimes in the low picosecond range [59]. Figure 5.15b shows delay time dependent curves of two different measurement signals, the amplitude of the direct sideband of the modulated probe pulse using a lock-in detection [61] and the boxcar averaged frequency shift. The data can be well fitted with an exponential decay leading to similar time constants in both cases, around 1 ps. Up to know, this result on LT-GaAs represents the best experimentally demonstrated time resolution for time-resolved KPFM.

5.4 Conclusion and Outlook

To improve the understanding if basic properties of materials and the performance of devices, knowledge about dynamic processes on the nanoscale is crucially important. KPFM and EFM can provide insight in charge-carrier and ionic dynamic processes with the same resolution as in regular imaging. In the simplest realization for such measurements of dynamic processes, the measurement signal is recorded in real time in a point measurement, providing a time resolution on the order of tens of millisecond, and even down to 100 μs in the case of EFM. Faster processes are accessible by using more advanced techniques, many of them relying on a modulated excitation signal, which can be an applied bias or light pulse. In these measurement modes the average KPFM or EFM signal is measured, which depends on the detailed time dependence of the underlying dynamic processes.

While the earliest reports of time-resolved KPFM and EFM measurements are already about 15 years old, in the last 5 years the field has received an increased attention. Nevertheless, access and understanding of the underlying physics is still rather limited and further work on time-resolved KPFM and EFM in the coming years is to be expected.

References

1. M. Nonnenmacher, M.P. O'Boyle, H.K. Wickramasinghe, Kelvin probe force microscopy. Appl. Phys. Lett. **58**, 2921 (1991)
2. K. Okamotoa, Y. Sugawarab, S. Morita, The elimination of the 'artifact' in the electrostatic force measurement using a novel noncontact atomic force microscope/electrostatic force microscope. Appl. Surf. Sci. **188**, 381–385 (2002)
3. E. Palleau, L. Ressier, Ł. Borowik, T. Mélin, Numerical simulations for a quantitative analysis of AFM electrostatic nanopatterning on PMMA by Kelvin force microscopy. Nanotechnology **21**, 225706 (2010)
4. K.M. Burson, W.G. Cullen, S. Adam, C.R. Dean, K. Watanabe, T. Taniguchi, P. Kim, M.S. Fuhrer, Direct imaging of charged impurity density in common graphene substrates. Nano Lett. **13**, 3576–3580 (2013)
5. L. Gross, F. Mohn, P. Liljeroth, J. Repp, F.J. Giessibl, G. Meyer, Measuring the charge state of an adatom with noncontact atomic force microscopy. Science **324**, 1428 (2009)
6. F. Mohn, L. Gross, N. Moll, G. Meyer, Imaging the charge distribution within a single molecule. Nat. Nanotechnol. **7**, 227–231 (2012)
7. S. Kawai, A. Sadeghi, X. Feng, P. Lifen, R. Pawlak, T. Glatzel, A. Willand, A. Orita, J. Otera, S. Goedecker, E. Meyer, Obtaining detailed structural information about supramolecular systems on surfaces by combining high-resolution force microscopy with ab initio calculations. ACS Nano **7**, 9098–9105 (2013)
8. S. Sadewasser, Th. Glatzel, M. Rusu, A. Jäger-Waldau, M.Ch. Lux-Steiner, High-resolution work function imaging of single grains of semiconductor surfaces. Appl. Phys. Lett. **80**, 2979 (2002)
9. S. Sadewasser, P. Jelinek, Ch.-K. Fang, O. Custance, Y. Yamada, Y. Sugimoto, M. Abe, S. Morita, New insights on atomic-resolution frequency-modulation Kelvin probe force microscopy imaging on semiconductors. Phys. Rev. Lett. **103**, 266103 (2009)

10. Th. Glatzel, D. Fuertes Marrón, Th. Schedel-Niedrig, S. Sadewasser, M.Ch. Lux-Steiner, $CuGaSe_2$ solar cell cross section studied by Kelvin probe force microscopy in ultrahigh vacuum. Appl. Phys. Lett. **81**, 2017 (2002)
11. Th. Glatzel, S. Sadewasser, R. Shikler, Y. Rosenwaks, M.Ch. Lux-Steiner, Kelvin probe force microscopy on III-V semiconductors: the effect of surface defects on the local work function. Mater. Sci. Eng. B **102**, 138 (2003)
12. S. Sadewasser, Th. Glatzel, M. Rusu, A. Jäger-Waldau, M.Ch. Lux-Steiner, Surface photo voltage measurements for the characterization of the CuGaSe2/ZnSe interface using Kelvin probe force microscopy, in *Proceedings of 17th EU Photovoltaics Solar Energy Conference* (München, 2001), p. 1155
13. D.C. Coffey, D.S. Ginger, Time-resolved electrostatic force microscopy of polymer solar cells. Nat. Mater. **5**, 735 (2006)
14. J.L. Luria, K.A. Schwarz, M.J. Jaquith, R.G. Hennig, J.A. Marohn, Spectroscopic characterization of charged defects in polycrystalline pentacene by time- and wavelength-resolved electric force microscopy. Adv. Mater. **23**, 624–628 (2011)
15. P.A. Cox, M.S. Glaz, J.S. Harrison, S.R. Peurifoy, D.C. Coffey, D.S. Ginger, Imaging charge transfer state excitations in polymer/fullerene solar cells with time-resolved electrostatic force microscopy. J. Phys. Chem. Lett. **6**, 2852–2858 (2015)
16. A. Schirmeisen, A. Taskiran, H. Fuchs, B. Roling, S. Murugavel, H. Bracht, F. Natrup, Probing ion transport at the nanoscale: time-domain electrostatic force spectroscopy on glassy electrolytes. Appl. Phys. Lett. **85**, 2053 (2004)
17. T.N. Ng, J.A. Marohn, M.L. Chabinyc, Comparing the kinetics of bias stress in organic field-effect transistors with different dielectric interfaces. J. Appl. Phys. **100**, 084505 (2006)
18. M. Jaquith, E.M. Muller, J.A. Marohn, Time-resolved electric force microscopy of charge trapping in polycrystalline pentacene. J. Phys. Chem. B **111**, 7711 (2007)
19. M.J. Jaquith, J.E. Anthony, J.A. Marohn, Long-lived charge traps in functionalized pentacene and anthradithiophene studied by time-resolved electric force microscopy. J. Mater. Chem. **19**, 6116–6123 (2009)
20. L. Bürgi, T. Richards, M. Chiesa, R.H. Friend, H. Sirringhaus, A microscopic view of charge transport in polymer transistors. Synth. Met. **146**, 297–309 (2004)
21. E. Strelcov, S. Jesse, Y.-L. Huang, Y.-C. Teng, I.I. Kravchenko, Y.-H. Chu, S.V. Kalinin, Space- and time-resolved mapping of ionic dynamic and electroresistive phenomena in lateral devices. ACS Nano **7**, 6806–6815 (2013)
22. R. Giridharagopal et al., Submicrosecond time resolution atomic force microscopy for probing nanoscale dynamics. Nano Lett. **12**, 893–898 (2012)
23. D.U. Karatay, J.S. Harrison, M.S. Glaz, R. Giridharagopal, D.S. Ginger, Fast time-resolved electrostatic force microscopy: achieving sub-cycle time resolution. Rev. Sci. Instrum. **87**, 053702 (2016)
24. M. Takihara, T. Takahashi, T. Ujihara, Minority carrier lifetime in polycrystalline silicon solar cells studied by photoassisted Kelvin probe force microscopy. Appl. Phys. Lett. **93**, 021902 (2008)
25. G. Shao, M.S. Glaz, F. Ma, H. Ju, D.S. Ginger, Intensity-modulated scanning Kelvin probe microscopy for probing recombination in organic photovoltaics. ACS Nano **8**, 10799–10807 (2014)
26. Ł. Borowik, H. Lepage, N. Chevalier, D. Mariolle, O. Renault, Measuring the lifetime of silicon nanocrystal solar cell photo-carriers by using Kelvin probe force microscopy and x-ray photoelectron spectroscopy. Nanotechnology **25**, 265703 (2014)
27. P.A. Fernández Garrillo, Ł. Borowik, F. Caffy, R. Demadrille, B. Grévin, Photo-carrier multi-dynamical imaging at the nanometer scale in organic and inorganic solar cells. ACS Appl. Mater. Interfaces **8**, 31460–31468 (2016)
28. D. Moerman, H. Kim, A.E. Colbert, S. Graham, D.S. Ginger, The impact of ultra-thin titania interlayers on open circuit voltage and carrier lifetime in thin film solar cells. Appl. Phys. Lett. **108**, 113301 (2016)

29. P. Narchi, R. Cariou, M. Foldyna, P. Prod'homme, P. Roca i Cabarrocas, Nanoscale investigation of carrier lifetime on the cross section of epitaxial silicon solar cells using Kelvin probe force microscopy. IEEE J. Photovolt. **6**, 1576–1580 (2016)
30. J. Murawski, T. Graupner, P. Milde, R. Raupach, U. Zerweck-Trogisch, L.M. Eng, Pump-probe Kelvin-probe force microscopy: principle of operation and resolution limits. J. Appl. Phys. **118**, 154302 (2015)
31. J. Murawski, T. Mönch, P. Milde, M.P. Hein, S. Nicht, U. Zerweck-Trogisch, L.M. Eng, Tracking speed bumps in organic field-effect transistors via pump-probe Kelvin-probe force microscopy. J. Appl. Phys. **118**, 244502 (2015)
32. Z. Schumacher, A. Spielhofer, Y. Miyahara, P. Grütter, The limit of time resolution in frequency modulation atomic force microscopy by a pump-probe approach. Appl. Phys. Lett. **110**, 053111 (2017)
33. T.R. Albrecht, P. Grütter, D. Horne, D. Rugar, Frequency modulation detection using high-Q cantilevers for enhanced force microscope sensitivity. J. Appl. Phys. **69**, 668 (1991)
34. B. Roling, A. Schirmeisen, H. Bracht, A. Taskiran, H. Fuchs, S. Murugavel, F. Natrup, Nanoscopic study of the ion dynamics in a LiAlSiO4 glass ceramic by means of electrostatic force spectroscopy. Phys. Chem. Chem. Phys. **7**, 1472 (2005)
35. A. Schirmeisen, A. Taskiran, H. Fuchs, H. Bracht, S. Murugavel, B. Roling, Fast interfacial ionic conduction in nanostructured glass ceramics. Phys. Rev. Lett. **98**, 225901 (2007)
36. A. Taskiran, A. Schirmeisen, H. Fuchs, H. Bracht, B. Roling, Time-domain electrostatic force spectroscopy on nanostructured lithium-ion conducting glass ceramics: analysis and interpretation of relaxation times. Phys. Chem. Chem. Phys. **11**, 5499–5505 (2009)
37. L. Kronik, Y. Shapira, Surface photovoltage phenomena: theory, experiment, and applications. Surf. Sci. Rep. **37**, 1–206 (1999)
38. Th. Dittrich, S. Bönisch, P. Zabel, S. Dube, High precision differential measurement of surface photovoltage transients on ultrathin CdS layers. Rev. Sci. Instr. **79**, 113903 (2008)
39. O.G. Reid, G.E. Rayermann, D.C. Coffey, D.S. Ginger, Imaging local trap formation in conjugated polymer solar cells: a comparison of time-resolved electrostatic force microscopy and scanning Kelvin probe imaging. J. Phys. Chem. C **114**, 20672–20677 (2010)
40. G. Shao, G.E. Rayermann, E.M. Smith, D.S. Ginger, Morphology-dependent trap formation in bulk heterojunction photodiodes. J. Phys. Chem. B **117**, 4654–4660 (2013)
41. T.M. Clarke, J.R. Durrant, Charge photogeneration in organic solar cells. Chem. Rev. **110**, 6736–6767 (2010)
42. A. Henning, G. Günzburger, R. Jöhr, Y. Rosenwaks, B. Bozic-Weber, C.E. Housecroft, E.C. Constable, E. Meyer, and Th. Glatzel, Kelvin probe force microscopy of nanocrystalline TiO_2 photoelectrodes. Beilstein J. Nanotechnol. **4**, 418–428 (2013)
43. M. Beu, K. Klinkmüller, D. Schlettwein, Use of Kelvin probe force microscopy to achieve a locally and time-resolved analysis of the photovoltage generated in dye-sensitized ZnO electrodes. Phys. Status Solidi A **211**, 1960–1965 (2014)
44. J.L. Garrett, E.M. Tennyson, M. Hu, J. Huang, J.N. Munday, M.S. Leite, Real-time nanoscale open-circuit voltage dynamics of perovskite solar cells. Nano Lett. **17**, 2554 (2017)
45. J.L. Garrett, J.N. Munday, Fast, high-resolution surface potential measurements in air with heterodyne Kelvin probe force microscopy. Nanotechnology **27**, 245705 (2016)
46. D.W. deQuilettes, W. Zhang, V.M. Burlakov, D.J. Graham, T. Leijtens, A. Osherov, V. Bulovic, H.J. Snaith, D.S. Ginger, S.D. Stranks, Photo-induced halide redistribution in organic-inorganic perovskite films. Nat. Commun. **7**, 11683 (2016)
47. Z. Xiao, Y. Yuan, Y. Shao, Q. Wang, Q. Dong, C. Bi, P. Sharma, A. Gruverman, J. Huang, Giant switchable photovoltaic effect in organometal trihalide perovskite devices. Nat. Mater. **14**, 193–198 (2014)
48. A. Salleo, R.A. Street, Light-induced bias stress reversal in polyfluorene thin-film transistors. J. Appl. Phys. **94**, 471 (2003)
49. Ch. Melzer, Ch. Siol, H. von Seggern, Transit phenomena in organic field-effect transistors through Kelvin-probe force microscopy. Adv. Mater. **25**, 4315–4319 (2013)

50. A. Heeger, Bulk heterojunction solar cells: understanding the mechanism of operation. Adv. Mater. **26**, 10–28 (2014)
51. S. Cowan, A. Roy, A. Heeger, Recombination in polymer-fullerene bulk heterojunction solar cells. Phys. Rev. B **82**, 245207 (2010)
52. C. Shuttle, N. Treat, J. Douglas, J. Fréchet, M. Chabinyc, Deep energetic trap states in organic photovoltaic devices. Adv. Energy Mater. **2**, 111–119 (2012)
53. M. Nyman, O. Sandberg, R. Österbacka, 2D and trap-assisted 2D Langevin recombination in polymer: fullerene blends. Adv. Energy Mater. **5**, 1400890 (2015)
54. C. McNeill, I. Hwang, N. Greenham, Photocurrent transients in all-polymer solar cells: trapping and detrapping effects. J. Appl. Phys. **106**, 024507 (2009)
55. C.L. Ma, P.O. Lauritzen, A simple power diode model with forward and reverse recovery. IEEE Trans. Power Electron. **8**, 342–346 (1993)
56. R.H. Kingston, Switching time in junction diodes and junction transistors. Proc. IRE **42**, 829–834 (1954)
57. M. Yamakazi, H. Kobayashi, S. Shinohara, Forward transient of PiN and super junction diodes, in *Proceeding 16th Symposium Power Semiconductor Devices ICs* (2004), pp. 197–200
58. D.C. Lewis, On the determination of the minority carrier lifetime from the reverse recovery transient of pnR diodes. Solid-State Electron. **18**, 87–91 (1975)
59. S. Gupta, M.Y. Frankel, J.A. Valdmanis, J.F. Whitaker, G.A. Mourou, F.W. Smith, A.R. Calawa, Subpicosecond carrier lifetime in GaAs grown by molecular beam epitaxy at low temperatures. Appl. Phys. Lett. **59**, 3276 (1991)
60. D.P.E. Smith, Limits of force microscopy. Rev. Sci. Instrum. **66**, 3191 (1995)
61. U. Zerweck, C. Loppacher, T. Otto, S. Grafström, L.M. Eng, Accuracy and resolution limits of Kelvin probe force microscopy. Phys. Rev. B **71**, 125424 (2005)

Part II
Data Interpretation and Theoretical Aspects

Chapter 6
Imaging Static Charge Distributions: A Comprehensive KPFM Theory

Philipp Rahe and Hagen Söngen

Abstract We analyze Kelvin probe force microscopy (KPFM) for tip-sample systems that contain static charges by presenting a rigorous derivation for the respective KPFM signal in all common KPFM modes, namely amplitude modulation, frequency modulation, or heterodyne detection in the static, open-loop or closed-loop variant. The electrostatic model employed in the derivation is based on a general electrostatic analysis of an arbitrary tip-sample geometry formed by two metals, and which can include a static charge distribution and dielectric material in-between. The effect of the electrostatic force on the oscillating tip is calculated from this model within the harmonic approximation, and the observables for each of the above KPFM modes are derived from the tip oscillation signal. Our calculation reveals that the KPFM signal can for all modes be written as a weighted sum over all charges, whereby each charge is multiplied with a position-dependent weighting factor depending on the tip-sample geometry, the KPFM mode, and the oscillation amplitude. Interestingly, as the weight function does not depend on the charges itself, the contribution of the void tip-sample system and the charge distribution can be well-separated in the KPFM signal. The weight function for charges allows for a detailed understanding of the KPFM contrast formation, and enables to trace the dependence of the KPFM signal on different parameters such as the tip-sample geometry or the oscillation amplitude.

P. Rahe (✉)
Fachbereich Physik, Universität Osnabrück, Barbarastrasse 7,
49076 Osnabrück, Germany
e-mail: prahe@uni-osnabrueck.de

H. Söngen
Institut für Physikalische Chemie, Johannes Gutenberg-Universität Mainz,
Duesbergweg 10-14, Mainz, Germany
e-mail: soengen@uni-mainz.de ; hagen.soengen@uni-bielefeld.de

H. Söngen
Graduate School Materials Science in Mainz, Staudinger Weg 9, 55128 Mainz, Germany

Present Address:
H. Söngen
Physical Chemistry I, Bielefeld University,
Universitätsstraße 25, 33615 Bielefeld, Germany

S. Sadewasser and T. Glatzel (eds.), *Kelvin Probe Force Microscopy*,
Springer Series in Surface Sciences 65, https://doi.org/10.1007/978-3-319-75687-5_6

6.1 Introduction

There is now a large body of experimental work available showing variations in the Kelvin probe force microscopy (KPFM) signal on a variety of samples, including contrast on adsorbed molecular systems [1–8], on metallic nanoclusters [5, 9], on charged species [10–13], and on the atomic scale [14–17]. Although KPFM has developed into an invaluable tool to investigate electric properties at the nanoscale, the general interpretation of the KPFM signal V_{KPFM} is still controversly discussed. For example, attempts to explain the KPFM signal of molecule-on-insulator systems following the concepts developed for metal surfaces have been made [1, 8, 18]. Furthermore, a number of explanations have been put forward that relate the KPFM signal V_{KPFM} to dipole and charge densities [10, 12, 13], the electrostatic surface potential [19], and the normal component of the electric field [20].

Besides the complexity of the KPFM signal interpretation due to the diverse range of the investigated samples, there are additionally a number of experimental KPFM modes available, namely the amplitude modulation (AM), frequency modulation (FM) and heterodyne mode used in static, open-loop, or closed-loop configuration [21, 22]. Each technique is optimized for usage in different environments and for different samples, but all techniques result in a voltage signal, the KPFM signal V_{KPFM}.

In this chapter, we will investigate the central question how the KPFM signal is related to the physical sample properties, namely the contact potential difference and the charge distribution within the tip-sample system, by a rigorous derivation for the formulae describing the KPFM signal V_{KPFM} for the different KPFM modes.

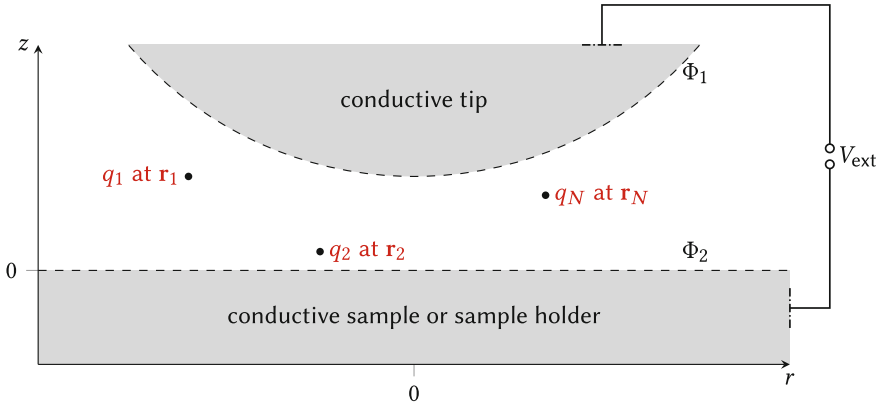

Fig. 6.1 Setup of a tip-sample system including a conductive tip and a conductive sample or conductive sample holder between which an external voltage V_{ext} is applied. Additionally, we have included exemplary point charges located in-between the two conductors. A dielectric sample and a dielectric medium would be considered by a different local dielectric permittivity in specific parts of the space between the two conductors

The system under consideration is sketched in Fig. 6.1. It is formed by a two-electrode setup with the upper electrode representing the tip and the lower representing the sample side, which is either the metallic sample, or a metallic sample back contact in case of dielectric material in the gap. Dielectric material is accounted for by assigning an according local dielectric permittivity to the respective region between the two metals. Moreover, we include a static charge distribution inside the tip-sample system formed by the two metals to model the presence of atomic or molecular species. This layout represents a common case of atomic or molecular species adsorbed and assembled on surfaces of insulating or conducting materials [3, 23, 24], as well as for species on insulating thick films [11, 12]. The derivation that is presented herein follows our recent work [25, 26], and also reflects similar evaluations for specific tip-sample systems [27, 28], or for short-range electrostatic forces [29].

The derivation starts in Sect. 6.2 with a general electrostatic description based on a model presented by Kantorovich et al. [30]. This model allows to calculate the electrostatic force on the probing tip for an arbitrary geometry. After a description of experimental measurement strategies in Sect. 6.3, we can analytically calculate in Sect. 6.4 the resulting KPFM signal for the different experimental KPFM modes.

The central result of this chapter is the introduction of the *KPFM weight function for charges*, W_{KPFM}, in Sect. 6.5, which allows to write the KPFM signal in a straightforward way as a sum over the weighted charges. Specifically, each charge q_i of a total of N charges is multiplied by the weight function W_{KPFM} evaluated at the position $\mathbf{r}_i$ of the respective charge,

$$V_{\mathrm{KPFM}} = V_{\mathrm{CPD}} + \sum_{i=1}^{N} q_i W_{\mathrm{KPFM}}(\mathbf{r}_i), \tag{6.1}$$

where V_{CPD} is the contact potential difference of the two metals due to the electric connection between them. W_{KPFM} is an implicit function of the tip-sample geometry, (which includes the tip position), as well as of the oscillation amplitude. The weight function furthermore depends on the KPFM mode used in the experiment, with the respective definitions for the FM and AM mode given in this chapter. The KPFM signal V_{KPFM} can therefore be understood as a convolution of the charge distribution with the weight function [25, 26], similar to earlier approaches using a point spread function to calculate the KPFM signal on conducting surfaces with different local work functions [31, 32].

6.2 Electrostatic Description

The common starting point to understand the physical origin of the KPFM signal for all KPFM modes and diverse sample systems is to calculate the *total electrostatic energy* U_{el} for the tip-sample system including external sources, i.e. batteries or power supplies, that fix the electric potentials on the conductors. The

KPFM signal then follows from evaluating specific observables for the different KPFM modes with respect to the externally applied voltage.

The electrostatic calculation fundamental to our KPFM model has initially been performed by Kantorovich et al. [30]. They have analyzed a system containing an arbitrary number of finite metallic conductors m at fixed potentials $\{\boldsymbol{\Phi}_m\}$, an arbitrary number of point charges $\{q_i\}$ located at positions $\{\mathbf{r}_i\}$ outside of the conductors, and external batteries keeping the potentials $\{\boldsymbol{\Phi}_m\}$ on the metals constant. Especially when spatially moving any metal within the system, the batteries facilitate the necessary charge exchange to keep the potentials constant. Consequently, the total energy consists of the energy stored in the electrostatic field as well as the energy contribution due to the external batteries.

Here, we adapt the original derivation from Kantorovich et al. [30] to the case of a KPFM tip-sample system by reducing their general case to two metals and N point charges, see also Fig. 6.1. In the KPFM setup, the upper metal (1) represents the metallic tip and the lower metal (2) represents the sample side, defined by the metallic sample or a metallic sample holder in case of dielectric material in the tip-sample gap.

Energy stored within an electrostatic field

For linear and isotropic media, the energy $U_{\mathrm{el,f}}$ stored within an electrostatic field is given by [33]

$$U_{\mathrm{el,f}} = \frac{1}{2}\int_V \mathbf{E}\cdot\mathbf{D}d\mathbf{r} \tag{6.2}$$

where $\mathbf{E}$ is the electrostatic field and $\mathbf{D}$ the dielectric displacement field. The integral is taken over the full volume V of the system. For the herein considered case of linear, isotropic dielectric materials we can write $\mathbf{D} = \varepsilon_0\varepsilon_r(\mathbf{r})\mathbf{E}$. With this description we furthermore assume that the dielectric material can be well described by the macroscopic relative permittivity ε_r. Additionally, the following derivation assumes that all charges are present on the surfaces of the metals and that the presence of the tip does not influence the sample structure, i.e. all charges stay fixed with respect to their initial positions. For the case of N point charges $\{q_i\}$ at positions $\{\mathbf{r}_i\}$ and two conductors at potentials $\boldsymbol{\Phi}_1$ and $\boldsymbol{\Phi}_2$ holding charges of Q_1 and Q_2, respectively, the electrostatic energy within the field $U_{\mathrm{el,f}}$ is then given by [30, 34]

$$U_{\mathrm{el,f}} = \frac{1}{2}\sum_i q_i\boldsymbol{\Phi}(\mathbf{r}_i) + \frac{1}{2}\left(\boldsymbol{\Phi}_1 Q_1 + \boldsymbol{\Phi}_2 Q_2\right) \tag{6.3}$$

whereby the electrostatic potential $\boldsymbol{\Phi}(\mathbf{r})$ within the system is produced by the dielectric media, the point charges, and the metals. The charge Q_m on metal m is given by the integral

$$Q_m = -\varepsilon\int_{S_m}\frac{\partial\boldsymbol{\Phi}}{\partial n}ds \tag{6.4}$$

where the integration is performed over the surface S_m of metal m with the local surface normal vector $\mathbf{n}$ and ε is the permittivity of the surrounding medium. This definition includes the assumption of finite metal surfaces and requires the classical situation where all charge is located on the metal surfaces. The electrostatic potentials $\boldsymbol{\Phi}_1$ and $\boldsymbol{\Phi}_2$ on the homogeneous metal surfaces include the contact potential difference between the two metals, which can build up after their electric contact via the battery V_{ext} as sketched in Fig. 6.1.

Energy due to the external battery

An external battery performs work to keep the potentials $\boldsymbol{\Phi}_1$, $\boldsymbol{\Phi}_2$ on the metal surfaces constant if these surfaces are moved with respect to each other. Consider moving the tip with respect to the sample by a distance δz_{ts} along $\mathbf{e}_z$. The work δA is performed against a force F_{ts} acting on the tip, namely [30]

$$\delta A = -F_{\text{ts}}\, \delta z_{\text{ts}}. \tag{6.5}$$

Three effects have to be considered when moving one metal with respect to the other by δz_{ts}. First, the electrostatic potential $\boldsymbol{\Phi}(\mathbf{r})$ of the full system will change by $\delta\boldsymbol{\Phi}(\mathbf{r})$ due to the change of the geometry. Second, the surface charges Q_1 and Q_2 on the tip and the sample side will change by δQ_1 and δQ_2, respectively, due to different influence[1] from the other conductor and from the point charges. The energy $U_{\text{el,f}}$ of the field will then change by

$$\delta U_{\text{el,f}} = \frac{1}{2}\sum_i q_i \delta\boldsymbol{\Phi}(\mathbf{r}_i) + \frac{1}{2}\left(\boldsymbol{\Phi}_1 \delta Q_1 + \boldsymbol{\Phi}_2 \delta Q_2\right). \tag{6.6}$$

Third, in order to modify the charges Q_1 and Q_2 on tip and sample side such that the potentials remain constant at $\boldsymbol{\Phi}_1$ and $\boldsymbol{\Phi}_2$, the external battery performs the work δA_b given by

$$\delta A_b = \boldsymbol{\Phi}_1 \delta Q_1 + \boldsymbol{\Phi}_2 \delta Q_2. \tag{6.7}$$

Finally, the total work performed when moving the tip by δz_{ts} is given from combining these contributions

$$\begin{aligned}\delta A &= -\delta A_b + \delta U_{\text{el,f}} \\ &= -\left(\boldsymbol{\Phi}_1 \delta Q_1 + \boldsymbol{\Phi}_2 \delta Q_2\right) \\ &\quad + \frac{1}{2}\sum_i q_i \delta\boldsymbol{\Phi}(\mathbf{r}_i) + \frac{1}{2}\left(\boldsymbol{\Phi}_1 \delta Q_1 + \boldsymbol{\Phi}_2 \delta Q_2\right).\end{aligned} \tag{6.8}$$

[1] We distinguish here between *influence* as the effect of shifting electron density within or between conductors due to an external field and *polarisation* as the result of generating a displacement field in a dielectric material.

The work done by the battery is taken with a negative sign as this work reduces the total potential energy of the whole system [30].

Total electrostatic energy

The sum of the electrostatic field energy and of the external battery energy contribution gives the total electrostatic energy U_{el} of the full system as

$$U_{\mathrm{el}} = \frac{1}{2}\sum_i q_i \boldsymbol{\Phi}(\mathbf{r}_i) - \frac{1}{2}\left(\boldsymbol{\Phi}_1 Q_1 + \boldsymbol{\Phi}_2 Q_2\right), \tag{6.9}$$

where we highlight the negative sign when comparing this result to (6.3). Equation (6.9) is, as it stands, of limited usability as the electrostatic potential $\boldsymbol{\Phi}(\mathbf{r})$ is not known, and a calculation needs to consider the implicit dependency on the charges $(q_i, \mathbf{r}_i)$ and on the potentials $\boldsymbol{\Phi}_1$, $\boldsymbol{\Phi}_2$. To challenge this difficulty, Kantorovich et al. [30] recognized that U_{el} can be split into different terms: one term describes the charges in the potential of the metal arrangement and a second term only includes the image interactions U_{im} caused by influence in the conductors and polarisation of the dielectric materials due to the point charges. Based on a Green function approach, they first derived a formal solution for the total electrostatic potential $\boldsymbol{\Phi}(\mathbf{r})$

$$\boldsymbol{\Phi}(\mathbf{r}) = {\sum_i}' \frac{1}{4\pi\varepsilon_0}\frac{q_i}{\left|\mathbf{r}-\mathbf{r}_i\right|} + \boldsymbol{\Phi}_{\mathrm{void}}(\mathbf{r}) + \boldsymbol{\Phi}_{\mathrm{im}}(\mathbf{r}) \tag{6.10}$$

with a potential $\boldsymbol{\Phi}_{\mathrm{void}}(\mathbf{r})$ not depending on the point charges, and the image potential $\boldsymbol{\Phi}_{\mathrm{im}}(\mathbf{r})$ due to the point charges $\{q_i\}$. The first term describes the potentials of the point charges whereby the prime indicates that $\mathbf{r} = \mathbf{r}_i$ is not included in the sum. Inserting (6.10) into (6.9) and reordering the terms give

$$\begin{aligned} U_{\mathrm{el}} = {} & \frac{1}{8\pi\varepsilon_0}\sum_i\sum_{i,i\neq j}\frac{q_i q_j}{\left|\mathbf{r}_i-\mathbf{r}_j\right|} + \frac{1}{2}\sum_i q_i \boldsymbol{\Phi}_{\mathrm{void}}(\mathbf{r}_i) \\ & + \frac{1}{2}\sum_i q_i \boldsymbol{\Phi}_{\mathrm{im}}(\mathbf{r}_i) - \frac{1}{2}\left(\boldsymbol{\Phi}_1 Q_1 + \boldsymbol{\Phi}_2 Q_2\right). \end{aligned} \tag{6.11}$$

The charges Q_m on the two metals representing the tip and sample side can furthermore be separated into charges $\{Q_m^{\mathrm{ind}}\}$ induced by the point charges $\{q_i\}$ and charges $\{Q_m^{\mathrm{ext}}\}$ maintained by the external battery with $Q_m = Q_m^{\mathrm{ind}} + Q_m^{\mathrm{ext}}$ for each m. Based on the Green function approach to introduce the formal solution, Kantorovich et al. [30] derived the identity

$$\frac{1}{2}\sum_i q_i \boldsymbol{\Phi}_{\mathrm{void}}(\mathbf{r}_i) = \frac{1}{2}\sum_m Q_m^{\mathrm{ext}} \boldsymbol{\Phi}_m - \frac{1}{2}\sum_m Q_m \boldsymbol{\Phi}_m. \tag{6.12}$$

This identity allows us to rewrite the last term in (6.11), and finally to separate the total eletrostatic energy U_{el} of this system into four contributions

$$\boxed{U_{\mathrm{el}} = U_{\mathrm{C}} + U_{\mathrm{q\text{-}C}} + U_{\mathrm{q\text{-}q}} + U_{\mathrm{im}}.} \tag{6.13}$$

The first term describes the capacitance of the charge-free ($N = 0$) system

$$U_{\mathrm{C}} = -\frac{1}{2}\left(\boldsymbol{\Phi}_1 Q_1^{\mathrm{ext}} + \boldsymbol{\Phi}_2 Q_2^{\mathrm{ext}}\right). \tag{6.14}$$

Without loss of generality [30], we can set the potential difference to $V = \boldsymbol{\Phi}_1 - \boldsymbol{\Phi}_2 = V_{\mathrm{ext}} - V_{\mathrm{CPD}}$ with an external bias V_{ext} and with the contact potential difference V_{CPD} between the two metals. By introducing a global contact potential difference, we assume that each metal surface is homogeneous with respect to their respective work function. The external battery requires $Q_1^{\mathrm{ext}} = -Q_2^{\mathrm{ext}} = Q_{\mathrm{ext}}$ and from furthermore introducing the capacitance $C_{\mathrm{void}} = Q_{\mathrm{ext}}/V$, we find for the first term the well-known result for the negative energy stored in a capacitor,

$$U_{\mathrm{C}} = -\frac{1}{2} C_{\mathrm{void}} V^2. \tag{6.15}$$

The second term describing the interaction between the point charges and the metal plates (excluding any image charges) is given by

$$U_{\mathrm{q\text{-}C}} = \sum_i q_i \boldsymbol{\Phi}_{\mathrm{void}}(\mathbf{r}_i). \tag{6.16}$$

In the case of a tip-sample system delimited by two metals, the electric potential $\boldsymbol{\Phi}_{\mathrm{void}}$ of the void capacitor directly scales with the potential between the plates, allowing us to introduce the normalized electric potential $\hat{\boldsymbol{\Phi}}_{\mathrm{void}} = \boldsymbol{\Phi}_{\mathrm{void}}/V$. We can then write

$$U_{\mathrm{q\text{-}C}} = \sum_i q_i \hat{\boldsymbol{\Phi}}_{\mathrm{void}}(\mathbf{r}_i) V. \tag{6.17}$$

The pairwise Coulomb-interaction between all point charges as considered in the third term is

$$U_{\mathrm{q\text{-}q}} = \frac{1}{8\pi\varepsilon_0} \sum_i \sum_{j, i \neq j} \frac{q_i q_j}{\left|\mathbf{r}_i - \mathbf{r}_j\right|}, \tag{6.18}$$

and finally the image energy in the fourth term follows from

$$U_{\mathrm{im}} = \frac{1}{2} \sum_i q_i \boldsymbol{\Phi}_{\mathrm{im}}(\mathbf{r}_i), \tag{6.19}$$

where the image potential $\boldsymbol{\Phi}_{\mathrm{im}}(\mathbf{r})$ can be expressed [30] as

$$\Phi_{\mathrm{im}}(\mathbf{r}) = \sum_j q_j \Phi_{\mathrm{ind}}(\mathbf{r}, \mathbf{r}_j). \tag{6.20}$$

Here, $\Phi_{\mathrm{ind}}(\mathbf{r}, \mathbf{r}_j)$ describes the potential at $\mathbf{r}$ due to the image charges caused by charge q_j at position $\mathbf{r}_j$.

As the final result of this section we can now calculate the electrostatic contribution F_{el} to the tip-sample force F_{ts}. The normal component of the electrostatic force results directly from the negative derivative of the total electrostatic energy (6.13) with respect to the tip-sample distance z_{ts},

$$\begin{aligned} F_{\mathrm{el}}(z_{\mathrm{ts}}, V) = \frac{1}{2}\frac{\partial C_{\mathrm{void}}}{\partial z_{\mathrm{ts}}} \cdot V^2 \\ - \sum_{i=1}^{N} q_i \frac{\partial \hat{\Phi}_{\mathrm{void}}(\mathbf{r}_i)}{\partial z_{\mathrm{ts}}} \cdot V \\ - \sum_{i=1}^{N}\sum_{j=1}^{N} q_i q_j \frac{\partial \Phi_{\mathrm{ind}}(\mathbf{r}_i, \mathbf{r}_j)}{\partial z_{\mathrm{ts}}}. \end{aligned} \tag{6.21}$$

The formula reduces to three terms as the Coulomb interaction is not dependent on the tip-sample distance z_{ts}. Before discussing this result, we briefly revisit the assumptions made for the derivation of this formula:

- All metals and dielectric materials are described macroscopically, and the dielectric materials modelled by a relative permittivity $\varepsilon_{\mathrm{r}}(\mathbf{r})$ are isotropic and linear.
- All metals have homogeneous surfaces and all charges reside on their surfaces.
- The presence of the tip does neither modify the position of the point charges $\{q_i\}$, nor the position of the dielectric media. Therefore, we do not consider relaxations due to the tip-sample interaction.
- The external battery is an ideal battery.

Equation (6.21) is in agreement with several findings known from experiments. First, the force scales quadratically with the voltage V, and a term $\propto q_i V$ will change the parabolic shape depending on the charges in the system. Second, for the charge-free system ($N = 0$), where all terms containing q_i evaluate to zero, (6.21) reduces to the first term. This term is identical to the description of a void tip-sample capacitor as given by (6.15), and it is furthermore the common starting point when describing the KPFM signal for conducting substrates [35].

The force described by (6.21) conveniently separates the contribution due to the void tip-sample system from the image interactions of the point charges. This is possible as the former contribution depends on the geometry of the two metals, the dielectric media, and the applied potential, but not on the point charges. In contrast, the latter image interactions depend on the charges and the geometry of the metals, but not on the external voltage. While a description of the void tip-sample capacitor by the capacitance C_{void} and the electrostatic potential Φ_{void} can be performed analytically [30, 36, 37], calculating the image interaction U_{im} analytically can be a rather

difficult challenge, in particular for realistic geometries and multiple charges. As one of the important results of this chapter, we will derive in the following section that the image interaction terms do not contribute to the KPFM signal and, consequently, do not have to be evaluated for a KPFM signal analysis.

6.3 KPFM Detection

Based on this electrostatic model, we now turn to the calculation of the KPFM signal for the various KPFM modes based on an analysis of the tip motion. In this and the next section, we will quantitatively derive observables that are recorded in the AM-KPFM mode, the FM-KPFM mode, and the heterodyne KPFM modes, each in the static, open-loop, and closed-loop variants [21, 22]. Despite the difference of the KPFM mode-specific observables, it is possible to condense all different observables into *one* generalized equation that allows for a quantitative description of KPFM for *all* operation modes. Our derivation does not rely on mode-specific assumptions or approximations—we will only employ the *harmonic approximation* [38], which is the prevalent approximation used for the quantitative analysis of atomic force microscopy (AFM) data.

The electrostatic force F_{el} (see (6.21)) contributes to the tip-sample force F_{ts}, which can also include, for example, chemical, van-der-Waals, or magnetic forces [39]. Generally, the tip-sample force $F_{\mathrm{ts}}(z_{\mathrm{ts}}, \dot{z}_{\mathrm{ts}}, V)$ depends on the tip-sample distance z_{ts}, the tip velocity $\dot{z}_{\mathrm{ts}}$ as well as the voltage V between the tip and sample side metals. We assume in the following that only the electrostatic contribution F_{el} to the total tip-sample force F_{ts} is dependent on the voltage between the metals.

In the most general case, the voltage V between the tip and the sample side metals is a sum of the negative contact potential difference V_{CPD} and an external bias V_{ext}, which in turn can be defined by the sum of a static (DC) bias V_{bias} and a sinusoidal voltage with amplitude V_{el} and electrostatic excitation frequency ν_{el},

$$V = -V_{\mathrm{CPD}} + V_{\mathrm{bias}} + V_{\mathrm{el}} \cos\left(2\pi\nu_{\mathrm{el}} t\right). \tag{6.22}$$

For KPFM experiments in which only the static voltage V_{bias} is applied, we can set $V_{\mathrm{el}} = 0$. Similarly, for treating experiments where no static voltage, but only a sinusoidal voltage is applied, we can set $V_{\mathrm{bias}} = 0$.

The electrostatic force F_{el} in (6.21) can be rewritten in the form of three terms when using the voltage V according to (6.22),[2]

[2]The three quantities $F_{\mathrm{el,a}}$, $F_{\mathrm{el,b}}$ and $F_{\mathrm{el,c}}$ might firsthand appear to be spectral components of F_{el}—they would represent a static component (at zero frequency), a first harmonic (at frequency ν_{el}) and a second harmonic (at frequency $2\nu_{\mathrm{el}}$). However, it is important to remember that during dynamic AFM and dynamic KPFM measurements, the tip-sample distance z_{ts} is also a function of time. Therefore, considering $F_{\mathrm{el,a}}$, $F_{\mathrm{el,b}}$ and $F_{\mathrm{el,c}}$ to be spectral components of F_{el} is only reasonable under the assumption that z_{ts} is fixed.

$$
\begin{aligned}
F_{\mathrm{el}}(z_{\mathrm{ts}}, V) = & F_{\mathrm{el,a}}(z_{\mathrm{ts}}) \\
& + F_{\mathrm{el,b}}(z_{\mathrm{ts}}) \cos\left(2\pi \nu_{\mathrm{el}} t\right) \\
& + F_{\mathrm{el,c}}(z_{\mathrm{ts}}) \cos\left(2\pi (2\nu_{\mathrm{el}}) t\right),
\end{aligned}
\tag{6.23}
$$

where

$$
\begin{aligned}
F_{\mathrm{el,a}}(z_{\mathrm{ts}}) = & + \frac{1}{2} \frac{\partial C_{\mathrm{void}}}{\partial z_{\mathrm{ts}}} \left(\left(V_{\mathrm{bias}} - V_{\mathrm{CPD}}\right)^2 + \frac{1}{2} V_{\mathrm{el}}^2 \right) \\
& - \left(V_{\mathrm{bias}} - V_{\mathrm{CPD}}\right) \sum_{i=1}^{N} q_i \frac{\partial \hat{\boldsymbol{\Phi}}_{\mathrm{void}}(\mathbf{r}_i)}{\partial z_{\mathrm{ts}}} \\
& - \frac{1}{2} \sum_{i=1}^{N} \sum_{j=1}^{N} q_i q_j \frac{\partial \boldsymbol{\Phi}_{\mathrm{ind}}(\mathbf{r}_i, \mathbf{r}_j)}{\partial z_{\mathrm{ts}}}
\end{aligned}
\tag{6.24}
$$

$$
F_{\mathrm{el,b}}(z_{\mathrm{ts}}) = + V_{\mathrm{el}} \left(\frac{\partial C_{\mathrm{void}}}{\partial z_{\mathrm{ts}}} (V_{\mathrm{bias}} - V_{\mathrm{CPD}}) - \sum_{i=1}^{N} q_i \frac{\partial \hat{\boldsymbol{\Phi}}_{\mathrm{void}}(\mathbf{r}_i)}{\partial z_{\mathrm{ts}}} \right) \tag{6.25}
$$

$$
F_{\mathrm{el,c}}(z_{\mathrm{ts}}) = + \frac{1}{4} \frac{\partial C_{\mathrm{void}}}{\partial z_{\mathrm{ts}}} V_{\mathrm{el}}^2. \tag{6.26}
$$

Because F_{el} contributes to the tip-sample force F_{ts}, the latter force can in analogy to (6.23) also be written in the form of three terms

$$
\begin{aligned}
F_{\mathrm{ts}}(z_{\mathrm{ts}}, \dot{z}_{\mathrm{ts}}, V) = & F_{\mathrm{ts,a}}(z_{\mathrm{ts}}, \dot{z}_{\mathrm{ts}}) \\
& + F_{\mathrm{ts,b}}(z_{\mathrm{ts}}, \dot{z}_{\mathrm{ts}}) \cos\left(2\pi \nu_{\mathrm{el}} t\right) \\
& + F_{\mathrm{ts,c}}(z_{\mathrm{ts}}, \dot{z}_{\mathrm{ts}}) \cos\left(2\pi (2\nu_{\mathrm{el}}) t\right).
\end{aligned}
\tag{6.27}
$$

Here, $F_{\mathrm{ts,a}}$ contains $F_{\mathrm{el,a}}$ and all other voltage-independent contributions to the interaction force. In contrast, the other two terms include *only* electrostatic forces, we can therefore use the identities $F_{\mathrm{ts,b}} = F_{\mathrm{el,b}}$ and $F_{\mathrm{ts,c}} = F_{\mathrm{el,c}}$.

Next, we discuss the effect of the tip-sample force (including F_{el}) on the motion of the AFM resonator [38]. This resonator is described as a harmonic oscillator with effective mass m, spring constant k, and damping constant γ and the most rigorous derivation of the oscillator behavior starts at the equation of motion considering all involved forces. Besides the tip-sample force F_{ts}, the force acting on the resonator consists of the restoring force $-kq$ and a damping force $-\gamma \dot{q}$. Moreover, for conventional dynamic AFM imaging, we consider an external excitation force $F_0 \cos\left(2\pi \nu_{\mathrm{exc}} t\right)$, where F_0 is the excitation force amplitude and ν_{exc} is the excitation frequency. The equation of motion is then given by

$$\begin{aligned} m\ddot{q} = &-kq - \gamma\dot{q} \\ &+ F_0 \cos\left(2\pi\nu_{\mathrm{exc}}t\right) \\ &+ F_{\mathrm{ts}}(z_{\mathrm{ts}}, \dot{z}_{\mathrm{ts}}, V). \end{aligned} \tag{6.28}$$

An analytical solution of (6.28) for an arbitrary tip-sample force is generally not possible since F_{ts} depends on the tip-sample distance z_{ts}. We therefore employ the *harmonic approximation*, in which the deflection of the resonator is approximated as

$$\tilde{q} = q_{\mathrm{s}} + A\cos\left(2\pi\nu_{\mathrm{exc}}t + \varphi\right) \tag{6.29}$$

and, consequently, the tip-sample distance z_{ts} is given as

$$\tilde{z}_{\mathrm{ts}} = z_{\mathrm{c}} + A\cos\left(2\pi\nu_{\mathrm{exc}}t + \varphi\right). \tag{6.30}$$

In the above equations, q_{s} is the static deflection, A is the oscillation amplitude, and φ is the phase shift between the excitation at frequency ν_{exc} and the deflection. The tip oscillates around z_{c}, the center position of the oscillation.

When *only* discussing dynamic AFM, this approximation can consistently be used for the deflection and the tip-sample distance by replacing q with $\tilde{q}$ and z_{ts} with $\tilde{z}_{\mathrm{ts}}$ in (6.28). However, the approximation implies that the only spectral components of the deflection are the static deflection and the first harmonic at frequency ν_{exc}—there would not be any additional spectral components for a KPFM measurement to detect. Therefore, we only use the harmonic approximation for the *sampling* of the tip-sample and electrostatic force in (6.28). This means that we only substitute $F_{\mathrm{ts}}(z_{\mathrm{ts}}, \dot{z}_{\mathrm{ts}}, V)$ with $F_{\mathrm{ts}}(\tilde{z}_{\mathrm{ts}}, \dot{\tilde{z}}_{\mathrm{ts}}, V)$ in (6.28), but do not replace the other occurrences of q, thereby allowing arbitrary spectral components to the deflection. The thought underlying this approximation is that the additional spectral components to the deflection, which are not expressed in (6.29), do not significantly affect the path along which the tip-sample force is sampled. Using the harmonic approximation, equations (6.28) and (6.23) result in

$$\begin{aligned} m\ddot{q} = &-kq - \gamma\dot{q} \\ &+ F_0 \cos\left(2\pi\nu_{\mathrm{exc}}t\right) \\ &+ F_{\mathrm{ts,a}}(\tilde{z}_{\mathrm{ts}}, \dot{\tilde{z}}_{\mathrm{ts}}) \\ &+ F_{\mathrm{el,b}}(\tilde{z}_{\mathrm{ts}}) \cos\left(2\pi\nu_{\mathrm{el}}t\right) \\ &+ F_{\mathrm{el,c}}(\tilde{z}_{\mathrm{ts}}) \cos\left(2\pi(2\nu_{\mathrm{el}})t\right). \end{aligned} \tag{6.31}$$

When F_{ts} is periodically sampled due to the oscillation of the tip-sample distance as defined in (6.30), $F_{\mathrm{ts,a}}$, $F_{\mathrm{el,b}}$ and $F_{\mathrm{el,c}}$ are periodic functions of time with period ν_{exc}^{-1} since they depend on the tip-sample distance. They can be developed in a Fourier series. However, before doing so, we split $F_{\mathrm{ts,a}}$ into an odd and an even part

according to $F_{\mathrm{ts,a}} = F_{\mathrm{even,\,a}} + F_{\mathrm{odd,\,a}}$. Here, the force $F_{\mathrm{even,\,a}}$ is even with respect to the tip-velocity ($F_{\mathrm{even,\,a}}(z_{\mathrm{ts}}, \dot{z}_{\mathrm{ts}}) = F_{\mathrm{even,\,a}}(z_{\mathrm{ts}}, -\dot{z}_{\mathrm{ts}})$), while $F_{\mathrm{odd,\,a}}$ is odd with respect to the tip velocity ($F_{\mathrm{odd,\,a}}(z_{\mathrm{ts}}, \dot{z}_{\mathrm{ts}}) = -F_{\mathrm{odd,\,a}}(z_{\mathrm{ts}}, -\dot{z}_{\mathrm{ts}})$). The Fourier series of $F_{\mathrm{ts,a}}$ can then be written as

$$F_{\mathrm{ts,a}} = F^{(0)}_{\mathrm{even,\,a}} + \sum_{n=1}^{\infty} F^{(n)}_{\mathrm{even,\,a}} \cos\left(2\pi n \nu_{\mathrm{exc}} t + \varphi\right) + F^{(n)}_{\mathrm{odd,\,a}} \sin\left(2\pi n \nu_{\mathrm{exc}} t + \varphi\right). \tag{6.32}$$

The model we use for the electrostatic description of the system results in a purely conservative electrostatic force F_{el}, which does not depend on the tip velocity. Therefore, $F_{\mathrm{el,b}}$ and $F_{\mathrm{el,c}}$ are even with respect to the tip-velocity and, consequently, do only carry the even-force terms in their Fourier series:

$$F_{\mathrm{el,b}} = F^{(0)}_{\mathrm{el,b}} + \sum_{n=1}^{\infty} F^{(n)}_{\mathrm{el,b}} \cos\left(2\pi n \nu_{\mathrm{exc}} t + \varphi\right) \tag{6.33}$$

$$F_{\mathrm{el,c}} = F^{(0)}_{\mathrm{el,c}} + \sum_{n=1}^{\infty} F^{(n)}_{\mathrm{el,c}} \cos\left(2\pi n \nu_{\mathrm{exc}} t + \varphi\right) \tag{6.34}$$

Within the harmonic approximation, this Fourier series is truncated after the term with $n = 1$. The resulting spectral components describing $F_{\mathrm{ts,a}}$, $F_{\mathrm{el,b}}$ and $F_{\mathrm{el,c}}$ can furthermore be written as weighted averages over the tip-sample distance range $[-A + z_{\mathrm{c}}, z_{\mathrm{c}} + A]$ (see [38]), namely

$$F_{\mathrm{ts,a}}(\tilde{z}_{\mathrm{ts}}, \dot{\tilde{z}}_{\mathrm{ts}}) \approx \langle F_{\mathrm{even,\,a}} \rangle_{\cup} + \langle k_{\mathrm{ts,a}} \rangle_{\cap} \cdot (z_{\mathrm{ts}} - z_{\mathrm{c}}) - \langle \gamma_{\mathrm{ts,a}} \rangle_{\cap} \cdot \dot{z}_{\mathrm{ts}}, \tag{6.35}$$

$$F_{\mathrm{el,b}}(\tilde{z}_{\mathrm{ts}}) \approx \langle F_{\mathrm{el,b}} \rangle_{\cup} + \langle k_{\mathrm{el,b}} \rangle_{\cap} \cdot (z_{\mathrm{ts}} - z_{\mathrm{c}}), \tag{6.36}$$

$$F_{\mathrm{el,c}}(\tilde{z}_{\mathrm{ts}}) \approx \langle F_{\mathrm{el,c}} \rangle_{\cup} + \langle k_{\mathrm{el,c}} \rangle_{\cap} \cdot (z_{\mathrm{ts}} - z_{\mathrm{c}}). \tag{6.37}$$

In above equations, we introduced the tip-sample force gradient $k_{\mathrm{ts,a}}$ and the electrostatic force gradients $k_{\mathrm{el,b}}$ and $k_{\mathrm{el,c}}$ as

$$k_{\mathrm{ts,a}} = \frac{\partial F_{\mathrm{even,\,a}}}{\partial z_{\mathrm{ts}}} \tag{6.38}$$

$$k_{\mathrm{el,b}} = \frac{\partial F_{\mathrm{el,b}}}{\partial z_{\mathrm{ts}}} \tag{6.39}$$

$$k_{\mathrm{el,c}} = \frac{\partial F_{\mathrm{el,c}}}{\partial z_{\mathrm{ts}}} \tag{6.40}$$

as well as the tip-sample damping coefficient $\gamma_{\mathrm{ts,a}}$ according to $F_{\mathrm{odd,a}} = -\gamma_{\mathrm{ts,a}} \dot{q}$. The cup ($\cup$) and cap ($\cap$) averages shown in Fig. 6.2 are defined by

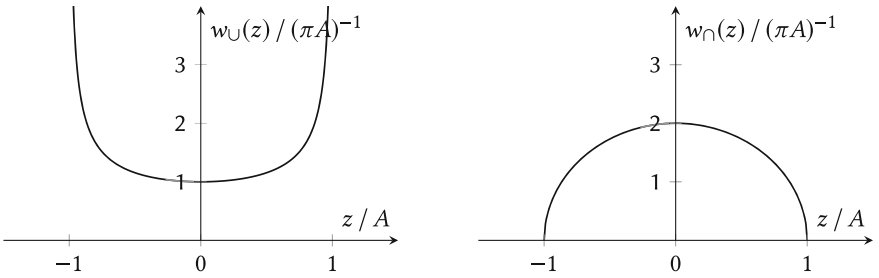

Fig. 6.2 Plots of the cup weight function $w_\cup(z)$ (left) and cap weight function $w_\cap(z)$ (right) as a function of z. Both functions are positive and normalized

$$\langle f\rangle_\cup = \int_{-A}^{A} f(z_\mathrm{c}+z)\,w_\cup(z)\mathrm{d}z, \quad w_\cup(z) = \frac{1}{\pi\sqrt{A^2-z^2}}, \tag{6.41}$$

$$\langle f\rangle_\cap = \int_{-A}^{A} f(z_\mathrm{c}+z)\,w_\cap(z)\mathrm{d}z, \quad w_\cap(z) = \frac{2}{\pi A^2}\sqrt{A^2-z^2} \tag{6.42}$$

and are each a function of the oscillation center position z_c.

Inserting (6.35), (6.36) and (6.37) into (6.31) results in the differential equation of the harmonic oscillator using the harmonic approximation and the modulated electrostatic forces,

$$\begin{aligned} m\ddot{q} \approx &-(k-\langle k_{\mathrm{ts,a}}\rangle_\cap)q \\ &-(\gamma+\langle\gamma_{\mathrm{ts,a}}\rangle_\cap)\dot{q} \\ &+F_0\cos\left(2\pi\nu_\mathrm{exc}t\right) \\ &+\langle F_{\mathrm{even,\,a}}\rangle_\cup \\ &+\langle F_{\mathrm{el,b}}\rangle_\cup\cos\left(2\pi\nu_\mathrm{el}t\right) \\ &+\langle F_{\mathrm{el,c}}\rangle_\cup\cos\left(2\pi(2\nu_\mathrm{el})t\right) \\ &+A/2\,\langle k_{\mathrm{el,b}}\rangle_\cap\cos\left(2\pi(\nu_\mathrm{exc}+\nu_\mathrm{el})t+\varphi\right) \\ &+A/2\,\langle k_{\mathrm{el,b}}\rangle_\cap\cos\left(2\pi(\nu_\mathrm{exc}-\nu_\mathrm{el})t+\varphi\right) \\ &+A/2\,\langle k_{\mathrm{el,c}}\rangle_\cap\cos\left(2\pi(\nu_\mathrm{exc}+2\nu_\mathrm{el})t+\varphi\right) \\ &+A/2\,\langle k_{\mathrm{el,c}}\rangle_\cap\cos\left(2\pi(\nu_\mathrm{exc}-2\nu_\mathrm{el})t+\varphi\right). \end{aligned} \tag{6.43}$$

The harmonic oscillator is now characterized by its effective mass m, effective spring constant $k' = k - \langle k_{\mathrm{ts,a}}\rangle_\cap$, and effective damping constant $\gamma' = \gamma + \langle\gamma_{\mathrm{ts,a}}\rangle_\cap$. For practical reasons, we consider all other contributions as being contributions to the excitation force. In contrast to (6.28), however, the excitation force components only depend on the center position z_c and not on z_ts. This allows us to solve the approximation in (6.43) analytically: The resulting spectrum of the deflection can be directly obtained by applying the Fourier transform to both sides of (6.43). Since the Fourier

transform of the first and second time-derivative is given by

$$\mathcal{F}[\dot{q}] = 2\pi \mathrm{i} \nu \mathcal{F}[q]$$
$$\mathcal{F}[\ddot{q}] = -(2\pi\nu)^2 \mathcal{F}[q],$$

we obtain the following relation between the spectrum of the deflection and the spectrum of the tip-sample and the excitation force

$$\begin{aligned}\mathcal{F}[q] = G'_{\mathrm{ho}}(\nu)\mathcal{F}\big[&+ F_0 \cos\left(2\pi \nu_{\mathrm{exc}} t\right) \\ &+ \langle F_{\mathrm{even,\,a}} \rangle_{\cup} \\ &+ \langle F_{\mathrm{el,b}} \rangle_{\cup} \cos\left(2\pi \nu_{\mathrm{el}} t\right) \\ &+ \langle F_{\mathrm{el,c}} \rangle_{\cup} \cos\left(2\pi (2\nu_{\mathrm{el}}) t\right) \\ &+ A/2\, \langle k_{\mathrm{el,b}} \rangle_{\cap} \cos\left(2\pi (\nu_{\mathrm{exc}} + \nu_{\mathrm{el}}) t + \varphi\right) \\ &+ A/2\, \langle k_{\mathrm{el,b}} \rangle_{\cap} \cos\left(2\pi (\nu_{\mathrm{exc}} - \nu_{\mathrm{el}}) t + \varphi\right) \\ &+ A/2\, \langle k_{\mathrm{el,c}} \rangle_{\cap} \cos\left(2\pi (\nu_{\mathrm{exc}} + 2\nu_{\mathrm{el}}) t + \varphi\right) \\ &+ A/2\, \langle k_{\mathrm{el,b}} \rangle_{\cap} \cos\left(2\pi (\nu_{\mathrm{exc}} - 2\nu_{\mathrm{el}}) t + \varphi\right) \big]. \end{aligned} \tag{6.44}$$

We can therefore conclude that the spectral components of the deflection are connected to the spectral components of the excitation force by the transfer function G'_{ho} defined as

$$G'_{\mathrm{ho}}(\nu) = \frac{1}{k' - (2\pi\nu)^2 m + 2\pi\nu \mathrm{i}\gamma'} = \left|G'_{\mathrm{ho}}(\nu)\right| \exp\left(\mathrm{i}\varphi'_{\mathrm{ho}}(\nu)\right). \tag{6.45}$$

The prime indicates that the transfer function depends on k' and γ', as opposed to k and γ. We can identify the spectral components of the cantilever deflection q by inspection of (6.44). As schematically plotted with respect to a frequency axis in Fig. 6.3a, the spectral components are given by

- a static deflection due to the static force components,
- a first harmonic or "fundamental" mode due to the external excitation at the frequency ν_{exc},
- a first harmonic or "fundamental" and second harmonic mode due to the electrostatic excitation at frequencies ν_{el} and $2\nu_{\mathrm{el}}$, and
- sidebands at $\nu_{\mathrm{exc}} \pm \nu_{\mathrm{el}}$ and $\nu_{\mathrm{exc}} \pm 2\nu_{\mathrm{el}}$.

All spectral components listed above can be measured experimentally although they can be subject to different noise contributions [40–42]. However, depending on the choice on the KPFM mode, the experimentalist only evaluates certain spectral components of the deflection as we will discuss in Sect. 6.4.

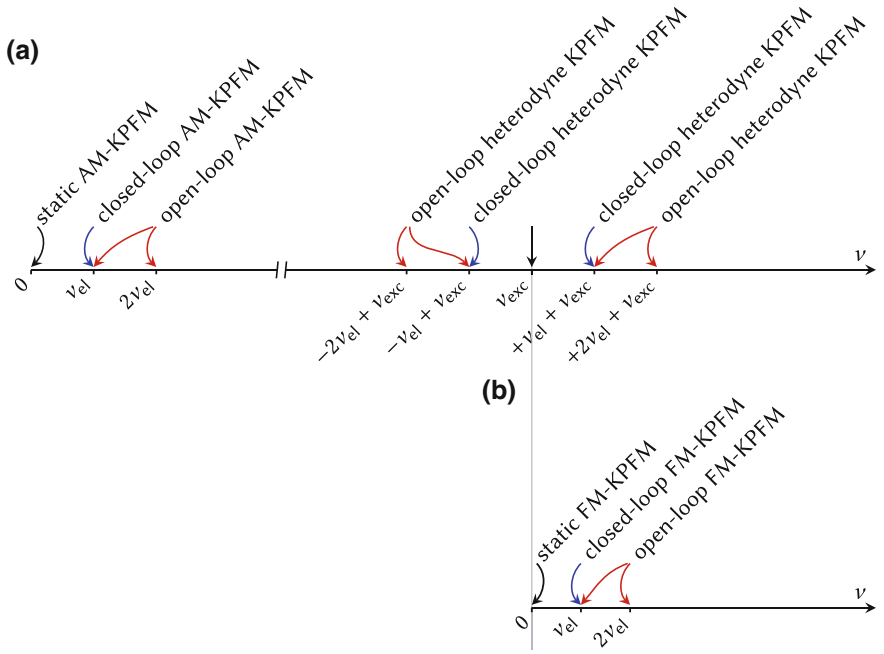

Fig. 6.3 Panel **a** shows the frequencies of all spectral components of the deflection that are described in 6.44. Although ν_{el} is depicted left of ν_{exc}, it is also often chosen as the first overtone of the oscillator at frequencies larger than ν_{exc}. Panel **b** presents the spectral components of the demodulated deflection signal (the demodulation is performed at the frequency ν_{exc}). The spectral components that are measured in the different KPFM modes are indicated by black arrows for the static modes, by blue arrows for the closed-loop methods, and by red arrows for the open-loop methods

6.4 The KPFM Signal

To calculate the KPFM signals obtained in the different KPFM modes, we start the categorization of the modes from the choice of the applied voltage as given by (6.22). First, the experimentalist chooses whether a static bias voltage and/or an sinusoidal voltage is applied (see Table 6.1). We refer to the case of only applying a DC bias voltage for measuring the KPFM signal from the extremal force interaction as *static* KPFM, while the case of only applying a sinusoidal voltage without DC bias is known as the *open-loop* KPFM mode. If the DC bias voltage is additionally regulated by an additional feedback loop and added to the sinusoidal voltage, this third mode is known as *closed-loop* KPFM.

Next, and depending on the above choice of the applied voltage, the experimentalist chooses which spectral components to detect. The schemes are classified using the terms *amplitude-modulation* (AM), *frequency-modulation* (FM) and *heterodyne* detection.

Table 6.1 Summary of the various KPFM implementations categorized via the applied voltage

No KPFM	$V_{\mathrm{bias}} = 0$	$V_{\mathrm{el}} = 0$
Static KPFM	$V_{\mathrm{bias}} \neq 0$	$V_{\mathrm{el}} = 0$
Open-loop KPFM	$V_{\mathrm{bias}} = 0$	$V_{\mathrm{el}} \neq 0$
Closed-loop KPFM	$V_{\mathrm{bias}} \neq 0$	$V_{\mathrm{el}} \neq 0$

6.4.1 *Excursus: Measuring Spectral Components*

Before starting the quantitative evaluation of the KPFM signal in these different modes in Sect. 6.4.2, we discuss the procedure of quantitatively measuring spectral components as we will frequently refer to measuring spectral components of the electrostatic force in the following. The experimentally accessible quantity is in all cases the deflection of the resonator. Measuring the spectral components of this deflection provides the basis for measuring spectral components of the electrostatic force.

In the laboratory, a lock-in amplifier usually performs this task. This device measures the Fourier components of a signal at a fixed frequency and within a given bandwidth. Since the spectrum of a signal is defined in the complex plane, the lock-in amplifier outputs either the real and imaginary part, or the magnitude ("amplitude") and the argument ("phase shift") of the input signal relative to the reference signal. Depending on the excitation frequency, both magnitude and phase shift of the spectral components can be modified according to the transfer function $G'_{\mathrm{ho}}(\nu)$.

To give one example, the inverse Fourier transform of the spectral component of the deflection at frequency ν_{el} is

$$\underbrace{\left|G'_{\mathrm{ho}}(\nu_{\mathrm{el}})\right| \cdot \left|\langle F_{\mathrm{el,b}}\rangle_{\cup}\right|}_{\text{amplitude } A(\nu_{\mathrm{el}})} \cos\left(2\pi\nu_{\mathrm{el}}t + \underbrace{\varphi'_{\mathrm{ho}}(\nu_{\mathrm{el}}) + \pi\Theta(-\langle F_{\mathrm{el,b}}\rangle_{\cup})}_{\text{phase shift } \varphi(\nu_{\mathrm{el}})}\right)$$

with the lock-in amplifier detected amplitude and phase shift marked. The reference signal is defined by ν_{el} in this example. Consequently, the amplitude $A(\nu_{\mathrm{el}})$ is the product of the gain function and the *magnitude* of the first spectral component of the electrostatic tip-sample force. To obtain the *sign* of the spectral component of the electrostatic excitation force, the phase shift $\varphi(\nu_{\mathrm{el}})$ needs to be evaluated additionally. The measured phase shift consists of the phase shift due to the harmonic oscillator ($\varphi'_{\mathrm{ho}}(\nu_{\mathrm{exc}})$) and an additional phase shift of π in case $\langle F_{\mathrm{el,b}}\rangle_{\cup} < 0$. For the above equation, the phase shift of π for negative spectral components of the electrostatic force is written using the Heaviside function Θ.

6.4.2 AM-KPFM

Static AM-KPFM

Only a DC bias voltage is applied in static AM–KPFM [43], therefore $V_{\mathrm{el}} = 0$. All spectral components of the electrostatic force except for the static term vanish in this case as is apparent from (6.44). Consequently, the only spectral components of the deflection that remain are the static deflection and the sinusoidal term at the excitation frequency ν_{exc} (see Fig. 6.3). The observable in static AM-KPFM is the static deflection as a function of the applied bias voltage, which can directly be accessed experimentally.

The contribution to the static deflection that depends on the bias voltage is according to (6.44) proportional to $\langle F_{\mathrm{el,a}} \rangle_{\cup}$. This term $\langle F_{\mathrm{el,a}} \rangle_{\cup}$ depends in turn quadratically on the bias voltage. We find the KPFM signal for static AM-KPFM directly as the bias voltage at the extremum of this term,

$$\begin{aligned} & \frac{\partial \mathcal{F}[q](0)}{\partial V_{\mathrm{bias}}} = 0 \\ \Leftrightarrow \quad & \frac{\partial \langle F_{\mathrm{even,\,a}} \rangle_{\cup}}{\partial V_{\mathrm{bias}}} = 0 \\ \Leftrightarrow \quad & \frac{\partial \langle F_{\mathrm{el,a}} \rangle_{\cup}}{\partial V_{\mathrm{bias}}} = 0 \quad \text{for} \quad V_{\mathrm{bias}} = V_{\mathrm{AM}} \ (\text{and } V_{\mathrm{el}} = 0). \end{aligned} \tag{6.46}$$

We can evaluate this condition using (6.24) and arrive at the AM-KPFM signal V_{AM}

$$V_{\mathrm{AM}} = V_{\mathrm{CPD}} + \sum_{i=1}^{N} q_i \frac{\left\langle \frac{\partial \hat{\Phi}_{\mathrm{void}}(\mathbf{r}_i)}{\partial z_{\mathrm{ts}}} \right\rangle_{\cup}}{\left\langle \frac{\partial C_{\mathrm{void}}}{\partial z_{\mathrm{ts}}} \right\rangle_{\cup}} \tag{6.47}$$

where the electrostatic potential Φ_{void} and the capacitance C_{void} of the charge-free tip-sample system are averaged using the cup averaging function $\langle . \rangle_{\cup}$.

Closed-loop AM-KPFM

The first harmonic signal resulting from the electrostatic excitation (at ν_{el}) is detected in closed-loop AM-KPFM from the deflection signal q of the oscillating cantilever [44, 45]. A feedback loop is used to nullify the amplitude of this spectral component by adjusting the bias voltage V_{bias},

$$\begin{aligned} & \mathcal{F}\left[q\right](\nu_{\mathrm{el}}) = 0 \\ \Leftrightarrow \quad & \langle F_{\mathrm{el,b}} \rangle_{\cup} = 0 \quad \text{for} \quad V_{\mathrm{bias}} = V_{\mathrm{AM}}. \end{aligned} \tag{6.48}$$

According to (6.25), the KPFM signal is

$$V_{\mathrm{AM}} = V_{\mathrm{CPD}} + \sum_{i=1}^{N} q_i \frac{\left\langle \frac{\partial \hat{\Phi}_{\mathrm{void}}(\mathbf{r}_i)}{\partial z_{\mathrm{ts}}} \right\rangle_{\cup}}{\left\langle \frac{\partial C_{\mathrm{void}}}{\partial z_{\mathrm{ts}}} \right\rangle_{\cup}}. \tag{6.49}$$

Thus, static AM-KPFM and closed-loop AM-KPFM give the same KPFM signal.

Open-loop AM-KPFM

Both, the first and the second harmonic signal at ν_{el} and $2\nu_{\mathrm{el}}$ due to the electrostatic excitation at ν_{el} are measured in open-loop AM-KPFM [46]. In a post-processing step, the components $\langle F_{\mathrm{el,b}} \rangle_{\cup}$ and $\langle F_{\mathrm{el,c}} \rangle_{\cup}$ of the electrostatic force are then evaluated from measuring the spectral components at ν_{el} and $2\nu_{\mathrm{el}}$ of the deflection signal as exemplified in Sect. 6.4.1. The open-loop AM-KPFM signal follows finally from

$$V_{\mathrm{AM}} = \frac{V_{\mathrm{el}}}{4} \frac{\langle F_{\mathrm{el,b}} \rangle_{\cup}}{\langle F_{\mathrm{el,c}} \rangle_{\cup}} = V_{\mathrm{CPD}} + \sum_{i=1}^{N} q_i \frac{\left\langle \frac{\partial \hat{\Phi}_{\mathrm{void}}(\mathbf{r}_i)}{\partial z_{\mathrm{ts}}} \right\rangle_{\cup}}{\left\langle \frac{\partial C_{\mathrm{void}}}{\partial z_{\mathrm{ts}}} \right\rangle_{\cup}}. \tag{6.50}$$

From this analysis we conclude that all AM-KPFM modes give the same measured signal despite the detection of different experimental observables.

6.4.3 FM-KPFM

In the AM-KPFM modes discussed before, spectral components are detected directly from the deflection signal. In contrast, the deflection signal is demodulated at frequency ν_{exc} using a demodulator in the FM-KPFM modes and observables are evaluated from this demodulated signal. The demodulator can be thought of effectively shifting all spectral components of the deflection by ν_{exc}, and is commonly implemented using a phase-locked loop in an experimental setup. A demodulation is based on multiplying the deflection q with a reference oscillation of $\cos(2\pi\nu_{\mathrm{exc}}t)$.

Static FM-KPFM

Similar to static AM-KPFM, only a DC bias voltage is applied in static FM-KPFM [4, 47–49], therefore $V_{\mathrm{el}} = 0$. In static FM-KPFM, the static component of the demodulated deflection signal[3] is recorded as function of the applied bias voltage V_{bias}. The KPFM signal corresponds in this case to the applied bias voltage, at which the demodulated signal is extremal

[3] In a FM-AFM experiment, the demodulated deflection signal is typically available as the excitation frequency or the frequency shift relative to a reference frequency.

$$\begin{aligned} & \frac{\partial \mathcal{F}[q\cos\left(2\pi\nu_{\mathrm{exc}}t\right)](0)}{\partial V_{\mathrm{bias}}} = 0 \\ \Leftrightarrow \quad & \frac{\partial \mathcal{F}[q](\nu_{\mathrm{el}})}{\partial V_{\mathrm{bias}}} = 0 \\ \Leftrightarrow \quad & \frac{\partial \langle k_{\mathrm{el,a}}\rangle}{\partial V_{\mathrm{bias}}} = 0 \quad \text{for} \quad V_{\mathrm{bias}} = V_{\mathrm{FM}}. \end{aligned} \tag{6.51}$$

When using (6.25) and (6.39), this condition yields the static mode FM-KPFM signal

$$V_{\mathrm{FM}} = V_{\mathrm{CPD}} + \sum_{i=1}^{N} q_i \frac{\left\langle \frac{\partial^2 \hat{\boldsymbol{\Phi}}_{\mathrm{void}}(\mathbf{r}_i)}{\partial z_{\mathrm{ts}}^2} \right\rangle_{\cap}}{\left\langle \frac{\partial^2 C_{\mathrm{void}}}{\partial z_{\mathrm{ts}}^2} \right\rangle_{\cap}}. \tag{6.52}$$

In contrast to the AM-KPFM modes, the second derivative of the electrostatic potential $\boldsymbol{\Phi}_{\mathrm{void}}$ and of the capacitance C_{void} of the charge-free tip-sample system is calculated here for FM-KPFM.

Closed-loop FM-KPFM

The first harmonic signal resulting from the electrostatic excitation at ν_{el} is detected from the demodulated deflection signal in closed-loop FM-KPFM and this signal is nullified by adjusting the bias voltage V_{bias} [21, 50]. This is experimentally achieved by using a feedback loop regulating V_{bias} to nullify the magnitude of this spectral component. In this case, the KPFM signal equals the adjusted bias voltage V_{bias} at which the magnitude of the spectral component is zero,

$$\begin{aligned} & \mathcal{F}\left[q\cos\left(2\pi\nu_{\mathrm{exc}}t\right)\right](\nu_{\mathrm{el}}) = 0 \\ & \Leftrightarrow \mathcal{F}\left[q\right](\nu_{\mathrm{exc}} \pm \nu_{\mathrm{el}}) = 0 \qquad (6.53) \\ & \Leftrightarrow \quad \langle k_{\mathrm{el,b}}\rangle_{\cap} = 0 \quad \text{for} \quad V_{\mathrm{bias}} = V_{\mathrm{FM}}. \qquad (6.54) \end{aligned}$$

According to (6.25), the KPFM signal is

$$V_{\mathrm{FM}} = V_{\mathrm{CPD}} + \sum_{i=1}^{N} q_i \frac{\left\langle \frac{\partial^2 \hat{\boldsymbol{\Phi}}_{\mathrm{void}}(\mathbf{r}_i)}{\partial z_{\mathrm{ts}}^2} \right\rangle_{\cap}}{\left\langle \frac{\partial^2 C_{\mathrm{void}}}{\partial z_{\mathrm{ts}}^2} \right\rangle_{\cap}}. \tag{6.55}$$

Open-loop FM-KPFM

The first and the second harmonic at ν_{el} and $2\nu_{\mathrm{el}}$, respectively, are both extracted from the demodulated deflection signal in open-loop FM-KPFM [51]. Similar to the open-loop AM-KPFM mode, the corresponding components of the electrostatic

interaction, here the force gradients $\langle k_{\mathrm{el,b}} \rangle_{\cap}$ and $\langle k_{\mathrm{el,c}} \rangle_{\cap}$ (see (6.44)), are calculated from the two spectral components in the demodulated signal using the transfer function of the demodulator, see also Sect. 6.4.1. The open-loop FM-KPFM signal follows from

$$V_{\mathrm{FM}} = \frac{V_{\mathrm{el}}}{4} \frac{\langle k_{\mathrm{el,b}} \rangle_{\cap}}{\langle k_{\mathrm{el,c}} \rangle_{\cap}} = V_{\mathrm{CPD}} + \sum_{i=1}^{N} q_i \frac{\left\langle \frac{\partial^2 \hat{\Phi}_{\mathrm{void}}(\mathbf{r}_i)}{\partial z_{\mathrm{ts}}^2} \right\rangle_{\cap}}{\left\langle \frac{\partial^2 C_{\mathrm{void}}}{\partial z_{\mathrm{ts}}^2} \right\rangle_{\cap}}. \tag{6.56}$$

Thus, the KPFM signals obtained in static FM-KPFM, open-loop FM-KPFM and closed-loop FM-KPFM are identical, but different to the AM-KPFM signal.

Heterodyne KPFM

The spectral components at the sidebands $\nu_{\mathrm{exc}} \pm \nu_{\mathrm{el}}$ and $\nu_{\mathrm{exc}} \pm 2\nu_{\mathrm{el}}$ are directly measured from the deflection signal in heterodyne KPFM [52]. Furthermore, also this detection scheme allows the implementation of a closed-loop and an open-loop method.

In closed-loop heterodyne KPFM, the spectral components at $\nu_{\mathrm{exc}} \pm \nu_{\mathrm{el}}$ are measured and nullified by adjusting V_{bias} with a feedback loop. This is described by (6.53). Therefore, closed-loop heterodyne KPFM gives the same signal as FM-KPFM.

In the open-loop variant of heterodyne KPFM, spectral components of the deflection at $\nu_{\mathrm{exc}} \pm \nu_{\mathrm{el}}$ and $\nu_{\mathrm{exc}} \pm 2\nu_{\mathrm{el}}$ are measured. Similar to the other open-loop methods, the components of the corresponding electrostatic tip-sample interaction are calculated in a post-processing step. The two components that can be obtained in the open-loop heterodyne mode are $\langle k_{\mathrm{el,b}} \rangle_{\cap}$ and $\langle k_{\mathrm{el,c}} \rangle_{\cap}$, and with the definition for V_{FM} in (6.56), the signal is identical to the open-loop FM-KPFM mode.

Consequently, heterodyne open-loop KPFM allows to obtain the same KPFM signal as heterodyne closed-loop KPFM and both signals are identical to the open- and closed-loop FM-KPFM modes.

6.4.4 Summary of the KPFM Modes

The detection schemes that have been discussed in the this chapter are summarized in Table 6.2 by listing the components of the deflection signal which are evaluated in each respective mode. Despite the formal difference of all terms, we derived before that all AM-KPFM modes result in the same KPFM signal V_{AM}, and all FM-KPFM modes give the same KPFM signal V_{FM}.

Table 6.2 Summary of the spectral components of the deflection q or the demodulated deflection $q\cos\left(2\pi\nu_{\mathrm{exc}}t\right)$ relevant in the KPFM modes discussed in this chapter (see also Fig. 6.3). The entries in the right column show either the condition for which the KPFM signal equal to V_{bias} is calculated, or the experimentally obtained quantity that is directly the KPFM signal

Static AM-KPFM	$\dfrac{\partial\mathcal{F}[q](0)}{\partial V_{\mathrm{bias}}}=0$
Static FM-KPFM	$\dfrac{\partial\mathcal{F}[q\cos\left(2\pi\nu_{\mathrm{exc}}t\right)](0)}{\partial V_{\mathrm{bias}}}=0$
Open-loop AM-KPFM	$(V_{\mathrm{el}}/4)\cdot\dfrac{\mathcal{F}[q](\nu_{\mathrm{el}})}{\mathcal{F}[q](2\nu_{\mathrm{el}})}$
Open-loop FM-KPFM	$(V_{\mathrm{el}}/4)\cdot\dfrac{\mathcal{F}[q\cos\left(2\pi\nu_{\mathrm{exc}}t\right)](\nu_{\mathrm{el}})}{\mathcal{F}[q\cos\left(2\pi\nu_{\mathrm{exc}}t\right)](2\nu_{\mathrm{el}})}$
Closed-loop AM-KPFM	$\mathcal{F}[q](\nu_{\mathrm{el}})=0$
Closed-loop FM-KPFM	$\mathcal{F}[q\cos\left(2\pi\nu_{\mathrm{exc}}t\right)](\nu_{\mathrm{el}})=0$

6.5 The Weight Function for Charges

The KPFM signal for all six KPFM modes discussed before can be written as

$$\boxed{V_{\mathrm{KPFM}}=V_{\mathrm{CPD}}+\sum_{i=1}^{N}q_i W_{\mathrm{KPFM}}(\mathbf{r}_i).} \tag{6.57}$$

This formula allows us to introduce the *KPFM weight function for charges* W_{KPFM}, which weights the contribution of each charge q_i at its position $\mathbf{r}_i$. The resulting KPFM signal is then given as the sum over all weighted charges with an additional offset given by the contact potential difference between the tip and sample side metals.

For the AM-KPFM modes, the weight function for charges is defined by the ratio of the cup-averaged first z_{ts}-derivative of $\hat{\boldsymbol{\Phi}}_{\mathrm{void}}$ and C_{void}

$$W_{\mathrm{AM}}(\mathbf{r})=\frac{\left\langle\frac{\partial\hat{\boldsymbol{\Phi}}_{\mathrm{void}}(\mathbf{r})}{\partial z_{\mathrm{ts}}}\right\rangle_{\cup}}{\left\langle\frac{\partial C_{\mathrm{void}}}{\partial z_{\mathrm{ts}}}\right\rangle_{\cup}}. \tag{6.58}$$

For the FM-KPFM modes, the weight function for charges is given by the ratio of the cap-averaged second z_{ts}-derivative of $\hat{\boldsymbol{\Phi}}_{\mathrm{void}}$ and C_{void}

$$W_{\mathrm{FM}}(\mathbf{r})=\frac{\left\langle\frac{\partial^2\hat{\boldsymbol{\Phi}}_{\mathrm{void}}(\mathbf{r})}{\partial z_{\mathrm{ts}}^2}\right\rangle_{\cap}}{\left\langle\frac{\partial^2 C_{\mathrm{void}}}{\partial z_{\mathrm{ts}}^2}\right\rangle_{\cap}}. \tag{6.59}$$

The cup $\langle . \rangle_{\cup}$ and cap $\langle . \rangle_{\cap}$ averages are each performed over the tip-sample distance interval that is probed by the oscillating tip, i.e. $z_{\mathrm{ts}} \in [-A + z_{\mathrm{c}}, z_{\mathrm{c}} + A]$. The weight of each charge therefore depends on the tip position range characterized by, e.g., the lower turning-point $z_{\mathrm{c}} - A$ of the oscillation and the oscillation amplitude A.

Moreover, the weight function only depends on two electrostatic quantities of the *void* (i.e. charge free) tip-sample system, namely the electrostatic potential $\boldsymbol{\Phi}_{\mathrm{void}}$ and the capacitance C_{void}. While the image charge interaction contributes to the total electrostatic force at any bias, it does not appear in the weight function and, therefore, does not contribute to the KPFM signal. The weight function is consequently a property of the charge-free tip sample system. This important conclusion simplifies the interpretation of KPFM data, and especially allows to calculate the KPFM signal for charge distributions in a straightforward manner.

6.6 Conclusions and Outlook

This chapter introduced the KPFM weight function for charges, which is identified to be the central quantity for the calculation and interpretation of KPFM data for physical systems that include charge distributions. Based on an electrostatic model describing a general tip-sample system with tip and sample formed by two metals, a charge distribution, and, optionally, dielectric material in the tip-sample gap, we derived the KPFM signal for all experimentally implemented KPFM modes. In all these KPFM modes, namely static, open-loop, and closed loop variants for the AM, FM, or heterodyne detection, the KPFM signal is given from a weighted sum over all charges in the tip-sample system.

The weight function for charges depends on the electrostatic properties of the charge-free tip-sample system, such as the sample geometry and composition, the tip geometry, the displacement between tip and sample, and the medium surrounding tip and sample. The weight function for charges, and thus the resulting KPFM signal, depends furthermore on the oscillation amplitude of the tip.

The next chapter will give a detailed account on several properties of this weight function, and will investigate the dependency on different parameters such as the tip-sample geometry or the oscillation amplitude.

Acknowledgements The authors are much obliged to Lev Kantorovich (King's College London), Ralf Bechstein and Angelika Kühnle (both from University of Mainz) for fruitful discussions. P.R. gratefully acknowledges financial support by the German Research Foundation (DFG) via grant RA2832/1-1. H.S. is a recipient of a DFG-funded position through the Excellence Initiative (DFG/GSC 266).

References

1. S.A. Burke, J.M. LeDue, Y. Miyahara, J.M. Topple, S. Fostner, P. Grütter, Nanotechnology **20**(26), 264012 (2009). https://doi.org/10.1088/0957-4484/20/26/264012
2. M. Kittelmann, P. Rahe, A. Gourdon, A. Kühnle, ACS Nano **6**(8), 7406 (2012). https://doi.org/10.1021/nn3025942
3. C. Barth, A.S. Foster, C.R. Henry, A.L. Shluger, Adv. Mater. **23**(4), 477 (2011). https://doi.org/10.1002/adma.201002270
4. L. Gross, F. Mohn, P. Liljeroth, J. Repp, F.J. Giessibl, G. Meyer, Science **324**(5933), 1428 (2009). https://doi.org/10.1126/science.1172273
5. C. Barth, C.R. Henry, Appl. Phys. Lett. **89**(25), 252119 (2006). https://doi.org/10.1063/1.2410223
6. B. Hoff, M. Gingras, R. Peresutti, C.R. Henry, A.S. Foster, C. Barth, J. Phys. Chem. C **118**(26), 14569 (2014). https://doi.org/10.1021/jp501738c
7. A. Hinaut, A. Pujol, F. Chaumeton, D. Martrou, A. Gourdon, S. Gauthier, Beilstein J. Nanotechnol. **3**, 221 (2012). https://doi.org/10.3762/bjnano.3.25
8. J.L. Neff, P. Milde, C. Pérez León, M.D. Kundrat, L.M. Eng, C.R. Jacob, R. Hoffmann-Vogel, ACS Nano **8**(4), 3294 (2014). https://doi.org/10.1021/nn404257v
9. C. Barth, C.R. Henry, J. Phys. Chem. C **113**(1), 247 (2009). https://doi.org/10.1021/Jp807340k
10. B. Hoff, C.R. Henry, C. Barth, Nanoscale **8**, 411 (2015). https://doi.org/10.1039/C5NR04541J
11. W. Steurer, J. Repp, L. Gross, I. Scivetti, M. Persson, G. Meyer, Phys. Rev. Lett. **114**(3), 036801 (2015). https://doi.org/10.1103/PhysRevLett.114.036801
12. W. Steurer, S. Fatayer, L. Gross, G. Meyer, Nat. Commun. **6**, 8353 (2015). https://doi.org/10.1038/ncomms9353
13. P. Rahe, R.P. Steele, C.C. Williams, Nano Lett. **16**, 911 (2016). https://doi.org/10.1021/acs.nanolett.5b03725
14. F. Bocquet, L. Nony, C. Loppacher, T. Glatzel, Phys. Rev. B **78**(3), 035410 (2008). https://doi.org/10.1103/PhysRevB.78.035410
15. L. Nony, A.S. Foster, F. Bocquet, C. Loppacher, Phys. Rev. Lett. **103**(3), 036802 (2009). https://doi.org/10.1103/PhysRevLett.103.036802
16. L. Nony, F. Bocquet, C. Loppacher, T. Glatzel, Nanotechnology **20**(26), 264014 (2009). https://doi.org/10.1088/0957-4484/20/26/264014
17. G.H. Enevoldsen, T. Glatzel, M.C. Christensen, J.V. Lauritsen, F. Besenbacher, Phys. Rev. Lett. **100**(23), 236104 (2008). https://doi.org/10.1103/PhysRevLett.100.236104
18. A. Liscio, V. Palermo, D. Gentilini, F. Nolde, K. Müllen, P. Samorì, Adv. Funct. Mater. **16**(11), 1407 (2006). https://doi.org/10.1002/adfm.200600145
19. C. Pérez León, H. Drees, S.M. Wippermann, M. Marz, R. Hoffmann-Vogel, J. Phys. Chem. Lett. **7**(3), 426 (2016). https://doi.org/10.1021/acs.jpclett.5b02650
20. B. Schuler, S.X. Liu, Y. Geng, S. Decurtins, G. Meyer, L. Gross, Nano Lett. **14**(6), 3342 (2014). https://doi.org/10.1021/nl500805x
21. W. Melitz, J. Shen, A.C. Kummel, S. Lee, Surf. Sci. Rep. **66**(1), 1 (2011). https://doi.org/10.1016/j.surfrep.2010.001
22. T. Glatzel, S. Sadewasser, M.C. Lux-Steiner, Appl. Surf. Sci. **210**(1–2), 84 (2003). https://doi.org/10.1016/S0169-4332(02)01484-8
23. P. Rahe, M. Kittelmann, J.L. Neff, M. Nimmrich, M. Reichling, P. Maass, A. Kühnle, Adv. Mater. **25**(29), 3948 (2013). https://doi.org/10.1002/adma.201300604
24. L. Bartels, Nat. Chem. **2**(2), 87 (2010). https://doi.org/10.1038/nchem.517
25. J.L. Neff, P. Rahe, Phys. Rev. B **91**(8), 085424 (2015). https://doi.org/10.1103/PhysRevB.91.085424
26. H. Söngen, P. Rahe, J.L. Neff, R. Bechstein, J. Ritala, A.S. Foster, A. Kühnle, J. Appl. Phys. **119**(2), 025304 (2016). https://doi.org/10.1063/1.4939619
27. C. Barth, T. Hynninen, M. Bieletzki, C.R. Henry, A.S. Foster, F. Esch, U. Heiz, New J. Phys. **12**, 093024 (2010). https://doi.org/10.1088/1367-2630/12/9/093024

28. T. Hynninen, A.S. Foster, C. Barth. e-J. Surf. Sci. Nanotechnol. **9**, 6 (2011). https://doi.org/10.1380/ejssnt.2011.6
29. A. Sadeghi, A. Baratoff, S.A. Ghasemi, S. Goedecker, T. Glatzel, S. Kawai, E. Meyer, Phys. Rev. B **86**(7), 075407 (2012). https://doi.org/10.1103/PhysRevB.86.075407
30. L.N. Kantorovich, A.I. Livshits, M. Stoneham, J. Phys. Condens. Matter **12**(6), 795 (2000). https://doi.org/10.1088/0953-8984/12/6/304
31. G. Elias, T. Glatzel, E. Meyer, A. Schwarzman, A. Boag, Y. Rosenwaks, Beilstein J. Nanotechnol. **2**, 252 (2011). https://doi.org/10.3762/bjnano.2.29
32. H.O. Jacobs, A. Stemmer, Surf. Interface Anal. **27**(5–6), 361 (1999). https://doi.org/10.1002/(SICI)1096-9918(199905/06)27:5/6<361::AID-SIA482>3.0.CO;2-8
33. J. Jackson, *Klassische Elektrodynamik, 3. Ausgabe.* De Gruyter Studium, (De Gruyter, 2002)
34. L. Landau, E. Lifschitz, *Elektrodynamik der Kontinua*. Lehrbuch der theoretischen Physik (Akademie-Verlag, 1990)
35. J.M.R. Weaver, D.W. Abraham, J. Vac. Sci. Technol. B: Microelectron. Nanometer Struct. **9**(3), 1559 (1991). https://doi.org/10.1116/1.585423
36. S. Hudlet, M.S. Jean, C. Guthmann, J. Berger, Eur. Phys. J. B: Condens. Matter Phys. **2**(1), 5 (1998). https://doi.org/10.1007/s100510050219
37. A. Sadeghi, A. Baratoff, S. Goedecker, Phys. Rev. B **88**(3), 035436 (2013). https://doi.org/10.1103/PhysRevB.88.035436
38. H. Söngen, R. Bechstein, A. Kühnle, J. Phys.: Condens. Matter **29**(27), 274001 (2017). https://doi.org/10.1088/1361-648X/aa6f8b
39. M. Guggisberg, M. Bammerlin, C. Loppacher, O. Pfeiffer, A. Abdurixit, V. Barwich, R. Bennewitz, A. Baratoff, E. Meyer, H.J. Güntherodt, Phys. Rev. B **61**(16), 11151 (2000). https://doi.org/10.1103/PhysRevB.61.11151
40. J. Polesel-Maris, M.A. Venegas de la Cerda, D. Martrou, S. Gauthier, Phys. Rev. B **79**(23), 235401 (2009). https://doi.org/10.1103/PhysRevB.79.235401
41. J. Lübbe, M. Temmen, P. Rahe, M. Reichling, Beilstein J. Nanotechnol. **7**, 1885 (2016). https://doi.org/10.3762/bjnano.7.181
42. H. Diesinger, D. Deresmes, T. Mélin, Beilstein J. Nanotechnol. **5**, 1 (2014). https://doi.org/10.3762/bjnano.5.1
43. M. Shimizu, H. Watanabe, K. Anazawa, T. Miyahara, C. Manabe, J. Chem. Phys. **110**(24), 12116 (1999). https://doi.org/10.1063/1.479147
44. M. Nonnenmacher, M.P. O'Boyle, H.K. Wickramasinghe, Appl. Phys. Lett. **58**(25), 2921 (1991). https://doi.org/10.1063/1.105227
45. U. Zerweck, C. Loppacher, T. Otto, S. Grafström, L.M. Eng, Phys. Rev. B **71**(12), 125424 (2005). https://doi.org/10.1103/PhysRevB.71.125424
46. L. Collins, J.I. Kilpatrick, S.A.L. Weber, A. Tselev, I.V. Vlassiouk, I.N. Ivanov, S. Jesse, S.V. Kalinin, B.J. Rodriguez, Nanotechnology **24**(47), 475702 (2013). https://doi.org/10.1088/0957-4484/24/47/475702
47. F. Mohn, L. Gross, N. Moll, G. Meyer, Nat. Nanotechnol. **7**, 227 (2012). https://doi.org/10.1038/nnano.2012.20
48. S. Kitamura, K. Suzuki, M. Iwatsuki, Appl. Surf. Sci. **140**, 265 (1999). https://doi.org/10.1016/S0169-4332(98)00538-8
49. F. Albrecht, J. Repp, M. Fleischmann, M. Scheer, M. Ondráček, P. Jelínek, Phys. Rev. Lett. **115**(7), 076101 (2015). https://doi.org/10.1103/PhysRevLett.115.076101
50. S. Kitamura, M. Iwatsuki, Applied Phys. Lett. **72**(24), 3154 (1998). https://doi.org/10.1063/1.121577
51. O. Takeuchi, Y. Ohrai, S. Yoshida, H. Shigekawa, Jpn. J. Appl. Phys. **46**(8S), 5626 (2007). https://doi.org/10.1143/JJAP.46.5626
52. Y. Sugawara, L. Kou, Z. Ma, T. Kamijo, Y. Naitoh, Y.J. Li, Appl. Phys. Lett. **100**(22), 223104 (2012). https://doi.org/10.1063/1.4723697

Chapter 7
Interpretation of KPFM Data with the Weight Function for Charges

Hagen Söngen, Philipp Rahe, Ralf Bechstein and Angelika Kühnle

Abstract The KPFM signal for systems containing local charges can be expressed as a weighted sum over all local charges. The *weight function for charges* quantifies the contribution of each charge, depending on its position. In this chapter, we evaluate the KPFM weight function for charges by analyzing several application-relevant model systems. The intention of this chapter is to provide insights into the KPFM contrast formation in order to facilitate the KPFM data interpretation. For this, we concentrate on three model systems: (A) a conductive sample in ultra-high vacuum, (B) a dielectric sample in ultra-high vacuum, and (C) a dielectric sample in water. We calculate the weight function for charges for each of these systems using a conductive sphere as a tip model. While the analysis substantiates a number of known experimental observations, it reveals surprising effects in some environments. For example, the sign of the FM-KPFM signal reflects the sign of the charges measured in the systems A and B, but in system C the sign of the KPFM signal is found to be tip-sample distance dependent. Additionally, we deduce the lateral KPFM resolution limits and

H. Söngen (✉) · R. Bechstein · A. Kühnle
Institut für Physikalische Chemie, Johannes Gutenberg-Universität Mainz,
Duesbergweg 10-14, Mainz, Germany
e-mail: soengen@uni-mainz.de; hagen.soengen@uni-bielefeld.de

R. Bechstein
e-mail: bechstein@uni-mainz.de

A. Kühnle
e-mail: kuehnle@uni-mainz.de; angelika.kuehnle@uni-bielefeld.de

H. Söngen
Graduate School Materials Science in Mainz, Staudinger Weg 9, 55128
Mainz, Germany

Present Address:
H. Söngen · A. Kühnle
Physical Chemistry I, Bielefeld University, Universitätsstraße 25, 33615
Bielefeld, Germany

P. Rahe
Fachbereich Physik, Universität Osnabrück, Barbarastrasse 7,
49076 Osnabrück, Germany
e-mail: prahe@uni-osnabrueck.de

S. Sadewasser and T. Glatzel (eds.), *Kelvin Probe Force Microscopy*,
Springer Series in Surface Sciences 65, https://doi.org/10.1007/978-3-319-75687-5_7

finally discuss the lateral decay of the weight function to assess how charges contribute to the signal. Our discussion is accompanied by an interactive visualization available at www.pc1.uni-bielefeld.de/kpfm.

7.1 Introduction

Atomic force microscopy (AFM) has most successfully been joined with the Kelvin probe technique to specifically probe voltage-dependent contributions to the tip-sample interaction force [1, 2]. This Kelvin probe force microscopy (KPFM) has extensively been used to investigate a large variety of different tip-sample systems, including conductive [3], semi-conductive [4] and dielectric [5, 6] materials in air [7], ultra-high vacuum [8, 9] and in liquid [10, 11] environments.

Recently, the KPFM signal has been derived for a most general system that consists of a conductive tip, a conductive sample or a dielectric sample with a metallic back contact, and N point charges q_i located at positions $\mathbf{r}_\mathrm{i}$ [12, 13]. This model also has been introduced in the preceding chapter within this book. Both major KPFM modes, namely the amplitude modulation (AM) and the frequency modulation (FM) mode [14] have been considered in their most prominent technical implementations, which are the static, closed-loop and open-loop methods. It was found that for all cases, the KPFM signal V_KPFM can be written as

$$V_\mathrm{KPFM} = V_\mathrm{CPD} + \sum_{i=1}^{N} q_i W_\mathrm{KPFM}(\mathbf{r}_i) \tag{7.1}$$

where the KPFM signal contains the contact potential difference V_CPD between the homogeneous tip and conductive sample (or the conductive sample back contact in case of insulating samples) and, most importantly, a weighted sum over all charges q_i located within the tip-sample system. Each charge in the sum is multiplied by a weight function W_KPFM that is evaluated at the position $\mathbf{r}_i$ of each charge. The weight function is fully defined by the properties of the charge-free tip-sample system, the oscillation amplitude of the tip and the KPFM mode.

In this chapter, we closely inspect (7.1) with the motivation to facilitate the interpretation of experimental KPFM data. In particular, we answer the following questions:

- How does the sign of the KPFM signal reflect the sign of the charges beneath the tip?
- How does the oscillation amplitude of the tip influence the KPFM signal?
- What is the lateral resolution for resolving charges with KPFM?
- What is the KPFM signal generated by electric dipoles?
- How large is the contribution of surface charges distributed across the whole sample to the KPFM signal?

For this, we first review the weight function for charges in Sect. 7.2 and also introduce the tip sample systems considered throughout this chapter. In Sect. 7.3 we discuss properties of the weight function for charges W_{KPFM}, in particular its sign. Next, in Sect. 7.4 we discuss both qualitative and quantitative aspects of the KPFM signal by using the weight function for charges. For the purpose of this discussion, we calculate the KPFM signal V_{KPFM} for simple charge distributions such as single point charges, dipoles and a layer of surface charges.

Most of the calculations we present in the following sections can also be explored with our interactive *KPFM visualization*. The KPFM visualization runs within the browser and is accessible at:

www.pc1.uni-bielefeld.de/kpfm

The visualization is also available from the authors, should the link be unaccessible.

7.2 The Weight Function for Charges

Depending on using AM or FM-KPFM, there are different expressions for the weight function for charges. Two different terms for the AM- and FM-KPFM weight functions have been derived in [12, 13] as is presented in the preceding chapter. The AM-KPFM weight function is given by

$$W_{\mathrm{AM}}(\mathbf{r}) = \frac{\left\langle \frac{\partial \hat{\Phi}_{\mathrm{void}}}{\partial z_{\mathrm{ts}}}(\mathbf{r}) \right\rangle_{\cup}}{\left\langle \frac{\partial C_{\mathrm{void}}}{\partial z_{\mathrm{ts}}} \right\rangle_{\cup}}, \tag{7.2}$$

and the FM-KPFM weight function is written as

$$W_{\mathrm{FM}}(\mathbf{r}) = \frac{\left\langle \frac{\partial^2 \hat{\Phi}_{\mathrm{void}}}{\partial z_{\mathrm{ts}}^2}(\mathbf{r}) \right\rangle_{\cap}}{\left\langle \frac{\partial^2 C_{\mathrm{void}}}{\partial z_{\mathrm{ts}}^2} \right\rangle_{\cap}}. \tag{7.3}$$

Both KPFM weight functions are determined by two electrostatic quantities: the normalized electric potential[1] $\hat{\Phi}_{\mathrm{void}}$ and the capacitance C_{void}, both calculated for the *void*, i.e., the charge-free tip-sample system. There are two distinct differences between the AM- and FM-KPFM weight function: First, depending on considering the AM- or the FM-mode, either the first or second derivative of $\hat{\Phi}_{\mathrm{void}}$ and C_{void} with respect to the tip-sample distance z_{ts} appears in the respective weight function. Second, different averages are calculated for the two KPFM modes. The two

[1]The quantity $\hat{\Phi}_{\mathrm{void}}$ is the electric potential normalized with respect to the voltage V between the conductive tip and sample (or sample back contact in case of dielectric samples), i.e., $\hat{\Phi}_{\mathrm{void}} = \Phi_{\mathrm{void}}/V$.

derivatives are averaged over the tip-sample distance range $[z_c - A,\ z_c + A]$ covered during the tip oscillation with amplitude A around the center position z_c. We introduce the cup average $\langle . \rangle_\cup$ and the cap average $\langle . \rangle_\cap$ for AM-KPFM and FM-KPFM, respectively [15]. The averaging functions are both positive and normalized (see also the previous chapter) and they are defined as

$$\langle f \rangle_\cup = \int_{-A}^{A} \mathrm{d}z f(z_c + z)\, w_\cup(z), \quad w_\cup(z) = \frac{1}{\pi\sqrt{A^2 - z^2}}, \tag{7.4}$$

$$\langle f \rangle_\cap = \int_{-A}^{A} \mathrm{d}z f(z_c + z)\, w_\cap(z), \quad w_\cap(z) = \frac{2}{\pi A^2}\sqrt{A^2 - z^2}. \tag{7.5}$$

The weight function W_{KPFM} for charges is evaluated at the position $\mathbf{r}_i$ of each charge to calculate the KPFM signal V_{KPFM} (7.1). The weight function depends on properties of the void tip-sample system, including the geometry of both tip and sample, as well as their relative displacement. Moreover, the weight function for charges depends on the electrostatic properties, such as the dielectric permittivity of the medium surrounding the tip. Since the weight function contains quantities that are averaged over the tip-sample distance oscillation range, the weight function additionally depends on the oscillation amplitude of the tip.

7.2.1 The Void Tip-Sample System

The quantitative evaluation of (7.1) requires to pick a suitable model for the geometry of the void tip-sample system. Within this chapter we use a simple, yet realistic, model consisting of a conductive sphere as a tip. The reader is free to pick a different model appropriate for their application (see Appendix A for an overview over available models). We are confident that the qualitative statements of this chapter regarding the properties of the weight function are correct irrespective of the choice of the model.

In the model we use here, the tip is placed above either a conductive or a dielectric sample filling the semi-infinite half-space at $z < 0$ below the surface located at $z = 0$. We denote the relative dielectric permittivity of the medium surrounding the tip as ε_m. In case of a dielectric sample, we denote the relative dielectric permittivity of the sample as ε_s. According to the electrostatic model we use, a conductive sample is obtained in the limiting case $\varepsilon_\mathrm{s} \to \infty$ (corresponding to setting the factor $\beta = (\varepsilon_\mathrm{s} - \varepsilon_\mathrm{m})/(\varepsilon_\mathrm{s} + \varepsilon_\mathrm{m})$ to 1, see Appendix A.3). Unless otherwise stated, the tip radius is in the following set to $R = 20\,\mathrm{nm}$. The tip-sample distance is denoted as z_ts (see Fig. 7.1a). More details on the calculation can be found in Appendix A.3.

Similar to our previous analysis of the weight function [13], we discuss here three different tip-sample systems as drawn in Fig. 7.1. First, we consider as "system A" a conductive substrate ($\beta = 1$) in ultra-high vacuum ($\varepsilon_\mathrm{m} = 1$). Second, we consider a thick dielectric sample in vacuum as "system B", where we set the permittivity of

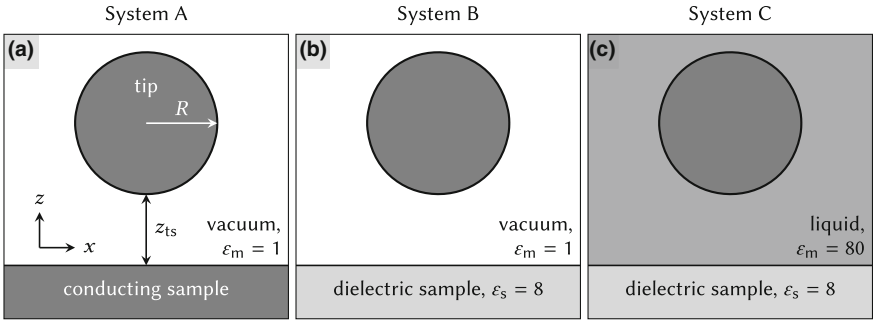

Fig. 7.1 Three *void* tip-sample systems we consider for calculating the KPFM weight functions. A conducting sample ($\beta = 1$) is present in system A. While the samples in system B and system C are given by dielectric material with $\varepsilon_s = 8$, the dielectric constant of the medium where the tip is located differs. System B represents the ultra-high vacuum environment where the tip is located in a vacuum ($\varepsilon_m = 1$), while system C is aligned with measurements in liquid environment using $\varepsilon_m = 80$

the sample to $\varepsilon_s = 8$ to exemplary resemble the bulk insulating material calcite [16]. Third, while we consider for "system C" again a dielectric sample with $\varepsilon_s = 8$, we set the permittivity of the medium to a value larger than the permittivity of the sample. Specifically, we choose $\varepsilon_m = 80$ to represent water [17]. In all considered cases, we set $V_{CPD} = 0$, i.e., we only consider the KPFM signal arising from charges in the tip-sample system. We thereby ignore any offset as a result of the contact potential difference between the two metallic electrodes. Note that within the electrostatic model we employ here, V_{CPD} is only a property of the metallic electrodes and does not depend on their geometry, the tip displacement and the oscillation amplitude.

7.3 Properties of the Weight Function for Charges

Using the electrostatic model introduced in the last section, we can evaluate the weight function for charges as is shown in Fig. 7.2.

The value of the weight function in the area below the tip (tip sphere is indicated by a white disk) is of primary interest as charges are typically located in the tip-sample gap and in close proximity to the sample surface. It is a common assumption that there is a simple relationship between the sign of the KPFM signal and the sign of the charges in the tip-sample gap [8, 18–20]. However, the sign assignment not only depends on whether tip or sample are biased, but, importantly, on the weight function for charges. As we will discuss in the following, simple relations between the sign of the KPFM signal and the sign of the charges can only be provided for specific tip-sample systems. For systems A and B in both the AM and FM-KPFM mode, we find indeed that the sign of the weight function below the tip is positive, thus the sign of the charges q_i in (7.1) is maintained in the KPFM signal V_{KPFM}.

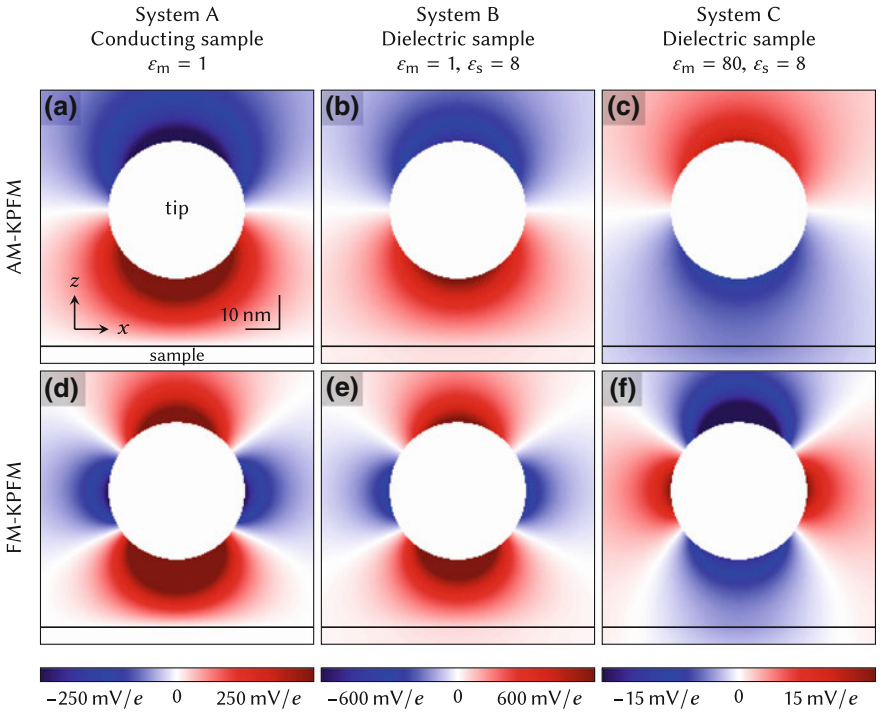

Fig. 7.2 Weight function for charges in AM-KPFM (top row) and FM-KPFM (bottom row). The considered tip-sample systems A, B and C are shown in the first, second and third column, respectively. The tip-sample distance is $z_{ts} = 20\,\text{nm}$, the tip radius is $R = 20\,\text{nm}$ and the amplitude is $A = 0\,\text{nm}$. The weight function corresponding to other parameters can be interactively explored at www.pc1.uni-bielefeld.de/kpfm. The coordinate system and scale bar shown in (**a**) apply to all panels. The sample surface at $z = 0$ is indicated by a horizontal black line

In sharp contrast, the sign of the KPFM weight function below the tip is negative in system C for the tip-sample distance evaluated in Fig. 7.2. The inversion of the sign of the weight function is readily explained by the sign of the derivative of the capacitance that enters the weight function, as detailed in [13] and in the following paragraph.

For the conductive sample (system A) the capacitance of the system is at its maximum when the distance between the tip and the conductive sample is at its minimum ($z_{ts} \to 0$), similar to a parallel-plate capacitor. Consequently, the capacitance decreases for increasing tip-sample distance, leading to a negative first derivative of C_{void} with respect to z_{ts}. For dielectric samples, the capacitance of the void tip-sample system is additionally influenced by the permittivity of both, sample and medium. For system B ($\varepsilon_m < \varepsilon_s$) the capacitance is again at its maximum when the tip is placed directly above the sample, since here the tip is surrounded by both, the dielectric sample and the dielectric medium. In the limit of a large tip-sample distance, the tip is only surrounded by the medium, which has a smaller permittivity

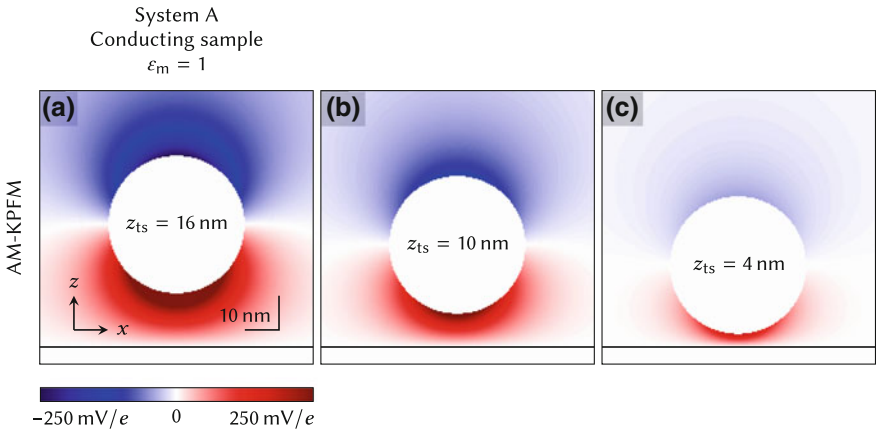

Fig. 7.3 The weight function for charges in AM-KPFM for system A is shown for different tip-sample distances z_{ts}. The color bar shown in (**a**) applies to all panels

than the sample. Therefore, for system B, the first derivative of C_{void} with respect to z_{ts} is again negative. In system C, however, the capacitance decreases for decreasing tip-sample distances, since the sample has a smaller dielectric permittivity compared to the medium. This effect readily explains the observation of an inversed sign when performing KPFM measurements in a medium with a permittivity ε_m larger than the permittivity ε_s of the sample [13]. We discuss the far-reaching consequences of this sign inversion in the next section.

Despite the change in sign for system C, a different overall magnitude of the weight function for charges as well as a different decay can be recognized in Fig. 7.2 when comparing different modes and sample systems – both aspects are again discussed in the next section. Finally, to illustrate that the KPFM weight function depends on the displacement between tip and sample, we exemplary plot the AM-KPFM weight function for system A in Fig. 7.3 for three different tip-sample distances. As the tip approaches the sample, the asymmetry of the weight function (when comparing the area beneath and above the tip) becomes more pronounced.

7.4 KPFM Signal for Relevant Charge Distributions

In this section, we calculate the KPFM signal V_{KPFM} using (7.1) for different charge distributions that resemble, for example, charged adsorbates such as molecules or atoms, deposited on metallic and insulating surfaces. The charges in the tip-sample system are all defined by their magnitudes q_i and positions $\mathbf{r}_i$. For a given displacement between tip and sample, the weight function is then evaluated at the positions of the charges.

We start with considering a single point charge in Sect. 7.4.1, for which we discuss the sign of the KPFM signal and the influence of the oscillation amplitude. Next, we investigate the signal for two point charges to quantify the lateral resolution of KPFM in Sect. 7.4.2, and the imaging of differently-oriented dipoles in Sect. 7.4.3. We continue with considering samples that exhibit a layer of surface charge in Sect. 7.4.4 to reveal the dependency of the KPFM signal on the sample size.

7.4.1 Imaging a Single Point Charge

We consider a single positive point charge of magnitude e, located at a height of $z = 0.2\,\text{nm}$ above the surface and in the center ($x = 0, y = 0$) of our coordinate system. To disentangle effects in the KPFM signal due to the tip-sample geometry from the averaging over the oscillation cycle, we start by setting the oscillation amplitude A to zero. This corresponds to experiments in the static AFM mode. We will close this section by discussing the effect of increasing the oscillation amplitude.

7.4.1.1 Lateral Images

We show images of the calculated KPFM signal as a function of x_{ts} and y_{ts} in Fig. 7.4, where the tip-sample distance z_{ts} is held constant at 0.5 nm. The upper panel of Fig. 7.4 shows the AM-KPFM signal, the lower panel shows the FM-KPFM signal.

For the conductive sample (system A, Fig. 7.4a, d) and the dielectric sample with $\varepsilon_{\text{m}} < \varepsilon_{\text{s}}$ (system B, Fig. 7.4b, e), the positive charge results in a positive KPFM signal at the position of the charge. Although the magnitude of V_{KPFM} is different for the different sample systems, the sign of the KPFM signal corresponds to the sign of the charge irrespective of using AM-KPFM or FM-KPFM. Moreover, the KPFM signal is at its maximum when the tip is positioned directly above the point charge. The charge is imaged with radial symmetry and with a lateral extent of the order of 10 nm.

In sharp contrast, the *positive* point charge yields within the shown image an overall *negative* AM-KPFM signal for the dielectric sample with $\varepsilon_{\text{m}} > \varepsilon_{\text{s}}$ (system C, Fig. 7.4c), and is furthermore in both modes (Fig. 7.4c, f) imaged as a toroidal ring with a local minimum at the position of the charge. Consequently, the qualitative interpretation of AM-KPFM in system C is different compared to systems A and B, especially since the sign of the KPFM signal reverses in the AM-KPFM mode. The physical reason for the sign reversal of the KPFM signal is the sign reversal of the derivatives of the capacitance as discussed in Sect. 7.2.1.

7.4.1.2 Vertical Slices

Next, we consider the same systems A, B and C, but evaluate the KPFM signal in the form of vertical slices as shown in Fig. 7.5. Thereby, we investigate the dependence of the KPFM signal on the tip-sample distance.

For systems A and B, we see that the KPFM signal for both the AM and the FM-KPFM mode has the same positive sign in the entire z_{ts} range of up to $z_{ts} = 75$ nm as shown in Figs. 7.5a, b, d and e. In contrast, the AM-KPFM signal obtained for system C (Fig. 7.5c) has an inverted sign throughout the investigated tip-sample distance regime, and the sign of the KPFM signal for system C in the FM mode (Fig. 7.5f) differs *within* the evaluated tip-sample distance regime. This finding highlights that qualitative statements regarding the sign of the point charge can be a challenge in AM-KPFM experiments for systems of type C (where $\varepsilon_m > \varepsilon_s$), and especially require knowledge of the tip-sample distance when using the FM-KPFM mode for systems of type C.

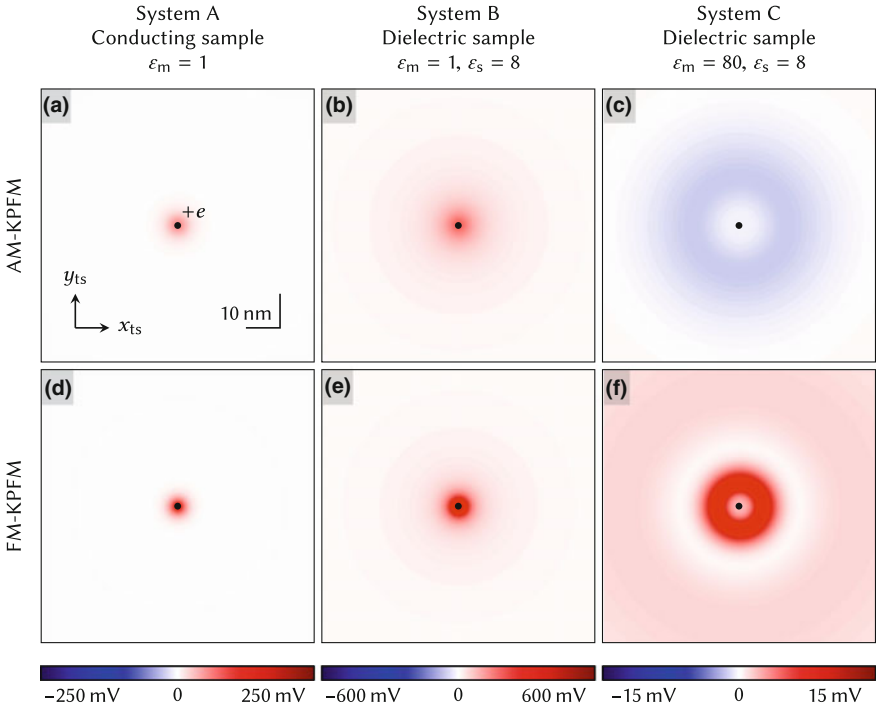

Fig. 7.4 Lateral images of the KPFM signal calculated for a point charge $+e$ (black dot) located at $x = 0$, $y = 0$ and $z = 0.2$ nm. The sample surface is located at $z = 0$. The oscillation amplitude A is set to zero and the tip-sample distance is $z_{ts} = 0.5$ nm. The coordinate system and scale bar shown in (**a**) apply to all panels, the color bars to both images above each bar

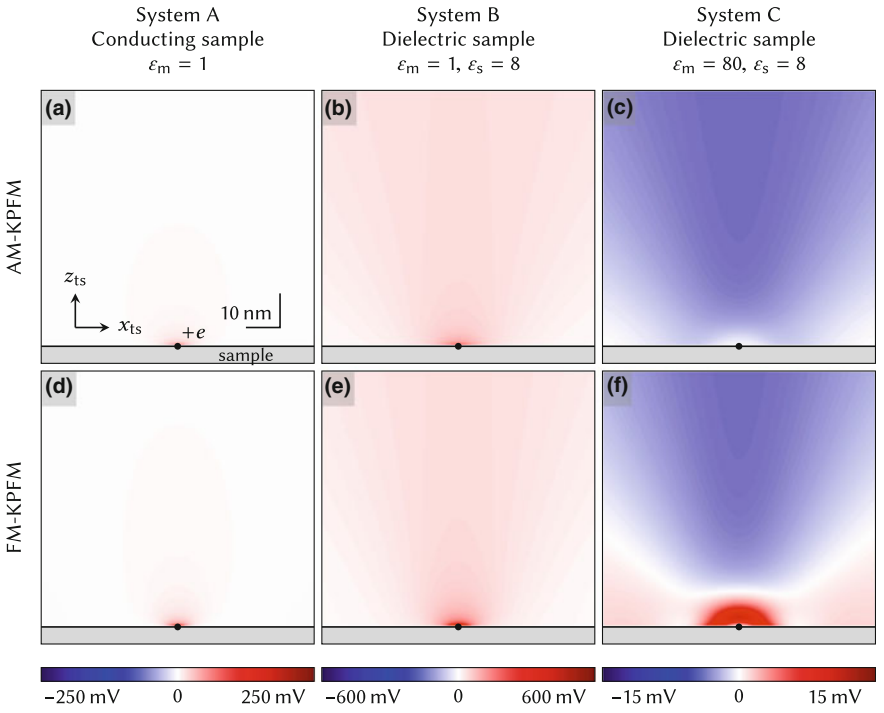

Fig. 7.5 Vertical slice of the KPFM signal calculated for a point charge $+e$ (black dot) located at $x = 0$, $y = 0$ and $z = 0.2$ nm. The oscillation amplitude A is set to zero. The coordinate system and scale bar shown in (**a**) apply to all panels, the color bars to both images above each bar

The vertical slices furthermore show that the KPFM signal changes monotonically upon approaching the tip closer to the charge for both system A and B, while the behavior for system C is more complex (see Fig. 7.5f).

7.4.1.3 Lateral and Vertical Profiles

It is common practice to experimentally measure the KPFM signal along specific surface directions in order to obtain the KPFM signal in profiles, e.g., as function of x_{ts} or z_{ts}. To facilitate comparison of these experiments with the KPFM signal of a single point charge, we show lateral and vertical profiles of the KPFM signal in this section. Using our model we calculate lateral profiles obtained at three different tip-sample distances ($z_{ts} = 0.5$, 2 and 10 nm) as shown in Fig. 7.6.

For systems A and B (black and blue lines), the KPFM signal shows a single peak in the lateral profiles, both for the AM- and the FM-KPFM mode. The signal is at its maximum when the tip is positioned centered on the charge. Moreover, the width of the peak increases for increasing tip-sample distances. As already discussed for the

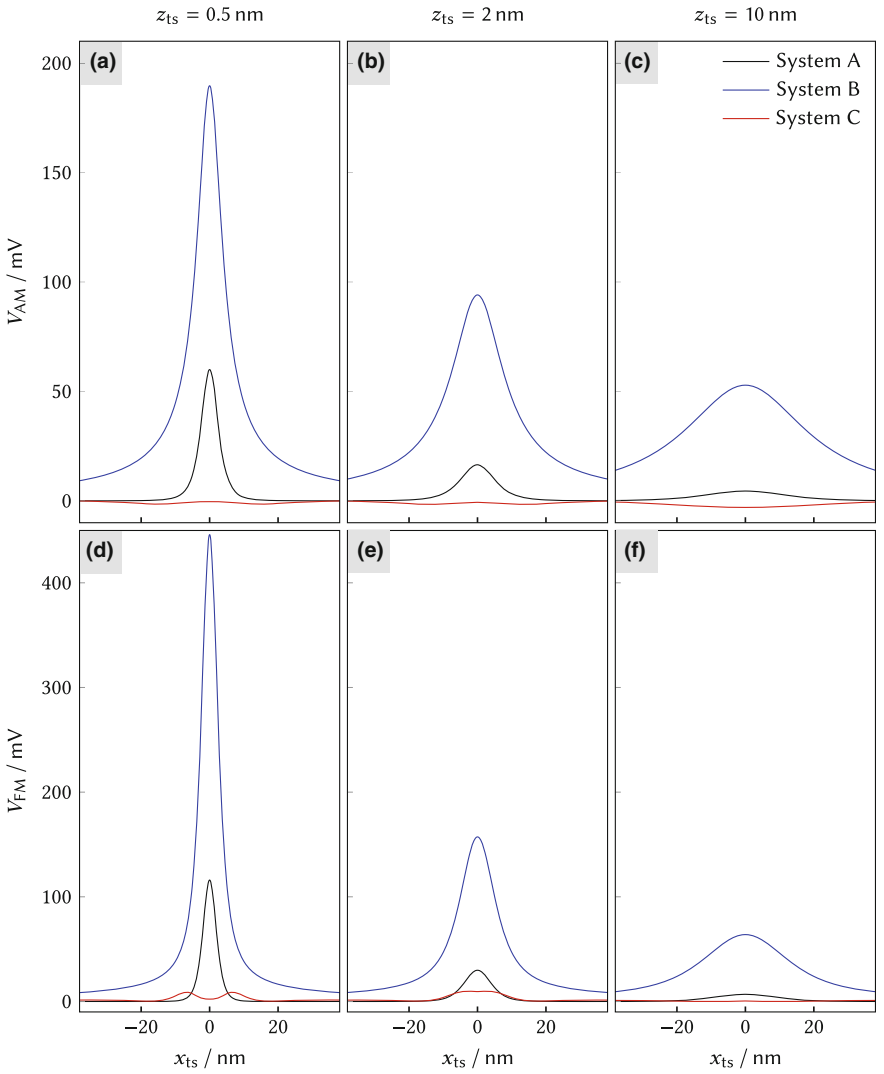

Fig. 7.6 Lateral profiles of the KPFM signal calculated for a point charge $+e$ located at $x = 0, y = 0$ and $z = 0.2$ nm. The oscillation amplitude A is set to zero. The tip-sample distance z_{ts} at which the tip has been scanned is indicated above the top panel

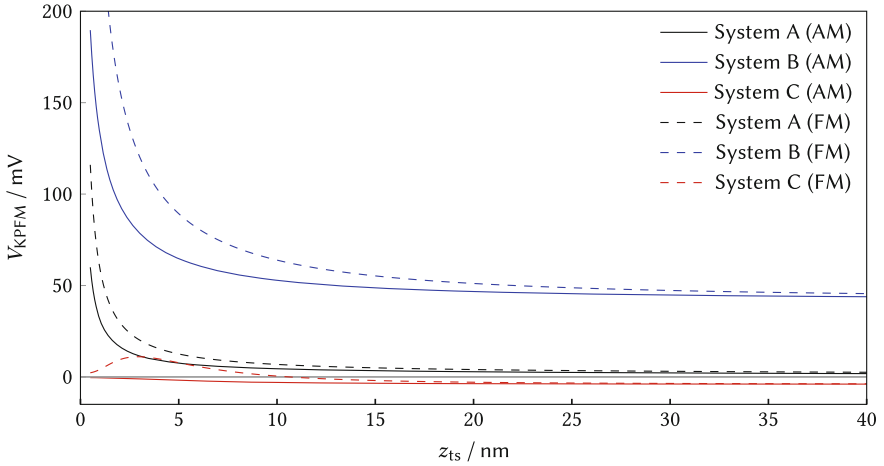

Fig. 7.7 Vertical profiles of the KPFM signal calculated for a point charge $+e$ located at $x = 0$, $y = 0$ and $z = 0.2\,\text{nm}$. The oscillation amplitude A is set to zero. The tip was positioned directly above the charge at $x_{ts} = 0$ and $y_{ts} = 0$

lateral and vertical slices, a non-monotonic shape of the KPFM signal is observed for system C when approaching the tip to the charge (red solid lines). Additionally, the AM-KPFM signal in system C is negative for all tip-sample distances shown in Fig. 7.6. In contrast, the FM-KPFM signal for system C changes depending on the tip-sample distance (Fig. 7.6e, f).

Vertical profiles of the KPFM signal extracted at the lateral position of the point charge are shown in Fig. 7.7. For system A and B, the KPFM signal increases for decreasing tip-sample distances. The increase in the KPFM signal is particularly steep when the tip is close to the sample and the signal magnitudes clearly differ for the different KPFM modes. The absolute value of the KPFM signal in system C decreases for the AM mode when increasing the tip-sample distance and, again, a non-monotonic behavior is observed for system C in the FM mode, where the KPFM signal exhibits a maximum in the vertical profile (red dashed line) as shown in Fig. 7.7.

7.4.1.4 Influence of the Oscillation Amplitude

We have so far chosen the oscillation amplitude A to be zero for all calculations of the KPFM signal, corresponding to the static AFM case. However, in dynamic AFM the oscillation amplitude is not zero. Therefore, we explore the effect of a non-zero oscillation amplitude on the KPFM signal in this section. According to the definition of the weight functions (7.2 and 7.3), both the derivative of the normalized electric potential of the void tip-sample system $\hat{\boldsymbol{\Phi}}_{\text{void}}$ and the corresponding derivative of the

capacitance C_{void} are averaged over the tip-sample distance range sampled during one oscillation cycle.

To illustrate the effect of this averaging, we calculate in Fig. 7.8 the KPFM signal along the same line profile shown in Fig. 7.6 with amplitudes of 0.1, 1, 10 and 100 nm and compare them with the $A = 0$ case. In all cases, we set the lower turning point of the tip oscillation to $z_{\mathrm{c}} - A = 0.5\,\mathrm{nm}$. Therefore, the tip-sample distance range considered for the averages (7.4 and 7.5) is $z_{\mathrm{ts}} \in [z_{\mathrm{c}} - A, z_{\mathrm{c}} + A]$.

Figure 7.8 a presents the AM-KPFM signal for a conductive sample (system A). The profile lines indicate that the KPFM signal at the position of the charge decreases for increasing oscillation amplitudes by a factor of about two. A qualitatively similar behavior can be found for FM-KPFM (Fig. 7.8f) in system A and for system B (Fig. 7.8b, g). For system C in FM-KPFM, even the sign of the KPFM signal can change depending on the oscillation amplitude (Fig. 7.8h). While the KPFM signal of a charge-free system does not depend on the oscillation amplitude [21], it is clearly emphasized from Fig. 7.8 that a quantitative comparison of KPFM signals between different experiments cannot be made without considering the amplitude when measuring systems containing charges.

For an investigation of the peak shape we normalize the profiles with respect to the maximum value of the peak (at $x_{\mathrm{ts}} = 0$). Normalized profiles are only calculated for systems A and B, since only here the KPFM signal has a consistent sign and peak-like shape in the lateral profiles. The results in Fig. 7.8d, e, i and j clearly show an increase in the width of the peaks with increasing oscillation amplitude. This finding is related to the peak-broadening observed for increasing tip-sample distances (Fig. 7.6) combined with the fact that the C_{void} and $\hat{\boldsymbol{\Phi}}_{\mathrm{void}}$ at larger tip-sample distances increasingly contribute with increasing oscillation amplitudes. As we will discuss in the next section, the lateral resolution in KPFM experiments is effectively reduced with larger peak widths.

These conclusions can also be drawn for system A in the FM-KPFM mode as well as for system B in both, the AM and the FM-KPFM mode as is apparent from Fig. 7.8. For system A and B, increasing oscillation amplitudes cause a decrease of the KPFM signal at the charge position and an increase of the peak width. However, the sign of the KPFM signal does not change as function of the oscillation amplitude, allowing qualitative statements regarding the sign of the charge to be made independent of the oscillation amplitude when considering system A and B.

7.4.2 Lateral Resolution for Imaging Charges with KPFM

The lateral resolution of KPFM experiments is an important figure to assess when aiming to image charge distributions with KPFM. We define the lateral resolution for imaging charges with KPFM by the minimal lateral distance at which two equally-charged point charges can be distinguished. Although KPFM experiments are always subject to measurement noise [22], a noise-free measurement is assumed here as a best-case scenario, where a minimum value between the two KPFM maxima at the

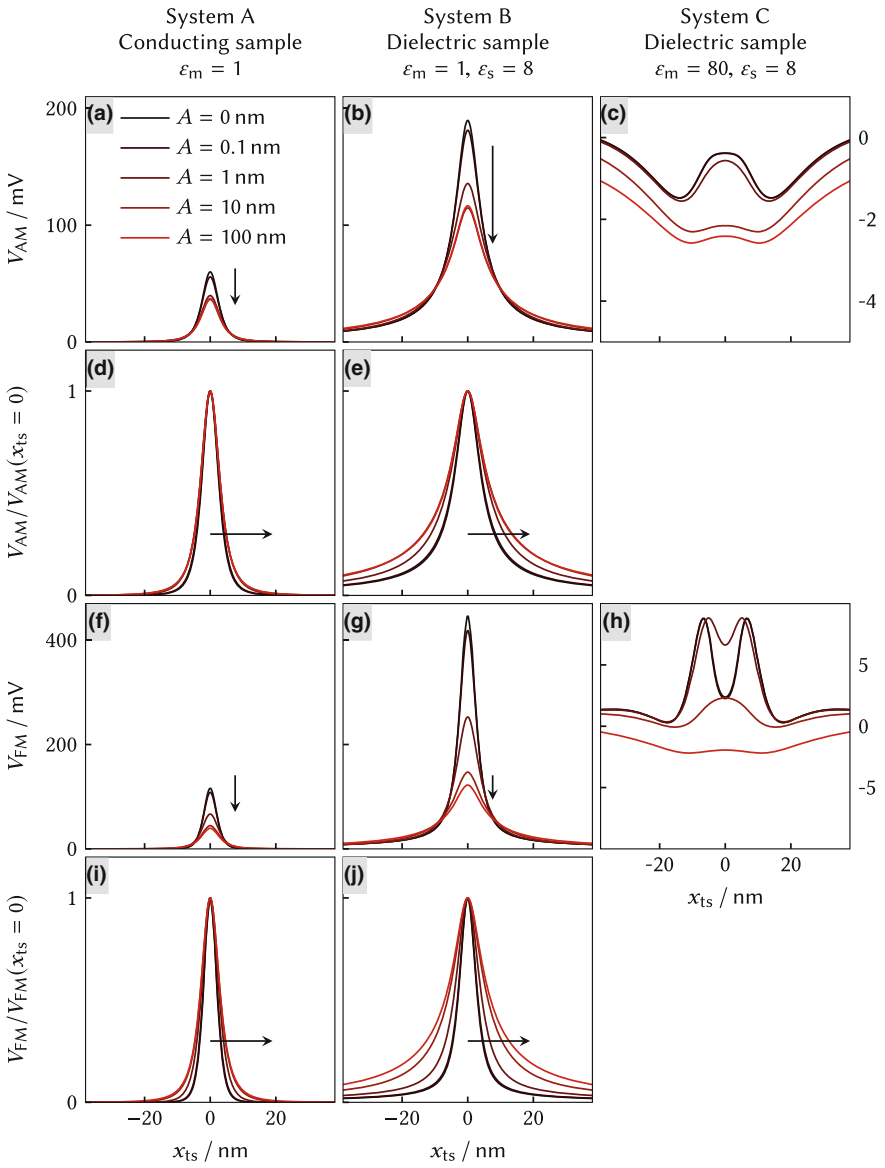

Fig. 7.8 Lateral profiles of the KPFM signal calculated for a point charge $+e$ located at $x = 0$, $y = 0$ and $z = 0.2$ nm calculated for several oscillation amplitudes A, namely 0, 1, 10 and 100 nm (increasing the amplitude is indicated by the black arrow). The lower turning point of the tip oscillation was held constant at $z_c - A = 0.5$ nm. Panels in the second and fourth row present the KPFM signal normalized to the respective maximum value at $x_{ts} = 0$

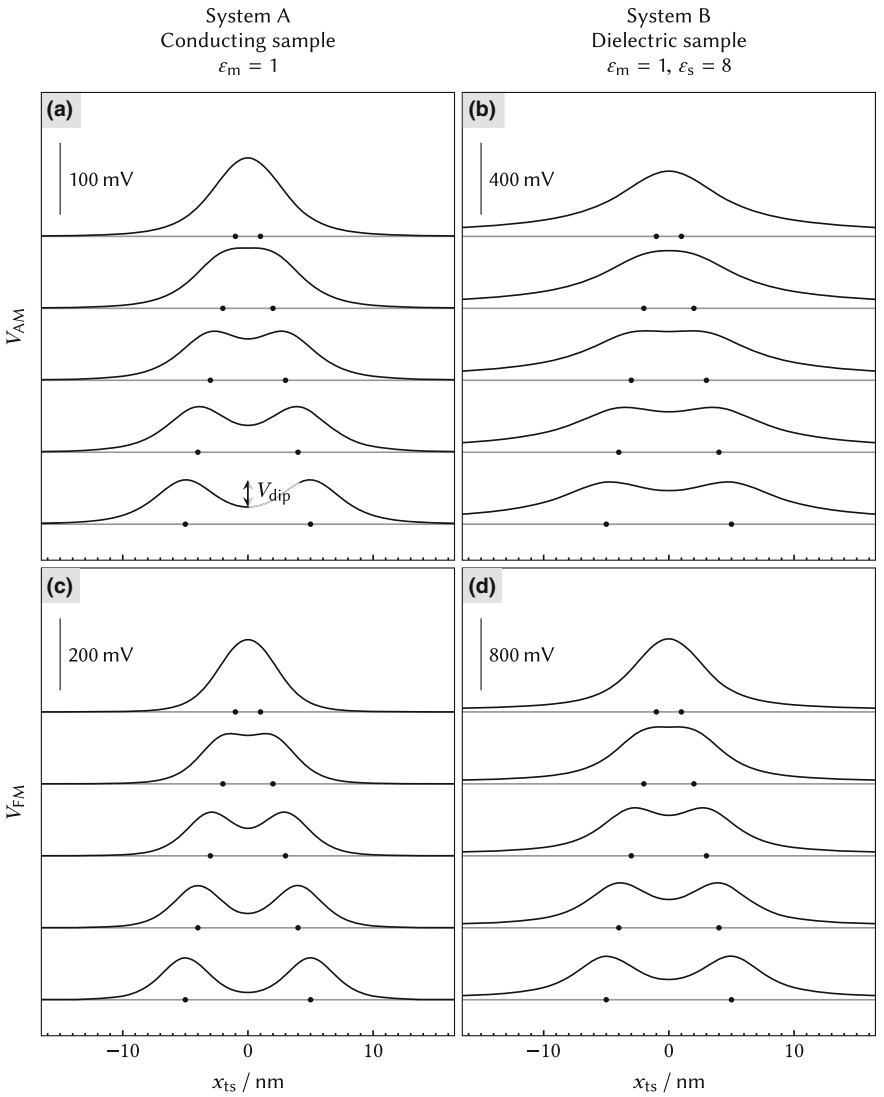

Fig. 7.9 Lateral profiles of the KPFM signal for two point charges ($+e$ located at $z = 0.2$ nm as indicated by the black dots) and separated by increasing distances ranging from 2 to 10 nm. The individual profiles are shifted by the amount stated at the scale bar. In all cases, the oscillation amplitude A was set to zero and the tip-sample distance z_{ts} was held constant at 0.5 nm

charge positions is revealed regardless of the depth magnitude V_{dip}. Practically, the resolution will be limited by a minimum detectable depth.

The lateral resolution is influenced by several parameters, such as the vertical tip position z_{ts} and the oscillation amplitude A. In the previous sections, we have found

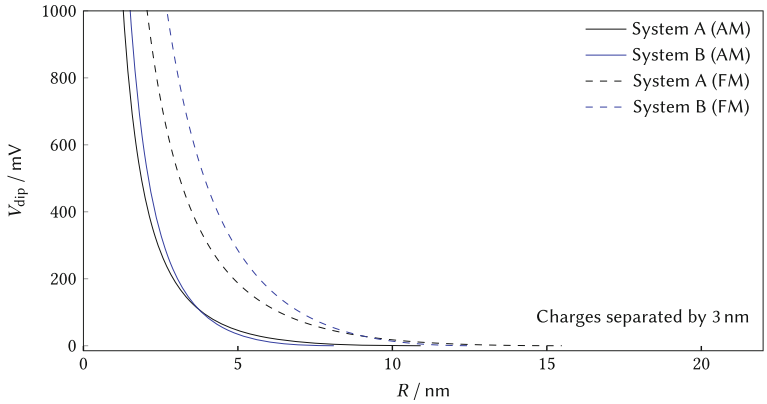

Fig. 7.10 Lateral resolution quantified by the depth of the minimum V_{dip} between the two charge peaks as function of the tip radius for two charges separated by an arbitrarily chosen distance of 3 nm. No data denotes the absence of a dip between the signals at the two charge positions

that the KPFM signal images a single point charge as a single peak (for systems A and B in both, AM- and FM-KPFM modes). We obtained the sharpest peaks for the smallest considered tip-sample distance of $z_{ts} = 0.5$ nm (Fig. 7.6) and for the smallest considered oscillation amplitude $A = 0$ (Fig. 7.8). We will use these two parameters in the following for illustrating the lateral resolution.

Figure 7.9 presents lateral profiles of the KPFM signal for two positive point charges (each $+e$, each located at $z = 0.2$ nm above the surface). The charges are positioned at different lateral distances indicated by the black dots. The corresponding KPFM line profiles are shifted vertically for clarity. When the charges are placed 10 nm apart, they appear as two clearly separable peaks in the profiles shown in Fig. 7.9. Upon moving the charges towards each other, eventually the two peaks merge to a single peak. For all considered cases (system A and B, AM-KPFM and FM-KPFM), they appear as one single peak at the smallest considered charge separation of 2 nm.

So far, we considered the lateral resolution for a fixed tip radius of $R = 20$ nm. To investigate the influence of the tip radius on the lateral resolution, we plot the depth of the minimum between the charges (the "dip" voltage indicated as V_{dip} in Fig. 7.9a) as a function of the tip radius R for two charges spaced 3 nm apart. Larger V_{dip} values lead to more robust measurements of the two charges as larger noise can be tolerated. If there is no minimum between the two charges, the charges cannot be distinguished.

The corresponding curves of V_{dip} vs. R are shown in Fig. 7.10 for system A and B in both, the AM- and FM-mode. In case there was no dip, no data is shown. With a tip radius of $R > 20$ nm, the two charges can not be separated, regardless of considering system A or B or by using AM-KPFM or FM-KPFM. Moreover, the dip voltage is consistently larger in the FM-KPFM modes (dashed lines) compared to the AM-KPFM modes (solid line), indicating that the resolution is increased in FM-KPFM

measurements when compared to AM-KPFM. This conclusion is in agreement with KPFM experiments on conducting surfaces of different local composition, where an increased lateral resolution was found for the FM-KPFM mode as well [14].

7.4.3 Imaging Dipoles

Molecules that adsorb on surfaces often exhibit a dipole moment. To investigate the KPFM signal produced by such a molecular adsorbate, we calculate the KPFM signal that arises from either a vertical or a horizontal dipole. In each case, the dipole results from placing two charges of opposite sign.

7.4.3.1 Vertical Dipole

First, we consider the KPFM signal for a system containing a *vertical* dipole centered at $x = 0$ and $y = 0$ as shown in Fig. 7.11. The dipole points upwards, i.e., a negative charge is located at $z = 0.15$ nm and a positive charge at $z = 0.25$ nm, which results in a dipole length of 0.1 nm and a dipole moment of $1e\text{Å} \approx 4.8$ D. The oscillation amplitude of the tip is set to zero.

For systems A and B, the vertical slice reveals a KPFM signal qualitatively similar to the one obtained for a single positive point charge (see Fig. 7.5). The KPFM signal for the upward-pointing dipole is positive in both, the AM- and FM-KPFM mode. This is a result from the weight function for charges having its maximum directly beneath the tip (for system A and B) and then falling off for increasing distances. Therefore, the upper charge of the dipole is closer to the tip and its contribution to the KFPM signal is larger compared to the lower charge. However, the presence of the lower charge of the dipole readily explains the overall smaller magnitude of the KPFM signal when compared to a single point charge (see Fig. 7.5).

In contrast to systems A and B, the vertical slice of the KPFM signal for the vertical dipole obtained for system C is qualitatively different compared to the vertical slice of the single point charge (Fig. 7.5). The KPFM signal in AM-KPFM is positive when the tip is directly above the dipole. In FM-KPFM, the vertical dipole produces negative side lobes. The sign of the KPFM signal in system C depends again on the tip-sample distance as was found for the single point charge in system C before, and the KPFM signal for the dipole is furthermore smaller than the point charge signal in Fig. 7.5.

7.4.3.2 Horizontal Dipole

A vertical slice of the KPFM signal corresponding to a *horizontal* dipole is shown in Fig. 7.12. The dipole is again centered at $y = 0$ and $z = 0.2$ nm and results from two charges, $-e$ at $x = -0.05$ nm and $+e$ at $x = +0.05$ nm. Consequently, the dipole

is pointing in the positive x direction. For systems A and B and in both, AM- and FM-KPFM mode (Figs. 7.12a–e), the dipole produces a negative KPFM signal for $x_{ts} < 0$ and a positive KPFM signal for $x_{ts} > 0$. Since the weight function has a radial symmetry for the spherical tip used within this chapter, the KPFM signal is zero at $x_{ts} = 0$ as both charges cancel each other. Imaging the horizontal dipole with a different sign in the KPFM signal in dependence on the horizontal position provides means to distinguish the horizontal dipole clearly from a single point charge. The KPFM signal obtained for system C shows a rather complex behavior including different signs depending on the vertical and horizontal tip position, as expected from the insights obtained for the single point charge.

7.4.4 *Surface Charge Distribution*

We have so far calculated the KPFM signal for one and two point charges, but neglected that a substrate, which is usually large compared to the tip dimensions,

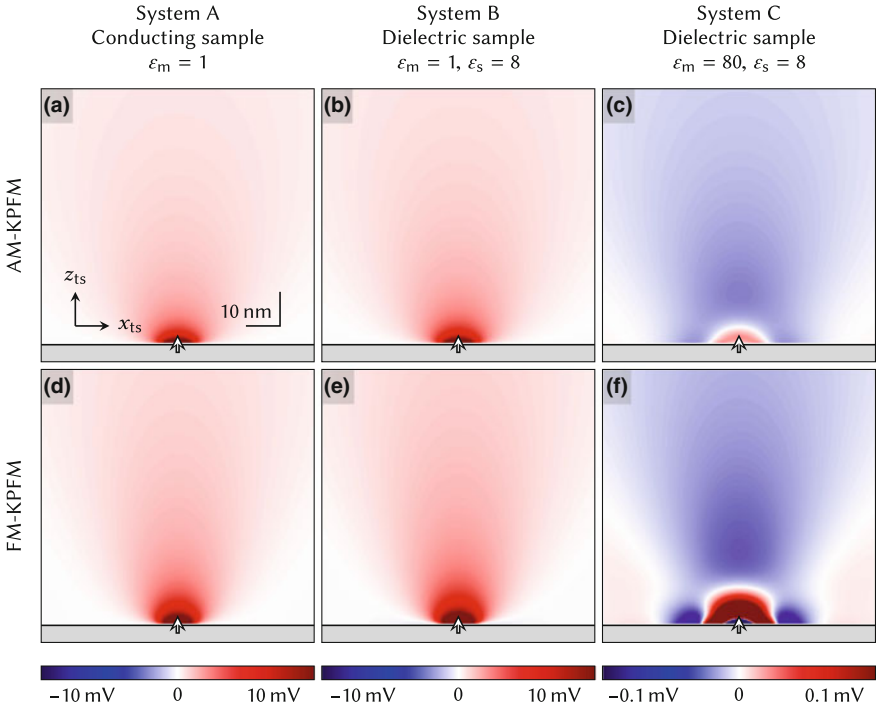

Fig. 7.11 Vertical slice of the KPFM signal calculated for a vertical dipole (pointing upwards) located at $x = 0$, $y = 0$ and $z = 0.2$ nm. The oscillation amplitude A is set to zero. The coordinate system and scale bar shown in (**a**) apply to all panels, the color bar to both images above each bar

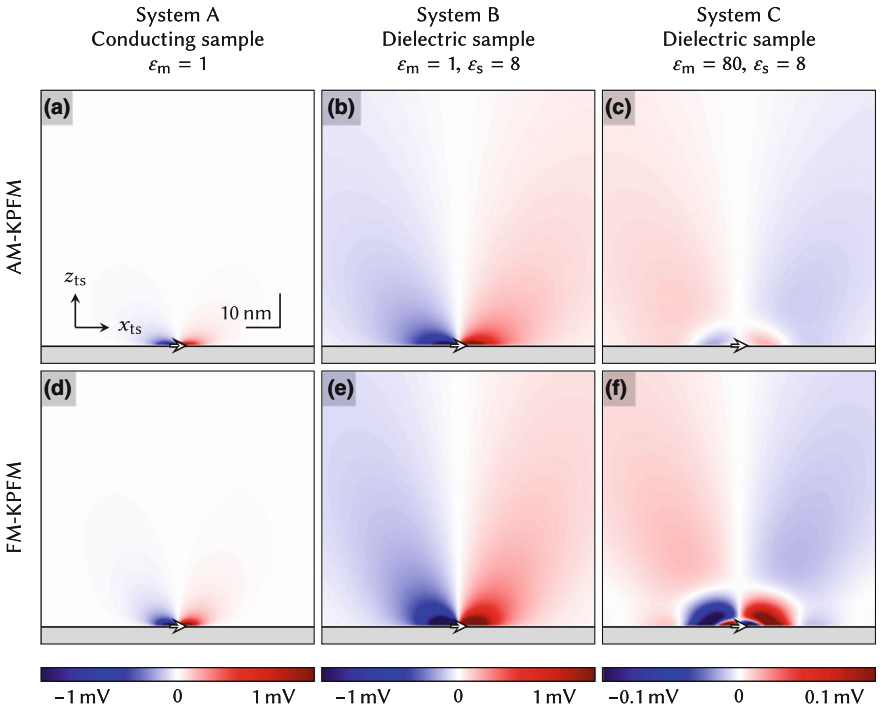

Fig. 7.12 Vertical slices of the KPFM signal calculated for a horizontal dipole pointing to the right (centered at $x = 0$, $y = 0$ and $z = 0.2$ nm. The oscillation amplitude A is set to zero. The coordinate system and scale bar shown in (**a**) apply to all panels, the color bar to both images above each bar

is often covered by e.g. charged defects, atoms or molecules. Therefore, we now extend the analysis by quantifying the contribution to the KPFM signal due to a large number of point charges, most of which are located at large distances from the tip.

We plot the KPFM weight function W_{KPFM} in Fig. 7.13 for a fixed tip position $\mathbf{r}_{ts} = (0, 0, 5\,\mathrm{nm})$ centered above the origin as function of the distance $r = \sqrt{x^2 + y^2 + z^2}$ of the charge from the origin. The horizontal distance interval is evaluated from $r = 0.2$ nm (i.e., close to the tip) up to $r = 1$ mm (representing the edge of the sample far away from the tip). The profile of the weight function is computed for a fixed height $z = 0.2$ nm (with the tip at $z_{ts} = 5$ nm) and we set again the oscillation amplitude A to zero.

For all considered tip-sample systems A, B and C and for both, the AM- and FM-KPFM modes, the weight function decays to zero in the limit $r \to \infty$. However, there is a striking difference in the fall-off behavior when comparing the conductive sample (system A) with the dielectric samples (systems B and C). The AM-KPFM and FM-KPFM weight functions decay both with r^{-3} for the conductive sample (system A).

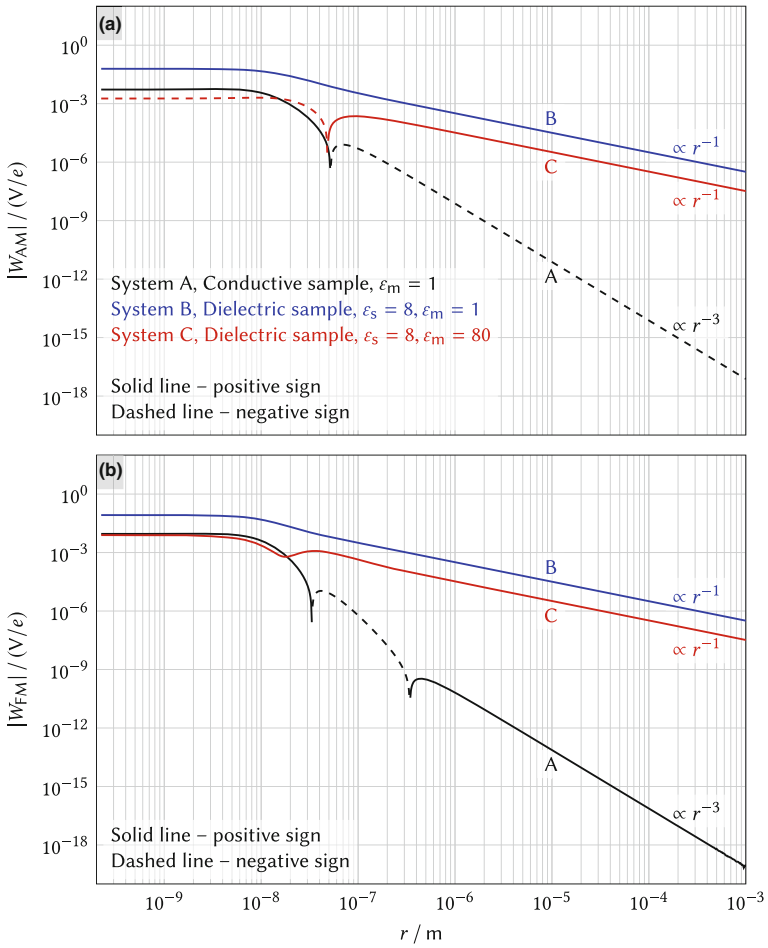

Fig. 7.13 Lateral profiles of the **a** AM-KPFM weight function for charges and the **b** FM-KPFM weight function for charges as function of the distance r from the origin in a double-logarithmic plot

On dielectric samples, however, the AM-KPFM and FM-KPFM weight functions both decay more slowly with r^{-1}.

To illustrate the consequences of the different lateral decays of the weight function, we consider a sample that is homogeneously covered with surface charges. These surface charges could, e.g., arise from defects as well as from polar or charged adsorbates. We model the surface charges as a charged circular-shaped island with surface charge density σ and radius r_σ (see Fig. 7.14). We assume that the charges are located at a height of $z = 0.2\,\text{nm}$ above the sample, i.e. at the same distance at which the weight function was analyzed in Fig. 7.13.

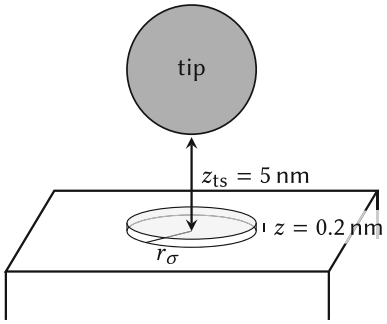

Fig. 7.14 Illustration showing the charged island (gray circle) with radius r_σ located at a height of $z = 0.2\,nm$ above the sample. The tip (with tip radius $R = 20\,nm$) is placed at a distance of $z_{ts} = 5\,nm$ above the sample. The illustration is not to scale

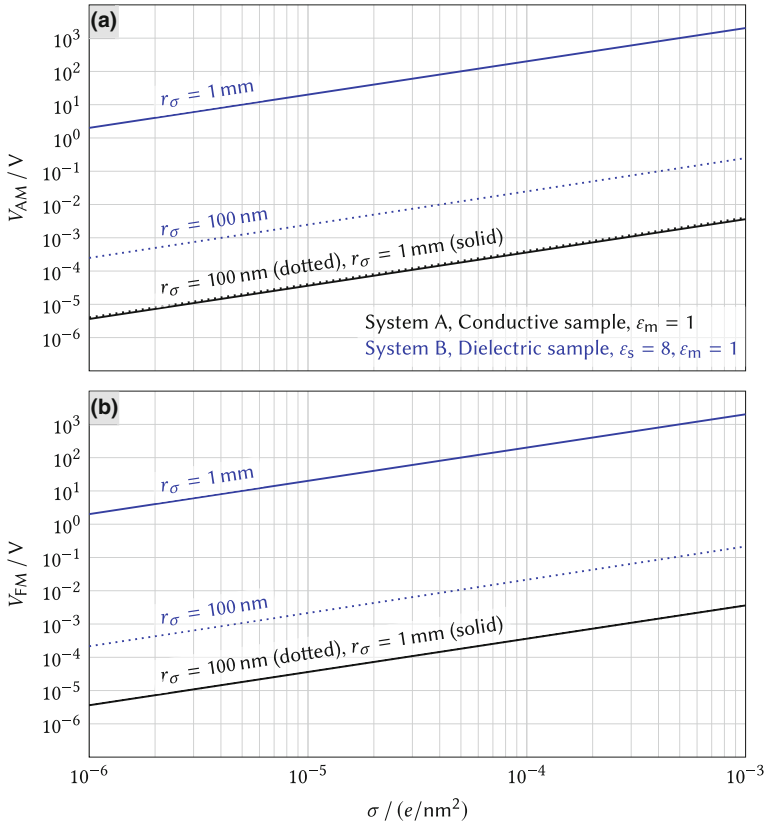

Fig. 7.15 Calculated AM-KPFM signal (**a**) and FM-KPFM signal (**b**) for a homogeneously charged island with radius r_σ as function of the island's surface charge density σ. The tip is positioned above the center of the charged island at $r_{ts} = 0$ and $z_{ts} = 5\,nm$. The charges within the island are located at $z = 0.2\,nm$, the oscillation amplitude is set to zero

Using this charge distribution, we first model a sample where an island with a radius of $r_\sigma = 100\,\text{nm}$ covers the surface. The corresponding KPFM signal is shown as a function of the surface charge density σ in Fig. 7.15 for the (a) AM-KPFM and (b) FM-KPFM modes and for systems A (conductive sample and $\varepsilon_\text{m} = 1$, dotted black lines) and B (dielectric sample with $\varepsilon_\text{s} = 8$ and $\varepsilon_\text{m} = 1$, dotted blue lines).

Next, we compare the KPFM signal with the signal that is produced by a charged island that covers a large portion of the sample by setting its radius to $r_\sigma = 1\,\text{mm}$. On the conductive sample (system A), the KPFM signal remains nearly constant (solid black lines in Fig. 7.15) when compared to the KPFM signal obtained for the smaller charged island with radius $r_\sigma = 100\,\text{nm}$. This indicates that the charges that contribute to the KPFM signal are overwhelmingly located beneath the tip.[2] In this case, the KPFM signal converges with respect to the radius of the charged island.

In sharp contrast, the KPFM signal obtained for the dielectric sample (system B) differs *several orders of magnitude* compared to the smaller island with $r_\sigma = 100\,\text{nm}$. In this case, even for a surface charge density of $\sigma = 10^{-6}\,e/\text{nm}^2$, the KPFM signal obtained for the dielectric sample is of the order of several volts. Indeed, Kelvin voltages on surfaces of especially freshly cleaved insulating materials have been found to be of the order of several 10 V [23]. As is already clear from the decay in Fig. 7.13, charges from the whole sample contribute critically to the KPFM signal when considering dielectric samples. Here, the KPFM signal does not converge with respect to the radius of the charged island.

Thus, the different lateral decay of the weight function for charges in KPFM that is obtained for a conductive sample compared to a dielectric sample has a significant impact on the interpretation of KPFM data. For conductive samples, the major contribution to the KPFM signal arises from charges that are in the proximity of the tip. On dielectric samples, in contrast, charges located on the *whole* sample can significantly contribute to the KPFM signal. In this case, the KPFM signal consequently depends on the size of the sample.

7.5 Conclusions and Outlook

In this chapter, we discussed the KPFM signal arising from charge distributions that represent charged adsorbates such as atoms or molecules on surfaces. As tip-sample system we considered a spherical tip surrounded by either vacuum, air, or liquid above either a conductive or dielectric sample. The KPFM signal of a single point charge, a pair of charges (dipole), a charged island, and a layer of charges was calculated by convolution of the respective charge distributions with the weight function for charges.

[2]The slight decrease in the KPFM signal when increasing r_σ from 100 nm to 1 mm originates from the negative sign of the weight function for system A in the distance range of $r \gtrsim 100\,\text{nm}$ (see black solid and dotted line in Fig. 7.13a).

For a single point charge we discussed horizontal and vertical images and profiles of the KPFM signal. Interestingly, on dielectric samples, the KPFM signal arising from a single positive point charge can be positive or negative, depending on the dielectric permittivities of medium and sample. In some cases, the sign even depends on the tip-sample distance. This demonstrates that knowledge of the weight function for charges and the tip-sample distance is crucial, even for a qualitative interpretation of charges beneath the tip. Furthermore, the quantitative value of the obtained KPFM signal depends on the oscillation amplitude of the probe tip.

We provided means to quantify the lateral resolution of KPFM. For the spherical tip model we used here, two charges can only be resolved if their distance is at least in the range of the tip radius.

We considered two charges of equal magnitude but different sign, i.e. dipoles. Considering a sample in vacuum and air, a vertical dipole produces a KPFM signal with the same sign as its upper point charge. Only dipoles that are oriented horizontally on the surface can be clearly differentiated from a single point charge, since the sign of the KPFM signal inverts depending on the lateral position of the tip.

We compared the KPFM signal generated by an island of charges for different island sizes. Our analysis revealed that the KPFM signal does not converge with respect to the island size when considering dielectric samples. In case of dielectric samples, charges can significantly contribute to the KPFM signal, even if they are far away (in the range of mm) from the tip. Therefore, the KPFM signal obtained for dielectric samples that are covered with a layer of charges depends on the sample size. In contrast, on conductive samples, the charges that contribute to the KPFM signal are more locally confined within several tens of nanometers, since here the KPFM signal converges.

With this discussion of the KPFM weight function for charges, we aim for a coherent understanding of the KPFM signal generation to enable KPFM data interpretation.

Acknowledgements H.S. is a recipient of a DFG-funded position through the Excellence Initiative (DFG/GSC 266). P.R. gratefully acknowledges financial support by the German Research Foundation (DFG) via grant RA2832/1-1.

Appendix A: Electrostatic Model

In this appendix we consider different electrostatic models that can be used to calculate the weight function for charges. Moreover, we also discuss the model for the tip-sample system that we use in this chapter.

There is a large number of both approximative and exact solutions available in literature for the electrostatic problem of tip-sample systems of various compositions and geometries. As the *weight function for charges* depends only on the normalized electrostatic potential $\hat{\Phi}_{\text{void}}$ and the capacitance C_{void} of the *void* tip-sample system (see also the previous chapter), we only consider void, i.e., charge-free tip-sample

systems. Thus, we here exclude solutions of the full electrostatic system including charges such as given by Pan et al. [24] for a hyperboloid tip and a point charge, by Uchida for a single charge in a series of parallel-plate capacitors [25], and by Terris et al. [26] for two point charges. We furthermore exclude the cases of a semiconducting substrate as well as non-metallic tips [27].

Models presented in literature can be separated into *approximative* and *exact* models, as we will discuss in the following.

A.1 Approximative Solutions

Several approximations have been put forward over the last years that allow for obtaining an approximative solution of the electrostatic potential and capacitance of the void tip-sample system. The *equivalent charge model (ECM)* [28–31], also known as the *generalized image charge method (GICM)* [32–35], has been employed by several authors, often to consider a more elaborate tip model by including a cone in addition to the tip sphere. In this model, a number of point charges are adjusted in their magnitudes and/or positions such that the boundary conditions for the electrostatic potential are matched on the tip and on the sample surface as good as possible. However, and in contrast to the infinite image charge series introduced later, the convergence of these models has not generally been tested.

Hudlet et al. [36] have presented a formula for the case of a metallic tip against a metallic surface using two assumptions: First, they consider the tip surface as a superposition of infinitesimal surface segments and second, they assume that the total electric field is given from the superposition of all electric field lines present between each surface segment and the sample in their respective geometry. This approach effectively models the field lines as circular segments. The authors could show a good agreement with the analytical model for a metallic sphere-metallic surface system [37].

Colchero et al. [38] and Gil et al. [39] solve the electrostatic problem of a system consisting of both cone and tip sphere under the same assumption that all field lines can be approximated by circular segments and that the potential varies linearly along these circular segments. Within this approximation, they calculate the electrostatic force for a rectangular cantilever tilted with respect to the surface, for a circular truncated cone representing the tip shank, and for a parabolic tip that smoothly joins the truncated cone.

A.2 Exact Solutions

For obtaining the electric potential and the capacitance of the tip-sample system, finite element and finite difference solvers [40] can be used. Most notably, a dedicated

solver named *CapSol* has been published recently, which allows to specifically model scanning-probe relevant setups [41].

A computationally less expensive way to calculate the electric potential and the capacitance of a tip-sample system is, in the simplest case, to consider a *parallel-plate capacitor* [29, 42, 43]. Thereby, both a purely metallic tip and sample as well as additionally included dielectric materials can be modeled. The sizes of the plates are approximated by the dimensions of the tip. However, since the electric potential resulting from this model is laterally homogeneous, this model is not capable of explaining lateral contrast.

To include the dependence on the probe position, a straightforward approach is to represent the tip by a single point charge [29, 37, 44]. The potential distribution of a sphere of radius R at constant potential V in a medium with dielectric constant ε_m can (outside of the sphere) be obtained by considering a single image charge with magnitude $q = 4\pi\varepsilon_0\varepsilon_\mathrm{m}VR$ located at the center of the sphere [37]. This model does, so far, not include the presence of the sample. However, when extending the finite number of charges to an infinite sum [37], the method of image charges is a powerful concept to solve the electrostatic problem of a metallic sphere in proximity to another metallic sphere [37, 45], a metallic plane [37], a dielectric slab [46], or a dielectric half-space [46]. The next section will revisit the solution for a metallic sphere against a dielectric or metallic sample following previous works [37, 46].

A.3 Infinite Charge Series Model

The method of infinite image charge series for both the sphere-conductor and the sphere-dielectric setup is based on two well-known textbook concepts for solving the electrostatic problem with boundary conditions using image charges: (a) the case of a point charge in front of a dielectric (or metallic) half-space and (b) the case of a point charge in front of a conducting sphere.

Point charge in front of conductive or dielectric half-space

For a point charge q in a medium with relative permittivity ε_m at a distance b in front of a dielectric or conductive half-space, an image charge with magnitude $\xi' = -\beta q$ placed at $b' = -b$ yields the correct boundary condition at the interface [44]. The factor β is defined by the dielectric permittivities according to

$$\beta = \frac{\varepsilon_\mathrm{s} - \varepsilon_\mathrm{m}}{\varepsilon_\mathrm{s} + \varepsilon_\mathrm{m}}, \tag{7.6}$$

where ε_s is the permittivity of the lower half-space. For a metal, $\beta = 1$ [46].

The potential for the upper half-space ($z \geq 0$) is then defined by the point charge q and image charge ξ'

$$\Phi(\mathbf{r}) = \frac{1}{4\pi\varepsilon_0\varepsilon_\mathrm{m}}\left(\frac{q}{\sqrt{x^2+y^2+(b-z)^2}} + \frac{-\beta q}{\sqrt{x^2+y^2+(b+z)^2}}\right). \tag{7.7}$$

To calculate the electrostatic potential for the lower half-space ($z < 0$) it is necessary to place a different image charge ξ'' with magnitude $\xi'' = q - \xi' = q(1+\beta)$ in the upper half space at the same position as the charge q. The potential for $z < 0$ then reads

$$\Phi(\mathbf{r}) = \frac{q(1+\beta)}{4\pi\varepsilon_0\varepsilon_\mathrm{s}\sqrt{x^2+y^2+(b-z)^2}}. \tag{7.8}$$

Point charge outside of a conductive sphere

For a point charge q located outside of a conducting sphere of radius R at a distance y from the center, an image charge ξ' is placed on the line connecting the point charge q with the center of the sphere. This image charge of magnitude $\xi' = -\frac{R}{y}q$ is placed at distance $d = \frac{R^2}{y}$ from the sphere center to match the boundary condition at the sphere surface [44]. Then, the total electrostatic potential for the conducting sphere of radius R at potential V in a medium with relative permittivity ε_m and a point charge at distance y is given from the sum of potentials for three point charges:

$$\Phi(\mathbf{r}) = \frac{1}{4\pi\varepsilon_0\varepsilon_\mathrm{m}}\left(\frac{q}{|\mathbf{r}-\mathbf{y}|} + \frac{-\frac{R}{y}q}{\left|\frac{R^2}{y^2}\mathbf{y}-\mathbf{r}\right|} + \frac{RV}{|\mathbf{r}|}\right) \tag{7.9}$$

for $|\mathbf{r}| \geq R$. While the first two terms ensure the boundary condition on the sphere surface for a neutral sphere due to the external charge, the last term includes the potential distribution due to the charged surface.

Conductive sphere in front of dielectric or conductive half-space

Using these two concepts, the solution for the conducting sphere in front of the conductive or dielectric half-space can be found using series of image charges [37, 46].

A single point charge $\xi_0 = 4\pi\varepsilon_0\varepsilon_\mathrm{m}RV$ is placed at $z_0 = R + z_\mathrm{ts}$, representing a conducting sphere of radius R at constant potential V in a medium with ε_m and with the center positioned at $R + z_\mathrm{ts}$ from the lower half-space, see also Figs. 7.1 and 7.16. The dielectric material ε_s is modeled with an infinite thickness where the metallic back contact resides at $z \to -\infty$. In practice, this approximation is usually fulfilled as the sample thickness is much larger compared to the sphere radius R and the tip-sample separation z_ts. Furthermore, and without loss of generality, the potential can be set to ground at this back electrode.

While the boundary condition at the sphere is fulfilled with the point charge ξ_0, the boundary condition at the dielectric boundary is not. The latter can be corrected by placing an image charge

$$\xi_0' = -\beta\xi_0 \quad \text{at} \quad z_0' = -z_0 \tag{7.10}$$

and $x = 0, y = 0$. The image charges series $\{\xi_i\}$ and $\{\xi_i'\}$ define the electrostatic potential in the upper half-space (above the sample, at $z \geq 0$). The electrostatic potential at $z < 0$ is given from placing an image charge of magnitude

$$\xi_0'' = \xi_0 - \xi_0' = (1 + \beta)\xi_0 \quad \text{at} \quad z_0'' = z_0 \tag{7.11}$$

in the upper half-space. Now the image charge ξ_0' violates the boundary condition on the sphere, which can again be fixed by placing according image charges. The concept of infinite charge series relies on an alternating correction of the two boundary conditions, whereby the infinite series fulfills all boundary conditions.

The infinite series of image charges continues with

$$\xi_1 = \frac{R}{2(R + z_{\text{ts}})}\beta\xi_0 \qquad \text{at} \quad z_1 = R + z_{\text{ts}} - \frac{R^2}{2(R + z_{\text{ts}})}, \tag{7.12}$$

fulfilling the boundary condition at the sphere for ξ_0'. The series of image charges ξ_i, ξ_i' and ξ_i'' is then continued to alternatively fulfill the boundary conditions at the sphere and at the dielectric boundary. The magnitudes ξ_i and positions z_i of these image charges placed inside the sphere are given by the following recursive equations (for $i > 0$)

$$z_i = z_0 - \frac{R^2}{z_0 + z_{i-1}} \quad \text{with} \quad z_0 = R + z_{\text{ts}} \tag{7.13}$$

$$\xi_i = \frac{R}{z_0 + z_{i-1}}\beta\xi_{i-1} \quad \text{with} \quad \xi_0 = 4\pi\varepsilon_0\varepsilon_{\text{m}}RV. \tag{7.14}$$

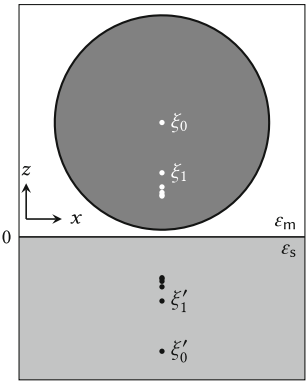

Fig. 7.16 Geometry of the sphere-dielectric system including the positions of the image charge series

This charge series is accompanied by two further image charge series, namely ξ_i' and ξ_i'' according to

$$z_i' = -z_i, \tag{7.15}$$
$$\xi_i' = -\beta\xi_i, \tag{7.16}$$
$$z_i'' = z_i, \tag{7.17}$$
$$\xi_i'' = (1+\beta)\xi_i. \tag{7.18}$$

Using the series of these charges, the potential $\boldsymbol{\Phi}_{\text{void}}$ for both half-spaces follows directly from the superposition of the point charge potentials, namely

$$\boldsymbol{\Phi}_{\text{void}}(\mathbf{r}) = \frac{1}{4\pi\varepsilon_0\varepsilon_{\text{m}}}\sum_{i=0}^{\infty}\left[\frac{\xi_i}{\sqrt{x^2+y^2+(z_i-z)^2}} + \frac{\xi_i'}{\sqrt{x^2+y^2+(z_i'-z)^2}}\right] \quad (\text{for } z \geq 0) \tag{7.19}$$

for the upper half-space and

$$\boldsymbol{\Phi}_{\text{void}}(\mathbf{r}) = \frac{1}{4\pi\varepsilon_0\varepsilon_{\text{s}}}\sum_{i=0}^{\infty}\frac{\xi_i''}{\sqrt{x^2+y^2+(z_i''-z)^2}} \quad (\text{for } z < 0) \tag{7.20}$$

for the lower half-space. The capacitance C_{void} of the system is given by the sum over all image charges ξ_i divided by the tip voltage V:

$$C_{\text{void}} = \frac{1}{V}\sum_{i=0}^{\infty}\xi_i. \tag{7.21}$$

As the magnitudes of the image charges converge quickly to zero, it is practical to only consider a finite number of terms. Since the positions of the charges converge quickly, the high-index elements can furthermore be represented by a single charge holding the sum of the remaining infinite charge series [45, 46].

For all calculations shown within this chapter, we truncated the infinite image charge series after 100 image charges and consider one additional point charges holding the sum of the remaining charges in the series [45, 46]. After calculating the normalized electric potential and the capacitance, we numerically determined the derivatives needed for computing the weight functions in (7.2) and (7.3) using a central finite difference scheme of second order.

References

1. M. Nonnenmacher, M.P. O'Boyle, H.K. Wickramasinghe, Appl. Phys. Lett. **58**(25), 2921 (1991). https://doi.org/10.1063/1.105227
2. J.M.R. Weaver, J. Vac. Sci. Technol. **9**(3), 1559 (1991). https://doi.org/10.1116/1.585423
3. U. Zerweck, C. Loppacher, T. Otto, S. Grafström, L.M. Eng, Nanotechnology **18**(8), 084006 (2007). https://doi.org/10.1088/0957-4484/18/8/084006
4. S. Kawai, T. Glatzel, H.J. Hug, E. Meyer, Nanotechnology **21**(24), 245704 (2010). https://doi.org/10.1088/0957-4484/21/24/245704
5. A. Hinaut, A. Pujol, F. Chaumeton, D. Martrou, A. Gourdon, S. Gauthier, Beilstein J. Nanotechnol. **3**, 221 (2012). https://doi.org/10.3762/bjnano.3.25
6. M. Kittelmann, P. Rahe, A. Gourdon, A. Kühnle, ACS Nano **6**(8), 7406 (2012). https://doi.org/10.1021/nn3025942
7. V.W. Bergmann, S.A.L. Weber, F.J. Ramos, M.K. Nazeeruddin, M. Grätzel, D. Li, A.L. Domanski, I. Lieberwirth, S. Ahmad, R. Berger, Nat. Commun. **5**, 5001 (2014). https://doi.org/10.1038/ncomms6001
8. L. Gross, F. Mohn, P. Liljeroth, J. Repp, F.J. Giessibl, G. Meyer, Science **324**(5933), 1428 (2009). https://doi.org/10.1126/science.1172273
9. L. Gross, B. Schuler, F. Mohn, N. Moll, N. Pavliček, W. Steurer, I. Scivetti, K. Kotsis, M. Persson, G. Meyer, Phys. Rev. B **90**(15), 155455 (2014). https://doi.org/10.1103/PhysRevB.90.155455
10. A.L. Domanski, E. Sengupta, K. Bley, M.B. Untch, S.A.L. Weber, K. Landfester, C.K. Weiss, H.J. Butt, R. Berger, Langmuir **28**(39), 13892 (2012). https://doi.org/10.1021/la302451h
11. L. Collins, J.I. Kilpatrick, I.V. Vlassiouk, A. Tselev, S.A.L. Weber, S. Jesse, S.V. Kalinin, B.J. Rodriguez, Appl. Phys. Lett. **104**(13), 133103 (2014). https://doi.org/10.1063/1.4870074
12. J.L. Neff, P. Rahe, Phys. Rev. B **91**(8), 085424 (2015). https://doi.org/10.1103/physrevb.91.085424
13. H. Söngen, P. Rahe, J.L. Neff, R. Bechstein, J. Ritala, A.S. Foster, A. Kühnle, J. Appl. Phys. **119**(2), 025304 (2016). https://doi.org/10.1063/1.4939619
14. T. Glatzel, S. Sadewasser, M.C. Lux-Steiner, Appl. Surf. Sci. **210**(1–2), 84 (2003). https://doi.org/10.1016/S0169-4332(02)01484-8
15. H. Söngen, R. Bechstein, A. Kühnle, J. Phys. Condens. Matter **29**, 274001 (2017). https://doi.org/10.1088/1361-648X/aa6f8b
16. K.S. Rao, K.V. Rao, Z. Physik **216**(3), 300 (1968). https://doi.org/10.1007/bf01392970
17. C.G. Malmberg, A.A. Maryott, J. Res. Nat. Bur. Stand. **56**(1), 369131 (1956)
18. W. Steurer, S. Fatayer, L. Gross, G. Meyer, Nat. Commun. **6**, 8353 (2015). https://doi.org/10.1038/ncomms9353
19. B. Hoff, C.R. Henry, C. Barth, Nanoscale **8**, 411 (2015). https://doi.org/10.1039/C5NR04541J
20. P. Rahe, R.P. Steele, C.C. Williams, Nano Lett. **16**, 911 (2016). https://doi.org/10.1021/acs.nanolett.5b03725
21. W. Melitz, J. Shen, A.C. Kummel, S. Lee, Surf. Sci. Rep. **66**(1), 1 (2011). https://doi.org/10.1016/j.surfrep.2010.001
22. H. Diesinger, D. Deresmes, T. Mélin, Beilstein J. Nanotechnol. **5**, 1 (2014). https://doi.org/10.3762/bjnano.5.1
23. C. Barth, C.R. Henry, Nanotechnology **17**(7), S155 (2006). https://doi.org/10.1088/0957-4484/17/7/S09
24. T.E. Pan, L.-H.and Sullivan, V.J. Peridier, P.H. Cutler, N.M. Miskovsky, Appl. Phys. Lett. **65**(17), 2151 (1994). https://doi.org/10.1063/1.112775
25. K. Uchida, in *Nanoelectronics and Information Technology*, ed. by R. Waser (Wiley, 2012)
26. B.D. Terris, J.E. Stern, D. Rugar, H.J. Mamin, Phys. Rev. Lett. **63**(24), 2669 (1989). https://doi.org/10.1103/PhysRevLett.63.2669
27. A. Passian, A. Wig, F. Meriaudeau, T.L. Ferrell, J. Vac. Sci. Technol. **20**(1), 76 (2002). https://doi.org/10.1116/1.1428268

28. G. Mesa, E. Dobado-Fuentes, J.J. Sáenz, J. Appl. Phys. **79**(1), 39 (1996). https://doi.org/10.1063/1.360951
29. S. Belaidi, P. Girard, G. Leveque, J. Appl. Phys. **81**(3), 1023 (1997). https://doi.org/10.1063/1.363884
30. H.W. Hao, A.M. Baró, J.J. Sáenz, J. Vac. Sci. Technol. **9**(2), 1323 (1991). https://doi.org/10.1116/1.585188
31. O. Cherniavskaya, L. Chen, V. Weng, L. Yuditsky, L.E. Brus, J. Phys. Chem. B **107**(7), 1525 (2003). https://doi.org/10.1021/jp0265438
32. S. Gómez-Mõivas, J.J. Sáenz, R. Carminati, J.J. Greffet, Appl. Phys. Lett. **76**(20), 2955 (2000). https://doi.org/10.1063/1.126528
33. S. Gómez-Mõivas, L.S. Froufe-Pérez, A.J. Caamaño, J.J. Sáenz, Appl. Phys. Lett. **79**(24), 4048 (2001). https://doi.org/10.1063/1.1424478
34. G.M. Sacha, J.J. Sáenz, Appl. Phys. Lett. **85**(13), 2610 (2004). https://doi.org/10.1063/1.1797539
35. G.M. Sacha, A. Verdaguer, J. Martínez, J.J. Sáenz, D.F. Ogletree, M. Salmeron, Appl. Phys. Lett. **86**(12), 123101 (2005). https://doi.org/10.1063/1.1884764
36. S. Hudlet, M.S. Jean, C. Guthmann, J. Berger, Eur. Phys. J. B **2**(1), 5 (1998). https://doi.org/10.1007/s100510050219
37. W.R. Smythe, *Static And Dynamic Electricity* (Taylor & Francis, 1989)
38. J. Colchero, A. Gil, A.M. Baró, Phys. Rev. B **64**(24), 245403 (2001). https://doi.org/10.1103/PhysRevB.64.245403
39. A. Gil, J. Colchero, J. Gómez-Herrero, A.M. Baró, Nanotechnology **14**(2), 332 (2003). https://doi.org/10.1088/0957-4484/14/2/345
40. G. Gramse, G. Gomila, L. Fumagalli, Nanotechnology **23**(20), 205703 (2012). https://doi.org/10.1088/0957-4484/23/20/205703
41. A. Sadeghi, A. Baratoff, S.A. Ghasemi, S. Goedecker, T. Glatzel, S. Kawai, E. Meyer, Phys. Rev. B **86**(7), 075407 (2012). https://doi.org/10.1103/PhysRevB.86.075407
42. Y. Martin, D.W. Abraham, H.K. Wickramasinghe, Appl. Phys. Lett. **52**(13), 1103 (1988). https://doi.org/10.1063/1.99224
43. S. Hudlet, M. Saint Jean, B. Roulet, J. Berger, C. Guthmann, J. Appl. Phys. **77**(7), 3308 (1995). https://doi.org/10.1063/1.358616
44. J.D. Jackson, *Classical Electrodynamics*, third edition edn. (De Gruyter, 2002)
45. L.N. Kantorovich, A.I. Livshits, M. Stoneham, J. Phys.: Condens. Matter **12**(6), 795 (2000). https://doi.org/10.1088/0953-8984/12/6/304
46. A. Sadeghi, A. Baratoff, S. Goedecker, Phys. Rev. B **88**(3), 035436 (2013). https://doi.org/10.1103/PhysRevB.88.035436

Chapter 8
Precise Modeling of Electrostatic Interactions with Dielectric Samples in Kelvin Probe Force Microscopy

Ali Sadeghi

Abstract Kelvin Probe Force Microscope (KPFM) maps the nanometer-scale variations of the electric potential over the probed sample surface. Since this is done by locally minimizing the force felt by the microscope tip with respect to the applied bias voltage, a true model of the bias-dependent contribution to the probe-sample interactions is essential when interpreting the KPFM maps. One requires to evaluate not only the long-range electrostatic force between tip and sample but also the electric field underneath the tip apex. The electric field influences greatly the short-range chemical interactions at the contact point. A rich complexity emerges as a result of penetration of the field into the dielectric samples. In this Chapter, we address the electrostatics of several tip-sample setups and aim to develop convenient models for understanding the measurements involving voltage-biased probes over dielectric samples, estimation of lateral resolution, and prediction of trends as a function of relevant parameters. Exact and compact approximate expressions for the capacitance and its first and second vertical gradients, and the profile and effective width of the electric field are derived for a spherical model tip atop thin or thick dielectric layers coated on a flat electrode. For more realistic tip-cantilever-sample geometries, a numeric finite-difference method on an adjustable nonuniform mesh is introduced to determine the same quantities with high accuracy.

8.1 Introduction

Numerous scanning probe microscopy techniques are nowadays available for studying local properties of various surfaces. Achieving spatial resolutions down to the atomic scale is possible in many of these techniques provided that the scanning tip mounted with a sharp apex comes so close to the surface that the detected signal is dominantly influenced by one or a few surface atoms in the vicinity of the tip apex. At the next step, a robust model of the imaging mechanism is needed to

A. Sadeghi (✉)
Department of Physics, Shahid Beheshti University, G. C., 19839 Tehran, Iran
e-mail: ali_sadeghi@sbu.ac.ir

S. Sadewasser and T. Glatzel (eds.), *Kelvin Probe Force Microscopy*,
Springer Series in Surface Sciences 65, https://doi.org/10.1007/978-3-319-75687-5_8

truly interpret the atomic scale variation of the recorded image map and to connect it to the physical properties of the sample surface.

One notable example is the non-contact atomic force microscopy (nc-AFM) in which the surface imaging is based on the deflection of the cantilever beam. The recorded signal, i.e. the shift in the vibration frequency of the cantilever, is interpreted as a signature of the tip-sample interaction (and hence surface topography). nc-AFM may be extended beyond topography measurements by focusing on only one type of tip-sample interaction. Of particular importance in this context is Kelvin probe force microscopy (KPFM) in which the so-called *local* contact potential difference (CPD) is mapped by locally minimizing the frequency shift with respect to the applied bias voltage between the tip and the sample back-electrode. A deep understanding of the atomic scale variations of KPFM images is possible only if the bias-dependence of both the long-range (capacitive) and the short-range (chemical) contributions to the tip-sample interactions are known. The situation can be rather complicated in case of KPFM experiments on non-conducting samples, because owing to electric field penetration into the dielectric sample, the tip shank and the cantilever affect the capacitive force and its gradient even at sub-nanometer tip-surface separations where atomic-scale contrast appears. In this Chapter, we first investigate the electrostatics of a model spherical tip over dielectric samples from an analytic point of view. We will then review efficient *numeric* solutions to the Poisson's equation that aim to present more reliable description of the tip-sample electrostatics by treating realistic model probes.

8.2 Analytic Approach

The most relevant length parameters influencing the atomic-scale contrast of imaging experiments are the tip radius R, its separation from the sample surface s, and the sample thickness h. To estimate the lateral resolution of the measurements, analytic expressions for the capacitance, electrostatic (ES) force, and its vertical gradient as functions of R, s, and h are highly desirable. Moreover, the lateral spread of the electric field at the top and bottom interfaces of a uniform dielectric layer coating a flat electrode provides useful estimates of the lateral resolution of local CPD or surface charge variations.

Metallic Samples

A system of an arbitrary arrangement of metallic electrodes, point charges and external batteries that maintain the electrodes at constant potentials has been addressed by Kantorovich et al. [1]. For a flat conducting sample, Hudlet et al. [2] proposed an approximate analytic model by dividing the tip surface into infinitesimal surface elements. They assumed that the electric field and thus the local charge density on each surface element is the same as that of a dihedral capacitor with infinite planes in the same relative orientation as the surface element and the sample plane. The capacitance of the tip-sample system is determined from the total charge accumulated

on the tip surface, which for example gives $C = 2\pi\epsilon_0 R \ln(1 + R/s)$ for the simplest case, i.e. a conducting sphere at distance s form a flat surface. But this expression falsely vanishes at the $s \to \infty$ limit while the exact solution for an isolated conducting sphere predicts a finite capacitance $C_{\text{sph}} = 4\pi\epsilon_0 R$. We will show that their expression is accurate if C_{sph} is added to it (see 8.20). The missing term is constant and does not affect the force

$$F = \frac{1}{2}\frac{\partial C}{\partial s}V^2 = -\pi\epsilon_0 V^2 \left(\frac{R^2}{s(s+R)}\right) \tag{8.1}$$

that the plane exerts on the sphere. This approximate expression deviates from the exact solution of the conducting sphere-plane electrodes by only a few percent over a rather large range of separations. Hudlet et al. [2] also suggested that if the probe is composed of a conic body of height H and half-angle θ that is terminated by a spherical cap of radius R (and thus of height $R_c = (1 - \sin\theta)R$), its interaction with a conducting sample at distance s can be approximated as

$$\frac{F}{-\pi\epsilon_0 V^2} = \frac{RR_c}{s(s+R_c)} + k^2 \times \left[\ln\frac{H}{s+R_c} - 1 + \frac{R\cos^2\theta}{(s+R_c)\sin\theta}\right],$$

where $k(\theta) = 1/\ln[\tan(\theta/2)]$, the accuracy of which was verified by later numerical calculations [3–5]. Hoping that an accurate description of the *force* is obtained by applying their *ad hoc* derivation to other probe geometries, a formally similar approach has been used to derive analytic expressions and estimates for the lateral resolution in KPFM for a parabolic tip and tilted cantilever [6]. Such analytic expressions for metallic samples are commonly adopted by the community.

Dielectric Samples

The presence of dielectric samples and coated layers, on the other hand, makes the electrostatic problem much complicated because of partial penetration of the electric field into the dielectrics. No exact analytic solution there exists even for a cylindrically symmetric probe, illustrated in Fig. 8.1a. A spherical tip on an infinitely thick insulating layer has an exact solution in terms of an infinite sequence of image charges. The solution may be extended to the case of a dielectric sample with finite thickness to give an estimation of the significance of thickness as a function of R and s [7]. By truncation the series, compact approximate expressions for the sphere-sample capacitance and force will be derived in the following which are useful for modeling and analysing the experiment results on dielectric samples.

8.2.1 Spherical Tip Against Semi-infinite Dielectric

The starting point is to decouple the problem of a sphere facing a semi-infinite dielectric into two textbook problems: a point charge near a conducting sphere, or

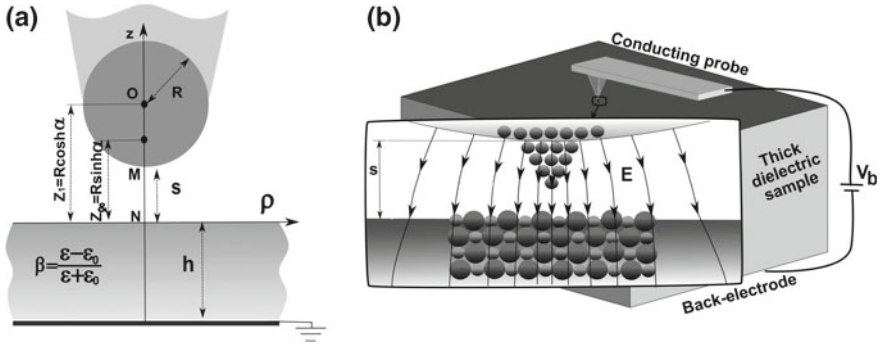

Fig. 8.1 **a** A model tip with cylindrical symmetry over a uniform dielectric slab of thickness h grounded at the bottom. The probe-sample separation is s. The apex is considered as a conducting sphere of the same radius R as the probe apex. Image charges which sum up to the charge on the sphere are located between z_1 and z_∞ (see text). The electric field on points M and N are of special importance because they polarize the sample and the apex atoms, respectively. **b** A realistic model probe with more complicated geometry and very different length scales. Zoom window illustrates how the electric field **E** is felt as an external field by the atomistic subsystem underneath the apex. Adapted with permission from [5, 7]. Copyrighted by the American Physical Society

a semi-infinite dielectric [8]. In the first problem, a point charge q a distance $r > R$ away from the center of a conducting sphere of radius R induces an image of magnitude $-qR/r$ inside the sphere at distance R^2/r from the center. The charge and its image are on the same radial line. One can show that the Coulomb potentials of these two point charges cancel each other out over the sphere surface, leaving it an equipotential surface. In the second problem, i.e. a point charge q in vacuum a distance z_q away from the surface of a semi-infinite dielectric of relative permittivity ϵ_r, the electric potential outside the dielectric ($z \geq 0$) equals the sum of the Coulomb potentials of the charge and its mirror image with respect to the dielectric surface (i.e. at $-z_q$) but with a magnitude reduced to $-\beta q$. For the sake of convenience, we characterize the dielectric by the unit-less quantity

$$\beta \equiv \frac{\epsilon_r - 1}{\epsilon_r + 1},$$

which ranges from 0 for vacuum to 1 for metals. In practice, β is rarely smaller than 0.6. Some typical values of β are 0.59 for PMMA and SiO_2, 0.71 for NaCl, 0.8 for Al_2O_3, 0.86 for Si, 0.92 for HfO_2, and 0.93–0.98 for $LiNbO_3$ [9].

The physical interpretation of an image charge put behind a surface is that it represents the effect of the polarization induced at that surface. If the sphere is atop the semi-infinite dielectric, the polarization on both surfaces should be represented at the same time. This needs more than a single image charge. The images are added iteratively until the boundary conditions is satisfied on both surfaces. The first point charge $q_1 = 4\pi\epsilon_0 RV$ is put at the sphere center ($z_1 = R + s$) to make the sphere surface a V-equipotential one. However, q_1 induces also an image $-\beta q_1$ at $-z_1$ within

the dielectric as explained above. When the charge $-\beta q_1$ is present, the potential on the sphere surface is no longer V unless a second point charge $q_2 = \beta q_1 R/2z_1$ is present at $z_2 = z_1 - R^2/2z_1$. Now, an image $-\beta q_2$ is induced at $-z_2$ to represent the polarization by q_2 on the dielectric surface. Then the image of q_2 within the sphere is required to bring its surface potential back to V and so forth. The series of point charges inside the sphere can be shown to be given by

$$q_1 = 4\pi\epsilon_0 RV \qquad q_{n+1} = \frac{\beta q_n R}{z_1 + z_n} \tag{8.2}$$

$$z_1 = R + s \qquad z_{n+1} = z_1 - \frac{R^2}{z_1 + z_n} \tag{8.3}$$

while the corresponding images below the dielectric surface (inside the dielectric) are $\{-\beta q_n, -z_n\}$. If there are additional localized charges/dipoles on the symmetry axis (attached to the tip apex or the sample surface), the same procedure gives the corresponding image charges/dipoles (see, e.g., [10]). Note that $q_{n+1}/q_n = \beta R/(R + s + z_n) < 1$, i.e. the series of charges is linearly convergent unless if $s \to 0$ and $\beta \to 1$ which corresponds to the unphysical case of a sphere at potential V touching a conducting plane at zero potential. The force felt by the sphere is equal to the sum of Coulomb forces exerted on all image charges inside the sphere by those inside the dielectric. Equation (8.13) gives the closed form of this force.

Green's Function of Semi-infinite Dielectric

The so-called Green's function (GF) is both technically and conceptually a very useful tool in our electrostatics approach. Generally, the Green's function $G(\mathbf{r}, \mathbf{r}')$ is the solution of the Poisson's equation at arbitrary point $\mathbf{r}$ in space if a point unit charge (in the Gaussian units system) is placed at position $\mathbf{r}'$. Once the GF is determined for the given boundary conditions, for a localized charge distribution $\rho(\mathbf{r})$ the superposition gives the electric potential as $\Phi(\mathbf{r}) = \frac{1}{4\pi\epsilon_0}\int \rho(\mathbf{r}')G(\mathbf{r}, \mathbf{r}')d^3r'$ in the SI units system.

The most trivial GF is that in vacuum, namely

$$G(\mathbf{r}, \mathbf{r}') = \frac{1}{|\mathbf{r} - \mathbf{r}'|}.$$

For a probe with cylindrical symmetry, all image charges are put on the z-axis of the coordinates system. In the ρ-z plane, for the sake of simplicity, we adopt the notation

$$\mathcal{G}(\mathbf{r}, z') = \frac{1}{\sqrt{\rho^2 + (z - z')^2}} \tag{8.4}$$

for the GF at point $\mathbf{r} = (\rho, z)$ due to an isolated unit charge at $\mathbf{r}' = (0, z')$. We will express the GF of several geometries in terms of (8.4). For instance, based on the image charges method, if a unit charge is placed on the z axis a distant z_n away from the dielectric surface, i.e. at point $(0, z_n)$, the geometry dependence of the

electrostatic potential in vacuum is given by

$$G_n^+(\mathbf{r}) = \mathcal{G}(\mathbf{r}, z_n) - \beta\mathcal{G}(\mathbf{r}, -z_n), \tag{8.5}$$

where $G_n^+(\mathbf{r}) \equiv G^+(\mathbf{r}, z_n)$ is the GF of the dielectric surface for the $z \geq 0$ region. Similarly, the GF inside the dielectric ($z \leq 0$) reads

$$G_n^-(\mathbf{r}) = (1 - \beta)\mathcal{G}(\mathbf{r}, z_n). \tag{8.6}$$

In the probe-dielectric system, a series of charges, e.g. (8.2), replace the probe and the resulting electric potential reads

$$\Phi(\mathbf{r}) = \frac{1}{4\pi\epsilon_0} \sum_{n=1}^{\infty} q_n G_n(\mathbf{r}). \tag{8.7}$$

Electric Field

The electric field $\mathbf{E} = \frac{-1}{4\pi\epsilon_0} \sum q_n \nabla G_n$ can be inserted into atomistic models [11, 12] or simulations [5] to take into account the bias-induced polarization of atoms underneath the tip apex, as illustrated in Fig. 8.1b. The resulting local dipoles greatly influence the atomic-scale contrast in KPFM [12]. On the sample surface, the electric field is dominantly determined by its vertical component given by

$$E_z\Big|_{z=0} = \frac{1 + \beta}{4\pi\epsilon_0} \sum_{n=1}^{\infty} \frac{q_n z_n}{(\rho^2 + z_n^2)^{3/2}} \tag{8.8}$$

The maximum strength of the electric field in the apex-sample gap occurs at ($\rho = 0, z = 0$) and reads

$$E_N = \frac{1 + \beta}{4\pi\epsilon_0} \sum_{n=1}^{\infty} \frac{q_n}{z_n^2}. \tag{8.9}$$

Away from this point, the electric field strength decreases monotonically. The variation of E_z over the sample surface, as a function of ρ is shown in Fig. 8.2a. To characterize field localization, one can define an effective width $\rho_{1/2}$ for the field as the radial distance at which $E_z|_{z=0}$ drops to $\frac{1}{2}E_N$. The separation dependence of $\rho_{1/2}$ is shown in Fig. 8.2b.

If the dielectric is very dilute ($\beta \simeq 0$) or if the sphere-dielectric distance is too large, then the sphere-dielectric combination becomes practically an isolated sphere the field from which is in turn identical to that of a single point charge q_1 at the sphere center. In that case the field width $\rho_{1/2}$ of the sphere approaches the asymptotic linear regime of a point-charge, i.e. $\rho_{1/2} = \sqrt{2^{2/3} - 1}(R + s) \simeq 0.766(R + s)$, as seen in Fig. 8.2b. On the other hand, for a conducting sample, i.e. $\beta = 1$, the effective width

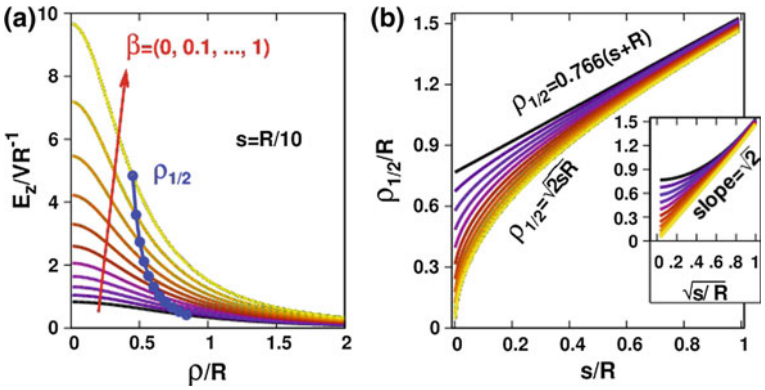

Fig. 8.2 **a** Field radial profile just outside the sample surface, $E_z|_{z=0}$, for a conducting sphere of radius R separated by $s = 0.1R$ from a semi-infinite dielectric for different values of β. Solid dots indicate $\rho_{1/2}$ at which the field drops to $\frac{1}{2}E_N$. **b** Variation of $\rho_{1/2}/R$ against s/R and $\sqrt{s/R}$ (inset). Adapted with permission from [7]. Copyrighted by the American Physical Society

approaches as $s^{1/2}$ towards zero (if the sphere touches the conducting sample surface E_N becomes infinite and thus $\rho_{1/2}$ vanishes). As better seen in the inset, $\rho_{1/2} = \sqrt{2Rs}$ for $s \ll R$. For many of commonly used solid dielectric samples $\beta > 0.6$, meaning that for very small separations, $\rho_{1/2}/R \ll 1$ and the field is highly localized.

An alternative definition of $\rho_{1/2}$ on the sample surface is the effective polarization radius, i.e. the radius of a circle that encloses half of surface polarization charge underneath the tip. This definition results in profiles very similar to those above. On the probe surface, the angular half-width defined as the angle that encloses half of surface polarization charge over the sphere surface which results in a formally similar conclusion [7].

Closed-Form Expressions

The sequence given by (8.2) may be expressed in a closed form. Similar to the case of two conducting spheres that is worked out in [13], eliminating z_n the sequence may be rearranged as a second order homogeneous difference equation

$$\frac{1}{q_n} = \left(\frac{2\cosh\alpha}{\beta}\right)\frac{1}{q_{n-1}} - \left(\frac{1}{\beta^2}\right)\frac{1}{q_{n-2}},$$

where $\cosh\alpha = 1 + s/R$, the solution of which can be expressed in terms of a linear combination of $\exp(\pm n\alpha)$ as

$$q_n = q_1 \sinh\alpha \times \frac{\beta^{n-1}}{\sinh n\alpha}, \tag{8.10}$$

$$z_n = R\sinh\alpha \times \coth n\alpha. \tag{8.11}$$

The latter equation is obtained by plugging (8.10) in (8.2). This general solution for semi-infinite dielectric sample of arbitrary β reduces to the solution for a conducting sample if $\beta = 1$. Now, a very convenient expression for the capacitance is also in hand

$$C = \frac{1}{V}\sum_{n=1}^{\infty} q_n = 4\pi\epsilon_0 R \sinh\alpha \times \sum_{n=1}^{\infty} \frac{\beta^{n-1}}{\sinh n\alpha}, \tag{8.12}$$

where the charge accumulated on the sphere surface is calculated as the sum of the image charges inside it. The vertical derivatives $C' = \partial C/\partial s$ and $C'' = \partial^2 C/\partial s^2$ provide corresponding closed-form expressions for the force on the tip ($F = \frac{1}{2}C'V^2$) as

$$F = 2\pi\epsilon_0 V^2 \sum_{n=2}^{\infty} \frac{\beta^{n-1}}{\sinh n\alpha}\big(\coth\alpha - n\coth n\alpha\big), \tag{8.13}$$

and for the force-gradient ($F' = \partial F/\partial s$) as

$$F' = \frac{2\pi\epsilon_0 V^2}{R\sinh\alpha}\sum_{n=2}^{\infty} \frac{\beta^{n-1}}{\sinh n\alpha} \times \left[\frac{n^2}{\sinh^2 n\alpha} - \frac{1}{\sinh^2\alpha} + n\coth n\alpha(n\coth n\alpha - \coth\alpha)\right]. \tag{8.14}$$

The latter is proportional to the shift of the resonance frequency of the deflection sensor in small amplitude experiments and thus can be used for controlling the tip-sample separation [14].

Note that the first term in the expression for the capacitance (q_1/V) represents the capacitance of an isolated conducting sphere in vacuum, $C_{\text{sph}} = 4\pi\epsilon_0 R$. This constant term in the series is eliminated by taking the derivatives to obtain the expressions for the force and force-gradient. As already mentioned, the same term is missing in Hedlet's [2] expression for C but does not affect their approximate expression for the force, (8.1). The term, however, contributes to the electric field, the maximum of which just outside the sample surface, (8.9), now reads

$$E_N = \frac{V}{R}\left(\frac{1+\beta}{\sinh\alpha}\right)\sum_{n=1}^{\infty} \frac{\beta^{n-1}\sinh n\alpha}{\cosh^2 n\alpha}. \tag{8.15}$$

Compact Approximate Expressions

For small separations, the charge series converges slowly and many terms must be considered for calculating (8.12–8.15). By adapting the procedure suggested by Kantorovich et al. [15], as explained here, the error induced by truncating the series becomes negligible. The idea is that the position of the image charges, (8.11), approaches $z_\infty = R\sinh\alpha$ exponentially, i.e. as $\exp(-2n\alpha)$, meaning that many of

charges are practically lumped at z_∞. In other words, the positions of the first k charges are calculated by (8.11) while for the rest $z_{n>k} \simeq z_\infty$. Noting that $q_{n+1}/q_{n>k} \simeq \beta R/(z_1 + z_\infty) = \beta e^{-\alpha}$, the magnitude of the lumped charge at z_∞ is obtained analytically

$$q_{corr}^{(k)} \equiv \sum_{n=k+1}^{\infty} q_n \simeq \frac{q_{k+1}}{1-\beta e^{-\alpha}} = \frac{q_1 \beta^k/(1-\beta e^{-\alpha})}{\sinh[(k+1)\alpha]/\sinh\alpha}. \tag{8.16}$$

If this correction is added to the truncated series at the kth term, the truncation error is drastically reduced. The maximum error of approximating the capacitance as

$$C^{(k)} = \frac{1}{V}\Big(\sum_{n=1}^{k} q_n + q_{corr}^{(k)}\Big) \tag{8.17}$$

is listed in Table 8.1 for several separations (from $s = R/10$ to $s = R$) for a dielectric or conducting surface. Compact, accurate analytical expressions may be gained by keeping few terms of the series but including also the corresponding correction given by (8.16). In particular, the capacitance, (8.12), is approximated within 5% by

$$C^{(1)} - C_{\text{sph}} \simeq 2\pi\epsilon_0 R\Big(\frac{\beta/(1-\beta e^{-\alpha})}{\cosh\alpha}\Big) \tag{8.18}$$

if only the first term is kept, and within 1% by

$$C^{(2)} - C_{\text{sph}} \simeq 2\pi\epsilon_0 R\Big(\frac{\beta}{\cosh\alpha} + \frac{\beta^2/(1-\beta e^{-\alpha})}{4\cosh^2\alpha - 1}\Big) \tag{8.19}$$

if two terms are included.

To see the efficiency of including the correction term, one may truncate the sum in (8.12) at the second term to obtain $C(s) \simeq 2\pi\epsilon_0 R\beta/(1 + s/R)$. This expression gives the correct asymptotic behavior $C - C_{\text{sph}} = 2\pi\epsilon_0\beta R^2/s$ for $s \gg R$. But for small separations the error is very large, (e.g. 33% at $s = R/10$). By including the correction

Table 8.1 Relative error of approximating the capacitance by (8.17), or using Hudlet's formula, (8.20) [2]

s/R	$\beta = 0.71$ (NaCl)				$\beta = 1$ (conductor)				Equation (8.20)
	k = 1	2	10	20	1	2	10	20	
0.1	0.02	0.004	10^{-7}	10^{-15}	0.05	0.01	10^{-7}	10^{-13}	0.0203
0.2	0.008	0.001	10^{-11}	$<10^{-16}$	0.02	0.002	10^{-8}	$<10^{-16}$	0.016
0.5	0.001	10^{-5}	10^{-16}	$<10^{-16}$	0.003	10^{-4}	10^{-14}	$<10^{-16}$	0.009
1.0	10^{-4}	10^{-6}	10^{-16}	$<10^{-16}$	10^{-4}	10^{-5}	10^{-16}	$<10^{-16}$	0.004

term $q^{(2)}_{\text{corr}}$, then (8.19) is obtained which is 1% accurate at $s = R/10$. As seen in the last column of Table 8.1, the approximation proposed by Hudlet et al. [2]

$$C - C_{\text{sph}} = 2\pi\epsilon_0 R \ln\left(1 + \frac{R}{s}\right), \tag{8.20}$$

(their original expression is corrected by adding C_{sph}) is remarkably accurate at moderate separations. Their expression is only applicable to conducting samples while the corresponding compact expressions are given by (8.18 and 8.19) is useful for theoretical modeling on insulating samples with an accuracy comparable to their expression.

Touching-Limit Values

The sphere-sample interaction increases as their separation decreases. When the sphere touches the sample surface (8.10) and (8.11) reduce to

$$q_n\big|_{s=0} = \frac{q_1\beta^{n-1}}{n},$$
$$z_n\big|_{s=0} = \frac{R}{n}.$$

For a perfect conducting sample, the capacitance $C|_{s=0} = 4\pi\epsilon_0 R\sum_{n=1}^{\infty} 1/n$ is infinite. The divergent harmonic series $\sum \frac{1}{n}$ appears also when evaluating the force and the field. However, note that the $s = 0, \beta = 0$ limit corresponds to an unphysical case mentioned before. In contrast, over a dielectric sample, the sum $\sum \beta^{n-1}/n$ remains finite, and the capacitance when the sphere touches the dielectric surface reads

$$C_{max} = -4\pi\epsilon_0 R\left(\frac{\ln(1-\beta)}{\beta}\right). \tag{8.21}$$

Similarly, the upper bounds of the force, force-gradient, and electric field at the contact point are attained at $s = 0$ as

$$F_{max} = -\frac{2}{3}\pi\epsilon_0 V^2\left[\frac{\ln(1-\beta)}{\beta} + \frac{1}{(1-\beta)^2}\right], \tag{8.22}$$

$$F'_{max} = \frac{4\pi\epsilon_0 V^2}{45R}\left[\frac{\ln(1-\beta)}{\beta} + \frac{1}{(1-\beta)^2} + \frac{21\beta}{(1-\beta)^4}\right], \tag{8.23}$$

$$E_{N,max} = \frac{V}{R}\frac{1+\beta}{(1-\beta)^2}. \tag{8.24}$$

Note that F_{max} is independent of R, because $z_n \propto q_n$ in the $s = 0$ limit [16]. The dependence of these quantities on β is shown on a semi-logarithmic scale in Fig. 8.3. The relevant range of $\beta > 0.6$ is highlighted. For the exemplified case of NaCl ($\beta = 0.71$, indicated by circles): $C_{max}/\pi\epsilon_0 R = 6.98$, $F_{max}/\pi\epsilon_0 V^2 = -6.77$ (i.e. $F_{max} = -0.188$ nN if $V = 1$ V), $F'_{max}/\pi\epsilon_0 V^2 R^{-1} = 188.7$, and $E_{N,max}/VR^{-1} = 20.4$. When

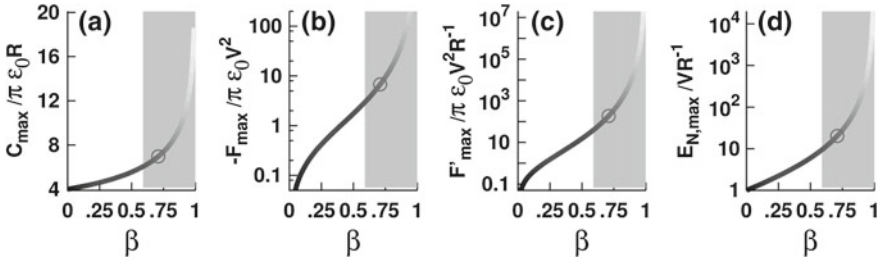

Fig. 8.3 Upper bounds of C, $-F$, F', and E_N (in units $\pi\epsilon_0 R$, $\pi\epsilon_0 V^2$, $\pi\epsilon_0 V^2 R^{-1}$, and VR^{-1}, respectively) as a function of β. The physically relevant range is shaded while the values for NaCl are indicated by circles ($\beta_{\mathrm{NaCl}} = 0.71$). The bounds are attained for a conducting sphere touching ($s = 0$) the semi-infinite dielectric surface. Adapted with permission from [7]. Copyrighted by the American Physical Society

the sphere-sample distance increases, all four quantities decrease monotonically. It will be shown that if the sphere is equipped with a tip shank and then a cantilever, the force, force gradient and field strength are weaker due to the spread of the polarized charges to those parts at least for very small separations (see Figs. 8.7c and 8.8). Therefore, the expressions introduced here provide useful upper bounds of the corresponding quantities.

8.2.2 Dielectric Slab

The availability of GF for a dielectric sample of infinitely large thickness, (8.5), allows one to address analytically the electrostatics of a sphere close to its surface. Here we derive an analytical GF for a dielectric slab sample with finite thickness grounded at the bottom surface. The GF is used to evaluate the capacitance and the field localization for a point-like probe and a spherical one in front of a dielectric slab sample.

Green's Function of Slab

Assume that a point charge is put on the z axis in vacuum a distant $z_n > 0$ away from the surface of a uniform dielectric slab of thickness h. As shown in Fig. 8.4a, the slab is grounded at the bottom while, similar to the semi-infinite dielectric, the plane $z = 0$ and the slab top surface coincide. The general form of the cylindrically symmetric GF [8] above and inside the slab is

$$G_n^+(\mathbf{r}) = \int_0^\infty \left(e^{-k|z-z_n|} + A_1 e^{-kz}\right) J_0(k\rho)dk, \tag{8.25}$$

$$G_n^-(\mathbf{r}) = \int_0^\infty \left(A_2 e^{-kz} + A_3 e^{+kz}\right) J_0(k\rho)dk, \tag{8.26}$$

where J_0 is the zero order Bessel function of the first kind for which [8]

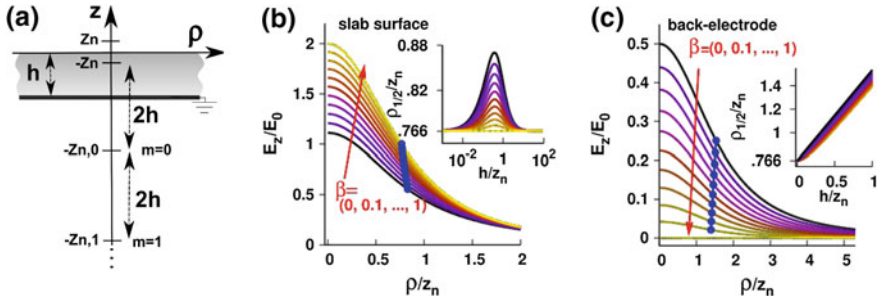

Fig. 8.4 **a** Positions of the image charges induced below a dielectric slab grounded on the bottom when a point charge is put at z_n. **b** Field radial profile just outside the dielectric slab ($E_z|_{z=0}$) if $h = z_n$. The length is normalized to z_n, and the electric field to $E_0 = q_n/4\pi\epsilon_0 z_n^2$ (the field at distance z_n from the point charge if were isolated in vacuum). Solid dots indicate the half-width $\rho_{1/2}$; its variation with h is depicted in the inset; **c** Same as (b) but on the slab-electrode interface. $\rho_{1/2} = 0.766(h + z_n)$ for $\beta = 0$. Adapted with permission from [7]. Copyrighted by the American Physical Society

$$\int_0^\infty e^{-k|z-z_n|} J_0(k\rho) dk = \frac{1}{\sqrt{\rho^2 + (z - z_n)^2}} = \mathcal{G}(\mathbf{r}, z_n) \tag{8.27}$$

(see 8.4). Three boundary conditions on the two surfaces of the slab

$$\begin{aligned} \frac{\partial G_n^+}{\partial z}\Big|_{z=0} &= \epsilon_r \frac{\partial G_n^-}{\partial z}\Big|_{z=0}, \\ G_n^+\Big|_{z=0} &= G_n^-\Big|_{z=0}, \\ G_n^-\Big|_{z=-h} &= 0 \end{aligned}$$

determine the coefficients

$$\begin{aligned} A_1 &= -(\beta + e^{-2kh}) A e^{-kz_n}, \\ A_2 &= (\beta - 1) e^{-2kh} A e^{-kz_n}, \\ A_3 &= (1 - \beta) A e^{-kz_n}, \end{aligned}$$

where

$$A = \frac{1}{1 + \beta e^{-2kh}} = \sum_{m=0}^{\infty} (-\beta)^m e^{-2mkh}.$$

Extending to the case of a multilayer slab needs that separate boundary conditions are applied to each interface. By substituting the coefficients and using (8.27), the GF at an arbitrary field point $\mathbf{r}$ above the surface or inside the slab is obtained as

$$G_n^+(\mathbf{r}) = \mathcal{G}(\mathbf{r}, z_n) - \beta\mathcal{G}(\mathbf{r}, -z_n) - (1-\beta^2)\sum_{m=0}^{\infty}(-\beta)^m\mathcal{G}(\mathbf{r}, -z_{nm}), \tag{8.28}$$

$$G_n^-(\mathbf{r}) = (1-\beta)\sum_{m=0}^{\infty}(-\beta)^m\Big[\mathcal{G}(\mathbf{r}, z_{nm-1}) - \mathcal{G}(\mathbf{r}, -z_{nm})\Big], \tag{8.29}$$

where

$$z_{nm} = z_n + 2(m+1)h.$$

A different approach for driving these expressions is presented by Lyuksyutov et al. [17].

Interpreting the obtained GF is instructive. First of all note that a conducting sample corresponds to either $\beta = 1$ or $h = 0$, for which the above expressions give the trivial GF of a metallic plane. On the other hand, in the $h \to \infty$ limit the sum in (8.28) vanishes and (8.5) is recovered, while the only non-vanishing term in (8.29) is $\mathcal{G}(\mathbf{r}, z_{n0} - 2h) = \mathcal{G}(\mathbf{r}, z_n)$, such that (8.6) is recovered. For a point charge q_n at distance z_n above an infinitely thick dielectric slab, the potential in vacuum equals the sum of the Coulomb potentials of q_n and that of an image $-\beta q_n$ at $(0, -z_n)$ if the whole region were vacuum, while a single point charge $(1-\beta)q_n$ at $(0, z_n)$ describes the potential inside the dielectric.

For finite h the field lines become perpendicular to the slab-electrode interface, a condition that is satisfied if the charge $(1-\beta)q_n$ at $(0, z_n)$ is mirror reflected with respect to the back-electrode. Therefore, a charge $-(1-\beta)q_n$ a distance $z_n + h$ below the back-electrode, i.e. at $(0, -z_n - 2h)$ is included. These two image charges correspond to the $m = 0$ terms in (8.29). The boundary conditions on the top surface of the slab is no longer satisfied unless the charge below the electrode is reflected with respect to the slab top face: a new image $\beta(1-\beta)q_n$ is therefore put at $(0, z_n + 2h)$. This in turn induces an image $-\beta(1-\beta)q_n$ with respect to the electrode at $(0, -z_n - 4h)$. The latter two charge are represented by the $m = 1$ terms in (8.29). Again the boundary conditions on the slab top surface need to be satisfied by including a new image charge, and so on. The image charges below the back-electrode make an infinite, alternating, convergent series of image charges $(1-\beta)(-\beta)^m q_n, m = 0, 1, 2, \ldots$, that are distributed at equal distances $2h$ as illustrated schematically in Fig. 8.4a. They, along with their images with respect to the back-electrode represent the polarization on the slab-electrode interface. This image charges series contributes to the potential in the vacuum above the slab top-face and appears as the third term in (8.28). (Note that a charge q below the vacuum-dielectric interface induces a potential in the vacuum side equivalent to that of a charge $(1+\beta)q$ at the same position if the whole space were filled with the same dielectric [8].)

Electric Field Profile for Point Charge Against Slab

The z-component of the electric field caused by a single point charge on the slab surface and on its interface with the back-electrode as a function of radial distance ρ is shown in Fig. 8.4b and c. With a larger β, the field penetration into the dielectric decreases resulting in a stronger field on the vacuum-slab interface but a weaker one

within the slab and over the back-electrode. The field half-width on either interface is almost insensitive to β variations, but depends on the slab thickness as seen in the insets (the charge-surface distance is used as the length unit). Over the back-electrode the half-width increases almost linearly with the slab thickness, close to the line $\rho_{1/2} = \sqrt{2^{2/3} - 1}(h + z_n) \simeq 0.766(h + z_n)$ for $\beta = 0$. Therefore, if the thickness is e.g. doubled the field localization over the electrode is halved. In contrast, over the slab surface $\rho_{1/2}$ shows a short peak when the slab thickness is comparable to its distance from the charge. Otherwise, the field half-width remains close to $\sim 0.77 z_n$ independent of the slab thickness: for a given charge distance smaller than h, the field localization over the slab surface does not change by further increasing h.

8.2.3 *Spherical Tip Atop Grounded Dielectric Slab*

Recall the sphere against semi-infinite dielectric sample. The sphere is replaced by a set of point charges inside it, on the symmetry axis and distributed between the sphere center and $z_\infty = R \sinh \alpha$. Each charge within the sphere induces a mirror image below the sample surface. Now, if the thickness of the dielectric is finite, (8.28) implies that an additional series of images are also induces below the back-electrode.

We are interested only in the images within the sphere (because their sum gives the net accumulated charge on the sphere surface and hence the capacitance). A point charge q at z_q (within the sphere) has a series of images below the slab surface, the images of which within the sphere are given by

$$Q_{-1}(q, z_q) = q\beta \left[\frac{R}{R + s + z_q} \right], \tag{8.30}$$

$$Q_m(q, z_q) = q(1 - \beta^2)(-\beta)^m \left[\frac{R}{R + s + z_q + 2(m + 1)h} \right], m \geq 0 \tag{8.31}$$

located at

$$Z_m(z_q) = R + s - \frac{R^2}{R + s + z_q + 2(m + 1)h}, m \geq -1. \tag{8.32}$$

Note that (8.2) and (8.3) have been incorporated in these expressions as the $m = -1$ term (if $h \to \infty$ those equations are recovered because only Q_{-1} is nonzero).

To solve the combined sphere-slab problem, one puts a first point charge $q = 4\pi\epsilon_0 RV$ at the sphere center $z_q = R + s$ to make an equipotential surface at potential V on it. An infinite sequence of images $Q_m(q, z_q), m \geq -1$ are induced inside the sphere, to compensate the effect of the image charges below the slab surface and bring the sphere surface potential back to V. Each Q_m induces in turn an infinite sequence of images $Q_l[Q_m, Z_m]$, and so on. The resulting infinite number of

sequences are to be approximately evaluated on computer by truncation each series at a small enough term. Summing up all the image charges within the sphere

$$CV = q + \sum_{m=-1}^{\infty} Q_m(q, z_q) + \sum_{l,m=-1}^{\infty} Q_l[Q_m(q, z_q), Z_m(z_q)] + \ldots , \tag{8.33}$$

where $q = 4\pi\epsilon_0 RV, z_q = R + s$, one calculates the capacitance of the sphere-slab system. In practice, $|Q_m(q, z_q)/q| < 10^{-16}$ already for $m \sim 10$ with a set of relevant geometrical parameters. The number of series that have at least one term greater than a given threshold (e.g. $10^{-16}q$) is also not so large. One makes a one-dimensional array $\{q_n\}$ out of those charges that are greater than that threshold (10^{-16} is the machine precision). The array length depends on the geometrical parameters, in particular s/R and h/R. The array $\{q_n\}$, along with the GF given by (8.28) and (8.29), determine the electric field $-(4\pi\epsilon_0)^{-1} \sum q_n \nabla G_n$ in vacuum and inside the slab.

Electric Field Profile

The profile of the vertical component of the electric field over the slab surface is plotted in Fig. 8.5 for two different separations. For thicknesses larger than R, as seen in the insets of Fig. 8.5a and c, $\rho_{1/2}$ becomes independent of h and equals the semi-infinite dielectric value for the corresponding s (see Fig. 8.2b). Thus once h is as large as R, the field localization over the slab surface behaves similar to that on a semi-infinite sample in particular for smaller separations. On the other hand, similar to a point charge atop the slab, field penetration decreases as β increases, enhancing the field over the slab surface. For large β (e.g. a depleted semiconductor capping layer), the localization resembles the conducting sample for any slab thickness. The field half-width on the slab-electrode interface increases almost linearly with the slab thickness (see insets of Fig. 8.5b and d). For missing dielectric layer, the variation is exactly linear $\rho_{1/2} = 0.766(s + R + h)$ in agreement with the inset of Fig. 8.4b if s replaced by $s + h$ for separations comparable to R where the sphere can be approximated by a lumped charge at its center. In the $h \to 0$ limit, the $\beta = 1$ value of Fig. 8.2b is obtained on both surfaces on the slab ($\rho_{1/2}/R = 1.02$ or 0.45 for $s = R/2$ or $R/10$, respectively.) Finally, one notes that for experimentally interesting case of $s \ll h \leq R$, the field is much more localized on the slab surface than on the electrode.

Capacitance

An accurate evaluation of the sphere-slab capacitance is given by (8.33). As a typical value, one obtains for a NaCl ($\beta = 0.71$) slab of thickness $0.2R$ separated by $s = 0.2R$ from a sphere of radius R, as $C/\pi\epsilon_0 R = 7.22$. Note that this value is within the two limiting values 5.86 and 7.46 calculated using (8.12) for a semi-infinite slab ($h \to \infty$) and a conducting sample ($h = 0$), respectively. The dependence of the capacitance,

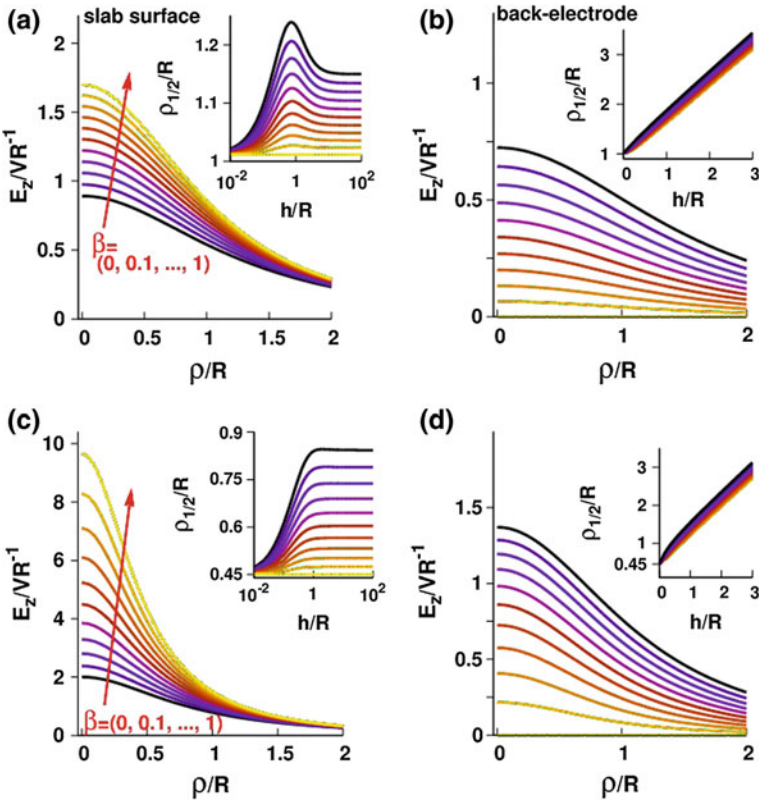

Fig. 8.5 Field radial profile just outside the surface of a slab of thickness $h = R/2$ (**a**, **c**) and on the slab-electrode interface (**b**, **d**) at two separations $s = R/2$ (**a**, **b**) and $R/10$ (**c**, **d**). Insets show the variation of half-widths with the slab thickness. Adapted with permission from [7]. Copyrighted by the American Physical Society

calculated by (8.33), on β, s, and h is shown in Fig. 8.6. The capacitance approximated by the Hudlet's formula [2], (8.20), is also plotted by dashed lines in Fig. 8.6a for companion. The latter should coincide the $\beta = 1$ curve for any separation s. The difference is within 2% for the examined range. However, for smaller separations than $R/100$ (not shown), the agreement is not good.

A strong dependence on β appears in the limit of small s/R. At large separations or for small slab thicknesses, the β-dependence of the capacitance is reduced. When s is very large, or for small β and very large thickness, the capacitance of the sphere-slab approaches the capacitance $C_{\text{sph}} = 4\pi\epsilon_0 R$ of an isolated sphere. The capacitance over an infinitely thick sample, given by (8.12), is plotted as straight dashed lines on Fig. 8.6b and c. This way one can see how the capacitance approaches (8.12) as the thickness increases to very large values. If h is at least two orders of magnitude larger than R the slab is thick enough to result the same capacitance as a semi-infinite one.

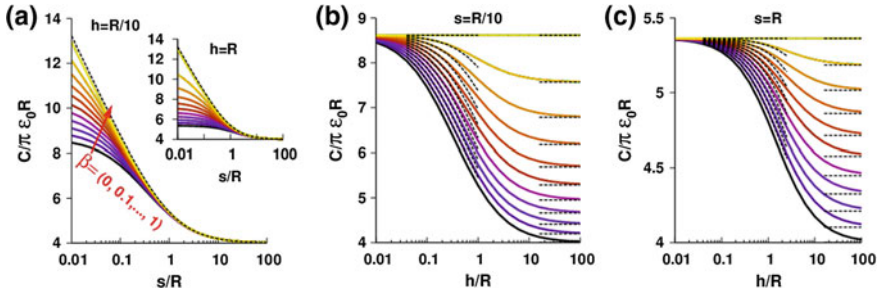

Fig. 8.6 Variation of the capacitance of a conducting sphere of radius R above a dielectric slab grounded at the bottom as a function of separation for $h = R/10$ (**a**) or $h = R$ (inset), or as a function of slab thickness for $s = R/10$ (**b**) or $s = R$ (**c**). Length is normalized to R, capacitance to $\pi\epsilon_0 R = \frac{1}{4}C_{\text{sph}}$. Dashed lines in (a) correspond to Hudlet's approximation [2], (8.20). In (**b**) and (**c**) the right dashed lines correspond to $h \to \infty$ (semi-infinite dielectric) while the left dashed lines correspond to replacing the slab with a vacuum layer of thickness h/ϵ_r. Adapted with permission from [7]. Copyrighted by the American Physical Society

Then the capacitance is approximately given by (8.12) within a few percent error (depending on β and s). This very slow approach is due to the significant polarization of the slab-electrode interface.

All curves are bounded by $\beta = 0$ and 1 cases which correspond to a biased sphere at respective separations $s + h$ and s from a perfect conductor. A very useful approximate expression is gained by interpolating between these two limits. Equation (8.12) for a conducting sample ($\beta = 1$) but a modified separation $s \to s + h/\epsilon_r$ is employed to plot dashed lines on the left hand side in Fig. 8.6b and c. For $s = R/10$, the difference between this approximation and the accurately calculated capacitance (solid lines) is less than one percent for $h \leq R/3$. For larger separations the error increases if h is small. However, for larger thicknesses up to $h = R$, as seen in Fig. 8.6c, the error does not excess one percent for separations as large as R. This observation implies that if an analytic solution is available for a non-spherical probe over a conducting sample (like Hudelt's formula [2]), it can be used for thin dielectric slabs as well by substituting s by $s + h/\epsilon_r$ within an accuracy that is estimated from Fig. 8.6b and c.

8.3 Numerical Approach

Deriving accurate analytic expressions is possible only for simple geometries. A general solution to the electrostatic boundary-value problem of the probe-sample with an arbitrary geometry needs numeric techniques. The main difficulty is the coexistence of different length scales (nm to μm, see Fig. 8.1b) that induces numerical errors and increases computational costs. We will review in the following some of the numeric methods and approximations proposed so far to address this non-trivial problem.

A simple, yet flexible finite-difference scheme to treat the electrostatic interactions between a conducting probe and dielectric samples is presented in details.

8.3.1 Numerical Image Charges Method

The application of the image charges method to the tip-sample electrostatics problem is already discussed in Sect. 8.2. The numerical variant of the image charges method is more flexible and can be applied to complex geometries. For a cylindrically symmetric probe, Belaidi et al. [18] placed a set of point charges on the probe axis and determined their positions and strengths by a nonlinear least squares fitting of the potential on the probe surface to the desired value. One may fix the positions of a set of point and line image charges on the symmetry axis while optimizing their magnitudes in the fitting procedure and study the role of the tip shape and the cantilever [19]. Such a *linearized* version of the numerical images charge method has been applied to conductive and *dielectric* samples [16, 20] and thin films on conducting substrates [21]. The implementation of the method, in particular in its linearized form, is straightforward and easier than other numeric method cited below. However, contrary to the analytic variant, the boundary conditions are satisfied only on a set of selected test points distributed rather arbitrarily on the probe surface and one has no estimation of the numerical error.

8.3.2 Real Space Discretization

A different class of numeric approaches to solve the Poisson's equation rely on discretization of the volume or surface using (adjustable) meshes. The most systematically accurate methods are reviewed here.

Finite Element Method

The *finite element methods* (FEM) represent a class of powerful techniques for solving different types of partial differential equations not only in science but also in industry. The FEM is based on 3D discretization of the domain, which has to be truncated at some finite length. The mesh resolution should be very carefully adjusted locally to get practically solvable matrix equations. Implementation of FEM is not easy and researchers usually use commercial software packages. Using such packages, probes of actual shape and size over a conducting sample with CPD discontinuity [22], or in the presence of charges or impurities [23, 24] have been simulated.

Boundary Element Method

In the *boundary element method* (BEM) the differential equation (Poisson's equation in our case) is transformed into integral equations on the surfaces (of probe and sample) [25, 26]. The accuracy of the solution depends on the resolution of the mesh

used for discretizing the surfaces. Although a much smaller system of equations is obtained compared to volumetric discretization methods, but solving the resulting fully populated matrix equation is numerically expensive and thus the computational cost is not necessarily decreased. Similar to the numerical image charges method, BEM uses GF formalism and is practically applicable to systems for which GF is available. A very useful feature of the BEM is its capability of reconstruction of local surface potentials and charge densities by deconvolution of the KPFM images [27] over conducting [25] or dielectric [3] sample surfaces. Since the contributions from local charges from a homogeneous flat dielectric sample are separated in this method, once the problem is solved for a given tip position over such a surface, solving it for several tip positions at the same height tip needs only a little additional computational cost [3, 26].

Finite Difference Method

The finite difference method (FDM), similar to the FEM, is based on discretizing the volume. The grid is, however, a rectangular one and the function value is calculated only on the grid points, making its implementation much easier than FEM and BEM. This is perhaps the most attractive feature of the FDM and is of great importance to scientists in this field.

A conductive tip was simulated by Müller et al. [28] over a uniform mesh. Such a regular grid results in too large matrices if dielectric thick samples, tip, and cantilever are considered in their actual sizes because the mesh resolution has to be tuned in accordance with the tip apex. However, the electrostatic potential varies smoothly and slowly at distances far from the tip apex and thus one may use a course mesh there. If the grid spacing increases exponentially away from the tip apex, increasing the truncation length of the simulation box induces only a small increment of the total computational cost. This allows one to simulate the cantilever and thick samples according to their actual sizes in experiments.

The CapSol Code

CapSol [29], a *capacitance solver* specialized for AFM experiments, is an implementation of the explained FDM on a non-uniform grid. This code is efficient enough to include cantilever [5] and simulate different samples types, e.g. metallic, multilayer thin dielectric films, and inhomogeneous dielectric samples [30].

The system consisting of a conducting probe at distance s from a sample surface is a capacitor. For fixed geometries, its capacitance depends only s. One can evaluate the capacitance $C(s)$ from the electrostatic energy

$$U_c(s, V) = \frac{1}{2} C(s) V^2 \tag{8.34}$$

when an effective voltage difference $V = V_b - V_{CPD}$ is applied between the conducting tip and back-electrode. The attractive electrostatic force between tip and sample,

$$F(s, V) = + \left(\frac{\partial U_c}{\partial s} \right)_V = + \frac{1}{2} C'(s) V^2, \tag{8.35}$$

is proportional to the capacitance gradient.[1] CapSol aims to calculate $C(s)$ from which the force ($\propto C'$) and force gradient ($\propto C''$) are determined.

To calculate $C(s)$, one notes that the the electric field propagated by the tip possesses an electrostatic energy density $\frac{1}{2}\epsilon(\mathbf{r})|\nabla\Phi|^2$ the volume integral of which equals the capacitive energy, (8.34), namely

$$\frac{1}{2}CV^2 = \frac{1}{2}\int \epsilon(\mathbf{r})|\nabla\Phi|^2\, d\mathbf{r}.$$

Based on the Gauss law $\nabla \cdot \mathbf{D} = \rho(\mathbf{r})$ where $\mathbf{D} = -\epsilon\nabla\Phi$, the electrostatic potential $\Phi(\mathbf{r}; s, V)$ satisfies

$$\nabla \cdot [\epsilon(\mathbf{r})\nabla\Phi(\mathbf{r})] = -\rho(\mathbf{r}), \tag{8.36}$$

where $\rho(\mathbf{r})$ is the real charge density. The latter is the appropriate form of the Poisson's equation when the dielectric constant $\epsilon(\mathbf{r})$ varies in scape. Note that if ϵ is a constant, the simple form $\nabla^2\Phi(\mathbf{r}) = -\rho(\mathbf{r})/\epsilon$ is recovered.

Within a variational approach, which is more convenient in numeric treatment, the solution of (8.36) minimizes the energy-like functional

$$I\left[\Psi(\mathbf{r})\right] = \frac{1}{2}\int \epsilon(\mathbf{r})\left|\nabla\Psi\right|^2 d\mathbf{r} - \int \rho\Psi d\mathbf{r}. \tag{8.37}$$

(i.e. $\frac{\partial I}{\partial\Psi}\big|_{\Psi=\Phi} = 0$) subject to the same Dirichlet boundary conditions [8].

Discretization

If the space is discretized using a rectangular mesh, the volume delimited by eight neighbouring nodes is taken as one volume element. For the volume element $\mathbf{n}$ all required quantities, i.e. $\Psi_{\mathbf{n}}$, $\rho_{\mathbf{n}}$, and $\epsilon_{\mathbf{n}}$, are evaluated at the center of the element by a linear interpolation between the values on the eight nodes. Moreover, the components of the electric field are effectively evaluated to the second order by the finite difference approximation.

In the special case of systems with cylindrical symmetry, the volume element labeled as $\mathbf{n} = (i, k)$, is presented in cylindrical coordinates by a tube of inner and

[1] It is a common mistake to take a wrong sign on the right hand side of (8.35). To calculate the tip-sample interaction force $F(s, V) = -\partial U_{\text{tot}}/\partial s$, one should distinguish between the total potential energy $U_{\text{tot}} = U_c + U_b$, and the capacitive contribution U_c. The difference, U_b, is the contributions from the biasing battery. Upon an infinitesimal vertical displacement δs of the tip, the battery maintains the potential difference at V by transferring a charge δQ between the tip and back-electrode with an energy cost of $\delta U_b = -\delta Q \cdot V$. In the same time, the capacitor energy gain is $\delta U_c = \frac{1}{2}\delta Q \cdot V$. Therefore $\delta U_{\text{tot}} = \delta U_c + \delta U_b = -\delta U_c$ and

$$F(s, V) = -\frac{\delta U_{\text{tot}}}{\delta s} = +\frac{\delta U_c}{\delta s} = +\frac{1}{2}\frac{\delta C}{\delta s}V^2.$$

Since the capacitance decreases if s increases ($C' < 0$) the force is attractive.

outer radii r_i and r_{i+1}, which is truncated by the horizontal planes $z = z_k$ and z_{k+1}. Then, (8.37) is discretized as

$$I\left(\{\Psi_{\mathbf{n}}\}\right) = \sum_{\mathbf{n}} \left(\frac{1}{2}\epsilon_{\mathbf{n}} |\nabla\Psi|^2_{\mathbf{n}} - \rho_{\mathbf{n}}\Psi_{\mathbf{n}}\right) v_{\mathbf{n}}. \tag{8.38}$$

For this volume element the radial and vertical components of the potential gradient (electric field) are approximated as $(\Psi_{i+1,k} - \Psi_{i,k})/h_i^{(r)}$ and $(\Psi_{i,k+1} - \Psi_{i,k})/h_k^{(z)}$, respectively, with grid spacings $h_i^{(r)} = r_{i+1} - r_i$ and $h_k^{(z)} = z_{k+1} - z_k$. In other words, $\nabla\Psi$ is represented as a linear combination of Ψ values on the neighboring nodes. Therefore $I\left(\{\Psi_{\mathbf{n}}\}\right)$ is quadratic versus $\Psi_{\mathbf{n}}$, and $\partial I/\partial\Psi_{\mathbf{n}} = 0$ yields a system of linear equations $A\boldsymbol{\Psi} = \mathbf{b}$. The unknowns of the problem, i.e. the potential value on the nodal points $\{\Psi_{\mathbf{n}}\}$ are arranged in the vector $\boldsymbol{\Psi}$ while any charge density and/or imposed boundary condition is described by the vector $\mathbf{b}$. The matrix $A_{\mathbf{mn}} = \partial^2 I/\partial\Psi_{\mathbf{m}}\partial\Psi_{\mathbf{n}}$ is sparse, symmetric and band, so that the matrix equation is solved efficiently using standard libraries like PARDISO [31, 32]. But due to the nonuniformity of the grid, the matrix can be ill-conditioned if it becomes too huge.

The electrostatic force felt by a conducting part of area S is

$$\mathbf{F} = \frac{1}{2\epsilon_0}\int_S \sigma(s)^2 \hat{n} dS, \tag{8.39}$$

where $\sigma(s) = -\epsilon\partial\Phi/\partial n$ is the surface charge density and $\hat{n}$ is the unit vector normal to the surface element dS. The contribution of a part of the probe delimited by two cylinders of radii $r_1 < r_2$ is given by $F = \pi\epsilon_0 \int_{r_1}^{r_2} |\nabla\Phi|^2 r dr$. However, the total force on the probe and its gradient are calculated from $C = \int \epsilon(\mathbf{r})|\nabla\Phi|^2 d\mathbf{r} \simeq \sum_{\mathbf{n}} \epsilon_{\mathbf{n}} |\nabla\Phi|^2_{\mathbf{n}} v_{\mathbf{n}}$.

8.3.3 Conductive Probe-Dielectric Sample Electrostatics

The model system with cylindrical symmetry illustrated in Fig. 8.7a consists of three parts: a spherical cap, a conical tip and a disk cantilever. All parts are conducting, and Dirichlet boundary conditions ($\Phi = V$) are applied to their surfaces. Dirichlet boundary conditions ($\Phi = 0$) are also applied to the walls of the very large cylindrical box of simulation. The sample is a NaCl ($\epsilon_r = 5.9$) slab of thickness 1 mm. The cap radius is $R = 20$ nm, the tip height 15 μm, and its half-opening angle 15°. The details of the cantilever geometry, except its area, seem to be not as important as those of the tip and apex. The cantilever is therefore modelled as a disk to benefit from the cylindrical symmetry. The disk edges are rounded to reduce numerical errors and its thickness is arbitrary set to 0.5 μm. The area of the disk equals that of a typical cantilever (disk radius is 35 μm). The radius of the simulation cylinder is $10^6 R = 20$ mm. The mesh resolution varies by six orders of magnitude from $R/400 = 0.05$ nm

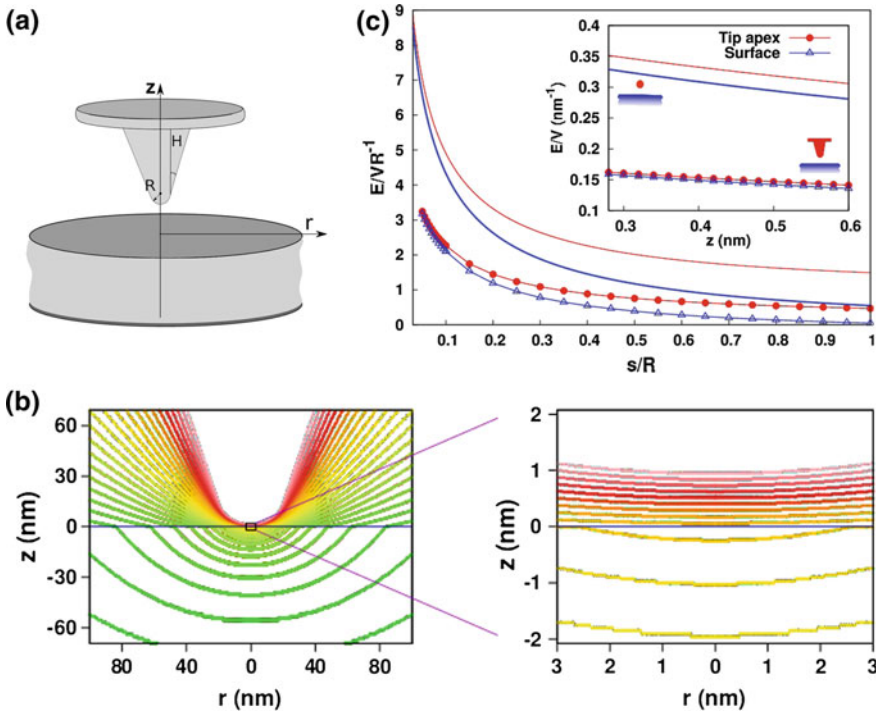

Fig. 8.7 **a** Schematic of the model AFM probe-sample system with cylindrical symmetry. The bias voltage V is applied to the conducting probe while the back electrode at the bottom and the surrounding enclosure of height and radius $10^6 R = 20$ mm (not shown) are grounded. **b** Normalized electrostatic potential Φ/V (successive contours differ by 0.01) for $s = 1$ nm and a zoom view into the apex-surface proximity region. The sample-vacuum interface is indicated by the horizontal line at $z = 0$. **c** Electric field in the vacuum on the tip and dielectric sample surfaces. Curves with symbols correspond to the model probe shown in (a) while continuous curves correspond to a spherical tip of the same radius (see Sect. 8.2.1). Inset: zoom into the range of separations where atomic-scale contrast appears. The horizontal axis is the actual separation $z = s - 0.7$ nm between the sample surface and a nanotip of height 0.7 nm mounted on the apex; $R = 20$ nm. Adapted with permission from [5]. Copyrighted by the American Physical Society

in the tip-sample gap to tens of μm close to the simulation box walls. To ensure that the chosen truncation length and mesh resolution are reliable, a set of convergence tests were performed for a spherical tip against a semi-infinite dielectric sample for which analytic solution.

The calculated electrostatic potential when $V = 1$ Vlot and $s = R/20 = 1$ nm, is shown in Fig. 8.7b along with a 30× zoom-in view in the contact point. The high resolution of the mesh is revealed by the smoothness of the contour at every position in the space. The inter-contour spacing in the tip-sample gap remains almost constant while, contrary to a parallel plate capacitor, the contours deviate from straight lines

within the dielectric sample and their spacing increases. Almost one tenth of the voltage drop occurs within the vacuum (successive contours differ by 0.01) and the reset in the thick dielectric sample.

Electric Field

At small separations the electric field at two regions is of great relevance: near the apex of the tip and on the sample surface underneath the tip. The s-dependence of the vertical component of the field at these two points is shown in Fig. 8.7c. Over the sample surface, the field practically vanishes for separations larger than R. Over the tip apex surface, on the other hand, already at $s \simeq R/3$ the field strength drops to V/R, which is the field strength on the surface of an insulated conducting sphere. For a spherical model tip as the most trivial approximation of the probe, the field strength at both mentioned points is overestimated by a factor $\sim$3 at any separation (see the continues curves). While modeling the probe with a conducting sphere results in a precise description of the electric field only when the sample surface is conducting, the same model over a thick dielectric slab gives only the order of magnitude of the electric field strength. The surfaces of the tip shank and cantilever adsorb a considerable fraction of the charges on the apex induced due to proximity to a dielectric sample surface.

Over the range relevant for atomic-scale contrast (shown in the inset of Fig. 8.7c), the z-component of the field changes by only a few percent, and is stronger than the radial component by almost two orders of magnitude. The same feature is also deduced by looking at the contour lines shown in the zoom-in view in Fig. 8.7b: the contours are essentially parallel to the sample surface and their separation remains constant in this region. The important consequent of this fact is that one can ignore the non-uniformity of the field in the atomistic scale simulations. In other words, to polarize the microscopic contents of the tip-sample system one may simply apply a uniform electric field normal to the sample surface the magnitude of which equals E_z at the gap in the macroscopic tip-sample problem.

Force and Force-Gradient

Two relevant quantities in KPFM are the electric force on the probe and its gradient. The variation of the force gradient and force (inset) with tip-sample distance is shown in Fig. 8.8. The model system described in Fig. 8.7a with three different geometries is used to study the influence of the cantilever. The first model probe is equipped with a large cantilever of radius 35 μm, having the same area as a typical rectangular cantilever. The second one has a smaller cantilever of radius 20 μm, equal to the typical width of rectangular cantilevers. Finally, for the third test, we exclude the cantilever, such that the probe consists of a conic tip terminated by a spherical apex. In this case, Hudlet's formula [2] can be used if the sample is conducting. Finally, we present also the results for a sphere-only model (no tip shank) obtained from the analytic solution of Sect. 8.2.

As expected, the inset of Fig. 8.8a shows that including a tip, including a cantilever, or enlarging the cantilever all result in increment of the attraction force on

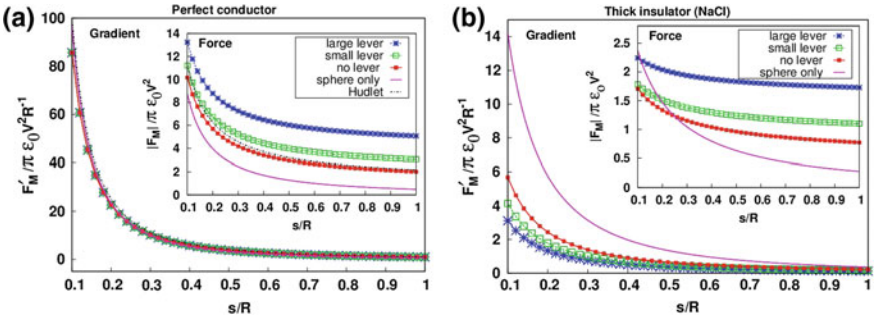

Fig. 8.8 Effect of the cantilever and its size on the electrostatic force-gradient and force (inset) at different normalized tip separations from a conducting (**a**) and dielectric (**b**) sample. The cantilever is modelled as either a small or a large disk with radii of 20 and 35 μm, respectively. Other parameters are as in caption of Fig. 8.7a. The solid lines show corresponding results for a tip approximated by a conducting sphere of the same radius. Adapted with permission from [5]. Copyrighted by the American Physical Society

the probe over a conducting sample. This is not true, however, for a dielectric sample. Inset of Fig. 8.8b shows that including a tip or a cantilever in the model probe causes either stronger or weaker interactions with the dielectric samples depending on the tip-sample separation.

Since the distance between the cantilever and the sample surface (the height of the conic part, ∼15 μm) is much larger than the apex-sample separation s, it is usually assumed that the cantilever contribution to the total force remains constant when s varies. This implies that the cantilever contribution to the force-gradient is negligible. Figure 8.8a shows that this assumption is valid for a conducting sample. Indeed, even the tip shank does not contribute, and the spherical cap determines almost completely the force-gradient. On the other hand, as shown in Fig. 8.8b and also emphasized in previous work [16, 19, 21], over a thick dielectric sample the force is significantly decreased, owing to field penetration into the sample at small s. Hence, ignoring their contributions causes an overestimation of the force-gradient if the sample is an insulator.

8.4 Concluding Remarks

The electrostatics of conducting probes over dielectric and conducting samples are quite different. A dielectric sample leads to a more complicated boundary value problem. Due to the cylindrical symmetry of the probe, it can be replaced by a set of image charges on the symmetry axis. The method of image charges is a convenient way to address this problem, both analytically and numerically. For a spherical tip facing a semi-infinite dielectric, an analytic exact solution is obtained as a simple generalization of the solution of the sphere-planar problem. This provides also accurate,

compact, approximate formulae for the capacitance and its gradient, as quantities of interest in electrostatic force microscopy of insulating layers on metal substrates. A dielectric slab with finite thickness can also be treated with the image charges methods and the interaction between the sphere and slabs are accurately evaluated within a simple numerical procedure for evaluating converging series. An experimentally interesting case is where both the slab thickness and tip-sample separation are much smaller than the tip apex radius. Then the sphere-thin film-back electrode setup is approximately equivalent to the sphere-electrode setup but with an effective separation $s + h/\epsilon_r$. The error of this approximation is less than one percent for relevant parameters, and thus acceptable.

Opposite to the conducting sample case, if the sample is dielectric the probe cannot be accurately presented simply by only a spherical cap. The electrostatic problem of the AFM probe by including the tip and the cantilever against a grounded dielectric sample needs numerical solutions. A convenient numerical method in this case is the finite difference method on a non-uniform mesh. Results obtained with and without the cantilever or the tip shank reveals that if the dielectric sample is thick, all three parts contribute to the force and force-gradient and the electric field even at small separations relevant for atomic-scale contrast.

Analytic expressions for dielectric slabs can be incorporated into atomistic simulation packages [15]. They can also be adopted for analytic modeling, e.g. by including localized point charges on dielectric samples [10]. Numeric results obtained for the more realistic probe geometries are useful for ab initio calculations [5]. Finally, the tip is typically oscillating close to the sample surface and the force or force-gradient need to be averaged over the tip trajectory [5, 14]. This requires that the description of the electrostatic interactions be valid for a large range of tip-sample separations.

Acknowledgements Fruitful discussions with Alexis Baratoff, Stefan Goedecker and S. Alireza Ghasemi are greatly acknowledged.

References

1. L.N. Kantorovich, A.I. Livshits, M. Stoneham, J. Phys. Condens. Matter **12**(6), 795 (2000)
2. S. Hudlet, M. Saint Jean, C. Guthmann, J. Berger, Eur. Phys. J. B **2**, 5 (1998)
3. Y. Shen, D.M. Barnett, P.M. Pinsky, Eng. Anal. Bound. Elem. **32**(8), 682 (2008)
4. C. Barth, T. Hynninen, M. Bieletzki, C.R. Henry, A.S. Foster, F. Esch, U. Heiz, New J. Phys. **12**, 093024 (2010)
5. A. Sadeghi, A. Baratoff, S.A. Ghasemi, S. Goedecker, T. Glatzel, S. Kawai, E. Meyer, Phys. Rev. B **86**, 075407 (2012)
6. J. Colchero, A. Gil, A.M. Baró, Phys. Rev. B **64**(24), 245403 (2001)
7. A. Sadeghi, A. Baratoff, S. Goedecker, Phys. Rev. B **88**, 035436 (2013)
8. J.D. Jackson, *Classical Electrodynamics* (Wiley, New York, 2001)
9. G.D. Wilk, R.M. Wallace, J.M. Anthony, J. Appl. Phys. **89**(10), 5243 (2001)
10. M. Orihuela, A. Somoza, J. Colchero, M. Ortuño, E. Palacios-Lidón, Nanotechnology **28**(2), 025703 (2016)
11. L. Nony, F. Bocquet, C. Loppacher, T. Glatzel, Nanotechnology **20**(26), 264014 (2009)

12. F. Bocquet, L. Nony, C. Loppacher, Phys. Rev. B **83**, 035411 (2011)
13. W.R. Smythe, *Static and Dynamic Electricity*, 2nd edn. (McGraw-Hill, New York, 1950)
14. F.J. Giessibl, Rev. Mod. Phys. **75**(3), 949 (2003)
15. L. Kantorovich, A. Foster, A. Shluger, A. Stoneham, Surf. Sci. **445**, 283 (2000)
16. S. Gómez-Moñivas, L.S. Froufe-Pérez, A.J. Caamaño, J.J. Sáenz, App. Phy. Lett. **79**(24), 4048 (2001)
17. S.F. Lyuksyutov, R.A. Sharipov, G. Sigalov, P.B. Paramonov, arXiv:cond-mat/0408247v2 (2004)
18. S. Belaidi, P. Girard, G. Leveque, J. Appl. Phys. **81**(3), 1023 (1997)
19. G.M. Sacha, J.J. Sáenz, Appl. Phys. Lett. **85**(13), 2610 (2004)
20. S. Gómez-Moñivas, L.S. Froufe, R. Carminati, J.J. Greffet, J.J. Sáenz, Nanotechnology **12**(4), 496 (2001)
21. G.M. Sacha, E. Sahagún, J.J. Sáenz, J. Appl. Phys. **101**(2), 024310 (2007)
22. G. Valdrè, D. Moro, Nanotechnology **19**(40), 405502 (2008)
23. T. Hochwitz, C. Henning, A.K.N.D. Levey, C. Daghlian, J. Slinkman, J. Vac. Sci. Technol. B **14**, 457 (1996)
24. D.S.H. Charrier, M. Kemerink, B.E. Smalbrugge, T. de Vries, R.A.J. Janssen, ACS Nano **2**(4), 622 (2008)
25. E. Strassburg, A. Boag, Y. Rosenwaks, Rev. Sci. Instrum. **76**(8), 083705 (2005)
26. Y. Shen, D.M. Barnett, P.M. Pinsky, Rev. Sci. Instrum. **79**, 023711 (2008)
27. G. Elias, T. Glatzel, E. Meyer, A. Schwarzman, A. Boag, Y. Rosenwaks, Beilstein J. Nanotechnol. **2**, 252 (2011)
28. U. Müller, S. Hofschen, C. Böhm, J. Sprengepiel, E. Kubalek, A. Beyer, Microelec. Eng. **31** (1–4), 235 (1996)
29. http://pages.unibas.ch/comphys/comphys/software
30. J.L. Neff, P. Rahe, Phys. Rev. B **91**(8), 085424 (2015)
31. O. Schenk, M. Bollhöfer, R.A. Römer, SIAM Rev. **50**(1), 91 (2008)
32. O. Schenk, A. Wächter, M. Hagemann, Comput. Optim. Appl. **36**(2–3), 321 (2007)

Chapter 9
Quantitative Analysis of Kelvin Probe Force Microscopy on Semiconductors

Leo Polak and Rinke J. Wijngaarden

Abstract As is well known, Kelvin Probe Force Microscopy (KPFM) is a powerful and versatile tool to measure the contact potential difference (CPD) in metals. Here, we discuss the application of KPFM for the investigation of semiconducting materials, where the interpretation of KPFM is complicated by band bending and surface charge. Nevertheless, it is demonstrated that the signal measured with KPFM in semiconductors should be interpreted as the contact potential difference (CPD). This interpretation enables the extraction of information related to semiconductor properties such as the dopant density, surface charge, density of surface states, and band bending. The CPD description and its validation are discussed in detail. Also, model calculations of the expected KPFM signal are presented for a wide range of doping concentrations and for various types of surface charge models, including surface states with a Fermi level dependent charge and surface states with fixed charge. It is demonstrated that the model calculations within the CPD model are consistent with experiments from the literature. As an example of how KPFM data on semiconductors can be analyzed, it is shown how information on surface charge is obtained from measurements on Si *pn*-junction dopant profiles. Combining KPFM with illumination provides many interesting possibilities for the study of semiconductors, which are briefly discussed at the end of this chapter.

9.1 Introduction

KPFM is a powerful tool to study semiconductors, as it can provide information with high lateral resolution on properties such as the dopant density, density of surface states, band bending, and charge carrier concentration [1–8]. Methods combining KPFM with sample illumination can probe still more properties, such as the band

L. Polak · R. J. Wijngaarden (✉)
Department of Physics and Astronomy, Vrije Universiteit Amsterdam, Amsterdam, The Netherlands
e-mail: r.j.wijngaarden@vu.nl; rw@nat.vu.nl

L. Polak
e-mail: l.polak@vu.nl

S. Sadewasser and T. Glatzel (eds.), *Kelvin Probe Force Microscopy*,
Springer Series in Surface Sciences 65, https://doi.org/10.1007/978-3-319-75687-5_9

gap, carrier diffusion length, and recombination rate [9–11]. The data analysis relies on the interpretation of the measured signal as the contact potential difference (CPD), i.e. the work function difference between probe and sample [12]. The sample work function is determined by the relative position of the Fermi level in the bulk, as well as the band bending. The latter depends on the surface charge density, which can be fixed, variable (when the charges reside in surface states near the Fermi level), or a combination of both. Also a (fixed) surface dipole will shift the work function. These influences are of great importance for a proper analysis of KPFM of semiconductors.

Brattain and Bardeen were the first to perform a detailed analysis for vibrating Kelvin probe measurements on semiconductors. They provided direct evidence for the existence of band bending at the free surface of a Ge-semiconductor [13]. The implementation in 1991 of Kelvin probe measurements on a scanning probe force microscope in the form of KPFM by Nonnemacher et al. [14] provided the big advancement of being able to perform the measurement with higher lateral resolution, making semiconductor samples with dopant profiles and semiconductor heterostructures a very natural and interesting subject of application.

Early applications of KPFM on semiconductors with doping profiles include the works of Kikukawa et al. [15], Henning et al. [16], and Hochwitz et al. [17]. In such studies it is generally found that the difference in measured Kelvin probe potential between differently doped areas is significantly less than what would be expected solely from the doping induced shift of the positioning of the band edges with respect to the Fermi level. This is a direct consequence of the band bending at the free surface of semiconductors in the presence of surface charge. Thus, the possibility of KPFM mapping with high lateral resolution made the effects of band bending apparent in a new way and provided opportunities to study it. For example, Glatzel et al. [18] studied band bending caused by defect states at step edges of cleaved GaAs and the resulting influence on the work function variation over a *pn*-junction. Similarly, Saraf and Rosenwaks [2] extracted the surface band bending and surface charge with high lateral resolution by performing KPFM over a Si *pn*-junction. Saraf et al. [1] even showed that it is possible to extract the energy distribution of surface states locally at the position of the junction, just from KPFM maps.

The study of semiconductor surfaces with KPFM also extends to the study of real devices, even under operation. As an example, Shikler et al. [19] mapped the potential on the cleaved surface of operating light emitting diodes, enabling a study of the built-in voltage under applied bias. KPFM can also provide valuable information on devices such as solar cells [20, 21] and transistors [22, 23] and it is used to study nanostructures, such as semiconductor nanowires [24–26].

In this chapter we first discuss some fundamentals of KPFM on semiconductors. Then we discuss how the CPD interpretation leads to a quantitative connection between KPFM measurements and semiconductor properties. As an example we analyze KPFM measurements on Si *pn*-junction doping profiles in a way that enables extraction of information on the nature of the surface charges. This discussion will be restricted to the situation in the dark, but at the end of this chapter also basic considerations for the analysis of the effects of illumination are discussed.

9.2 Fundamentals of KPFM Measurements on Semiconductors

In KPFM an oscillating potential $V = V_{\mathrm{DC}} + V_{\mathrm{AC}} \cos \omega t$ is applied between the sample and a conducting AFM probe. This voltage generates an electrostatic force per unit area, which has a 'first harmonic' component F_ω at frequency ω. There are two main classes of KPFM: amplitude modulation (AM) and frequency modulation (FM). In closed loop AM-KPFM, V_{DC} is adjusted by a feedback loop to a value V_K that nullifies a signal that is proportional to F_ω, i.e.,

$$F_\omega\big|_{V_{\mathrm{DC}}=V_K} = 0. \tag{9.1}$$

In closed loop FM-KPFM, the feedback loop nullifies a signal that is approximately proportional to the amplitude of the first harmonic of the gradient of the electrostatic force (see e.g. 2.18 of [27]), i.e.

$$\left.\frac{\partial F_\omega}{\partial z}\right|_{V_{\mathrm{DC}}=V_K} = 0. \tag{9.2}$$

In both cases, we refer to V_K as the 'Kelvin voltage' in analogy to the voltage measured by conventional Kelvin probes. To discuss the interpretation and modeling of the quantity V_K obtained with KPFM on *semiconductor* samples we will now introduce some theoretical background.

If two conducting bodies with different work functions are electrically connected, a potential difference is generated between their surfaces. This potential difference is called V_{CPD}, i.e. the contact potential difference. V_{CPD} arises due to different work functions Φ of the two conducting bodies, leading to charge transfer upon contact. The work function Φ of an object is the energy needed to move an electron from the bulk of the object to a position just outside its surface, in the absence of a net charge on the object and of any external electric fields originating from other objects. Φ often varies over the surface of an object with homogeneous bulk properties, because it contains contributions from potential drops at the surface. These can e.g. be caused by band bending at the semiconductor surface or by a fixed surface charge density.

To further discuss the theory of KPFM measurements, a one-dimensional geometry will be assumed, where KPFM probe and sample are opposite to each other and form a parallel plate capacitor, while each has a single work function (for discussions of the effects of non-flat samples and lateral work function variations, see e.g. [28–31]). In this approximation,

$$V_{\mathrm{CPD}} \equiv (\Phi_s - \Phi_p)/e, \tag{9.3}$$

where e is the positive elementary charge and Φ_s and Φ_p are the sample (s) and probe (p) work functions, respectively.

For ideal conductors with surface properties that are independent of any applied potential, the total charge on each body is proportional to the total potential difference $V - V_{\mathrm{CPD}}$ with V the applied potential, which is defined positive when a positive potential is applied to the sample with respect to the probe. In the one-dimensional geometry, the total net charge per unit area is thus:

$$\sigma_s = C\left(V - V_{\mathrm{CPD}}\right), \tag{9.4}$$

where the proportionality constant C is the capacitance per unit area. At a plate distance z, $C = \varepsilon/z$ and thus the electrostatic force per unit area is

$$F = \frac{\sigma_s^2}{2\varepsilon}, \tag{9.5}$$

where ε is the permittivity of the medium in the gap (usually air or vacuum). Under these conditions, the first harmonic is given by

$$F_\omega = \frac{\varepsilon}{z^2}\left(V_{\mathrm{DC}} - V_{\mathrm{CPD}}\right) V_{\mathrm{AC}}. \tag{9.6}$$

When substituting this in (9.1) and (9.2), it is found that both AM- and FM-KPFM lead to

$$V_K = V_{\mathrm{CPD}}, \tag{9.7}$$

which is the CPD interpretation of V_K, i.e. the KPFM set-up measures the contact potential difference between the two metals (in this case probe and sample) brought into contact. When the work function of the probe is known, the work function of the sample can be determined using (9.3) and (9.7). If the geometry is not one-dimensional, V_K can be interpreted as an approximation for the difference between the work functions of the tip of the probe and a small area of the sample directly underneath it.

Now the situation for a semiconducting sample will be addressed. In all cases to be discussed, the probe will be assumed metallic to avoid complications. In semiconducting samples, electrical fields penetrate the sample and influence the charge distribution inside the sample. Also fixed charge distributions may be present, in particular at the sample surface. It is the main purpose of this chapter to evaluate how KPFM results for such semiconducting samples should be interpreted.

The penetration of electrical fields in the sample is usually described by conduction- and valence-band levels that are dependent upon the distance from the semiconducting surfaces. This is the well-known *band-bending* at semiconducting surfaces (for a recent discussion see: Kronik and Shapira [9]), which changes the total potential difference between probe and sample. Thus σ_s is not simply proportional to the sum of the applied potential and the work function difference, as in (9.4). Instead, the charge-voltage relation must be described by a voltage dependent capacitance per unit area, $C(V)$, as

$$\sigma_s = \int_{V_{\mathrm{CPD}}}^{V} C(V')dV'. \tag{9.8}$$

As a consequence, one might (erroneously) think that (9.7) is not valid for semiconducting samples and hence that the CPD interpretation of V_K is wrong. However, we will now present strong arguments for the validity of the CPD interpretation of V_K even in the more complicated case of semiconductor samples.

We note that also for semiconductor samples, the electrostatic force can be written as in (9.5) [32], but since the capacitance is now voltage dependent, (9.8) must be used to substitute for σ_s. Without AC modulation of the applied potential V, i.e. $V_{\mathrm{AC}} = 0$, the force F is zero for $V = V_{\mathrm{DC}} = V_{\mathrm{CPD}}$ because the integral in (9.8) is over an interval of zero length. Nevertheless, in the presence of modulation, F_ω may be non-zero (the interval of integration now becomes time-dependent even for $V = V_{\mathrm{DC}} = V_{\mathrm{CPD}}$). To find F_ω for this situation, we use an approximation similar to that of Hudlet et al. [32]. The first order Taylor expansion of the force $F(V)$ around V_{DC} is given by

$$F(V) \approx V_{\mathrm{AC}} \cos \omega t \left.\frac{\partial F}{\partial V}\right|_{V=V_{\mathrm{DC}}} \tag{9.9}$$

thus

$$F_\omega \approx V_{\mathrm{AC}} \left.\frac{\partial F}{\partial V}\right|_{V=V_{\mathrm{DC}}} = \frac{V_{\mathrm{AC}}}{2\varepsilon} \frac{\partial}{\partial V} \left(\int_{V_{\mathrm{CPD}}}^{V} C(V')dV' \right)^2 \Bigg|_{V=V_{\mathrm{DC}}} \tag{9.10}$$

where we used (9.5) and (9.8) for the second equal sign. With $I(V)$ defined as the antiderivative of $C(V)$, we thus obtain

$$F_\omega \approx \frac{V_{\mathrm{AC}}}{\varepsilon} \left(I\left(V_{\mathrm{DC}}\right) - I\left(V_{\mathrm{CPD}}\right) \right) C\left(V_{\mathrm{DC}}\right).$$

We note that $C(V)$ is always positive and hence I is a monotonically increasing function. As a consequence, $I\left(V_{\mathrm{DC}}\right) - I\left(V_{\mathrm{CPD}}\right) = 0$ and also $F_\omega = 0$ if and only if $V_{\mathrm{DC}} = V_{\mathrm{CPD}}$. Somewhat surprisingly perhaps, we find that despite the voltage dependence of the capacitance C in the case of semiconducting samples, the nullifying feedback potential is equal to V_{CPD}. In other words: for semiconducting samples we measure with AM-KPFM also the contact potential difference, just as in the case of metals. For FM-KPFM, a $\partial/\partial z$ must be added in front of (9.10), see (9.2), and with analogous arguments as just given, we find that (9.7) is also valid for FM-KPFM. Hence we conclude that KPFM measurements on semiconductors should be interpreted in terms of the contact potential difference, i.e. the CPD interpretation of KPFM is valid for semiconductors. That this conclusion is not trivial is demonstrated by the fact that it is questioned in the literature (e.g. [33–35]).

Of course, the above derivation is jeopardized if the limitation to the first order Taylor term is invalid. This can be avoided by keeping V_{AC} small. We note that the second order Taylor term does not contribute to F_{ω}, which alleviates this requirement somewhat. Complications that are outside our present scope could arise from frequency dependent dynamics of the surface charges and the space charge layer, leading to a frequency or time dependence of $C(V)$.

9.3 The Work Function of Semiconductors

The KPFM technique is sensitive to the total potential difference over the semiconductor sample, from the back contact to just outside the surface. As a consequence, KPFM is sensitive to the band bending. Figure 9.1 shows schematically the energy levels in a *p*-type semiconductor with the band bending at the surface (at the right hand side of the sample in the Figure) and the band structure in the bulk (at the left hand side of the sample in the Figure). Band bending is strongly influenced by the (surface) charge state of the semiconductor. Figure 9.1a is for nonzero net charge, while Fig. 9.1b depicts the situation for an uncharged semiconductor. Note that (according to convention) the electron energy increases towards the top of the figure, hence electric potential increases towards the bottom. Indicated are the Fermi level E_F, which is flat in equilibrium, the valence (E_v) and conduction (E_c) band energies, and the local vacuum level E_l, defined (see Marshak [36]) as the energy of an electron at rest and free from the microscopic potentials of the semiconductor lattice, but not free from macroscopic potentials, such as those generated at surfaces or interfaces. Also indicated is the bulk electron affinity (χ), which is the energy required to bring an electron from the conduction band to the local vacuum level in the bulk of the material. If there are surface charges on the semiconductor, or if an external electrical field is applied, a so-called space charge region with non-zero net charge forms below the surface over a non-negligible depth, due to the low charge carrier density in semiconductors. This spatial charge distribution is the cause of band bending: E_v and E_c are now dependent upon the distance from the surface. As a result, a potential difference, V_s, arises between the bulk and the surface.

In the presence of a fixed dipole layer at the surface, which can be caused by the surface termination or by a molecular layer adhered to the surface, a potential step ϕ_s arises. To simplify our treatment below, we will assume that ϕ_s is independent of external electrical fields and also that ϕ_s is equal for the *p*- and *n*-sides of a *pn*-junction.

It is important to note that even if the semiconductor has zero net charge, usually band bending still occurs as indicated in Fig. 9.1b. In this situation, the charge in the space charge region is exactly compensated by surface charges. The band bending potential in this uncharged situation is defined as V_s^0. The work function Φ_s is the energy needed to bring an electron from the Fermi level E_F to the local vacuum level E_l outside the semiconductor in this uncharged case. These definitions lead to the relation

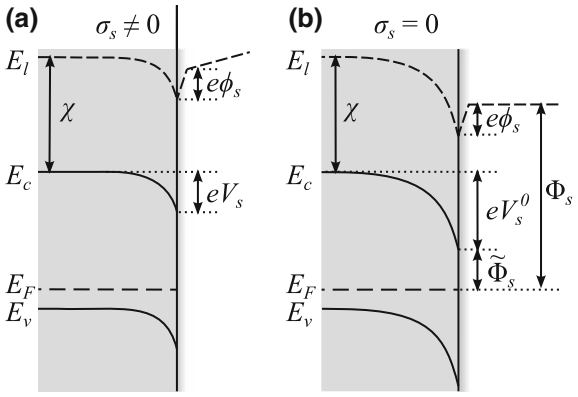

Fig. 9.1 Energy levels in a semiconductor with **a** nonzero net charge σ_s and **b** zero net charge σ_s. The bulk of the semiconductor is at the left hand side of each graph, while its surface is at the right hand side. E_F refers to the Fermi level, E_v to the valence band, E_c to the conduction band and E_l to the local vacuum level. The amount of band bending is quantified by V_s. A surface dipole may give rise to an additional potential step ϕ_s. Note that the work function Φ_s and the related quantity $\widetilde{\Phi}_s$ are defined in the uncharged condition (adapted from [12])

$$\Phi_s = E_c - E_F + \chi - e\phi_s - eV_s^0 \tag{9.11}$$

(note that in the figure V_s^0 is positive, while ϕ_s is negative). In order to proceed with the interpretation of KPFM measurements, the effects of various types of surface charge on Φ_s are discussed below.

9.4 Surface Charge on Semiconductors

In this chapter we explore the effect that various types of surface charge have on the band levels and band bending, and thus on Φ_s. To do this, we first need an expression for the position of the Fermi level in the bulk. For a non-degenerate *n*-type semiconductor, the position of the *band edges in the bulk* with respect to the Fermi level can be obtained from [37]:

$$N_c \exp\left(-\frac{E_c - E_F}{kT}\right) \approx \frac{N_D}{1 + g_D \exp[(E_F - E_D)/kT]}. \tag{9.12}$$

Here N_c is the effective density of states in the conduction band, N_D is the donor concentration, E_D is the donor energy level and g_D is the ground state degeneracy of the donor level. For a *p*-type semiconductor a similar expression holds. To investigate the effect of various types of surface charge, we note that the total charge on the semiconductor, σ_s, is the sum of the net charge in the space charge layer σ_{sc} and

all surface charges. Two types of surface charge densities are distinguished here: a surface state charge density, σ_{ss}, which depends on the energy between the Fermi level and the *band edges at the surface*, and a fixed surface charge density, σ_{sf}. Thus the total charge on the semiconductor is given by

$$\sigma_s = \sigma_{sc} + \sigma_{ss} + \sigma_{sf}. \tag{9.13}$$

These three contributions to σ_s are now discussed in detail.

The dependence of the *space charge density* σ_{sc} on the band bending potential V_s for a p-type semiconductor is approximated by [37]:

$$\sigma_{sc} = -\text{sgn}\left[V_s\right]\sqrt{2\varepsilon_s N_A kT}\,G(V_s), \tag{9.14}$$

Here ε_s is the permittivity of the semiconductor, N_A is the acceptor concentration, k is the Boltzmann constant, T is the temperature, and

$$G(V_s) = \sqrt{\exp[-\beta V_s] + \beta V_s - 1 + \frac{n_e}{n_h}(\exp[\beta V_s] - \beta V_s - 1)}, \tag{9.15}$$

where $\beta = e/kT$, and n_e and n_h are respectively the equilibrium electron and hole densities in the bulk. For non-degenerate p-type semiconductors we use the additional approximation [37] $n_e/n_h \approx n_i^2/N_A^2$, where n_i is the intrinsic carrier density. A similar expression holds for an n -type semiconductor.

Now we discuss the *variable surface state charge density* σ_{ss}, which depends on the band bending potential V_s. Charged surface states are donor or acceptor type. Just as the position of the conduction and valence band near the surface, they are shifted by band bending. According to Fermi-Dirac statistics, the charge in acceptor surface states, σ_{ss}^A, can be written as

$$\sigma_{ss}^A = \int_{E_v}^{E_c} \frac{-en_{ss}^A(E)}{1 + \exp[(E - E_F - eV_s)/kT]}dE. \tag{9.16}$$

Here $n_{ss}^A(E)$ is the acceptor density of surface states (DOSS) (per unit area and energy) in case of zero band bending, ignoring the surface state degeneracy. A similar expression holds for donor surface states. We write the combination of donor and acceptor DOSS as $n_{ss}(E)$ and the total number of surface states as N_{ss}.

For an atomically clean Si surface, N_{ss} can be of the order of the density of surface atoms [38], i.e. 10^{15} cm^{-2}, while on a hydrogen terminated Si surface it can be as low as 10^{10} cm^{-2} [39]. In the literature various functional dependences $n_{ss}(E)$ have been reported [40] for Si. Often, $n_{ss}(E)$ is considered to have a U-shape, with acceptor states above and donor states below the minimum density [39, 40]. Also, Gaussian [1, 41], Lorentzian [6], delta [9, 42], and constant [43] functions for $n_{ss}(E)$ have been considered.

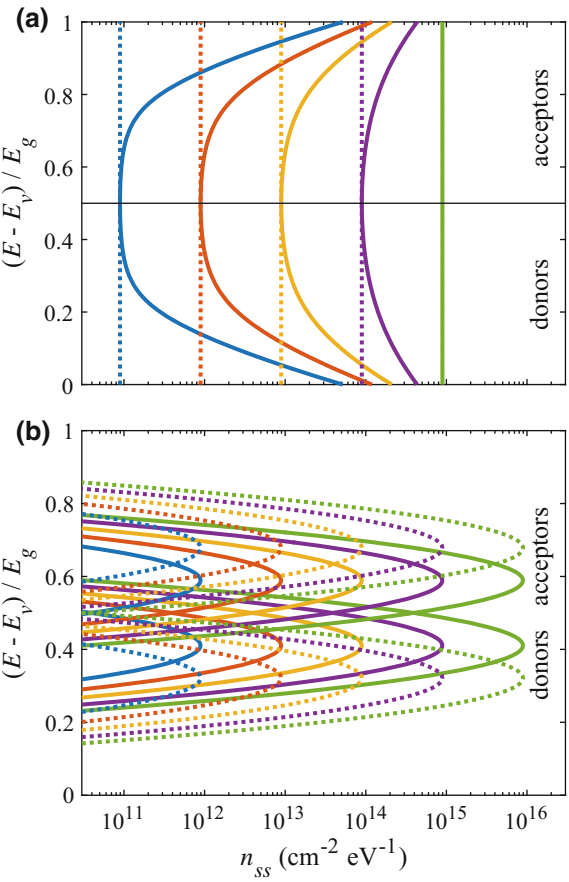

Fig. 9.2 Plots of the density of surface state (n_{ss}) models that are used in (9.16). **a** U-shaped (solid lines) and constant (dotted lines) densities **b** double Gaussian densities, which have 0.04 eV standard deviation and are centered at $E_g/2 \pm 0.1$ eV (solid lines) and at $E_g/2 \pm 0.2$ eV (dotted lines). In both (**a**) and (**b**) donor states are in the lower half of the bandgap and acceptor states in the upper half. The constant and Gaussian densities in blue, red, orange, purple, and green (from the left to right) correspond, respectively, to $N_{ss} = 10^{11}$, 10^{12}, 10^{13}, 10^{14} and 10^{15} cm^{-2}. The U-shaped densities have the same n_{ss} at $E_g/2$ as the constant densities with the same color, but higher N_{ss} (adapted from [12])

To capture the main phenomenology of $n_{ss}(E)$ in our calculations, we use three types of DOSS: U-shaped, constant, and double Gaussian. Examples of the U-shaped (solid lines) and constant (dotted lines) densities that we use below are given in Fig. 9.2a. These consist of donor states in the lower half of the bandgap (also lower half of the figure) and of acceptor states in the upper half. The U-shaped densities were chosen similar to those of [39] for Si/SiO_2 interfaces with various surface treatments (to be specific: we used $n_{ss}(E) = \alpha \exp[(E-\beta)^2/\gamma] + \delta$). Examples of double Gaussian densities are shown in Fig. 9.2b. These have 0.04 eV standard deviation and are centered at $E_g/2 \pm 0.1$ eV (solid lines) and $E_g/2 \pm 0.2$ eV (dotted lines). The Gaussian densities centered below $E_g/2$ (lower half of the figure) represent donor states, while those centered above $E_g/2$ represent acceptor states. Close to the center of the bandgap these Gaussian densities roughly correspond to results obtained by Angermann [44] on an HF-etched Si surface. Due to the symmetry of all these DOSS models, σ_{ss} will be zero if, at the surface of the semiconductor, the Fermi level is in the center of the gap.

A *fixed surface charge density* σ_{sf} is known to intrinsically exist at the Si/SiO_2 interface and to depend on sample treatment [45]. Also, ions from the environment can deposit on the surface during sample preparation or during measurement [13, 46] thus modifying σ_{sf}. For these reasons, the value of σ_{sf} is often unknown in an experiment. Another complication is that the deposited ions can either remain on the surface or migrate to the sub-surface. In our analysis we will neglect such migration and thus a possible distance between the Si surface and the fixed "surface" charges. In any case, this distance will be expected to be small.

9.5 Model Calculations for *pn*-Junctions

To demonstrate that the concepts discussed above enable a quantitative discussion of KPFM on selected semiconductors, we proceed by discussing the expected difference ΔV_K in the KPFM signal between the *p*- and *n*-sides of a single *pn*-junction:

$$\Delta V_K \equiv V_{K,p} - V_{K,n}, \tag{9.17}$$

where the subscripts p and n indicate values at the *p*- and *n*-type regions far away from the interface, respectively.

From 9.3 we find:

$$e\Delta V_K = \Phi_{s,p} - \Phi_{s,n}, \tag{9.18}$$

which is clearly independent of the probe work function. Therefore, we only need to consider the semiconductor work function in the modeling. This can be further simplified since we assume that ϕ_s is equal for the *p*- and *n*-side of a *pn*-junction and thus that $\chi - e\phi_s = \text{const}$ in 9.11, if we also assume that ϕ_s is independent of external electrical fields.

With the definition

$$\widetilde{\Phi}_s = E_c - E_F - eV_s^0, \tag{9.19}$$

which is the energy difference between the Fermi level and the conduction band at the surface (see Fig. 9.1b), we find from the last two equations that

$$e\Delta V_K = \widetilde{\Phi}_{s,p} - \widetilde{\Phi}_{s,n}, \tag{9.20}$$

and thus that ΔV_K is determined by the positions of the conduction band levels in the bulk with respect to the Fermi level, and V_s^0. As defined above, the *zero net charge band bending potential*, V_s^0, (see Fig. 9.1) is the value of V_s for which the total net charge on the semiconductor is zero, i.e. $\sigma_s = 0$.

To do model calculations and to predict ΔV_K, we thus need to calculate (i) the position of the conduction band edge in the bulk with respect to the Fermi level, $E_c - E_F$, and (ii) the zero net charge band bending potential V_s^0. The position of the band edges in the bulk with respect to the Fermi level is calculated by numerically solving (9.12). V_s^0 is obtained by taking a model DOSS, $n_{ss}(E)$, or a fixed surface charge, σ_{sf}, and numerically solving $\sigma_s = 0$ for V_s, using (9.13)–(9.16).

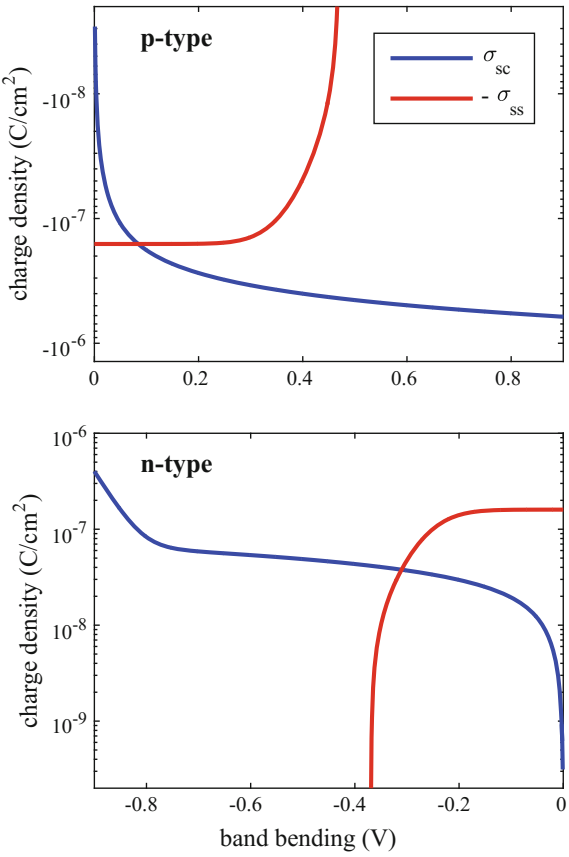

Fig. 9.3 Example of the space charge density σ_{sc} and the surface charge density σ_{ss} (in the plot multiplied by -1) of a Si *pn*-junction with a Gaussian surface state model (for details and parameters see text) as obtained from our model. The resulting equilibrium band bendings on the *p*-type and *n*-type sides are determined by the intersections of the curves. The position of the conduction band edge in the bulk with respect to the Fermi level, $E_c - E_F$, is in this case 1.0 eV and 0.2 eV respectively, such that with the band bending we obtain $\Delta V_K = 445$ mV

An example of the relation between surface charge density and band bending for a Si *pn*-junction is given in Fig. 9.3. In the same figure also the corresponding space charge density is shown (multiplied by -1 in the graph for display purposes). The resulting equilibrium band bendings on the *p*-type and *n*-type sides correspond to zero total charge and thus are given by the intersections of the plotted charge densities. This example is for the Gaussian surface state density corresponding to the solid red line of Fig. 9.2b, where we assumed B doped Si for the *p*-type material with a carrier density of 1.3×10^{18} cm^{-3} and P doped Si for the *n*-type material with a carrier density of 1.5×10^{16} cm^{-3}. The other parameters used for all our calculations on Si throughout this chapter are taken from [37]. These are: $\epsilon_s = 1.05 \times 10^{-10}$ F/m, $E_g = 1.12$ eV, $N_v = 2.65 \times 10^{19}$ cm^{-3}, $N_c = 2.8 \times 10^{19}$ cm^{-3}, $n_i = 9.65 \times 10^9$ cm^{-3}, $g_D = 2$, $g_A = 4$, $E_D(\mathrm{P}) = E_v + 1.075$ eV, $E_D(\mathrm{As}) = E_v + 1.066$ eV, and $E_A(\mathrm{B}) = E_v + 0.045$ eV. In addition, we assume $T = 293$ K.

Since the KPFM signal difference ΔV_K is expressed in terms of $\widetilde{\Phi}_s$, see (9.20), we also express the results of our calculations in terms of $\widetilde{\Phi}_s$. Figure 9.4a and b

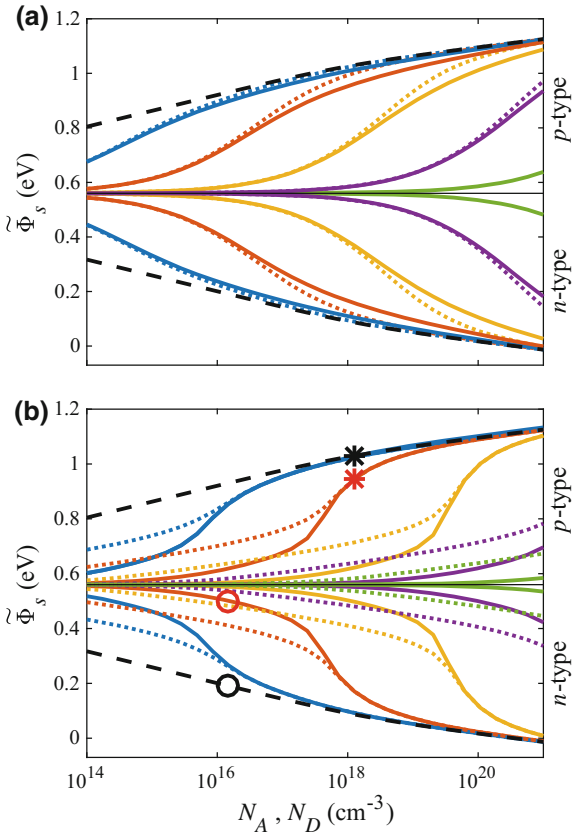

Fig. 9.4 $\widetilde{\Phi}_s$ as a function of dopant concentration, calculated for Si with $\sigma_{sf} \equiv 0$ and various surface state distributions $n_{ss}(E)$. The lines in the upper half of each figure correspond to B-doped p-type Si and the lines in the lower half to P-doped n-type Si (for parameters see text). The black dashed lines correspond to zero n_{ss} and, hence, $V_s = 0$. The other results in (**a**) and (**b**) correspond, respectively, to the n_{ss} shown in Fig. 9.2a, b with the same color and linestyle. The expected value of ΔV_K for any Si pn-junction with these n_{ss} can be obtained from this data using (9.20). The red circle and star correspond to the pn-junction of Fig. 9.3. The black circle and star correspond to that pn-junction as well, but without any surface states (adapted from [12])

show $\widetilde{\Phi}_s$ as a function of dopant concentration, calculated for Si with $\sigma_{sf} = 0$ and the various model DOSSs shown in Fig. 9.2a, b, respectively, using identical line colors and types. The lower half of each sub-figure corresponds to n-type P-doped Si and the upper half to p-type B-doped Si. The black dashed lines correspond to zero band bending, i.e. $V_s = 0$, which is the situation without surface states.

For each DOSS shown in Fig. 9.2, the expected value of ΔV_K for any Si pn-junction can be read from Fig. 9.4 using (9.20). As an example, consider the same Si pn-junction as in Fig. 9.3. with the DOSS given by the solid red line in Fig. 9.2b, which has $N_{ss} = 10^{12}$ cm^{-2}. The values of $\widetilde{\Phi}_s$ on the p-type and n-type side are 946 meV and 501 meV and are indicated in Fig. 9.4b with a red star and circle, respectively. Hence, the predicted ΔV_K is 445 mV. In the absence of surface states and fixed surface charge there would be zero band bending and $\widetilde{\Phi}_s$ for the p-type and n-type would lie on the black dashed lines as indicated by the black star and circle, respectively. In this case, the predicted ΔV_K would be 839 mV.

In a naive approach to the CPD interpretation, one might wish to ignore the effect of band bending, which corresponds to using the black dashed lines in Fig. 9.4.

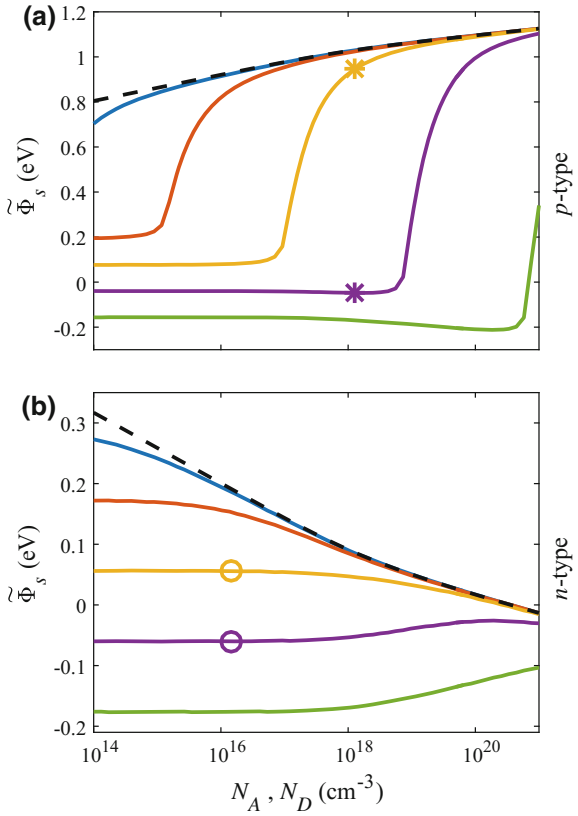

Fig. 9.5 $\widetilde{\Phi}_s$ as a function of dopant concentration, calculated for Si with $n_{ss} \equiv 0$ and $\sigma_{sf}/e = 10^{10}$, 10^{11}, 10^{12}, 10^{13} and 10^{14} cm^{-2} in blue, red, orange, purple, and green (from top to bottom), respectively. The lines in **a** correspond to B-doped p-type Si and the lines in **b** to P-doped n-type Si. The black dashed lines correspond to zero σ_{sf} and, hence, $V_s = 0$ (adapted from [12])

Our calculations show for which range of parameters band bending is significant and, hence, where such naive approach fails. It clearly fails where $\widetilde{\Phi}_s$ is close to the $E_g/2$. This corresponds to the type of Fermi level pinning that was first suggested by Bardeen [43], where V_s^0 can be approximated by the value of V_s at which $\sigma_{ss} = 0$ (instead of $\sigma_s = 0$). For our symmetric model DOSSs this leads to $\widetilde{\Phi}_s = E_g/2$.

Figure 9.5 shows $\widetilde{\Phi}_s$ as a function of dopant concentration, calculated for Si with positive fixed surface charge densities between $\sigma_{sf}/e = 10^{10}$ cm^{-2} and 10^{14} cm^{-2}. Subfigure (a) corresponds to p-type B-doped Si and (b) to n-type P-doped Si. The black dashed lines correspond to zero band bending, i.e. the case without fixed surface charge. Negative fixed surface charge densities lead to similar results, but with opposite sign of $\widetilde{\Phi}_s$ and p- and n-type reversed.

It is clear from Fig. 9.5 that a fixed surface charge density can have a dramatic influence on the work function $\widetilde{\Phi}_s$ and, therefore, also on ΔV_K. To illustrate this in more detail, we consider again the same pn-junction as above, but now with fixed surface charge densities. For $\sigma_{sf}/e = 10^{12}$ cm^{-2}, indicated with an orange circle and star, we obtain $\Delta V_K = 944$ mV, while for $\sigma_{sf}/e = 10^{13}$ cm^{-2}, indicated with a purple

circle and star, we obtain $\Delta V_K = 12$ mV, which is dramatically smaller. Although this demonstrates the strong influence of a fixed surface charge density, the precise values should be used with care since these calculations are less accurate for $\widetilde{\Phi}_s < 0$ and $\widetilde{\Phi}_s > E_g$, because then the Boltzmann statistics assumed in (9.12) and (9.14) is not very accurate. This problem arises for the case in the example with $\sigma_{sf}/e = 10^{13}$ cm^{-2}, where $\widetilde{\Phi}_s < 0$ on both the *p*- and the *n*-side. Nevertheless, on both sides the Fermi level can be expected to be slightly above the conduction band edge at the surface, i.e. $\widetilde{\Phi}_s$ is slightly below zero, and thus ΔV_K can be expected to be very small. Hence, the conclusion that ΔV_K is much smaller for $\sigma_{sf}/e = 10^{13}$ cm^{-2} than for $\sigma_{sf}/e = 10^{12}$ cm^{-2} still holds.

9.6 Comparison with Selected Experiments

The capability to predict ΔV_K for *pn*-junctions as defined and discussed above enables testing the ideas presented above with experiments. In particular, this may be interpreted as an experimental test for the contact potential difference (CPD) interpretation of KPFM measurements on semiconductors. Ten relevant published experiments on Si *pn*-junctions are listed in Table 9.1. In the first column the corresponding reference to the literature is listed, while in the second column a label is introduced for reference in the discussion below. In the third and fourth column the dopant concentrations and dopant types of the two sides of the *pn*-junction are given. The fifth column presents the experimental values of ΔV_K. All data in the table was taken from the references given in the first column unless otherwise noted.

Table 9.1 Ten KPFM experiments on Si *pn*-junctions. From left to right, the columns give the reference, a label used for reference in the text to the experiment, the reported dopant concentrations, and the measured ΔV_K (adapted from [12])

Refs.	Experiment	N_A (cm^{-3})	N_D (cm^{-3})	ΔV_K^{exp} (V)
[33]	(i)	2×10^{16}(B)	2×10^{17}(P)	0.30
[33]	(ii)	2×10^{16}(B)	2×10^{20}(As)	0.20
[33]	(iii)	4.7×10^{16}(B)	1.4×10^{15}(P)	0.44
[33]	(iv)	1×10^{15}(B)	6.5×10^{15}(P)	0.47
[2]	(v)	1.8×10^{15}(B)	2.1×10^{20}(As)	0.69
[5]	(vi)	5×10^{14}(B)	2×10^{20}(As)[a]	0.23
[5]	(vii)	5×10^{14}(B)	2×10^{20}(As)[a]	0.02[b]
[6]	(viii)	1×10^{19}(B)	3.5×10^{15}(P)	0.07
[6]	(ix)	5×10^{18}(B)	3.5×10^{15}(P)	0.05
[6]	(x)	1×10^{18}(B)	3.5×10^{15}(P)	0.03

[a] N_D was extrapolated from Fig. 9 and the given ΔV_K in [5]
[b] ΔV_K was estimated from Fig. 6c in [5]

We now proceed to compare these experimental results with predictions according to our model detailed above. In this CPD model, to obtain ΔV_K one needs to know the DOSS and the fixed surface charge density. Since these are generally unknown and difficult to measure, we fit the experiment to the CPD model with five surface charge models as described below. These models are fitted to each experimental result listed in Table 9.1 using the reported dopant concentrations as reproduced in this table. Although fitting does not allow to test the CPD interpretation thoroughly, it turns out that a test can be made—even by fitting—since the fit parameter of each model (the total surface state density N_{ss} for the DOSS models and fixed surface charge density σ_{sf} for the fixed surface charge models) must be of reasonable value (to be further discussed below).

The five surface charge models used are: (i) a constant $n_{ss}(E)$ with acceptor states in the upper half of the bandgap and donor states in the lower half (labeled hereafter as 'constant'), (ii) a $n_{ss}(E)$ with Gaussian distributed acceptor and donor states centered at $\mu = E_g/2 \pm 0.1$ eV respectively, and with a standard deviation of 0.04 eV (labeled 'Gauss1'), (iii) a $n_{ss}(E)$ with Gaussian distributed acceptor and donor states centered at $\mu = E_g/2 \pm 0.2$ respectively, and with the same standard deviation of 0.04 eV (labeled 'Gauss2'), (iv) a positive σ_{sf} (labeled '$\sigma_{sf} > 0$') and (v) a negative σ_{sf} (labeled '$\sigma_{sf} < 0$'). Note that in our calculations we consider only cases with either surface states (σ_{ss}) or fixed surface charge (σ_{sf}), but not both at the same time.

Like for ϕ_s, we assume that the DOSS or fixed surface charge is the same on both sides of the *pn*-junctions. For a given set of Si bulk parameters, the remaining fit parameter is N_{ss} for the Gaussian and constant DOSS models and σ_{sf} for the fixed surface charge models. The other parameters needed for our calculations on Si, are taken from [37] and are given above in Sect. 9.5.

Fitting was performed through iterative adjustment of the fit parameter, until the calculated ΔV_K was within 1 mV of the experimental value. We have not used the U-shaped DOSSs for fitting to experimental results, because, as shown in Fig. 9.4a above, its results are very similar to a constant DOSS, which is simpler to use. We assume in our procedure that the DOSS or fixed surface charge is the same on both sides of the *pn*-junction.

The values of the fit parameters N_{ss} and σ_{sf} that were determined for our five models from these ten experiments are presented in Fig. 9.6. We determined the sensitivity of the fit parameters by fitting them to the experimental values varied by ±5 mV. It was found that the resulting range of values is smaller than the symbols plotted in Fig. 9.6. A small complication is that, due to the complicated behavior of the $\widetilde{\Phi}_s$ in the fixed surface charge models, there can be multiple solutions σ_{sf} that reproduce a certain value of ΔV_K. However, we checked that within the charge density range 10^{10} cm$^{-2} > |\sigma_{sf}/e| > 10^{14}$ cm^{-2} there is only one solution for each case.

We consider values of N_{ss} and σ_{sf}/e below 10^{13} cm^{-2}, i.e. the values in roughly the lower half of Fig. 9.6, to be reasonable, see [39, 45]. Higher values are increasingly unlikely. Surface state densities above the density of surface atoms ($\sim 10^{15}$ cm^{-2}) are very unlikely for Si surfaces that have been exposed to air. As a result, the main conclusion from Fig. 9.6 is that all experimental cases can be fit

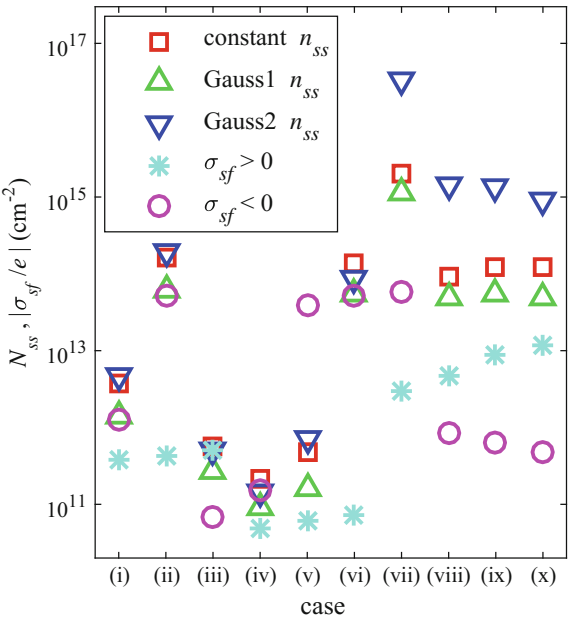

Fig. 9.6 Fit parameter values obtained by fitting our CPD model, as described in the text, to the experimental ΔV_K values listed in Table 9.1. The legend indicates the corresponding surface charge model as described in the text (adapted from [12])

with a reasonable value of the fit parameter by at least one surface charge model. This shows that all ten experimental observations can be interpreted in the CPD interpretation. We now proceed to investigate the validity of each particular surface charge model for each of the ten experiments.

Experiment (i) can be fitted with all five models with reasonable fit parameter values (i.e. below 10^{13} cm^{-2}), while for experiment (ii) only the fixed positive surface charge model (σ_{sf}) leads to reasonable parameter values; the other models lead to unrealistically high charge densities. Note that a positive fixed surface charge causes band bending in the same direction on both sides. What enables the small ΔV_K (compared to the value expected without any surface charges) as a fitting result is the fact that on the moderately doped p-type side, the resulting band bending is much larger than on the n-type side (see Fig. 9.4), causing the difference in work function, and hence ΔV_K, to become very small. Thus, although both bands bend in the same direction, the difference in the amount of bending between p-type and n-type (due to different doping) causes a reduction of ΔV_K. The experimental ΔV_K values of experiments (i) and (ii) were obtained from a single KPFM scan on a single sample with multiple pn-junctions. Hence, these junctions have undergone similar surface treatments, suggesting that their surface state density or fixed surface charge should be similar. Therefore, since only the fixed positive surface charge model gives nearly identical fit results for experiments (i) and (ii), this is the most likely model for both experiments. In addition, for experiment (ii) all other models lead to unrealistic parameter values.

In cases (iii) and (iv) all surface state models lead to reasonable fit parameter values. The reason is that in these two cases the measured ΔV_K is relatively close to the value expected in the naive approach to the CPD interpretation, i.e. without taking surface charges into account. As a result, for a good fit only a small adjustment is needed. Thus, for the surface state models, which bend both sides towards each other, the amount of required band bending to fit the experimental result is small, leading to low, reasonable values for N_{ss}. Similarly, a small amount of fixed surface charge causes enough difference in band bending between the *p*- and *n*-side to reach the required value of ΔV_K.

In case (v) the measured ΔV_K is even bigger and all models fit this case with reasonable fit parameter value, except for the negative fixed surface charge model. The reason that this model fails and the fixed positive surface charge doesn't is that the *n*-type side has a very high doping concentration. With the negative fixed surface charge, it is this side that should obtain more band bending than the other side to bring their work functions just a bit closer, but due to the high doping concentration this only happens at very high fixed surface charge density. Thus for cases (iii) to (v) the only conclusion that may be drawn from the fitting procedure is that in case (v) a negative fixed surface charge is very unlikely, while in the other cases all the considered models are possible.

Experiments (vi) and (vii) correspond to samples with identical *pn*-junctions, as far as dopant concentrations are concerned, but with different surface treatment. In case (vi) the sample was dipped in HF and not thermally oxidized, while in case (vii) the sample was thermally oxidized and not dipped in HF. The significantly different ΔV_K (by 0.21 V) can be easily interpreted in the CPD interpretation as a consequence of a different band bending V_s, due to a different N_{ss} or σ_{sf}. Since all models, except the fixed positive surface charge model, lead to rather high surface charge densities for these experiments, the most likely explanation for the observed difference in ΔV_K is that the positive fixed surface charge density σ_{sf} in experiment (vii) is higher than in experiment (vi).

Like experiments (i) and (ii), also experiments (viii) to (x) correspond to a single Si sample with several *pn*-junctions that went through a single preparation process. Thus, it is also reasonable for these experiments to assume that the surface state density or fixed surface charge should be similar. Interestingly, this corresponds well with the observation that for all models the fit parameter values for these three experiments are very similar. However, the surface state models lead to rather high surface state densities and are therefore less likely. The negative fixed surface charge model is the only that leads to densities that are significantly below 10^{13} cm^{-2}, but also the positive fixed surface charge model appears to be reasonable.

In their analysis of experiments (viii) to (x), Volotsenko et al. [6] assumed zero band bending, i.e. $V_s = 0$, for the highest doped region, which is the *p*-side in experiment (viii). However, in our calculations V_s is larger than 400 mV in this region for all fitted models, except for the negative fixed surface charge model, where it is only −9 mV. This suggests that either the assumption was not justified, or there was a fixed negative surface charge.

9.7 KPFM and Surface Photovoltage

KPFM measurements on semiconductors are mostly done in the dark to avoid any influence of light induced charge carriers. In contrast, an extension of the KPFM method combines scans with and without illumination. This is preferably done with a metallic probe to avoid light induced effects in the KPFM probe. Under this condition, i.e. that the *probe* work function is not altered by the illumination, the surface photovoltage (SPV), defined by the difference in work function with and without illumination, can be directly related to the measured change in V_K as

$$\mathrm{SPV} \equiv \left(\Phi_s^{\mathrm{light}} - \Phi_s^{\mathrm{dark}}\right)/e = V_K^{\mathrm{light}} - V_K^{\mathrm{dark}}. \tag{9.21}$$

Before discussing SPV as a very useful tool for the characterization of semiconductors, we note that many different methods for combining KPFM with illumination have been developed. For example, Schikler et al. [47] determined the minority carrier diffusion length in a single crystal of GaP by analyzing the potential profile measured with KPFM with and without illumination over a *pn*-junction cross-section. Many polycrystalline semiconductor materials have been studied with KPFM in combination with illumination techniques, providing insight into possible band bending variation on the crystallites or near their interfaces [48–50], into the influence of buried junctions [51, 52] or into the effect of surface layers [53, 54]. Similar methods can be applied to study isolated single crystals. For example, Zhu et al. [55] measured the SPV difference between different crystal facets on single crystals of the water splitting photocatalyst $BiVO_3$, finding evidence for the separation of photogenerated charge to different facets. Many of these methods are extended to the study of organic semiconductors [56–60]. Often KPFM studies of the SPV also include or focus specifically on the analysis of the KPFM signal as a function of time when changing the illumination, providing information on properties such as recombination rates and carrier lifetimes [51, 53, 60, 61]. For more details on the possible methods for SPV measurements with KPFM we refer the reader to the above mentioned references and the work of Kronik and Shapira [9], which treats SPV measurements in general and includes a good discussion of problems related specifically to SPV measurements with KPFM.

Here, we briefly discuss a simple SPV method, which nevertheless yields valuable information on properties such as band bending, dopant type, and band gap. Consider a SPV measurement with illumination by photons with an energy larger than the band gap and an absorption that is associated solely to the excitation of an electron from the valence band to the conduction band. Near the surface, where most photons are absorbed, the created mobile electron and hole are under influence of the gradient in local potential due to the band bending close to the surface, which leads to a spatial separation of the electron and hole. One of these is pulled into the space charge region, thus increasing the local charge density, and thus causing a reduction of the band bending. Assuming no other changes in charge distribution, such as from a

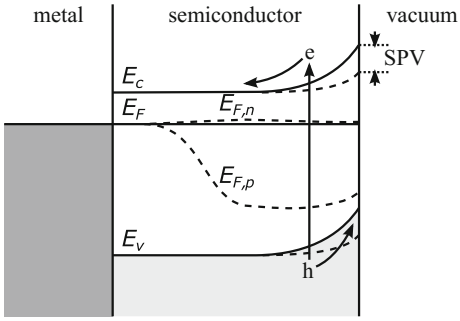

Fig. 9.7 Schematic energy diagram of a semiconductor sample with metallic back contact in dark and under illumination. The conduction band edge E_c and valence band edge E_v in dark are depicted by solid lines, and under illumination by dashed lines, illustrating that the band bending is reduced by illumination. The Fermi level E_F in dark is depicted by a solid line; under illumination it splits into electron and hole quasi-Fermi levels depicted by the dashed lines labeled with $E_{F,n}$ and $E_{F,p}$, respectively

change of the surface dipole or the Dember effect [9, 62], the SPV is related to the change in band bending as

$$\mathrm{SPV} = -\left(V_s^{\mathrm{light}} - V_s^{\mathrm{dark}}\right). \tag{9.22}$$

This situation is depicted in Fig. 9.7.

Since the sign of the band bending is directly related to sign of the surface charge, the sign of the surface charge can be directly determined by SPV measurement. Under the definitions described here, a positive SPV corresponds to a net positive surface charge in dark. Furthermore, when the band bending in the dark is caused by surface states, the sign of the SPV directly tells whether the semiconductor is *n*-type or *p*-type. For example in Fig. 9.7 the negative SPV gives away that the semiconductor is *n*-type (note that V_s in this Figure is negative).

In equilibrium, the balance between excitation and the various recombination pathways will determine the resulting change in band bending, which in general will depend on the illumination intensity [9]. Under photosaturation, i.e. illumination intensity that is increased until the SPV no longer depends on the intensity, the band bending is in some cases almost completely removed such that the SPV is approximately equal to the total band bending in dark [9].

Assuming that no absorption of photons with energy smaller than the band gap takes place, KPFM photovoltage spectroscopy provides in principle a direct method to locally map the band gap of a sample [49]. More specifically, one expects an onset of the SPV at a photon energy equal to the band gap. Above this onset, and with low illumination intensity, the SPV is approximately proportional to the absorption coefficient [9]. Often the situation is more complicated, for example due to excitation from trap states within the band gap, which can exist both in the bulk and at the surface [9].

Acknowledgements This chapter is largely based on a previous publication by the same authors [12], and we thank the American Physical Society for the right given to authors to reuse their figures in another publication. This work is part of the research program of the Foundation for Fundamental Research on Matter (FOM), which is part of the Netherlands Organization for Scientific Research (NWO) and was carried out within the research program of BioSolar Cells, co-financed by the Dutch Ministry of Economic Affairs.

References

1. S. Saraf, M. Molotskii, Y. Rosenwaks, Appl. Phys. Lett. **86**, 172104 (2005)
2. S. Saraf, Y. Rosenwaks, Surf. Sci. **574**, L35 (2005)
3. S.D. Tzeng, S. Gwo, J. Appl. Phys. **100**, 023711 (2006)
4. S. Barbet, R. Aubry, M.A. di Forte-Poisson, J.C. Jacquet, D. Deresmes, T. Melin, D. Theron, Appl. Phys. Lett. **93**, 212107 (2008)
5. B.Y. Tsui, C.M. Hsieh, P.C. Su, S.D. Tzeng, S. Gwo, Jap. J. Appl. Phys. **47**, 4448 (2008)
6. I. Volotsenko, M. Molotskii, Z. Barkay, J. Marczewski, P. Grabiec, B. Jaroszewicz, G. Meshulam, E. Grunbaum, Y. Rosenwaks, J. Appl. Phys. **107**, 014510 (2010)
7. M. Arita, K. Torigoe, T. Yamauchi, T. Nagaoka, T. Aiso, Y. Yamashita, T. Motooka, Appl. Phys. Lett. **104**, 132103 (2014)
8. C. Maragliano, S. Lilliu, M. Dahlem, M. Chiesa, T. Souier, M. Stefancich, Sci. Rep. **4**, 4203 (2014)
9. L. Kronik, Y. Shapira, Surf. Sci. Rep. **37**, 1 (1999)
10. T. Meoded, R. Shikler, N. Fried, Y. Rosenwaks, Appl. Phys. Lett. **75**, 2435 (1999)
11. F. Streicher, S. Sadewasser, M.C. Lux-Steiner, Rev. Sci. Instrum. **80**, 013907 (2009)
12. L. Polak, R.J. Wijngaarden, Phys. Rev. B **93**, 195320 (2016)
13. W.H. Brattain, J. Bardeen, Bell Syst. Tech. J. **32**, 1 (1953)
14. M. Nonnenmacher, M. O'Boyle, H. Wickramasinghe, Appl. Phys. Lett. **58**, 2921 (1991)
15. A. Kikukawa, S. Hosaka, R. Imura, Appl. Phys. Lett. **66**, 3510 (1995)
16. A.K. Henning, T. Hochwitz, J. Slinkman, J. Never, S. Hoffmann, P. Kaszuba, C. Daghlian, J. Appl. Phys. **77**, 1888 (1995)
17. T. Hochwitz, A.K. Henning, C. Levey, C. Daghlian, J. Slinkman, J. Never, P. Kaszuba, R. Gluck, R. Wells, J. Pekarik et al., J. Vac. Sci. Technol. B **14**, 440 (1996)
18. T. Glatzel, S. Sadewasser, R. Shikler, Y. Rosenwaks, M.C. Lux-Steiner, Mater. Sci. Eng. B **102**, 138 (2003)
19. R. Shikler, T. Meoded, N. Fried, B. Mishori, Y. Rosenwaks, J. Appl. Phys. **86**, 107 (1999)
20. T. Glatzel, D.F. Marrón, T. Schedel-Niedrig, S. Sadewasser, M.C. Lux-Steiner, Appl. Phys. Lett. **81**, 2017 (2002)
21. V.W. Bergmann, S.A.L. Weber, F.J. Ramos, M.K. Nazeeruddin, M. Grätzel, D. Li, A.L. Domanski, I. Lieberwirth, S. Ahmad, R. Berger, Nat. Commun. **5** (2014)
22. C.H. Lin, D.R. Doutt, U.K. Mishra, T.A. Merz, L.J. Brillson, Appl. Phys. Lett. **97**, 223502 (2010)
23. A.M. Hilton, J.L. Brown, E.A. Moore, J.A. Hoelscher, E.R. Heller, D.L. Dorsey, J. Electron. Mater. **44**, 3259 (2015)
24. S. Vinaji, A. Lochthofen, W. Mertin, I. Regolin, C. Gutsche, W. Prost, F. Tegude, G. Bacher, Nanotechnology **20**, 385702 (2009)
25. C. Van Ben, H.D. Cho, T.W. Kang, W. Yang, Thin Solid Films **520**, 4622 (2012)
26. E. Halpern, A. Henning, H. Shtrikman, R. Rurali, X. Cartoixà, Y. Rosenwaks, Nano Lett. **15**, 481 (2014)
27. S. Sadewasser, in *Kelvin Probe Force Microscopy*, ed. by S. Sadewasser, T. Glatzel (Springer, 2012), chap. 2

28. T. Hochwitz, A.K. Henning, C. Levey, C. Daghlian, J. Slinkman, J. Vac. Sci. Technol. B **14**, 457 (1996)
29. S. Sadewasser, C. Leendertz, F. Streicher, M.C. Lux-Steiner, Nanotechnology **20**, 505503 (2009)
30. S. Sadewasser, T. Glatzel, R. Shikler, Y. Rosenwaks, M.C. Lux-Steiner, Appl. Surf. Sci. **210**, 32 (2003)
31. L. Polak, R.J. Wijngaarden, Ultramicroscopy **171**, 158 (2016)
32. S. Hudlet, M. Saint Jean, B. Roulet, J. Berger, C. Guthmann, J. Appl. Phys. **77**, 3308 (1995)
33. C. Baumgart, M. Helm, H. Schmidt, Phys. Rev. B **80**, 085305 (2009)
34. C. Baumgart, A.D. Müller, F. Müller, H. Schmidt, Phys. Status Solidi A **208**, 777 (2011)
35. C. Baumgart, Dissertation, Helmoltz Zentrum Dresden Rossendorf, 2012
36. A.H. Marshak, IEEE Trans. Electron Dev. **36**, 1764 (1989)
37. S.M. Sze, K.K. Ng, *Physics of Semiconductor Devices* (Wiley, 2006)
38. F.G. Allen, G.W. Gobeli, Phys. Rev. **127**, 150 (1962)
39. H. Flietner, Surf. Sci. **200**, 463 (1988)
40. H. Hasegawa, T. Sawada, Thin Solid Films **103**, 119 (1983)
41. L.Å. Ragnarsson, P. Lundgren, J. Appl. Phys. **88**, 938 (2000)
42. W. Mönch, *Semiconductor Surfaces and Interfaces* (Springer, Berlin, Heidelberg, 2001)
43. J. Bardeen, Phys. Rev. **71**, 717 (1947)
44. H. Angermann, Solid State Phenom. **103**, 23 (2005)
45. B.E. Deal, M. Sklar, A.S. Grove, E.H. Snow, J. Electrochem. Soc. **114**, 266 (1967)
46. H.F. Okorn-Schmidt, IBM, J. Res. Dev. **43**, 351 (1999)
47. R. Shikler, N. Fried, T. Meoded, Y. Rosenwaks, Phys. Rev. B **61**, 11041 (2000)
48. S. Sadewasser, Phys. Status Solidi A **203**, 2571 (2006)
49. F. Streicher, S. Sadewasser, T. Enzenhofer, H.W. Schock, M.C. Lux-Steiner, Thin Solid Films **517**, 2349 (2009)
50. E.M. Tennyson, J.L. Garrett, J.A. Frantz, J.D. Myers, R.Y. Bekele, J.S. Sanghera, J.N. Munday, M.S. Leite, Adv. Energy Mater. **5** (2015)
51. M. Gwon, A. Sohn, Y. Cho, S.H. Phark, J. Ko, Y.S. Kim, D.W. Kim, Sci. Rep. **5**, 16727 (2015)
52. I. Sharma, B.R. Mehta, Appl. Phys. Lett. **110**, 061602 (2017)
53. A. Henning, G. Günzburger, R. Jöhr, Y. Rosenwaks, B. Bozic-Weber, C.E. Housecroft, E.C. Constable, E. Meyer, T. Glatzel, Beilstein J. Nanotechnol. **4**, 418 (2013)
54. E. Kim, Y. Cho, A. Sohn, D.W. Kim, H.H. Park, J. Kim, Curr. Appl. Phys. **16**, 141 (2016)
55. J. Zhu, F. Fan, R. Chen, H. An, Z. Feng, C. Li, Angew. Chem. **127**, 9239 (2015)
56. V. Palermo, M. Palma, P. Samorì, Adv. Mater. **18**, 145 (2006)
57. V. Palermo, G. Ridolfi, A.M. Talarico, L. Favaretto, G. Barbarella, N. Camaioni, P. Samori, Adv. Funct. Mater. **17**, 472 (2007)
58. S. Watanabe, Y. Fukuchi, M. Fukasawa, T. Sassa, A. Kimoto, Y. Tajima, M. Uchiyama, T. Yamashita, M. Matsumoto, T. Aoyama, A.C.S. Appl, Mater. Interfaces **6**, 1481 (2014)
59. F. Fuchs, F. Caffy, R. Demadrille, T. Mélin, B. Grevin, ACS Nano **10**, 739 (2016)
60. G. Shao, M.S. Glaz, F. Ma, H. Ju, D.S. Ginger, ACS Nano **8**, 10799 (2014)
61. L. Borowik, H. Lepage, N. Chevalier, D. Mariolle, O. Renault, Nanotechnology **25**, 265703 (2014)
62. H. Dember, Zeitschrift für Physik **32**, 554 (1931)

Part III
Application to Device Characterization

Chapter 10
Nanoscale Transport Imaging of Active Lateral Devices: Static and Frequency Dependent Modes

Evgheni Strelcov, Mahshid Ahmadi and Sergei V. Kalinin

Abstract Electronic and ionic transport in semiconductors, ionic conductors, and dielectrics underpins multiple applications from information technology devices to electroactive ceramics, batteries, fuel cells, and photovoltaics. In this chapter, we review the applications of Kelvin Probe Force Microscopy (or Scanning Surface Potential Microscopy) to map the charge transport in lateral devices. In these measurements, the SPM probe serves as a non-invasive probe of potentials created by the external electrodes, similar to the four-probe resistance measurements. We briefly discuss the invasiveness of such measurements, as exemplified by Scanning Gate Microscopy. We further discuss extensions of the KPFM based transport measurements to probe frequency dependent transport, an analog to impedance spectroscopy, and frequency mixing phenomena. Finally, implementations of lateral transport measurements in liquids are discussed.

10.1 Introduction

One of the hallmarks of our times is a constant drive for the miniaturization of electronic devices. The conventional electronics is now approaching the realization of the 5-nm node, with examples of single atom devices being developed [1, 2],

E. Strelcov
Institute for Research in Electronics and Applied Physics,
University of Maryland, College Park, MD 20742, USA
e-mail: evgheni.strelcov@nist.gov

M. Ahmadi
Department of Materials Science and Engineering,
University of Tennessee, Knoxville, TN 37996, USA
e-mail: mahmadi3@utk.edu

S. V. Kalinin (✉)
Oak Ridge National Laboratory, The Center for Nanophase Materials Sciences,
Oak Ridge, TN 37831, USA
e-mail: sergei2@ornl.gov

S. Sadewasser and T. Glatzel (eds.), *Kelvin Probe Force Microscopy*,
Springer Series in Surface Sciences 65, https://doi.org/10.1007/978-3-319-75687-5_10

explored, and commercialized in the context of quantum computing. Similarly, the emergence of novel concepts such as neuromorphic computing [3, 4], magneto— and optoelectronics stimulate exploration of coupling between transport and other physical and chemical functionalities [5, 6]. These developments gain significant prominence in the context of the Internet of Things applications, calling for low cost low energy multifunctional devices, but reducing requirements on the bandwidth and miniaturization. This difference in requirements allows for emergence of technological trees different from classical semiconductors, but necessitates a large body of exploratory work on materials and device behavior. Finally, a significant scientific and industrial effort is focused on the "bottom-up" assembly of electronic and molecular machine devices from molecular and cluster-sized building blocks, contributing to the rapidly developing fields of nanoscience and nanotechnology.

In addition to the device applications, nanoscale systems often exhibit unusual physical properties that have attracted attention of experimentalists and theorists alike [7]. The range of available methods for the fabrication of functional nanodevices has grown immensely in the last decades and encompasses a wide range of techniques from traditional photo- and e-beam lithography, to self-assembly and nanopatterning, to STM based atomic manipulation. However, the advances in fabrication necessitate device characterization and failure analysis. Since most electronic devices are based on electronic phenomena, the transport measurements on the nanoscale present an important challenge for nanotechnology. Equally important are the changes of the device structure induced by current flow, ranging from electroforming and electromigration to breakdown and failure.

Currently there exist multiple electric characterization techniques ranging from traditional *I-V*, *C-V* and Hall measurements, impedance spectroscopies and time domain response measurements to relatively complicated and rarely used techniques such as deep level transient spectroscopy (DLTS). The vast majority of these techniques is ultimately based on the detection of the AC and DC currents induced by probing bias applied to the sample, which requires the fabrication of relatively large-scale contacts to the device. The spatial resolution of these techniques is determined by the contact separation, which in most cases is limited to >10 μm. However, even when smaller structures can be fabricated, the interpretation of measured transport behaviors and establishing their link with the materials structure remains complex. This concept can be illustrated with such relatively large (>1 μm length) objects as carbon nanotubes. The latter can contain a number of defects, which can be imaged using techniques such as Scanning Gate Microscopy (SGM) [8–10] as illustrated in Fig. 10.1 [11–14]. However, differentiation of individual defect contribution to device transport properties using conventional current based semiconductor characterization techniques is impossible, since defect spacing is often in the 100-nm range, precluding contact fabrication to individual nanotube segments. Similar considerations can be applied to transport in polycrystalline materials, in which only average properties can be determined from macroscopic measurements and differentiation of contribution of individual microstructural elements to transport behavior presents a complex problem.

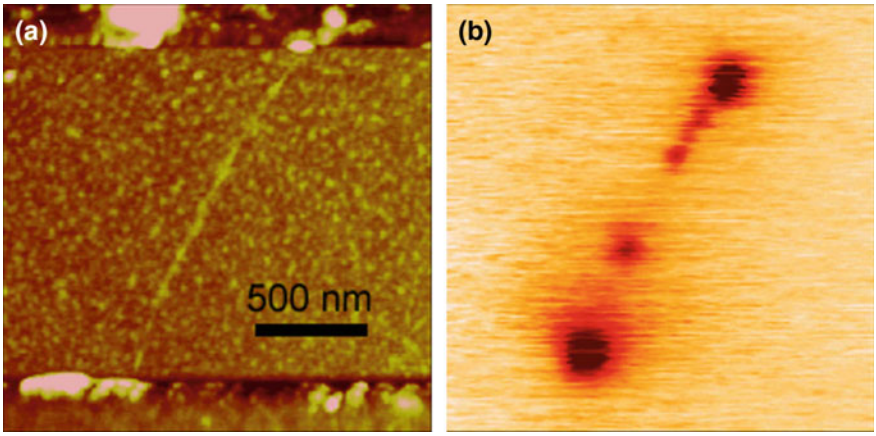

Fig. 10.1 **a** Surface topography and **b** scanning gate microscopy (SGM) images of a carbon nanotube circuit. Several defects are clearly seen in the SGM image. Adapted from [15]

Some of these problems can be circumvented by using techniques such as impedance spectroscopy [16]. The frequency dependence of the bias induced AC current can be analyzed to reveal the major relaxation processes in the solid that can be assigned to specific microstructural elements. Fitting the impedance spectroscopy data to a relevant equivalent circuit equation helps deconvoluting the behavior of the grain boundaries and interiors in a polycrystalline material. However, even this procedure does not yield information on the behavior of the individual elements. Several approaches have been suggested to separate the impedance response of individual structural elements, such as microimpedance spectroscopy using patterned contact arrays [16–18]. However, the small contact area inevitably leads to high contact resistance and precludes quantitative measurements even in the four-probe configuration [19].

10.2 Techniques

These days, SPM of transport phenomena is a large and rapidly developing field, spanning areas from low-temperature physics to materials science. This progress has been associated with the emergence of many techniques implemented in different tip-surface interaction regimes (contact, non-contact, intermittent contact) and utilizing a number of modulation (mechanical, voltage) and detection (force, current to the tip, current through the device) schemes for probing the local properties.

The general framework for the classification of SPM-based transport measurements is illustrated in Fig. 10.2. The SPM tip is considered as a moving electrode of the virtual device structure. In the single-terminal measurements, the properties of

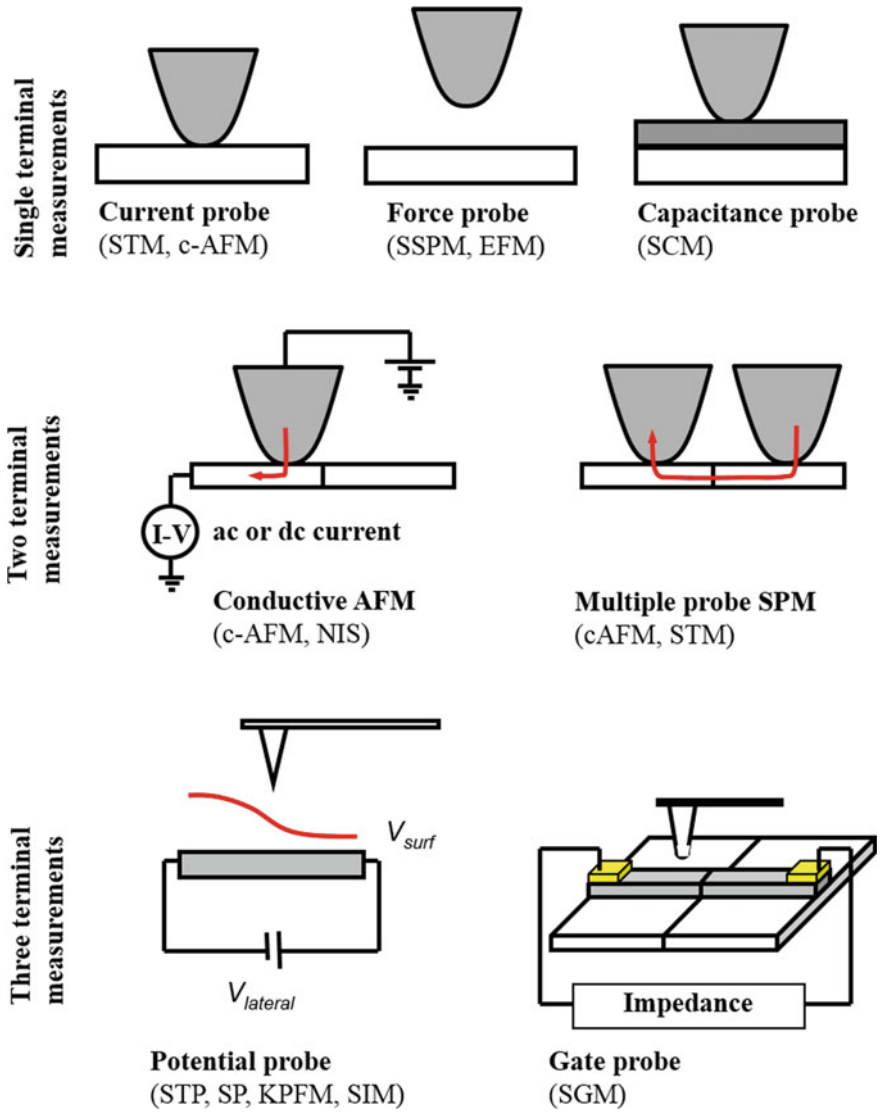

Fig. 10.2 General framework for transport measurements by SPM. For abbreviations, see Table 10.1. Adapted from [15]

the material directly below the tip are probed. The local character of these measurements owes to the fact that properties are typically dominated by the near-contact region (albeit a number of exceptions exist [20, 21], as will be discussed below). The rest of the sample provides a current sink (ground) and its detailed structure is not reflected in SPM measurements. In the two terminal setup, the current path between the SPM probe and macroscopic electrode or two SPM

Table 10.1 Local electric property measurements by SPM[a]

Technique	Topography feedback	Probe principle
Kelvin probe force microscopy—KPFM	Contact, non-contact or intermittent contact	The first harmonic of tip-surface force is nulled by varying DC tip bias. Tip acts as a moving voltage probe
Electrostatic force microscopy—EFM	Contact, non-contact or intermittent contact	Measured is electrostatic force gradient between a DC biased tip and the surface
Dissipation force EFM	Contact, non-contact or intermittent contact	Measured are losses in the material induced by mechanically modulated DC biased tip
Conductive AFM (c-AFM)	Contact mode	Measured is the tip-surface current
Tunneling AFM	Intermittent contact	Tip-surface tunneling current
Scanning spreading resistance microscopy —SSRM	Contact mode	Current probe
Scanning capacitance Microscopy—SCM	Contact mode	Tip-surface capacitance voltage derivative, dC/dV
Scanning tunneling Microscopy—STM	Current	Tunneling current
ac-STM	Current	AC current
Piezoresponse force microscopy—PFM	Contact mode	Electromechanical response of the surface to AC tip bias

[a]T is topographic feedback, S is excitation

probes is defined and the properties of material between the probes are studied. In the three-terminal measurements, the current is applied across the system through macroscopic contacts, while SPM tip acts as a voltage probe or a local gate probe providing the information on the lateral transport properties of the sample. Some of these modes are summarized in Table 10.1.

Non-contact techniques such as Kelvin Probe Force Microscopy (KPFM) [22] (also known as Scanning Surface Potential Microscopy, SSPM) and Electrostatic Force Microscopy (EFM) [23, 24] can be used to measure local potential and work function. In these techniques, the probe is capacitively coupled to the surface and capacitive force-induced changes in the dynamic behavior of the cantilever are recorded. The combination of KPFM with photoexcitation allows imaging of various photoelectric phenomena, such as diffusion length measurements of minority carriers [25]. Contact techniques such as Scanning Spreading Resistance Microscopy (SSRM) [26, 27] and Scanning Capacitance Microscopy (SCM) [28] are based on the detection of tip surface current. In SSRM and conductive AFM the DC tip-surface current is measured, providing the information on the contact and spreading resistance below the tip, from which local conductivity can be determined. These techniques require a highly conductive tip-surface contact in order to

Table 10.2 Two-terminal measurements by SPM[a]

Technique	Feedbacks and modulation	Probe principle
Conductive AFM	**T**: force **S**: DC bias	DC current probe
Nanoimpedance spectroscopy	**T**: force **S**: AC bias	AC current probe

[a]T is topographic feedback, S is excitation

obtain quantitative information. In SCM the voltage derivative of the tip-surface capacitance is measured. Here, the tip-surface coupling is purely capacitive and current leakage can hinder the measurements. Combination of SCM and SSRM can be employed to probe local carrier concentration and doping level in semiconductors and, hence, characterize *p-n* junctions [29–31]. Scanning Tunneling Microscopy (STM) and spectroscopy (STS) are used to decipher local electronic and atomic structure [32–34]. Due to the potential of atomic spatial resolution, STM is by far the most extensively developed SPM technique. The applicability of conventional STM is limited to conductive surfaces only; however, a number of approaches utilizing an AC current feedback for STM imaging on insulators (e.g. glass) were reported [35].

In certain cases, e.g. in the presence of highly resistive elements, well-defined sites for electrochemical counter-reaction, the localization of the second electrode becomes relevant, giving rise to two-terminal measurements. These techniques are limited to the current detection; conductive AFM and nanoimpedance spectroscopy can be differentiated based on whether a DC or AC current is measured. It should be noted that the techniques listed in Table 10.2 rely on the force feedback for topography (T is topographic feedback, S is excitation). The use of the topographic current feedback requires a conductive substrate thus imposing limitations on the range of the systems that can be studied with this approach. Overall, until now the two-terminal setup is the least used variety of SPM transport measurements, partially due to the generic problems associated with the high resistance of the tip-surface contact. However, transition from purely transport imaging to electrochemical measurements (i.e. electrochemical process at the tip-surface junction) necessitates two terminal measurements to render the system electrochemically well defined. Alternatively, the spurious water layers serve as a counter electrode, limiting the fidelity of information obtained by these techniques [21].

Finally, the three-terminal configuration provides several paradigms for SPM transport measurements. One type of conductivity measurements is based on using potential-sensitive SPM techniques, such as scanning tunneling potentiometry (STP), [36–40] scanning surface potential microscopy (SSPM, or Kelvin Probe Force Microscopy, KPFM) [41–44] or Scanning Potentiometry (SP) [45] on laterally biased surfaces as shown in Fig. 10.3.

This approach is similar to the classical 4-probe resistivity measurements, but instead of two fixed sensing electrodes, the SPM tip acts as a moving voltage probe providing the advantage of spatial resolution. The voltage sensitivity is enabled

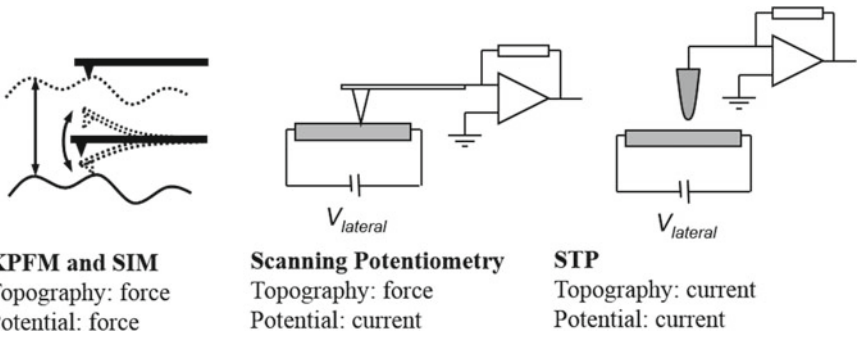

Fig. 10.3 Three-terminal potential probes for lateral transport measurements in the lift mode KPFM, and scanning impedance microscopy (SIM), and schematics of the scanning potentiometry and scanning tunneling potentiometry (STP) modes. Adapted from [15]

either by nulling the tunneling current (STP), capacitive force (KPFM) or direct connection to a high input impedance electrometer (equivalent to nulling the spreading current, SP).

In these measurements, the probe is often approximated as non-invasive, i.e. the presence of the AFM tip does not affect the potential and current distribution in the device under investigation. This assumption is sufficiently justified in macroscopic systems with high conductivity or pinned surface Fermi level, in which the tip-surface displacement current does not alter the electrostatic state of the surface. This is not always true in the mesoscopic systems [46] in which a biased SPM tip can introduce significant perturbation in the current and potential distribution, or systems with significant ionic mobility. The perturbation effect is employed in Scanning Gate Microscopy [47–50]. Three-terminal SPM techniques are classified by the type of topography feedback (T), probe type (P) and sample modulation (S) and are summarized in Table 10.3.

10.2.1 DC Transport by KPFM

The DC transport imaging techniques such as KPFM provide direct information on the potential distribution in the device under different lateral bias conditions [44, 51, 52]. Different from the classical two or 4-probe current measurement techniques, KPFM probes the local potential, leaving current undetected. To amend this, current in the single lateral interface systems (bicrystals, metal-semiconductor junctions) can be extracted from an equivalent circuit model. The elements of the equivalent circuit are now associated with the individual microstructural features as observed in topographic images, or by another microscopic technique (e.g. Scanning Electron Microscopy or optical microscopy). Such analysis can be readily extended to multiple interface systems with 1D current flow. For 2D and 3D systems with multiple

Table 10.3 Lateral transport measurements by SPM[a]

Technique	Feedbacks and modulation	Probe principle
Scanning tunneling potentiometry	**T**: current **P**: current **S**: DC bias	DC voltage probe
Scanning surface potential Microscopy (or KPFM)	**T**: force **P**: force **S**: DC bias	DC voltage probe
Scanning impedance microscopy (including non-linear SIM) and scanning frequency mixing microscopy	**T**: force **P**: force **S**: AC bias	AC voltage
Scanning potentiometry	**T**: force **P**: DC current **S**: DC bias	Voltage probe
Scanning capacitance microscopy	**T**: force **P**: AC current **S**: DC bias	Capacitance probe
Scanning gate microscopy	**T**: force **S**: DC bias	Gate probe
AC-Scanning gate microscopy	**T**: force **S**: AC bias	Gate probe

[a]T is topography feedback, P is probe type and S is sample modulation

interfaces, the analysis is more complex, but some estimates of local properties can still be obtained.

The SPM tip in a typical DC transport measurement setup is protected from high current by two limiting resistors connected in series with the biased interface (Fig. 10.4e). For such a circuit, the total resistivity of the sample R_Σ, is $R_\Sigma = 2R + R_d(V_d)$, where V_d is the potential across the interface, $R_d(V_d)$ is the voltage-dependent resistivity of the interface, and R is the resistivity of the external protective resistor. The dependence of the interfacial potential drop on the applied bias is directly measurable by SPM and is referred to as the voltage characteristics of the interface. Quantitative characterization of the interfacial transport is possible in this case, as some of the circuit parameters (e.g. resistivity of current limiting resistors, R) are known and can be varied deliberately.

Reconstruction of the interfacial transport IV characteristics in general case (when their functional form is unknown) can be performed, if the values of the protective resistors are known. In this case,

$$I(V_d) = (V - V_d)/2R \tag{10.1}$$

where $I(V_d)$ is the current-voltage characteristics of the non-linear element, and V is the applied bias. Such measurements can be conveniently done by applying a slow (approximately mHz range) triangular voltage ramp across the interface with the slow scan disengaged (i.e. scanning is performed along the same spatial line many

times). The first image is then the KPFM image in which each line corresponds to different lateral bias conditions (i.e. potential profile across the interface, from which $V_d(V)$ is obtained), the second image stores the actual lateral bias (V) and the third image is the current in the circuit measured by an I-V converter ($I = I_d$). A similar approach can be extended to systems with multiple interfaces.

The applicability of this approach to interfaces with highly asymmetric I-V characteristics, such as metal-semiconductor interfaces, is limited. In such case, the potential drop under the forward bias conditions is small compared to the typical noise in the potential measurements and direct I-V curve reconstruction yields erroneous results. For such systems, transport behavior can be established by varying the protective resistor. For example, for a metal-semiconductor junction the current is given by:

$$I_d = I_0\left(\exp\left(\frac{qV_d}{nkT}\right) - 1\right), \tag{10.2}$$

where $V_d = V_2 - V_1$ is the potential across the junction, $q = 1.6 \cdot 10^{-19}$ C is the elementary charge, n is the quality factor, k is the Boltzmann constant, T is the temperature, and I_0 is the saturation current. In this case, the potential drop across the interface is:

$$V = 2RI_0\left(\exp\left(\frac{qV_d}{nkT}\right) - 1\right) + V_d, \tag{10.3}$$

which in the limit of a large forward bias simplifies to $V_d = \frac{kT}{q}\ln(V/2RI_0)$, and for a large reverse bias to $V_d = V + 2RI_0$. Hence, for a forward biased diode the interfacial potential drop is on the order of a few mV and hardly detectable by KPFM. On the contrary, reverse biasing leads to a large potential drop at the interface. Switching between the two regimes occurs around the voltage point of $V = -2RI_0$. Description of real systems biased reversely necessarily includes a leakage term, $I_l = \sigma V_d$. Adding it to (10.3) yields:

$$V_d = (V + 2RI_0)/(1 + 2R\sigma) \tag{10.4}$$

Thus, potential profiling of the biased interface with KPFM can be used to obtain both the saturation and leakage current components of the diode resistivity. An example of such study on a cross-sectioned Schottky diode is shown in Fig. 10.4. The metal and silicon have clearly different topographic structures. Surface potential under a slowly varying sample voltage is shown in Fig. 10.4b presents an evolution of the surface potential (measures along line 1–2 in Fig. 10.4a) as a function of varying sample bias. When the interface is biased positively, no potential drops on it (light blue regions of the evolvent). At negative polarity, large potential drops are seen at the Schottky barrier (dark blue regions in Fig. 10.4b), as expected. The observed potential drop is dependent on the passing current and can

be tuned by selecting the protective resistor value. This behavior is attributed to photoinduced carrier generation in the junction region at a level equivalent to constant current element of opposite polarity in the circuit. For larger protective resistors, this effect is suppressed (cf. Fig. 10.4c—500 Ω, d—100 kΩ).

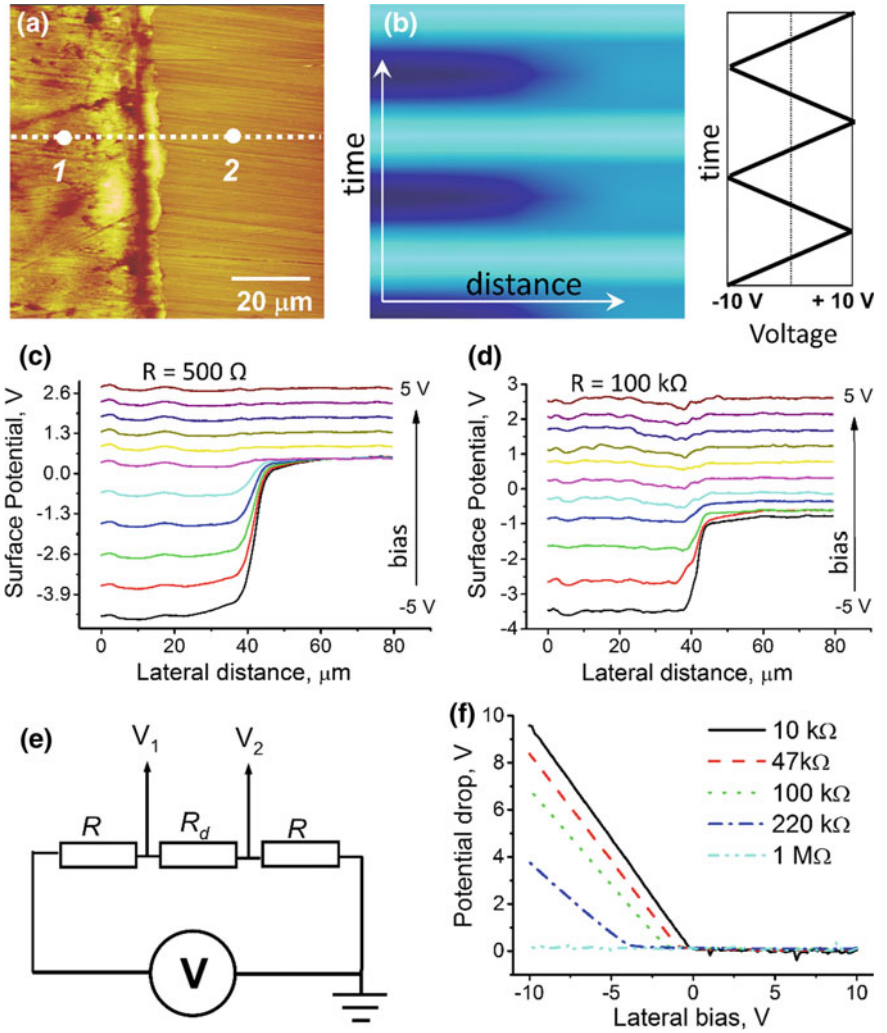

Fig. 10.4 DC transport in a diode: **a** surface topography of a cross-sectioned diode. Potential, phase and amplitude were measured along the 1–2 line. **b** Surface potential along 1–2 during a 2 MHz triangular voltage ramp to the sample with R = 500 Ω. The full colorscale is 300 nm for (**a**) and 10 V for (**b**). Potential profiles across the interface for different lateral biases for R = 500 Ω (**c**) and 100 kΩ (**d**). Profiles are acquired with a 1 V interval. Note that the onset of the reverse bias condition is shifted for high resistivity circuit terminations. Equivalent circuit (**e**) for KPFM. Potential drop at the interface (**f**) as a function of lateral bias for various values of the limiting resitor. Adapted with permission from [43]

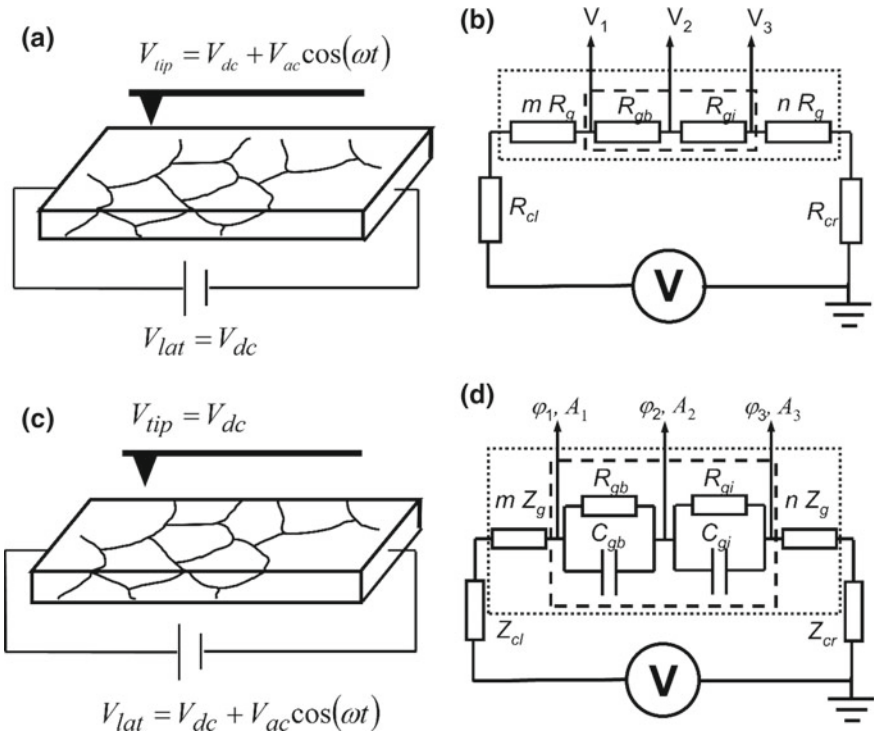

Fig. 10.5 Experimental set-up for DC transport measurements by KPFM in multiple interface systems: **a** and the corresponding equivalent circuit (**b**). Experimental set-up for AC transport measurements by SIM in multiple interface systems (**c**) and the corresponding equivalent circuit (**d**). Adapted from [15]

Figure 10.4c, d shows how the potential distribution across the interface changes as a function of lateral bias when low and high value current limiting resistors are used. The forward-reverse bias switching point for small R is $V = 0$. For the larger resitance the switching is shifted to negative biases. Figure 10.4f summarizes the dependence of the interfacial potential drop on the lateral bias and R. The observed behavior, predicted by (10.4): no potential drop in the forward bias regime and a linear drop under the reverse biasing. The saturation current and leakage can be derived from the observed dependences in a straightforward manner, and are found in excellent agreement with macroscopic IV measurements [43]. Note that the variation of resistors in this case allows access to the full I(V) curve by varying potential distribution across known and unknown circuit elements.

This approach can be trivially extended to multiple interface systems, for example polycrystalline ceramics or semiconductors, as shown in Fig. 10.5. In this case, the current flow is not uniform and not limited to a single direction. For 2D systems (e.g. thin films), the quantitative description of DC transport properties can be still achieved by either numerical solution of the corresponding Kirchhoff

equations for individual grain boundary resistivities or by finite element modeling (e.g. using models developed by Fleig et al. [53]). In the 3D case (e.g. bulk ceramics), the potential distribution *inside* the material cannot be accessed by SPM. In this case, the estimate for interface and bulk resistivity can be obtained; however, the properties of individual structural elements cannot be unambiguously determined.

10.2.2 Frequency and Time Dependent Transport Imaging

The DC transport measurements approach via KPFM can be generalized to probe AC transport, as implemented in Scanning Impedance Microscopy (SIM) [43, 54, 55]. SIM is performed in the dual-pass mode (each line scanned twice: first topography is recorded and then played back, while SIM measurement is performed). The tip is held at constant bias V_{dc} and a lateral bias $V_{lat} = V_{dc} + V_{ac}\cos(\omega t)$, is applied across the sample. This lateral bias affects the surface potential

$$V_{surf} = V_s + V_{ac}(x)\cos(\omega t + \varphi(x)), \tag{10.5}$$

where $\varphi(x)$ and $V_{ac}(x)$ are the position dependent phase shift and voltage oscillation amplitude and V_s is the DC surface potential (Fig. 10.6).

The variation in surface potential results in a capacitive tip-surface force. The first harmonic of the force is $F_{1\omega}^{cap}(z) = C_z^{'}(V_{dc} - V_s)V_{ac}$, where C_z is the tip-surface capacitance gradient, z is the tip-surface separation and V_s is the surface potential. The magnitude, $A(\omega)$, and phase, φ_c, of the cantilever response to the periodic force induced by the voltage are:

$$A(\omega) = \frac{F_{1\omega}^{cap}}{m}\frac{1}{\sqrt{\left(\omega^2 - \omega_{rc}^2\right)^2 + \omega^2\gamma^2}} \text{ and } \tan(\varphi_c) = \frac{\omega\gamma}{\omega^2 - \omega_{rc}^2} \tag{10.6a, b}$$

where m is the effective mass, γ is the damping coefficient, and ω_{rc} is the resonant frequency of the cantilever. The local phase shift between the applied voltage and the cantilever oscillation is $\varphi(x) + \varphi_c$ and the oscillation amplitude $A(\omega)$ is proportional to the local voltage oscillation amplitude $V_{ac}(x)$. Thus, the collected phase image reflects the variation in the true voltage phase shift with a constant offset due to the inertia between the sample and tip. The spatially resolved phase shift signal thus constitutes the SIM phase image of the device. The SIM amplitude image is given by the tip oscillation amplitude, which is proportional to the local voltage oscillation amplitude.

Determination of the absolute value of local amplitude, $V_{ac}(x)$, is possible by reconfiguring the microscope to the open-loop KPFM mode (disengaged feedback) and measuring the tip oscillation response to an AC bias applied to the tip. The local voltage oscillation amplitude is then

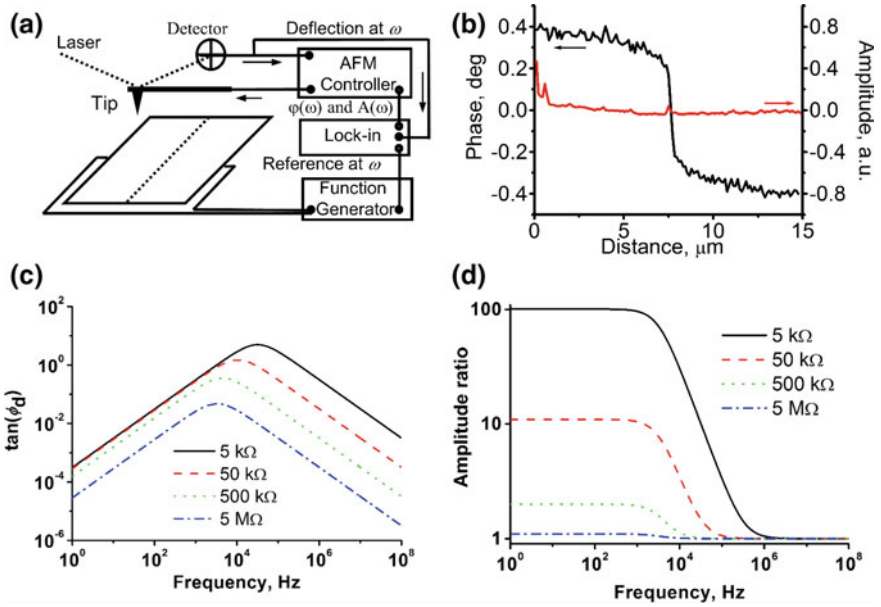

Fig. 10.6 Experimental setup for scanning impedance microscopy: (**a**) and typical phase and amplitude profiles across a grain boundary in a $SrTiO_3$ bicrystal in the high frequency regime (**b**). Adapted with permission from [55]. Calculated phase shift (**c**) and amplitude ratios (**d**) across the interface for different circuit terminations. The interface resistance and capacitance are taken to be $C_d = 1.0 \cdot 10^{-10}$ F, $R_d = 500$ kΩ for various values of the current limiting resistor. Adapted with permission from [43]

$$V_{ac}(x) = \frac{V_{ac}A_{sim}(x)\left(V_{surf}(x) - V_{tip}^{kpfm}\right)}{A_{kpfm}(x)\left(V_{surf}(x) - V_{tip}^{sim}\right)} \tag{10.7}$$

where A is the oscillation amplitude, V_{tip} is the tip DC bias, V_{ac} is the tip AC bias and *sim* and *kpfm* refer to the SIM and open-loop KPFM modes respectively. $V_{surf}(x)$ is the surface potential which varies with x in the presence of a lateral bias and can be determined by an independent KPFM measurement.

The SIM imaging mechanism is analyzed similar to KPFM. For the equivalent circuit of a single interface system in Fig. 10.7, the total impedance of the circuit, Z_Σ, is $Z_\Sigma = 2R + Z_d$, where Z_d is the interface impedance. The interface equivalent circuit is represented by a parallel *R-C* element and the impedance is $Z_d^{-1} = 1/R_d + i\omega C_d$, where R_d and C_d are the voltage dependent interface resistance and capacitance, respectively. The voltage phase difference $\varphi_d = \varphi_2 - \varphi_1$ across the interface measured by SIM is calculated from the ratio of impedances on each side, $\beta = R/(Z_d + R)$ as $\tan(\varphi_d) = \mathrm{Im}(\beta)/\mathrm{Re}(\beta)$. For the equivalent circuit in Fig. 10.7a,

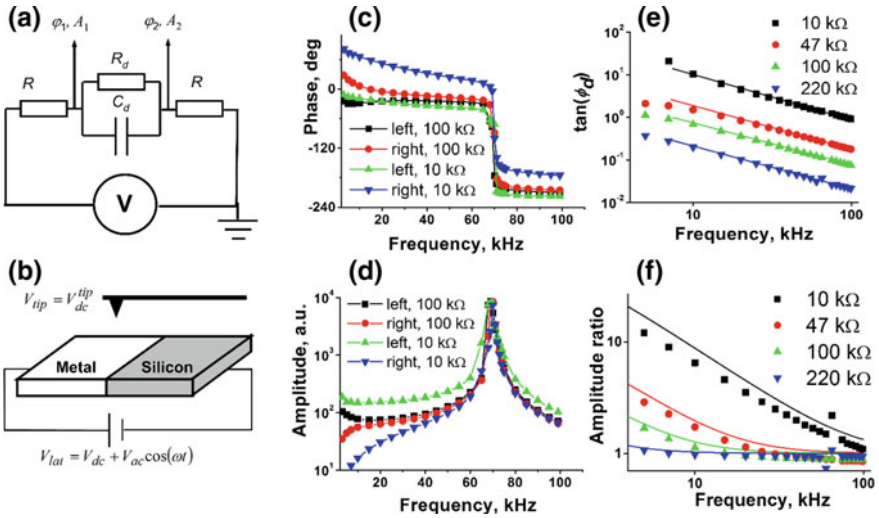

Fig. 10.7 SIM imaging of interfaces: **a** Equivalent circuit for SIM of a single interface. **b** Schematics of the schottky diode. Frequency dependence of the tip oscillation phase (**c**) and amplitude (**d**) to the left and to the right of the junction for various R values. Frequency dependence of the phase shift (**e**) and amplitude (**f**) for various R values. Solid lines are linear fits (**e**) and (**f**) amplitude ratios calculated with interface capacitance determined from the slopes in (**f**). Adapted with permission from [43]

$$\tan(\varphi_d) = \frac{\omega C_d R_d^2}{(R+R_d) + R\omega^2 C_d^2 R_d^2}. \tag{10.8}$$

The voltage amplitude ratio, $A_1/A_2 = |\beta|^{-1}$ can be calculated as

$$\beta^{-2} = \frac{\left\{(R+R_d) + R\omega^2 C_d^2 R_d^2\right\}^2 + \omega^2 C_d^2 R_d^4}{R^2\left(1+\omega^2 C_d^2 R_d^2\right)^2}. \tag{10.9}$$

Equations (10.8) and (10.9) provide information on different aspects of the interface conductance. In the low frequency limit, $\omega \ll \omega_0 = 1/(C_d R_d)$, the voltage phase shift across the interface is $\tan(\varphi_d) = \omega C_d R_d^2/(R+R_d)$, whereas the amplitude ratio is $A_1/A_2 = (R+R_d)/R$. In the high frequency limit, $\omega \gg \omega_0$, $\tan(\varphi_d) = 1/(\omega C_d R)$, while the amplitude ratio is equal to unity. The crossover between low and high frequency limits occurs at the voltage relaxation frequency of the interface, ω_r, defined as

$$\omega_r = \sqrt{\frac{R+R_d}{R}}\frac{1}{R_d C_d}, \tag{10.10}$$

at which the voltage phase angle attains its maximal value

$$\tan(\varphi_d) = \frac{R_d}{2\sqrt{R(R+R_d)}} \tag{10.11}$$

In the low frequency limit the voltage phase shift at the interface is determined by the interface capacitance and resistance, as well as by the resistance of the current limiting resistors. In the high frequency limit, however, it is determined by the interface capacitance and circuit termination only. At the same time, the amplitude ratio is determined by the interface and current limiting resistors at low frequencies and is unity in the high frequency regime. Therefore, SIM amplitude imaging at frequencies *below* the interface relaxation frequency visualizes resistive barriers at the interfaces and provides quantitative measure of interfacial resistance. SIM phase imaging at frequencies *above* the interface relaxation frequency visualizes *capacitive* barriers at the interfaces and provides a quantitative measure of interface capacitance. Equations (10.10) and (10.11) are validated by varying the protective resistance R. For other circuit terminations, including both resistive and capacitive elements, a similar but more complex analysis is required [56].

An example of SIM characterization of the Schottky diode interface is illustrated in Fig. 10.7. The tip dynamics is complex, being determined by a convolution of the harmonic response of the tip to the periodic bias and the frequency dependence of position dependent voltage phase and amplitude induced by the lateral bias. The abrupt phase change by *ca*. 180° and the tip oscillation amplitude maximum at $f = 72$ kHz are indicative of a mechanical cantilever resonance. Figure 10.7c displays the frequency dependence of the phase shift for different current limiting resistors. The relaxation frequency of the junction was estimated from the macroscopic impedance measurements to be 1.5 kHz at −5 V reverse bias. Therefore, SIM measurements are performed in the high frequency region, in which $\tan(\varphi_d)$ is inversely proportional to frequency with the proportionality coefficient determined by the product of the interfacial capacitance and circuit termination resistance. The experimental data were described by $\log(\tan(\varphi_d)) = a + b\log(f)$. The interfacial capacitance can be determined as $C_d = 10^{-a}/(2\pi R)$, and is found to increase with the current limiting resistor and was larger than the capacitance extracted from macroscopic impedance spectroscopy in all cases.

SIM can be used to obtain local capacitance-voltage characteristics of the interface. To this end, the interfacial phase shift was recorded as a function of the lateral DC bias for different protective resistors. The data in Fig. 10.7 was used to determine the interfacial capacitance. On the other hand, the interfacial potential drop was directly measured by KPFM. Combination of the two determines the *C-V* characteristics of the interface, presented in Fig. 10.8b. The universal behavior manifested by the resulting curve is independent of the protective resistance. The Schottky barrier height $\phi_B = 0.6 \pm 0.1$ V was calculated from an ideal metal-semiconductor junction relation [57]. Macroscopic *I-V* measurements yield a similar value of $\phi_B = 0.55$ V. From the line slope, the dopant concentration for the material is $N_b = 1.06 \cdot 10^{24}$ m^{-3}. The close match between the results of local

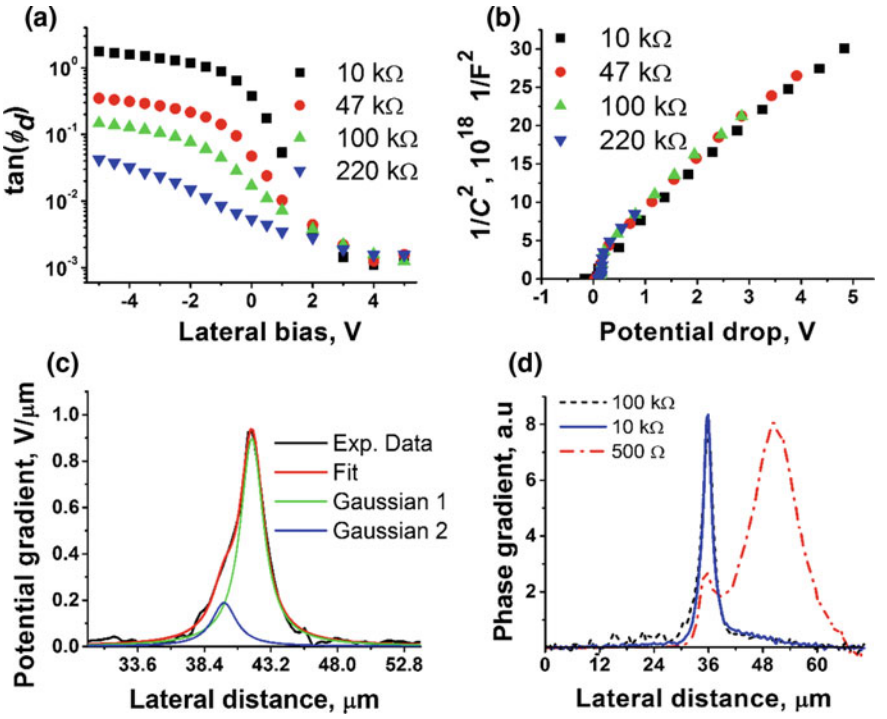

Fig. 10.8 **a** Voltage phase angle tangent as a function of lateral bias for various current limiting resistances. **b** Calculated $1/C^2$ versus V_d for different R values. Although $\tan(\varphi_d)$ varies by 2 orders of magnitude, $1/C^2$ exhibits a universal behavior. **a**, **b** Adapted with permission from [43]. **c** Lateral potential gradient across the diode junction deconvoluted into two gaussian peaks and (**d**) SIM phase angle gradient across the junction. Note that for small $R = 500\ \Omega$ a large phase angle feature exists on the right of the interface. This effect is completely suppressed at R values of 10 kΩ and higher. Adapted from [15]

SIM imaging of a metal-semiconductor interface and macroscopic measurements of the same verify the quantitativeness of the SIM approach.

Further insight into the potential, field and current distribution in the junction region can be obtained from the analysis of KPFM and SIM profiles. Shown in Fig. 10.8c is the lateral gradient of surface potential across the junction under reverse bias conditions, $V = -5$ V. The peak is asymmetric and can be deconvoluted into two Gaussian profiles of effective width ≈2.1 μm corresponding to a total effective width of ≈2.8 μm. The half-width of the SIM phase profile is 2.8 μm for $R = 10$ and 100 kΩ. Therefore, the resolution achievable in both techniques is comparable as expected due to the similarities of tip-surface interactions employed in the imaging mechanism. The phase angle gradient across the surface for low resistance termination $R = 500\ \Omega$ clearly exhibits two junction peaks with half-widths of 2 and 11 μm. This phenomenon is attributed to photoinduced carrier generation in the junction area. Analysis of the SIM profile shape allows

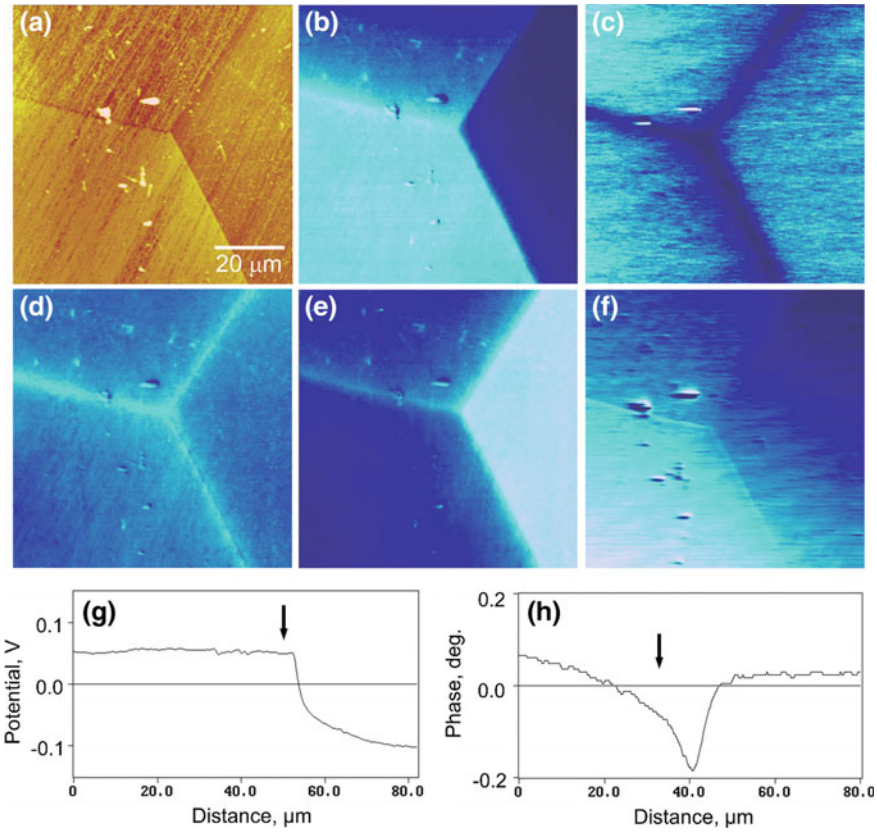

Fig. 10.9 SIM imaging of grain boundaries: **a** Surface topography and surface potential of (**d**) grounded, **b** positively, and **e** negatively biased polycrystalline *p*-doped silicon surface, where bias is applied laterally between macroscopic contacts. **c** SIM phase and **f** amplitude images of the same region at 90 kHz. Full color scale is 200 nm (**a**), 200 mV (**b**, **d**, **e**), 0.36° (**c**). **g** Potential profile across the grain boundary (bottom segment) for positive lateral bias. Position of the grain boundary is indicated by the arrow. **h** SIM phase profile across the same boundary. Adapted with permission from [43]

distinguishing the spatial localization of the two effects thus clarifying the origin of the anomalous phase-shift effect.

The quantitative extension of this approach to more complex structures is illustrated with polycrystalline silicon. Figure 10.9a, d compares the topography and surface potential of a 3-way grain boundary on a p-type polished silicon surface.

Potential on the grain boundaries is raised by ca. 30 mV relative to the grains, as expected for positively charged boundaries in a *p*-type semiconductor. A 10 V lateral bias forms potential drops at the grain boundaries confirming their high resistivity (Fig. 10.9b). Inverting the lateral bias (−10 V) results in inversion of the direction of the potential. SIM phase and amplitude maps are shown in Fig. 10.9c, f.

The potential drop at this interface yields an 18% contribution to the total sample resistivity. The linear dependence of the SIM phase signal on frequency in the range 50–100 kHz suggests that this region represents the low frequency limit of the interface. The relaxation frequency of the interface was measured by macroscopic impedance spectroscopy as 400 kHz. As can be seen from the SIM amplitude image, the interfacial AC resistance is comparable to that of the bulk.

The shape of the SIM phase signal is more complex than in the case of diode. In particular, the grain boundary is characterized by a minimum, rather than a step (Fig. 10.9b). These observations can be explained by assuming generation of minority carriers in the interfacial region under the applied AC bias. The minority carrier dynamics is given by

$$\frac{\partial n}{\partial t} = D\frac{\partial^2 n}{\partial x^2} - \frac{n}{\tau}, \tag{10.12}$$

where n is the minority carrier concentration, D is the diffusion coefficient and τ is the relaxation time. The solution of (10.12) with boundary conditions at the grain boundary $n(0) = n_0 e^{i\omega t}$ (and in the bulk $n(\infty) = 0$ is $n = n_0 \exp\left(-x\sqrt{(i\omega + \tau^{-1})/D}\right)e^{i\omega t}$.

In the low frequency limit, $\tau^{-1} \gg \omega$, the solution is $n = n_0 e^{-x/L} e^{i\omega\tau/2} e^{i\omega t}$, where the diffusion length is $L = \sqrt{D\tau}$. The surface potential is related to the minority carrier concentration as $V_s = V_{s0} + \alpha n$, where V_{s0} is potential of the surface far from the interface and α is a proportionality coefficient. The surface potential near the interface contains contributions from the applied lateral bias and the minority carrier current, $V = V_{s0} + V_{ac} e^{i\omega t} + \alpha n_0 e^{-x/L} e^{i\omega\tau/2} e^{i\omega t}$. Therefore, the SIM phase shift is

$$\tan(\varphi) = \frac{\alpha n}{V_{ac}} e^{-x/L} \frac{\omega\tau}{2}. \tag{10.13}$$

Equation (10.13) predicts an exponential decay of the SIM phase shift on the length scale comparable to the minority carrier diffusion length. The phase shift is expected to be linear in frequency, in a good agreement with the experimental observations.

As a second example, shown in Fig. 10.10 is a SIM image of a carbon nanotube network embedded in polymer [58]. The surface topography images are dominated by the substrate roughness and partial dewetting, precluding identification of the nanotubes. However, SIM amplitude images clearly illustrate the potential distribution along the network. Noteworthy is that SIM probes the transport along the nanotubes 0–100 nm deep *inside* the polymer matrix, providing an approach for local non-invasive transport measurements of thin film composite materials. Figure 10.10 shows large scale SIM amplitude and phase images when the top, bottom, and both electrodes are biased. Note that the potential amplitude decreases

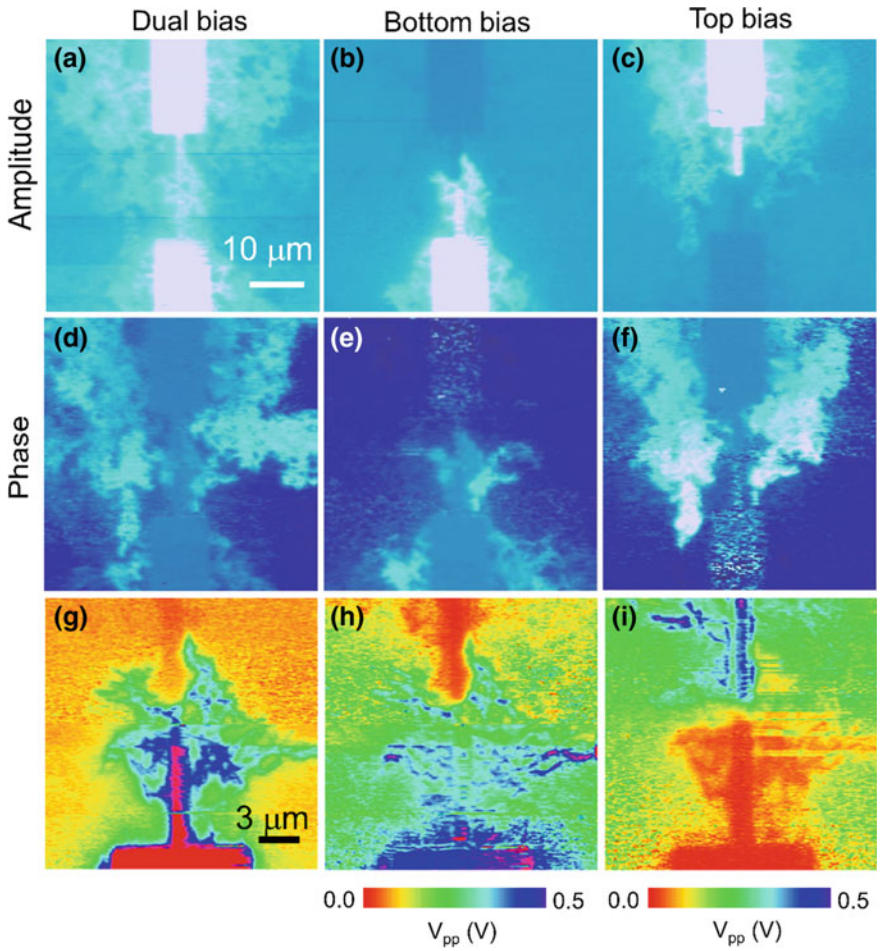

Fig. 10.10 SIM imaging of carbon nanotube networks: SIM amplitude and phase images in the dual, bottom, and top biased electrode configurations. The lateral electrodes are visible as white rectangles in the amplitude images. SIM amplitude (**a**, **b**, **c**) and phase (**d**, **e**, **f**) images in the dual (**a**, **d**), bottom (**b**, **e**), and top (**c**, **f**) biased configurations. The full color scale of the phase images is 60°. **g** a SIM amplitude image in the bottom biased configuration (replotted image of panel (**b**)). Note the significant amplitude change at the nanotube-electrode contact due to the capacitance differences. **h** Normalized SIM voltage image in the bottom-biased configuration obtained by dividing the image of panel (**b**) by the image of panel (**a**) and normalizing by the V_{ac}. Note the absence of any potential drop at the tube-contact interface. **i** Normalized SIM voltage image in the top-biased configuration.

away from the biased electrodes even when both electrodes are biased, while SIM phase images exhibit phase variations along the network.

This behavior can be understood noting the fundamental difference between the AC and DC transport. Whereas DC transport requires a well-defined transport path

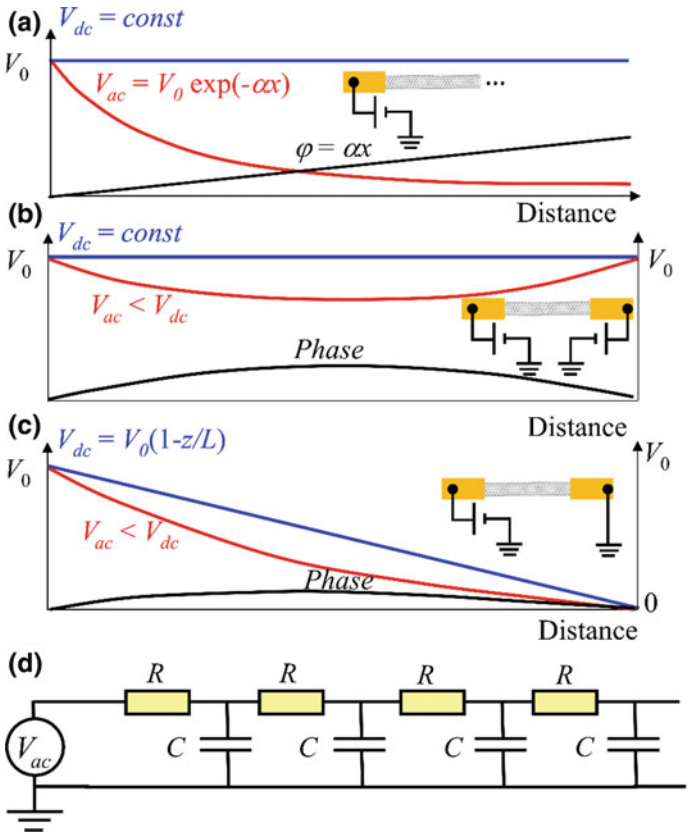

Fig. 10.11 Predicted potential, amplitude, and phase distributions across conductive segments within a network for various boundary conditions. DC (blue), potential and AC potential amplitude (red), and phase lag (black) distributed along an individual nanotube for (**a**) an infinite nanotube, **b** dual electrode biased nanotube, and (**c**) single electrode biased nanotube. **d** The equivalent circuit of a transmission line capacitively coupled to ground.

(or leakage resistances), AC transport can be capacitively shunted via the oxide. This behavior can be quantitatively described using a transmission line model (Fig. 10.11) [57] $d^2V_{ac}(x)/dx^2 = i\omega RCV_{ac}(x)$, where $V_{ac}(x)$ is the position-dependent local AC bias amplitude, R is the resistivity of the nanotube, C is the specific nanotube-substrate capacitance and ω is the signal frequency. The boundary conditions for an infinitely long nanotube biased on one end at the electrode are $V(0) = V_{ac}$ and $V(\infty) = 0$. The potential distribution along the nanotube is then given by $V_{ac}(x) = V_{ac}\exp\left(-x\sqrt{iR\omega C}\right)$, or

$$V_{ac}(x) = V_{ac}\exp(-\alpha x)(\cos\alpha x + i\,\sin\alpha x) \tag{10.14}$$

where $\alpha = \sqrt{R\omega C/2}$. SIM experimentally measures the force amplitude proportional to $V_{ac}(x)$, and phase, $\varphi(x)$, of voltage oscillations on the surface. From (10.14) these are $V_{ac}(x) = V_{ac}\exp(-\alpha x)$ and $\varphi(x) = \alpha x$. This implies that the voltage amplitude along the nanotube drops exponentially with a decay length, α, while the phase angle increases linearly in the same direction. Figure 10.11 illustrates this case, as well as two other cases when a finite nanotube is laterally biased at both ends or only at one end.

A highly conductive nanotube biased at both ends shows a uniform potential distribution along its length at low frequencies, $\omega \ll 1/RCL^2$, and small decay lengths. A steady potential drop is observed for a nanotube between a biased and a grounded electrode. In this case, the decay constant can be calculated from the phase signal, which is independent of the tip-tube capacitance (the amplitude, on the contrary, is proportional to this capacitance and the nanotube diameter). Further analysis of the frequency dependence of phase images allows relevant materials characteristics to be obtained.

Finally, the true potential distribution within the network and nanotube-contact junction was also mapped out by SIM. The measurements were performed on a uniformly biased network (with $V_{ac}(x) = const$) to account for the local variations in the tip-surface capacitance. This is equivalent to the case of nanotube biased at both ends and low frequencies, when the capacitive coupling of the network to the gate does not influence the potential distribution. Under these conditions, the potential map of the network is calculated by dividing the single-electrode biased SIM amplitude image by the dual electrode biased image and then renormalizing the resultant map by the value of the applied bias, V_{ac}, as illustrated in Fig. 10.10h, i. Note that the potential drop appears only at the interface between the network and the top contact.

10.2.3 Non-linear Transport Imaging via Scanning Probe Microscopy

KPFM and SIM measurements provide insight into linear transport behavior of lateral device structures. At the same time, of interest are non-linear phenomena such as rectification, harmonic generation, etc., that can be related to the non-linearity of an *I-V* curve, bias dependence of capacitance, etc. These phenomena can be addressed via non-linear SIM (NL-SIM) [59] and Scanning Frequency Mixing Microscopy (SFMM) [60], described below.

10.2.3.1 Non-linear SIM

In non-linear SIM (NL-SIM), a lateral excitation bias $V_{lat} = V_{dc} + V_{ac}\cos(\omega t)$ is applied across the sample. This excitation induces a DC, $V_{0\omega}(x)$, and AC, $V_{1\omega}(x)$,

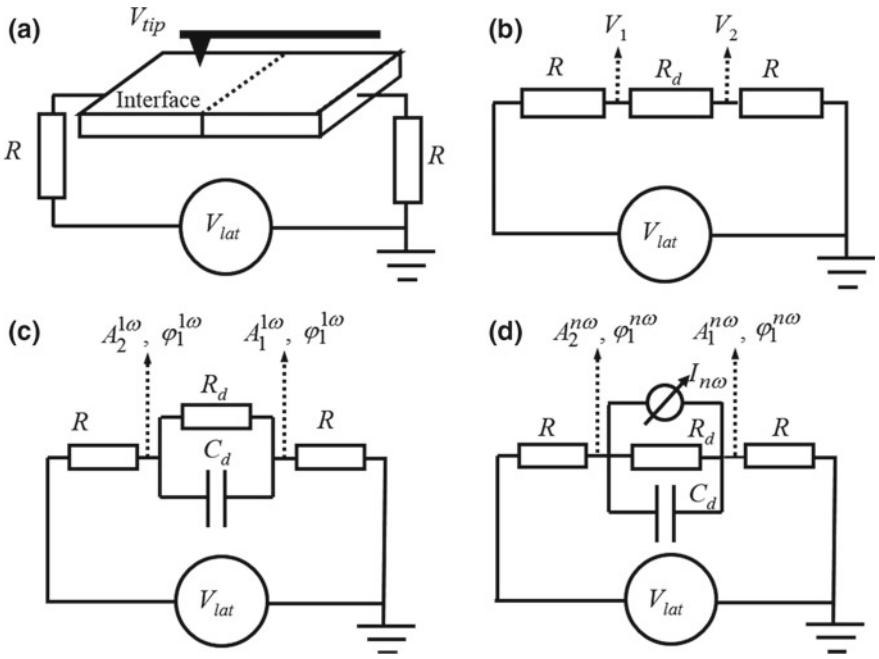

Fig. 10.12 **a** Experimental set-up for DC and AC SPM transport measurements. **b** Equivalent circuit for KPFM based DC transport measurements. The tip measures the DC potential distribution induced by a lateral bias applied across the sample, thus imaging resistive elements of the equivalent circuit. **c** Equivalent circuit for linear SIM measurements. The tip measures the distribution of the phase and amplitude of the AC voltage, thus imaging the resistive and capacitive elements of equivalent circuit. **d** Equivalent circuit for non-linear SIM. The tip measures the higher harmonics of potential oscillations in the sample generated due to frequency mixing on nonlinear interfaces, which act as current sources at harmonics of the applied bias. Adapted with permission from [59]

potential distributions across the device (x is the spatial coordinate). The resistive elements of the equivalent circuit uniquely control the DC component of the potential field, while the AC part ($V_{1\omega}$) is determined by both resistive and capacitive elements (Fig. 10.12). Hence, imaging the two components can help establishing the C-V characteristics of the interface, as demonstrated above for SIM.

However, the inherently non-linear nature of the interface gives rise to higher-order response harmonics at 2ω, 3ω, … In particular, the sample's surface potential will be given by:

$$V_{surf} = V_{0\omega} + \sum_{n=1} V_{n\omega} \cos\left(n\omega t + \varphi_{n\omega}\right), \tag{10.15}$$

where $V_{n\omega}$ is the amplitude and $\varphi_{n\omega}$ the phase of the n-th harmonic of the surface potential. The bias oscillations induce a capacitive force acting on the DC biased tip. The NL-SIM detects the phase and amplitude of the tip oscillations at all harmonics. For $\varphi_{n\omega} = 0$,

$$F_{1\omega} \sim 2\left(V_{tip} - V_{0\omega}\right)V_{1\omega} + V_{1\omega}V_{2\omega} + V_{2\omega}V_{3\omega} + \cdots, \tag{10.16a}$$

$$F_{2\omega} \sim 2V_{2\omega}\left(V_{tip} - V_{0\omega}\right) + 0.5V_{1\omega}^2 + V_{1\omega}V_{3\omega} + \cdots, \tag{10.16b}$$

$$F_{3\omega} \sim 2V_{3\omega}\left(V_{tip} - V_{0\omega}\right) + V_{1\omega}V_{2\omega} + \cdots. \tag{10.16c}$$

The second and higher harmonics of the force are a result of the non-linear behaviors of the electroactive interface and of the tip-surface junction. Generally, the harmonic amplitude decreases with order, $V_{1\omega} \gg V_{2\omega} \gg V_{3\omega}$, thus, making only the first term in (10.16a) and only the first and second terms in (10.16b, 10.16c) dominant.

The second and third order harmonics can be viewed as the sum of the intrinsic frequency mixing signal generated in the device, $F_{n\omega}^{\text{int}}$, and the tip-surface junction signal, $F_{n\omega}^{j}$: $F_{n\omega} = F_{n\omega}^{\text{int}} + F_{n\omega}^{j} = 2V_{n\omega}\left(V_{tip} - V_{0\omega}\right) + V_{1\omega}V_{(n-1)\omega}$. Thus, the intrinsic and junction signals can be separated based on the tip-bias dependence of the cantilever oscillation amplitude. While not incorporated originally, presently the use of open-loop KPFM spectroscopy [61–63] can enable this imaging mode. The third harmonic response is an unambiguous signature of non-linearity in the system, and is only generated at the intrinsically non-linear interfaces.

Like in the linear SIM, the tip oscillation amplitude depends on the corresponding harmonic of the excitation bias, whereas the phase shift is determined by a position-independent term. Thus, the surface potential variations (both in amplitude and phase) can be imaged via monitoring the tip's oscillation phase and amplitude. The mechanical resonance of the n-th harmonic signal appears at the driving frequency $\omega = \omega_0/n$, and the experimental conditions can be tuned for selective measurement of the chosen harmonics. As an alternative, the higher-order harmonics generated by a strong excitation can be recorded as a function of frequency, revealing frequency-dependent non-linear transport at the interfaces.

Deeper understanding of the NL-SIM fundamental mechanisms can be achieved by considering harmonic generation at an electroactive interface. At low excitation biases, the interfacial transport I-V curve can be expanded in a Taylor series as $I(V_0 + \delta V) = I_0 + \sum_{n=1} I_n \delta V^n/n!$, where $I_n = d^n I(V_0)/dV^n$ is the n-th derivative of the I-V curve around the DC bias, V_0, across the interface. The non-linear element acts as a current source at n-th ($n \geq 2$) harmonic of the signal in parallel with non-linear interface resistance and grounded through circuit termination resistances (Fig. 10.12d). For a symmetric circuit, the amplitudes of the intrinsic 2nd and 3rd harmonic of the signal [first terms in (10.16a–10.16c)] are expected to be equal on both sides of the interface, while the phase must flip by 180° due to current

conservation. The amplitude is related to the second and third derivatives of the *I-V* curve as:

$$V_{2\omega} = \frac{I_2 R}{(1+2I_1R)^3} V_{ac}^2, \tag{10.17a}$$

$$V_{3\omega} = \left[\frac{I_3 R}{3(1+2I_1R)^4} - \frac{2I_2^2R^2}{(1+2I_1R)^5}\right] V_{ac}^3. \tag{10.17b}$$

For small values of the protective resistor, $I_1R \ll 1$, (10.17a, 10.17b) predict that the measured second and third harmonic signals contain information on the second, $I_2(V_0)$, and third, $I_3(V_0)$, derivatives of the *I-V* curve as a function of DC bias across the interface. Thus, the non-linear transport characteristics of interfaces can be measured by probing the dependence of the non-linear voltage harmonics on the lateral DC bias.

This non-linear transport spectroscopy is illustrated in Fig. 10.13. The DC potential drop across the interface can be determined as a function of lateral bias, as shown above. Amplitude and phase of the first harmonic signal across the interface are directly related to linear interface resistance and capacitance. The DC bias dependence of the second harmonic response is displayed in Fig. 10.13d. According to (10.16b) the latter has contributions from both $V_{1\omega}$ and $V_{2\omega}$. Comparing Fig. 10.13c, d, we see that the peak of $V_{2\omega}$ for $V_{lat} \approx 0$ is due to the intrinsic non-linearity of the interface, rather than originates in the second harmonic generation at the tip-surface junction. It is also clear that at large negative biases the tip-surface junction (the second term in (10.16b)) has largest contribution to the signal. The intrinsic term can exceed the surface junction term by an order of magnitude at certain DC biases. Only a weak dependence of $V_{2\omega}$ on R is observed for $R = 1$, 3, and 10 kΩ, as expected from the assumption $I_1R \ll 1$. The behavior of $V_{3\omega}$ as a function of lateral excitation is shown in Fig. 10.13e, f. The observed dependence is explained by the fact that $V_{3\omega}$ is proportional to the derivative of $V_{2\omega}$ for small R, while for higher resistances, the full (10.16b) must be used.

10.2.3.2 Scanning Frequency Mixing Microscopy

Transport imaging at high frequencies can be performed with Scanning Frequency Mixing Microscopy (SFMM). This technique detects a mixed frequency signal at non-linear electroactive interfaces. In SFMM, the modulation signal $V_{lat} = V_{dc} + V_1\cos(\omega t) + V_2\cos((\omega + \delta\omega)t)$ is applied across the sample as shown in Fig. 10.14a, where ω is chosen in the 1 kHz–40 MHz range and $\delta\omega$ is typically 10 kHz.

The resultant surface potential has a DC component, $V_{0\omega}(x)$, and components at the frequencies of lateral bias, $V_{\omega}(x)$ and $V_{\omega+\delta\omega}(x)$. In non-linear systems, additional terms appear at higher-order and mixed harmonics of the modulation signal

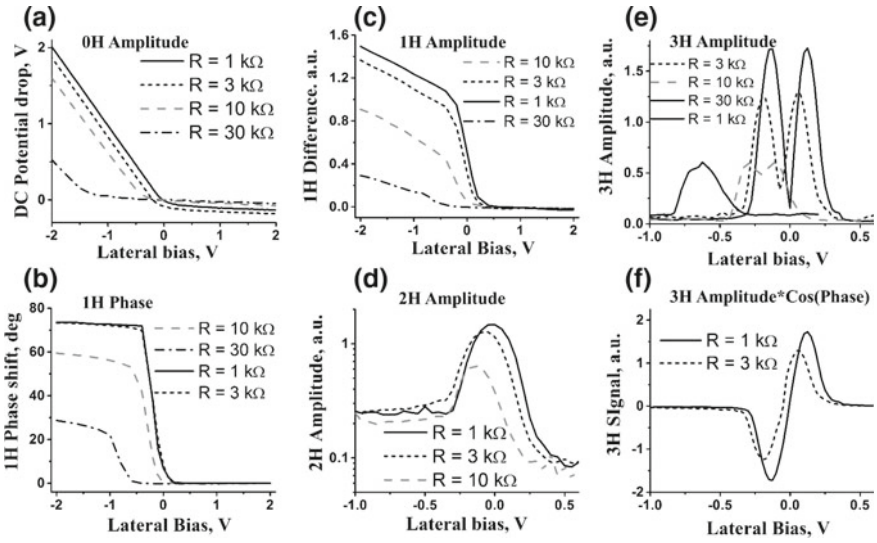

Fig. 10.13 **a** The DC potential drop across the Au–Si Schottky diode interface as a function of lateral bias. **b** Phase and **c** amplitude change of the first harmonic signal across the interface. **d** The second harmonic signal on the biased side of the interface. **e** Amplitude and **f** *x*-component, $A_{3\omega}\cos(\varphi_{3\omega})$ of the third harmonic signal. Adapted with permission from [59]

due to frequency mixing at the interface. The low-frequency component, $V_{\delta\omega}\cos(\delta\omega t)$, can be tuned to be within the bandwidth of optical detection for arbitrarily high (ω), and therefore is of particular interest.

The analysis of SFMM can be performed similar to NL-SIM. The measured signal is a combination of an intrinsic (device-generated) signal, $F_{\delta\omega}^{\text{int}}$, and an extrinsic signal originating from the tip-surface junction, $F_{\delta\omega}^{j}$:

$$F_{\delta\omega} = F_{\delta\omega}^{\text{int}} + F_{\delta\omega}^{j} \sim V_{\delta\omega}\left(V_{tip} - V_{0\omega}\right) + V_1 V_2 \tag{10.18}$$

The intrinsic term depends linearly on the tip bias, whereas the extrinsic term is tip bias independent. Thus, separation of the intrinsic signal can be done by performing measurements at several (e.g., 3) tip bias values and calculating the slope of the local response-bias curve. Alternatively, an additional lock-in amplifier can be used to determine the linear component by periodically varying the tip bias, V_{tip}.

As in the case of SIM, the tip oscillation amplitude depends on the corresponding excitation bias harmonic, with the phase shift being position independent. Hence, again, the mapping of the surface potential is performed by detecting the amplitude and phase of tip's oscillations.

SFMM potential mapping is presented in Fig. 10.15 for the same diode device as shown in Figs. 10.7 and 10.8. The the first harmonic amplitude and phase signal is mapped as a function of lateral bias in Fig. 10.15a, b. The mixed signal (SFMM) maps are shown in Fig. 10.15c, d. As can be seen, for high reverse biases the

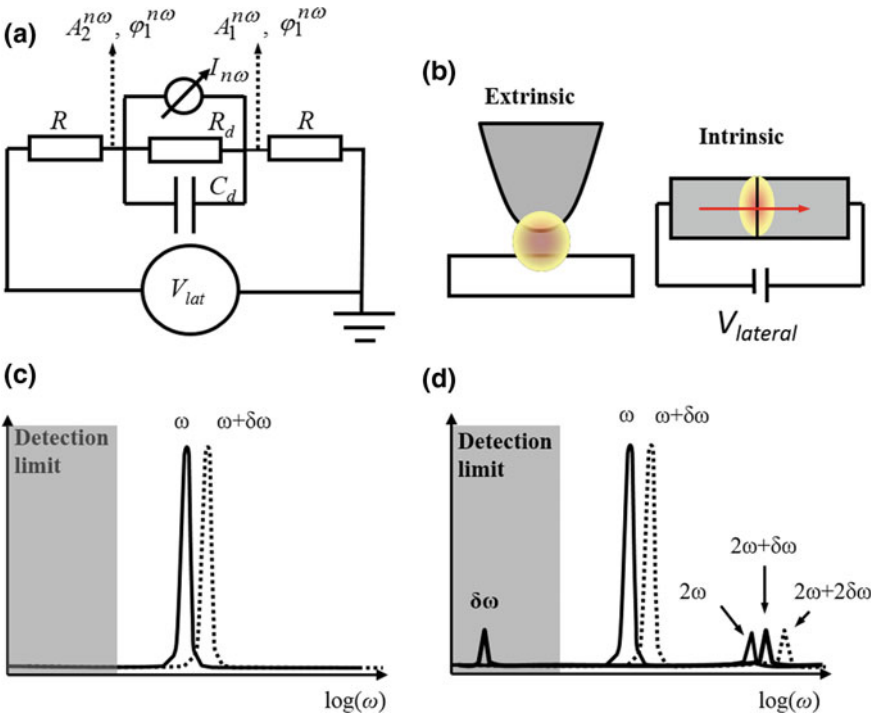

Fig. 10.14 SFMM: **a** Equivalent circuit of SFMM. **b** Extrinsic and intrinsic contributions to SFMM signals. **c** In a linear system, the application of a high frequency probing signal generates potential oscillations only on the main harmonics of the signal. **d** In a non-linear system, frequency mixing on the non-linear element induces potential oscillations on the main harmonics of the probing signal, as well as second harmonics, sum signal and difference signals. Adapted with permission from [60]

amplitude changes in a step. For forward biases it is zero, and at zero biases it has a sharp feature, revealing a region of maximum non-linearity in the *I-V* curve.

Distinguishing between these contributions is possible by numerically determining the intercept of the corresponding best linear fit at each point in the (V_{lat}, x) phase space. Figure 10.15e, f shows the resultant slope and intercept images, deconvoluting the intrinsic and extrinsic components. Furthermore, Fig. 10.16a, b shows line profiles along the voltage axis. These graphs reveal a clear advantage of SFMM over SIM, showing that the extrinsic signal is independent of the surface work function.

The SFMM dynamics can be analyzed by simultaneous measurement of the responses at ω (SIM), 2ω, 3ω (NL-SIM) and $\delta\omega$ (SFMM) as a function of frequency (ω varied, $\delta\omega = 10$ kHz), as illustrated in Fig. 10.16c. Note that the SFMM signal only has a weak frequency dependence, whereas the harmonic signals, being influenced by the cantilever dynamics, are strongly affected by frequency change. The phase signal clearly separates the regions of resistive and capacitive coupling at

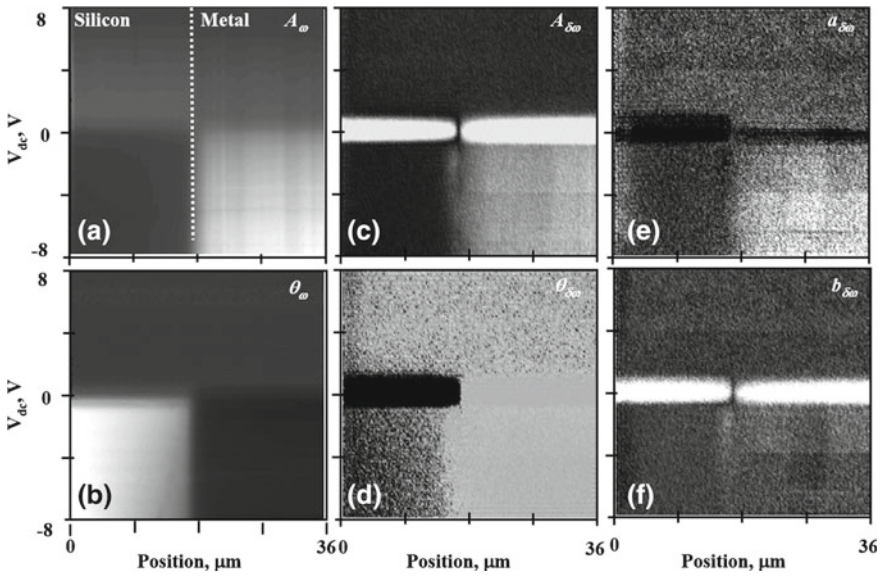

Fig. 10.15 SFMM diode mapping: Maps of DC bias dependence of the **a**, **c** amplitude and **b**, **d** phase of the (**a**, **b**) first harmonic and (**c**, **d**) mixed frequency signals. The position of the interface is indicated with a dotted line in (**a**). The strong feature around 0 V in frequency mixing signal (**c**) is due to the intrinsic contribution. **e** Intrinsic and **f** extrinsic parts of the mixed frequency signal. Adapted with permission from [60]

the interface. The decay of the SFMM signal above the cross-over frequency is due to reduced interface impedance. Importantly, the SFMM response is detectable well above the SIM limit, allowing for high-frequency probing of electroactive interfaces.

To extract the device properties from the SFMM signal, we expand the *I-V* curve of the interface in a Taylor series as $I(V_0+\delta V)=I_0+(\partial I/\partial V)\delta V+0.5\left(\partial^2 I/\partial V^2\right)\delta V^2+o(\delta V^3)$, where the derivatives of the *I-V* curve are calculated around the DC bias, V_0, across the interface. The expansion converges for a potential drop across the diode $\tilde{V}_0 < 27$ mV. At $\delta\omega$ the non-linear element acts as a current source, connected in parallel with the non-linear interface resistance and grounded via current limiting resistors. The amplitudes of the SFMM signal are given by:

$$V_{mixing}=\frac{V_1 V_2\cdot R}{4}\frac{\partial^2 I}{\partial V^2}\left(\frac{R\left(\tilde{V}_0\right)}{2R+R\left(\tilde{V}_0\right)}\right)^3, \tag{10.19}$$

where $\tilde{V}_0=V_{Lat}\left(R(V_{0\omega})/(R(V_{0\omega})+2R)\right)$.

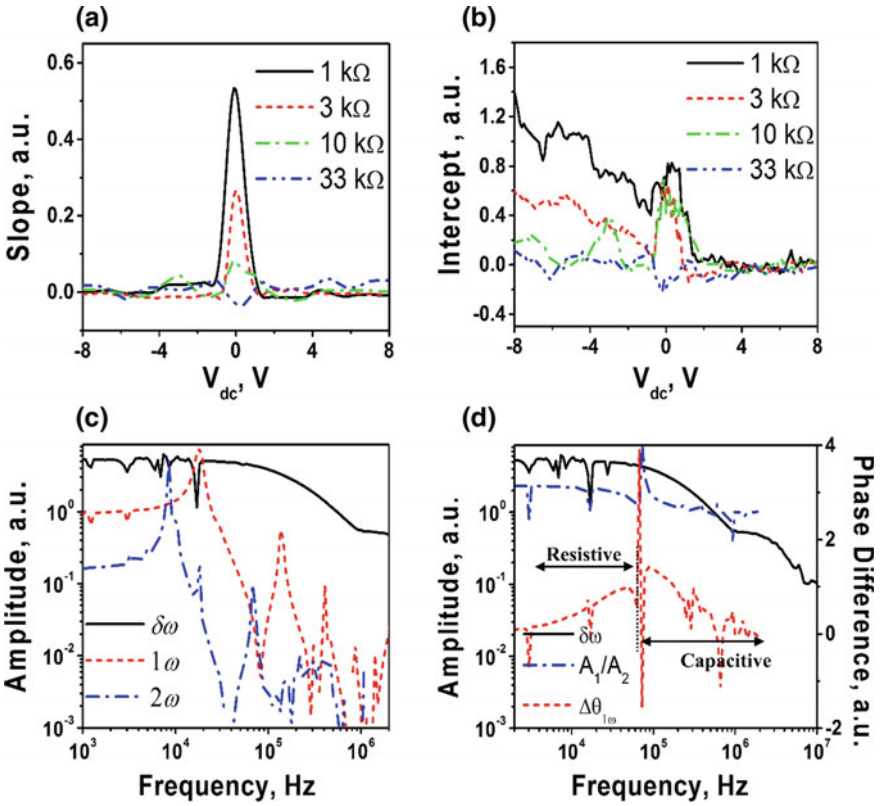

Fig. 10.16 Bias dependence of **a** intrinsic and **b** extrinsic contributions to the mixed frequency signal in scanning non-linear frequency microscopy. **c** Frequency dependence of the mixed frequency (solid) and first (dot) and second (dash-dot) responses. **d** Frequency dependence of mixed frequency (solid), and phase difference (dash) and amplitude ratio (dash-dot) of the first harmonic response. Adapted with permission from [60]

10.2.4 Time-Resolved and Pump-Probe KPFM Methods

In many cases, bias induced phenomena in lateral devices ranging from transport to electrochemistry are associated with time scales well below that of classical KPFM imaging [64]. This has stimulated the development of fast KPFM variants, extensively reviewed in Chaps. 3 and 5. Here, we discuss the modification of KPFM specifically developed for probing phenomena in laterally biased devices with a temporal resolution of 10 ms, referred to as time-resolved KPFM (tr-KPFM) [65]. Figure 10.17 shows the tr-KPFM setup that can be implemented on a conventional AFM. The AFM tip is positioned a fixed distance (z_0) above the surface on a predefined spatial grid. Then a 2-step DC excitation voltage waveform V_1 is applied to the lateral electrodes to activate charge transport, while the tip bias is modulated

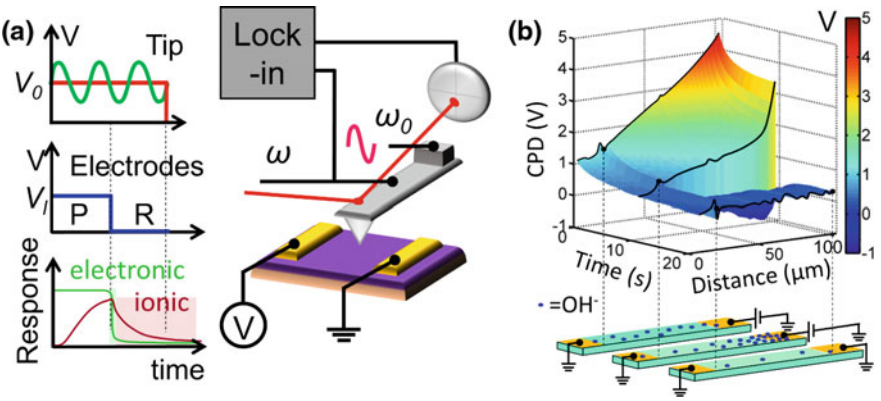

Fig. 10.17 **Tr-KPFM**: **a** A tr-KPFM schematic showing a device with two lateral electrodes and the AFM cantilever, whose oscillation is monitored by a lock-in amplifier and is affected by the local surface potential; graphs on the left display the voltage excitation signals that are applied to the AFM tip and lateral electrodes; the response of the electronic and ionic carriers to the excitation will occur on different timescales, allowing their separate detection; **b** An example of a tr-KPFM measurement: a 3D potential map of a Ca-BFO sample; At 5 V the DC excitation activated electromigration of the surface OH-groups, which changed potential distribution between the electrodes. Reprinted with permission from [65]

by a high-frequency AC probing signal: $V_{tip} = V_0 + V_{ac} \cdot cos(\omega t)$. To avoid cross-talk, an AC frequency ω is chosen to be far away from the free resonance frequency of the cantilever, ω_0. Following activation, both lateral electrodes are grounded, allowing the material to relax, while the tip bias waveform is kept unchanged. As the surface potential changes over time, so does the tip-surface force, which is reflected in the deflection signal and is detected by a lock-in. Application of the voltage waveforms and data recording is repeated for each pixel of the grid. The duration of the activation and relaxation steps is typically equal, although any pulse sequences and durations can be chosen depending on the nature of the physical phenomena under investigation.

The periodic interaction force due to a capacitive coupling between the surface (with the tip contact potential difference, CPD $= V_s$) and tip distance (z) is given by the usual linear equation, in which tip and surface potentials are now time dependent [66–68] The recorded amplitude and phase can be used to calculate the surface potential (more precisely—CPD) at each point of the grid as:

$$V_s = V_0 - \frac{1}{f_{1\omega} \cdot \frac{\partial C(z)}{\partial z}\Big|_{z_0}} \cdot V_{ac} \cdot A = V_0 - K \cdot A sin(\theta), \tag{10.20}$$

where K is the calibration coefficient and $f_{1\omega}$ is the transfer function of the cantilever for the first harmonic.

Since the tip-surface capacitance and its dependence on z are generally unknown, K can be found by performing a measurement on a grounded metal electrode. Such calibration is valid only if the capacitance gradient is independent of time and tip position in the x-y plane. Verifying this assumption is possible by measuring the response at the second harmonic, which is given by:

$$R_{2\omega}(\omega) = \frac{1}{4} f_{2\omega}(\omega) \cdot \frac{\partial C(z)}{\partial z} \cdot V_{ac}^2 \tag{10.21}$$

Here $f_{2\omega}$ is the cantilever transfer function for the second harmonic, which is typically different from $f_{1\omega}$. The slope of $R_{2\omega}$ versus V_{ac}^2 dependence measured across the sample reflects changes in $f_{2\omega}(\omega) \cdot \frac{\partial C(z)}{\partial z}$ both spatially and in time.

Since maximal perturbation in the system happens at the electrode boundary, where a step-like jump of the cantilever takes place, Fig. 10.18 shows the slope measured at the boundary region for a Ca-substituted $BiFeO_3$ (Ca-BFO) sample. As can be seen, the gradient-related slope is not affected by the boundary, but is sensitive to switching off the lateral excitation voltage. Biasing the lateral electrodes may change the cantilever transfer function due to its flexure in the electrostatic field. Therefore, the CPD calibration must be performed separately for bias-on and bias-off states.

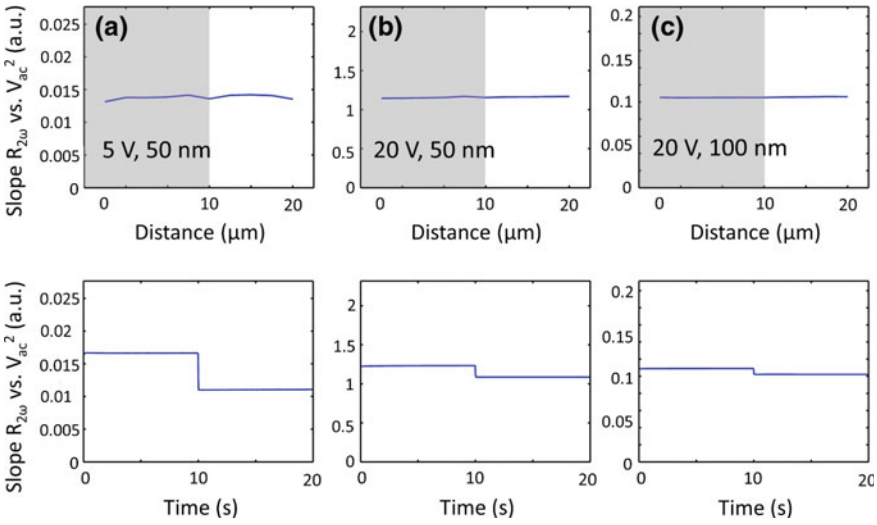

Fig. 10.18 Slopes of the second harmonic tr-KPFM response versus tip AC voltage as a function of distance and time for a Ca-BFO sample: **a** Slope averaged over distance parallel to the biased electrode (marked in grey) *versus* distance perpendicular to the electrode, and whole grid-averaged Slope versus time at 5 V polarizing bias and 50 nm tip-surface distance; **b** same for 20 V and 50 nm, and **c** same for 20 V and 100 nm. The lateral bias was switched off at 10 s. Reprinted with permission from [65]

The local CPD measurement by tr-KPFM is subject to several systematic corrections. First, the abrupt height jumps at the film-electrode interface or nanoparticles on the surface may affect the V_s—A linear dependence and the measured CPD. Secondly, the measured potential distribution may be influenced by geometrical aspects of the tip-surface and cantilever-surface interactions, affecting the spatial resolution [69–71]. It is noteworthy that the open-loop detection scheme of tr-KPFM eliminates the feedback errors typical of classical KPFM [72–74].

Figure 10.17b shows an example of tr-KPFM potential mapping. Here, CPD was measured on a 100 nm thick film of Ca-BFO on a 20 × 30 grid overlaying a 20 μm × 105 μm interelectrode region. Film activation was triggered by a polarization pulse of 5 V lasting for 10 s. The CPD data were averaged for pixels equidistant from the electrodes and plotted as a function of time (after switching the lateral bias on) and distance perpendicular to the electrodes (Fig. 10.17b). The potential profile between the electrodes changes from nearly linear right after application of polarizing bias to curved after 10 s of polarization. At time t = 10 s, both electrodes are grounded and the measured CPD shows a negative pit in the vicinity of the formerly-biased electrode, indicating accumulation of negative charge (presumably, surface OH^- ions) in that region. During the following 10 s of relaxation, this charge dissipates, and the potential profile becomes a flat zero line throughout the film. Thus, although the extension of the measurement deep into the time domain decreased the spatial resolution of tr-KPFM as compared to standard EFM or KPFM techniques, it simultaneously provided much more information on the surface potential dynamics, which is now accessible to about ms scale. Note that in principle spatial resolution of the tr-KPFM technique is not inferior to that of EFM and KPFM, but rather is a trade-off between the chosen temporal resolution and total time spent on acquiring one image. The spatial resolution can be ultimately sacrificed in favor of capturing potential dynamics with millisecond resolution, as was proposed recently in a closed-loop time-resolved KPFM method [75]. This approach implies positioning of the AFM tip at one single location on a sample and recording the KPFM feedback signal (CPD) in response to a step-like DC gate voltage pulse. In the future, the obvious advance for tr-KPFM is the incorporation of the general mode acquisition paradigm [76, 77], recently implemented in G-mode KPFM [78]. This paradigm will help simplify the signal detection, capture the whole cantilever response in the frequency domain, eliminate frequency-shift artifacts, and improve temporal resolution to microseconds.

An alternative approach for time resolution in KPFM was demonstrated by employing a pump-probe method [79]. The pump-probe KPFM (pp-KPFM) detection scheme takes advantage of the fact that the electrostatic interaction between the tip and surface is independent of the cantilever dynamics and is not limited by the bandwidth of the controller electronics. Nullifying this interaction in pp-KPFM is achieved not by a DC voltage offset applied to the tip as in standard KPFM, but by a pulsed modulation of AC voltage, V_{AC}. This probing waveform, shown in Fig. 10.19a, consists of an AC envelope intermitted by short grounding pulses, which can be synchronized with the pumping DC square pulses applied between the lateral electrodes (Fig. 10.19a, b). The delay time between the pump

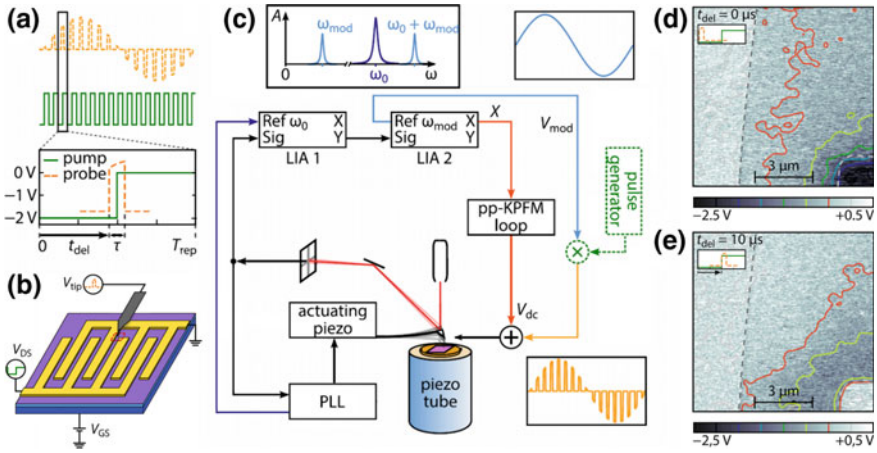

Fig. 10.19 Pump-probe KPFM: **a** The pump (green line) and probe (yellow line) pulses of the pp-KPFM; **b** An organic field effect transistor with interdigitated electrodes in pp-KPFM configuration; **c** A schematic of the single-loop pp-KPFM setup. The modulation AC signal is modified with a pulse generator and used as a probe signal. It is applied to the tip together with the feedback V_{dc} signal resulting in response, whose spectrum is shown in the inset. **d** and **e** CPD maps measured with pp-KPFM in the region indicated by the red square in panel (**b**). The organic film in between the source and drain electrodes becomes polarized after application of −2 V to the source electrode (panel d). The material retains some negative charge immediately after grounding of the electrodes (panel d), indicating the presence of space-charge limited transport in this region. Adapted with permission from [79]

and probe pulses can be varied to detect the sample state at a certain moment relative to the excitation signal. The sample response to the pump excitation pulses is a time-varying CPD, which induces frequency shifts of the mechanical resonance frequency ω_0. This modulation can be detected by a lock-in amplifier around the sideband frequency $\omega_0 + \omega_{mod}$, where ω_{mod} is the AC excitation frequency. Then, the pp-KPFM control loop nullifies the lock-in signal by applying a compensating voltage to the tip. The overall schematic of a single-loop pp-KPFM is shown in Fig. 10.19c. This simplest setup is prone to producing a significant topographic crosstalk arising from incomplete time-averaged potential compensation (i.e. the force is only nullified during the probe time τ in Fig. 10.19a). To correct for this, Eng's group introduced a second, standard KPFM loop, which compensates the time-averaged CPD, but cannot capture the fast CPD changes accessible by the pp-KPFM. As an example of potential mapping, Fig. 10.19d presents a CPD distribution between the source (cornered) and drain (flat) electrodes in a pentacene thin film. When the source electrode is biased at −2 V (delay time is 0 μs), an expected potential drop is seen between the electrodes. However, right after grounding of the source electrode (delay time 10 μs, Fig. 10.19e), although its potential returned to zero, the neighboring film is still negatively charged. The charge will dissipate in a matter of 8 μs, indicating the space-charge limited

transport regime in the film. In this example, the pp-KPFM temporal resolution is 2 μs within the probing time range (repetition period) of 20 μs.

The spatial resolution of pp-KPFM is equal to that of standard KPFM. The temporal resolution is limited by the pulse generator speed, and currently can reach 4 ns, allowing probing electrodynamic processes on the nanoscale in the nanosecond regimes. The total probing time at duty cycles lower than 5% is limited by various cross-talking at low repetition frequencies. The signal-to-noise ratio significantly decreases at repetition frequency of 10 Hz (probing time 0.1 s), which makes the pp-KPFM unsuitable for tracking material response to short excitations for long (seconds and tens of seconds) times. Note also that whereas one tr-KPFM dataset contains potential maps for any moment within the total probing time range (at a given time resolution), a pp-KPFM dataset is one potential map at a certain delay time (i.e. certain moment after excitation). Thus, the pp-KPFM allows for higher flexibility in choosing the moments of interest for capturing the instantaneous potential distribution, and tr-KPFM shows potential maps at all times providing deeper insight into physics of transport and charging phenomena.

10.2.5 Gating Probes

The AFM tip placed above the sample can act not only as a sensitive probe for detecting local electrical or magnetic properties through the long-range interaction, but also as an active electrode that influences the local charge transport. This idea was realized in 1990-s in form of the scanning gate microscopy (SGM) technique [49, 80, 81]. In SGM, a biased conductive AFM tip is scanned over the nanostructure in non-contact mode, while the electron transport through it is monitored using lateral electrodes. The tip, via its electric field (capacitive coupling), influences the transport measurements by locally perturbing the electron gas density, thus acting as a movable gate. No tunneling current flows between the tip and sample. For semiconductor-based quantum systems, the measurements are performed at liquid nitrogen or helium temperatures. Therefore, in order to avoid laser heating, quartz tuning forks and soft piezoresistive cantilevers are often used in place of the common optical AFM detection scheme [82]. The spatial resolution of SGM is on the order of half of the Fermi wavelength in the semiconductor nanostructure [49]. Unlike STM, SGM allows probing subsurface features, such as two-dimensional electron gas buried tens of nanometers below the surface. The variations in conductance measured by SGM were shown to be related to local current flows [83] or local density of states [84], depending on the studied system. This method was also used to probe the electron wave functions by mapping the probability densities in quantum rings. For 1D systems, such as carbon nanotubes, SGM measurements can be performed in ambient conditions; however, energy and spatial resolution drastically improve in low noise, low T environments.

Extending the SGM technique to scanning gate spectroscopy (SGS) by continuously varying the tip's potential allowed resolving the energy spectra of electron

scattering in the device [14]. Another modification of SGM comes from employing a tip coated in magnetized metal, and was used to map transverse voltage in graphene Hall devices [9]. Reduction of parasitic electric field effects was achieved via a KPFM feedback loop that kept the probe-surface potential difference at zero. Further evolution of the SGM approach is currently focused on design of coaxial probes that improve spatial resolution by reducing parasitic capacitance [85] and development of comprehensive theory that provides interpretation of the experimental SGM results [8].

The SGM methods have been used to study a variety of systems, ranging from quantum point contacts, two-dimensional electron gas, quantum dots, carbon nanotubes, InAs and Si nanowires, graphene, to more complex structures (see [8, 82] and references therein). Figure 10.20 presents several examples of SGM measurements. Panel (a) shows an SGM setup for probing transport in a two-dimensional electron gas buried 25 nm deep in a GaInAs/AlInAs heterostructure. The region of interest includes a quantum ring, whose magnetoresistance maps are shown in Fig. 10.20b. Measurements performed in high magnetic field (quantum Hall regime), reveal existence of localized states ("Coulomb islands") inside the device that can be manipulated individually [82]. Another example (Fig. 10.20c) shows maps of electron flows as measured by SGM in two quantum point contacts formed in a GaAs/AlGaAs heterostructure. Unexpectedly, the current flows out of the point contact not continuously, but forming a complex branching pattern due to focusing of the electron paths by ripples in the background potential [81]. A scanning gate spectroscopic map is presented in Fig. 10.20d, which shows variation of resistance

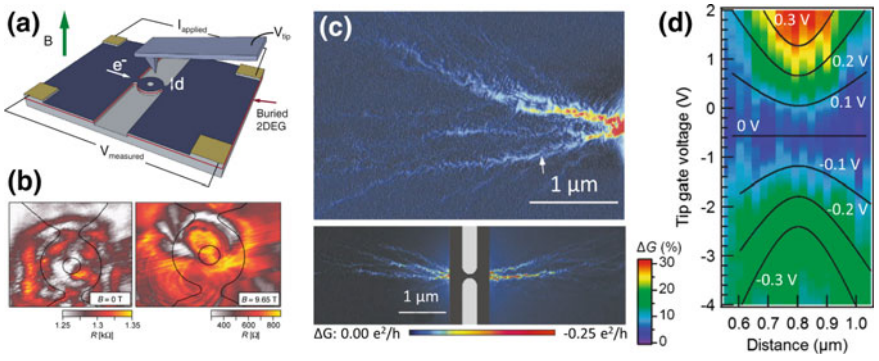

Fig. 10.20 **SGM**: **a** SGM setup for measuring buried two-dimensional electron gas in a quantum ring; AFM tip is positioned at distance d = 20–50 nm above the surface; An external magnetic field B can be applied perpendicular to the surface; **b** Magnetoresitance maps of a GaInAs/AlInAs heterostructure quantum ring as measured by SGM in the absence and presence of magnetic field; reprinted with permission from [82]; **c** SGM images of a quantum point contact measured at 1.7 K; Reprinted with permission from [81]; **d** An example of SGS: resistance change map of a defect in a carbon nanotube as a function of tip voltage; the plotted distance is measured along the nanotube length; the defect is close to its middle; The black lines with voltage values show a family of contours of the defect site electrostatic potential; Adapted with permission from [14]

in a carbon nanotube defect as a function of tip voltage. As can be seen, the defect is very sensitive to SGS probing. Simple modeling in this case allowed extracting the defect's electrostatic potential, determination of the defect and nanotube band alignments and barrier dimensions associated with the defect [14].

SGM has several limitations, some of which are shared by other SPM techniques [82]. One of the technique's complications is the complex shape of the tip that influences the electron transport. Proper understanding of SGM images, thus, requires correct modeling of the electric field produced by the tip in the measurement location. As in any other SPM method, caution must be taken to avoid tip-induced artifacts due to tip damage or accumulation of particles. SGM imaging is also negatively affected by stray residual charges (electronic traps, surface ions, etc.) that may plague the device. At low temperatures, these charges are immobile and can be identified in SGM maps as concentric rings that shift around under illumination or thermal cycling. Lastly, a too high voltage on the tip must be avoided, as it may result in irreversible changes in the device.

10.3 Tip Calibration and Imaging Artefacts

10.3.1 Tip Calibration in Electrostatic SPMs

The resolution of the force-based electrostatic SPMs, such as KPFM and SIM, for quantitative nanoscale imaging is limited by the geometric size of the tip [86, 87]. The tip geometry corrections can be estimated from the spherical tip approximation for small tip-surface separations by recording dependencies of the electrostatic force- or force gradient on distance and bias [67, 88]. Such a calibration is often laborious, and frequent re-calibrations are required due to mechanical tip instabilities [89]. The tip contribution to the measured properties can also be quantified directly by employing an alternative calibration method [90]. The separation of the tip contribution can be done using the tip-surface transfer function [70, 91–93].

Well-defined metal-semiconductor interfaces have been proposed as a sample standards for such deconvolution [94]. However, humidity-sensitive mobile charges and surface states [95, 96] alter the step-like surface potential profiles even across grounded interfaces. An improved approach for calibration of the tip shape in the voltage modulation methods can be based on the SIM of active device structures, more specifically, carbon nanotubes [93]. Here, the nanotube is AC voltage biased making the SPM tip above it oscillate due to capacitive coupling (SIM amplitude imaging). Having a diameter much smaller than the AFM tip, the nanotube effectively probes its geometry. Furthermore, AC biasing precludes the effect of lateral charge migration.

The force between the tip and the surface depends on capacitances as:

$$2F_z = C_{ts}^{'}(V_t - V_s)^2 + C_{ns}^{'}(V_n - V_s)^2 + C_{tn}^{'}(V_t - V_n)^2 \tag{10.22}$$

where V_t is the tip potential, V_n is the nanotube potential and V_s is the surface potential, C_{ts} is the tip-surface capacitance, C_{ns} is the nanotube-surface capacitance and C_{tn} is the tip-nanotube capacitance. C' refers to the derivative of capacitance with respect to the z direction perpendicular to the surface. When an AC bias is applied to the nanotube, $V_n = V_0 + V_{ac}\cos(\omega t)$ and $V_s = V_0$. Thus, the first harmonic of the tip-surface force is:

$$F_{1\omega} = C_{tn}^{'} V_{ac}(V_t - V_0) \tag{10.23}$$

In comparison, application of an AC bias to the tip, $V_t = V_{dc} + V_{ac}\cos(\omega t)$ yields

$$F_{1\omega} = C_{tn}^{'} V_{ac}(V_{dc} - V_0) + C_{ts}^{'} V_{ac}(V_{dc} - V_s) \tag{10.24}$$

Hence, applying an AC bias directly to the carbon nanotube allows the tip-surface capacitance to be excluded from the overall force.

This equation can be rewritten using the tip-surface transfer function $C'_z(x,y)$, defined as the capacitance gradient between the tip and a region $dxdy$ on the surface (Fig. 10.21a) [86] as

$$F_{1\omega} = (V_t - V_0) \int C_z^{'}(x,y) V_{ac}(x,y) dxdy \tag{10.25}$$

For the nanotube oriented in the y-direction and taking into account small width, w_0, of the nanotube compared to the tip radius of curvature, (10.25) can be integrated as

$$F_{1\omega}(a) = w_0 V_{ac}(V_t - V_0) \int C_z^{'}(a,y) dy \tag{10.26}$$

where a is the distance between the projection of the tip and the nanotube. Assuming a rotationally invariant tip, the differential tip-surface capacitance is $C_z(x, y) = C_z(r)$, where $r = \sqrt{x^2 + y^2}$ and (10.26) can be rewritten as a function of a single variable, a. Therefore, the partial tip-surface capacitance gradient $C_z^{'}(r)$ can be found by numerically solving (10.25) using experimental force profiles across the nanotube, $F_{1\omega}(a)$.

This calibration approach is validated in Fig. 10.21. The biased electrode-tip interactions can be minimized by performing the measurements 1–2 μm away from electrode, where the nanotube potential is uniform. Figure 10.21b, c presents topographic and SIM amplitude images of the nanotube. The nanotube is 2.7 nm tall and ca. 40 nm wide (the measured width is convoluted with the tip shape). Simple geometric considerations yield a tip radius of curvature as $R \approx 75$ nm.

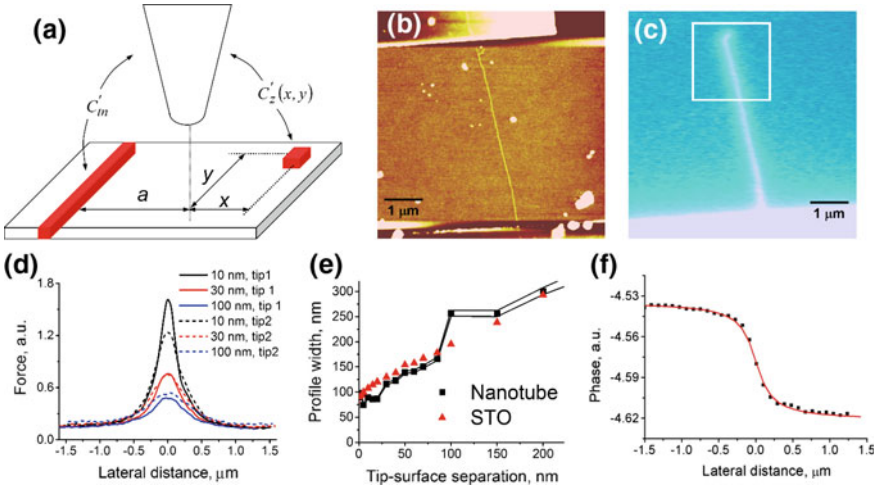

Fig. 10.21 **a** The tip-surface transfer function is defined as the capacitance gradient, $C'_z(x,y)$, between the tip and the region *dxdy* located at position *x*, *y*. Experimentally determined is an integral of $C'_z(x,y)$ as a function of distance from a nanotube, *a*. **b** Topographic image and **c** SIM amplitude image across a carbon nanotube on SiO_2 substrate. **d** Force profiles for various lift heights and two different tips. **e** Profile width for carbon nanotube standard and SIM phase image of $SrTiO_3$ (STO) grain boundary as a function of lift height (**a**). **f** Measured (■) and simulated (line) phase profiles across STO GB. Adapted with permission from [93]

The full width at half maximum (FWHM) of the amplitude profile can be as small as ≈100 nm and increases with the tip-surface separation. The tip-surface transfer function can be extracted from this profile using (10.25). Analysis of the distance dependence and properties of the $F_{1\omega}$, amplitude profiles can be done by fitting it a Lorentzian function:

$$y = y_0 + \frac{2A}{\pi}\frac{w}{4(x-x_c)^2 + w^2}, \tag{10.27}$$

where y_0 is an offset, A is the area below the peak, w is the peak width and x_c is the position of the peak. Obviously, (10.27) describes well the experimental data. The non-local contribution of the cantilever and tip cone to the measured response is quantified by the offset y_0 [64, 97, 98]. The profile shape is tip dependent and Fig. 10.21d presents profiles for two different tips showing that profiles are sensitive to the tip shape. The distance dependence of the peak height $h = 2A/\pi w$ is shown in Fig. 10.21e. For large tip-surface separations $h \sim 1/d$. The distance dependence of the width, w, is shown in Fig. 10.21f and is almost linear in distance for $d > 100$ nm. A similar picture was observed for profile width for "potential step" type standards, e.g. ferroelectric domain walls and biased interfaces [99].

In the case of the amplitude profile given by (10.27), the local part of the differential tip-surface capacitance can be found by solving (10.26) as

$$C_z^{'} = \frac{2A}{\pi} \frac{w}{\left(4r^2 + w^2\right)^{3/2}} \tag{10.28}$$

where A and w are z-dependent parameters determined in (10.27) and r is radial distance.

Equation (10.25) can be used to determine the tip shape contribution to electrostatic SPM measurements in systems with arbitrary surface potential distributions. For a stepwise surface potential distribution, $V_{surf} = V_1 + (V_2 - V_1)\theta(x)$, where $\theta(x)$ is a Heaviside step function, the measured potential profile is $V_{eff} = V_1 + V_2 \arctan(2x/w)/\pi$, provided that the cantilever contribution to the measured potential is small. Figure 10.21f shows excellent agreement between the measured and simulated profile shape.

10.3.2 Imaging Artifacts and Some Considerations on Invasiveness

Qualitative and sometimes even quantitative SPM studies of fundamental physical phenomena on the micron and nanometer level are often hindered by SPM imaging artifacts. In fact, wide availability of advanced SPM techniques and lack of universal standards and reference handbooks in the field have contributed to a large number of papers with dubious and even obviously erroneous interpretation of SPM data. Here, we briefly discuss the major sources of artifacts in electrostatic measurements by SPM.

One of the possibilities for erroneous potential measurements in KPFM is DC and AC voltage drops in the circuit including the probe tip. DC voltage drops in the electronics can be important if the tip-surface resistance is very small. One of the weakest links in the measurement set-up is the contact between the tip holder and tip substrate that typically has resistances on the order of several kΩ and larger depending on the type of tip coating. However, during KPFM imaging the tip-surface separation is usually large (>10 nm), therefore, the resistance is also large ($\gg$ GΩ) and DC voltage drops in the electronics are negligible. If the tip accidentally touches the surface so that there is a significant current flow the effects are easy to notice: for a nonconductive or contaminated metal surface, a charged patch will form. Overall, DC leakage is negligible with a possible exception of extremely small tip-surface separations, in which case tip-surface charge transfer is possible. This is not quite true for AC leakage. Modest capacitive coupling between the AC biased channel and the rest of the microscope on the order of ≈nF at the typical frequencies of 10–100 kHz is equivalent to a leakage resistance on the order of 10–100 kΩ. For cantilevers with semiconductive coatings and large probe-tip

holder contact resistances, this leakage resistance can be (but usually is not) comparable to the contact resistance between tip holder and the substrate, resulting in significant attenuation of driving voltage. This effect can be compensated by improving probe holder contact, e.g. by placing a drop of silver paint or a piece of indium on the contact area.

Another source of error in potential measurements are feedback effects and non-local cantilever effects. Due to feedback non-ideality, the first harmonic of the cantilever response is not nullified; rather it is reduced to some small, but finite value. In addition, simple calculations suggest that at typical tip surface separations on the order of 10–100 nm, tip-surface and cantilever-surface capacitive gradients are comparable [67]. Therefore, both contributions are important and the signal picked up by the probe can be subdivided into the local tip part and non-local cantilever part.

In this case, the nulling condition in KPFM corresponds to

$$F_{loc}(V_{dc} - V_s) + F_{nl}(V_{dc} - V_{av}) = \delta / V_{ac}, \tag{10.29}$$

where F_{loc} is the local part of the tip surface capacitance gradient, F_{nl} is the non-local and cantilever part, V_s is the local potential below the tip, V_{av} is the surface potential averaged over the cantilever length, V_{ac} is the tip AC bias, and δ is the feedback constant (which, of course, depends on the gain values for the feedback loop). The nulling voltage V_{dc} is then

$$V_{dc} = V_s \frac{F_{loc}}{F_{loc} + F_{nl}} + V_{av} \frac{F_{nl}}{F_{loc} + F_{nl}} + \frac{\delta}{V_{ac}(F_{loc} + F_{nl})}. \tag{10.30}$$

Reliable measurement of local surface potential is possible if and only if $F_{loc} \gg F_{nl}$, i.e. tip is close to the surface, and the third term is small, i.e. the feedback error is minimized. Noteworthy is that the relative potential variations across the surface are independent of feedback effects, i.e. the measured potential difference between two points relates to the true potential difference as:

$$(V_1 - V_2)_{measured} = (V_1 - V_2) \frac{F_{loc}}{F_{loc} + F_{nl}}. \tag{10.31}$$

The absolute surface potential value, however, depends on feedback effects:

$$V_{dc} = V_{av} + \frac{\delta}{V_{ac}(F_{loc} + F_{nl})}. \tag{10.32}$$

The implications of (10.31) and (10.32) are twofold. Measurements of absolute surface potential (or CPD) by KPFM are subject to errors due to the feedback effect. The reciprocal dependence of absolute surface potential on driving voltage can be easily confirmed experimentally by variation of the driving amplitude [72]. Doing so at different tip-surface separations allows the effect of F_{loc} and F_{nl} to be

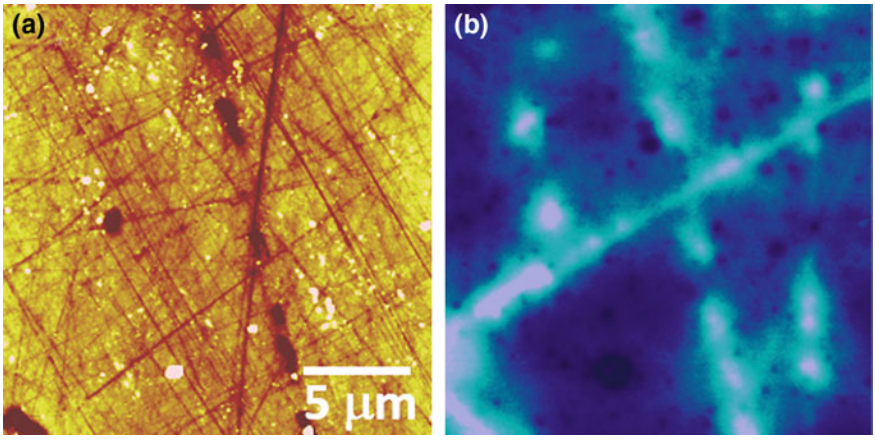

Fig. 10.22 **a** Surface topography and **b** surface potential of a polished $SrTiO_3$ surface. Notice a correspondence between the topographic and potential images. Adapted from [15]

determined and the true surface potential can be obtained from the analysis of the data.[1] At the same time, potential variations across the surface do not depend on V_{ac} (except that small driving amplitudes result in increased noise level), but the effective potential difference between two spots on the surface (say, 10–40 μm apart) decays logarithmically with lift height. For very large tip-surface separations, the potential contrast along the surface disappears [98].

KPFM metrology of laterally biased devices is limited by a significant cantilever contribution to the measured potential, minimization of which requires imaging at small tip-surface separations. Under optimal conditions, the potential drop measured at the interface (i.e., ±500 nm from the interface) is approximately 90% of its true value. The rest decays at the lateral distances on order of approximately 10 μm from the interface, i.e., comparable to the cantilever widths. Therefore, by measuring potential distribution in ceramics with grain sizes on order of 10–20 μm, the grain boundary conductivity can be determined reliably, whereas the grain bulk conductivity cannot. Similar problems exist for carbon nanotube circuits. Due to the fact that interaction area of KPFM (30–100 nm) is much larger than the diameter of a nanotube, the measured potential is a weighted average of nanotube potential and back gate potential [93]. Of course, more complex artifacts are possible. For example, capacitive crosstalk between the tip bias channel and photodiode detector channel will result in an error signal proportional to the driving voltage and this effect can be minimized only by decreasing the tip surface separation, but not by increasing driving amplitude. Also, significant role can be played by surface roughness (via second derivative of capacitance) and contaminations, as illustrated in Fig. 10.22.

[1]Of course, in ambient conditions, mobile surface charges contribute to the measured potential. Here we only consider the *measurement* artifacts.

As a concluding remark, the CPD detection quality in all of the described techniques and examples can be improved by using shielded conductive AFM probes. The long-range interaction and stray capacitive coupling between the AFM probe and sample surface limits the spatial resolution of potential mapping and introduces artifacts and offsets. The use of coaxial probes, in which the cantilever and cone are shielded by a conductive shell eliminates these shortcomings and significantly improves the quality of data. These probes have been introduced more than a decade ago [100], are still developed and improved [85, 101, 102] and not widely available. Employing them in characterizing lateral devices presents an ample opportunity.

10.3.3 Invasiveness

A very interesting, and almost unstudied issue is the tip effect on surface properties [103]. Voltage or mechanical modulation of the biased tip induces an AC current in the region directly below the tip proportional to $VdC/dt + CdV/dt$, where first term originates from oscillation in tip position and second from voltage oscillations. For a voltage modulated tip with a driving amplitude of 10 V, driving frequency of 100 kHz and a (heavily underestimated) tip surface capacitance of 10 aF, the corresponding displacement current amplitude is ≈100 pA. Assuming the lateral size of the biased region to be ≈100 nm, variations in surface potential due to the displacement current become significant for resistivities higher than 10^{-2} Ωm. For well conducting surfaces or semiconductor surfaces with pinned Fermi levels, changes in surface potential due to displacement current are negligible. However, this might not be the case for surfaces with unpinned Fermi levels, where tip-induced band bending and associated variations in surface potential can be important. Another interesting case is imaging of nanoscale objects, for which injection of even several electrons can severely affect properties. This analysis has several interesting implications for lateral transport measurements on biased nanoscale devices as discussed in Sect. 10.2.5.

10.4 Applications to Non-invasive Electronic Transport

Charge transport and, hence, device operation in traditional and emerging electronic devices is controlled by a number of parameters, such as the interfaces, nanostructure, dopant distribution, and existence of traps. The SPM techniques described in previous sections provide an excellent way of probing these parameters and correlating them to the overall performance of the device. Here we will focus on SPM imaging of various materials in lateral configuration, including semiconductors, ceramics, nanowires, nanotubes and 2D materials. Over the course of the last several decades, these material systems have been studied in a range of devices

from p-n junctions, to field effect transistors (FET), conductometric gas sensors, light-emitting diodes, lasers, and solar cells. Each class of these applications has its own set of problems that need to be solved to improve their characteristics, necessitating adaptation of measurement setup and problem-specific data analysis.

KPFM and EFM emerged as the most popular methods for studying these systems in real space. These techniques can be used to monitor potential distribution in the channel in different bias states or at different gate voltages. As described below, this allows extracting information on the charge carrier density and mobility; density of charge traps; and rates of trapping/detrapping; injection rates from the electrodes; distribution of resistance and barriers in defects (interfaces, grain and domain boundaries); and, finally, the transport mechanisms in the channel. The field of organic electronics has, probably, benefited more from these potentiometric SPM methods than studies of any other class of devices. The reason for this is that unlike inorganic semiconductors, organic materials suffer significantly from nanoscale heterogeneity in the form of disordered regions, phase-separated domains, and non-ideal molecular packing. These features affect nanoscale charge transport by determining the trap density and mobility, injection, generation and recombination rates. Hence, a significant effort was made to unravel transport details in organic field effect transistor (OFET). A short review on this topic can be found in [104].

A series of early works has demonstrated the simple possibility of potential profiling in active lateral devices using SPM methods [44, 105–109]. Later publications went further to extract more useful information from the potential distribution maps. Puntambekar et al. [110] have investigated behavior of thin-film pentacene transistors in two configurations: with lateral electrodes deposited on top of the film and below it (Fig. 10.23a, c schematics). Using KPFM they mapped potential distribution between the electrodes at different values of the source-drain voltage (V_{SD}) and gate voltage (V_G). Profiles of these maps are shown in Fig. 10.23a–d. For the bottom contact device, they observed a sharp drop in potential on the film-source electrode boundary, and a smaller step on the drain electrode interface. These barriers tend to increase at negative gate voltage and are nearly eliminated at $V_G > 27$ V, when the device is switched into the "ON" state. Thus, in this configuration the FET is contact-limited. On the contrary, for the top contact configuration, potential profiles stay linear between the electrodes at all V_G values, only inflecting down at +40 V. Increasing V_{SD} at a constant V_G leads to a transition from the linear to the pinch-off regime (Fig. 10.23d). To quantify contributions of the channel and electrodes to the overall device conductivity in different states, authors converted potential drops across respective elements to their resistances using measured current values (Fig. 10.23e, f). For the bottom electrode configuration, a clear transition between the channel-dominated and source-controlled regimes is seen around $V_G = 0$ V (Fig. 10.23e). In the top electrode device, as expected, the electrode contribution is minimal (1 to 2 orders of magnitude lower than the channel's).

An early attempt to use KPFM potential profiling to extract useful information on charge transport beyond resistance measurements was undertaken by Bürgi et al.

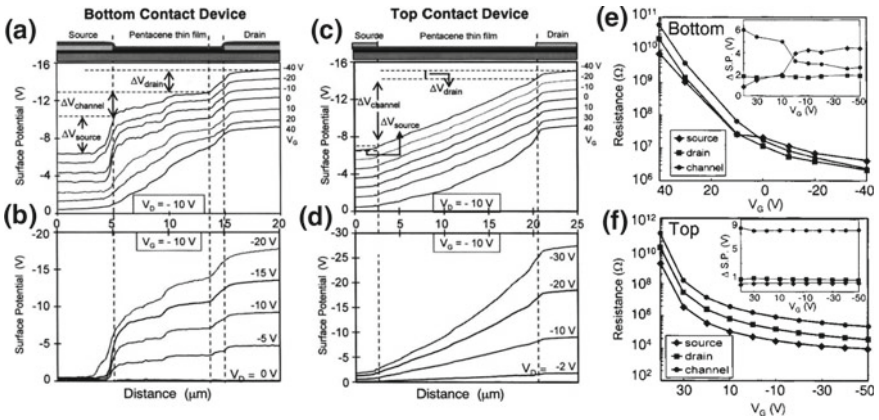

Fig. 10.23 Determining contact resistance in an organic FET: **a** A pentacene device schematic in bottom contact configuration and measured potential profiles at constant $V_D = -10$ V and gate voltage varying from −40 to 40 V in 10 V steps. Profiles are offset for clarity; **b** Potential profiles for same device as in (**a**) with $V_G = -10$ V and V_D varying from 0 to −20 V; **c** A pentacene device schematic in top contact configuration and measured potential profiles at constant $V_D = -10$ V and gate voltage varying from −40 to 40 V in 10 V steps. Profiles are offset for clarity; **d** Potential profiles for same device as in (**c**) with $V_G = -10$ V and V_D varying from −2 to −30 V; **e** and **f** extracted resistances of the source, drain and channel as a function of V_G for bottom and top electrode configurations, respectively. The insets show surface potential drops associated with these resistances. Adapted with permission from [110]

[41]. This work investigated operation of an FET based on a thin film of regioregular head-to-tail coupled poly(3-hexylthiophene). The CPD data collected on an active FET at various temperatures and gate voltages were converted into the hole mobility versus temperature and hole mobility versus carrier concentration dependencies. It was concluded, that transport was limited by the Poole-Frenkel emission.

Another example of deep quantitative analysis of potentiometric data is given by Silveira et al. [111]. The authors investigated charge injection from a metallic (gold) electrode into the π-conjugated system of a triarylamine (in polystyrene—TPD-PS). Thin films of TPD-PS were formed on a quartz substrate with pre-deposited lateral electrodes as shown in the schematic of Fig. 10.24a. Potential profiling was performed in vacuum using EFM. The shift in the resonance frequency was recalibrated to yield CPD and $\partial^2 C/\partial z^2$. Figure 10.24a shows interelectrode potential profiles as a function of lateral electrodes voltage. They are linear at low voltages and slowly curve upward at bias >15 V. The distribution of electric field along the x-axis can be obtained by differentiating the potential by x (Fig. 10.24b). At low voltage, the electric field is distributed uniformly within the channel, as expected for ohmic transport. However, at higher bias, the electric field at the drain electrode is significantly stronger than at the source electrode, which is typical of a space charge limited (SCL) regime. Furthermore, the behavior of electric field at the interfaces was used to evaluate the degree to which the interelectrode current is space-charge

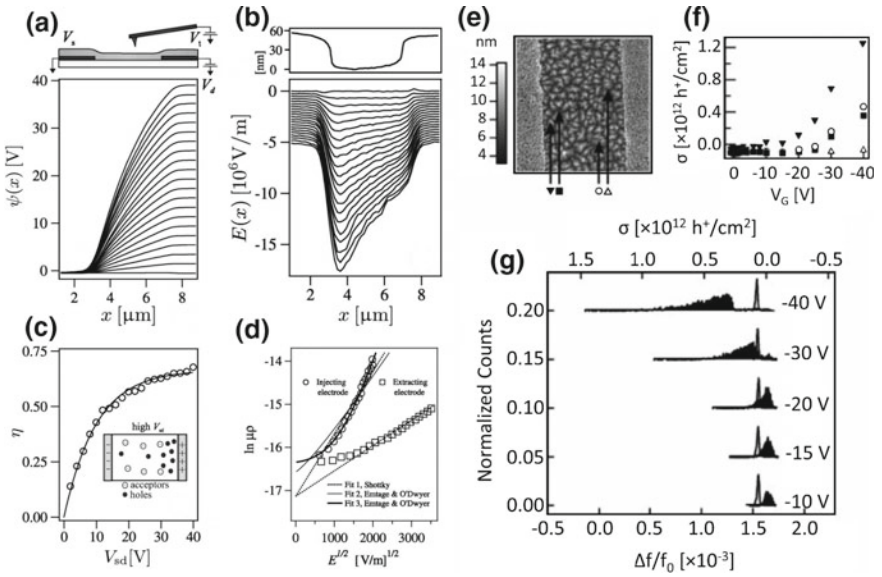

Fig. 10.24 Probing the space-charge limited conductance in an organic FET: **a** A device schematic and measured CPD distribution between the lateral electrodes as a function of voltage between them, which is varied from 0 to 40 V in a 2 V interval; **b** Topographic profile between the electrodes and electric field distribution for all source-drain voltages calculated from the data in panel (**a**). Each curve is offset for clarity by $0.25 \cdot 10^6$ V/m from the ground curve; **c** Degree to which space-charge limited conductance dominates transport as a function of the source-drain voltage. The inset shows free charge distribution; **d** The product of the charge density and mobility as a function of electric field for injecting and extracting electrodes. Adapted with permission from [111]. **e** Topographic image of a pentacene thin film on SiO_2 in FET configuration; **f** calculated electron hole trap density versus gate voltage at several location indicated in panel (**e**); **g** histograms of trap density at various gate voltages. Adapted with permission from [112]

limited: $\eta = -\sigma_\epsilon/\sigma_L$. Here, σ_ϵ and σ_L are the two-dimensional charge densities in the material and at the drain electrode, respectively. In case of the space-charge limited conductance, both of these will be comparable and much higher than the charge density at the source electrode σ_0. Pure ohmic transport, on the other hand, will be characterized by $\eta = 0$. Considering Gauss' Law and charge conservation, η can be expressed as $\eta = (E_L - E_0)/E_L$, where E_L and E_0 are the electric filed strengths at the extracting and injection electrodes, respectively. Figure 10.24c shows dependence of the calculated η on the source-drain voltage. The degree of SCL conductance rapidly increases with voltage and nearly saturates above 25 V. The data can be fitted to an exponential dependence $\eta = \eta\,[1 - \exp(-V/V_0)]$, with $\eta = 0.667$ and $V_0 = 10$ V, indicative of a crossover between the ohmic and SCL transport around this voltage. Simultaneous collection of the current data allowed the authors to also estimate the mobility (μ) behavior at the electrodes: $\mu\rho = J/E$ (ρ is the volumetric charge density, J is the current density, and E is the electric field). The data show an exponential increase of the $\mu\rho$ product, which, for the

extracting electrode and high field, can be explained by lowering of the injection barrier (Fig. 10.24d). Thus, a simple combination of transport and EFM measurements allowed determining the crossover point between the ohmic and SCL regimes and evaluate injection barriers at the electrodes.

A subsequent work from the same group investigated charge trapping in pentacene-based FETs using EFM [112]. The posed question was whether the charge trapping originates in the bulk defect sites or is associated with the grain boundaries and other microscopic features. Muller and Marohn [112] have measured the shift in cantilever's resonance frequency (Δf) as a function of the gate voltage, and calculated the trap density (σ) maps according to: $\Delta\varphi \approx \frac{\Delta f}{f_0}\frac{2k}{C''V_t} \approx \frac{\sigma d}{\kappa\varepsilon_0}$. Here f_0 is the resonance frequency, k is a constant, C'' is the second derivative of capacitance by z, V_t is the tip voltage, d is the SiO_2 layer thickness, κ is the SiO_2 dielectric constant, ε_0 is the vacuum permittivity. Figure 10.24e shows a topographic image of the device with 4 selected locations, for which the hole trap density versus gate voltage graphs are displayed in Fig. 10.24f. Apparently, the trap density is not a static quantity, but more traps are created in the presence of free holes at higher charging voltage. Traps are unevenly distributed within the channel and their density does not correlate well with the outlines of the grain boundaries. The charging voltage also affects the trap distribution in the histogram (Fig. 10.24g), changing it from Gaussian at low V_G to highly asymmetric at high V_G. The detection limit of this method, estimated by Muller and Marohn, is about 3 trapped holes underneath the tip.

Another useful piece of information that can be acquired via KPFM measurements in OFETs is the electronic density of states (DOS). This methodology was first proposed in 2005, when Tal et al. [113]. Successfully probed DOS in two doped and undoped organic semiconductors. It was shown that the DOS spectra of the undoped film recorded on the interfaces between regions of different surface potential had an anomalous peak. The doped films showed broadening of the peaks and additional peaks in the main distribution. A similar work that investigated oligothiophene FETs was published later by Salmeron's group [114]. Devices were prepared by depositing monolayers of D5TBA oligothiophene onto a thermally-grown silicon oxide layer on a p-doped Si wafer as shown in Fig. 10.25a, b. The SiO_2 surface was either kept pristine, or pre-treated with (3-aminopropyl)triethoxysilane (APTES) to block the surface-adsorbed hydroxyl groups. The Si substrate was used as a gate, while both lateral electrodes were kept grounded. The KPFM measurements were performed by positioning the AFM tip over the film at one location and monitoring the CPD change as the gate voltage (V_G) was slowly ramped. For the non-passivated SiO_2 device (Fig. 10.25c) at V_G above the threshold voltage (V_t) the film is insulating and the surface potential follows V_G with a slope of 0.6 (charge trapping hysteresis). At lower gate voltages, there is a wide hump in the spectrum before the surface potential reached the constant −0.4 V value. The APTES-passivated silica FET does not have that hump and its slope in the linear regime is 1, indicative of the absence of charge trapping (Fig. 10.25d). These data can be converted into the DOS spectra by assuming field uniformity in the z-direction of the channel and neglecting thermal

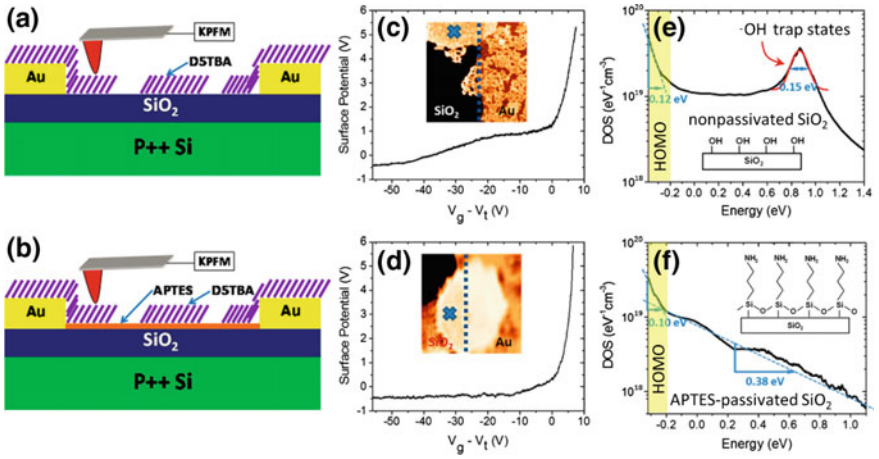

Fig. 10.25 Resolving the density of states: **a** and **b** schematics of oligo-thiophene monolayer FETs fabricated on Si wafer with pristine and APTES-passivated thermally-grown SiO_2 layer, respectively; **c** and **d** are the FET's surface potential versus gate voltage plots for pristine and passivated devices; the insets show topographic images of the film-electrode interfaces with crosses indicating the position of the tip during measurements; **e** and **f** are the calculated DOS spectra for both devices. The insets show the surface structure of SiO_2 before thiophene deposition. Adapted with permission from [114]

broadening of the Fermi-Dirac distribution at room temperature. Then, by simple parallel plate capacitor model, the carrier density in the channel will be given by: $N = C_{ox}[(V_G - V_t) - V_s]/tq$, where C_{ox} is the oxide capacitance per unit area, t is the channel thickness, V_s is the surface potential, and q is the elementary charge. The energy level in the channels is $E = qV_s$, and DOS is:

$$\frac{dN}{dE} = \frac{C_{ox}}{tq}\left(\frac{1}{\frac{dV_s}{dV_G}} - 1\right) \tag{10.35}$$

The DOS distributions calculated for both types of devices are shown in Fig. 10.25e, f. They both show an exponential HOMO band edge ($DOS \propto exp(-E/E_0)$) with the characteristic energy values ($E_0 \approx 0.1$ eV) similar to those found by optical methods. The non-passivated device has a Gaussian peak around 0.87 eV in the band gap region, absent in the APTES-treated FET. The authors attribute this peak to the surface hydroxyl groups that play the role of deep electron traps. The researchers also conclude that the characteristic slope of 0.38 eV in the passivated device spectrum (Fig. 10.25f) is due to charge trapping in the bulk silica. It should be noted, that the successful application of KPFM in this study relied on the fact that the thiophene monolayer in the channel was only 1.5 nm thick, which prevented significant band bending in the z-direction and increased accuracy of the DOS measurements. Other publications on OFETs include studies of how stress influences device operation [115]; correlation of the potential drop across the device

with the film's grain boundaries [116]; probing band bending at an organic heterojunction interface [117]; determination of resistance distribution and carrier mobility in a FET [118, 119]; trapped charge mapping [120]; and observing interlayer resistance and edge-specific charging in layered molecular crystals [121].

Probing kinetic parameters of charge transport, such as charge mobility, injection rate, rate of trap filling/emptying, etc., is possible using time-resolved SPM methods. As described above, the Marohn group published a series of works [111, 112] on trap distribution in organic FETs. Having realized that the trap density changes over time, they introduced a time-resolved EFM technique [122] to investigate the trap dynamics. Applying a DC step pulse to the gate electrode of a FET, they caused accumulation of charge at the channel-dielectric (pentacene-SiO_2) interface. Some of this charge became trapped over time, and was detected by measuring the surface potential after grounding the gate. As the trapping process was very slow (decay time constant 45–140 min), they used simple line scanning to map the FET surface in terms of frequency shift, which is proportional to the trapped charge. The maximal measured trap charge was about one charge per 640 pentacene molecules. They also observed a power law dependence of the trapping rate on the free surface charge density, and concluded that the rate-limiting step in trap generation is a chemical reaction or formation of bipolarons, which proceed in several steps. The authors indicate that one of the possibilities is interaction of pentacene with the ambient water, which is supposedly catalyzed by structural defects in the film. The defect distribution, in turn, is governed by the fabrication method that determines the film's microstructure. Therefore, in their next publication [123] they studied the effects of device fabrication techniques on the charge trapping. It was found that charge trapping was very sensitive to the preparation technique and that in a certain type of device (6,13-bis(triisopropylsilylethynyl) pentacene with gold electrodes), trapping can be reversed by electron injection.

While Marohn's tr-EFM featured a time resolution of about 2 s [123], the later works of Zhang et al. (Salmeron's group) [114] and Moscatello et al. [75] used time-resolved KPFM methods with a 3 ms resolution. In both works a decay of the surface potential in an OFET in response to a step-like change in the gate voltage was recorded and fitted to a sum of two exponentials: $\varphi(t) = A_1 e^{-t/\tau_1} + A_2 e^{-t/\tau_2}$. Obviously, the physical interpretation of a 4-parameter fit is very ambiguous. Therefore, Moscatello et al. have introduced a weighted average time constant (calculated from the A and τ parameters of the fit), and determined how it depended on the gate voltage. It was assumed that the decay is due to charge trapping. Zhang et al., on the other hand, went further. As described above, they calculated the DOS spectra in two devices and found OH-groups-related charge trapping states in the non-passivated device. It turned out, then, that a passivated device showed a potential decay with only one exponential and a characteristic time $\tau = 0.8$ s. The potential transient of the non-passivated device was fitted to two exponentials, with τ_1 fixed at 0.8 s, which yielded $\tau_2 = 6.2$ s. Zhang et al. assigned the slower process to the traps generated by the OH-groups, and the faster process to trapping in the bulk SiO_2 dielectric. Unlike these two works, Yamagishi et al. [124] did not fit the

measured OFET potential transients to an exponential decay, but rather focused on the dependence of potential spikes (ΔV) on the gate voltage (V_G). This dependence turned out to be linear, indicating that the trapped charge density is proportional to the density of the injected carriers. The researchers concluded that the amplitude of the potential spike is proportional to the amount of charge in deep trap states with lifetime longer than the 3 ms resolution of KPFM. Thus, about 80% of the charge diffused into the electrodes too quickly to be measured, and the rest got trapped, making the ΔV versus V_G slope less than one. Yamagishi et al., then proceeded to record potential variation in response to triangular sweeps of the gate voltage and converted the obtained data into maps of the charge density remaining after the sweep and charge density ejected during the sweep.

Melzer et al. [125] also used voltage sweeps to study transport in an OFET. However, they biased not the gate, but the drain electrode. The surface potential in the channel showed very non-linear dependence on this drain-source lateral voltage (U_C). Measurements were performed in a manner similar to the tr-KPFM method described above: [65] as the AFM tip was placed at each spatial location of a grid that spanned lateral electrodes, U_C was swept as shown in Fig. 10.26a, bottom graph. The surface potential measurement was limited to the time intervals, where non-linearity was observed (colorized in Fig. 10.26a). At $U_C < -9$ V and $U_C > -4$ V the channel is filled with the electron and hole carriers, respectively, and, therefore, linearly responds to the lateral bias. In the intermediate regime, the channel is depleted of carriers and the surface potential cannot follow changes in U_C fast enough, giving rise to the non-linearity (Fig. 10.26a, top graph). Melzer et al. note that it is challenging to measure carrier's mobility in this depletion regime. Indeed, as described above, mobility can be determined from the potential maps, if the flowing current is known, but in the off state only some parasitic current flows through the channel, and this method is not applicable. Melzer et al. solve this problem by recording the time evolution of the surface potential, from which they calculate three quantities: (i) the electric field in the channel as $F(x, t) = -\partial_x \varphi(x, t)$; (ii) the surface hole density as $p_a(x, t) = (\varphi(x, t) - \varphi_0(x))C_0/q$; and (iii) the charging current from the continuity equation as $I(x,t) = WC_0 \int_0^x \partial_x \varphi(\gamma, t)\partial y$. Here φ is the time-dependent surface potential at every x location between the lateral electrodes, φ_0 is the location-dependent threshold surface potential (corresponding to the inflection at -9 V in Fig. 10.26a, top graph), C_0 is the gate oxide capacitance per unit area, q is the elementary charge, W is the channel thickness, and integration is performed from the middle of the transistor channel at $x = 0$ μm towards the contacts. These three quantities are related by $I(\mathrm{x}, \mathrm{t}) = Wq\mu \cdot p_a(x, t) \cdot F(x, t)$, where μ is the sought-for mobility. Figure 10.26b shows this relation in a graphic way, as a product of the calculated maps across the channel. Although the accuracy of the mobility calculations is limited by the signal-to-noise ratio, and Mezel et al. used extensive averaging, their method allowed determining dependencies of the hole mobility on the hole density and electric field (Fig. 10.26c, d).

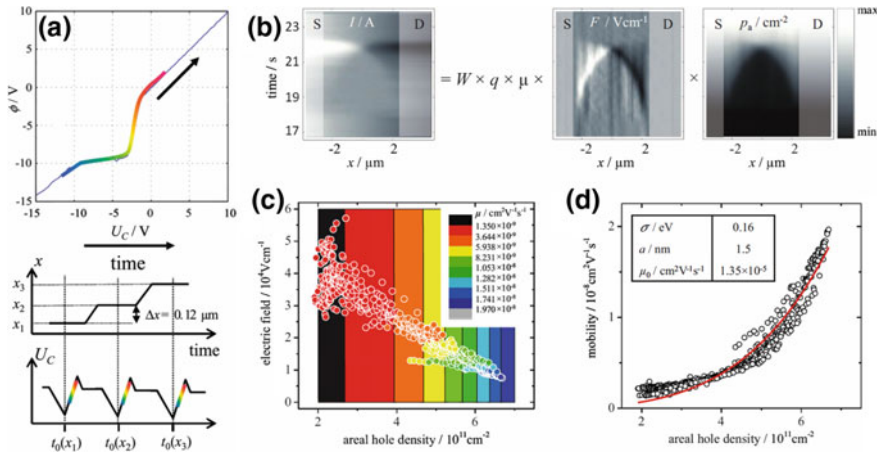

Fig. 10.26 Time-resolved KPFM study of an OFET: **a** A plot of surface potential at one location in the FET channel versus source-drain voltage showing non-linearity in the off state; bottom graphs are time dependencies of the tip position between the lateral electrodes and later bias waveforms (colors indicate measurement sequence); **b** Relationship between the time-distance maps of the channel current, electric field and surface charge density; the colorbar limits are –1.35 pA $< I <$ 1.23 pA, –52 kV cm^{-1} $< F <$ 59 kV cm^{-1}, 0 cm^{-2} $< p_a <$ 10^{12} cm^{-2}; **c** Electric field versus surface hole density plot; **d** mobility versus surface hole density plot. Adapted with permission from [125]

Finally, the highest reported to date KPFM temporal resolution—nanoseconds—was demonstrated by Murawski et al. [126] with the pump-probe technique. They studied response of a pentacene-based OFET to lateral bias within a 20 µs time frame and compared it to an ideal transistor (transmission line model) by fitting the potential decay curves to a single exponential decay. It was found that the OFET behavior deviates from operation of an ideal FET due to the presence of Schottky barriers at the lateral electrodes. Both the transient behavior and switching speed were limited by the barriers. Murawski et al. suggested solving this problem either by better energy level matching between the electrodes and pentacene (via global doping of the latter), or by local doping of the injection region with self-assembled molecules.

Inorganic and traditional semiconducting material devices also have been extensively studied. A number of publications describe KPFM/EFM/SIM potential mapping of a Schottky diode [43], p-n junctions [105, 106, 127, 128], transistors [129–131], ferroelectrics [56, 132], bicrystals [133, 134], ZnO and TiO_2 varistors [135–138], ceramic capacitors [56, 139, 140], microelectromechanical electrodes [141], light emitting diodes [107, 142, 143], solar cells [144, 145], and conductometric gas sensors [146, 147]. A few of these works go further, endeavoring to correlate the acquired maps to the device microstructure and electron microscopy data [136, 142, 145]; extract the contact resistance contributions and frequency dependence of transport; [43, 56, 131, 133–135]; and time constants for potential

relaxation transients [129]. Similar research has been conducted on nanostructured materials: nanowires (NWs), single and multiwalled carbon nanotubes (SWCNT, MWCNT), and graphene. Integration of nanostructures into lateral devices allows the probing of uni- or two-dimensional transport, which is often subject to effects absent in the bulk materials: quantum confinement [148], single-defect transport control [149], and transduction of the surface charge into the conduction channel [95]. Besides exploring these effects, researchers have been focusing on mapping the distribution of impurities, traps and doping levels in NWs [150–152]; visualizing the contact resistance and resistivity spread along the NW length [153]; and determining the transport regimes [47]. The most popular nanostructure materials in these studies were silicon [150–152, 154] III–V semiconductors [10, 148, 155–157], metal oxides [95, 153, 158] and carbon [11–14, 47, 58, 93, 149, 159, 160]. Below we will illustrate this rich research with several interesting examples to highlight the capabilities of different techniques and approaches as applied to a variety of systems.

Semiconducting oxide ceramics are characterized by 3-dimensional grains with boundaries that control their electrical properties. A typical representative of this class of materials is zinc oxide—a commercial polycrystalline material used in varistors. At the turn of the century Bonnell's group published several works that explored the effects of grain boundaries on potential distribution in ZnO lateral devices. In Huey et al. [161] KPFM was used to map the surface potential as either individual or multiple grains were biased via micropatterned electrodes. Figure 10.27a shows schematics of the carrier concentration profile, band diagram and measured potential across an *npn* grain boundary in unbiased and biased states. For comparison, the band diagram of the conductive AFM tip is also shown. Qualitatively, the measured potential follows the flat band diagram. The grain boundary is not prominent in the topographic image of a polycrystalline ZnO, as well as KPFM potential map (Figs. 10.27b and c, respectively), but become visible upon biasing the sample laterally (Fig. 10.27d, e) [138]. The height of the sharp potential barrier (φ) between the two grains can be calculated using the thermionic emission model with the assumption of an abrupt junction:

$$\varphi(V) = -E_F - kTln\left[\frac{1}{AT^2}\frac{j}{1-\exp\left(-V_{app}/kT\right)}\right] \tag{10.36}$$

Here, V_{app} is the measured voltage drop at the interface, j is the current density, T is the temperature, A is the Richardson's constant, and E_F is the Fermi level with respect to the conduction band. In addition to the potential barrier, the interfacial charge density can be calculated as follows:

$$Q_{gb}(V) = \sqrt{2eN_D\epsilon\epsilon_0\left[V_{app} + \left(2\varphi + 2\sqrt{\varphi^2 + V_{app}\varphi}\right)\right]} \tag{10.37}$$

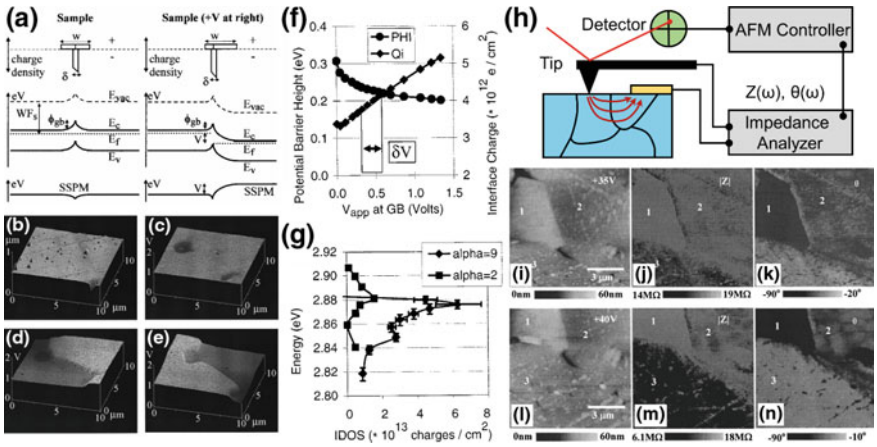

Fig. 10.27 Zinc oxide ceramic varistor: **a** schematic of the charge density, band diagram and KPFM-measured potential on an *npn* grain boundary (left—unbiased, right—positively biased from right). Adapted with permission from [161]; **b** sample topography in the vicinity of a grain boundary; **c** surface potential of the same region of unbiased sample; **d** and **e** surface potential maps of the sample biased at +1 V and −1 V, respectively (voltage applied to a lateral electrode outside of the field of view); **f** potential barrier and interfacial charge at the grain boundary as a function of bias; **g** density of states at two different grain boundaries in the same material with different nonlinearity factor alpha; Adapted with permission from [138]; **h** a schematic of NIM measurements with a lateral electrode; **i** and **l** topography, **j** and **m** impedance, **k** and **n** phase angle images of a region with several grains; for **i**–**k** panels $V_{DC} = 35$ V, for **l**–**n** panels $V_{DC} = 40$ V. Reprinted with permission from [135]

N_D is the bulk carrier density (calculated from *IV* and capacitance measurements), ϵ is the ZnO dielectric constant, and ϵ_0 is vacuum permittivity. The dependence of both the potential barrier and the interfacial charge density on the applied lateral bias is shown in Fig. 10.27f. The visible increase of the interfacial charge is explained by filling previously unoccupied boundary states, as they shift below the Fermi level of the interface due to reduction of the potential barrier. The interfacial density of states can be calculated as:

$$IDOS(E) = \frac{Q_{gb}^{\delta V} - Q_{gb}^{0}}{E_F^{\delta V} - E_F^{0}}, \tag{10.38}$$

where $Q_{gb}^{\delta V}$ and $E_F^{\delta V}$ are the charge density and Fermi level after application of a step voltage δV. Comparison of interfacial carrier densities of two dissimilar grain boundaries (with different nonlinearity coefficients $\alpha = \partial logI/\partial logV$) is presented in Fig. 10.27g. Huey and Bonnell [138] point out that such variation in grain boundary properties can be brought about by difference in their atomic structure, dopant segregation and homogeneity.

Their next publication on the topic went beyond static DC measurements by employing nanoimpedance microscopy (NIM) [135]. Probing AC transport gives

the advantage of distinguishing between relaxation processes in the bulk, at the grain boundaries, electrode interfaces and tip-surface junction. A schematic of an impedance NIM measurement in lateral electrode configuration is shown in Fig. 10.27h. A constant DC and a probing AC bias ($V(\omega)$) are applied between the tip and a lateral electrode and impedance is calculated as the ratio between the probing voltage and measured current: $Z(\omega) = V(\omega)/I(\omega) = |Z|exp(i\theta)$. The sample surface, then, can be mapped in terms of impedance modulus $|Z|$ and phase angle θ. Figure 10.27i, l show a ZnO sample topography with multiple grain boundaries. The corresponding panels j and m present $\log|Z|$ images of these regions when a 35 and a 40 V DC bias was applied between the tip and lateral electrode. As can be seen, the impedances of grains 2 and 3 decrease as a function of DC bias, indicative of the varistor behavior. Figure 10.27k, n show corresponding phase angle images, that reveal that transport in grain 1 is purely capacitive ($\theta = -90°$). Besides imaging, SIM can be used in spectroscopic mode, recording spatially-resolved impedance spectra. The latter can be fitted to equivalent circuit models, helping to extract electrical parameters of the individual circuit elements.

An example of KPFM usage for probing doping in NWs can be found in Hazut et al. [150]. By combining the KPFM potentiometric and conductometric data (Fig. 10.28a, b), the authors calculated the local doping N_D by:

$$N_{(D)}(x) = \frac{J}{q\mu_n(N_D)\frac{d\Phi}{dx}}. \tag{10.39}$$

Here J is the current density through the device, q is the elementary charge, μ_n is the electron mobility for phosphorous-doped silicon, Φ is the surface potential, and x is the distance coordinate along the NW length. The calculated effective doping level turned out to be quite uniform (Fig. 10.28c).

An interesting study demonstrating the advantages of both lateral device configuration and combined AFM/STM measurements was reported by Person et al. [155]. The publication focused on exploring transport in a heterostructure nanowire comprised of two sections of InAs and GaSb with a gradual change in composition at the NW middle point. The NW was placed on an insulating substrate and contacted with two lateral electrodes, thus forming an Esaki diode. Person et al. used AFM to locate the NW (Fig. 10.28d) and position the STM tip on it to perform *dI/dV* spectroscopy (STS) measurements as a function of the tip and lateral voltage. An example of STS imaging across the junction is presented in Fig. 10.28e alongside a height profile in this area, which shows how the NW narrows down towards the InAs region. The STS map reveals the change of the bandgap across the GaSb-InAs interface. Averaged *dI/dV* spectra for regions corresponding to both materials are shown in Fig. 10.28g. The lateral electrode configuration allows operating the diode during imaging and monitoring its state in situ. A typical *IV* curve of the device is shown in Fig. 10.28f. After initial device characterization, Person et al. proceed to correlate the device functionality to its specific surface properties. By recording STS maps as a function of the lateral voltage, they observed spectral shifts proportional to the local potential drop inside the NW.

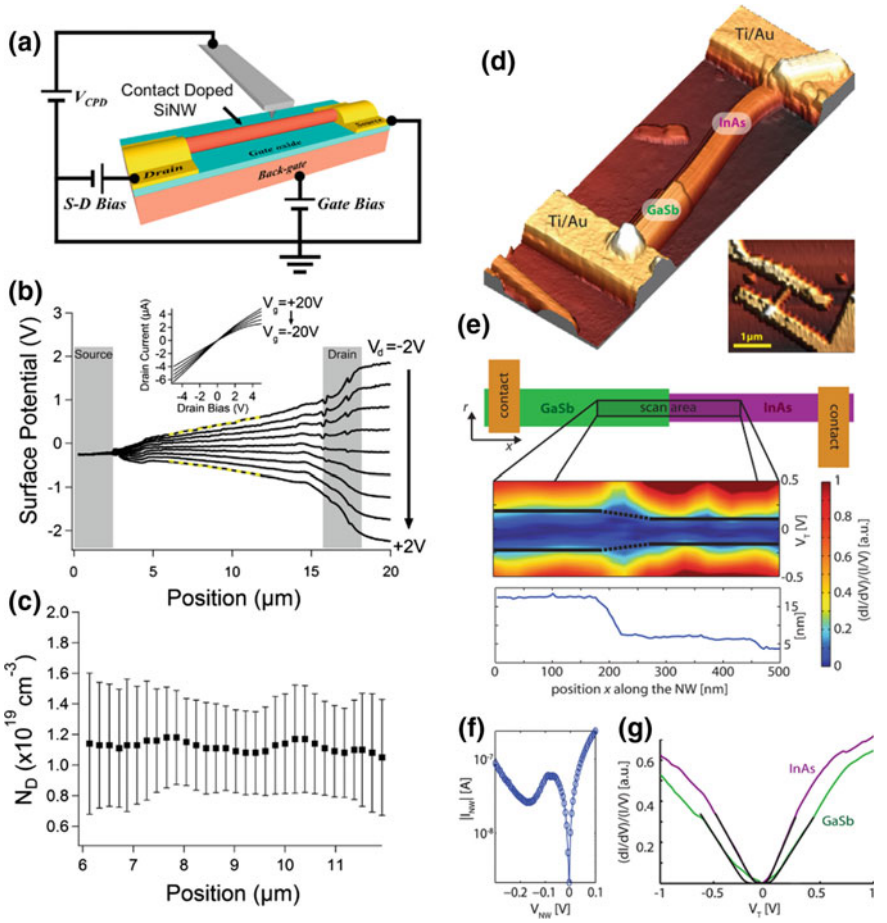

Fig. 10.28 Lateral devices with nanowires: **a** A schematic of KPFM measurements on a doped Si NW device; **b** measured potential profiles across the device as a function of the drain voltage; the gray rectangles represent electrodes; the inset shows the device IV curves as a function of the gate voltage; **c** local doping profile along the NW length calculated from the KPFM data. Reprinted with permission from [150]. **d** AFM topographic images of an Esaki diode made of a heterostructured NW with two segments; **e** An STS map of the GaSb-InAs interfacial region in the nanowire device showing the change in the bandgap along the NW length; the shown topographic profile highlights the narrowing of the NW in the region of interest; **f** An IV curve of the operating NW Esaki diode; **g** STS spectra averaged over regions of the NW corresponding to two different compositions. Adapted with permission from [155]

Thus, the use of STS in lateral device configuration allows the simultaneous probing of the potential distribution and surface electronic structure.

The transport properties of carbon nanotubes have been explored since the year 2000 using KPFM, EFM, SGM and SIM techniques. It is known from DC electrical measurements that metallic SWCNT are ballistic conductors over micron lengths,

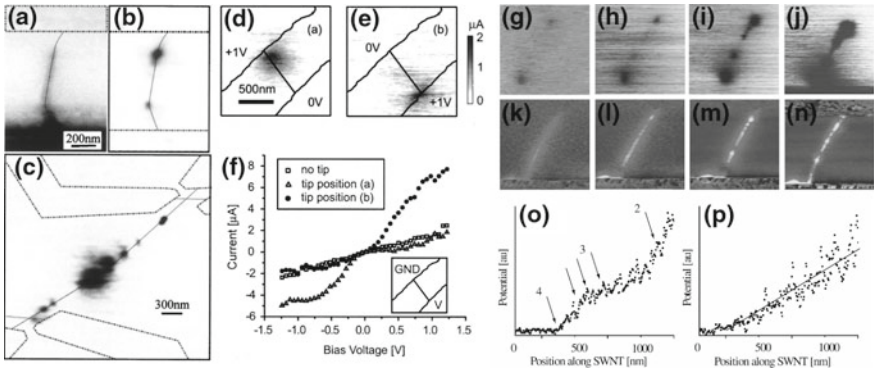

Fig. 10.29 Lateral devices with carbon nanotubes: **a** an EFM image of a 3 nm diameter semiconductor SWCNT bundle; **b** an SGM image of the same bundle; black color indicates very large resistance in the defect sites; electrodes are indicated by dashed boxes; **c** an SGM image of another semiconducting SWCNT integrated into a device with electrodes outlined; Reprinted with permission from [47]; **d** and **e** SGM images of a semiconducting SWCNT FET oppositely biased; the nanotubes and electrodes are sketched for clarity; **f** *IV* curves of the same device as measured with the AFM tip at two different locations and without tip; Reprinted with permission from [12]; **g**–**j** SGM and **k**–**n** simultaneous SIM images of a nanotube FET device with tip voltage 1, 4, 6 and 8 V, respectively; top and bottom of the images are lateral electrodes; strong defects are clearly visible; **o** and **p** are SIM potential profiles in the FET OFF and ON states, respectively; Reprinted with permission from [13]

whereas transport in semiconducting SWCNT is hampered by a series of large transport barriers along their lengths. Kalinin et al. [162] were one of the first who were able to visualize these barrier sites. Figure 10.29a–c show EFM and SGM images of two semiconducting SWCNT bundles with clearly seen defect sites with strong transport barriers. The authors note that these points are likely to have minimal local electron densities, but are unaware of the origin of these scattering sites. Johnson's group has shown that the Schottky barrier formed between the SWCNT and metallic contact determines the transport regimes in the nanotube [12, 159]. When a +1 V DC voltage is applied between the nanotube-based FET's lateral electrodes, a −2 V-biased SGM tip detects a strong barrier at the positively-biased electrode, independent of the polarity (Fig. 10.29d, e). *IV* curves of the device are symmetric in the absence of the tip, but become rectifying, with the forward bias direction determined only by the tip position relative to the lateral electrodes (invasive measurement). Freitag et al. [12] explain this behavior by proposing formation of back-to-back Schottky barriers at the nanotube-electrode contacts. In the biased state, the barrier at the positive electrode is the transport bottleneck, as its depletion region is widened compared to the other one. The presence of the negatively-charged SGM tip near this barrier, suppresses it by inducing holes in this region. Thus, transport becomes enhanced. Note, that imaging barriers at both electrodes in one measurement is possible by performing

AC-SGM, when the lateral AC bias ensures that both electrodes are positively charged half of the AC cycle.

The publications that followed have demonstrated mapping of the defect distribution in a SWCNT [163]; described the role of single defects in operation of nanotube-based FET [13]; and proposed using nanotube-containing circuits for characterization of the geometric shape of the AFM tip [93]. Figure 10.29 illustrates defect mapping by a combination of SGM (panels g-j) and SIM (panels k-n) [13]. Several strong defects are visible along the nanotube length. Their observed diameters linearly increase as a function of the tip voltage, which allows determining the relative strength of the defects. Taking into account electrostatic considerations, the authors [13] derive a relationship between the imaged defect diameter D and its depletion surface potential (V^*): $D = (V_{tip}/V^*)4\alpha R/(\kappa + 1)$, where α is the ratio of the tip-surface capacitance to that of a sphere of radius R, and κ is the dielectric constant of the FET dielectric layer. Depletion surface potentials can be used to estimate the Fermi energy of each defect as: $E_F \approx V^* C/e^2\lambda$ (C is the total capacitance of the defect region per unit length, e is the elementary charge, and λ is the density of states per unit length). The estimated Fermi energies of the defects in Fig. 10.29g–j are from 20 to 50 mV. Weak defects, even if they neighbor strong ones, can be resolved using SIM imaging. Figure 10.29o shows a SIM potential profile along the nanotube FET in the OFF state. Strong defects 2 and 4 are clearly resolved, but in addition, a series of smaller scattering sites is seen around defect #3. When the nanotube is in the ON state (high conductance), it exhibits a uniform potential drop along its length (Fig. 10.29p).

More recently, Collin's group studied point functionalization of SWCNTs by various chemicals (water, H_2SO_4, HCl), and successfully distinguished between the three chemical defect types using SGS [11]. Later they employed a parametrized KPFM method to measure resistance per unit length in semiconducting and semimetallic nanotubes [164], as well as discover that a 1-dimesional Poole-Frenkel mechanism describes defect scattering transport in a semimetallic SWCNT [149]. Finally, graphene has also been studied in the lateral device configuration by KPFM [160, 165, 166].

10.5 Voltage Modifications in Lateral Devices

Strong electric fields in lateral electronic devices may trigger processes that are typically omitted in the description of device operation. Activation of the ionic subsystem, including bulk and surface ionic transport, related electrochemical and ferroelectric polarization, and electrochemical transformations of the solid-state device material, metallic contacts and gaseous species on their surfaces—all these phenomena may contribute to or plague the device operation. Unlike the electronic processes, the ionic and electrochemical phenomena can be semi-reversible or irreversible, and highly non-linear. Two most important classes of electrochemical applications that can be studied by SPM methods in the lateral device configuration

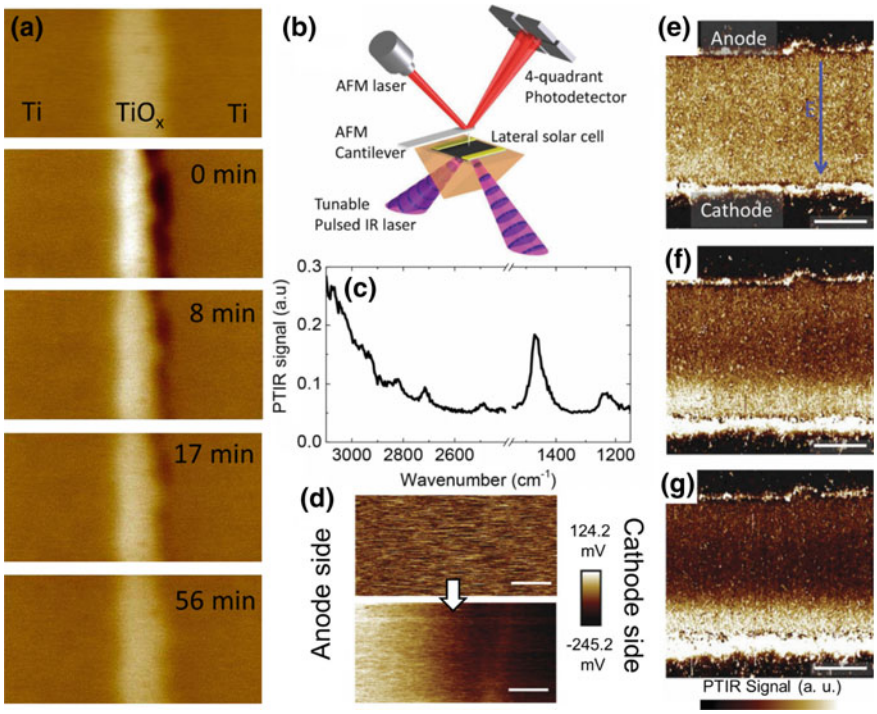

Fig. 10.30 **Bulk ion migration**: **a** A series of KPFM images of a planar Ti/TiO_x/Ti structure; the top image is pristine device, and the subsequent images were taken the indicated time past polarization; a clear dissipation of oxygen vacancies is seen; the full color scale is 220 mV, except for the top image where it is 3.5 V; Adapted with permission from [168]; **b** a schematic of PTIR setup for lateral configuration; a perovskite thin film and lateral electrodes are deposited onto an optical prism and laser-excited from below; the AFM tip detects the material's thermal response as a function of laser frequency, lateral voltage and position; **c** a PTIR absorption spectrum of $MAPbI_3$; **d** KPFM maps of an interelectrode region of the film before (top) and after (bottom) polarization (1.2 V/μm for 100 s); the scale bar is 6 μm; **e**–**g** PTIR maps of the CH_3 asymmetric deformation absorption of the methylammonium ion (1468 cm^{-1}) recorded (**e**) on the pristine device, **f** after 100 s and **g** 200 s of polarization. Adapted with permission from [172]

are memristive/electroresistive memory devices and energy-relevant systems: solid state batteries and fuel cells. Although many groups have used SPM techniques to explore these applications [167], very few studies took advantage of the planar geometry.

Batko and Batkova [168, 169] used KPFM to explore resistive switching in a Ti/TiO_x/Ti lateral structure. Figure 10.30a shows a sequence of CPD maps of the device with grounded electrodes taken at different times following device polarization with a 3 V bias. The first image shows the pristine structure, with the central band being the oxide strip flanked by Ti electrodes. The subsequent images reveal the process of gradual dissipation of oxygen vacancies, on the time scale of tens of minutes. Similar studies were conducted by Kim et al. [170] and Kim and Kim

[171] on a Pt/TiO_2/Ti planar junctions. They noticed that application of a large voltage (±40 V) to the lateral electrodes significantly alters the device conductivity. KPFM surface imaging revealed that following activation with lateral field, the oxide surface becomes charged oppositely to the applied voltage. It was proposed that these changes were due to several concurring processes: bulk oxygen vacancies electromigration; electric-field driven desorption of oxygen and water molecules from the surface with subsequent modulation of the space-charge layer and conductivity; and the electrochemical reaction of vacancy filling with the ambient gas oxygen molecules.

The photo-thermal induced resonance (PTIR) technique has been used by Yuan et al. [172] to map out electromigration of ions in an organic perovskite material. Triiodoplumbate(II) of methylammonium ($MAPbI_3$) is a very promising solar cell material, whose photovoltaic properties might be related to the MA^+ ion mobility in its bulk. Yuan et al. have spin-coated a thin film of $MAPbI_3$ onto a surface of an optical prism with pre-deposited gold electrodes as shown in Fig. 10.30b. The material was then excited with a tunable IR laser from below, while the AFM tip recorded its thermal response. This way PTIR allows circumventing the diffraction limit and obtaining material spectra similar to IR with nanoscale resolution. An example of pristine $MAPbI_3$ PTIR absorption spectrum is presented in Fig. 10.30c. The spectrum features a pronounced peak around 1468 cm^{-1}, which corresponds to asymmetric deformation of the CH_3 group in methylammonium ion. By locking the laser at this frequency and scanning the device surface synchronously with the laser pulsing, Yuan et al. mapped out the distribution of the MA^+ ion between the electrode in the pristine device (Fig. 10.30e) and after 100 s and 200 s of polarization (Figs. 10.30f and g, respectively). The pristine perovskite PTIR map is uniform, whereas the polarized maps show progressive accumulation of the MA^+ ions near the cathode. KPFM mapping clearly confirms charge re-distribution (Fig. 10.30d). Ion electromigration in semiconductors leads to a change in the local doping levels, local conductivity and typically causes formation of a p-n junction in the material (e.g. the Ca-BFO case [128]). Although MA^+ ions do not directly participate in the formation of the conduction and valence bands of $MAPbI_3$, their vacancies act as p-dopants by attracting electronic holes to maintain charge neutrality. The researchers concluded that the ionic electromigration is the origin of the switchable photovoltaic effect in this perovskite and that it can be triggered by photovoltage, causing deterioration of the solar cell performance.

Unlike the perovskite, ion conductors used in solid oxide fuel cells (SOFC) have very low ion mobility at room temperature. Thus, activation of ionic transport in them either requires a high temperature (beyond what is typically available for the common SPMs), or very large electric fields, such as ones generated at the tip-surface junction. It is for this reason, that SOFC materials were so far studied by SPM methods in the stacking, rather than planar configuration: the lateral electric field is much weaker than the tip-generated. However, recently Nonnenmann et al. [173] introduced a high-temperature environmental chamber that was used to probe SOFCs at 600 °C. A schematic of the chamber is shown in Fig. 10.31b. The key element of this method is to enclose the hot operating SOFC in a gases-fed chamber

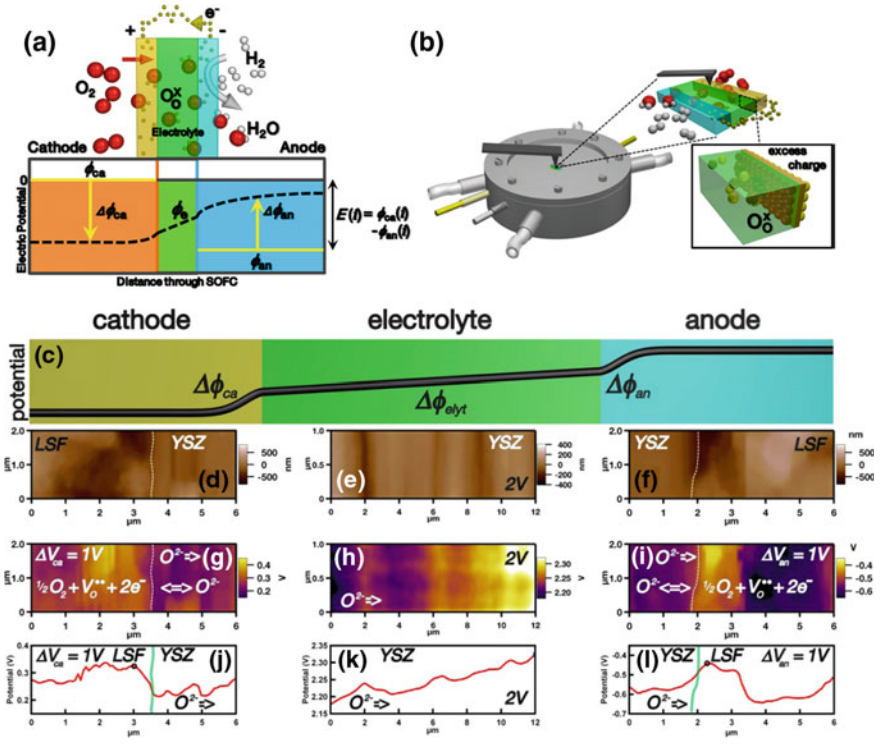

Fig. 10.31 Ionic transport in SOFCs: **a** A schematic depiction of an operational SOFC with cathodic and anodic reactions and potential drop between the electrodes; **b** a drawing of the environmental hot stage chamber for AFM imaging lateral SOFC devices in operando; **c** potential profile in an ideal SOFC; **d–f** AFM topographic images, **g–i** potential maps, and **j–l** potential profiles in at biased symmetrical LSF-YSZ SOFC at 600 °C; vertical lines represent interfaces. Adapted with permission from [173]

with a small opening in the lid that can be used to perform AFM potential or current measurements without exposing the sensitive AFM electronics to the damaging heat. Nonnenmann et al. demonstrated KPFM mapping of an operating SOFC (Fig. 10.31c–l) and estimated the change in activation barrier from the potentiometric data. In the subsequent publications [174–176] they have explored other similar systems. It is expected that this approach will provide important insights into the SOFC operation in the near future.

Ionic transport may occur not only in the bulk of the active material, but also on its surface, playing an important role in operation of various devices. The surface ion dynamics has plagued microelectronics since Shockley's times [177]; it affects polarization switching in ferroelectric memory devices, and is crucial for electrocatalysis and gas sensorics. As with the bulk charge transport, a significant impediment in studying the surface ion migration is the need to separate the electronic flows from the ionic ones with high spatial resolution. Standard

electrochemical techniques, such as electrochemical impedance spectroscopy (EIS) [178, 179], surface conductometry [180–182] and vibrating reed electrometry [177], suffer from poor spatial resolution. ESM and KPFM only detect the total potential due to both electronic and ionic processes. Fortunately, the mobilities and transport coefficients of electronic and ionic charge carriers are vastly different in most materials. Therefore, separation of the electronic and ionic responses to an electrical stimulus should be possible in the time domain [183].

Several studies took advantage of this fact to probe surface electrochemistry with tr-KPFM [65], which merges the high spatial resolution of KPFM with a 10-ms time resolution permitting the detection of ionic dynamics on solid surfaces. A tr-KPFM measurement yields a 3D dataset (*Potential* = $f(x, y, t)$), which is hard to visualize. Therefore, the data is typically averaged over the spatial dimension that runs parallel to the electrodes. Figure 10.32a–d shows a tr-KPFM potential profiling for various materials: activated Ca-substituted $BiFeO_3$ (Ca-BFO), a $LiNbO_3$ crystal, nanostructured ceria film and pristine Ca-BFO, respectively. Here the two sets of curves denote the lateral voltage on (dark blue to green) and off (green to red) periods. As can be seen, the surface potential evolution in these materials is very different, foretelling the difference in the stimulated surface processes and their mechanisms. In the pristine Ca-BFO, the initial interelectrode potential distribution is close to linear (dark blue line, Fig. 10.32d), as a 5 V lateral bias is applied to the device. Later, after 10 s in the bias-on state, the film polarizes and the potential profile curves downward near the biased electrode (upper green line in Fig. 10.32d). This curving is indicative of the negative charge accumulation in that region. When the voltage is switched off, the whole film acquires a negative surface potential (lower green line in Fig. 10.32d), confirming the presence of negative charges. As the material relaxes during the next 10 s this charge dissipates, and the potential profile flattens out to zero (dark red line in Fig. 10.32d). A different picture is observed in an activated Ca-BFO, which has positively-charged oxygen vacancies racked up by the grounded electrode. Other film regions become depleted of oxygen vacancies and turns almost metallic (p-doped semiconductor) [65]. This virtual electrode region is seen in Fig. 10.32a (right hand side of the graph). In the voltage-off period a slow dissipation of oxygen vacancies is seen, as the positive potential hump relaxes to zero.

Whereas charge dynamics in Ca-BFO can be activated with a low voltage, it takes 90 V to trigger any processes in a ferroelectric $LiNbO_3$ crystal. Figure 10.32b demonstrates injection of a positive charge from the biased electrode in $LiNbO_3$ [184]. This charge rapidly disperses during the bias-on period and no relaxation is seen in the bias-off time. A similar phenomenon is observed at high voltage in nanostructured ceria. A substantial flow of positive charge from the biased electrode occurs in this typical oxygen-ion conductor (Fig. 10.32c). This charge is retained by the ceria film. Unlike the $LiNbO_3$ behavior, the ceria sample shows migration of the charge to the grounded electrode and its dissipation during the bias-off stage. The presented assorted cases exemplify the tr-KPFM efficiency in probing various charge redistribution processes on insulating surfaces, where the flowing currents are undetectable by the existing current amplifiers. Note that the standard scanning

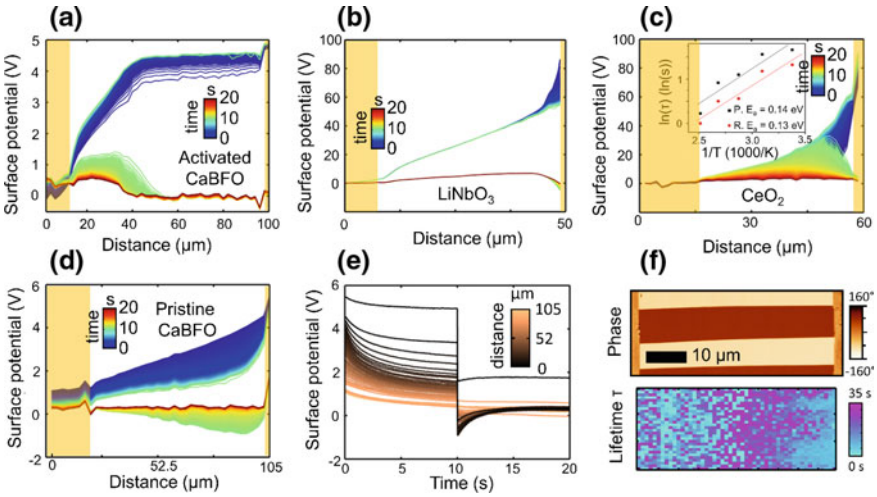

Fig. 10.32 Surface ionic dynamics captured by tr-KPFM: **a–d** Potential profiles for activated BFO, $LiNbO_3$, nanostructured CeO_2 and pristine BFO samples showing a diversity of the activated processes; golden stripes represent the lateral electrodes (right electrode is biased); the inset shows an Arrhenius plot of the mean lifetime of charged species on Ca-BFO surface with activation energies for the polarization (P.) and relaxation (R.) periods; **e** Potential versus time curves for the pristine Ca-BFO sample for different positions (same data as in (**d**)); **f** A PFM phase image and tr-KPFM lifetime map of a periodically-poled ferroelectric $LiNBO_3$ crystal; ferroelectric domains are seen in the PFM Phase image as brown and beige horizontal bands; the brown stripes on the sides of the PFM image are the metallic electrodes. Adapted with permission from [65, 184, 185]

KPFM, having a time resolution of tens of seconds to tens of minutes (time it takes to capture an image), would only capture the last, fully relaxed, state of the system (i.e. the red line in Fig. 10.32a–d).

To determine which charge carriers—electronic or ionic—are responsible for the observed potential evolution, we recall that the response times of the charged species are determined by the RC constant of the circuit (electrons/holes) and ionic diffusion coefficients (ions) in the studied material. In the shown ceria example [185], the RC constant was ca. 100 s, which is much larger than the 10 s timeframe used for the tr-KPFM measurements. Hence, it is unlikely that the electronic dynamics has been recorded in this case. The activated Ca-BFO sample [186] is the opposite case, where in about 60% of the film the electronic conductivity is higher than 0.2 S/m, and oxygen vacancy mobility is low. The estimated electron response time in this case is lower than 1 μs, and, thus, no relaxation was observed in the metallic region during the bias-off stage (Fig. 10.32a red line between 65 and 100 μm). A more quantitative consideration can be found by looking at the potential versus time curves (Fig. 10.32e), which can be fitted to a single exponential decay equation: $Potential(t) = A + B \cdot e^{-t/\tau}$. Here A and B are constants and τ is the mean lifetime of the charged species that caused the potential variation. The mean lifetime measured on a Ca-BFO sample is plotted in an Arrhenius plot in the

inset of Fig. 10.32c. The corresponding activation energies for both bias-on and bias-off states are ca. 0.14 eV [186]. Secondly, the diffusion coefficient of charged species can be estimated as: $D \approx \frac{d^2}{\tau}$, where d is the interelectrode distance. The estimated room temperature diffusivity ($2 \cdot 10^{-9}$ m^2/s), and E_a values are very similar to those for proton transport in bulk water ($D \sim 10^{-8}$ m^2/s, $E_a = 0.12$ eV) [186]. Another important observation pointing at the ionic nature of the surface charge species is the fact that the changes in the surface potential are strongly dependent on the ambient gas humidity [177]. Taken together, these considerations imply that migration of the adsorbed protons on the surface must be responsible for the potential evolution in the $LiNbO_3$, ceria and pristine Ca-BFO samples. The response of the activated Ca-BFO film may also have been influenced by the bulk oxygen vacancies and electronic hole transport.

In addition to potential profiling, tr-KPFM can also be used for functional imaging. Figure 10.32f shows a piezoresponse force microscopy (PFM) phase image of a periodically poled $LiNbO_3$. A series of horizontal ferroelectric domains is seen. This image can be compared to a mean lifetime map obtained by fitting the tr-KPFM data with an exponential decay. The dark horizontal band in upper Fig. 10.33f is a ferroelectric domain with polarization pointing into the plane of the image. This domain is screened by positive surface charges (surface-adsorbed

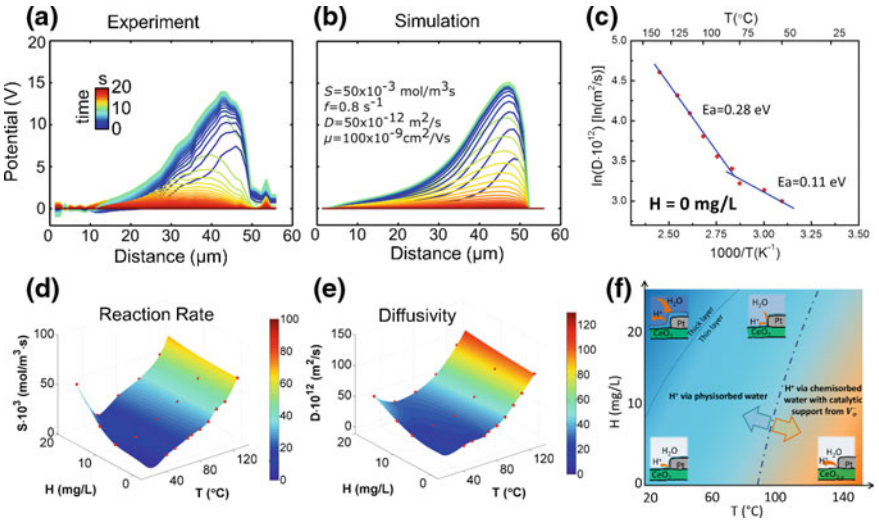

Fig. 10.33 The energy discovery platform approach: **a** Experimental and **b** simulated potential profiles for a nanostructured ceria sample; tr-KPFM measurements were performed at 135 °C and 0% relative humidity; for the experimental data, potential profiles at the end of the bias-on and -off periods were subtracted from the profile curves at other moments of time; **c** an Arrhenius plot of the surface proton diffusivity extracted from the fits shows a crossover at ca. 100 °C; **d** and **e** dependence of the deconvoluted reaction rate and proton diffusivity on air humidity (H) and temperature; **f** a schematic phase diagram of the different proton conduction regimes in nanostructured ceria, as extracted from the tr-KPFM data. Adapted with permission from [187]

protons in ambient conditions). The difference in the mobility of these ionic species creates the contrast in the lifetime map of Fig. 10.32f (right side of the τ map), where the dwell time on the central domain is ca. 12 s and is twice as low on the side domains. The detection of this difference, or imaging partly exposed ferroelectric domains in general, cannot be done with the standard KPFM.

Quantitative analysis of the tr-KPFM data is an integral part of the so called energy discovery platform (EDP) approach [185, 187, 188]. The EDP endeavors to unravel the surface electrochemistry and ionic transport in the studied material by a synergistic conjunction of device microfabrication, tr-KPFM and numerical modeling. To recall, in the nanostructured ceria sample, protons flow into material from the positively-biased electrode. The source of these protons is the water splitting reaction that occurs at the triple-phase boundary (platinum electrode, ceria, and air):

$$2H_2O \rightleftarrows 4H^+(aq) + O_2 + 4e^- \tag{10.40a}$$

The generated protons subsequently diffuse and electromigrate along the adsorbed water layers on the ceria surface, according to the Grotthuss mechanism [187]:

$$Ce_{Ce}^{\times} - OH_3^{\cdot} + Ce_{Ce}^{\times} - OH_2 \rightleftarrows Ce_{Ce}^{\times} - OH_2 + Ce_{Ce}^{\times} - OH_3^{\cdot} \tag{10.40b}$$

Importantly, the CPD detected by tr-KPFM is affected by both processes of diffusion/migration and generation/annihilation of protons. Disentangling this complexity can be achieved by simultaneous solution of the transport, reaction and electrostatics equations [185]:

$$\frac{\partial n_i}{\partial t} = \nabla \cdot (-D_i \nabla n_i + z_i \mu_i n_i F \nabla \Phi) + (S_i - f_i n_i) \tag{10.41}$$

$$\nabla^2 \Phi = -\Sigma n_i z_i q_0 F / \varepsilon_0 \varepsilon_r \tag{10.42}$$

Here, n_i is the local time-dependent concentration of ions $(\mathrm{i} = H^+, OH^-)$, D is the ionic diffusivity, z is the ion charge, μ is mobility in the electric field, F is the Faraday constant, Φ is the surface potential, S is the rate of generation reaction (for protons rate of (10.2)), f is the rate of annihilation reaction (inverse of (10.40a)), q_0 is the elementary charge and $\varepsilon_0\varepsilon_r$ is the ceria permittivity. The rates of proton generation and annihilation are given by (10.40b) as:

$$S_{H^+} = \frac{d[H^+]}{dt} = 2k \cdot [H_2O]; \tag{10.43}$$

$$f_{H^+} n_{H^+} = -\frac{d[H^+]}{dt} = 2k' \cdot [H^+]^2 \cdot p_{O_2}^{1/2} \tag{10.44}$$

Finite element modeling can be used to solve this set of equations with appropriate boundary conditions. Matching the simulation results to the experimental

data allows extracting four parameters that characterize the observed processes: D, μ, S and f [185, 187]. The dependence of the system-governing parameters on the temperature and air humidity is plotted in the phase diagrams of Fig. 10.33d, e. The distinct difference in the shapes of these 3D plots makes it clear that the diffusivity and reaction rate have different contributions to the overall potential in different conditions. An Arrhenius plot of the extracted proton diffusivity in dry conditions (Fig. 10.33c) shows a crossover between two transport regimes around 100 °C, when the activation energy changes from 0.11 to 0.28 eV. This is a clear indication of the physisorbed water desorption with inevitable impediment to transport.

The explored proton generation and transport regimes are summarized in the schematic of Fig. 10.33f, where an interplay between the temperature and humidity thermodynamic factors favor existence of several surface conditions. At low temperature and high humidity, a thick physisorbed layer of surface water facilitates proton transport. At intermediate temperatures and humidity, only a thin physisorbed water layer exist, hampering transport and giving rise to a minimum in the phase diagram of Fig. 10.33d, e. Finally, at high temperatures and low humidity, only chemisorbed water is left on the surface. In this regime, the proton transport is enhanced by catalytic influence of oxygen vacancies and high thermal driving force.

As a concluding remark, Strelcov et al. [189] note that "…the power of the EDP approach can be limited for some complex systems that feature concurrent processes with similar time constants (e.g. double layer charging or discharging versus bulk diffusion). In such cases interpretation and deconvolution of the tr-KPFM signal may become ambiguous or impossible and other methods should be used to understands the system. However, these problems also affect interpretations based on classical impedance spectroscopies, which do not allow for spatial resolution."

10.6 Light Effects

In addition to electric field and temperature, photoexcitation is another external stimulus that can affect charge transport in opto-electronic devices. As discussed previously, ion migration was demonstrated as one of the reason for several anomalous phenomena in organometallic halide perovskites [190–192]. Generally, in mixed conductors characterization of ionic conductivity, mobility, and the effective carrier concentration of the mobile ion species, can be particularly challenging. The typical approach of using transient current measurements can be instructive, and helps establishing qualitative trends in conductivity [193–197]. Impedance spectroscopy (IS) on lateral electrode devices can separate ionic conductivity from that of electronic carriers. However, these methods lack spatial resolution. Recently, the formation of internal tunneling junctions due to ion migration was observed using KPFM in thin films of methyl ammonium lead bromide ($MAPbBr_3$) perovskite with lateral electrode spacing of 50 μm [198]. In this work, the surface potential of the electrically biased (poled) perovskite solar

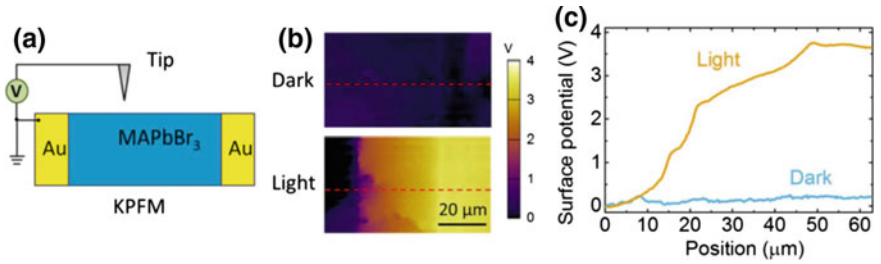

Fig. 10.34 **a** A schematic of the KPFM characterization on a lateral electrode design, where one electrode was grounded. **b** Surface potential distribution of the $MAPbBr_3$ device measured in the dark and under illumination (in N_2 atmosphere), respectively. **c** The respective surface potential profiles at the position marked in (**b**). Reprinted with permission from [198]

cells was measured by KPFM in N_2 atmosphere (Fig. 10.34a). Under white light illumination with an intensity of ≈100 mW/cm^2, a cathode-anode potential difference of 3.5 V was observed under open-circuit conditions, which is above the bandgap of $MAPbBr_3$ ($Eg = 2.2$ eV) (Fig. 10.34b, c). It was explained that the anomalously large open circuit voltage (V_{oc}) in this class of perovskite device is similar to that of ferroelectric photovoltaic devices. The anomalous large V_{oc} known as bulk photovoltaic (BPV) effect was previously identified in ferroelectric inorganic perovskites including bismuth ferrite (BFO) [199] and barium titanite (BTO) [200] under illumination. Two mechanisms are proposed for bulk photovoltaic effect which are ballistic and shift (this mechanism was briefly explained in [200]). However, $MAPbBr_3$ at room temperature is cubic and can not be ferroelectric. In the case of $MAPbI_3$ with non-centrosymmetric structure at room temperature, the anomalous V_{oc} has been only observed after poling $MAPbI_3$ devices at temperature around 330 K which is above the phase transition to cubic for this compound. This contradicts the ferroelectric mechanism since if ferroelectricity exists, then the spontaneous polarization should disappear above the phase transition temperature. The dependence of the anomalous V_{oc} on the polarization direction of the incident light is considered as a fingerprint of the BPV in ferroelectric materials [199]. Therefore, in this experiment the lack of response to the light polarization direction excluded the effect of ferroelectricity.

As noted earlier, poling of perovskite devices can lead to the formation of p-i-n or p-n structures with small V_{oc}. During poling, MA^+ ions migrate creating n- and p-doped regions. These ions can accumulate at the grain boundaries (GBs) due to trapping. The ion build-up creates heavily doped regions at GBs forming interfacial tunneling junctions. However, these junctions are randomly distributed along the GBs, and are hard to be detected by KPFM. Additionally, the GBs thickness is lower than the KPFM resolution. Therefore, Yuan et al. artificially broadened the thickness of GBs with an electron beam (E-beam) (Fig. 10.35a) to control ion accumulation at the GBs. This resulted in formation of two clear band-bending regions in the surface potential mapping image (Fig. 10.35c) in accordance with the E-beam written regions. It was proposed that the band bending induced by local

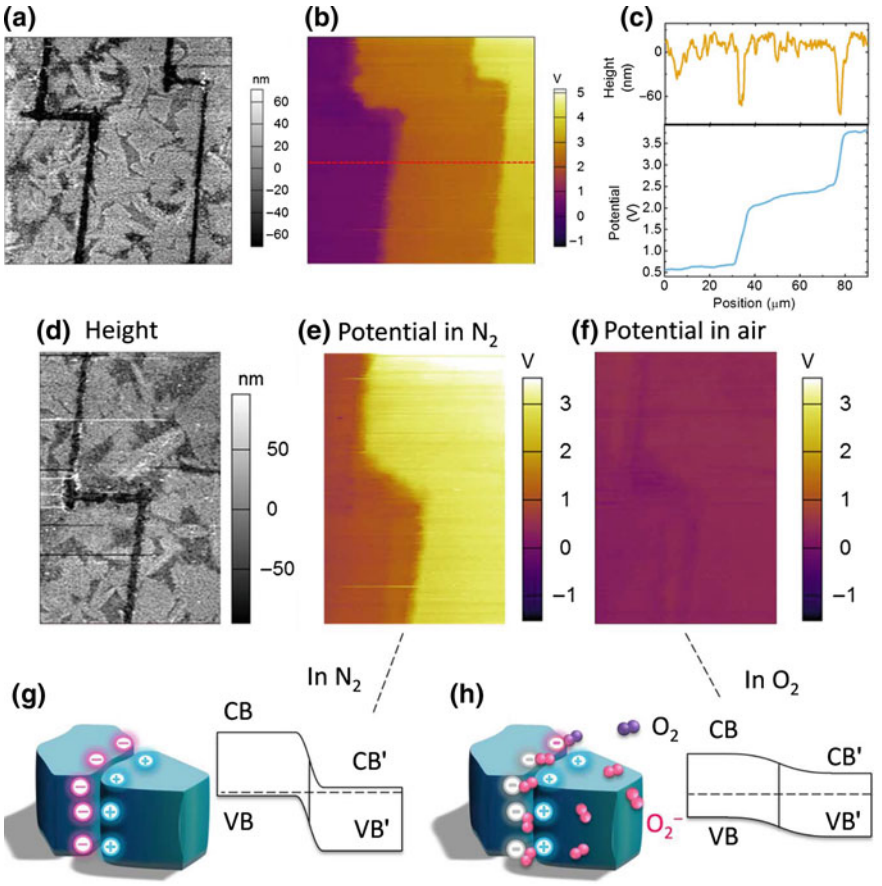

Fig. 10.35 **a** Topography and **b** surface potential of an E-beam–treated $MAPbBr_3$ film with controlled ion accumulation pattern with "Z" shapes. **c** Topography and surface potential profiles of the position marked in (**b**). **d** Topography of the E-beam–patterned $MAPbBr_3$ film, where the measured area was 60 mm × 90 mm. **e** and **f** Show the surface potential images of the electrically poled $MAPbBr_3$ film in N_2 and air, respectively, where the abrupt potential change vanished because of oxygen absorption. **g** and **h** Show the schematic energy diagrams at interfaces in N_2 and air, respectively, where the ion accumulation–induced tunneling junction vanished because of oxygen absorption. (CB, conduction band; VB, valence band). Reprinted with permission from [198]

tunneling junctions can be an additional driving force for the separation and collection of photogenerated charge carriers in these materials, which lead to above bandgap V_{oc}. The surface potential in $MAPbBr_3$ devices with controlled ion accumulation disappeared after the sample was exposed to air (Fig. 10.35e, f). This was attributed to the much lower doping concentration at GBs by the charge trapping effect of absorbed oxygen (Fig. 10.35g, h).

10.7 Transport Imaging in Liquids

Electrostatic interactions in liquid media determine the processes in polyelectrolytes, electrical double layers, biological cells and membranes. In addition, several bio—and chemical technologies, such as electrophoresis and dielectrophoresis, employ electric forces in solutions to control molecular and particle motion. The recent decades have seen development of microelectrodes used to trap and micro-manipulate cells and viruses, and micro—and nanofabrication methods utilizing electrophoretic [201] and electrostatic [202] self-assembly. A thorough understanding of elestrostatic forces in solutions at the nanoscale is required for these applications, necessitating extending the lateral transport measurements to liquid environments. However, the same presence of double layers, electromigration, electrochemical reactions, and convective motion, in the solution can affect the electrostatic probe-surface interactions.

Studies of electrostatic interactions in liquid media employed direct static force detection and force-distance spectroscopy [203–205]. These techniques rely on the control of the surface charge density on the sample via solution pH. To our knowledge, this methodology has not been applied to lateral devices. At the same time, it has been demonstrated that an electromechanical response of a ferroelectric in solution can be measured by an AC-biased AFM [206–208]. Additionally, biasing the tip with a DC voltage could be used in some liquids to induce

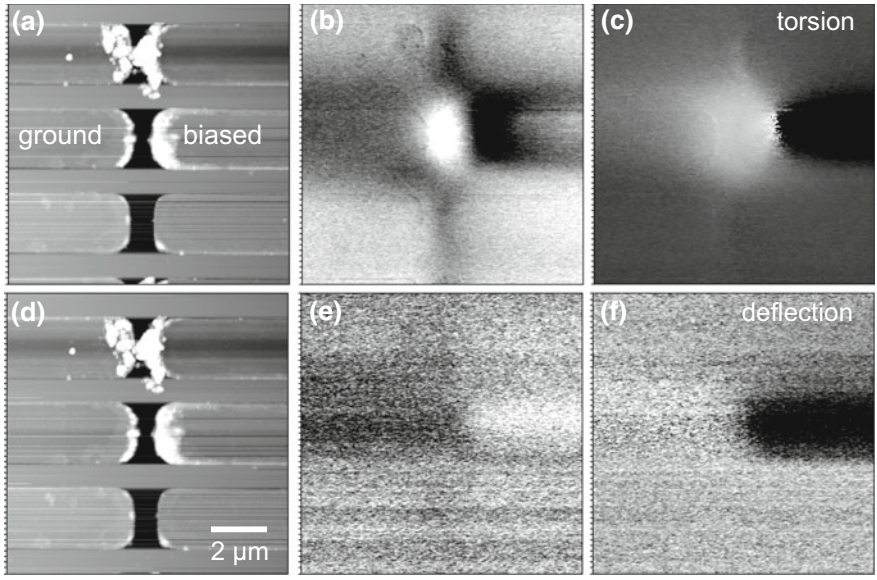

Fig. 10.36 **a**, **d** AC-mode height images of the AC-biased electrodes in DI water, and (**b**, **e**) amplitude and (**c**, **f**) phase images of tip torsion and deflection signals, respectively. Reprinted with permission from [210]

ferroelectric switching, thus probing DC electric field localization in the liquid media [209]. Importantly, these studies suggest that at certain conditions (sufficiently high frequencies, low ionic strength) the electric field from the tip is screened only partially or not at all, enabling the implementation of ambient-based lateral transport measurements in liquid environment.

The direct measurement of an electric force between two periodically biased electrodes in a liquid was demonstrated by Rodriguez et al. [210]. The topography and electric force amplitude and phase maps of an AC-biased interdigitated metal electrode structure are shown in Fig. 10.36. The tip deflection and torsion amplitude images were recorded between the same electrode pair. It appeared that the lateral forces were strongest in the gap between the polarized electrodes, as revealed by the torsion amplitude map. The flexural force, on the other hand, is maximal on the biased electrode. These observations agree with the simple electrostatic considerations. The signal measured by a biased tip on the biased electrode in air depends linearly on the voltage (Faradaic reactions were avoided by keeping the tip bias low). For a grounded tip, over grounded or biased electrodes, the signal remains linear above a certain threshold. DI water media changes this behavior,

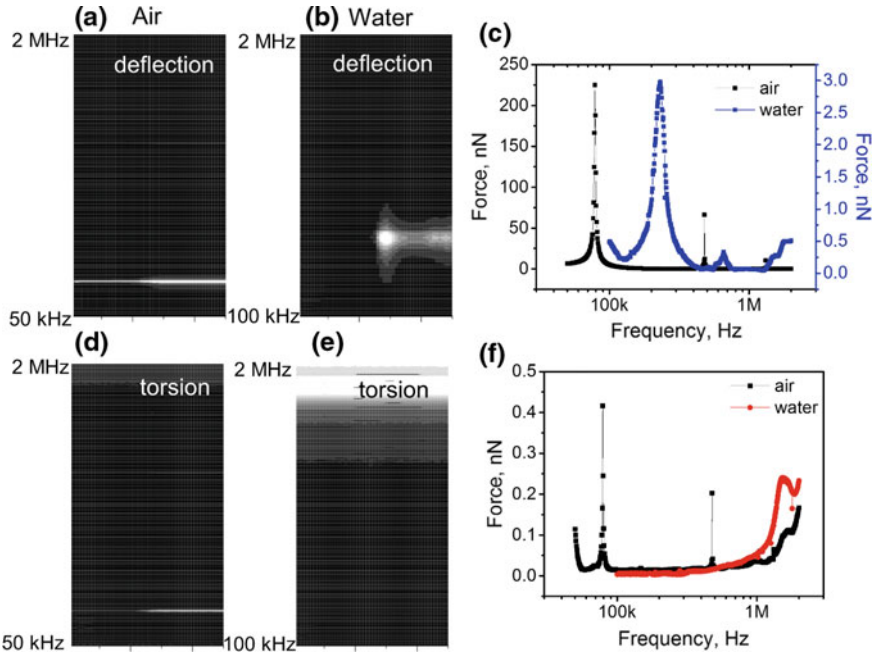

Fig. 10.37 Maps of the amplitude of the (**a**, **b**) deflection and (**d**, **e**) torsion signals as a function of position and frequency in air and DI water, respectively for a 12 μ slow-axis-disabled scan. (**c**, **f**) The averaged amplitude signal as a function of frequency for tip deflection and torsion, respectively. The frequency range in liquid is limited by the onset of electrochemical processes. Reprinted with permission from [210]

zeroing the signal over the grounded electrode and making it proportional to AC voltage over the biased one.

The torsional force on the cantilever due to electric field scales linearly with the AC bias in air, whereas in DI water the dependence is more complex. Figure 10.37 summarizes the frequency dependence of the force on the cantilever. The in-air deflection and torsion signal amplitudes are mapped in Fig. 10.37a, d as a function of frequency and position. Figure 10.37b, e plot the same for DI water. The effective electrical force deflecting the cantilever (Fig. 10.37c) can be converted into to the absolute force as: $F = F_{eff}/Q$, where Q is the quality factor. The absolute forces at second resonance as measured in air and water are 0.1 and 0.8 nN, suggesting that the cantilever dynamics is governed by the AC-bias induced macroscopic convection flows in liquid.

10.8 Perspectives

Lateral transport measurements on active device structures ranging from ceramics and thin films to OFET to carbon nanotube circuits provide a wealth of information on the internal charge behaviors such as quantum and ballistic transport, ionic motion, filling of trap states, and surface electrochemistry. The vast majority of these studies have been performed using commercially available KPFM and EFM measurement modes, even though a number of advanced KPFM modes were developed for analysis of the time- and voltage dependent phenomena in specific materials classes, as summarized throughout this book. However, often these developments are limited to a single group and specific materials system. Below, we summarize some of the integrative challenges for the field, as well as pathways for the future development. These include (a) development of novel techniques in a systematic fashion, (b) controlled environments, (c) quantification of the imaging data, separation of contributing mechanisms, and signal conversion to materials specific behavior. These targets can be further enabled by transitioning from single group-led developments to a community-wide crowd sourced development, now underway in many areas of science.

10.8.1 New Techniques

Development of new SPM modalities that can be incorporated on the extant hardware platforms is one of the primary vectors of the field development, largely enabled by (relatively) open architecture of the existing SPM systems electronics and sample environments. This progress includes two primary components, namely development of novel spectroscopic techniques and new universal driving methods. The spectroscopic techniques generally refer to the imaging based on the sampling of a broad parameter space, for example potential at each spatial location as a

function of time, as exemplified by tr-KPFM. Alternatively, it includes measurements of the potential distributions as a function of lateral bias, gate potential, etc. Here, the sampling of the parameter space is often determined by the data acquisition time for individual measurement, availability of the automated measurement interfaces, and software for consistent data analysis. The extensive set of spectroscopic imaging modes was developed in the context of Piezoresponse force microscopy [211–217]. Notably, the same machinery can be implemented for laterally-biased KPFM methods. Here, of significant benefit will be the development of universal guidelines for experimental design and planning, allowing problem-specific configurations of bias waveforms to the lateral and gate electrodes and tip. These configurations can be implemented at a relatively low level in which device operation is controlled but the microscope is operated in a packaged KPFM mode (i.e. only synchronization via line and frame TTL signals). This level of integration can be trivially achieved via LabView interfaces, low-cost Raspberry Pi, or Arduino controllers, and requires minimal access to the microscope signals. Alternatively, the use of fast cards combined with open microscope electronics further allows the synchronizing of the device probing waveforms with specific tip bias sequences, as exemplified by Jesse et al. [218].

The second component of this process is the development of universal detection methods, as described at length in Chap. 3. For example, prior to ca. 2000 the detection was universally based on the heterodyne lock-in amplifier and phase locked loops, often further integrated with a certain type of feedback. These approaches are necessarily limited by the time constants of the heterodyne detection and feedback, often resulting in a fairly slow imaging that also severely limited the amount of obtained information and lead to systematic cross-talks. The revolution in this field occurred in 2000–2005, when commercially available IO cards have approached the 10 MHz barrier required for SPM imaging. The immediate emergence of band excitation [218–220] method in 2006 and the G-Mode [77, 221] in 2016 have enabled more comprehensive methodologies for capturing tip-surface interactions. Theoretically, G-Mode is based on full information capture from the tip-surface junction, and hence should allow for achieving the physical limits for data collection in SPM. Notably, the spectroscopic mode and detection methods can be combined, giving rise to a new variation of the lateral KPFM techniques. The advantage of this two-tiered approach is that the detection scheme provides information on the local functionality (e.g. local potential and capacitance), while the spectroscopic sweeps change the relevant device variables and probe their dependence on the external stimuli. This separation simplifies data interpretation.

Given the rapid rate at which spectroscopic and detection techniques have been developing and that these developments are often limited to a single research group (and commercialization takes long times, and often is difficult to justify for niche applications or latent markets), there is a strong incentive to community-wide adoption of measurements protocols and file formats, and open–sourced development and sharing of these tools, as will be discussed below. The necessary corollary from this is the concurrent standardization and opening of the microscopic platforms by the manufacturers.

10.8.2 Probes and Controlled Environments

The second development vector for techniques is the microscopic platforms, probes, and measurement environments. We do not discuss the first aspect here, since the development of force-sensitive SPMs represents a big area spanning multiple disciplines, well beyond the KPFM and especially KPFM of lateral devices. However, KPFM imaging imposes specific requirement on the probes and sample environments.

For ambient imaging, probe development predominantly targets the spatial resolution. For a technique sensitive to the capacitive gradient, the spatial resolution is determined as a balance between the local force acting on the spherical part of the probe, and the non-local cantilever and conical part of the tip contributions [67, 72, 134]. These considerations preclude the classical pathway of increasing the spatial resolution via the introduction of sharper probes. The alternative can be engineered probes with microelectrodes or dielectric or conductive shielding that limit the effective electrical size of the probe, while maintaining the mechanical integrity [222]. Furthermore, the presence of several individually addressable electrodes will allow the modification of the field structure, enabling e.g. differential electrostatic imaging. The key limitation here is that such probes must be available commercially in reasonable quantities and with reproducible characteristics, a feat that is still in the future. Note, that while these requirements are softened by the frequency-shift based methods sensitive to the second derivative of capacitance, these methods have more stringent limitation on the measurement speed, potentially limiting their applicability.

The probe development is, however, much more crucial for the imaging in liquid and conductive environments [223–225]. Multiple examples of shielded and insulated probes have been reported by several groups in US and worldwide [226, 227]. Particularly promising are the scuba probes for liquid imaging developed by the Ashby group [228], combining electrical insulation of probe body and mechanical decoupling of the cantilever from the environment. However, these probes only recently became commercially available.

Finally, often of interest is the functional imaging under controllable environment. In some cases, the need for the environmental control stems from the functionality of the materials or device of interest, for example a chemical sensor or a fuel cell, for which the gaseous component is the inherent part of the device. However, the environmental control is also crucial for systems with purely electronic or internal ionic functionality. For example, the signatures of serendipitous electrochemical processes in the water layer covering oxide surfaces in ambient are indistinguishable from physical phenomena such as charge injection, etc. [95, 229–232]. While multiple reports of these behaviors are available since the late 1990s, the recognition of the role these phenomena can play in the lateral KPFM measurement is still limited. Correspondingly, crucial is the development of the glove box, environmental cell, and vacuum platforms, as well as comparative studies under varying environmental conditions.

10.8.3 Data Analysis and Knowledge Extraction

In a predominant number of publications on KPFM under lateral bias (or many other imaging techniques for that matter), the emphasis is made on the development of the technique and/or materials study. The resultant images are generally published as is after minor image processing with qualitative explanations, or relatively minor analysis is performed (e.g. spatial differentiation to extract the lateral fields). At the same time, KPFM provides high-fidelity and often quantitative images of potential distributions inside the materials, suggesting that considerably more information can be extracted. This process comprises three intertwined stages, as discussed below.

The first limitation of the KPFM imaging is that the measured contrast is a result of the interplay between the local potential distribution in the material, dielectric properties (sometimes), and the probe. In certain cases, this effect can be represented as a linear convolution between the probe function and potential distribution in the material. The limitations imposed by these effects on the device analysis are straightforward—for example, potential gradients in the operational devices can be a signature of the resistive (IR) drops within the grains, or the effect of the cantilever surface interactions.

Correspondingly, of interest are deconvolution methods (e.g. based on the regularized reconstructions) that allow the reconstruction of the intrinsic potential (or charge) distribution in the device. Necessary for this is the development of reliable standards (e.g. nanotube based). Closely related, but significantly more complex, is the reconstruction of potential distributions on topographically non-uniform surfaces, which may require numerical solution at each step of the deconvolution process. Furthermore, ideally reconstruction will provide the associated reconstruction uncertainties, e.g. via Bayesian inference. As a note, the use of the reconstruction methods should also allow for uncertainties related to materials behaviors, e.g. presence of ionic charges on metallic surfaces.

The second critical aspect in data analysis in KPFM and other potential imaging techniques is the multitude of possible materials-specific mechanisms, including bulk electronic and ionic transport, surface ionic transport, electrochemistry, etc. For example, the potential measurements above the sample surface cannot distinguish the injection of electrons in the bulk trap states versus, bulk ionic dynamics versus electrochemical reactions of the water layer. This limitation stems from the nature of the KPFM measurements (very few parameters versus multiple degrees of freedom in material behaviors), and are common to SPM. The way to address these is a better experiment design, use of proper materials systems, capturing charge dynamics, temperature and environment control to reduce side reactions.

Finally, of interest is the reconstruction of materials specific behaviors, once the predominant mechanism is established. The lateral KPFM and related measurements are by definition non-local, i.e. the measured local response is determined by all other equivalent elements in the circuit. The multiple examples considered in this chapter typically use strongly simplifying assumptions, e.g. known current in

the (quasi) 1 D system to reconstruct the field distributions or local current-voltage characteristics. Here, the reconstruction algorithms based on the realistic device models and suitable fitting routines as demonstrated for energy discovery platforms for KPFM or for particle growth in liquids [233] offer a way forward.

10.8.4 Towards Community Science

As mentioned above, most of the technique and analysis developments are driven by individual groups and remain accessible only to the group members (or even vanish upon change of the scientific portfolio or personnel). Correspondingly, in the coming years particular premium can be put on the development of the community wide tools and codes using platforms such as GitHub. These developments include microscope operation codes and universal file formats, a development requiring a close integration with the instrument manufacturers. It further requires a community wide development and distribution of the image reconstruction codes and software for data fitting. Note, that this transition is now happening in many scientific areas, albeit it still has to enter the SPM domain. Once available, it will significantly increase the knowledge-generation potential of KPFM and contribute to a faster growth in the field.

Acknowledgements This research was conducted at and supported by the Center for Nanophase Materials Sciences, which is a DOE Office of Science User Facility. ES acknowledges support under the Cooperative Research Agreement between the University of Maryland and the National Institute of Standards and Technology Center for Nanoscale Science and Technology, Award 70NANB14H209, through the University of Maryland.

References

1. M. Fuechsle, J.A. Miwa, S. Mahapatra, H. Ryu, S. Lee, O. Warschkow, L.C.L. Hollenberg, G. Klimeck, M.Y. Simmons, Nat. Nanotechnol. **7**(4), 242–246 (2012)
2. S.R. Schofield, N.J. Curson, M.Y. Simmons, F.J. Ruess, T. Hallam, L. Oberbeck, R.G. Clark, Phys. Rev. Lett. **91**(13) (2003)
3. I. Valov, R. Waser, J.R. Jameson, M.N. Kozicki, Nanotechnology **22**(25) (2011)
4. R. Waser, Nanoelectron. Inf. Technol. (2012)
5. N.A. Spaldin, M. Fiebig, Science **309**(5733), 391–392 (2005)
6. S.V. Kalinin, N.A. Spaldin, Science **341**(6148), 858–859 (2013)
7. S. Datta, Phys. Rev. Lett. **79**, 2530 (1997)
8. C. Gorini, R.A. Jalabert, W. Szewc, S. Tomsovic, D. Weinmann, Phys. Rev. B **88**(3), 035406 (2013)
9. R.K. Rajkumar, A. Asenjo, V. Panchal, A. Manzin, Ó. Iglesias-Freire, O. Kazakova, J. Appl. Phys. **115**(17), 172606 (2014)
10. J.L. Webb, O. Persson, K.A. Dick, C. Thelander, R. Timm, A. Mikkelsen, Nano Res. **7**(6), 877–887 (2014)
11. S.R. Hunt, E.J. Fuller, B.L. Corso, P.G. Collins, Phys. Rev. B **85**(23), 235418 (2012)

12. M. Freitag, M. Radosavljevic, Y. Zhou, A.T. Johnson, W.F. Smith, Appl. Phys. Lett. **79**(20), 3326–3328 (2001)
13. M. Freitag, A.T. Johnson, S.V. Kalinin, D.A. Bonnell, Phys. Rev. Lett. **89**(21), 216801 (2002)
14. S.R. Hunt, D. Wan, V.R. Khalap, B.L. Corso, P.G. Collins, Nano Lett. **11**(3), 1055–1060 (2011)
15. S.V. Kalinin, Ph.D. Thesis, University of Pennsylvania, 2002
16. S. Rodewald, J. Fleig, J. Maier, J. Am. Ceram. Soc. **84**(3), 521–530 (2001)
17. K. Seong-Ho, S. Jun-Hyuk, P. Jae-Gwan, K. Yoonho, Jpn. J. Appl. Phys. **39**(4R), 1788 (2000)
18. A.S. Škapin, J. Jamnik, S. Pejovnik, Solid State Ion. **133**(1–2), 129–138 (2000)
19. D.D. Edwards, J.H. Hwang, S.J. Ford, T.O. Mason, Solid State Ion. **99**(1–2), 85–93 (1997)
20. R. Shao, S.V. Kalinin, D.A. Bonnell, in *Spatially Resolved Characterization of Local Phenomena in Materials and Nanostructures*, ed. by J. Piqueras, F.R. Zypman, D.A. Bonnell, A.P. Shreve, vol. 738 (2003), pp. 163–168
21. T.M. Arruda, A. Kumar, S. Jesse, G.M. Veith, A. Tselev, A.P. Baddorf, N. Balke, S.V. Kalinin, ACS Nano **7**(9), 8175–8182 (2013)
22. M. Nonnenmacher, M.P. Oboyle, H.K. Wickramasinghe, Appl. Phys. Lett. **58**(25), 2921–2923 (1991)
23. T.R. Albrecht, P. Grutter, D. Horne, D. Rugar, J. Appl. Phys. **69**(2), 668–673 (1991)
24. B.D. Terris, J.E. Stern, D. Rugar, H.J. Mamin, Phys. Rev. Lett. **63**(24), 2669–2672 (1989)
25. R. Shikler, N. Fried, T. Meoded, Y. Rosenwaks, Phys. Rev. B **61**(16), 11041–11046 (2000)
26. P.D. Wolf, J. Snauwaert, L. Hellemans, T. Clarysse, W. Vandervorst, M. D'Olieslaeger, D. Quaeyhaegens, J. Vac. Sci. Technol. A Vac. Surf Films **13**(3), 1699–1704 (1995)
27. P.D. Wolf, R. Stephenson, T. Trenkler, T. Clarysse, T. Hantschel, W. Vandervorst, J. Vac. Sci. Technol. B Microelectron. Nanometer Struct. Process. Meas. Phenom. **18**(1), 361–368 (2000)
28. C.C. Williams, Annu. Rev. Mater. Sci. **29**(1), 471–504 (1999)
29. H. Edwards, V.A. Ukraintsev, R.S. Martin, F.S. Johnson, P. Menz, S. Walsh, S. Ashburn, K. S. Wills, K. Harvey, M.-C. Chang, J. Appl. Phys. **87**(3), 1485–1495 (2000)
30. J.N. Nxumalo, D.T. Shimizu, D.J. Thomson, J. Vac. Sci. Technol. B Microelectron. Nanometer Struct. Process. Meas. Phenom. **14**(1), 386–389 (1996)
31. M.L. O'Malley, G.L. Timp, S.V. Moccio, J.P. Garno, R.N. Kleiman, Appl. Phys. Lett. **74**(2), 272–274 (1999)
32. R.M. Silver, J.A. Dagata, W. Tseng, J. Vac. Sci. Technol. A Vac. Surf. Films **13**(3), 1705–1708 (1995)
33. W. Wu, S.L. Skala, J.R. Tucker, J.W. Lyding, A. Seabaugh, E.A. Beam III, D. Jovanovic, J. Vac. Sci. Technol. A Vac. Surf. Films **13**(3), 602–606 (1995)
34. E.T. Yu, K. Barmak, P. Ronsheim, M.B. Johnson, P. McFarland, J.M. Halbout, J. Appl. Phys. **79**(4), 2115–2121 (1996)
35. S.J. Stranick, P.S. Weiss, Rev. Sci. Instrum. **64**(5), 1232–1234 (1993)
36. D.G. Cahill, R.J. Hamers, J. Vac. Sci. Technol. B Microelectron. Nanometer Struct. Process. Meas. Phenom. **9**(2), 564–567 (1991)
37. B. Grévin, I. Maggio-Aprile, A. Bentzen, L. Ranno, A. Llobet, Ø. Fischer, Phys. Rev. B **62** (13), 8596–8599 (2000)
38. J.R. Kirtley, S. Washburn, M.J. Brady, Phys. Rev. Lett. **60**(15), 1546–1549 (1988)
39. P. Muralt, D.W. Pohl, Appl. Phys. Lett. **48**(8), 514–516 (1986)
40. M. Tanimoto, K. Arai, J. Vac. Sci. Technol. B Microelectron. Nanometer Struct. Process. Meas. Phenom. **12**(3), 2125–2128 (1994)
41. L. Bürgi, H. Sirringhaus, R.H. Friend, Appl. Phys. Lett. **80**(16), 2913–2915 (2002)
42. A. Chavez-Pirson, O. Vatel, M. Tanimoto, H. Ando, H. Iwamura, H. Kanbe, Appl. Phys. Lett. **67**(21), 3069–3071 (1995)
43. S.V. Kalinin, D.A. Bonnell, J. Appl. Phys. **91**(2), 832–839 (2002)
44. O. Vatel, M. Tanimoto, J. Appl. Phys. **77**(6), 2358–2362 (1995)

45. T. Trenkler, P.D. Wolf, W. Vandervorst, L. Hellemans, J. Vac. Sci. Technol. B Microelectron. Nanometer Struct. Process. Meas. Phenom. **16**(1), 367–372 (1998)
46. T. Gramespacher, M. Büttiker, Phys. Rev. B **56**(20), 13026–13034 (1997)
47. A. Bachtold, M.S. Fuhrer, S. Plyasunov, M. Forero, E.H. Anderson, A. Zettl, P.L. McEuen, Phys. Rev. Lett. **84**(26), 6082–6085 (2000)
48. R. Crook, C.G. Smith, M.Y. Simmons, D.A. Ritchie, J. Phys. Condens. Matter **12**(50), L735 (2000)
49. M.A. Eriksson, R.G. Beck, M. Topinka, J.A. Katine, R.M. Westervelt, K.L. Campman, A.C. Gossard, Appl. Phys. Lett. **69**(5), 671–673 (1996)
50. M.T. Woodside, C. Vale, P.L. McEuen, C. Kadow, K.D. Maranowski, A.C. Gossard, Phys. Rev. B **64**(4), 041310 (2001)
51. M. Tanimoto, O. Vatel, J. Vac. Sci. Technol. B **14**(2), 1547–1551 (1996)
52. O. Vatel, M. Tanimoto, J. Appl. Phys. **77**(6), 2358–2362 (1995)
53. J. Fleig, S. Rodewald, J. Maier, J. Appl. Phys. **87**(5), 2372–2381 (2000)
54. S.V. Kalinin, D.A. Bonnell, in *Electrically Based Microstructural Characterization III*, ed. by R.A. Gerhardt, A.P. Washabaugh, M.A. Alim, G.M. Choi, vol. 699 (2002), pp. 101–106
55. S.V. Kalinin, D.A. Bonnell, Appl. Phys. Lett. **78**(9), 1306–1308 (2001)
56. S.V. Kalinin, M.R. Suchomel, P.K. Davies, D.A. Bonnell, J. Am. Ceram. Soc. **85**(12), 3011–3017 (2002)
57. S.M. Sze, *Physics of Semiconductor Devices* (Wiley, New York, 1981)
58. S.V. Kalinin, S. Jesse, J. Shin, A.P. Baddorf, M.A. Guillorn, D.B. Geohegan, Nanotechnology **15**(8), 907 (2004)
59. J. Shin, V. Meunier, A.P. Baddorf, S.V. Kalinin, Appl. Phys. Lett. **85**(18), 4240–4242 (2004)
60. B.J. Rodriguez, S. Jesse, V. Meunier, S.V. Kalinin, Appl. Phys. Lett. **88**(14), 143128 (2006)
61. L. Collins, J.I. Kilpatrick, S.A.L. Weber, A. Tselev, I.V. Vlassiouk, I.N. Ivanov, S. Jesse, S. V. Kalinin, B.J. Rodriguez, Nanotechnology **24**(47), 475702 (2013)
62. S.L. Guo, S.V. Kalinin, S. Jesse, Nanotechnology **23**(12), 125704 (2012)
63. N. Kobayashi, H. Asakawa, T. Fukuma, J. Appl. Phys. **110**(4), 044315 (2011)
64. S.V. Kalinin, D.A. Bonnell, Phys. Rev. B **63**(12) (2001)
65. E. Strelcov, S. Jesse, Y.-L. Huang, Y.-C. Teng, I.I. Kravchenko, Y.-H. Chu, S.V. Kalinin, ACS Nano **7**(8), 6806–6815 (2013)
66. S.V. Kalinin, D.A. Bonnell, Phys. Rev. B **63**(12), 125411–125424 (2001)
67. S. Belaidi, P. Girard, G. Leveque, J. Appl. Phys. **81**(3), 1023–1030 (1997)
68. E.S. Sadewasser, T. Glatzel (Springer Science + Business Media, New York, 2011)
69. D.J. Bayerl, X. Wang, Adv. Funct. Mater. **22**(3), 652–660 (2012)
70. E. Strassburg, A. Boag, Y. Rosenwaks, Rev. Sci. Instrum. **76**(8), 083705 (2005)
71. S. Sadewasser, T. Glatzel, R. Shikler, Y. Rosenwaks, M.C. Lux-Steiner, Appl. Surf. Sci. **210** (1–2), 32–36 (2003)
72. S.V. Kalinin, D.A. Bonnell, Phys. Rev. B **63**(12), 125411 (2001)
73. A. Liscio, V. Palermo, P. Samori, Acc. Chem. Res. **43**(4), 541–550 (2010)
74. D.S.H. Charrier, M. Kemerink, B.E. Smalbrugge, T. de Vries, R.A.J. Janssen, ACS Nano **2** (4), 622–626 (2008)
75. J.P. Moscatello, C.V. Castaneda, A. Zaidi, M.X. Cao, O. Usluer, A.L. Briseno, K.E. Aidala, Org. Electron. **41**, 26–32 (2017)
76. A. Belianinov, S.V. Kalinin, S. Jesse, Nat. Commun. **6** (2015)
77. S. Somnath, A. Belianinov, S.V. Kalinin, S. Jesse, Appl. Phys. Lett. **107**(26), 263102 (2015)
78. C. Liam, B. Alex, S. Suhas, J.R. Brian, B. Nina, V.K. Sergei, J. Stephen, Nanotechnology **27** (10), 105706 (2016)
79. J. Murawski, T. Graupner, P. Milde, R. Raupach, U. Zerweck-Trogisch, L.M. Eng, J. Appl. Phys. **118**(15), 8 (2015)
80. M.A. Topinka, B.J. LeRoy, S.E.J. Shaw, E.J. Heller, R.M. Westervelt, K.D. Maranowski, A. C. Gossard, Science **289**(5488), 2323–2326 (2000)

81. M.A. Topinka, B.J. LeRoy, R.M. Westervelt, S.E.J. Shaw, R. Fleischmann, E.J. Heller, K.D. Maranowski, A.C. Gossard, Nature **410**(6825), 183–186 (2001)
82. H. Sellier, B. Hackens, M.G. Pala, F. Martins, S. Baltazar, X. Wallart, L. Desplanque, V. Bayot, S. Huant, Semicond. Sci. Technol. **26**(6), 064008 (2011)
83. K.E. Aidala, R.E. Parrott, T. Kramer, E.J. Heller, R.M. Westervelt, M.P. Hanson, A.C. Gossard, Nat. Phys. **3**(7), 464–468 (2007)
84. F. Martins, B. Hackens, M.G. Pala, T. Ouisse, H. Sellier, X. Wallart, S. Bollaert, A. Cappy, J. Chevrier, V. Bayot, S. Huant, Phys. Rev. Lett. **99**(13), 136807 (2007)
85. A.J. Haemmerli, N. Harjee, M. Koenig, A.G.F. Garcia, D. Goldhaber-Gordon, B.L. Pruitt, J. Appl. Phys. **118**(3), 034306 (2015)
86. A. Efimov, S.R. Cohen, J. Vac. Sci. Technol. A Vac. Surf. Films **18**(4), 1051–1055 (2000)
87. Z.-Y. Li, B.-Y. Gu, G.-Z. Yang, Phys. Rev. B **57**(15), 9225–9233 (1998)
88. L. Olsson, N. Lin, V. Yakimov, R. Erlandsson, J. Appl. Phys. **84**(8), 4060–4064 (1998)
89. H.O. Jacobs, H.F. Knapp, A. Stemmer, Rev. Sci. Instrum. **70**(3), 1756–1760 (1999)
90. F. Robin, H. Jacobs, O. Homan, A. Stemmer, W. Bächtold, Appl. Phys. Lett. **76**(20), 2907–2909 (2000)
91. A. Liscio, V. Palermo, P. Samori, Acc. Chem. Res. **43**(4), 541–550 (2010)
92. A. Blumel, H. Plank, A. Klug, E. Fisslthaler, M. Sezen, W. Grogger, E.J.W. List, Rev. Sci. Instrum. **81**(5), 056107 (2010)
93. S.V. Kalinin, D.A. Bonnell, M. Freitag, A.T. Johnson, Appl. Phys. Lett. **81**(4), 754–756 (2002)
94. H.O. Jacobs, P. Leuchtmann, O.J. Homan, A. Stemmer, J. Appl. Phys. **84**(3), 1168–1173 (1998)
95. S.V. Kalinin, J. Shin, S. Jesse, D. Geohegan, A.P. Baddorf, Y. Lilach, M. Moskovits, A. Kolmakov, J. Appl. Phys. **98**(4), 044503 (2005)
96. H. Sugimura, Y. Ishida, K. Hayashi, O. Takai, N. Nakagiri, Appl. Phys. Lett. **80**(8), 1459–1461 (2002)
97. A.K. Henning, T. Hochwitz, J. Slinkman, J. Never, S. Hoffmann, P. Kaszuba, C. Daghlian, J. Appl. Phys. **77**(5), 1888–1896 (1995)
98. G. Koley, M.G. Spencer, H.R. Bhangale, Appl. Phys. Lett. **79**(4), 545–547 (2001)
99. P. Maksymovych, M.H. Pan, P. Yu, R. Ramesh, A.P. Baddorf, S.V. Kalinin, Nanotechnology **22**(25) (2011)
100. B.T. Rosner, T. Bork, V. Agrawal, D.W. van der Weide, Sens. Actuators A **102**(1–2), 185–194 (2002)
101. N. Harjee, A.G.F. Garcia, M. König, J.C. Doll, D. Goldhaber-Gordon, B.L. Pruitt, presented at the 2010 *IEEE 23rd International Conference on Micro Electro Mechanical Systems (MEMS)*, 2010 (unpublished)
102. A.B. Keith, J.S. Kevin, M.W. Robert, Nanotechnology **23**(11), 115703 (2012)
103. A. Ishtiaq, T.F. Muhammad, World Appl. Sci. J. **19**(4), 464–469 (2012)
104. L.S.C. Pingree, O.G. Reid, D.S. Ginger, Adv. Mater. **21**(1), 19–28 (2009)
105. A. Kikukawa, S. Hosaka, R. Imura, Appl. Phys. Lett. **66**(25), 3510–3512 (1995)
106. G.H. Buh, H.J. Chung, J.H. Yi, I.T. Yoon, Y. Kuk, J. Appl. Phys. **90**(1), 443–448 (2001)
107. G. Leveque, P. Girard, E. Skouri, D. Yarekha, Appl. Surf. Sci. **157**(4), 251–255 (2000)
108. K. Nakagami, Y. Ohno, S. Kishimoto, K. Maezawa, T. Mizutani, Appl. Phys. Lett. **85**(24), 6028–6029 (2004)
109. J.A. Nichols, D.J. Gundlach, T.N. Jackson, Appl. Phys. Lett. **83**(12), 2366–2368 (2003)
110. K.P. Puntambekar, P.V. Pesavento, C.D. Frisbie, Appl. Phys. Lett. **83**(26), 5539–5541 (2003)
111. W.R. Silveira, J.A. Marohn, Phys. Rev. Lett. **93**(11), 4 (2004)
112. E.M. Muller, J.A. Marohn, Adv. Mater. **17**(11), 1410–1414 (2005)
113. O. Tal, Y. Rosenwaks, Y. Preezant, N. Tessler, C.K. Chan, A. Kahn, Phys. Rev. Lett. **95**(25) (2005)
114. Y.J. Zhang, D. Ziegler, M. Salmeron, ACS Nano **7**(9), 8258–8265 (2013)

115. S.G.J. Mathijssen, M. Colle, A.J.G. Mank, M. Kemerink, P.A. Bobbert, D.M. de Leeuw, Appl. Phys. Lett. **90**(19), 3 (2007)
116. P. Annibale, C. Albonetti, P. Stoliar, F. Biscarini, J. Phys. Chem. A **111**(49), 12854–12858 (2007)
117. H.B. Wang, X.J. Wang, H.C. Huang, D.H. Yan, Appl. Phys. Lett. **93**(10), 3 (2008)
118. S. Bain, D.C. Smith, N.R. Wilson, M. Carrasco-Orozco, Appl. Phys. Lett. **95**(14), 143304 (2009)
119. F. Luttich, D. Lehmann, H. Graaf, D.R.T. Zahn, C. von Borczyskowski, in *Physica Status Solidi C: Current Topics in Solid State Physics,* vol. 7, no 2 (Wiley-V C H Verlag Gmbh, Weinheim, 2010), pp. 452–455
120. M. Ando, S. Heike, M. Kawasaki, T. Hashizume, Appl. Phys. Lett. **105**(19), 4 (2014)
121. Y. Yamagishi, K. Noda, K. Kobayashi, H. Yamada, J. Phys. Chem. C **119**(6), 3006–3011 (2015)
122. M. Jaquith, E.M. Muller, J.A. Marohn, J. Phys. Chem. B **111**(27), 7711–7714 (2007)
123. M.J. Jaquith, J.E. Anthony, J.A. Marohn, J. Mater. Chem. **19**(34), 6116–6123 (2009)
124. Y. Yamagishi, K. Kobayashi, K. Noda, H. Yamada, Appl. Phys. Lett. **108**(9), 5 (2016)
125. C. Melzer, C. Siol, H. von Seggern, Adv. Mater. **25**(31), 4315–4319 (2013)
126. J. Murawski, T. Monch, P. Milde, M.P. Hein, S. Nicht, U. Zerweck-Trogisch, L.M. Eng, J. Appl. Phys. **118**(24), 6 (2015)
127. R. Nowak, D. Moraru, T. Mizuno, R. Jablonski, M. Tabe, Appl. Phys. Lett. **102**(8), 083109 (2013)
128. K.K. Bharathi, W.-M. Lee, J.H. Sung, J.S. Lim, S.J. Kim, K. Chu, J.W. Park, J.H. Song, M.-H. Jo, C.-H. Yang, Appl. Phys. Lett. **102**(1), 012908 (2013)
129. S. Kamiya, M. Iwami, T. Tsuchiya, M. Kurouchi, J. Kikawa, T. Yamada, A. Wakejima, H. Miyamoto, A. Suzuki, A. Hinoki, T. Araki, Y. Nanishi, Appl. Phys. Lett. **90**(21), 213511 (2007)
130. C.H. Lin, T.A. Merz, D.R. Doutt, M.J. Hetzer, J. Joh, J.A. del Alamo, U.K. Mishra, L. J. Brillson, Appl. Phys. Lett. **95**(3), 3 (2009)
131. Z.H. Han, G.W. Xu, W. Wang, C.Y. Lu, N.D. Lu, Z.Y. Ji, L. Li, M. Liu, Appl. Phys. Lett. **109**(2), 4 (2016)
132. D.Y. Fan, J. Zhu, X.L. Wang, S.Y. Wang, Y. Liu, R.T. Chen, Z.C. Feng, F.T. Fan, C. Li, ACS Appl. Mater. Interfaces **8**(22), 13857–13864 (2016)
133. S.V. Kalinin, D.A. Bonnell, Phys. Rev. B **70**(23), 235304 (2004)
134. S.V. Kalinin, D.A. Bonnell, Phys. Rev. B **62**(15), 10419–10430 (2000)
135. R. Shao, S.V. Kalinin, D.A. Bonnell, Appl. Phys. Lett. **82**(12), 1869–1871 (2003)
136. A. Nevosad, M. Hofstaetter, M. Wiessner, P. Supancic, C. Teichert, in *Oxide-Based Materials and Devices IV*, ed. by F.H. Teherani, D.C. Look, D.J. Rogers, vol. 8626 (Spie-Int Soc Optical Engineering, Bellingham, 2013)
137. D.A. Bonnell, B. Huey, D. Carroll, Solid State Ion. **75**, 35–42 (1995)
138. B.D. Huey, D.A. Bonnell, Appl. Phys. Lett. **76**(8), 1012–1014 (2000)
139. C. Sakai, N. Ishida, H. Masuda, S. Nagano, M. Kitahara, Y. Ogata, D. Fujita, Appl. Phys. Lett. **109**(5), 051603 (2016)
140. S.-Y. Chung, I.-D. Kim, S.-J.L. Kang, Nat. Mater. **3**(11), 774–778 (2004)
141. L. Ian, F. Nassim, F. Maxwell, S. Mohammad, C. Carlo, M. Roya, B. Qing, L. Maozi, H. Storrs, J. Micromech. Microeng. **22**(6), 065031 (2012)
142. W. Bergbauer, T. Lutz, W. Frammelsberger, G. Benstetter, Microelectron. Reliab. **46**(9–11), 1736–1740 (2006)
143. R. Shikler, T. Meoded, N. Fried, Y. Rosenwaks, Appl. Phys. Lett. **74**(20), 2972–2974 (1999)
144. M. Moczala, N. Sosa, A. Topol, T. Gotszalk, Ultramicroscopy **141**, 1–8 (2014)
145. P. Narchi, V. Neplokh, V. Piazza, T. Bearda, F. Bayle, M. Foldyna, C. Toccafondi, P. Prod'homme, M. Tchernycheva, P.R.I. Cabarrocas, Sol. Energy Mater. Sol. Cells **161**, 263–269 (2017)
146. X.J. Wang, S.L. Ji, H.B. Wang, D.H. Yan, Org. Electron. **12**(12), 2230–2235 (2011)

147. K. Smaali, D. Guerin, V. Passi, L. Ordronneau, A. Carella, T. Melin, E. Dubois, D. Vuillaume, J.P. Simonato, S. Lenfant, J. Phys. Chem. C **120**(20), 11180–11191 (2016)
148. E. Halpern, A. Henning, H. Shtrikman, R. Rurali, X. Cartoixà, Y. Rosenwaks, Nano Lett. **15** (1), 481–485 (2015)
149. D. Pan, E.J. Fuller, O.T. Gül, P.G. Collins, Nano Lett. **15**(8), 5248–5253 (2015)
150. O. Hazut, A. Agarwala, I. Amit, T. Subramani, S. Zaidiner, Y. Rosenwaks, R. Yerushalmi, ACS Nano **6**(11), 10311–10318 (2012)
151. E. Koren, G. Elias, A. Boag, E.R. Hemesath, L.J. Lauhon, Y. Rosenwaks, Nano Lett. **11**(6), 2499–2502 (2011)
152. S.S. Bae, N. Prokopuk, N.J. Quitoriano, S.M. Adams, R. Ragan, Nanotechnology **23**(40), 9 (2012)
153. H. Jeong, Y.H. Ahn, S. Lee, J.-Y. Park, Appl. Phys. Lett. **104**(21), 213102 (2014)
154. I. Amit, N. Jeon, L.J. Lauhon, Y. Rosenwaks, ACS Appl. Mater. Interfaces **8**(1), 128–134 (2016)
155. O. Persson, J.L. Webb, K.A. Dick, C. Thelander, A. Mikkelsen, R. Timm, Nano Lett. **15**(6), 3684–3691 (2015)
156. T. Wagner, H. Beyer, P. Reissner, P. Mensch, H. Riel, B. Gotsmann, A. Stemmer, Beilstein J. Nanotechnol. **6**, 2193–2206 (2015)
157. S. Masaki, Y. Xiang, K. Ryota, K. Seiya, Jpn. J. Appl. Phys. **55**(2S), 02BD01 (2016)
158. D.J. Bayerl, X. Wang, Adv. Func. Mater. **22**(3), 652–660 (2012)
159. M. Radosavljević, M. Freitag, K.V. Thadani, A.T. Johnson, Nano Lett. **2**(7), 761–764 (2002)
160. Y.-J. Yu, Y. Zhao, S. Ryu, L.E. Brus, K.S. Kim, P. Kim, Nano Lett. **9**(10), 3430–3434 (2009)
161. B.D. Huey, D. Lisjak, D.A. Bonnell, J. Am. Ceram. Soc. **82**(7), 1941–1944 (1999)
162. S.V. Kalinin, B.J. Rodriguez, S. Jesse, K. Seal, R. Proksch, S. Hohlbauch, I. Revenko, G.L. Thompson, A.A. Vertegel, Nanotechnology **18**(42), 424020 (2007)
163. S.V. Kalinin, D.A. Bonnell, M. Freitag, A.T. Johnson, Appl. Phys. Lett. **81**(27), 5219–5221 (2002)
164. E.J. Fuller, D. Pan, B.L. Corso, O.T. Gul, J.R. Gomez, P.G. Collins, Appl. Phys. Lett. **102** (8), 083503 (2013)
165. L. Yan, C. Punckt, I.A. Aksay, W. Mertin, G. Bacher, Nano Lett. **11**(9), 3543–3549 (2011)
166. V. Panchal, C. Giusca, A. Lartsev, R. Yakimova, O. Kazakova, Front. Phys. **2**(3) (2014)
167. S.V. Kalinin, N. Balke, Adv. Mater. **22**(35), E193–E209 (2010)
168. I. Batko, M. Batkova, Eur. Phys. J. Appl. Phys. **58**(2), 20102 (2012)
169. I. Batko, M. Batkova, arXiv:1106.5006 (2011)
170. H. Kim, D.-W. Kim, S.-H. Phark, J. Phys. D Appl. Phys. **43**(50), 505305 (2010)
171. H. Kim, D.-W. Kim, Appl. Phys. A Mater. Sci. Process. **102**(4), 949–953 (2011)
172. Y. Yuan, J. Chae, Y. Shao, Q. Wang, Z. Xiao, A. Centrone, J. Huang, Adv. Energy Mater. **5** (15), 1500615-n/a (2015)
173. S.S. Nonnenmann, R. Kungas, J. Vohs, D.A. Bonnell, ACS Nano **7**(7), 6330–6336 (2013)
174. J. Zhu, C.R. Pérez, T.-S. Oh, R. Küngas, J.M. Vohs, D.A. Bonnell, S.S. Nonnenmann, J. Mater. Res. **30**(3), 357–363 (2014)
175. J. Zhu, J. Wang, D.S. Mebane, S.S. Nonnenmann, APL Mater. **5**(4), 042503 (2017)
176. S.S. Nonnenmann, Nanoscale **8**(6), 3164–3180 (2016)
177. W. Shockley, W.W. Hooper, H.J. Queisser, W. Schroen, Surf. Sci. **2**, 277–287 (1964)
178. E. Barsoukov, J.R. Macdonald, *Impedance Spectroscopy: Theory, Experiment, and Applications* (Wiley, Hoboken, NJ, 2005)
179. R. O'Hayre, M. Lee, F.B. Prinz, J. Appl. Phys. **95**(12), 8382–8392 (2004)
180. E.S. Schlegel, G.L. Schnable, R.F. Schwarz, J.P. Spratt, IEEE Trans. Electron Devices **ED15** (12), 973-& (1968)
181. I. Kiselev, M. Sommer, Thin Solid Films **518**(16), 4533–4536 (2010)
182. I. Kiselev, M. Sommer, V.V. Sysoev, S.L. Skorokhodov, Phys. Status Solidi A Appl. Mater. Sci. **208**(12), 2889–2899 (2011)

183. S.V. Kalinin, N. Balke, A.Y. Borisevich, S. Jesse, P. Maksymovych, Y. Kim, E. Strelcov (Google Patents, 2014)
184. E. Strelcov, A.V. Ievlev, S. Jesse, I.I. Kravchenko, V.Y. Shur, S.V. Kalinin, Adv. Mater. **26** (6), 958–963 (2014)
185. J. Ding, E. Strelcov, S.V. Kalinin, N. Bassiri-Gharb, Nano Lett. **15**(6), 3669–3676 (2015)
186. E. Strelcov, S. Jesse, Y.L. Huang, Y.C. Teng, I.I. Kravchenko, Y.H. Chu, S.V. Kalinin, ACS Nano **7**(8), 6806–6815 (2013)
187. J. Ding, E. Strelcov, V.S. Kalinin, N. Bassiri-Gharb, Nanotechnology **27**(34), 345401-345401-345411 (2016)
188. J. Ding, E. Strelcov, N. Bassiri-Gharb, J. Am. Ceram. Soc. **00**, 1–10 (2017)
189. E. Strelcov, S.M. Yang, S. Jesse, N. Balke, R.K. Vasudevan, S.V. Kalinin, Nanoscale **8**(29), 13838–13858 (2016)
190. J.M. Azpiroz, E. Mosconi, J. Bisquert, F. De Angelis, Energy Environ. Sci. **8**(7), 2118–2127 (2015)
191. P. Calado, A.M. Telford, D. Bryant, X. Li, J. Nelson, B.C. O'Regan, P.R.F. Barnes, Nat. Commun. **7**, 13831 (2016)
192. H.J. Snaith, A. Abate, J.M. Ball, G.E. Eperon, T. Leijtens, N.K. Noel, S.D. Stranks, J.T.-W. Wang, K. Wojciechowski, W. Zhang, J. Phys. Chem. Lett. **5**(9), 1511–1515 (2014)
193. C.H.W. Cheng, F. Lin, M.C. Lonergan, J. Phys. Chem. B **109**(20), 10168–10178 (2005)
194. D. Tordera, M. Kuik, Z.D. Rengert, E. Bandiello, H.J. Bolink, G.C. Bazan, T.-Q. Nguyen, J. Am. Chem. Soc. **136**(24), 8500–8503 (2014)
195. A. Garcia, J.Z. Brzezinski, T.-Q. Nguyen, J. Phys. Chem. C **113**(7), 2950–2954 (2009)
196. C. Hoven, R. Yang, A. Garcia, A.J. Heeger, T.-Q. Nguyen, G.C. Bazan, J. Am. Chem. Soc. **129**(36), 10976–10977 (2007)
197. D. Li, H. Wu, H.-C. Cheng, G. Wang, Y. Huang, X. Duan, ACS Nano **10**(7), 6933–6941 (2016)
198. Y. Yuan, T. Li, Q. Wang, J. Xing, A. Gruverman, J. Huang, Sci. Adv. **3** (3)(2017)
199. T. Choi, S. Lee, Y.J. Choi, V. Kiryukhin, S.-W. Cheong, Science **324**(5923), 63–66 (2009)
200. J.E. Spanier, V.M. Fridkin, A.M. Rappe, A.R. Akbashev, A. Polemi, Y. Qi, Z. Gu, S.M. Young, C.J. Hawley, D. Imbrenda, G. Xiao, A.L. Bennett-Jackson, C.L. Johnson, Nat. Photon **10**(9), 611–616 (2016)
201. R.C. Hayward, D.A. Saville, I.A. Aksay, Nature **404**(6773), 56–59 (2000)
202. K. Hu, A.J. Bard, Langmuir **13**(20), 5418–5425 (1997)
203. A.S. Johnson, C.L. Nehl, M.G. Mason, J.H. Hafner, Langmuir **19**(24), 10007–10010 (2003)
204. D.J. Müller, D. Fotiadis, S. Scheuring, S.A. Müller, A. Engel, Biophys. J. **76**(2), 1101–1111 (1999)
205. Y. Yang, K.M. Mayer, J.H. Hafner, Biophys. J. **92**(6), 1966–1974 (2007)
206. B.J. Rodriguez, S. Jesse, A.P. Baddorf, S.V. Kalinin, Phys. Rev. Lett. **96**(23) (2006)
207. N. Balke, A. Tselev, T.M. Arruda, S. Jesse, Y.H. Chu, S.V. Kalinin, ACS Nano **6**(11), 10139–10146 (2012)
208. N. Balke, S. Jesse, Y.H. Chu, S.V. Kalinin, ACS Nano **6**(6), 5559–5565 (2012)
209. B.J. Rodriguez, S. Jesse, A.P. Baddorf, S.H. Kim, S.V. Kalinin, Phys. Rev. Lett. **98**(24) (2007)
210. B.J. Rodriguez, S. Jesse, K. Seal, A.P. Baddorf, S.V. Kalinin, J. Appl. Phys. **103**(1), 014306 (2008)
211. S. Guo, O.S. Ovchinnikov, M.E. Curtis, M.B. Johnson, S. Jesse, S.V. Kalinin, J. Appl. Phys. **108**(8), 084103 (2010)
212. S. Wicks, K. Seal, S. Jesse, V. Anbusathaiah, S. Leach, R.E. Garcia, S.V. Kalinin, V. Nagarajan, Acta Mater. **58**(1), 67–75 (2010)
213. O. Ovchinnikov, S. Jesse, S. Guo, K. Seal, P. Bintachitt, I. Fujii, S. Trolier-McKinstry, S.V. Kalinin, Appl. Phys. Lett. **96**(11), 112906 (2010)
214. N. Balke, I. Bdikin, S.V. Kalinin, A.L. Kholkin, J. Am. Ceram. Soc. **92**(8), 1629–1647 (2009)

215. D.A. Bonnell, S.V. Kalinin, A.L. Kholkin, A. Gruverman, MRS Bull. **34**(9), 648–657 (2009)
216. P. Bintachitt, S. Trolier-McKinstry, K. Seal, S. Jesse, S.V. Kalinin, Appl. Phys. Lett. **94**(4), 042906 (2009)
217. S.V. Kalinin, A.N. Morozovska, L.Q. Chen, B.J. Rodriguez, Rep. Prog. Phys. **73**(5), 056502 (2010)
218. S. Jesse, S. Kalinin, V.R. Proksch, A.P. Baddorf, B.J. Rodriguez, Nanotechnology **18**(43), 435503 (2007)
219. S. Jesse, S.V. Kalinin, J. Phys. D Appl. Phys. **44**(46), 464006 (2011)
220. S. Jesse, R.K. Vasudevan, L. Collins, E. Strelcov, M.B. Okatan, A. Belianinov, A. P. Baddorf, R. Proksch, S.V. Kalinin, Annu. Rev. Phys. Chem. **65**(65), 519–536 (2014)
221. A. Belianinov, S.V. Kalinin, S. Jesse, Nat. Commun. **6** (2015)
222. E.A. Eliseev, S.V. Kalinin, S. Jesse, S.L. Bravina, A.N. Morozovska, J. Appl. Phys. **102**(1) (2007)
223. A.B. Keith, M.W. Robert, Nanotechnology **20**(38), 385302 (2009)
224. K.A. Brown, J.A. Aguilar, R.M. Westervelt, Appl. Phys. Lett. **96**(12), 123109 (2010)
225. A.G. Onaran, M. Balantekin, W. Lee, W.L. Hughes, B.A. Buchine, R.O. Guldiken, Z. Parlak, C.F. Quate, F.L. Degertekin, Rev. Sci. Instrum. **77**(2), 023501 (2006)
226. J.H. Noh, M. Nikiforov, S.V. Kalinin, A.A. Vertegel, P.D. Rack, Nanotechnology **21**(36) (2010)
227. B.J. Rodriguez, S. Jesse, K. Seal, A.P. Baddorf, S.V. Kalinin, P.D. Rack, Appl. Phys. Lett. **91**(9) (2007)
228. D. Ziegler, A. Klaassen, D. Bahri, D. Chmielewski, A. Nievergelt, F. Mugele, J.E. Sader, P. D. Ashby, in *2014 IEEE 27th International Conference on Micro Electro Mechanical Systems (Mems)*, (2014), pp. 128–131
229. S.V. Kalinin, D.A. Bonnell, Nano Lett. **4**(4), 555–560 (2004)
230. Y. Nan, D. Sandra, K. Amit, J. Jae Hyuck, M.A. Thomas, T. Antonello, J. Stephen, N.I. Ilia, P.B. Arthur, S. Evgheni, L. Silvia, Y.B. Albina, B. Giuseppe, V.K. Sergei, Nanotechnology **25**(7), 075701 (2014)
231. A.V. Ievlev, S. Jesse, A.N. Morozovska, E. Strelcov, E.A. Eliseev, Y.V. Pershin, A. Kumar, V.Y. Shur, S.V. Kalinin, Nat. Phys. **10**(1), 59–66 (2014)
232. D. Brunel, A. Mayer, T. Mélin, ACS Nano **4**(10), 5978–5984 (2010)
233. A.V. Ievlev, S. Jesse, T.J. Cochell, R.R. Unocic, V.A. Protopopescu, S.V. Kalinin, ACS Nano **9**(12), 11784–11791 (2015)

Chapter 11
Kelvin Probe Force Microscopy Characterization of Organic and Hybrid Perovskite Solar Cells

Benjamin Grévin

Abstract Nowadays, solution processed solar cells based on organic and hybrid-perovskite semi-conductors are serious competitors for silicon-based and inorganic photovoltaic technologies in terms of production costs, performance to weight ratio, flexibility, and easy manufacturing. Since the beginning of this century, the power conversion efficiency (PCE) values of polymer solar cells have continuously increased, and now exceed ten percent. More recently, following the development of dye-sensitized solar cells, lead-halide perovskite based devices with various architectures have been developed leading to PCE exceeding twenty percent. The goal of this chapter is to show how KPFM can contribute to further improve the performances of these solution-processed photovoltaic devices, by gaining a deeper insight in the local mechanisms governing the charge carrier generation, recombination, transport, and extraction at the electrodes. This chapter will focus more specifically on KPFM investigations of the surface potential and surface photo-voltage of organic donor-acceptor interfaces and polycrystalline lead halide perovskites in relation with the sample morphology and structural defects at the mesoscopic and nanometer scales, cross sectional KPFM investigations, and time-resolved measurements of the charge dynamics by KPFM under frequency modulated illumination.

11.1 Introduction

11.1.1 Organic Solar Cells

One of the biggest challenges of the 21st century consists in finding a solution to the world's increasing energy demand. Photovoltaics (PV) technologies have a huge potential for the development of carbon-free renewable energies, and can contribute

B. Grévin (✉)
National Center for Scientific Research – CNRS, UMR5819 CEA-CNRS-UGA, CEA-INAC/SYMMES, 17 rue des Martyrs, 38054 Grenoble Cedex 9, France
e-mail: benjamin.grevin@cea.fr

S. Sadewasser and T. Glatzel (eds.), *Kelvin Probe Force Microscopy*,
Springer Series in Surface Sciences 65, https://doi.org/10.1007/978-3-319-75687-5_11

significantly to counteract the climate changes. Most of today's installed solar panels are single junction cells based on multi-crystalline silicon. However, other emerging PV technologies show continuously increasing efficiencies.

Organic solar cells constitute a promising approach for the development of alternative PV technologies. These "plastic" cells can potentially be constructed on lightweight flexible substrates, thereby offering possibilities for new applications. This past decade, the performance of "all organic" photovoltaic (OPV) devices based on blends of electron donor and acceptor materials has improved continuously, with power conversion efficiency record values above 10% for single junctions [1–4]. However, these record values are still far away from the maximum theoretical efficiencies [5].

Solution processed organic solar cells [6] combine electron donor (D, polymers or small molecules) and acceptor (A, most often fullerene derivatives) π-conjugated materials displaying suitable energy offset between their highest occupied molecular orbitals (HOMO) and lowest unoccupied molecular orbitals (LUMO) levels. These energetic offsets define a type-II heterojunction (Fig. 11.1a), enabling to dissociate singlet excitons into Coulomb-bound electron-hole pairs which will be referred to in the following as charge-transfer states (CT). The CT state may either recombine or split up into free charges, which can ultimately reach the collection electrodes of the device. It is necessary to establish Ohmic contacts for efficient charge extraction [7]. A proper interface engineering [8, 9] is also crucial to achieve selective electrical contacts for holes at the anode and electrons at the cathode in bulk-heterojunctions. Basically, this is achieved by using materials with a low work function and a high work function for the electron extraction and the hole extraction, respectively.

A milestone in the field was the development of the bulk heterojunction (BHJ) architecture [10] in which donor and acceptor materials are processed to form two interpenetrated networks phase-segregated at the ten nanometer scale (Fig. 11.1b). This blend morphology maximizes the interfacial area for exciton dissociation, keeping in mind that the typical exciton diffusion length is on the order of ten nanometers in solution-processed organic semiconductors. Percolating and ordered (ideally crystalline) donor and acceptor networks are moreover required to achieve a reasonably high carrier mobility and avoid losses by recombination [11] during the charge transport to the electrodes.

Generally, the losses in BHJ may originate from: (i) the relaxation of excitons, (ii) the recombination of geminate polaron pairs (CT state) which fail to escape their mutual Coulomb interaction; this event is qualified as "geminate recombination", and (iii) the electron-hole annihilation of free carriers generated by different absorption events on their way towards the electrodes (bimolecular non-geminate recombination).

Last, due to energetic and spatial disorder, free charges can also be trapped in tail states [6, 12] with low de-trapping rates. These trapped charges can eventually recombine with a free non-geminate counter charge; this process is called a (non-geminate) trap-assisted recombination (also referred as trap-delayed recombination). As the charge carrier mobility is low in solution processed BHJ, the

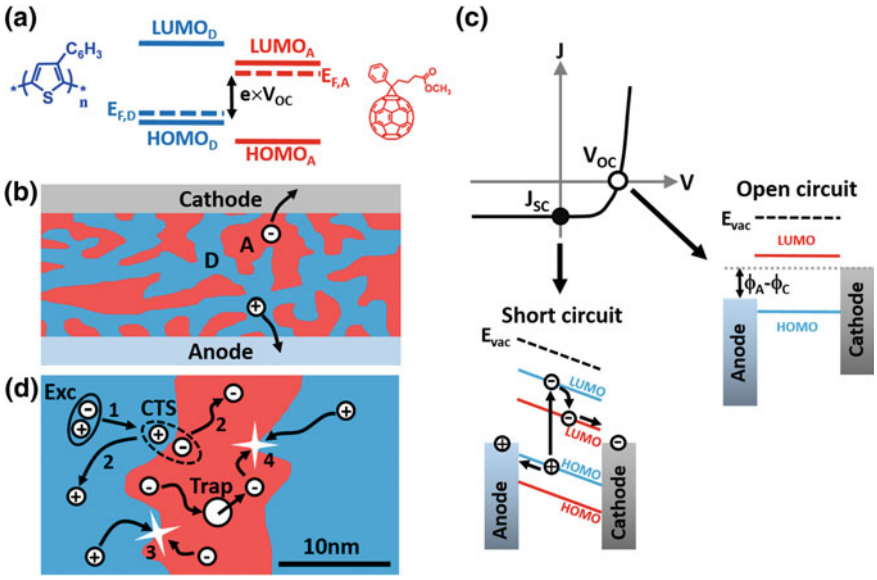

Fig. 11.1 **a** Illustration of a type-II energy level alignment between a π-conjugated electron donor polymer (here, P3HT) and a π-conjugated electron acceptor molecule (PCBM). The open circuit voltage is determined by the splitting of holes and electrons quasi Fermi levels (symbolized by dotted lines) under illumination. **b** Organic bulk heterojunction solar cell. **c** Current density versus voltage of an organic donor-acceptor solar cell. The energy level alignment has been represented for short circuit and open circuit conditions in the idealized case of a metal-insulator-metal junction (here band bending or energy offsets at the organic/metal interfaces are not considered). Under short circuit the built in electric field promotes carrier transport (sweep out) by drift. With this representation, the device open circuit voltage would be equal to the work function difference between the anode and the cathode. This is not generally true. **d** Schematic diagram showing some major steps of charge generation and recombination. (1) Exciton diffusion (represented in a "classical picture") to the D-A interface and creation of the charge transfer state; (2) separation of the bound polaron pair into free charges (alternatively geminate recombination can occur); (3) non-geminate recombination of free charge carriers; (4) charge trapping, release, and trap-delayed recombination with a free counter charge

competition between charge extraction to the electrodes and non-geminate recombination processes limits significantly the performances of operating devices. It has been shown that non-geminate recombination (NGR) is a major loss mechanism limiting the performances under standard operating conditions. The internal built-in field plays a crucial role in the charge collection process [13], because it promotes carrier transport via drift. This so called carrier sweep out process competes with recombination and is especially efficient in short circuit conditions (Fig. 11.1c) where the internal electric field can be high.

Several models have been developed to describe NGR process in BHJ, such as adaptations of the well-known Langevin model for bimolecular recombination, or the model proposed by Shockley, Read and Hall (SRH) for trap-assisted recombination [14]. So far, there is no universal model to describe the NGR processes in

BHJ devices. However, it is obvious that the nanostructure has a critical impact on the photo-carrier dynamics. In the case of "canonical" blends such as P3HT:PCBM, it has been shown [15] that the relative strength of bimolecular and trap-assisted recombination process is strongly sample processing-dependent; some reports also demonstrated that bimolecular recombination can be significantly reduced by thermal annealing which promotes P3HT crystallization [16].

Significant progress has been achieved this past decade in understanding the photo-carrier generation and transport mechanisms in relation with the nanostructure in BHJs. Many efforts have been devoted to understanding the nature of the mechanisms behind the CT state separation into free charges [17, 18]. Several works pointed out the importance of investigating the local micro-electrostatics in relation with the molecular organization [17], because interfacial molecular dipoles can dramatically impact the energetics landscape and the CT state separation at D/A interfaces [19]. However, many questions are not definitely settled, largely due to the highly complex phase morphology of BHJs [20]. It is now established that many blends display a three-component organization in pure donor, pure acceptor and inter-mixed phases [21–23], where the donor and acceptor molecules are finely mixed at the sub-10 nm scale. Several reports concluded that ultra-fast (sub-100 fs timescale) CT state separation occurs in regions where the polymer and fullerene are molecularly intermixed [24, 25]. The co-existence with neat domains allows separating the Coulomb-bound electron-hole pairs and transporting the charges towards the electrodes. On the basis of current knowledge, however, a number of questions remain widely open concerning the impact of the ternary phase morphology on the photo-carrier dynamics and transports.

11.1.2 Hybrid Perovskites Solar Cells

The most promising perovskites used in solar cells are organic-inorganic methylammonium lead trihalides ($CH_3NH_3PbX_3$, X = I-, Br-, Cl-, see Fig. 11.2a) and mixed cation lead trihalides. They are excellent PV materials displaying direct band gaps, large absorption coefficients, high carrier mobility (on the order of 10 cm^2 V^{-1} s^{-1} for electrons and holes [26]), and high diffusion lengths [27]. Thanks to these remarkable properties, the power conversion efficiencies of perovskite solar cells (PSCs) have been dramatically increased within a few years and exceed nowadays 20% [28].

Initially, organic-inorganic perovskites have been used as sensitizers [29] in dye sensitized solar cells (DSSC, see Fig. 11.2c), in combination with mesoporous n-type TiO_2 and with a solid state hole-transporting material such as Spiro-OMeTAD. In standard DSSCs, the electrons are transferred from the photo-excited dye to the conduction band of the mesoporous oxide, which is used to drive the

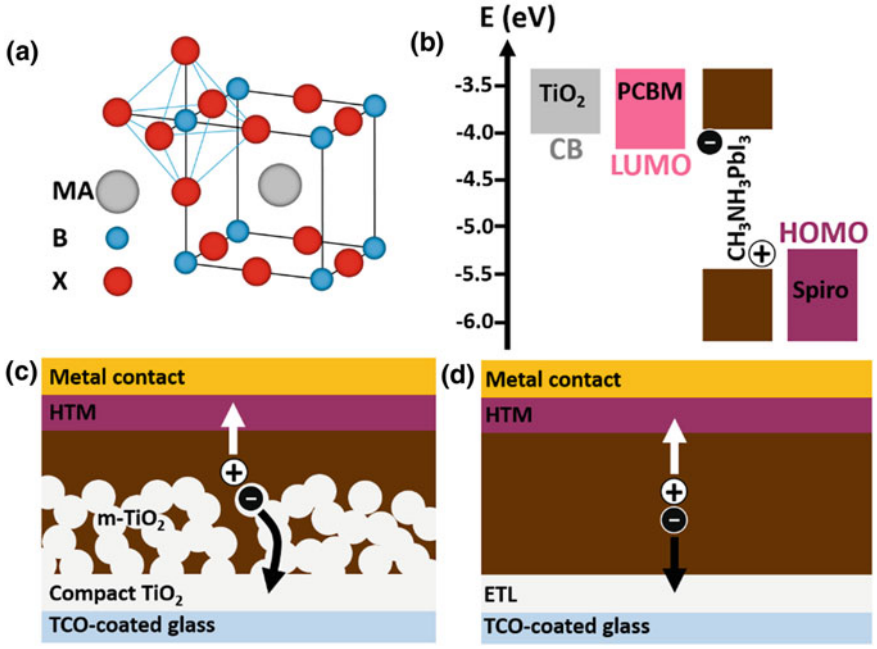

Fig. 11.2 **a** $MABX_3$ perovskite structure (MA: methylammonium cation, B: metal cation, X: halide anion). NB: depending of the composition, the crystal structure of hybrid perovskite can differ from the cubic phase at room temperature (for instance $MAPbI_3$ displays a tetragonal phase). **b** Illustration showing the relative position of the energy levels of two electron transporting materials (TiO_2 and PCBM), of the perovskite $CH_3NH_3PbI_3$, and of a hole transporting material (Spiro-OMeTAD). **c** Perovskite solar cell in DSSC or MSSC configuration (m-TiO_2: mesoporous TiO_2, HTM: hole-transporting material, TCO: transparent conducting oxide). In DSSC devices the electrons are injected in the conduction band of the mesoporous oxide. In MSSC devices the mesoporous oxide is replaced by an insulating scaffold and the electron transport is insured by the perovskite layer. **d** Planar perovskite solar cell (ETL: electron transporting layer)

carriers to the photo-anode. Quickly, it was shown that the perovskites can be used as both absorbers and electron transporters, and the mesoporous TiO_2 layer was replaced by an insulating mesoporous alumina scaffold (which improves the uniformity of coating [26]) in the so-called meso-superstructured solar cell (MSSC) configuration [30]. MSSCs have further evolved towards quasi planar heterojunction architectures, as a consequence of the significant thinning of the alumina scaffold. Finally, it was shown that a scaffold layer is not necessarily required to achieve high efficiencies. Thus, thin-film like perovskite solar cells in planar configuration (sometimes referred to as planar heterojunction configuration) have been developed (Fig. 11.2d), in which the perovskite layer is sandwiched between an electron transporting/hole blocking layer (ETL) and a hole transporting/electron

blocking layer (HTL). Examples of ETL materials include (but are not limited to): TiO_2 [27], ZnO [31] and fullerene derivatives [32]. Spiro-OMeTAD [33] and PEDOT:PSS [32] have frequently been used for the HTL. Depending of the electrode configuration (i.e. ETL at the top or at the bottom), the planar cells are referred to as "regular" n-i-p or "inverted" p-i-n devices.

The nature of the charge generation and transport mechanisms in hybrid-perovskites are still the subject of intensive investigations. Photo-physical studies have shown extremely long electron and hole diffusion lengths, on the order of hundred nanometers and even exceeding one micron for mixed halides [27]. In these materials, free charge carriers can be directly generated at room temperature under optical excitation due to the low exciton binding energy. The charge carriers can be directly driven to the electrodes by the internal electric field (due to the work function difference between the contacts). Even in the case of a low built-in electric field, selective contacts can still drive the electron and hole flows thanks to the large carrier diffusion lengths. In fact, electron beam-induced current profiling [34] revealed that planar cells can indeed operate as p-i-n devices, implying that the perovskite can be considered as a high quality low-doped intrinsic semiconductor. It is noteworthy, however, that the internal built-in electric field may be spatially inhomogeneous in contrast to the case of an ideal p-i-n device [34].

Like the case of organic devices, a proper interface engineering is essential to achieve highly efficient planar PSCs [35], and it is crucial to investigate the energy level alignment at the interfaces between the perovskite film and the selective layers [36].

The impact of structural and chemical defects on the perovskite solar cell performance remains also intensively investigated. It has been argued that the influence of grain boundaries shall be benign [34], but several studies have shown that grain boundaries are detrimental to the overall device performances. Several reports have shown that grain boundaries (GBs) can be the source of charge trapping and trap-delayed recombination [32, 37]. Nowadays, it is widely admitted that trap-states can limit the performance of PSCs as the source of losses by recombination. Moreover, it has been shown that trap states can also exist at the surface of the film (and not only at the GBs), due to a non-stoichiometric composition and defect sites [38–40]. Actually, the types of structural/chemical defects that act as carrier traps are far from being fully identified (see for instance [41] or [42]).

A last important point that we would like to stress relates to ion migration mechanisms. There is now overwhelming evidence that photo-induced (and electric-field induced) ion-migration can impact the optoelectronic properties of organic-inorganic halide perovskites [43]. Ion-defect migration is especially likely to be involved in the slow photoconductivity response and solar cell hysteresis phenomena [44]. Recent works revealed that a complex interplay can exist between the charge carrier populations, the traps, and mobile halides [45, 46]. It is important to bear in mind this particularity when analyzing the results of KPFM investigations on organic-inorganic halide perovskites.

11.1.3 Using KPFM for Local Investigations of Solution Processed Solar Cells

From what precedes, there is obviously a crucial need to use local probes to investigate the interplay between the sample morphology, the structural and chemical defects and the opto-electronic properties in organic and perovskite solar cells. For both PV technologies, it is also essential to characterize the energy level alignment at the device interfaces and the internal built-in electric field distribution. Last, local investigations of the photo-carrier dynamics are highly desirable to identify the source losses by recombination and to improve the device performances.

KPFM [47] is a method which provides a high spatial resolution for imaging surface potentials and charge distributions. Here, we just remind that the surface potential imaging is performed by minimizing the electrostatic force (in amplitude modulation KPFM, AM-KPFM) or its gradient (in frequency modulation KPFM, FM-KPFM) between the tip and the sample. This is done by applying an appropriate dc-voltage between the tip and the sample. This compensation bias yields a measurement of the work function difference (divided by the electronic charge) between a metallic tip and a metallic surface, the so-called contact potential difference (CPD). This CPD description in terms of work function difference is very popular but can become ambiguous when performing investigations on non-metallic samples. It is thus preferable to define the CPD as the difference between the vacuum levels at the tip and at the sample surface (here the vacuum level is defined as the energy of an electron at rest just outside the surface of the solid [48]). This last definition is especially relevant when discussing the results of KPFM in terms of band bending or band offsets effects because all surface electronic levels (including the sample vacuum level) follow the band bending (offsets) [48]. We also remind that proper polarities conventions (see for instance [49]) shall be used to define the CPD depending of the configuration of the experimental setup (compensation bias applied at the tip or at the sample). Further details about the fundamentals of KPFM and its operational modes can be found in review articles [50] or in Chap. 1 of this book.

Besides its ability to image permanent charge distributions, KPFM can be used to probe the photo-generated charge carriers by analyzing the surface potential shift under illumination, i.e. the surface photo-voltage [51]. In principle, the surface photo-voltage yields a local measurement of the electron-hole quasi Fermi levels splitting under illumination [52]. Very early on, it became clear that KPFM was well suited for local investigation of the permanent and photo-generated charge carriers in nanostructured and heterogeneous photovoltaic devices. The first proof of concept experiments on solution processed organic blends have been carried out a little more than a decade ago. When reading the following, the reader should bear in mind that our comprehension of the mechanisms behind the charge carrier generation and transport in BHJs has continuously evolved (sometimes considerably) in the past ten years. It is not our intent here to systematically re-visit the

results of earlier works in view of the most recent advances in the field of organic photovoltaics. Our purpose is rather to illustrate through selected examples what progresses have been achieved in using KPFM to investigate organic and perovskite solar cell materials and operating devices.

The remainder of this chapter is organized as follows. Section 11.2 will review KPFM investigations of the surface potential and surface photo-voltage in organic donor-acceptor blends and dyads (Sect. 11.2). The case of hybrid perovskites thin films will be discussed in Sect. 11.3. Section 11.4 will be devoted to KPFM investigations of cross sections from organic and perovskite solar cell devices. Last, Sect. 11.5 will introduce time-resolved measurements of the charge dynamics by KPFM under frequency modulated illumination.

11.2 KPFM Investigations of Donor-Acceptor Interfaces

Surface scientists began to investigate the opto-electronic properties of organic solar cells with KPFM a little more than a decade ago. At the beginning of the twenty-first century, a significant step in OPV performances was achieved by Shaheen and co-workers [53] who demonstrated that the conversion efficiency of cells based on MDMO-PPV/PCBM blends was dramatically affected by the nature of the donor-acceptor blend morphology. In short, the authors demonstrated that the blend morphology could be optimized by a proper choice of the casting solvent. A much finer phase segregation between the donor and acceptor components was obtained by using chlorobenzene instead of toluene, enabling at that time to achieve an almost threefold improvement in the solar cells power conversion efficiency (with respect to the former published values). The MDMO-PPV/PCBM tandem remained a material platform for basic research over several years [54]. In that frame, a first comprehensive KPFM work on MDMO-PPV/PCBM solar cells was published by Hoppe et al. in 2005 [55]. In this study, the authors took benefit of the ability to control the nanoscale morphology by changing the casting solvent. They combined nc-AFM with amplitude modulation-KPFM (under UHV) in dark and under selective illumination with cross-sectional scanning electron microscopy to characterize films casted from chlorobenzene and toluene. Consistently with earlier reports, they observed that the films cast from chlorobenzene display a much finer phase separation than the ones cast from toluene. The last samples featured mesoscopic PCBM clusters embedded in a polymer enriched matrix, which forms also a skin layer on the top of the PCBM clusters. Surface photo-voltages (SPV) of a few hundreds of mV were observed for both kinds of samples. From the analysis of the SPV contrasts detected over the mesoscopic PCBM clusters, the authors concluded that the skin layer around the PCBM clusters in toluene-cast samples hinders the electron transport toward the cathode electrode in operating devices.

A second report was published in 2005 by Chiesa and co-worker [56], who also used non-contact AFM/KPFM under UHV but to investigate another class of heterojunctions based on hole and electron-accepting polyfluorene polymers (more

precisely PFB for the electron donor and F8BT for the electron acceptor). Before considering the case of bulk heterojunctions, they performed preliminary KPFM investigations on planar PFB/F8BT bilayers. A logarithmic dependence of the surface potential as a function of the illumination intensity was observed, a behavior already reported for the open circuit voltage of operating devices based on PFB/F8BT bilayers (the SPV logarithmic dependency versus illumination intensity will be illustrated hereafter in the case of FG1:[70]PCBM blends, see Fig. 11.5j).

This last result was used by Chiesa et al. to establish the validity of using KPFM as a local probe of the photo-carrier generation in polymer solar cells. This may seem obvious, but actually the question of the relation between the surface photo-voltage and the open circuit voltage is not always so straightforward, as we will see later on. A second series of experiments was performed on PFB/F8BT blends displaying PFB-rich and F8BT-rich domains phase-separated at the micron-scale [56]. A third "interfacial" F8BT-rich phase was moreover identified in these samples. By correlating the morphology with the surface photo-voltage contrasts, the authors were able to propose a model for the blend morphology. The surface potential curves as a function of the illumination intensity displayed again a logarithmic dependency. Remarkably, different slopes were extracted from the curves acquired on domains of the PFB-rich, interfacial and F8BT-rich phases. In view of our current understanding of the carrier recombination dynamics in BHJs, this last result indicates that the relative weight of mono-molecular (trap-delayed) and bi-molecular non-geminate recombination varies significantly between the different phases. Last, long decays of the surface potential after switching off the light source were observed, revealing the existence of deep traps levels in the PFB-rich and F8BT-rich phases.

These two pioneering works [55, 56] demonstrated unambiguously that KPFM can probe the photo-induced charge generation mechanisms in organic solar cells, and they have been used as reference works and technical basis in many following studies. They also raised a number of questions especially with regards to the interpretation of the surface potential and surface photo-voltage contrasts on organic bulk heterojunction.

The first important question concerns the origin of contrasts in the surface potential images acquired without illumination (referred hereafter as "in-dark" SP images). In the original report by Chiesa et al., it was argued that in the absence of free charge carriers the energy bands should not be bent across the film thickness [56]. Alternatively, the authors proposed that permanently trapped charge carriers are responsible for the existence of in-dark electrostatic contrasts. Maturova and co-workers reopened the debate on the origin of the SP contrasts a few years later [57]. The authors investigated MDMO-PPV:PCBM blends processed to display large scale PCBM clusters embedded in a MDMO-PPV-rich matrix (this morphology is similar to the one described in the former report by Hoppe et al.). KPFM experiments were carried out in lift mode in combination with tapping-AFM in a glove box under N_2 atmosphere. Clear in-dark SP contrasts were observed over the PCBM aggregates (displaying a lower SP with respect to the surrounding MDMO-PPV matrix) for blends deposited on indium tin oxide (ITO) substrates

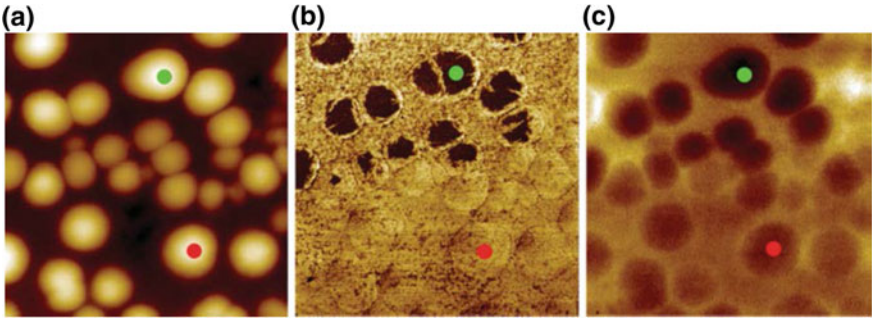

Fig. 11.3 Surface topography (left), phase contrast (middle) and KFPM surface potential (right) images (2 × 2 μm) of a MDMO-PPV:PCBM blend deposited on ITO/PEDOT:PSS. Mesosopic PCBM aggregates appear as elevations in the topographic image (vertical scale 150 nm). The phase contrast image reveals the existence of two kinds of PCBM clusters, covered or uncovered by a thin MDMO-PPV rich skin layer. All clusters appear as dark spots in the surface potential image (scale 0.1 V). This contrast originates from band bending (or energy level offset) effects at the substrate/organic interface (see Fig. 11.4a). Reproduced with permission from [57], "Scanning Kelvin Probe Microscopy on Bulk Heterojunction Polymer Blends" by K. Maturova, M. Kemerink, M. M. Wienk, D. S. H. Charrier, R. A. J. Janssen, Adv. Funct. Mater. 2009, **19**, 1379–1386. Copyright Wiley-VCH Verlag GmbH & Co. KGaA

coated with PEDOT:PSS (Fig. 11.3). This last material is a hole-transporting chemically doped polymer, which is very widely used by the OPV community to realize bulk-heterojunction solar cells in standard configuration. It smoothens the surface of ITO, and fixes the work function of the anode allowing a proper extraction of holes. In turn, much weaker SP contrasts were observed for blends displaying the same morphology, but casted on ZnO-coated and Al_2O_3-coated ITO substrates. This last result led the authors to conclude that the "in-dark" SP contrasts observed for the samples cast on PEDOT:PSS/ITO substrates (Fig. 11.3) effectively took their origin from band bending effects [57]. More precisely, they invoked the existence of an effective charge transfer between the PEDOT:PSS and the MDMO-PPV matrix, resulting in a positive shift of its surface potential with respect to the one of the PCBM clusters (Fig. 11.4a).

At this stage it is necessary to step back and consider what meaning is (or shall be) given to the concept of band bending. This notion is well established in inorganic semiconductor physics and is often introduced by considering the interface between a metal and a n-doped (or p-doped) semiconductor. The Fermi level equalization is realized at these interfaces by a charge transfer, resulting in the formation of a carrier depleted zone extending to a certain distance into the semiconductor. In that zone, dopant impurities create a net charge density and an internal electric field, the corresponding electrical potential bending therefore the energy bands in the depletion region. Strictly speaking, band bending should not occur in organic semiconductors. Firstly, π-conjugated polymers and molecules do not display a real band structure but rather localized electronic states (here we do not consider the case of organic single crystals). As stressed by Ishii et al. [58], it

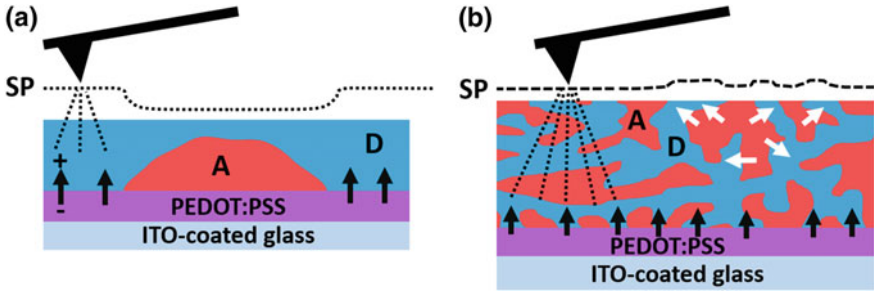

Fig. 11.4 **a** Schematic illustration showing how energy level offsets at the organic blend/substrate interface can account for the existence of surface potential contrasts in samples displaying large-scale phase separated domains. Here, we assume that charge transfer occurs from the donor (or donor-rich, D) phase to the PEDOT:PSS. This results in the formation of an interface dipole (dark arrows) oriented upward. Due to the long range nature of the electrostatic forces, this dipole gives rise to a positive surface potential contrast over the donor-rich phase. As a consequence, the acceptor (or acceptor-rich) clusters appear as dark spots (see Fig. 11.3) in the potentiometric image. The same reasoning applies if the charge transfer process results in the formation of a space charge area. **b** In the case of nano-phase segregated blends, recessed dipoles (dark arrows) at the organic/substrate interface shall not be detected by KPFM due to convolution effects. Local surface potential contrasts are more likely to take their origin from permanent charges localized at the donor-acceptor interfaces. They can originate from band bending or from interfacial molecular dipoles (symbolized by white arrows)

would therefore be preferable to describe a variation of the molecular energy levels (if any) as a function of the distance from the interface in terms of energy level bending. Secondly, in their pristine state π-conjugated materials are non-doped and the concentration of thermally excited carriers should be very low, in that case the analogy with doped organic semiconductors becomes meaningless. However, nowadays it is definitely established that charge transfer can occur across metal/organic interfaces. The real question is more about the nature of the physical and chemical mechanisms behind the charge transfer, and about the spatial extension of the space charge area.

First, band bending like behavior (i.e. a shift of the molecular energy levels as a function of the distance to the organic/metal interface) can occur if the organic layer is lightly doped [58]. That doping can be due to residual impurities left from the synthesis process, or can be induced by partial oxidation of the organic film if processed under ambient conditions. In that frame, Bisquert and Garcia-Belmonte proposed that D-A blends may be globally treated as a p-doped semiconductor [59], leading to the formation of a hole depletion zone at the vicinity of the cathode contact.

Besides, it has been shown that energy level alignment and Fermi level pinning can occur at organic/metal interfaces even in the absence of dopants. The integer charge transfer (ICT) and induced density of states models (IDIS) have been especially developed to account for the physics of interfaces formed between organic molecules and metals featuring no hybridization (for the ICT model) or

weak hybridization (for the IDIS model) of their electronic states [60]. In the ICT model, an integer amount of charge tunnels from or into well-defined charge states (basically polaron states) on the π-conjugated material. In turn, partial charges can be transferred in the case of weakly hybridized interfaces due to the mixing of the metal and organic SC orbitals. In both cases, the charge transfer is restricted to π-conjugated molecules (or polymer chains) residing in the close vicinity of the metal/organic interface [60]. Thus, one expects the formation of an interface dipole but there should be no space charge area. However, new electrostatic models have been recently developed that predict in some cases the development of extended band-bending regions within the organic semiconductor [61].

Returning to the discussion of the in-dark surface potentials, it is clear that charge transfer and Fermi level pinning at the organic/substrate interface can reasonably account for the contrasts observed over D-A blends displaying large-scale phase separated domains. Whatever the underlying mechanism, the charge transfer will differ as a function of the nature of the material in contact with the bottom electrode, resulting in the appearance of SP contrasts at the mesoscopic scale (Fig. 11.4a). However, since the substrate/organic interface is recessed well below the surface it is in practice impossible to conclude if the band alignment results in the formation of dipoles or in the existence of a spatially extended space charge area. Further complexity is added by the fact that charge transfer and band bending can also occur at donor-acceptor interfaces [60]. Interfacial dipoles at the donor-acceptor interface can also originate from mutual polarization effects between the interacting molecules [62]. In principle, all these effects can simultaneously contribute to the formation of a complex micro-electrostatic landscape giving rise to the formation of "in-dark" SP contrasts both at the mesoscopic and nanometer scale. In our opinion, SP contrasts at the local scale are more likely to take their origin in energy level alignment or polarization effects at the donor-acceptor interfaces (Fig. 11.4b). By local scale, we mean something smaller than the film thickness, which is on the order of a few tens of nanometers to one hundred nanometers in optimized bulk heterojunction thin films. We justify this assumption as follows. Permanent charges localized at the vicinity of the organic/substrate interface can give rise to SP contrasts thanks to the long range nature of the electrostatic forces. In turn, recessed charged domains with a lateral extension smaller than the film thickness shall not (in principle) be detected in SP images due to convolutions effects.

In that frame, we note that some teams tentatively used the in-dark KPFM contrasts to identify the donor and acceptor sub-networks at the surface of bulk heterojunction thin films. For instance, Wessendorf et al. applied this strategy [63] to analyze the scale of the phase segregation in blends of PCBM and oligomers processed with and without solvent vapor annealing. In this work mesoscopic structures were observed in the contact potential difference images, but the authors concluded that they were too large to originate from pure donor and acceptor phases. The observed SP contrasts were instead attributed to PCBM-enriched and oligomer-enriched domains, but no conclusion was drawn about the physical origin of the permanent charges.

To investigate furthermore the "in-dark" potential contrasts in relation with the nanoscale morphology, it might be useful to combine KPFM with phase imaging (in amplitude modulation AFM) or damping imaging (in frequency modulation imaging). The phase and the damping signals are related the energy dissipated in the tip-surface interaction. Thus, both phase and damping imaging can be used to perform a compositional mapping at the surface of soft materials [64]. Comparing the dissipation and the KPFM images should allow to better specify if the SP contrasts originate from interface dipoles (or space charge areas) at the vicinity of the substrate, or from the electrostatics of the top layers of the blends.

Whatever the experimental strategy, resolving the exact morphology of nano-phase segregated donor and acceptor networks in optimized samples (i.e. with a phase segregation at the ten nanometer scale) remains a real challenge. For that reason, many groups limited their investigations to case studies on model systems featuring very large-scale donor and/or acceptor domains [65], which are non-relevant for true photovoltaic applications. Here, we remind that high power conversion efficiencies can in principle only be achieved if the donor and acceptor networks are segregated at the scale of a few tens nanometers. Besides, as above-mentioned, more complex blend morphologies involve inter-mixed phases where donor and acceptor components are mixed at the sub-10 nm scale. In order to address the physics of energy level alignment and photo-carrier generation at the relevant scales, it is essential to develop high resolution topographic, compositional, and potentiometric AFM modes.

In 2010, we demonstrated that surface potential contrasts could be resolved on optimized P3HT:PCBM blends with a sub-10 nm resolution by using non-contact AFM combined with AM-KPFM under UHV [66]. In these experiments, a clear chemical contrast between the donor and acceptor sub-networks was also achieved by dissipation imaging. More recently, we investigated another kind of photovoltaic blends [49] based on [70]PCBM and on an oligothiophene-fluorenone oligomer named FG1 (Fig. 11.5a). We took benefit of the liquid crystalline properties of this molecule to create model samples for KPFM investigations, featuring nanometer-sized [70]PCBM clusters buried in the sub-surface of a matrix of self-assembled pi-stacked donor molecular wires (Fig. 11.5b). This time the KPFM experiments were carried out in frequency modulation mode, and a sub-10 nm lateral resolution was achieved both for in-dark surface potential and surface photo-voltage imaging (SPV). The SPV images were calculated as the difference between the compensation bias images recorded under selective illumination and in dark (Fig. 11.5e, g, h). When calculating such SPV images, it is crucial to quantify what is the lateral misalignment between the images used for the SPV calculation. This can be done by performing a cross-sectional or cross-correlation analysis between the topographic or dissipation channels acquired simultaneously with the SP data, as shown by Fig. 11.5i. Beyond the validation of sub-10 nm resolved SP and SPV imaging by FM-KPFM, these investigations also confirmed that the local in-dark contrast originate from an uneven distribution of permanent charges at the donor-acceptor interfaces [49]. The experimental data were furthermore compared with the results of electrostatic simulations, showing that the SP contrasts may be

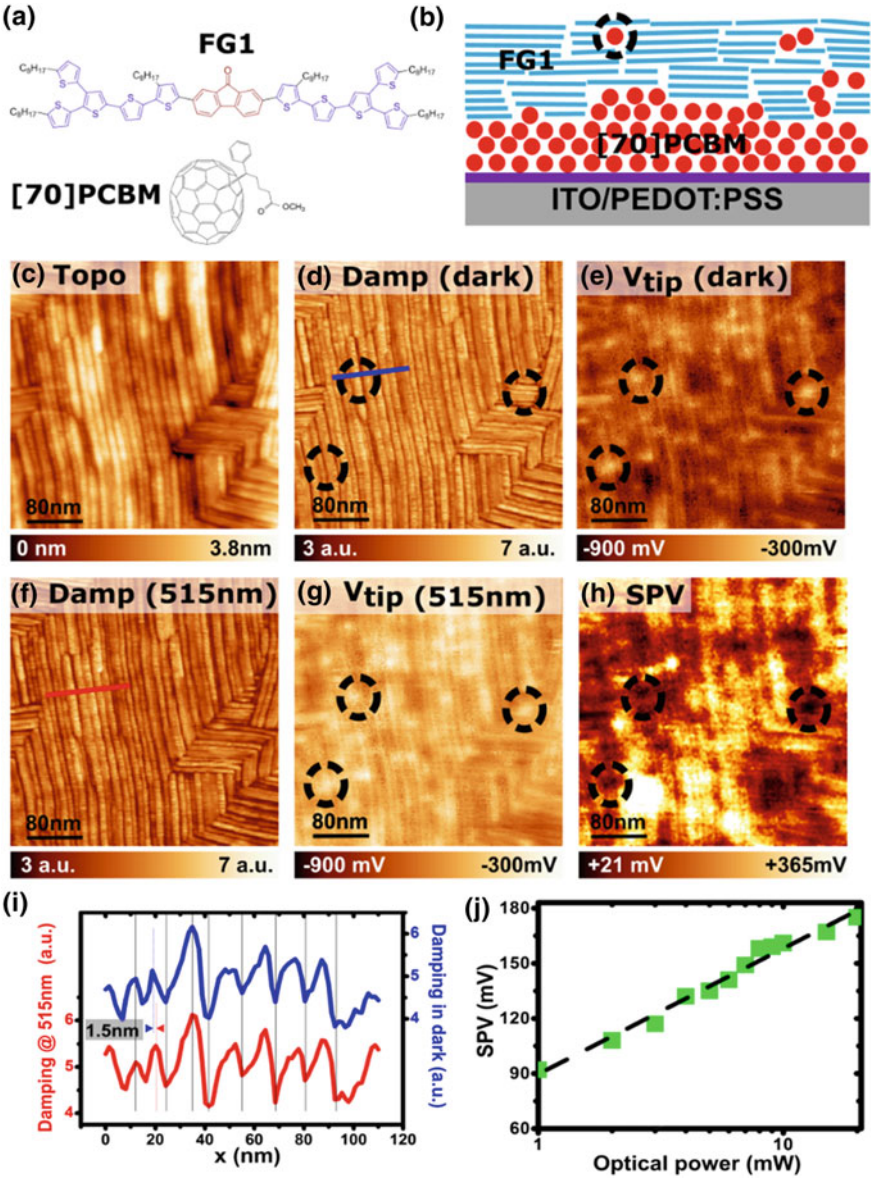
(a)
FG1
[70]PCBM
(b)
FG1
[70]PCBM
ITO/PEDOT:PSS
(c) Topo
80nm
0 nm
3.8nm
(d) Damp (dark)
80nm
3 a.u.
7 a.u.
(e) Vtip (dark)
80nm
-900 mV
-300mV
(f) Damp (515nm)
80nm
3 a.u.
7 a.u.
(g) Vtip (515nm)
80nm
-900 mV
-300mV
(h) SPV
80nm
+21 mV
+365mV
(i)
Damping @ 515nm (a.u.)
Damping in dark (a.u.)
1.5nm
x (nm)
(j)
SPV (mV)
Optical power (mW)

Fig. 11.5 **a** Chemical structures of FG1 (electron donor) and [70]PCBM (electron acceptor) molecules. **b** Model proposed for the morphology of the donor-rich phase (see [49]) of FG1:[70]PCBM blends after annealing. In the FG1-rich phase nanometer-sized [70]PCBM clusters are buried in the subsurface of a matrix of self-assembled π-stacked FG1 molecular wires (one of these clusters is highlighted by a black-dotted circle). Most of the fullerene derivatives are buried deeper in the bulk with a concentration increase toward the ITO/PEDOT:PSS electrode. **c–g** High-resolution (400 × 400 nm^2) topographic (**c**), damping (**d**, **f**), and KPFM potential (**e**, **g**) images recorded above a "FG1-rich" area in the dark (**c–e**) and under illumination at 515 nm (**f**, **g**). **h** Surface photo-voltage (SPV) image calculated as the difference between images (**e**) and (**g**). Black-dotted circles in (**d**, **e**, **g**) and **h** highlight subsurface [70]PCBM aggregates. The surface is uniformly covered by a capping layer of FG1, and most of the [70]PCBM is recessed at the ITO/PEDOT:PSS interface: as a consequence, the mean surface photo-voltage is positive, and subsurface [70]PCBM clusters appear as local minima in SPV images. **i** Damping profiles extracted simultaneously using multiple profiling analysis from **(d)** and **(f)**. The comparison between the damping profiles in dark and under illumination shows that the lateral misalignment is at maximum of 1.5 nm. **j** Dependence of the surface photo-voltage (mean value over an FG1-rich area) as a function of the illumination intensity at 515 nm in logarithmic scale. The slope of the SPV as a function of the natural logarithm of the intensity is equal to ca. $1.15k_BT/e$. This indicates that the recombination is mainly bimolecular [11]. Adapted and reprinted with permission from [49], "High-Resolution Kelvin Probe Force Microscopy Imaging of Interface Dipoles and Photogenerated Charges in Organic Donor–Acceptor Photovoltaic Blends", by F. Fuchs, F. Caffy, R. Demadrille, T. Mélin, B. Grévin, ACS Nano **10**, 739–746 (2016). Copyright 2016 American Chemical Society

accounted by considering the existence of effective dipoles. However, it was not possible to conclude whether the effective dipoles are related to the intrinsic molecular polarization, or if they originate from a charge transfer process at the donor-acceptor interfaces. Resolving the details of the electrostatic landscape at the molecular scale on BHJs remains unfortunately beyond the resolution limits of beam-deflection KPFM at room temperature.

Interpreting properly the SPV data on BHJ blends is another crucial issue. In principle, the surface photo-voltage may be expected to yield a local measurement of electron and holes quasi-Fermi levels splitting across the donor-acceptor interfaces, but is it real? First, it may be interesting to check the validity of this assumption in the case of planar donor-acceptor interfaces. This has been done by Ellison and co-workers, who investigated planar interfaces based on thermally evaporated C_{60}/donor interfaces deposited on indium tin oxide (ITO) substrates [67]. Their results revealed that the surface photo-voltage calculated by subtracting the in-dark SP from the one recorded under illumination does not probe the full value of the quasi-Fermi level splitting. This is simply due to the energy level alignment and Fermi level pinning at the substrate/donor interface, which results in a shift of the in-dark surface potential measured over the bilayer with respect to the one measured over the ITO. As a consequence, the surface photo-voltage yields an underestimated value of the quasi Fermi level splitting. A correct value can be obtained by subtracting the surface potential measured over the bare substrate from the one measured over the bilayer heterojunction under illumination as shown in Fig. 11.6. This situation will be at play whenever the local vacuum level is shifted by the energy level alignment at the organic/substrate interface. This should be the

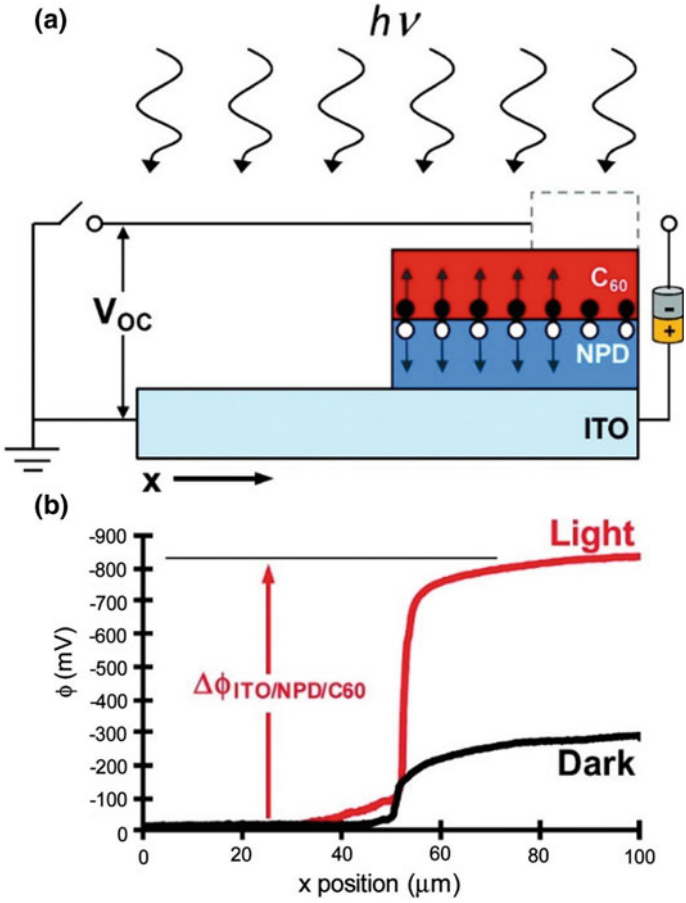

Fig. 11.6 **a** Schematic illustration of a planar donor-acceptor interface realized by sequential evaporation of NPD (electron donor) and C_{60} (electron acceptor) molecules on ITO. **b** Surface potential line scans of the bilayer device in the dark (black curve) and under illumination (red curve). The full open circuit voltage is calculated as the difference between the surface potential measured over the bare ITO substrate and the surface potential measured over the bilayer under illumination. Reprinted with permission from [67], "Determination of Quasi-Fermi Levels across Illuminated Organic Donor/Acceptor Heterojunctions by Kelvin Probe Force Microscopy" by F. D. J. Ellison, J. Y. Kim, D. M. Stevens, C. D. Frisbie, J. Am. Chem. Soc. **133**, 13802–13805 (2011). Copyright 2011 American Chemical Society

case for a large fraction of bulk heterojunctions thin films. Besides, in the case of nano-phase segregated blends convolution effects are highly likely to reduce the magnitude of the SPV.

Fortunately, however, it has been shown that despite these effects the SPV remains directly related to the open circuit voltage. In particular, Shao et al. carried out a comparison between the V_{OC} deduced from conventional electrical

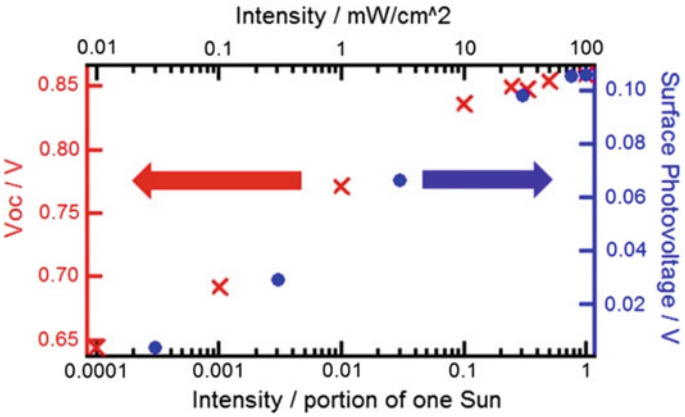

Fig. 11.7 Comparison between the open circuit voltage values measured as a function of the illumination intensity on operational solar cell devices based on PCDTBT:$PC_{71}BM$ heterojunctions, and the surface photo-voltage values deduced from KPFM measurements on the same organic blend without the top metallic electrode. Reprinted with permission from [68], "Intensity-Modulated Scanning Kelvin Probe Microscopy for Probing Recombination in Organic Photovoltaics" by G. Shao, M. S. Glaz, F. Ma, H. Ju, D. S. Ginger, ACS Nano **8**, 10799–10807 (2014). Copyright 2014 American Chemical Society

characterization (on complete devices) and the SPV probed by KPFM (on the bare surface) of optimized PCDTBT:$PC_{71}BM$ heterojunctions [68]. Their data (Fig. 11.7) show that the surface photo-voltage is almost ten times smaller than the V_{OC} for a given illumination intensity. However, both parameters display nearly identical functional forms when plotted as a function of the illumination intensity.

Thus, while there can be no absolute measurement of the V_{OC} on BHJs, the SPV remains related to the electron-hole quasi Fermi levels splitting. As a consequence, the local SPV contrasts and their dependency as the function of the illumination intensity [56] are highly likely to take their origin from variations of the carrier trapping and recombination dynamics at the local scale (this point will be further discussed in the section devoted to time-resolved SPV measurements). In addition, many other valuable information can be deduced from the analysis of the SPV data. For instance, the global polarity of the SPV can indicate the existence of an unfavorable compositional gradient (as demonstrated in the case of FG1:[70]PCBM blends, see Fig. 11.5) of the acceptor (or donor depending on the configuration of the solar cell) within the bulk or at the surface of the film.

Despite all the progress achieved, it may remain challenging to perform a clear identification of the donor and acceptor phases in blends displaying complex morphologies at the nanoscale. In that frame, we recently proposed to use self-assembled acceptor-donor dyads (A-D) as model nanostructured heterojunctions for local KPFM investigations [69]. The experiments were performed on samples consisting in A-D block co-oligomers deposited as thin films on ITO/PEDOT:PSS substrates. In these samples, the molecular self-assembly results in the

formation of lamellar A-D structures where the co-oligomers are oriented in an edge-on configuration. Surface photo-voltage contrasts were successfully resolved at the scale of the lattice constant of the supramolecular network. This was achieved by applying a post data acquisition correction procedure, allowing to reduce the lateral misalignment between the set of images used to calculate the SPV to a few nanometers. However, achieving a direct visualization of the donor and acceptor sub-units in the SPV images remained beyond the limits of resolution of the experiment. This underscores the necessity to develop new KPFM-based techniques, allowing to directly measure the surface potential difference between illuminated and dark states.

11.3 KPFM Investigations of Hybrid Perovskite Thin Films

The first KPFM investigations of solution-processed perovskite-based solar cells have been carried out a few years ago only. Since a great majority of solution-processed perovskite thin films display a high density of grain boundaries at the micron or sub-micron scales, earlier KPFM works were naturally aimed at investigating the impact of grain boundaries on the photo-carrier transport. Several studies were motivated by the assumption that these structural defects may be beneficial to the PSCs performance (similarly to the case of CIGS or CdTe solar cells), due to the existence of built-in potentials at the GBs facilitating a selective carrier extraction and suppressing electron-hole recombination.

Several reports concluded on the existence of a downward band bending at the GBs (Fig. 11.8), resulting in a positive surface potential contrast in the in-dark KPFM images [70–73]. However, it remains difficult to draw definitive conclusion about the impact of the GBs on the photo-carrier transport and dynamics. In $CH_3NH_3PbI_3$ films, Yun et al. observed that the GBs display an enhanced SPV compared to the grain interior [74], and that this SPV contrast became more prominent when increasing the light intensity. Thus, they concluded that the photo-generated carriers are more effectively separated at the GBs. In turn, Li et al. reported that the surface potential difference between the grains interior and GBs in $CH_3NH_3PbI_3$ films was unchanged under illumination [72]. Moreover, they observed reduced photo-voltages over GBs for solvent-annealed films. Thus, despite the existence of a built in potential they concluded that GBs mostly act as recombination centers (at least in solvent-annealed $CH_3NH_3PbI_3$ films).

The uncertainty about the nature of the charge carrier transport and recombination mechanisms at the GBs stems also from the contributions of the ionic species to the surface potential contrasts. To investigate the ionic electrostatics, an interesting approach [75, 76] consists in using the AFM tip to apply a pre-conditioning bias voltage to the sample during a first scan. A second pass can be performed with an active KPFM compensation bias loop to monitor the changes induced by the

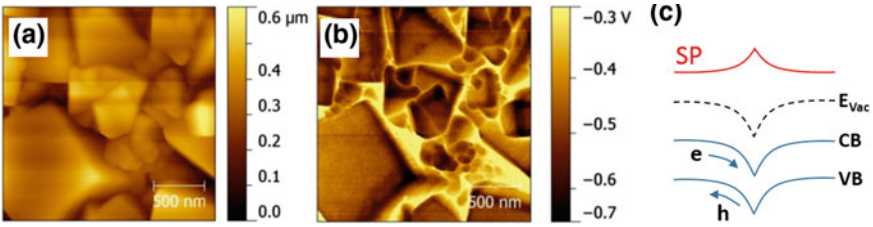

Fig. 11.8 Topography (**a**) and surface potential (**b**) images of a $CH_3NH_3PbI_3$ thin film deposited on compact TiO_2. **c** Schematic illustration of a downward band bending at the grain boundary, resulting in a positive shift of the surface potential probed by KPFM. The built-in potential at the GB may facilitate a selective carrier extraction and suppress electron-hole recombination. Panels (**a**) and (**b**) adapted and reprinted with permission from [70], "Interfacial Study to Suppress Charge Carrier Recombination for High Efficiency Perovskite Solar Cells" by N. Adhikari, A. Dubey, D. Khatiwada, A. F. Mitul, Q. Wang, S. Venkatesan, A. Iefanova, J. Zai, X. Qian, M. Kumar, Q. Qiao, ACS Appl. Mater. Interfaces **7**, 26445–26454 (2015). Copyright 2015 American Chemical Society

ion-migration on the surface potential. In this way, Yun et al. investigated the effect of ion-migration [75] in mixed-cation lead iodine perovskite thin films. Amongst the observed effects, their measurements revealed that ion-migration can induce an inversion of the surface potential contrast over the GBs. These experiments also revealed that several minutes were needed to achieve a complete reversibility of the surface potential after removing the polarization bias, implying long ionic migration time constants.

Very recently, Garrett and co-workers applied heterodyne KPFM [77] to investigate further the ion-dynamics under illumination in $CH_3NH_3PbI_3$ solar cells [78]. This newly developed extension of KPFM allows recording several surface potential maps per minute [79], which enables investigating dynamical processes occurring at the time scale of a few seconds. Their measurements revealed that after illumination, the surface potential evolves slowly and returns to an equilibrium state only after several minutes (Fig. 11.9). This behavior was attributed to ion-migration mechanisms within the perovskite film [78]. We point out that in principle, these slow potential dynamics shall not be interpreted in terms of surface photo-voltage (or local open circuit voltage) transients, because they do not reflect the dynamics of photo-carriers but the ones of ionic species. Besides, we note that it may be difficult to exclude the cumulative contribution of slow carrier de-trapping to the surface potential dynamics. Disentangling the contributions of permanent charges, photo-carriers, and ionic species to the surface potential remains a major challenge for forthcoming KPFM studies.

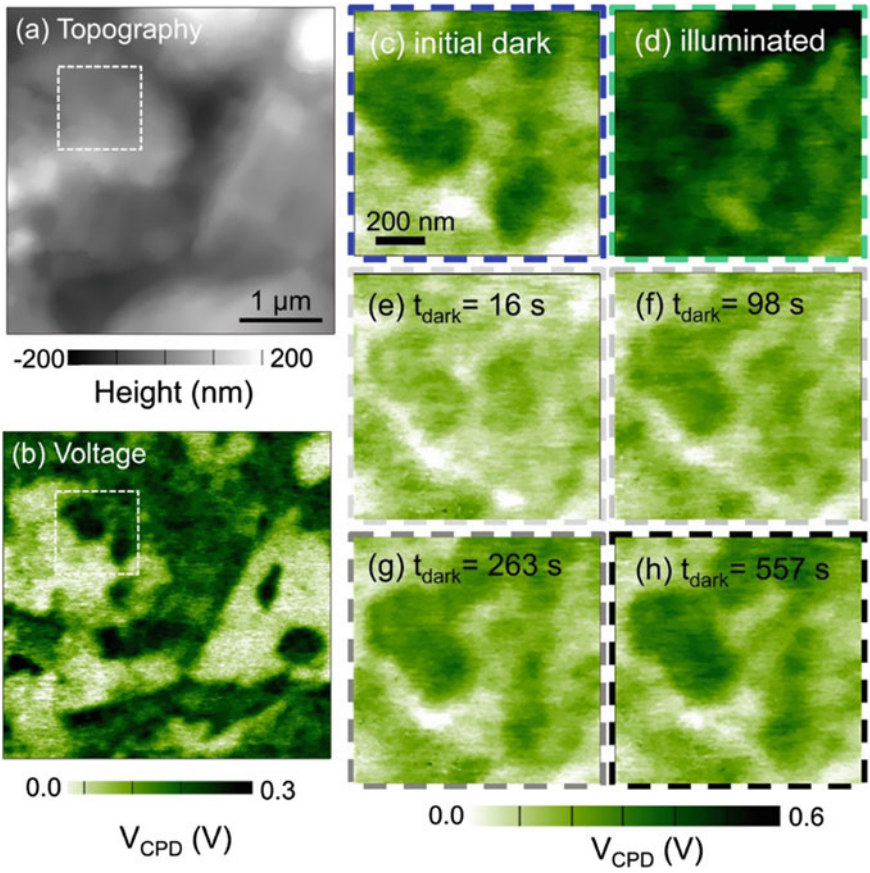

Fig. 11.9 Heterodyne KPFM investigations of thin films realized by sequential spin-coating deposition of a perovskite layer ($CH_3NH_3PbI_3$) and a PCBM layer (substrate: ITO-coated glass covered by an interfacial PEDOT:PSS layer). **a** Topography and **b** dark surface potential. **c**–**h** Sequence of fast-KPFM measurements performed on the area delimited by the white dashed square in (**a**) and (**b**). **c** Dark surface potential. **d** Surface potential under illumination. **e**–**h** Surface potential measured in dark as a function of time. Reprinted with permission from [78], "Real-Time Nanoscale Open-Circuit Voltage Dynamics of Perovskite Solar Cells" by L. Garrett, E. M. Tennyson, M. Hu, J. Huang, J. N. Munday, M. S. Leite, Nano Lett. **17,** 2554–2560 (2017). Copyright 2017 American Chemical Society

11.4 Cross-Sectional KPFM Investigations

As we saw in the previous sections, KPFM surface potential imaging presents some limitations, notably with regards to the analysis of the energy level alignment and band bending at the recessed interfaces. Another issue concerns the discrepancy between the surface photo-voltage values probed by KPFM on the bare photoactive layers, and the open circuit voltages measured on operating devices with

top-metallic electrodes. These issues can be overcome by recording cross sectional KPFM profiles on transversal sections of operating devices. Cross sectional KPFM allows mapping the internal electric field distribution within the device which is intrinsically related to the band alignment and the presence of space charge regions at the interfaces and within the active layer. The existence (or absence) of homogeneous or heterogeneous internal electric fields is indeed known to dramatically impact the carrier collection processes both in organic and hybrid-perovskite solar cells, by varying the relative weight of the carrier drift and diffusion mechanisms. It is moreover possible to carry out investigations under external biasing. The quality of the electrical contacts can then be clarified by measuring the voltage drops at the interfaces between the photo-active layer and the device electrodes. Operando investigations under illumination can also be performed, allowing a straightforward comparison between the KPFM surface photo-voltage data and the open circuit voltage values measured by conventional electrical characterization methods. Last, we note that convolutions effects (especially in amplitude modulation KPFM) shall be treated with a great care, for they can dramatically limit the lateral and energy resolution of cross sectional potentiometric profiles.

The first cross sectional investigations by KPFM of bulk-heterojunction solar cells (Fig. 11.10) were reported by Lee et al. in 2011 [80]. The authors investigated P3HT:PCBM blends deposited on indium tin oxide (ITO) functionalized with PEDOT:PSS (acting as the hole transporting material at the anode side) and

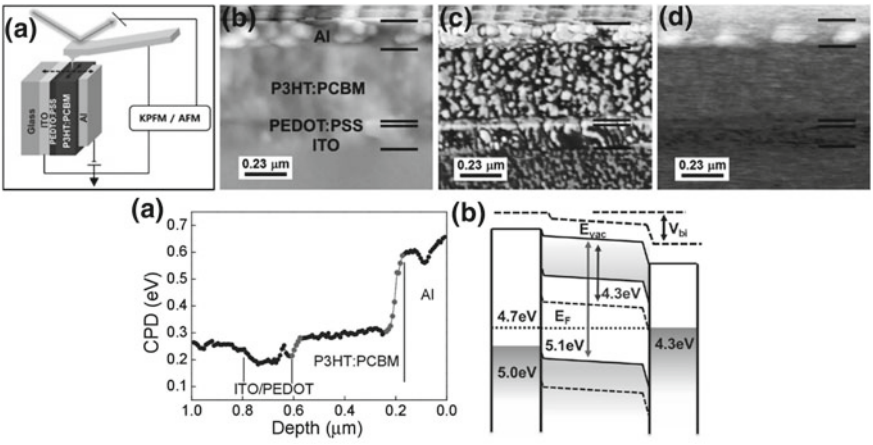

Fig. 11.10 Cross sectional AFM/KPFM investigations of a P3HT:PCBM bulk heterojunction solar cell. Top panels (from left to right): schematic illustration of the experiment, topographic image, phase contrast image, and CPD image. Bottom panels: cross-sectional profile of the CPD acquired in short circuit conditions and device energy band diagram (V_{bi}: internal built in potential). Reprinted from [80], "Direct observation of internal potential distributions in a bulk heterojunction solar cell" by J. Lee, J. Kong, H. Kim, S.-O. Kang, K. Lee, Appl. Phys. Lett. 99, 243301 (2011), with the permission of AIP Publishing. Copyright 2011 American Institute of Physics

top-coated with an aluminum layer (cathode electrode). The cross sectional potentiometric profiles recorded by FM-KPFM in dark under short circuit conditions revealed that the internal electric field was in majority confined at the cathode interface, while the bulk BHJ was found to be nearly field-free. In a subsequent study, the same group applied FM-KPFM to analyze the potential profiles under forward and reverse external bias in P3HT:$PC_{70}BM$ BHJ solar cells [81]. In these devices TiO_x was used as an electron transporting layer between the photoactive BHJ film and the aluminum top cathode. Again, a large fraction of the potential drops was observed to be confined at the cathode interface. It is noteworthy that a very good lateral resolution in potentiometric profiling was demonstrated thanks to the use of frequency-modulation KPFM (FM-KPFM). This allowed to determine accurately the extension of the space charge area at the TiO_x/blend interface. The bulk of the active layer was found to be nearly field free even for a bias voltage corresponding to the maximum power point of the operating device. Based on these results, the authors concluded that the free photo-generated charge carriers were mainly transported by diffusion in the nearly field-free bulk regions of the active layer.

Another comprehensive work was carried out in 2013 by Saive and co-workers, who investigated both the in-dark potentials (including measurements under external bias) and the surface photo-voltages in standard and inverted P3HT:PCBM solar cells [82]. Standard devices were prepared by depositing the blends on ITO substrates coated with PEDOT:PSS, and by using thermally evaporated LiF/Al as the top cathode. Inverted devices consisted in blends deposited on PEIE-coated ITO (bottom cathode), with a top anode made of MoO_3/Al. In the case of the standard devices, the authors noticed that the CPD difference between the BHJ and the ITO substrate was not consistent with the results of the former work by Lee and co-workers [80]. Here, we stress that morphological variations between the blends may have been invoked to account for the observed differences. In particular, the energy level alignment at the PEDOT:PSS anode (and the subsequent hole injection barrier) may strongly depend on the local concentration of the donor and acceptor in the adjacent BHJ (this also holds for electron injection barrier at the cathode). The nature of the vertical phase separation and the existence of favorable (or unfavorable) concentration gradients of the donor and acceptor have been the subject of many reports and are still investigated [83, 84].

In their work, Saive et al. used the potentiometric profiles acquired in short circuit as baselines that were subsequently subtracted from the data recorded under illumination or external bias (Fig. 11.11). This contact potential difference compensation procedure originally introduced by Bürgi et al. to investigate organic field effect transistors [85] yields potentiometric profiles containing only the effects of the photo-voltage or of the applied bias. In this way, it was shown that the applied voltage drops mostly at the interface between each contact and the BHJ in standard cells, whereas the drop occurs along the bulk of the BHJ in inverted devices. Here again, the existence of vertical concentration gradients of the donor and acceptor species is likely to account for the observed differences. Many reports demonstrated that P3HT and PCBM species can present favorable concentration gradients at the

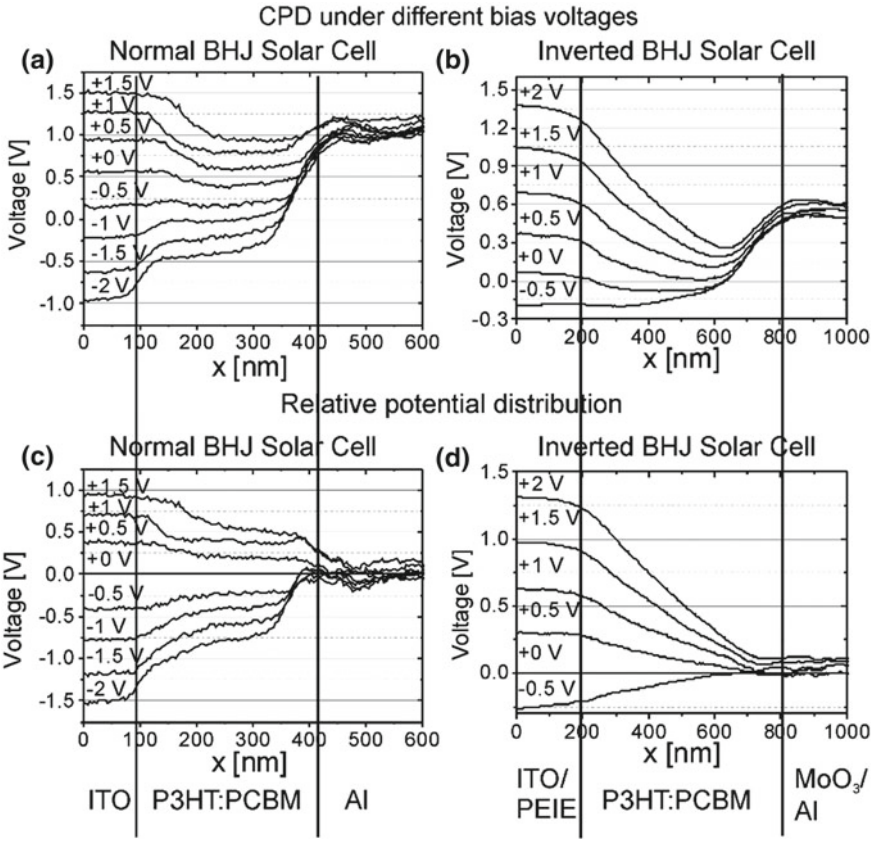

Fig. 11.11 CPD cross-sectional profiles under external voltage biasing of **a** a P3HT:PCBM BHJ solar cell in standard configuration and **b** a P3HT:PCBM BHJ solar cell in inverted configuration. **c**, **d** Potential distributions calculated by subtracting the baseline recorded in short circuit from the data acquired under bias. Reproduced with permission from [82], "Imaging the Electric Potential within Organic Solar Cells" by R. Saive, M. Scherer, C. Mueller, D. Daume, J. Schinke, M. Kroeger, W. Kowalsky, Adv. Funct. Mater. 2013, **23,** 5854–5860. Copyright Wiley-VCH Verlag GmbH & Co. KGaA

top-anode and bottom-cathode interfaces in inverted devices. However, as noted by the authors, the nanoscale morphology was not spatially resolved in these KPFM experiments. Generally, the lateral resolution of cross sectional data acquired on BHJs does not match the best performances achieved in AFM/KPFM surface imaging. Moreover, as mentioned earlier, achieving a clear identification of the donor and acceptor networks remains a difficult task in the case of nano-phase segregated bulk-heterojunctions, whatever the sample configuration (i.e. cross sectional or planar).

The same methodology was applied by Saive et al. to perform comparative investigations of P3HT:PCBM cells displaying regular diode and s-shape

current-voltage characteristics [86]. In that case it was shown that the s-shape behavior was caused by a poor electrical contact at the BHJ/cathode interface. Once again, this work demonstrated that it is crucial to apply a proper CPD-compensation to analyze properly the voltage drops under bias at the contacts.

Obviously, the quality of the sample surface is a key determinant of high resolution cross sectional scanning probe microscopy imaging. The pros and cons of focus ion beam (FIB) milling, cleavage and microtome cutting for sample preparation were compared by Scherer et al. [87]. The authors concluded that FIB milling is the most reliable technique to prepare smooth surfaces, allowing therefore to perform cross sectional KPFM measurements with higher lateral and energy resolutions.

Another work on BHJ has been recently published by Chen and co-workers [88]. The authors used amplitude modulation KPFM to characterize FIB-milled P3HT:PCBM and P3HT:ICBA solar cells. Since their measurements suffered from a poor lateral resolution due to convolution effects (which are an intrinsic limitation of AM-KPFM), the authors proposed a so-called bias voltage-compensation method to perform a true quantitative measurement of the built-in voltage (V_{bi}) and open circuit voltage (V_{OC}). Basically, their approach consists in applying an external bias V_{ext} such that both the anode and cathode match the same CPD yielding $V_{ext} = V_{bi}$, or such that the floating electrode potential under bias is equal to its potential under illumination yielding $V_{ext} = V_{OC}$. However, contrary to what is stated in their report, this method does not provide a true deconvolution of the cross sectional profiles from the convolution effects. As demonstrated in the earlier work of Kong et al., a much better lateral resolution can be simply achieved by carrying out the KPFM potentiometric profiling in the frequency-modulation mode (FM-KPFM).

All these studies on BHJs demonstrated that whatever the technical difficulties, cross sectional KPFM can be fruitfully applied to map the internal potential and photo-potential distributions in solution processed solar cells. Doubtlessly, this motivated the realization of similar experiments on hybrid-perovskites based devices. Two reports were almost simultaneously published in 2014 on devices realized with $CH_3NH_3PbI_{3-x}Cl_x$ [89] or $CH_3NH_3PbI_3$ [90] as the absorber, and TiO_2 and Spiro-OMeTAD as the electron and hole transporting materials at the collection electrodes, respectively. In-dark cross sections recorded on $CH_3NH_3PbI_{3-x}Cl_x$ layers [89] deposited on compact TiO_2 revealed the existence of a non-uniform electrical field within the perovskite film, which was interpreted by the authors in terms of carrier depletion zone (extending approximately half of the absorber thickness) in the frame of a p-n heterojunction model. Nevertheless, this effect was not reproduced in the experiments of Bergmann et al., who observed a homogeneous electric field distribution [90] through the whole thickness of $CH_3NH_3PbI_3$ films deposited on mesoporous TiO_2 (this last result being consistent with a p-i-n type solar cell). In this work [90], potential profiles were also recorded under illumination under short circuit conditions (Fig. 11.12). Positive CPD shifts within the active layer under illumination were interpreted as a consequence of unbalanced electron-hole transport in the device. Trapped charges inside the perovskite and TiO_2

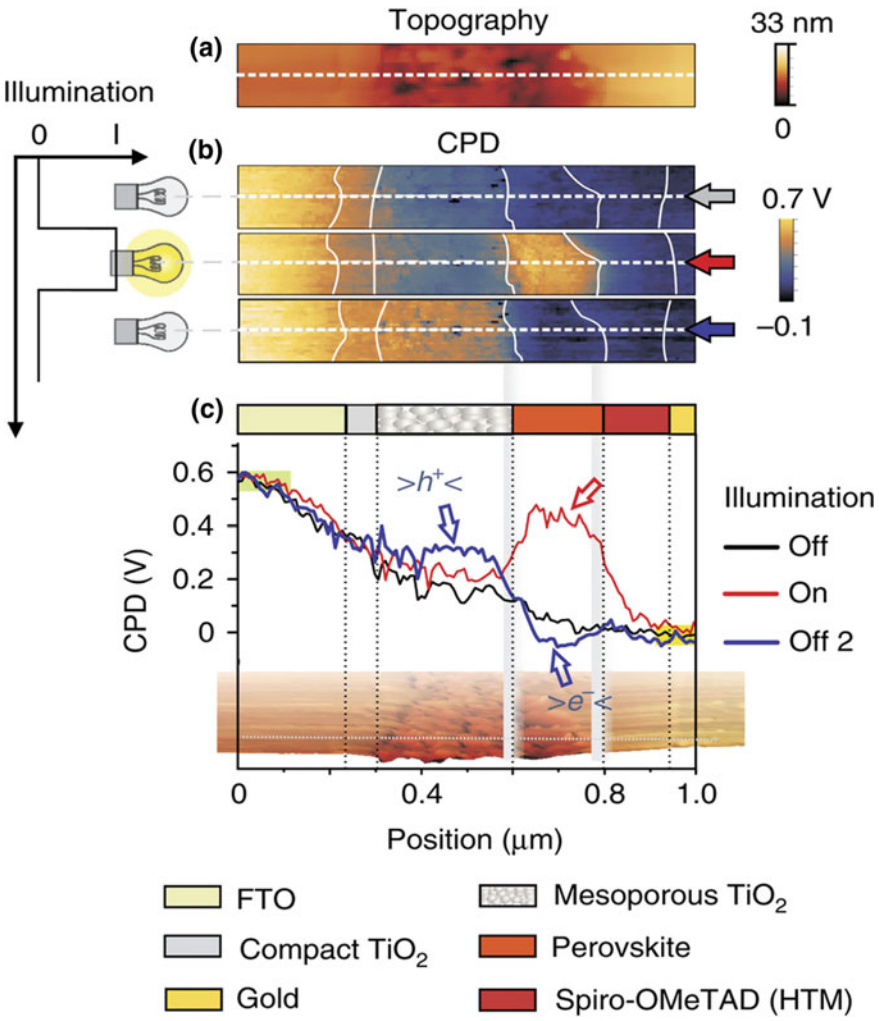

Fig. 11.12 Cross sectional KPFM investigations of a perovskite solar cell. **a** AFM topographic image **b** CPD maps recorded in short circuit before illumination, under illumination and after turning the illumination off. **c** Line profiles extracted from the CPD maps. The increase in potential after turning on the illumination reveals an accumulation of holes inside the perovskite layer. The comparison between the initial dark profile and the one recorded after switching off the illumination reveals the existence of trapped holes and electrons inside the mesoporous TiO_2 and the perovskite film, respectively. Reproduced with permission (CC BY license) from [90], "Real-space observation of unbalanced charge distribution inside a perovskite-sensitized solar cell" by V. W. Bergmann, S. A. L. Weber, F. J. Ramos, M. K. Nazeeruddin, M. Grätzel, D. Li, A. L. Domanski, I. Lieberwirth, S. Ahmad, R. Berger, Nat. Commun **5**, 5001 (2014). Copyright 2014 Macmillan Publishers Limited

layers were also revealed by recording potentiometric profiles immediately after light illumination (Fig. 11.12).

A subsequent work on planar methylammonium lead tri-iodide (MAPI) perovskite solar cells was published by Bergmann et al. in 2016 [91]. In this study, cross sectional photo-potential profiles were extracted by subtracting the in dark profiles acquired with both electrodes grounded from the profiles recorded under illumination leaving one electrode floating (Fig. 11.13). An excellent agreement was observed between the open circuit voltage measured by conventional electrical characterization and the surface photo-potential between the ITO and Ag electrodes, demonstrating the absence of significant cross-talk or convolution effects in FM-KPFM. The most remarkable feature of this work lies in the realization of time-dependent measurements in cross sectional configuration. Firstly, this was done by recording series of photo-potential profiles under illumination at different time intervals, after switching the device configuration from short-circuit to open circuit conditions. These measurements revealed a time-dependent accumulation of positive charges at the TiO_2/MAPI interface at the scale of a few seconds (Fig. 11.13). The potential time-evolution was also investigated while switching the device from open-circuit conditions under illumination to short-circuit conditions in the dark, revealing this time an accumulation of negative charges in the MAPI layer at the vicinity of the anode and cathode contacts. These results were interpreted in terms of ion-migration and charge trapping effects, contributing both to current-voltage hysteresis and device preconditioning effects in these solar cells.

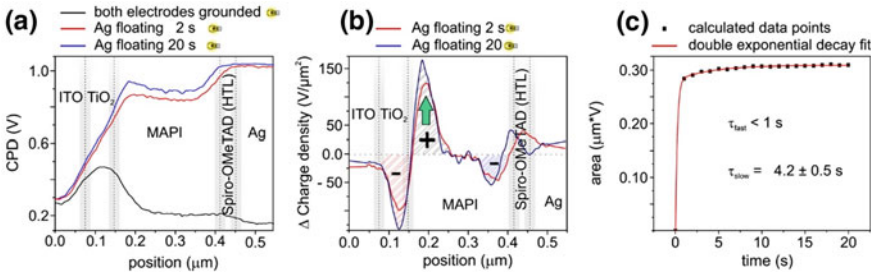

Fig. 11.13 Time-dependent cross sectional KPFM investigations of a perovskite solar cell. **a** CPD profiles acquired under illumination with both electrodes grounded, and as a function of time after leaving the Ag hole-collecting electrode floating. Time-dependent photo-potential profiles (not shown here) can be calculated by subtracting the in dark profile from the ones recorded under illumination. **b** Charge density profiles numerically derived from the photo-potential profiles. **c** Time evolution of the integrated area of the potentiometric profiles. The slower time constant can be attributed to the formation of a surface dipole or the migration of positive ions toward the TiO_2/MAPI interface. Reprinted with permission from [91], "Local Time-Dependent Charging in a Perovskite Solar Cell" by V. W. Bergmann, Y. Guo, H. Tanaka, I. M. Hermes, D. Li, A. Klasen, S. A. Bretschneider, E. Nakamura, R. Berger, S. A. L. Weber, ACS Appl. Mater. Interfaces **8**, 19402–19409 (2016). Copyright 2016 American Chemical Society

11.5 Time-Resolved Surface Photo-Voltage Measurements

With surface photo-voltage imaging, one performs a kind of local mapping of the open circuit voltage, i.e. the splitting of electron and holes quasi Fermi levels across D-A interfaces in organic solar cells. Basically, V_{OC} is related to the energy gap between the LUMO of the acceptor and the HOMO of the donor. However, many other parameters can impact the V_{OC} such as the electrode work functions, the illumination intensity, the charge carrier mobility and the charge carrier recombination rate. In particular, the recombination dynamics have been shown to be a key determinant of the V_{OC}. Therefore, it is highly likely that some of the contrasts observed in the SPV images acquired on BHJ take their origin from variations of the carrier dynamics at the local scale. However, it is impossible to disentangle the contributions of energetics (i.e. variations of the donor-acceptor gap) and of charge carrier dynamics to the SPV contrasts solely on the basis of data acquired under continuous wave illumination.

In this section, we explain how this issue can be (at least to some extent) addressed by performing KPFM experiments under frequency-modulated illumination (referred to as intensity-modulated KPFM hereafter). More precisely, we show that intensity-modulated KPFM can be used to map local non-geminate recombination rates in BHJs.

The basic principle of these dynamical measurements consists in monitoring the dependence of the average surface potential probed by KPFM as a function of the modulation frequency of an illumination source. Intensity-modulated KPFM operating principle can be described as follow. Under illumination a charged state builds-up and if the pulse duration is long enough the photo-potential reaches an equilibrium value equaling the one measured under continuous wave illumination. When the illumination source is switched off, the photo-potential decays with a functional form that depends on the underlying recombination processes. The KPFM bias compensation loop yields an averaged value of the instantaneous potential, with typical integration time constants in the range of a few tens of ms to hundreds of ms. In the regime where the pulse duration is much longer than the charge build-up time (case of an "instantaneous" photo-charging), the average potential will continuously increase with the modulation frequency to saturate at its maximum (equilibrium) value when the time between pulses is much shorter than the photo-potential time decay (Fig. 11.14). By analyzing the dependency of the average potential as a function of the modulation frequency, it is possible to extract decay time constants giving access to the photo-carrier lifetime.

This technique has been initially introduced by Takihara and co-workers [92] to probe the local minority carrier lifetime in polycrystalline silicon solar cells, and it was applied a few years later by Borowik et al. and Shao et al. to investigate silicon nanocrystal solar cells [93] and donor-acceptor blends [68], respectively. In all these reports, the dynamical measurements were performed in "point mode", i.e. the curves of the surface potential as a function of the illumination modulation frequency were only recorded at selected locations on the surface.

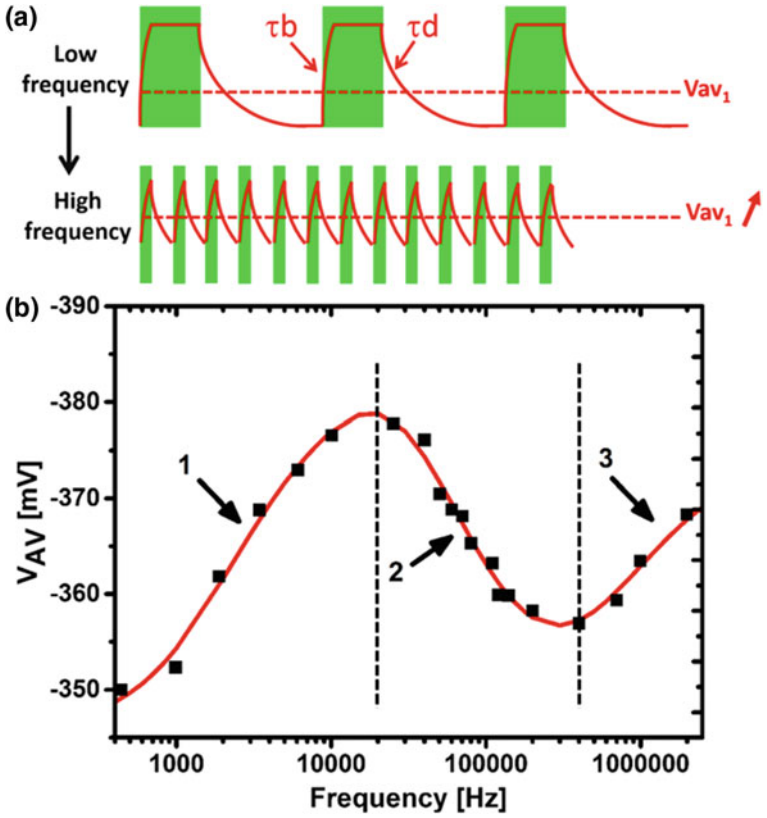

Fig. 11.14 **a** Scheme of the KPFM surface potential time-response under frequency modulated illumination. The KPFM compensation bias yields a time-integrated average value V_{av} of the instantaneous surface potential. The photo-potential decay dynamics (time constant τd) determine the average signal frequency-evolution. The average potential increases with frequency and is expected to saturate when the time interval between the light pulses becomes much smaller than the decay time constant. Actually, the experimental data indicate that multiple decay and build up dynamics determine the average signal frequency-evolution. **b** Spectroscopic curve of the average potential as a function of the illumination modulation frequency (515 nm, 10% duty, 3.8 mW/mm^2) acquired on a nano-phase segregated PDBS-TQx/$PC_{71}BM$ blend. The photo-voltage (with a negative polarity) displays a non-monotonic evolution with respect to the frequency, revealing the existence of several phenomena occurring at different time scales. The SPV increases (in absolute value) when raising the frequency from 400 Hz to ca. 20 kHz (frequency domain labeled 1), this effect can be accounted by using a first decay time constant. When pushing further the frequency, the SPV does not saturate but decreases (frequency domain 2). This behavior is attributed to the effect of a non- instantaneous SPV build up during the light pulse. Last, the SPV increases again for frequencies above ca. 300 kHz, revealing the existence of an additional contribution to the photo-voltage characterized by faster decay dynamics. Panel (**b**) adapted and reproduced with permission (ACS AuthorChoice License) from [94], "Photo-Carrier Multi-Dynamical Imaging at the Nanometer Scale in Organic and Inorganic Solar Cells", P. A. Fernández Garrillo, Ł. Borowik, F. Caffy, R. Demadrille, B. Grévin, ACS Appl. Mater. Interfaces **8**, 31460–31468 (2016). Copyright 2016 American Chemical Society

In organic PCDTBT/$PC_{71}BM$ bulk heterojunctions, millisecond scale surface photo-voltage decays were observed by Shao et al. in quantitative agreement with the kinetics measured at the macroscopic scale by using a conventional transient photo-voltage (TPV) setup [68]. Here, we stress that it is in practice highly challenging (almost impossible in some cases) to operate illumination-modulated KPFM in a true non-perturbative regime. Conventional TPV measurements are indeed performed by fixing the average carrier density with a continuous wave illumination source. Then, a small optical perturbation is applied in such a way that the voltage transient is less than a few percent of the open circuit voltage average. In the case of KPFM experiments carried out on bare BHJ blends, the surface photo-voltage measured under continuous wave illumination is reduced compared to the open circuit voltage of the full solar cell device with a top metallic electrode. With photo-voltages of a few tens of mV, it is almost impossible to operate KPFM under frequency-modulated illumination in a real non-perturbative regime. For future works on BHJ samples, it would be therefore preferable to compare the results of intensity-modulated KPFM measurements with the ones of macroscopic large perturbation transient photo-voltage (LPTV) experiments.

Another major technical issue is related to the acquisition time of spectroscopic curves of the KPFM potential over a broad frequency range. Achieving a proper signal to noise ratio may imply acquisition times of a few tens of seconds. Then, it becomes highly desirable to operate the frequency-spectroscopy in close loop mode without interrupting the z-regulation. This is what is done when KPFM measurements are performed in single-pass mode in combination with beam-deflection non-contact AFM (nc-AFM) under ultra-high vacuum. This approach has been recently used by our research teams [94] to record spectroscopic curves on a 2D grid (with acquisition times of a few tens of hours for the matrix of curves). Then, by fitting the full set of curves it becomes possible to recalculate 2D images of the photo-voltage dynamical time constants.

We recently applied this spectroscopic imaging (Fig. 11.15) to investigate a series of PDBS-TQx/$PC_{71}BM$ [95] blends. These experiments demonstrated the ability to map 2D images of the surface photo-voltage dynamics with a sub-10 nm resolution [94]. Furthermore, by pushing the illumination modulation frequency at higher frequencies than the ones previously used by Shao et al. [68], these experiments revealed that multiple phenomena occurring at different time scales can contribute to the average potential measured under modulated illumination (Fig. 11.14b). Non-monotonic dependencies of the average potential as a function of the illumination modulation frequency were indeed observed (Fig. 11.14b). They were tentatively attributed to the combined effects of non-instantaneous charge build-ups, and of multiple decays originating from different recombination mechanisms. A dual set of dynamical parameters was used to adjust the spectroscopic curves, characterized by different decay and build-up time constants (see [94] for more details). We attributed short decays (in the range of a few microseconds to a few tens of microseconds) to non-geminate recombination processes of free carriers, and long decays (a few hundreds of microseconds) to trap-delayed recombination processes (Fig. 11.15). The short and long decay time constants display indeed

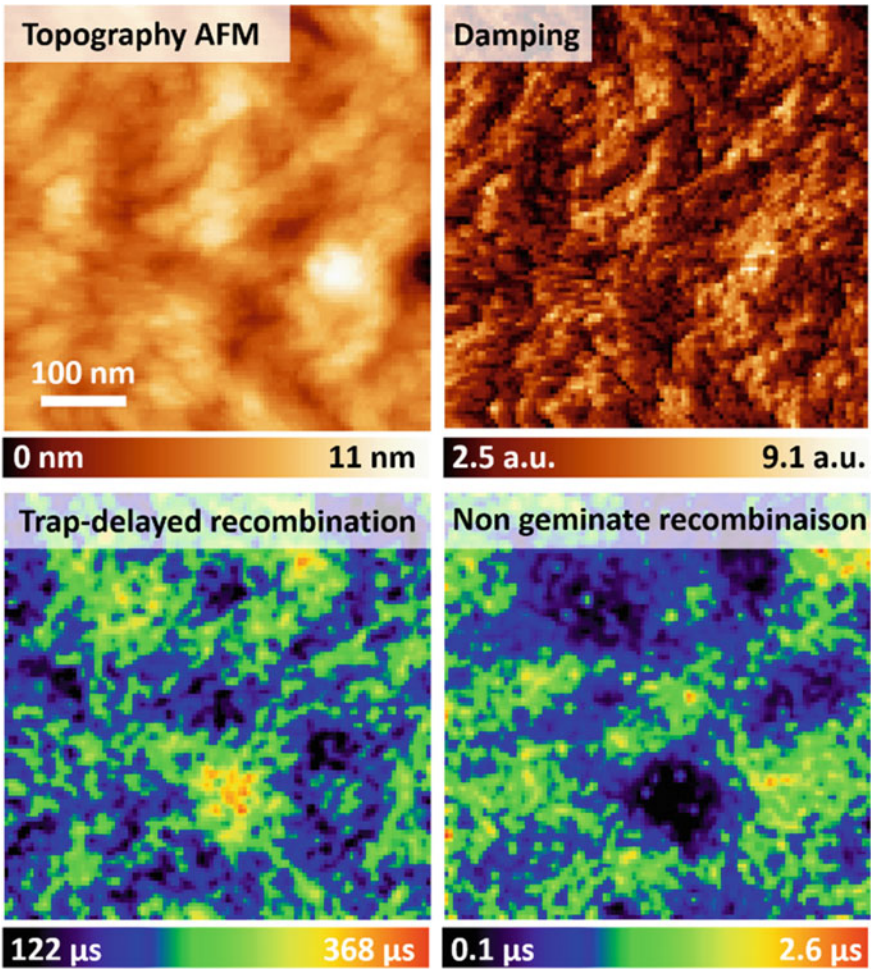

Fig. 11.15 Time resolved surface photo-voltage imaging of a nanophase segregated PDBS-TQx/$PC_{71}BM$ donor-acceptor blend. nc-AFM/KPFM topographic, damping and surface photo-voltage decay time constants images acquired in 2D spectroscopic mode under frequency-modulated illumination (515 nm, 10% duty, 3.8 mW/mm^2). Two decay time constants have been used to fit the curves of the photo-potential as a function of the frequency modulation of the illumination source. The longer has been attributed to trap-delayed recombination processes, and the shorter to non-geminate recombination of free carriers. Reprinted with permission (ACS AuthorChoice License) from [94], "Photo-Carrier Multi-Dynamical Imaging at the Nanometer Scale in Organic and Inorganic Solar Cells", P. A. Fernández Garrillo, Ł. Borowik, F. Caffy, R. Demadrille, B. Grévin, ACS Appl. Mater. Interfaces **8**, 31460–31468 (2016). Copyright 2016 American Chemical Society

different dependencies as a function of the illumination intensity. The latter was found to be nearly intensity-independent, while the former displayed a strong reduction when increasing the optical fluence (which is consistent with a carrier-concentration dependent bimolecular process).

In order to get a deeper understanding of how the intensity-modulated KPFM data shall be interpreted, it may be mandatory to investigate other kinds of bulk heterojunctions. The exact nature of the defects at the origin of the carrier trapping in PDBS-TQx/$PC_{71}BM$ blends remains indeed unclear [94]. In this respect, it could be interesting to investigate BHJs in which trapping (and recombination) centers can be added in a controlled manner. For instance, [6,6]-phenyl-C_{84}-butyric acid methyl ester (PCBM-84) has been shown to function as electron trap in PCDTBT: $PC_{60}BM$ blends [96].

Last, an open question concerns the possible influence of changes in capacitance gradients on the measured average KPFM signal under modulated illumination. In a recent work, Schumacher et al. demonstrated that the KPFM output under pulsed illumination is not only sensitive to changes in the contact potential difference but also to changes in the capacitance gradient [97]. This motivated their development of an alternative measurement technique of the surface photo-voltage, based on a gated-integration of the frequency shift synchronized with the pulsed illumination. This time-domain KPFM (TD KPFM) allows an instantaneous acquisition of the surface photo-voltage, however, its capability in terms of 2D SPV dynamical imaging of solar cell materials remains to be demonstrated. Anyhow, it is now clearly important to quantify the contributions of capacitive gradients to the averaged potential measured by KPFM on solution processed solar cells under modulated illumination. In the future, this will be done by monitoring simultaneously the dependency of the compensation bias and of the second harmonic KPFM channel (giving access to the capacitive signal) as a function of the illumination modulation frequency. This will allow applying a correction procedure by weighting the different time-domains of the function used to fit the compensation potential curves with constants calculated from the second harmonic data.

11.6 Summary and Outlook

The focus of this chapter was to present the applications of KPFM for investigations of the local micro-electrostatics in relation with charge transfer and energy alignment processes, carrier photo-generation mechanisms, and electronic transport in organic and perovskite solution-processed solar cells.

By reviewing the literature, it was shown that many valuable information on the phase morphology, phase composition, and opto-electronic properties of organic donor acceptor blends can be deduced from the surface potential and surface photo-voltage images. It is now clear that both band bending at the organic-substrate and permanent charges at the donor-acceptor interfaces can give rise to the formation of in-dark surface potential (SP) contrasts. Equally clearly, the

surface photo-voltage (SPV) is related to the open circuit voltage, i.e. the electron-hole quasi Fermi level splitting across the donor-acceptor interfaces. A sub-10 nm resolution can be achieved in SP and SPV imaging, however, it remains challenging to perform a clear identification of the donor and acceptor phases in blends displaying complex morphologies (such as intermixed phases) at the nanoscale. KPFM investigations demonstrated unambiguously the existence of local built in potentials at the grain boundaries in hybrid perovskite thin films. Nevertheless, the beneficial or detrimental impact of GBs on the carrier recombination remains difficult to establish on the sole basis of KPFM images acquired in steady state conditions. This stems from the concomitant contributions of ionic species and permanent charges to the micro-electrostatic landscape. Recent reports tend to demonstrate that specific experimental protocols (including sample pre-conditioning under illumination or bias stress) or advanced time-resolved modes may be mandatory to disentangle the ion contributions from the ones of the permanent and photo-generated charges to the SP and SPV contrasts.

Through this review, we have also shown that cross sectional KPFM can successfully be used to investigate the internal electric field and photo-potential distributions within the active layers of organic and perovskite solar cells.

Last, we have shown that KPFM under frequency-modulated illumination can be used to map two dimensional images of the photo-potential decays, paving the way for local investigations of the recombination processes. We anticipate that time-resolved KPFM measurements will become increasingly important to characterize the sources of carrier losses in solution-processed solar cells. We also foresee that significant progresses will be achieved by combining the capabilities of time-resolved surface photo-voltage imaging with the advantages offered by KPFM operations in cross-sectional configuration.

References

1. Y. Liu, J. Zhao, Z. Li, C. Mu, W. Ma, H. Hu, K. Jiang, H. Lin, H. Ade, H. Yan, Nat. Commun. **5**, 5293 (2014)
2. Z. He, B. Xiao, F. Liu, H. Wu, Y. Yang, S. Xiao, C. Wang, T.P. Russell, Y. Cao, Nat. Photonics **9**, 174 (2015)
3. J. Zhao, Y. Li, G. Yang, K. Jiang, H. Lin, H. Ade, W. Ma, H. Yan, Nat. Energy **1**, 15027 (2016)
4. W. Zhao, D. Qian, S. Zhang, S. Li, O. Inganäs, F. Gao, J. Hou, Adv. Mater. **28**, 4734 (2016)
5. R.A. Janssen, J. Nelson, Adv. Mater. **25**, 1847 (2013)
6. A.J. Heeger, Adv. Mater. **26**, 10 (2014)
7. Z. He, C. Zhong, S. Su, M. Xu, H. Wu, Y. Cao, Nat. Photonics **6**, 591 (2012)
8. L.-M. Chen, Z. Xu, Z. Hong, Y. Yang, J. Mater. Chem. **20**, 2575 (2010)
9. T.-H. Lai, S.-W. Tsang, J.R. Manders, S. Chen, F. So, Mater. Today **16**, 424 (2013)
10. G. Yu, J. Gao, J.C. Hummelen, F. Wudl, A.J. Heeger, Science **270**, 1789 (1995)
11. S.R. Cowan, A. Roy, A.J. Heeger, Phys. Rev. B **82**, 245207 (2010)
12. C.G. Shuttle, R. Hamilton, J. Nelson, B.C. O'Regan, J.R. Durrant, Adv. Funct. Mater. **20**, 698 (2010)

13. S.R. Cowan, N. Banerji, W.L. Leong, A.J. Heeger, Adv. Funct. Mater. **22**, 1116 (2012)
14. T. Kirchartz, B.E. Pieters, J. Kirkpatrick, U. Rau, J. Nelson, Phys. Rev. B. **83**, 115209 (2011)
15. K.S. Nalwa, H.K. Kodali, B. Ganapathysubramanian, S. Chaudhary, Appl. Phys. Lett. **99**, 263301 (2011)
16. S. Venkatesan, J. Chen, E.C. Ngo, A. Dubey, D. Khatiwada, C. Zhang, Q. Qiao, Nano Energy **12**, 457 (2015)
17. F. Sheridan, J.M. Frost, J. Nelson, Phys. Chem. Chem. Phys. **17**, 2311 (2015)
18. R.A. Street, Adv. Mater. **28**, 3814 (2016)
19. G. D'Avino, S. Mothy, L. Muccioli, C. Zannoni, L. Wang, J. Cornil, D. Beljonne, F. Castet, J. Phys. Chem. C **117**, 12981 (2013)
20. N. Banerji, Chimia **70**, 512 (2016)
21. E. Buchaca-Domingo, A.J. Ferguson, F.C. Jamieson, T. McCarthy-Ward, S. Shoaee, J.R. Tumbleston, O.G. Reid, L. Yu, M.-B. Madec, M. Pfannmöller, F. Hermerschmidt, R.R. Schröder, S.E. Watkins, N. Kopidakis, G. Portale, A. Amassian, M. Heeney, H. Ade, G. Rumbles, J.R. Durrant, N. Stingelin, Mater. Horiz. **1**, 270 (2014)
22. T.M. Burke, M.D. McGehee, Adv. Mater. **26**, 1923 (2014)
23. J. Razzell-Hollis, S. Limbu, J.-S. Kim, J. Phys. Chem. C **120**, 10806 (2016)
24. M. Causa, J. De Jonghe-Risse, M. Scarongella, J.C. Brauer, E. Buchaca-Domingo, J.-E. Moser, N. Stingelin, N. Banerji, Nat. Commun. **7**, 12556 (2016)
25. M. Scarongella, J. De Jonghe-Risse, E. Buchaca-Domingo, M. Causa, Z. Fei, M. Heeney, J.-E. Moser, N. Stingelin, N. Banerji, J. Am. Chem. Soc. **137**, 2908 (2015)
26. C. Wehrenfennig, G.E. Eperon, M.B. Johnston, H.J. Snaith, L.M. Herz, Adv. Mater. **26**, 1584 (2014)
27. S.D. Stranks, G.E. Eperon, G. Grancini, C. Menelaou, M.J.P. Alcocer, T. Leijtens, L.M. Herz, A. Petrozza, H.J. Snaith, Science **342**, 341 (2013)
28. X. Li, D. Bi, C. Yi, J.-D. Décoppet, J. Luo, S.M. Zakeeruddin, A. Hagfeldt, M. Grätzel, Science **353**, 58 (2016)
29. A. Kojima, K. Teshima, Y. Shirai, T. Miyasaka, J. Am. Chem. Soc. **131**, 6050 (2009)
30. M.M. Lee, J. Teuscher, T. Miyasaka, T.N. Murakami, H.J. Snaith, Science **338**, 643 (2012)
31. D. Liu, T.L. Kelly, Nat. Photonics **8**, 133 (2014)
32. W. Nie, H. Tsai, R. Asadpour, J. Blancon, A.J. Neukirch, G. Gupta, J.J. Crochet, M. Chhowalla, S. Tretiak, M.A. Alam, H.L. Wang, A.D. Mohite, Science **347**, 522 (2015)
33. H. Nagaoka, F. Ma, D.W. deQuilettes, S.M. Vorpahl, M.S. Glaz, A.E. Colbert, M.E. Ziffer, D. S. Ginger, J. Phys. Chem. Lett. **6**, 669 (2015)
34. E. Edri, S. Kirmayer, S. Mukopadhyay, K. Gartsman, G. Hodes, D. Cahen, Nat. Commun. **5**, 3461 (2014)
35. G. Yang, C. Wang, H. Lei, X. Zheng, P. Qin, L. Xiong, X. Zhao, Y. Yan, G. Fang, J. Mater. Chem. A **5**, 1658 (2017)
36. P. Schulz, L.L. Whittaker-Brooks, B.A. MacLeod, D.C. Olson, Y.-L. Loo, A. Kahn, Adv. Mater. Int. **2**, 1400532 (2015)
37. D.W. de Quilettes, S.M. Vorpahl, S.D. Stranks, H. Nagaoka, G.E. Eperon, M.E. Ziffer, H.J. Snaith, D.S. Ginger, Science **348**, 683 (2015)
38. A. Abate, M. Saliba, D.J. Hollman, S.D. Stranks, K. Wojciechowski, R. Avolio, G. Grancini, A. Petrozza, H.J. Snaith, Nano Lett. **14**, 3247 (2014)
39. Y. Shao, Z. Xiao, C. Bi, Y. Yuan, J. Huang, Nat. Commun. **5**, 5784 (2014)
40. D.W. deQuilettes, S. Koch, S. Burke, R.K. Paranji, A.J. Shropshire, M.E. Ziffer, D.S. Ginger, ACS Energy Lett. **1**, 438 (2016)
41. D. Kiermasch, P. Rieder, K. Tvingstedt, A. Baumann, V. Dyakonov, Sci. Rep. **6**, 39333 (2016)
42. H. Uratani, K. Yamashita, J. Phys. Chem. Lett. **8**, 742 (2017)
43. R. Gottesman, A. Zaban, Acc. Chem. Res. **49**, 320 (2016)
44. J.M. Azpiroz, E. Mosconi, J. Bisquert, F.D. Angelis, Energy Environ. Sci. **8**, 2118 (2015)
45. S. van Reenen, M. Kemerink, H.J. Snaith, J. Phys. Chem. Lett. **6**, 3808 (2015)

46. D.W. deQuilettes, W. Zhang, V.M. Burlakov, D.J. Graham, T. Leijtens, A. Osherov, V. Bulović, H.J. Snaith, D.S. Ginger, S.D. Stranks, Nat. Commun. **7**, 11683 (2016)
47. M. Nonnenmacher, M.P. O'Boyle, H.K. Wickramasinghe, Appl. Phys. Lett. **58**, 2921 (1991)
48. D. Cahen, A. Kahn, Adv. Mater. **15**, 271 (2003)
49. F. Fuchs, F. Caffy, R. Demadrille, T. Mélin, B. Grévin, ACS Nano **10**, 739 (2016)
50. W. Melitz, J. Shen, A.C. Kummel, S. Lee, Surf. Sci. Rep. **66**, 1 (2011)
51. L. Kronik, Y. Shapira, Surf. Sci. Rep. **37**, 1 (1999)
52. D.K. Schroder, Meas. Sci. Technol. **12**, R16 (2001)
53. S.E. Shaheen, C.J. Brabec, N.S. Sariciftci, F. Padinger, T. Fromherz, J. Hummelen, Appl. Phys. Lett. **78**, 841 (2001)
54. C.J. Brabec, S. Gowrisanker, J.J.M. Halls, D. Laird, S. Jia, S.P. Williams, Adv. Mater. **22**, 3839 (2010)
55. H. Hoppe, T. Glatzel, M. Niggemann, A. Hinsch, MCh. Lux-Steiner, N.S. Sariciftci, Nano Lett. **5**, 269 (2005)
56. M. Chiesa, L. Bürgi, J.-S. Kim, R. Shikler, R.H. Friend, H. Sirringhaus, Nano Lett. **5**, 559 (2005)
57. K. Maturova, M. Kemerink, M.M. Wienk, D.S.H. Charrier, R.A.J. Janssen, Adv. Funct. Mater. **19**, 1379 (2009)
58. H. Ishii, N. Hayashi, E. Ito, Y. Washizu, K. Sugi, Y. Kimura, M. Niwano, Y. Ouchi, K. Seki, Phys. Status Solidi (A) **201**, 1075 (2004)
59. J. Bisquert, G. Garcia-Belmonte, J. Phys. Chem. Lett. **2**, 1950 (2011)
60. S. Braun, W.R. Salaneck, M. Fahlman, Adv. Mater. **21**, 1450 (2009)
61. M. Oehzelt, N. Koch, G. Heimel, Nat. Commun. **5**, 4174 (2014)
62. M. Linares, D. Beljonne, J. Cornil, K. Lancaster, J.-L. Brédas, S. Verlaak, A. Mityashin, P. Heremans, A. Fuchs, C. Lennartz, J. Idé, R. Méreau, P. Aurel, L. Ducasse, F. Castet, J. Phys. Chem. C **114**, 3215 (2010)
63. C.D. Wessendorf, A. Perez-Rodriguez, J. Hanisch, A.P. Arndt, I. Ata, G.L. Schulz, A. Quintilla, P. Bäuerle, U. Lemmer, P. Wochner, E. Ahlswede, E. Barrena, J. Mater. Chem. A **4**, 2571 (2016)
64. R. García, R. Magerle, R. Perez, Nat. Mater. **6**, 405 (2007)
65. V. Palermo, G. Ridolfi, A.M. Talarico, L. Favaretto, G. Barbarella, N. Camaioni, P. Samorì, Adv. Funct. Mater. **17**, 472 (2007)
66. E.J. Spadafora, R. Demadrille, B. Ratier, B. Grévin, Nano Lett. **10**, 3337 (2010)
67. D.J. Ellison, J.Y. Kim, D.M. Stevens, C.D. Frisbie, J. Am. Chem. Soc. **133**, 13802 (2011)
68. G. Shao, M.S. Glaz, F. Ma, H. Ju, D.S. Ginger, ACS Nano **8**, 10799 (2014)
69. B. Grévin, P.-O. Schwartz, L. Biniek, M. Brinkmann, N. Leclerc, E. Zaborova, S. Méry, Beilstein J. Nanotechnol. **7**, 799 (2016)
70. N. Adhikari, A. Dubey, D. Khatiwada, A.F. Mitul, Q. Wang, S. Venkatesan, A. Iefanova, J. Zai, X. Qian, M. Kumar, Q. Qiao, A.C.S. Appl, Mater. Interfaces **7**, 26445 (2015)
71. J.-J. Li, J.-Y. Ma, Q.-Q. Ge, J.-S. Hu, D. Wang, L.-J. Wan, A.C.S. Appl, Mater. Interfaces **7**, 28518 (2015)
72. J.-J. Li, J.-Y. Ma, J.-S. Hu, D. Wang, L.-J. Wan, A.C.S. Appl, Mater. Interfaces **8**, 26002 (2016)
73. D. Kim, G.Y. Kim, C. Ko, S.R. Pae, Y.S. Lee, O. Gunawan, D.F. Ogletree, W. Jo, B. Shin, J. Phys. Chem. C **120**, 21330 (2016)
74. J.S. Yun, A. Ho-Baillie, S. Huang, S.H. Woo, Y. Heo, J. Seidel, F. Huang, Y.-B. Cheng, M.A. Green, J. Phys. Chem. Lett. **6**, 875 (2015)
75. J.S. Yun, J. Seidel, J. Kim, A.M. Soufiani, S. Huang, J. Lau, N.J. Jeon, S.I. Seok, M.A. Green, A. Ho-Baillie, Adv. Energy Mater. **6**, 1600330 (2016)
76. Y.C. Kim, N.J. Jeon, J.H. Noh, W.S. Yang, J. Seo, J.S. Yun, A. Ho-Baillie, S. Huang, M.A. Green, J. Seidel, T.K. Ahn, S.I. Seok, Adv. Energy Mater. **6**, 1502104 (2016)
77. Y. Sugawara, L. Kou, Z. Ma, T. Kamijo, Y. Naitoh, Y.J. Li, Appl. Phys. Lett. **100**, 223104 (2012)

78. J.L. Garrett, E.M. Tennyson, M. Hu, J. Huang, J.N. Munday, M.S. Leite, Nano Lett. **17**, 2554 (2017)
79. J.L. Garrett, J.N. Munday, Nanotechnology **27**, 245705 (2016)
80. J. Lee, J. Kong, H. Kim, S.-O. Kang, K. Lee, Appl. Phys. Lett. **99**, 243301 (2011)
81. J. Kong, J. Lee, Y. Jeong, M. Kim, S.-O. Kang, K. Lee, Appl. Phys. Lett. **100**, 213305 (2012)
82. R. Saive, M. Scherer, C. Mueller, D. Daume, J. Schinke, M. Kroeger, W. Kowalsky, Adv. Funct. Mater. **23**, 5854 (2013)
83. M.D. Clark, M.L. Jespersen, R.J. Patel, B.J. Leever, A.C.S. Appl, Mater. Interfaces **5**, 4799 (2013)
84. B. Cao, X. He, C.R. Fetterly, B.C. Olsen, E.J. Luber, J.M. Buriak, A.C.S. Appl, Mater. Interfaces **8**, 18238 (2016)
85. L. Bürgi, H. Sirringhaus, R.H. Friend, Appl. Phys. Lett. **80**, 2913 (2002)
86. R. Saive, C. Mueller, J. Schinke, R. Lovrincic, W. Kowalsky, Appl. Phys. Lett. **103**, 243303 (2013)
87. M. Scherer, R. Saive, D. Daume, M. Kröger, W. Kowalsky, AIP Adv. **3**, 092134 (2013)
88. Q. Chen, L. Mao, Y. Li, T. Kong, N. Wu, C. Ma, S. Bai, Y. Jin, D. Wu, W. Lu, B. Wang, L. Chen, Nat. Commun. **6**, 7745 (2015)
89. A. Guerrero, E.J. Juarez-Perez, J. Bisquert, I. Mora-Sero, G. Garcia-Belmonte, Appl. Phys. Lett. **105**, 133902 (2014)
90. V.W. Bergmann, S.A.L. Weber, F.J. Ramos, M.K. Nazeeruddin, M. Grätzel, D. Li, A.L. Domanski, I. Lieberwirth, S. Ahmad, R. Berger, Nat. Commun. **5**, 5001 (2014)
91. V.W. Bergmann, Y. Guo, H. Tanaka, I.M. Hermes, D. Li, A. Klasen, S.A. Bretschneider, E. Nakamura, R. Berger, S.A.L. Weber, A.C.S. Appl, Mater. Interfaces **8**, 19402 (2016)
92. M. Takihara, T. Takahashi, T. Ujihara, Appl. Phys. Lett. **93**, 021902 (2008)
93. Ł. Borowik, H. Lepage, N. Chevalier, D. Mariolle, O. Renault, Nanotechnology **25**, 265703 (2014)
94. P.A. Fernández Garrillo, Ł. Borowik, F. Caffy, R. Demadrille, B. Grévin, ACS Appl. Mater. Interfaces **8**, 31460 (2016)
95. F. Caffy, N. Delbosc, P. Chávez, P. Lévêque, J. Faure-Vincent, J.-P. Travers, D. Djurado, J. Pécaut, B. Grévin, N. Lemaitre, N. Leclerc, R. Demadrille, Polym. Chem. **7**, 4160 (2016)
96. L. Kaake, X.-D. Dang, W.L. Leong, Y. Zhang, A. Heeger, T.-Q. Nguyen, Adv. Mater. **25**, 1706 (2013)
97. Z. Schumacher, Y. Miyahara, A. Spielhofer, P. Grutter, Phys. Rev. Applied **5**, 044018 (2016)

Chapter 12
KPFM of Nanostructured Electrochemical Sensors

Alex Henning and Yossi Rosenwaks

Abstract Integrating sensor arrays with microelectronic devices enables applications such as disease diagnostics and environmental monitoring. The most advanced chemical sensor concepts, compatible with integrated circuits, comprise a semiconductor with a nanostructured sensing area that can be modified to be more selective and sensitive to specific analytes. The target molecules react with the exposed surface area and may dope the semiconductor, alter the surface charge density, and polarize the surface, which in turn affects the current that flows through the semiconductor via field-effect and charge transfer. KPFM allows probing the smallest variations of the surface charge density and band bending on a nanometer scale. Unique in this sense, KPFM can be used to detect the work function changes following adsorption and map the potential landscape of a nanostructured sensor surface to locate the most sensitive region. The chapter describes how KPFM helps to advance research and development of chemical sensors.

12.1 Introduction

Environmental and health monitoring is envisioned with nanostructured electrochemical transducers integrated into mobile electronics such as smartphones and wearables. Nanostructured chemical sensors encompass devices based on state-of-the-art semiconductor technology such as multiple gate field-effect transistors (FETs) and fin field-effect transistors (finFETs), as well as bottom-up grown nanomaterials such as nanowires (NWs) and carbon nanotubes (CNTs), as prospective candidates to augment or replace silicon (Si) technology in the future. The research and

A. Henning (✉)
Department of Materials Science and Engineering, Northwestern University, Evanston, IL, USA
e-mail: alex.henning@northwestern.edu

Y. Rosenwaks
Faculty of Engineering, Department of Physical Electronics, Tel Aviv University, Tel Aviv, Israel
e-mail: yossir@tauex.tau.ac.il

S. Sadewasser and T. Glatzel (eds.), *Kelvin Probe Force Microscopy*,
Springer Series in Surface Sciences 65, https://doi.org/10.1007/978-3-319-75687-5_12

development of nanostructured chemical sensors require high-resolution metrology tools related to charge and transport. Surface characterization techniques, such as X-ray photoelectron spectroscopy (XPS), micro-photoluminescence, and Raman spectroscopy, are limited in their spatial resolution by optical diffraction. Secondary ion mass spectrometry (SIMS) can be used for imaging with a spatial resolution down to 50 nm [1, 2] but is a destructive method. Related scanning probe microscopy (SPM) methods such as scanning capacitance microscopy (SCM) and scanning spreading resistance microscopy (SSRM) require operation in contact mode and thus damage the sample surface. KPFM is highly sensitive to surface potential variations following chemical interaction with target molecules, and thus provides means to assess the sensor selectivity and sensitivity on a nanometer scale during device operation. This way, it allows the monitoring of sensor stability and degradation in real time, and to this end, it allows to explore analyte-surface interaction and to optimize chemical sensors.

12.1.1 Nanostructured Chemical Sensors

To date, silicon is the semiconductor of choice despite its significantly lower mobility, larger power consumption, and stronger short-channel effects compared with other semiconductors, e.g. III-V NWs. Moreover, its mobility degradation at elevated temperatures can be a limiting factor for temperature-assisted chemical sensors. Low-dimensional materials including two-dimensional (2D) layered materials [3–9], one-dimensional (1D) nanowires [10–17] and CNTs [18–20], and zero-dimensional (0D) nanocrystals [21, 22] were demonstrated as selective and sensitive chemical sensors. Detection limits down to parts per billion (ppb) [23] and even parts per trillion (ppt) [20, 24] were achieved with CNT and NW FET-based gas sensors for NO_2 and trinitrotoluene (TNT), respectively. In particular, Si NW-based FETs were established for selective detection at room temperature [13, 15, 16, 25, 26]. Most commonly, the surface is chemically modified to tailor the sensitivity of NW-based sensors to specific target molecules, typically volatile organic compounds (VOCs) [10, 23, 27–29]. An electronic nose (e-nose) based on Si NW sensors allows for the analysis and discrimination of complex multi-component chemical analytes, for instance, to distinguish between ‘healthy’ and ‘cancerous’ breath by detection of specific biomarkers [30, 31].

Figure 12.1 shows two types of nanostructured FET-based chemical sensors, a silicon finFET sensor (Fig. 12.1a, b) as an example for state-of-the-art Si technology and a CNT sensor (Fig. 12.1c, d), representative for a device based on emerging nanomaterials.

Bottom-up grown nanomaterials such as NWs, quantum dots (QDs) and van der Waals (vdW) materials are prospective candidates that may replace silicon in the future. However, these emerging materials are not yet compatible with state-of-the-art nanoelectronics. The major challenges preventing integration with standard semiconductor technology are related to the complex growth process at elevated

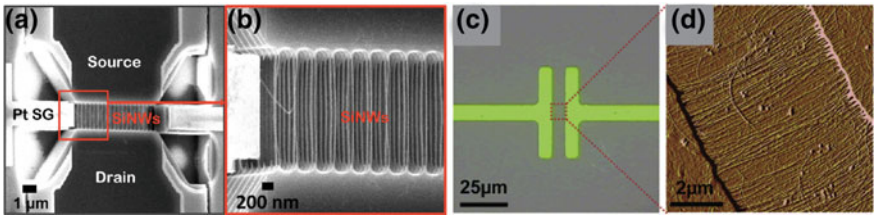

Fig. 12.1 **a**, **b** Scanning electron microscopy (SEM) images of a finFET sensor. Reprinted from [32], with permission from Elsevier. **c** Optical microscopy and **d** AFM image of a multi CNT sensor. Adapted with permission from [33]. Copyright 2006 American Chemical Society

temperatures and the challenges in achieving alignment with nanometer precision on a large scale. The general credo is that progress in nanoelectronics will come from improving Si technology by integrating emerging materials.

Top-down fabricated NW FETs and finFETs are both non-planar (nanostructured) transistors compatible with complementary metal-oxide-semiconductor (CMOS) technology, allowing for mass production. FinFETs have recently been demonstrated as highly sensitive and stable pH detectors and biosensors [34]. An interesting question is whether the larger surface-to-volume ratio, S/V, of finFETs and NW FETs results in a higher sensor sensitivity. The intrinsic sensitivity is unaffected by S/V considering the case where analytes are uniformly distributed, e.g. for ionic sensing in solution. However, detection of low analyte concentrations, e.g. single biomarkers, is more efficient (i.e., faster) with a larger S/V due to an increased chance of analyte-surface interaction.

Finally, planar FETs based on silicon-on-insulator (SOI) technology were demonstrated for high-sensitivity chemical sensing using a multiple gate transistor platform [35, 36], in which a nanowire-like channel is formed electrostatically (Sect. 12.2), and with an ultra-thin (3.5 nm) SOI-based sensor for selective gas detection [37]. In general, the transducer signal and therefore the extrinsic sensor response is larger for a smaller transistor channel, in close proximity to the sensing event near the surface.

12.1.2 Principles of Operation of Electrochemical Transducers

One can conditionally divide into two transducer principles, charge transfer and field-effect. In the first case, the analyte may covalently bond to the surface and chemically dope the semiconductor changing the carrier concentration in the transistor channel. Charges can be transferred for example by tunneling through a thin surface dielectric (e.g., native SiO_2) or after analyte reaction with crystal defects (e.g., vacancies) on the surface of a vdW material such as graphene [5]. An example for surface charge transfer doping in 2D materials [38] is shown in Sect. 12.3.2.1. In the second case, the adsorbed analyte electrostatically impacts the carrier density

via field-effect inducing a band bending of the conduction band edge, E_C. In other words, the relative position of the Fermi level, E_F, is shifted with respect to E_C.

Chemical sensors based on FETs with an exposed gate dielectric were thoroughly explored since their introduction in 1970 by Bergveld [39, 40], mainly for biosensing and as pH sensors in liquid. The ion-sensitive field-effect transistor (ISFET) is considered robust but its main drawback is the need for a reference electrode which is challenging to integrate on-chip. A catalytic palladium gate was introduced for hydrogen detection in 1975 by Lundström et al. [41]. This latter approach provides endless possibilities of tailoring the surface reactivity when combined with today's nanofabrication technology and deposition techniques.

Both charge transfer and field-effect affect the work function, $\Phi = E_{vac} - E_F$, defined as the energy difference between the local vacuum level, E_{vac}, and the Fermi level, E_F, of the sample (here sensor surface). KPFM probes the contact potential difference (CPD), $CPD \times e = \Phi - \Phi_{tip}$, defined as the difference between the work functions of sample and AFM tip, Φ_{tip}, multiplied by the elementary charge, e.

The exposed dielectric layer of a FET-based sensor acts as a 'molecular gate' because adsorbed molecules may change the surface charge distribution and thus alter the measured work function, Φ, of the sensor surface. [28, 42] The principle of operation involves analytes that adsorb on the surface of the semiconductor and induce a change in the work function, $\Delta\Phi$, and electric field across the exposed dielectric layer of the sensor, which in turn entails a shift in the channel current, I_D, and the effective gate dielectric capacitance, C_{eff}. Molecules that interact with the top gate dielectric, acting as a molecular gate, can lead to a charge carrier accumulation, depletion, or inversion in the semiconductor and at the interface. In case of a metal-oxide-semiconductor field-effect transistor (MOSFET) with an exposed gate dielectric, the adsorbed molecules induce a threshold voltage shift with respect to the back gate voltage, $\Delta V_{th}^{BG} = \frac{\Delta\Phi}{e} - V_{th}^{BG}$, of the transistor transfer characteristics ($I_D - V_{BG}$), due to $\Delta\Phi$ (12.1),

$$I_D = \mu_{FE} \frac{w}{l} Q V_D = \mu_{FE} \frac{w}{l} C_{eff} \left(V_{BG} + \frac{\Delta\Phi}{e} - V_{th}^{BG} \right) V_D, \tag{12.1}$$

where μ_{FE} is the majority carrier field-effect mobility, w and l are the effective channel dimensions, V_D is the source-drain voltage, and V_{BG} is the back gate voltage.

12.1.3 Effect of Surface Adsorption on the Work Function

The distinction between chemi- and physisorption is empirical since also intermediate levels of adsorption exist. Nonetheless, it is helpful to separately describe the two extremes to understand how molecule adsorption contributes to $\Delta\Phi$. In the case of physisorption, molecules are not chemically altered during interaction with the surface (associative adsorption). Instead, the adsorbate (e.g., ethanol) is bound via comparably weak electrostatic forces, with a binding energy typically below ~100 meV,

on the adsorbent (e.g., SiO_2). Such an adsorbate layer may result in a surface dipole changing the electron affinity, thus the measured work function of the sensor surface (see Fig. 12.4). Physisorption is reversible and the temperature dependency of the formed surface dipole on $\Delta\Phi$ can by studied by KPFM. Chemisorbed molecules are chemically altered or cleaved (dissociative adsorption) during the adsorption and exhibit a relatively strong binding to the surface with an energy above ~500 meV, mainly through covalent binding and ionic interaction. Chemisorption on the gate dielectric of a FET sensor may contribute to charged surface states affecting the carrier density in the semiconductor underneath.

KPFM detects the CPD following molecular adsorption with mV sensitivity and nanometer spatial resolution. A significant change in the measured CPD is not necessarily observed in the AFM topography. Remarkably, the charge distribution within a single naphthalocyanine molecule adsorbed on NaCl on Cu(111) was measured by KPFM, albeit at low temperatures in ultra-high vacuum [43]. In ambient air, all solid surfaces are covered by molecules like water, oxygen, and hydrocarbons [44]. Consequently, the electric field between tip and sample is partially screened by adsorbed water molecules when measuring samples exposed to ambient air [45]. Nonetheless, a significant shift in the work function was measured following chemisorption of hexadecane thiol on Au in a liquid [46] demonstrating that KPFM can be potentially used to probe biosensor surfaces in-situ. Furthermore, KPFM was employed as a label-free method to detect circulating tumor cells immobilized by CNTs modified with specific receptors [47, 48]. The functionalized CNTs were not used as transducers but as receptors, and the analyte-surface interaction was read-out as a change in the CPD, ΔCPD. Label-free detection down to a concentration limit of 1 pM was demonstrated with KPFM, which is comparable to the detection limit of fluorescence imaging, a technique that relies on signal amplification by labeling. CPD measurements of CNTs before and after exposure to toluene solvent showed that changes in the CNT work function upon exposure to the solvent are consistent with the increased negative charge on the CNT [49].

12.2 Molecular Gate

12.2.1 CPD Map of a Multiple Gate FET Sensor

A schematic illustration of a multiple gate FET sensor and the electronic circuit for KPFM under device operation are shown in Fig. 12.2. This device is a planar FET sensor, in which the spatial confinement of the transistor channel is achieved electrostatically after fabrication. This FET sensor consists of an silicon-on-insulator layer, separated by SiO_2 (green) from the wafer base (red) and covered with a 6 nm thin, thermally grown, SiO_2 layer. There is a trade-off between device stability and sensor sensitivity with a regular gate dielectric. The extent of the fringing field of the adsorbed molecules limits the range of detection. Therefore, devices with too thick

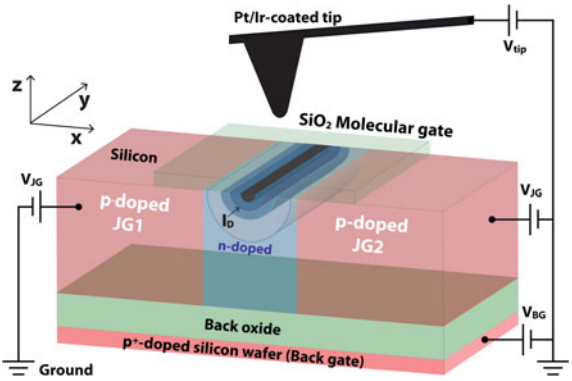

Fig. 12.2 An illustration of the KPFM measurement configuration of an SOI-based chemical FET sensor. By applying voltages to the two junction gates (V_{JG}) and the back gate (V_{BG}), a nanowire-like channel forms inside the n-doped silicon region along the y-axis of the device. Reproduced from [50], with permission from Wiley Publishing

sensor surface oxide layers do not respond to adsorbed molecules, as the externally sensible field of a dipole rapidly decays with the inverse cube of the distance ($\frac{1}{r^3}$).

The current flows from source to drain through the 500 nm narrow n-doped Si region (dark blue) when a bias, V_D, is applied to the drain electrode while the source electrode is grounded. The bias, V_{JG}, applied to the junction gates (JG1, JG1) controls the p-n junction depletion layer width and thus determines the effective channel width (grey-blue). The active carrier concentration within the n-doped channel region is additionally controlled with the back gate voltage, V_{BG}, applied to the degenerately p-doped handle wafer (red). The cross-sectional area of the channel and concurrently the current density are controlled with the transistor bias configuration; the conductive channel is confined to a cross-sectional diameter of tens of nanometers under reverse biased V_{JG}. KPFM provides means to measure the built-in potential of a p-n junction, as well as the areal extent of the space charge region (SCR).

Figure 12.3a shows a typical CPD (top) and topography (bottom) image of the sensors' active area while the voltages applied to the surrounding gate electrodes (V_{JG}, V_S, V_D and V_{BG}) were kept at ground potential. Notably, the measurements were conducted in a nitrogen glove box with less than 1 ppm of water. A higher or lower work function is expected for p- or n-type doping, respectively. While the sensor surface topography is perfectly flat (with the exception of the quadratic window defining the active area), the CPD map reveals the p-doped (bright) and n-doped (dark) regions within the chemo-sensitive area.

Figure 12.3b shows CPD profiles and their first and second derivates across the p-n-p structure of the sensor surface (white arrow in Fig. 12.3a). Potential pitfalls for measurement and interpretation of the CPD of semiconductor devices are discussed below and in Chaps. 1 and 9 of this book. The measured potential difference of ca. 0.23 V between p- and n-doped region is lower than the analytically calculated built-in potential of 1 V using doping densities for n-doped (4×10^{17} cm^{-3}) and p-doped (2×10^{19} cm^{-3}) regions measured by SIMS. The charges due to ionized donors and acceptors within the SCR of the Si layer is screened due to the following reasons. First of all, the active sensor area is covered with a 6 nm thick gate

oxide layer. Defect states at the Si/SiO_2 interface are present up to a concentration of 1×10^{11} cm^{-2}. Secondly, the surface was exposed to ambient air and the device was treated with organic solvents during fabrication. An adsorbate layer is present, and the SiO_2 is likely charged (fixed charges) resulting in screening of the electric field from the SCRs of the p-n junctions [45, 51]. Note that the measured width of the depletion layer is overestimated (Fig. 12.3b, top). For AFM in general, the spatial resolution is limited by the geometry (sharpness and aspect ratio) of the AFM probe tip (here with a nominal radius of 30 nm, PPP-EFM, Nanosensors). In particular for KPFM, the spatial resolution of the CPD is hampered due to capacitive coupling of the AFM probe with long-range electrostatic-forces from neighboring sample regions with different work functions. Tip-sample convolution is reduced by decreasing the tip-sample distance and is highly dependent on the mode of operation; frequency modulation detection provides higher spatial CPD resolution because it is sensitive to the derivative of the force. To account for the tip-limited CPD resolution it is necessary to determine the point spread function of the tip [52, 53], for example by measuring the CPD across the interface between two metals or degenerately doped semiconductors. Experimentally, the lateral electric fields, generated at the depletion regions of the p-n junctions, are obtained from the measured CPD profiles, $E_x = \mathrm{d}CPD/\mathrm{d}x$ and $E_y = \mathrm{d}CPD/\mathrm{d}y$, by taking the derivative of the measured CPD with respect to the x- or y-axis, respectively. Note that for Fig. 12.3b E_x and E_y are orthogonal to each other. The electric field is largest at the metallurgical junctions of the p-n regions, which are clearly identified as peaks in the measured electric field profile across the channel. The n-doped silicon region is 500 ± 20 nm wide, in accordance to the transistor design, confirmed with the measured electric field profiles. The electric field, E, is related to the charge density in the silicon SCR through Gauss' law, $\nabla E = \frac{eN_D}{\epsilon_0 \epsilon_{rel}}$, where N_D is the density of ionized dopants and ϵ_{rel} is the relative dielectric constant. Therefore, the second derivative of the measured CPD profile, $\mathrm{d}^2CPD/\mathrm{d}x^2$, correlates with the charge density within the SCR of the p-n junctions. Profiles of $\mathrm{d}^2CPD/\mathrm{d}x^2$ visualize the distribution of ionized donors and acceptors within the SCR (Fig. 12.3b, bottom).

12.2.2 CPD Changes Following Chemical Modification

Sensor stability, sensitivity, and selectivity can be enhanced with surface modifications, e.g. with a self-assembled monolayer (SAM) [54]. Surface modifications may also ensure sensor recovery at favorable temperatures by providing binding sites that weakly interact with the target molecules. Ambient temperature determines the

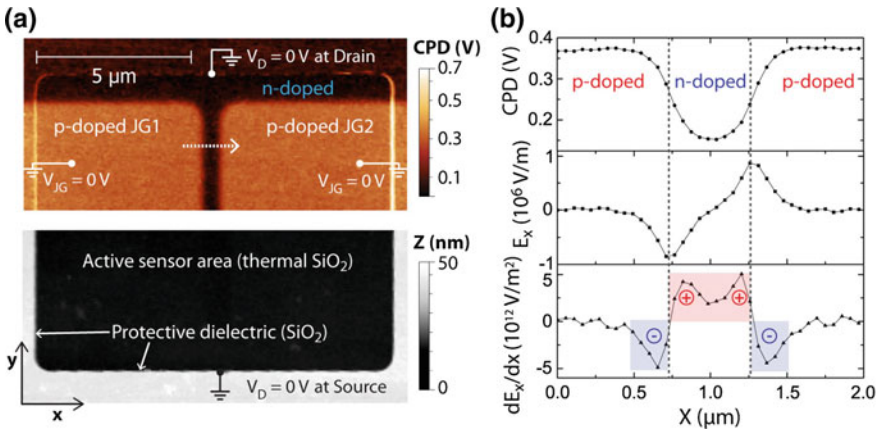

Fig. 12.3 **a** CPD (top) and topography (bottom) images of the sensor active area. **b** CPD profile (top) and its first (middle) and second derivatives (bottom), extracted from the CPD image in (**a**) indicated by the white arrow

balance (thermal equilibrium) between adsorption and desorption. Ideally for chemical sensors, analytes are physisorbed such that the reaction is reversible at room temperature. KPFM provides means to assess the quality and uniformity of the surface modification on a nanometer scale. For example, the CPD on linear alkanethiols of different length self-assembled as monolayers on Au substrates was reported to shift by $\Delta\Phi = (14.1 \pm 3.1)$ meV with every $-CH_2-$ unit in the chain [55]. CPD measurements of a CNT-based sensor revealed a shift in the Schottky barrier height at the interface between chemically modified gold electrode and CNT network (transistor channel) after analyte reaction with the receptors on the gold electrodes modified with a SAM [56]. KPFM has been also demonstrated as a tool to assess and evaluate surface modifications of sensors based on nanomaterials such as NWs and CNTs. For example, KPFM was used to locate segments with functional binding sites on single CNTs [57]. Tsai et al. characterized SiNW based biosensors by KPFM before and after NW surface functionalization with linker molecules, biotin-immobilization, and avidin-binding [58].

12.2.2.1 CPD Decomposition

The observed ΔCPD after modification of a FET-based sensor dielectric has two main contributions: $\Delta CPD \times e = \Delta\Phi = \Delta\Phi_D + \Delta\Phi_S$, where $\Delta\Phi_D = \Delta\chi$ is the change in the electron affinity after surface modification, and $\Delta\Phi_S$ is the change in band bending caused by molecular gating (Fig. 12.4). The field-effect induces a shift in the Fermi level position relative to the E_C of the semiconductor to change Φ. The electron affinity changes with the formation of a (microscopic) surface dipole layer resulting in an effective electron affinity, $\chi^* = \chi + \Delta\Phi$.

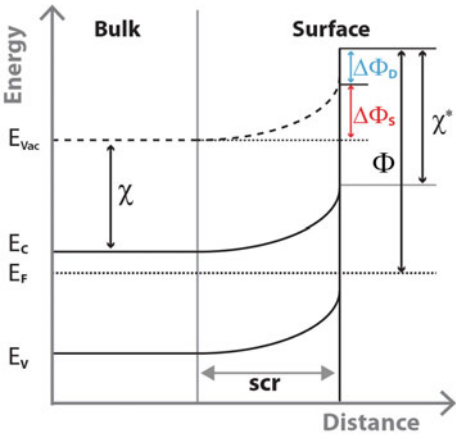

Fig. 12.4 A schematic band diagram of an n-type semiconductor surface in the presence of a microscopic surface dipole. E_C and E_V denote the conduction and valence band edge, respectively. E_F and E_{vac} are Fermi and vacuum level, respectively. Φ is the work function of the sample surface. $\Delta\Phi_S$ is the work function change due to energy band bending in the semiconductor and $\Delta\Phi_D$ is the work function change induced by a surface dipole. χ denotes the electron affinity and χ^* the effective electron affinity

The work function change induced by a surface dipole layer, $\Delta\Phi_D$, is related to the surface dipole density through the Helmholtz equation [59],

$$\Delta\Phi_D = 4\pi \frac{NP_0 \cos\theta}{A\,\varepsilon \cdot \varepsilon_0}, \tag{12.2}$$

where $n = \frac{N}{A}$ is the number of dipoles per surface area, P_0 is the dipole moment of the free molecule in the vacuum, $\varepsilon \equiv \frac{P_0}{P}$ is the effective dielectric constant of a molecular monolayer, P is the surface dipole moment, and ε_0 is the vacuum permittivity. The strength of the surface dipole depends on the orientation at an angle, θ, relative to the surface plane normal.

Shaya et al. [42] measured $\Delta\Phi$ of SOI wafers after the following treatments, summarized in Fig. 12.5a in sequential order from bottom to top: solvent cleaning, ultraviolet (UV) activation, and self-assembly. The measured changes in work function of the surface above the transistor channel are in agreement with $\Delta\Phi$ of the wafers following the same treatments where Φ increased by about 0.9 eV following UV activation and then decreased by about 1.6 eV after self-assembly. Figure 12.5b shows typical $I_D - V_{BG}$ characteristics of an SOI-based chemical sensor after UV activation and different modifications. The surface charge density is estimated from the measured ΔV_{th}^{BG} using the relationship $\Delta V_{th}^{BG} = -\frac{\sigma}{C_{box}} = -\frac{\sigma}{\varepsilon_{ox}} t_{box}$ derived from the 1D Poisson equation for an SOI MOSFET assuming a fully depleted silicon. The increase of V_{th}^{BG} following the UV treatment (relative to the solvent clean value) is

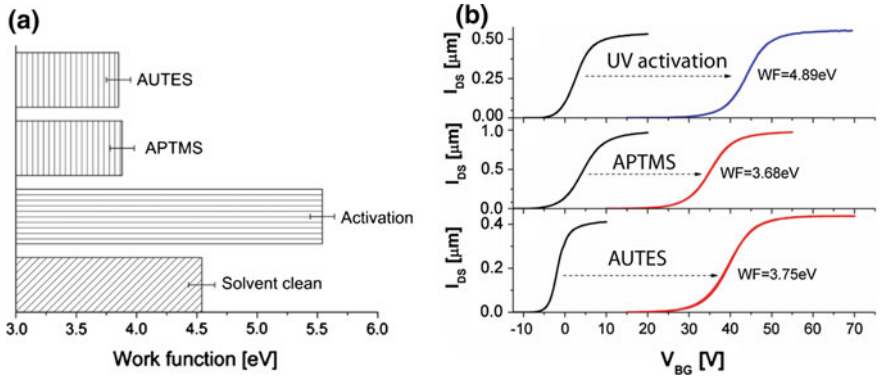

Fig. 12.5 **a** $\Delta\Phi$ measured at different stages of sample preparations following solvent cleaning, UV activation, APTMS, and amino-undecilenyltriethoxysilane (AUTES) self-assembly, respectively. **b** Current-voltage curves of the molecular-gated transistor following UV activation (blue), APTMS self assembly (red) and AUTES self assembly (red) compared to the I-V curves measured before treatment (black). Reprinted with permission from [42]. Copyright 2009 American Chemical Society

attributed to negative charging due to ozone oxidation of Si–O–Si. The decrease of V_{th}^{BG} following self-assembly of (3-Aminopropyl)trimethoxysilane (APTMS) after UV activation is a result of positive charging, or screening of the negative surface charges due to modification of the (partially negative) Si–O– surface sites, calculated to be $\sigma = 1.5 \times 10^{11}$ cm^{-2}. APTMS is known to be polar with a net molecular dipole moment of 1.5 Debye for the primary amine (RNH_2) state [60].

The contribution of $\Delta\Phi_S$ to the measured ΔCPD is extracted as follows. The FET-based sensor was modeled using an electrostatic device simulator (Sentaurus, Synopsys). The electrostatic potential throughout the entire device was calculated for three different surface charge densities, σ, corresponding to the following three cases: solvent clean, UV activation, and molecular self-assembly (Fig. 12.6). ΔV_{th}^{BG}, extracted from the I_D-I_{BG} plots served as an input to compute σ. The calculated change in band bending between the UV activation and the APTMS modification is $\Delta\Phi_S = 0.26$ V. A CPD difference of 1.21 V was measured resulting in $\Delta\chi = 1.21 - 0.26$ V $= 0.95$ V.

In summary, Shaya et al. [42] elaborated a strategy that combines KPFM, I-V characteristics and electrostatic simulation to decompose the measured CPD changes. This allows to separately determine the contributions of surface polarization ($\Delta\Phi_D$) and field-effect induced band bending ($\Delta\Phi_S$) to the measured CPD change. $\Delta\Phi_S$ is a measure of the sensor transduction.

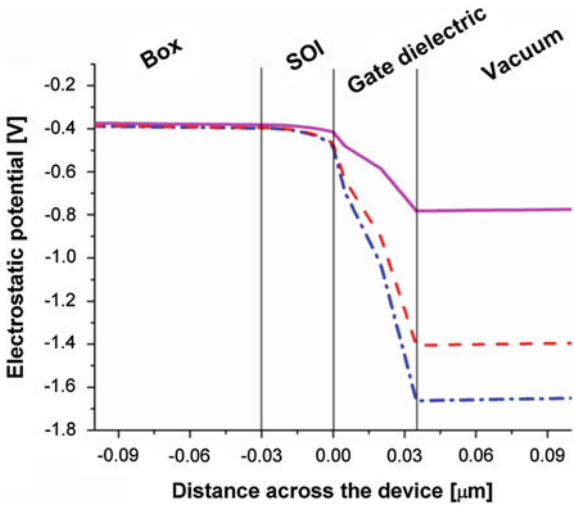

Fig. 12.6 Electrostatic potential throughout the chemical FET at zero applied bias simulated for three values of the surface charge density, σ, corresponding to the device after solvent-cleaning (solid line), UV activation (dash-dot), and APTMS modification (dashed line). Reprinted with permission from [42]. Copyright 2016 American Chemical Society

12.2.3 Coupling Between Front and Back Gate Potentials

KPFM is used to estimate the sensor sensitivity by measuring ΔCPD as a function of the back gate voltage. An applied back gate voltage induces a change in the carrier density of the semiconductor resulting in the measured ΔCPD of the molecular front gate, and vice versa. These measurements are demonstrated with an enhancement mode SOI-based multiple gate FET sensor introduced in Sect. 12.2.

12.2.3.1 Relation Between Sensor Work Function of the Molecular Gate and Back Gate Voltage

Figure 12.7a shows the CPD of the sensor surface as a function of the back gate voltage. Applying V_{BG} varies the relative position of E_F in the semiconductor with respect to E_{vac} and is detected as a work function change $\Delta\Phi_S$ of the sensor surface (see Sect. 12.2.2). The correlation factor between ΔV_{BG} and $\Delta\Phi_S$ provides an estimate of the transducer sensitivity; the measured $\Delta\Phi_S$ by KPFM translates into a threshold voltage shift with respect to the back gate voltage obtained from the transfer characteristics of the device. A correlation factor, $\Delta V_{BG}/\Delta\Phi_S = 90$, is obtained from a linear fit to the V_{BG}-CPD plot (Fig. 12.7). In this regard, KPFM provides a direct measurement of the transducer amplification ($\Delta V_{BG}/\Delta\Phi_S = 90$).

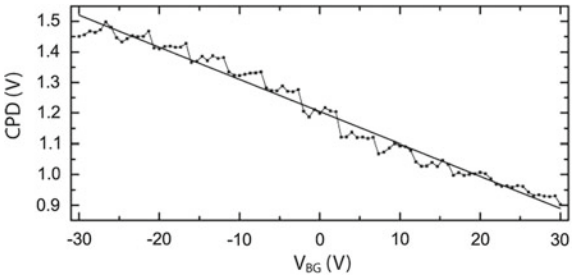

Fig. 12.7 Capacative coupling of the EFN transistor. *CPD* is shown as a function of V_{BG}. The correlation factor, $\Delta V_{BG}/\Delta CPD$, is determined from a linear curve fit

12.2.3.2 Emulating a Molecular Gate with an AFM Tip Gate

The platinum-iridium-coated AFM tip (PPP-EFM, Nanosensors) with a nominal apex radius of 30 nm is placed with nanometer precision above the transistor channel. Depending on the polarity of the tip voltage, V_{tip}, the tip either induces ($V_{tip} < 0$ V) or reduces ($V_{tip} > 0$ V) depletion of electrons in the conductive channel. The measurements were performed in intermittent contact mode instead of contact mode to avoid permanent and irreversible charging of the SiO_2 top layer, known as contact electrification. Figure 12.8a presents a typical CPD map of the channel region and Fig. 12.8b shows measurements of the drain current as a function of the tip position (indicated by dashed arrows in Fig. 12.8a) at $V_{tip} = -1$ V. The tip has the strongest effect on the drain current, I_D, when it is placed in the lateral and transversal center of the NW. The spatial resolution of this method is limited by the probe geometry and its distance to the sample surface.

Figure 12.9 shows $I_D - V_{BG}$ characteristics in a semi-logarithmic plot while the tip was placed at a fixed average height ($\delta \approx 15$ nm) above the transistor channel center, for three different tip voltages, $V_{tip} = 1$ V (red plot), $V_{tip} = 0$ V (black plot) and $V_{tip} = -1$ V (blue plot). It is evident that the effect of the positive tip bias is weaker than the effect of the negative tip bias inherent to a depletion mode FET: A tip induced negative charge induces depletion while a tip induced positive charge reduces depletion in the transistor. The upper boundary of the electron density in the transistor channel (i.e., the undepleted domain in the n-doped Si) is limited by the doping density. Since a positive charge cannot induce majority carrier accumulation, it is less sensitive. Inversion at the n-doped Si/SiO_2 interface can be achieved with a strongly negatively charged surface either after analyte exposure (e.g. high concentrations of polar analytes), treatments (e.g., UV/ozone), or with a negatively biased tip gate ($V_{tip} \leq -10$ V).

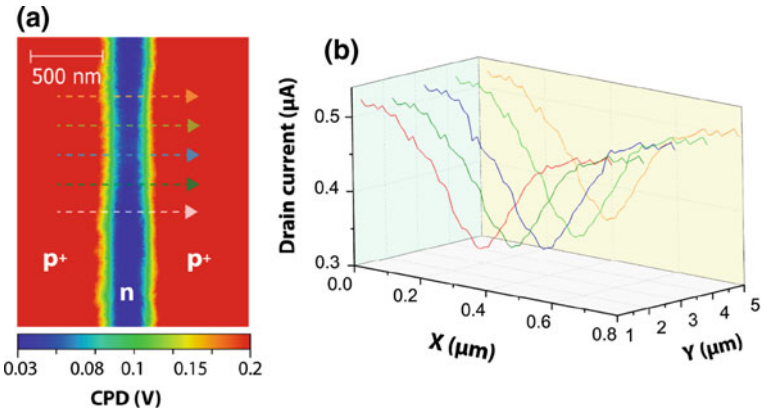

Fig. 12.8 **a** CPD image of a multiple gate FET under operation for $V_D = 1$ V and $V_{JG} = 0$ V. The dashed arrows indicate the AFM tip scans across the p-n-p junction. **b** The 3D plot shows the drain current as a function of the tip position on the x- and y-axis for $V_{tip} = -1$ V. The average tip-sample distance, δ, was kept constant at ca. 15 nm. Reproduced from [50], with permission from Wiley Publishing

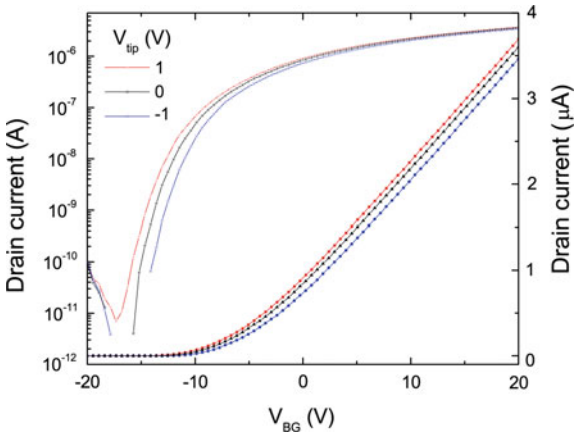

Fig. 12.9 The AFM tip emulates adsorbed molecules. $I_D - V_{BG}$ characteristics in a semi-logarithmic (left y-axis) and linear (right y-axis) plot while the tip was placed at a fixed position and an average distance, $\delta \approx$ 15 nm, above the NW center, for $V_{tip} = 1$ V (red plot), $V_{tip} = 0$ V (black plot) and $V_{tip} = -1$ V (blue plot). $V_D = 1$ V and $V_{JG} = -2$ V

12.2.4 Molecular Gating of a Multiple Gate FET Sensor

KPFM was used to evaluate a multiple-gate FET-based sensor and exemplify molecular gating as a consequence of adsorbed ethanol on the active area (Fig. 12.10). Figure 12.10a shows CPD images of the sensor surface under device operation before and after exposure to ≈3000 ppm of ethanol. It is evident from the CPD profiles along the p-n-p region (Fig. 12.10b) that adsorbed ethanol induces a positive CPD shift of ≈50 mV and ≈180 mV at the p-doped and n-doped (channel) region, respectively. The surface charge density is affected as a consequence of analyte adsorption on the top layer dielectric acting as a molecular gate. The molecular gate induced

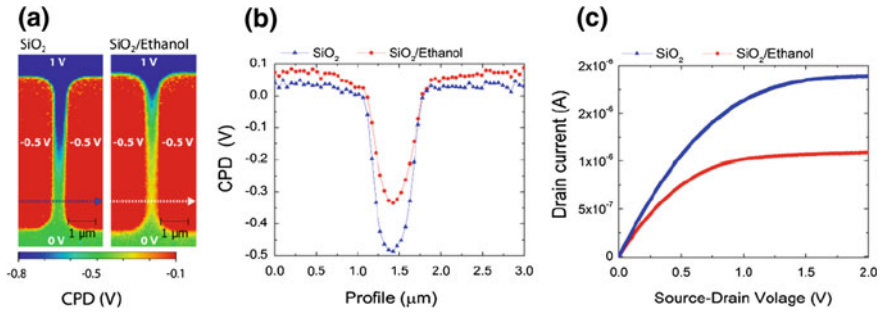

Fig. 12.10 **a** CPD images of the sensor active area before and after ethanol exposure (≈3000 ppm) under device operation at $V_D = 1$ V and $V_{JG} = -0.5$ V. **b** CPD line profiles, indicated by dashed arrows in (**a**), across the p-n-p junction of the sensor before and after ethanol adsorption. Ethanol alters the surface potential causing depletion in the n-doped region reflected in the more positive CPD compared with the pristine device. **c** The corresponding I_D-V_D characteristics show two times decrease in I_D following ethanol exposure. Reproduced from [50], with permission from Wiley Publishing

field-effect is also observed as a reduction of the drain current after ethanol adsorption (Fig. 12.10c) supporting the KPFM results.

The positive CPD shift of the device active area indicates negative charging of the SiO_2. Preferential orientation of ethanol molecules as opposed to a random orientation may lead to the formation of a surface dipole and polarization [61] resulting in a surface dipole, which would explain the observed CPD shift (≈50 mV). Additionally, the molecular gate (adsorbed ethanol on SiO_2) depletes the n-doped region leading to an upward bending of the conduction band edge, E_C. As a result, the measured CPD shift is larger (≈180 mV) than the CPD shift above the highly p-doped region where surface band bending is expected to be negligible small. The highly complex interaction of ethanol with a SiO_2 surface was studied in previous works, e.g., by Chang and Shu [62]. The number of dipoles (ethanol molecules) per surface area, $n = \frac{N}{A}$, is estimated with (12.2) to be $n_{eth} \approx 1.9\,\mathrm{nm}^{-2}$, using measured $\Delta\Phi = 50 \pm 20$ meV for the adsorbed ethanol on the highly p-doped region, and known values for the molecular dipole moment ($P_D = 1.7$ D) and dielectric constant ($\varepsilon_{eth} = 24.5$) of ethanol [63], assuming vertically oriented molecules at $\theta = 0°$ for simplicity. This result is in the range of reported values of $n_{eth} = 1\ \mathrm{nm}^{-2}$ [64] and $n_{eth} = 0.28\ \mathrm{nm}^{-2}$ [65] that were extracted from the measured adsorption isotherms of ethanol on SiO_2.

12.3 KPFM as a Tool to Evaluate Sensor Selectivity and Sensitivity on a Nanoscale

12.3.1 Multiple Gate FET-based Sensor Surface After Analyte Adsorption

KPFM is used to identify the active sensor region and the optimum operation condition, as well as to elucidate the surface-analyte interaction with the goal to optimize the sensor design. Figure 12.11 shows CPD images of the sensor active area of a multiple gate FET-based chemical sensor for different conditions. The CPD image of the grounded device and before analyte exposure (Fig. 12.11a) shows variations due to n- and p-doped regions. The Fermi level is aligned, and no current flows in thermal and chemical equilibrium. Figure 12.11b shows the CPD map of the operating device while biased at $V_{JG} = -0.5$ V, $V_D = 1$ V, and $V_{BG} = 0$ V. The FET sensor was exposed to ~3000 ppm of ethanol for 30 s while biased at $V_{JG} = -0.5$ V, $V_D = 1$ V, and $V_{BG} = 0$ V. Figure 12.11c depicts the CPD image of the biased device after analyte exposure, which reveals an increase in the CPD of the channel region, especially near the drain contact. The effect of the adsorbed ethanol molecules appears more pronounced in the CPD map of the grounded device after ethanol exposure (Fig. 12.11d). The observed CPD pattern is similar to reported measurements of biased p-n junctions in a humid atmosphere [66–68]. The images of Fig. 12.11a and d differ distinctly from each other: A CPD shift of ca. 250 mV near the p-n junctions next to the drain contact is observed. The fringing electric field, generated by the shallow p-n junctions underneath the thin gate oxide layer, reaches a maximum at the pinch-off point near the biased drain contact ($V_D = 1$ V). The fringing electric fields may orient the ethanol molecules due to their dipole moment of 1.7 D in the vicinity of the surface, and therefore influence the way they adsorb on the surface. Ethanol can be regarded as a 'marker' to spatially resolve the fringing electric field. Figure 12.11e shows the CPD of the sensor surface after heating to 70 °C for 10 min, indicating physisorption of ethanol, e.g. via hydrogen bonding with the siloxane sites at the SiO_2 layer.

Figure 12.12a compares the CPD profiles across the pristine (black curve) and the exposed sensor surface (blue curve), across the p-n-p structure, indicated by the arrows in Fig. 12.11a and d, respectively. The corrected CPD profile (red triangles, Fig. 12.12a) is obtained by subtracting the built-in potential profile before analyte exposure (black squares, Fig. 12.12a) from the CPD profile after ethanol adsorption (blue circles, Fig. 12.12a). A CPD change of ~200 mV is observed at the transverse center of the channel while a CPD difference of about −50 mV is measured at the highly p-doped (2×10^{19} cm^{-3}) junction gate area.

Figures 12.12b shows CPD profiles of the biased device along the transistor channel, i.e., along the y-axis from source to drain, indicated by the arrows in Fig. 12.11b and c, respectively. The measured potential difference between source and drain corresponds nearly to the applied voltage of 1 V. The slope of the CPD is zero above

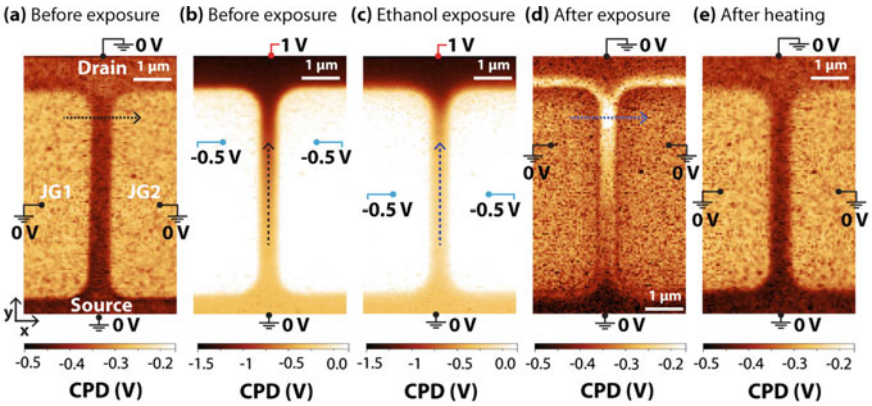

Fig. 12.11 CPD images of an EFN device before analyte adsorption **a** at ground potential and **b** biased at $V_D = 1$ V, $V_{JG} = -0.5$ V, and $V_{BG} = 0$ V, as well as **c** biased and **d** grounded after analyte adsorption, and **e** after surface recovery by heating in ambient air

the source contact region, then it increases (region I) before it gradually decreases (region II and III) along the channel approaching the drain contact. The CPD increases in region I as a consequence of the reverse biased junction gates ($V_{JG} = -0.5$ V) depleting the n-doped channel region. The slope of the CPD increases along the y-axis due to the decreasing channel width shaped by the source-drain potential difference. The channel resistance is largest and the channel width is smallest at the pinch-off point near the drain contact (region III). Therefore, the potential drop and the CPD slope are larger at channel segment III. The CPD drops more uniformly along the channel before ethanol exposure (black triangles) after ethanol exposure (blue squares) because the channel is more depleted of free carriers and therefore more resistive due to adsorbed ethanol molecules. The largest potential drop of ca. 600 mV is at the pinch-off point. Note that the CPD profile shows only the moderately n-doped channel region since the highly n-doped contact regions are protected by a 40 nm thick dielectric layer. Therefore, the potential is not constant at the drain contact region.

KPFM reveals that the fringing electric fields arising from the biased p-n junctions of the multiple gate sensor affect the interaction of vapor molecules with the top gate dielectric layer. While the charge read-out mechanism of this multiple gate sensor is well-understood, the mechanism of fringing-field-controlled sensing remains vague and is object of future studies.

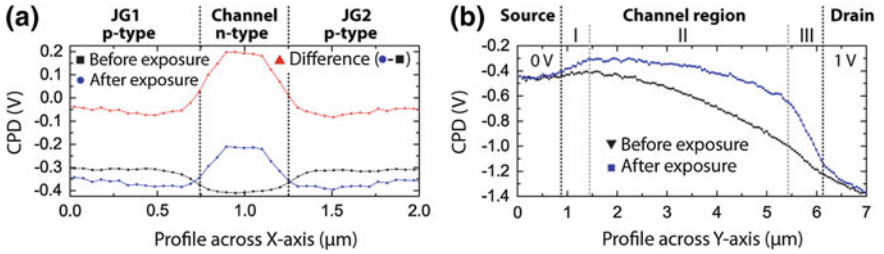

Fig. 12.12 **a** CPD profiles across the p-n-p structure before (black) and after analyte exposure (blue) indicated by the dashed arrows in Fig. 12.12 while the device was grounded. The corrected CPD profile after subtraction of the built-in potential is shown in red. **b** CPD profiles (top) while the EFN sensor was biased

12.3.2 Recent Examples for KPFM of Nanostructured Sensors

12.3.2.1 Van der Waals Materials

KPFM was employed to identify the sensitive areas with high spatial resolution and to quantify the amount of charge transferred to reduced graphene oxide after exposure to acetone or ammonia [69]. In another example, KPFM was used to measure the work function of 2D materials following adsorption of gas molecules and to probe the band alignment at the heterojunction formed between black phosphorus (BP) and molybdenum diselenide ($MoSe_2$) [38]. The vdW material heterojunction responds to NO_2 concentrations down to 25 ppb. Figure 12.13a shows device images measured by AFM and optical microscopy (OM). The flake thicknesses are 17 and 5 nm for BP and $MoSe_2$, respectively. For a multilayer vdW material the measured work function difference between BP and $MoSe_2$ approximately corresponds to the built-in potential, V_{bi}, at the heterojunction, assuming negligible surface band bending. Figure 12.13b shows CPD images of the highlighted area in the optical microscopy image. A V_{bi} of 0.15 V is measured at the BP and $MoSe_2$ junction (Fig. 12.13b, top). A ΔCPD of approximately 30 mV is observed at the BP surface after exposure to 500 ppb of NO_2 (Fig. 12.13b, middle) attributed to chemical doping. The initial sensor state is re-established after recovery in ambient without the analyte (Fig. 12.13b, bottom). The CPD images after analyte exposure and after a dwell time (tens of seconds) without the analyte are nearly identical (Fig. 12.13b, top and bottom images) demonstrating complete recovery. The CPD profiles in 12.13c show a CPD increase of 30 mV of the BP following exposure to NO_2, which likely increases V_{bi} from 0.15 to 0.18 V. The CPD of $MoSe_2$ is defined as reference zero to simplify the analysis. The average CPD differences are depicted in Fig. 12.13d for comparison. KPFM was used to determine V_{bi} and to compare with the finite element model used to predict the BP/$MoSe_2$ band alignment. The authors attribute the measured ΔCPD after

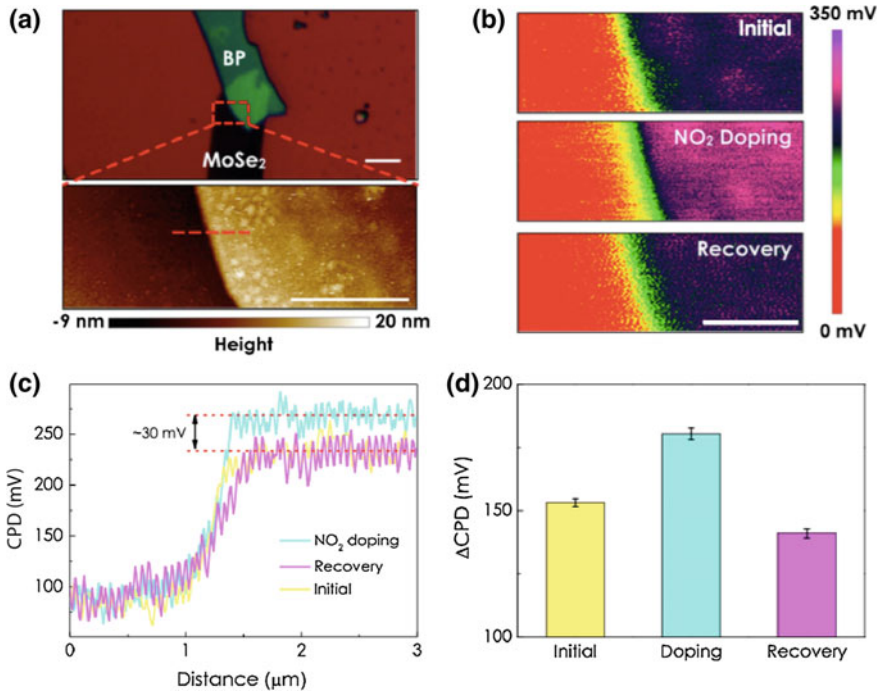

Fig. 12.13 **a** Optical microscope (top) and topography image (bottom) of the BP/$MoSe_2$ heterostructure measured by KPFM. The thickness of the BP film is 17 nm. Scale bars are 5 μm (top image) and 1 μm (bottom image). **b** CPD images of the same region as shown in **a** before (top) and after (middle) exposure to 500 ppb of NO_2, as well as after recovery (bottom). The CPD of $MoSe_2$ is defined as the minimum in the color scale and the scale bar is 1 μm. **c** CPD profiles along the red dashed line shown in the image in (a). A CPD increase of ∼30 mV of the BP sensor surface is observed after NO_2 doping. **d** Average *ΔCPD* for different measurements and standard deviations. *ΔCPD* after doping with NO_2 is significantly larger than the standard deviation. Reprinted from [38] and with permission from IOP Publishing Ltd

analyte exposure to changes in both the total built-in potential (via molecular gating) and the ratio between majority carrier density (doping) in both materials.

12.3.2.2 Nanoribbons

KPFM was used to characterize a Si nanoribbon FET-based sensor [70]. Figure 12.14 shows AFM topography and CPD images, as well as the corresponding CPD profiles, of a nanoribbon (NR) FET sensor before and after chemical functionalization with a SAM (TABINOL) and after exposure to an analyte (diphenylchlorophosphate, DPCP). The KPFM images show a CPD increase for the Si NR after functionalization and a decrease after analyte exposure. The authors attributed the measured

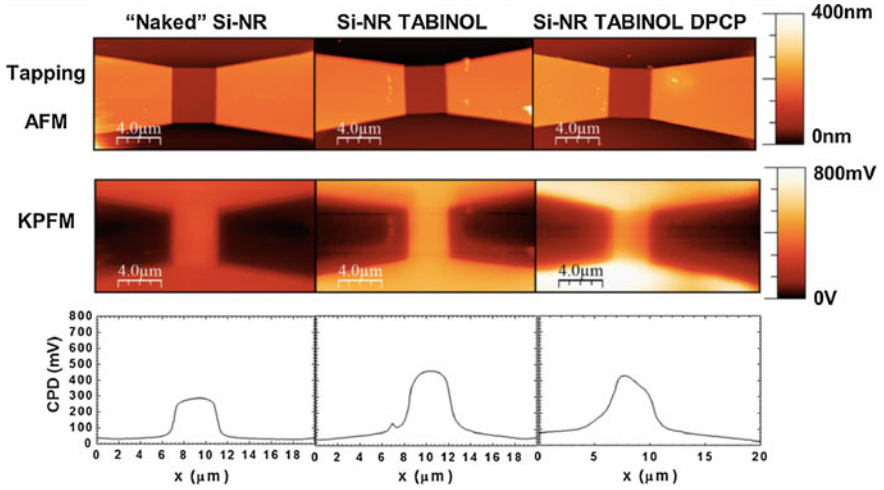

Fig. 12.14 Images of AFM topography and CPD of a silicon nanoribbon FET. The corresponding CPD profiles across the device before and after functionalization and after analyte (diphenylchlorophosphate, DPCP) exposure. With permission from ACS

ΔCPD to formation of a surface dipole after functionalization and charging following DPCP exposure.

12.3.3 Sensor Surface Recovery and Degradation

A major avenue of FET-based sensor research focuses on improving the reliability of the gate material. The top gate dielectric of a planar FET may degrade when continuously exposed to ambient air and analytes. The effect of humidity on semiconductor device operation has been studied since 1963. Shockley et al. demonstrated with a Kelvin probe that surface ions, formed in the presence of water vapor, migrate and accumulate above the SCR of a biased and buried p-n junction underneath a thermal oxide layer [66, 71]. Mobile surface ions were measured using a Kelvin probe on alumina before and after surface treatments with an acid or base [72].

So far, KPFM has been sparsely used to to study the effect of sensor surface degradation as a consequence of external factors, e.g. after repetitive cycles of heating and sensing, exposure to ambient air or UV illumination despite its compatibility conducting such measurements in-operando. A few examples are provided below. Domansky et al. observed a charge build-up on the oxide layer above a p-n junction that was exposed to different humidity levels using electrostatic force microscopy [67]. Individual SnO_2 crossed-nanowires sensors in a three-terminal field-effect transistor configuration were investigated using a combination of macroscopic transport measurements and KPFM [73]. Under ambient conditions, the dc transport

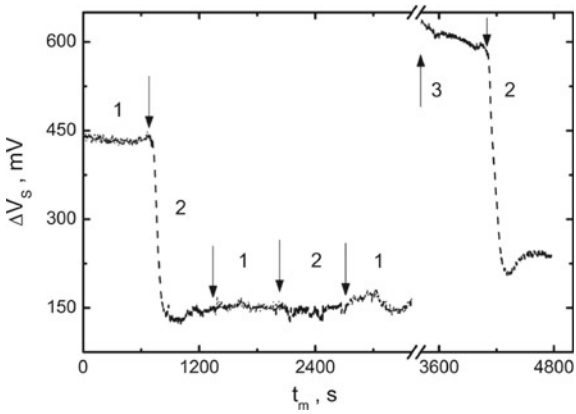

Fig. 12.15 Surface potential change over time of a TiO_2 gas sensor in air (1), under exposure to H_2 gas (2) and then reactivation with UV light (3). Reprinted from [74], with permission from Elsevier

measurements were found to be strongly affected by field-induced surface charges on the nanostructure and the gate oxide.

Spatial and time-resolved CPD measurements of a nanostructured chemical sensor surface are effective to probe analyte-surface interactions and gain knowledge about the sensing mechanism. There are only a couple of time-resolved KPFM studies on chemical sensors: The CPD of the sensor surface was measured during exposure to H_2 and recovery upon UV illumination [74] (Fig. 12.15). Grover et al. demonstrated KPFM as a tool to study chemical sensors and showed time-resolved CPD change on a porphyrine surface following pyridine gas exposure [75].

12.4 Summary and Perspective

Development of sensors based on emerging bottom-up grown nanomaterials and state-of-the-art nanoelectronics relies firmly on the proper metrology tools. KPFM allows probing local variations of the sensor work function and it was demonstrated as a tool to evaluate chemical modifications of a FET-based sensor surface and to elucidate analyte-surface interactions on a nanometer scale. The work function change following analyte-surface interactions is directly related to the intrinsic sensor response. Time-resolved and operando KPFM of nanostructured chemical sensors allows exploring adsorption kinetics on a nanoscale, however, to date, there are only a few studies. Corrosion and gas adsorption on the AFM tip surface are challenges to overcome for in-operando and real-time characterization of sensors during analyte exposure. In the long run, we envision that KPFM will establish as a major metrology tool for the development and optimization of chemical sensors and surface modifications.

References

1. B. Hagenhoff, Microchim. Acta **132**(2–4), 259 (2000)
2. N. Winograd, Anal. Chem. **77**(7), 142 (2005)
3. K.R. Ratinac, W. Yang, S.P. Ringer, F. Braet, Environ. Sci. Technol. **44**(4), 1167 (2010)
4. G. Lu, L.E. Ocola, J. Chen, Nanotechnology **20**(44), 445502 (2009)
5. F. Schedin, A. Geim, S. Morozov, E. Hill, P. Blake, M. Katsnelson, K. Novoselov, Nat. Mater. **6**(9), 652 (2007)
6. J.D. Fowler, M.J. Allen, V.C. Tung, Y. Yang, R.B. Kaner, B.H. Weiller, ACS Nano **3**(2), 301 (2009)
7. Y. Liu, X. Dong, P. Chen, Chem. Soc. Rev. **41**(6), 2283 (2012)
8. J.T. Robinson, F.K. Perkins, E.S. Snow, Z. Wei, P.E. Sheehan, Nano Lett. **8**(10), 3137 (2008)
9. F.K. Perkins, A.L. Friedman, E. Cobas, P. Campbell, G. Jernigan, B.T. Jonker, Nano Lett. **13**(2), 668 (2013)
10. Y. Cui, Q. Wei, H. Park, C.M. Lieber, Science **293**(5533), 1289 (2001)
11. A. Kolmakov, M. Moskovits, Annu. Rev. Mater. Res. **34**, 151 (2004)
12. D. Zhang, Z. Liu, C. Li, T. Tang, X. Liu, S. Han, B. Lei, C. Zhou, Nano Lett. **4**(10), 1919 (2004)
13. G. Zheng, F. Patolsky, Y. Cui, W.U. Wang, C.M. Lieber, Nat. Biotechnol. **23**(10), 1294 (2005)
14. X.J. Huang, Y.K. Choi, Sens. Actuators B Chem. **122**(2), 659 (2007)
15. A. Cao, E.J. Sudhölter, L.C. de Smet, Sensors **14**(1), 245 (2013)
16. Y. Paska, T. Stelzner, S. Christiansen, H. Haick, ACS Nano **5**(7), 5620 (2011)
17. X. Zhao, B. Cai, Q. Tang, Y. Tong, Y. Liu, Sensors **14**(8), 13999 (2014)
18. J. Kong, N.R. Franklin, C. Zhou, M.G. Chapline, S. Peng, K. Cho, H. Dai, Science **287**(5453), 622 (2000)
19. P.G. Collins, K. Bradley, M. Ishigami, A. Zettl, Science **287**(5459), 1801 (2000)
20. J. Li, Y. Lu, Q. Ye, M. Cinke, J. Han, M. Meyyappan, Nano Lett. **3**(7), 929 (2003)
21. P. Alivisatos, Nat. Biotechnol. **22**(1), 47 (2004)
22. G. Peng, U. Tisch, O. Adams, M. Hakim, N. Shehada, Y.Y. Broza, S. Billan, R. Abdah-Bortnyak, A. Kuten, H. Haick, Nat. Nanotechnol. **4**(10), 669 (2009)
23. M.C. McAlpine, H. Ahmad, D. Wang, J.R. Heath, Nat. Mater. **6**(5), 379 (2007)
24. Y. Engel, R. Elnathan, A. Pevzner, G. Davidi, E. Flaxer, F. Patolsky, Angew. Chem. Int. Ed. **49**(38), 6830 (2010)
25. F. Patolsky, C.M. Lieber, Mat. Today **8**(4), 20 (2005)
26. C.J. Chu, C.S. Yeh, C.K. Liao, L.C. Tsai, C.M. Huang, H.Y. Lin, J.J. Shyue, Y.T. Chen, C.D. Chen, Nano Lett. **13**(6), 2564 (2013)
27. A. Niskanen, A. Colli, R. White, H. Li, E. Spigone, J. Kivioja, Nanotechnology **22**(29), 295502 (2011)
28. Y. Paska, T. Stelzner, O. Assad, U. Tisch, S. Christiansen, H. Haick, ACS Nano **6**(1), 335 (2012)
29. B. Wang, J.C. Cancilla, J.S. Torrecilla, H. Haick, Nano Lett. **14**(2), 933 (2014)
30. F. Patolsky, G. Zheng, C.M. Lieber, Nanomedicine **1**(1), 51 (2006)
31. O. Assad, H. Haick, in *IEEE International Symposium on, Industrial Electronics, 2008. ISIE 2008.* (IEEE, 2008), pp. 2040–2044
32. E. Buitrago, M. Fernández-Bolaños, S. Rigante, C.F. Zilch, N.S. Schröter, A.M. Nightingale, A.M. Ionescu, Sens. Actuators B Chem. **193**, 400 (2014)
33. C.Y. Lee, S. Baik, J. Zhang, R.I. Masel, M.S. Strano, J. Phys. Chem. B **110**(23), 11055 (2006)
34. S. Rigante, P. Scarbolo, M. Wipf, R.L. Stoop, K. Bedner, E. Buitrago, A. Bazigos, D. Bouvet, M. Calame, C. Schnenberger et al., ACS Nano **9**(5), 4872 (2015)
35. G. Shalev, G. Landman, I. Amit, Y. Rosenwaks, I. Levy, NPG Asia Mater. **5**(3), e41 (2013)
36. A. Henning, N. Swaminathan, A. Godkin, G. Shalev, I. Amit, Y. Rosenwaks, Nano Res. **8**(7), 2206 (2015)
37. H.M. Fahad, H. Shiraki, M. Amani, C. Zhang, V.S. Hebbar, W. Gao, H. Ota, M. Hettick, D. Kiriya, Y.Z. Chen et al., Sci. Adv. **3**(3), e1602557 (2017)

38. Z. Feng, B. Chen, S. Qian, L. Xu, L. Feng, Y. Yu, R. Zhang, J. Chen, Q. Li, Q. Li, C. Sun, H. Zhang, J. Liu, W. Pang, D. Zhang, 2D Materials **3**(3), 035021 (2016). http://stacks.iop.org/2053-1583/3/i=3/a=035021
39. P. Bergveld, IEEE Trans. Biomed. Eng. **1**(BME-17), 70 (1970)
40. P. Bergveld, Sens. Actuators **8**(2), 109 (1985)
41. I. Lundstrom, S. Shivaraman, C. Svensson, L. Lundkvist, Appl. Phys. Lett. **26**(2), 55 (1975)
42. O. Shaya, M. Shaked, Y. Usherenko, E. Halpern, G. Shalev, A. Doron, I. Levy, Y. Rosenwaks, J. Phys. Chem. C **113**(15), 6163 (2009)
43. F. Mohn, L. Gross, N. Moll, G. Meyer, Nat. Nanotechnol. **7**(4), 227 (2012)
44. J. Voorthuyzen, K. Keskin, P. Bergveld, Surf. Sci. **187**(1), 201 (1987)
45. H. Sugimura, Y. Ishida, K. Hayashi, O. Takai, N. Nakagiri, Appl. Phys. Lett. **80**(8), 1459 (2002)
46. A.L. Domanski, E. Sengupta, K. Bley, M.B. Untch, S.A.L. Weber, K. Landfester, C.K. Weiss, H.J. Butt, R. Berger, Langmuir **28**(39), 13892 (2012). https://doi.org/10.1021/la302451h. http://dx.doi.org/10.1021/la302451h. PMID: 22946889
47. K. Nam, K. Eom, J. Yang, J. Park, G. Lee, K. Jang, H. Lee, S.W. Lee, D.S. Yoon, C.Y. Lee et al., J. Mater. Chem. **22**(44), 23348 (2012)
48. T. Kwon, J. Park, G. Lee, K. Nam, Y.M. Huh, S.W. Lee, J. Yang, C.Y. Lee, K. Eom, J. Phys. Chem. Lett. **4**(7), 1126 (2013). https://doi.org/10.1021/jz400087m. http://dx.doi.org/10.1021/jz400087m. PMID: 26282031
49. R.W. Friddle, M.C. Lemieux, G. Cicero, A.B. Artyukhin, V.V. Tsukruk, J.C. Grossman, G. Galli, A. Noy, Nat. Nanotechnol. **2**(11), 692 (2007)
50. A. Henning, M. Molotskii, N. Swaminathan, Y. Vaknin, A. Godkin, G. Shalev, Y. Rosenwaks, Small **11**(37), 4931 (2015)
51. S.V. Kalinin, D.A. Bonnell, Nano Lett. **4**(4), 555 (2004)
52. F. Robin, H. Jacobs, O. Homan, A. Stemmer, W. Bächtold, Appl. Phys. Lett. **76**(20), 2907 (2000)
53. E. Strassburg, A. Boag, Y. Rosenwaks, Rev. Sci. Instrum. **76**(8), 083705 (2005)
54. D. Cahen, R. Naaman, Z. Vager, Adv. Funct. Mater. **15**(10), 1571 (2005)
55. J. Lü, E. Delamarche, L. Eng, R. Bennewitz, E. Meyer, H.J. Güntherodt, Langmuir **15**(23), 8184 (1999)
56. M. Delalande, S. Clavaguera, M. Toure, A. Carella, S. Lenfant, D. Deresmes, D. Vuillaume, J.P. Simonato, Chem. Commun. **47**(21), 6048 (2011)
57. B.R. Goldsmith, J.G. Coroneus, J.A. Lamboy, G.A. Weiss, P.G. Collins, J. Mater. Res. **23**(05), 1197 (2008)
58. C.C. Tsai, P.L. Chiang, C.J. Sun, T.W. Lin, M.H. Tsai, Y.C. Chang, Y.T. Chen, Nanotechnology **22**(13), 135503 (2011). http://stacks.iop.org/0957-4484/22/i=13/a=135503
59. D.M. Taylor, O.N.D. Oliveira, H. Morgan, J. Colloid Interface Sci. **139**(2), 508 (1990). https://doi.org/10.1016/0021-9797(90)90123-6. http://www.sciencedirect.com/science/article/pii/0021979790901236
60. C.H. Kuo, C.P. Liu, S.H. Lee, H.Y. Chang, W.C. Lin, Y.W. You, H.Y. Liao, J.J. Shyue, Phys. Chem. Chem. Phys. **13**(33), 15122 (2011)
61. E. Atanassova, T. Dimitrova, Solid-State Electron. **36**(12), 1711 (1993)
62. C.C. Chang, M.C. Shu, J. Phys. Chem. B **107**(29), 7076 (2003)
63. D.R. Lide, CRC handbook of chemistry and physics 2004–2005: a ready-reference book of chemical and physical data (2004)
64. S. Mizushima, Metrologia **41**(3), 137 (2004)
65. A.L. McClellan, H. Harnsberger, J. Colloid Interface Sci. **23**(4), 577 (1967)
66. W. Shockley, H. Queisser, W. Hooper, Phys. Rev. Lett. **11**(11), 489 (1963)
67. K. Domanskỳ, Y. Leng, C.C. Williams, J. Janata, D. Petelenz, Appl. Phys. Lett. **63**(11), 1513 (1993)
68. R.F. Gouveia, C.A. Costa, F. Galembeck, J. Phys. Chem. C **112**(44), 17193 (2008)
69. C.E. Kehayias, S. MacNaughton, S. Sonkusale, C. Staii, Nanotechnology **24**(24), 245502 (2013)

70. K. Smaali, D. Guerin, V. Passi, L. Ordronneau, A. Carella, T. Mlin, E. Dubois, D. Vuillaume, J.P. Simonato, S. Lenfant, J. Phys. Chem. C **120**(20), 11180 (2016)
71. W. Shockley, W. Hooper, H. Queisser, W. Schroen, Surf. Sci. **2**, 277 (1964)
72. B. Salgin, R.F. Hamou, M. Rohwerder, Electrochim. Acta **110**, 526 (2013)
73. S.V. Kalinin, J. Shin, S. Jesse, D. Geohegan, A. Baddorf, Y. Lilach, M. Moskovits, A. Kolmakov, J. Appl. Phys. **98**(4), 044503 (2005)
74. Š. Vaškelis, V. Bukauskas, A. Mironas, A. Šetkus, Procedia Eng. **87**, 1063 (2014). https://doi.org/10.1016/j.proeng.2014.11.346. http://www.sciencedirect.com/science/article/pii/S1877705814024618. EUROSENSORS 2014, the 28th European Conference on Solid-State Transducers
75. R. Grover, B.M. Carthy, Y. Zhao, G.E. Jabbour, D. Sarid, G.M. Laws, B.R. Takulapalli, T.J. Thornton, D. Gust, Appl. Phys. Lett. **85**(17), 3926 (2004). https://doi.org/10.1063/1.1810209. http://dx.doi.org/10.1063/1.1810209

Chapter 13
Applications of KPFM-Based Approaches for Surface Potential and Electrochemical Measurements in Liquid

Liam Collins, Stefan A. L. Weber and Brian J. Rodriguez

Abstract Kelvin probe force microscopy (KPFM) has been widely used to map nanoscale surface potentials of materials in ambient and ultra-high vacuum environments. However, to study and ultimately understand charge-related processes, e.g., in biological systems or to further improve energy storage devices such as electrochemical batteries, nanoscale surface potential measurements in liquid environments are required. Here, we describe the various implementations of KPFM-based approaches for measuring surface potentials in liquid environments. We provide practical guidelines for surface potential measurements and describe what other information can be obtained. Finally, we discuss potential applications and limitations of existing approaches and present possible solutions for the successful implementation of liquid KPFM.

13.1 Introduction

The solid-liquid interface plays a fundamental role in a diverse range of physical, chemical, and electrochemical phenomena, including catalysis [1, 2], corrosion [3, 4], energy storage [5], sensing [6, 7], crystal growth [8], and biological

L. Collins
Center for Nanophase Materials Sciences and Institute for Functional Imaging of Materials, Oak Ridge National Laboratory, Oak Ridge, TN 37831, USA
e-mail: collinslf@ornl.gov

S. A. L. Weber (✉)
Max Planck Institute for Polymer Research, Ackermannweg 10, 55128 Mainz, Germany
e-mail: stefan.weber@mpip-mainz.mpg.de

B. J. Rodriguez
School of Physics and Conway Institute of Biomedical and Biomolecular Research, University College Dublin, Belfield, Dublin 4, Dublin, Ireland
e-mail: brian.rodriguez@ucd.ie

S. Sadewasser and T. Glatzel (eds.), *Kelvin Probe Force Microscopy*,
Springer Series in Surface Sciences 65, https://doi.org/10.1007/978-3-319-75687-5_13

processes [9]. Electrostatic potentials, which govern many of these processes, are ultimately controlled by electric field driven migration and diffusion of mobile charged ion species and electrochemical reactions at the solid-liquid interface [10]. Crucially, the ability to detect and quantify electrochemical potentials and charge dynamics is needed for the development of next generation energy materials and devices such as supercapacitors [11], batteries [12, 13], and biocatalysts [9]. Local inhomogeneities such as surface roughness, grain boundaries, and impurities can act, for example, as nucleation centers of pitting corrosion [14], locations of increased ionic transport in solid state electrolytes [15] or higher energy storage in supercapacitors due to increased surface areas [16]. Therefore, in order to achieve knowledge-driven design and optimization, the surface functionality must be correlated with microstructure on the level of individual structural elements (e.g., defects, step edges, grain boundaries). While macroscopic electrochemical measurements are capable of probing materials properties on the device level, few techniques can operate with submicron resolution.

In the past two decades, considerable progress has been achieved using voltage modulated (VM) atomic force microscopy (AFM) methods such as electrostatic force microscopy (EFM) and Kelvin probe force microscopy (KPFM) for combined electrostatic and structural characterization of materials at the solid-gas interface. An important distinction between EFM and KPFM approaches is that the latter is believed to give a quantitative measure of electrochemical potentials (i.e., contact potential difference, CPD). In contrast, results from EFM experiments without exact knowledge of the tip shape and numerical modelling of the tip-sample geometry remain mostly qualitative. KPFM has been shown to be a powerful technique, having been applied to a broad range of materials as diverse as ferroelectrics [17, 18], photovoltaics [19], lipid membranes [20–22] and DNA [23, 24]. While KPFM is considered quantitative, the interpretation of measurements in ambient is often complicated by the presence of a water layer and adsorbates, which can mask the true electronic properties of the sample. AFM operation in ambient is further prone to strong adhesive forces (van der Waals and capillary forces), which can inhibit meaningful investigation of some materials. Most importantly, for biological systems or battery materials it is necessary to maintain a natural environment for viable in situ or inoperandi operation. The combination of VM AFM with liquid imaging might seem to be a mismatch, as many liquids are electrically conductive. Nevertheless, successful KPFM measurements in liquid could elucidate the relationship between structure and electrochemical functionality on submicron length scales and provide a unique opportunity to study electrostatic double layers (EDLs) , electrochemical reactions, and diffuse charge dynamics at the solid-liquid interface. At the same time, the presence of mobile ions drastically complicates the direct implementation of conventional [25] KPFM. In this chapter, we describe the background and recent technique developments designed to overcome these technical hurdles, highlighting the applications of KPFM-based approaches for probing dielectric properties, EDLs electric surface potentials, and electrochemical processes in liquid.

13.2 Understanding Electrostatic Forces in Liquid

In this section, we consider the theory governing the electrostatic force at the solid-liquid interface. We start by briefly outlining the standard models used for describing the electrostatic potentials and ionic structures near solid-liquid interfaces under equilibrium conditions. We then provide a theoretical description for understanding EDL dynamics. We also discuss the breakdown of these standard models for realistic conditions (i.e., applied voltages in excess of the thermal potential, $\Psi_{th} > \frac{k_B T}{e} \approx 25$ mV) during VM AFM. Furthermore, we briefly describe the development of modified models to address non-linear steric effects at large voltages (e.g., ion crowding [26, 27]). Finally, we outline the body of experimental work directly related to understanding tip-sample capacitive forces in KPFM and EFM measurements in the presence of mobile ions.

13.2.1 Standard EDL Models

Electrostatic interactions in liquid follow different rules from electrostatics in air or in vacuum. The reasons for these differences are the dipolar nature of the water molecules and the presence of mobile ions. Any electric field in water, e.g., generated by an isolated ion or a surface charge at a solid-liquid interface, attracts ions of opposite charge and repels ions of the same charge. At the same time, thermal fluctuations prevent the formation of a static shell of counterions forming around the charged species. Helmholtz first described charge screening at flat electrified interfaces as an EDL comprising two compact layers of charge having opposite polarity [28]. The first description of the 'diffuse' double layer was introduced by Gouy [29] and Chapman [30] (GC), who considered charge screening by asymmetric distribution of ions and counterions as a function of distance from the electrode surface described by Boltzmann statistics. The GC model considered the coupled influence of diffusion and electrostatic forces on mobile ions near a charged surface [31]. Later, Stern combined the compact charge layer described by Helmholtz with the diffuse layer in the GC models in one theory, referred to as the Gouy Chapman Stern (GCS) model [32]. He proposed that at surface potentials larger than Ψ_{th}, a certain part of the ions in the EDL will be concentrated in a static layer of adsorbed ions directly at the electrode interface (see Fig. 13.1).

13.2.1.1 The Diffuse EDL

The basic equation that describes the competition between electrostatic or electrochemical energy and entropy is the Poisson-Boltzmann equation for a salt containing i different ionic species:

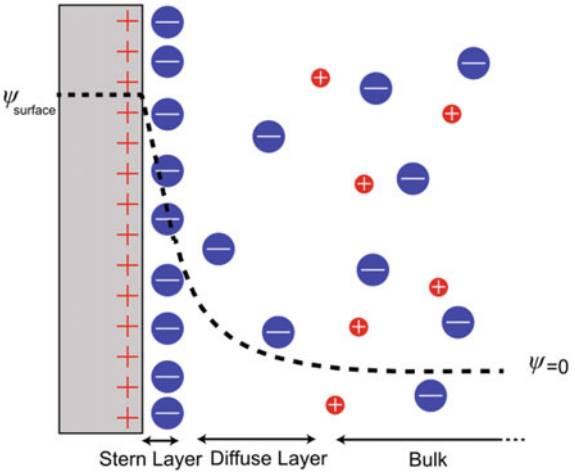

Fig. 13.1 Simple schematic of the Gouy Chapman Stern model of the electric double layer and the corresponding electrostatic potential, $\Psi(\vec{r})$. Close to the surface, a layer of static ions is forming as their finite radius does not allow them to get any closer to the surface (Stern layer)

$$\nabla^2\Psi(\vec{r}) = \sum_i \frac{z_i e c_0^i}{\epsilon\epsilon_0} exp\left(\frac{-z_i e\Psi(\vec{r})}{k_B T}\right) \tag{13.1}$$

Here, $\Psi(\vec{r})$ is the electrochemical potential, c_0^i and z_i are the equilibrium salt concentration and valence of the i-th ionic species, respectively, ϵ and ϵ_0 are the relative and vacuum permittivity, respectively, e is the positive elemental charge, k_B is the Boltzmann factor, and T is the temperature. As the name implies, the Poisson-Boltzmann equation combines elements of the Poisson equation used for the determination of the electrostatic potential at any point from the surface with calculations of the charge density away from the surface determined by a Boltzmann distribution. The Poisson-Boltzmann equation is valid under the assumption that (i) ions act as point-like charges interacting through their mean field interaction, (ii) the permittivity is constant throughout the bulk and double layer regions, and (iii) the solvent acts as a structure-less continuum (i.e., molecular effects are ignored) [31].

The full Poisson-Boltzmann equation is difficult to solve analytically, hence, linear approximations are often required to allow for analytical progress. For simple geometries, such as an infinite plane, and small voltages ($\Psi \lesssim \Psi_{\text{th}}$), the potential distribution can be calculated analytically. Following the Debye-Hückel linearization of the Poisson-Boltzmann equation, the electrochemical potential distribution in the EDL at an infinite plane can be calculated as [33]:

$$\Psi(x) = \Psi_0 exp\left(-\frac{x}{\lambda_D}\right); \tag{13.2}$$

$$\lambda_D^{mono} = \sqrt{\frac{\epsilon\epsilon_0 k_B T}{2c_0 e^2}}; \quad \lambda_D^{multi} = \sqrt{\frac{\epsilon\epsilon_0 k_B T}{e^2}\left(\sum_i c_0^i z^{i2}\right)^{-1}} \tag{13.3}$$

Here, λ_D^{mono} and λ_D^{multi} are the characteristic Debye screening lengths that corresponds to the width of the EDL for mono and multivalent electrolyte solutions, respectively. At a given temperature and salt concentration, the Debye length only depends on natural constants and the dielectric properties of the medium. For example, a solution of 100 mM NaCl has a Debye length of ~1 nm; it is slightly smaller in blood plasma: ~0.8 nm [33]. In pure water, the Debye length is up to ~600–700 nm due to the presence of OH^- and H_3O^+ ions. Thus, the EDL is a nanoscale structure, acting over distances of less than a nanometer up to ~1 μm.

The Poisson-Boltzmann description of the EDL is a good starting point for understanding electrostatic interactions in a liquid environment. However, as soon as length scales and ion concentrations relevant for biomolecular systems or realistic voltages during VM AFM $\left(V_{tip} \gg \Psi_{th}\right)$ are considered, limitations of the theory arise:

- The Poisson-Boltzmann description ignores the finite size of the charge and any inhomogeneities in the medium, such as variations in the dielectric permittivity or the molecular nature of the solvent.
- At surface potentials larger than the thermal potential $(\Psi > \Psi_{th})$, (13.1) can no longer be linearized. Here, the Boltzmann factor causes the electrolyte concentration at the interface to saturate due to a finite ion size [31]. This is termed the steric limit potential, which marks the start of the strongly non-linear electrochemical regime [34–36].
- The introduction of a finite molecular size of the ions in the framework of the GCS model required that there was some distance of closest approach to the surface. This region of surface-adsorbed ions is commonly called the compact Stern layer (Fig. 13.1) [31]. For a non-planar geometry, it is difficult to predict how the charges distribute between the Stern and the diffuse layer.
- More complex geometries than planar or spherical surfaces or the incorporation of ion dynamics require numerical solutions of the Poisson-Boltzmann equation or—on smaller length scales—molecular dynamics simulations.

There is no universal theory that fully describes electrostatic interactions on molecular length scales. Thus, the EDL remains a topic of intense research, even a century after its first discovery [31, 37].

13.2.1.2 EDL Dynamics

An important consideration in any attempt at liquid KPFM is the formation and re-arrangement of the EDL, e.g., as a response to a change in surface potential. As a first step, it is important to understand the processes which lead to the establishment of the EDL, as this is not an instantaneous process and includes several processes having a broad distribution of relaxation times. A general understanding of EDL dynamics can be found when one considers these relaxation timescales. To aid this

description we consider a simplified 1D plate capacitor geometry, Fig. 13.2a, made of an idealized polarized electrode (i.e., no Faradaic reactions), in a 1:1 molar solution.

Once a potential is applied across the capacitor, EDL dynamics are governed by two main driving forces, migration and diffusion, both of which are intrinsically related, but controlled by fundamentally different parameters. Migration (or electro-migration) is relevant only to charged particles and involves the transport of ions driven by an electric field or more specifically by the violation of local charge neutrality. Diffusion, on the other hand is a purely statistical process, where the net diffusion of ions is governed by the concentration gradient. Initially ions undergo electro-migration in response to the applied electric field. This charge relaxation of the EDL (i.e., the time it takes an ion to migrate across the EDL) is generally described by the Debye time, $\tau_D = \lambda_D^2/D$, where λ_D is the Debye screening length and D is the ion diffusivity in the liquid.

The resultant ion concentration gradient away from the electrode surface induces diffusion of ions towards the electrodes, resulting in a net uptake of ions from the bulk electrolyte into the EDL. This process takes place on the timescale $\tau_L = (L/2)^2/D$, where L is surface separation between electrodes. As L is usually much larger than λ_D, τ_L is much longer than τ_D, as it is governed by the geometry of the system. Overall, charging of the EDL happens through the electrical resistance of the bulk electrolyte, and can be shown to be governed by $\tau_C = \sqrt{\tau_D \tau_L} = \lambda_D(L/2)/D$ [31]. In macroscopic electrochemical measurements, equivalent circuit models are often used to understand the system dynamics, mainly due to their simplicity and compression of the system response into a small number of elements [10]. In equivalent circuit theory, τ_C, is equivalent to the EDL charging time (i.e., the *RC* time of the circuit) [31]. Note that even after the EDL charging time has been reached (i.e., $\tau = \tau_C$), the system has yet to achieve electrochemical equilibrium (i.e., ion redistribution continues).

The different relaxation processes were considered as a function of ion concentration for a simplified 1D capacitor geometry, Fig. 13.2a, one with a small electrode separation (50 nm) representing the tip-sample interaction, and a second with a much larger electrode separation (15 μm) representing the cantilever-sample interaction. In Fig. 13.2b, the red box indicates the frequency space currently accessible using commercial AFM systems (DC—~10 MHz). Within this frequency range, ion dynamics and electrochemical processes can be split into three different regimes: In regime (I), Faradaic and in (II), ion diffusion processes are expected to dominate the response, whereas in regime (III), ion dynamics are largely absent (i.e., quasistatic equilibrium). Notably, when operating in region III, where EDL dynamics are too slow to exert an influence within the measurement response time it may be possible to determine the electronic properties (e.g., CPD and dielectric constant) of the sample by means of VM AFM techniques. While measurements of CPD in higher (>100 mM) ion concentrations are attractive for many electrochemical phenomena, e.g., important for energy and biological systems, they become impractical due to extremely fast response times ($\ll$ 10 ns, or frequencies $\gg$ 10 MHz) in concentrated

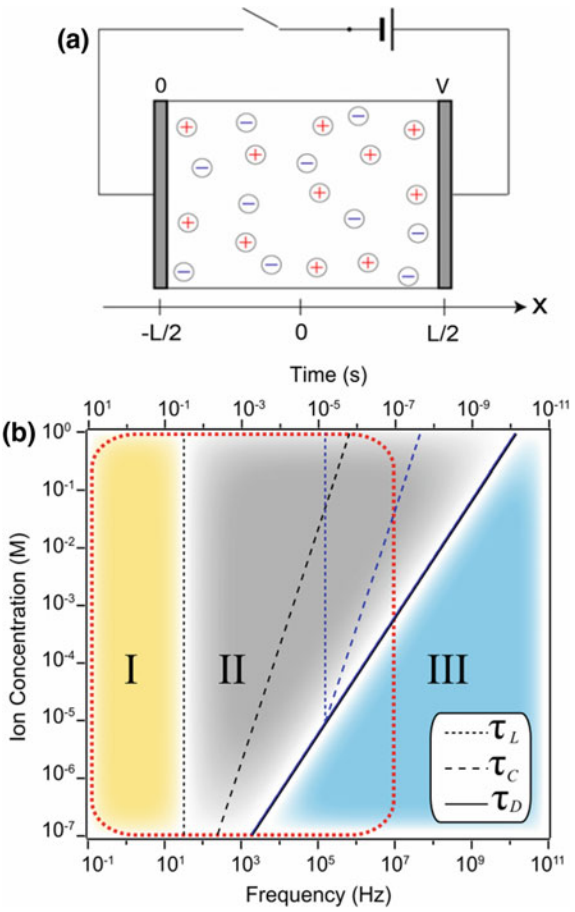

Fig. 13.2 **a** Simplified 1D capacitor model in which the electrodes have a separation L. **b** Phase diagram of the characteristic timescales (Debye time, τ_D), bulk diffusion, τ_L, and charge relaxation, τ_C as a function of NaCl concentration for L = 200 nm (blue) and 15 μm (black) electrode separation representing tip- and cantilever-sample, respectively. The region enclosed by the red dashed line indicates the frequency space accessible by AFM. The shaded regions indicate the different electrochemical regimes where (I) Faradaic and (II) ion diffusion processes are expected to dominate the response and (III) where ion dynamics are largely absent (i.e., quasistatic equilibrium). Adapted from permission [38]

solutions (>10 mM, region I and II). These time scales are outside the frequency space addressable with existing AFM methods.

13.2.1.3 Poisson-Nernst-Planck Equation

In the above descriptions of EDL dynamics, the equations only give a very rough estimate of the expected relaxation times. A full numerical description of electrolyte behavior (e.g., evolution of concentration, charge and potential gradients) as a function of bias and time requires solving the Nernst-Planck equation [31, 34, 39]. This equation is an extension of Fick's law of diffusion and describes the influence an electric field has on the motion of ions in a fluid. The gradient of the chemical potential of the i-th ionic species, μ_i, has the form:

$$\nabla \mu_i = \frac{k_b T}{c_i} \nabla c_i + z_i e \nabla \Psi \tag{13.4}$$

Here, z_i is the valence of the i-th ionic species and e the elemental charge. Any gradient in chemical potential will lead to a flux $\vec{F}_i$ of ions given by:

$$F_i = -M_i c_i \nabla \mu_i \tag{13.5}$$

Combining (13.4) with the Einstein relation, $M_i = D_i / k_B T$, relating ion mobility (M_i) and diffusivity (D_i), we can write the ionic flux $\vec{F}_i$ as:

$$F_i = -D_i \left(\nabla c_i + \frac{e z_i c_i}{k_B T} \nabla \Psi \right) \tag{13.6}$$

The first term in the bracket is the flux due to diffusion and the second term the flux due to electromigration. The general continuity equation for a static fluid (i.e., vanishing average fluid velocity) is given by:

$$\frac{\partial c_i}{\partial t} + \nabla F_i = 0 \tag{13.7}$$

leading to the Nernst-Planck equation:

$$\frac{\partial c_i}{\partial t} - D_i \nabla \left[\nabla c_i + \frac{e z_i c_i}{k_B T} \nabla \Psi \right] = 0 \tag{13.8}$$

The equation is closed by the Poisson equation used to relate charge and potential:

$$\Delta \Psi = \frac{1}{\epsilon \epsilon_0} \sum e z_i c_i \tag{13.9}$$

With ϵ and ϵ_0 being the relative and absolute dielectric permittivity. Equations (13.8) and (13.9) are referred to as the Poisson-Nernst-Planck equations. For concentrated solutions, and/or high voltages $\left(V_{tip} \gg \Psi_{th}\right)$, the Poisson-Nernst-Plank equation requires modifications to overcome the approximations made in its formulation (i.e., dilute solution of point-like charges, interacting through their mean-field electrostatic force). In particular, even for dilute solutions, the Poisson-Boltzmann theory becomes strongly non-linear and predicts unphysical ion concentrations at the solid-liquid interface, even at relatively low potentials (e.g., a few times Ψ_{th}). In the high potential regime $(\Psi \gg \Psi_{th})$, the assumption of a dilute solution of point-like charges breaks down near the electrode surface and steric effects need to be considered [35]. This has motivated researchers to modify the standard equations to overcome its limitation in concentrated solutions and at large potentials [31, 34, 40, 41].

Collins et al. modelled the time-dependent potential, ion concentration, and charge density distribution in a plate capacitor, mimicking a simplified tip/cantilever gap at high voltages $\left(V_{tip} \gg \Psi_{th}\right)$, as shown in Fig. 13.3 [38]. Following Kilic et al. [34], the authors numerically solved modified Poisson-Nernst-Planck equations taking into account steric effects, corresponding to the following model for the chemical potential:

$$\mu_{\pm} = k_B T \ln(c_{\pm}) \pm z_i e\psi - k_B T \ln(1 - c_+ a^3 - c_- a^3) \tag{13.10}$$

where c_+ and c_- are the concentration of positively and negatively charged ions, respectively, which for simplicity are assumed to have the same effective molecular length scale, a. The modified Poisson-Nernst-Planck equation becomes [34]:

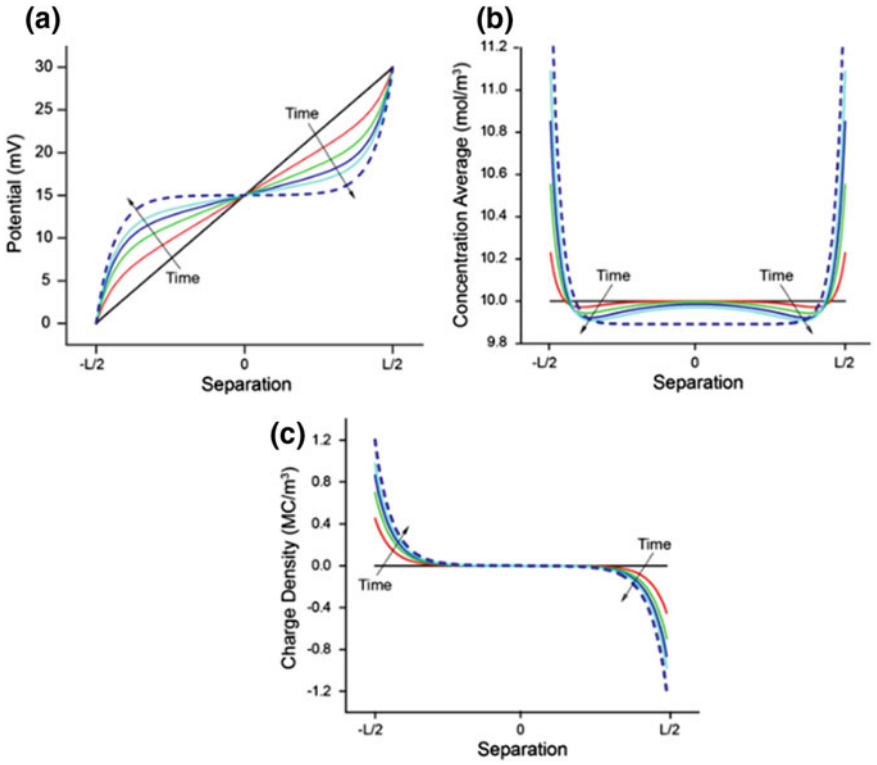

Fig. 13.3 Calculated evolution of the **a** potential **b** average ion concentration and **c** charge density distributions between parallel plate electrodes in a 10 mM, 1:1 electrolyte (ion diffusivities: D + = D− = 10^{-9} m^2/s) in response to the application of a 30 mV voltage step (electrode separation: L = 200 nm). Solid lines show density distributions in 30 ns time steps after application of the voltage at t = 0. The dashed line shows the distribution at t = 50 μs. Reproduced with permission [38]

$$\frac{\partial c_i}{\partial t} = D\nabla^2 c_{\pm} \pm \frac{D}{k_B T} ze\nabla \cdot (c_{\pm}\nabla\psi) + a^3 D\nabla \cdot \left(\frac{c_{\pm}\nabla(c_+ + c_-)}{1 - c_+ a^3 - c_- a^3}\right) \tag{13.11}$$

Since we do not account for Faradaic reactions at the electrode surface (i.e., an ideally polarized electrode) a no-flux boundary condition ($F_i = 0$) for ions at the electrodes was used. To account for the effect of ion crowding at the interface, a condensed layer boundary condition for the potential at the electrode (as discussed by Bazant et al. [31]) was used as:

$$\psi(x=0) = \psi_{electrode} + \lambda_s \frac{\partial \psi}{\partial x}(x=0) \tag{13.12}$$

where $\psi_{electrode}$ is the electrode potential, which is reduced by the condensed layer by $\psi_{x=0}$ at the surface of the electrolyte and $\lambda_s = \varepsilon / C_s$ is a measure of its thickness, where C_s is the fixed capacitance of the layer.

A time-dependent potential, ion concentration, and charge distribution in the electrode junction was observed, reaching a steady state condition in less than 50 μs (dashed line in Fig. 13.3). Once the circuit was closed, ions underwent electro-migration in response to the applied electric field, forming EDLs which eventually screened the electrode potential. The ion concentration gradient away from the electrode surface induced diffusion of ions towards the electrodes, resulting in a net uptake of ions from the neutral bulk electrolyte (e.g., midplane between the capacitor plates) into the EDL. This process took place on the timescale τ_L, which is much slower than the Debye time, as it is governed by the geometry of the system. Notice also in Fig. 13.3b, that the neutral bulk ion concentration was reduced initially in a region just outside the diffuse charge layer. Diffusion of ions from the bulk electrolyte (outside the EDL) slowly filled in the depleted regions, until a uniform equilibrium was achieved. This type of numerical analysis can be used to develop a deeper understanding regarding the type of spatial and temporal dynamics which are impossible to capture analytically and are crucial for understanding VM AFM force interactions in the presence of mobile ions.

The net force acting on the electrode will be heavily influenced by both electrostatic and osmotic pressure. The total pressure on the surface of the electrode or at any point of the electrolyte solution, P_{total}, can be calculated as the sum of hydrostatic pressure P_0, the osmotic pressure, P_{osm}, and the electrostatic pressure, P_{el} (i.e., $P_{total} = P_{el} + P_{osm}$). The electrostatic pressure, governed by Maxwell stress acting on the uncompensated charge at the electrode, can be obtained from the solution of the modified Poisson-Nernst-Planck equation [34, 38] given by $P_{osm} = \frac{\sigma^2}{2\varepsilon_0 \varepsilon}$, where σ is the electrode surface charge density. The osmotic pressure, on the other hand, is caused by ion concentration gradients and is given by [41]:

$$P_{osm} = \frac{k_B T}{a^3} \ln\left(\frac{1 - c_+ a^3 - c_- a^3}{1 - c_+^0 a^3 - c_-^0 a^3}\right) \tag{13.13}$$

At equilibrium, the forces at any point in the solution are balanced. In the following, we consider a plate capacitor with a fixed 50 nm electrode separation with identical electrodes (i.e., no CPD) with an AC voltage of 1 V amplitude at a frequency of $f_{el} = 30$ kHz applied across the electrode plates. The force on the plates, determined from the solution of a modified Poisson-Nernst-Planck equation [34, 38] and (13.13), was purely capacitive (i.e., no CPD between the plates), having only a second harmonic response at double the excitation frequency $(2f_{el})$. Figure 13.4b shows the normalized net pressure at the terminal plate as a function of increasing ion concentration. In deionized water, the response was shown to be purely capacitive at this drive frequency with no significant deviation from a sinusoidal pressure acting on the electrode. However, even in the presence of a very low ion concentration (100 μM) the response became distorted, i.e., deviated from a sine wave, becoming increasingly non-linear with increasing salt concentration. The non-linearities arise from the coupled charge dynamics that influence both P_{el} and $P_{osm.}$ These results demonstrate that, at a frequency typical for VM AFM experiments, the response transitions from an almost perfect sine response in deionized water to a highly non-linear response even at ion concentration as low as 1 mM. In Fig. 13.4c, we provide a frequency spectrum of the deflection signal (a thermal noise spectrum) of a voltage modulated cantilever in 250 mM NaCl over a HOPG electrode. As many as 5 harmonics of the drive voltage frequency were detected above the noise floor of the cantilever, indicating that the cantilever dynamics are highly non-linear. While it is difficult to ascribe these higher harmonics to ion dynamics alone, as non-linearities can also arise from cantilever dynamics, including surface tapping, and hydrodynamic effects, as well as Faradaic reactions, the results shown in Fig. 13.4b can qualitatively explain these observations. To investigate the precise physical mechanism of such non-linearities, techniques such as intermodulation EFM [42] and G-Mode KPFM [43, 44], which can capture multiple channels of information simultaneously, could prove useful (see the chapter by Jesse et al. in this book).

The above mentioned numerical models are based on continuum and mean field theories, where the behavior of the liquid and the ionic charges can be described on length scales much larger than molecular length scales. To understand electrostatic interactions on molecular length scales important for protein folding, for example, new and more sophisticated models are required. Here, VM AFM offers the unique opportunity to test these theories on the relevant molecular length scales. In the following section, we outline the basic physical principles for measuring electrostatic forces using AFM.

13.2.2 Practical Implementations of VM AFM

The electrostatic force caused by an alternating voltage between an electrically conducting tip and sample can be derived from the energy $E = 1/2CV_{TS}^2$ stored in the

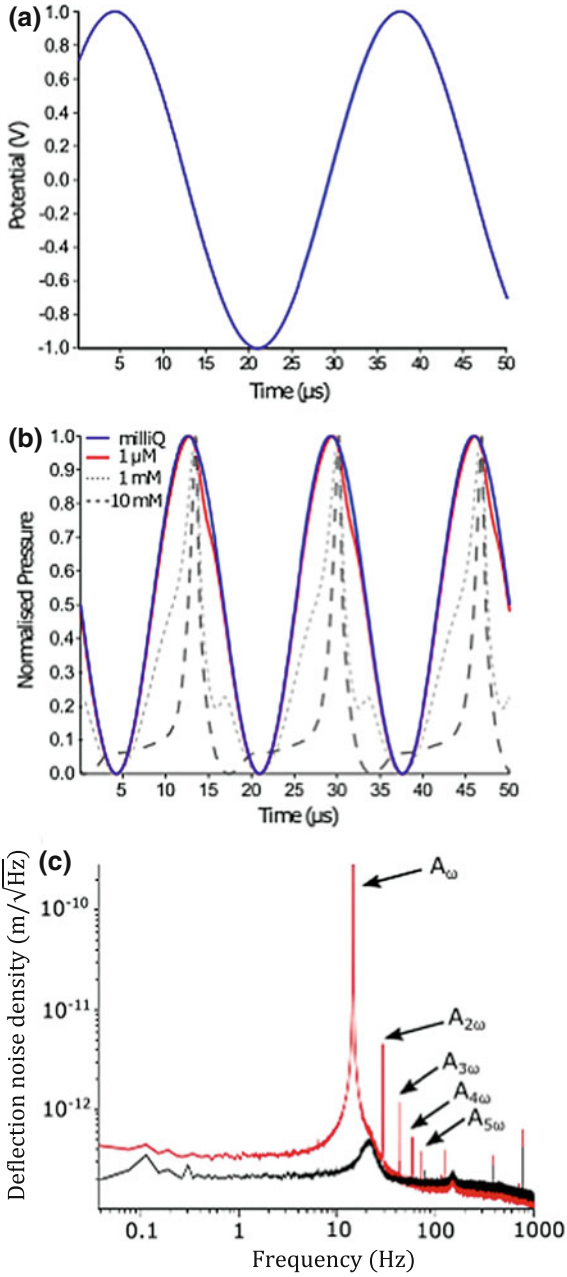

Fig. 13.4 **a** A segment of the AC voltage excitation applied between parallel plate electrodes (Amplitude = $2V_{p\text{-}p}$; frequency = 30 kHz. Evolution of the **b** Normalized total pressure demonstrating increased non-linearity of the response with increasing ion concentration. (ion diffusivities: $D_+ = D_- = 10^{-9}$ m^2/s; electrode separation: L = 50 nm) **c** Deflection spectra of a Pt/Ir coated cantilever located 150 nm above a grounded HOPG surface in 250 mM NaCl while the cantilever is grounded (black) and voltage modulated with a V_{ac} of 3 $V_{p\text{-}p}$ at a frequency of 12.5 kHz (red). Arrows highlight presence of higher harmonics in the VM case

capacitor C formed by the tip-sample gap. Here, $V_{TS} = V_{tip} - V_{CPD}$ is the voltage between tip and sample, consisting of the externally applied tip voltage $V_{tip} = V_{DC} + V_{AC}\sin(2\pi f_{el} t)$ and the CPD between tip and sample, V_{CPD}. The force

can be derived by differentiating the energy with respect to the tip-sample distance z. The dynamic forces at the first and second harmonic frequency are:

$$F_f = C_z^{'} V_{AC}(V_{DC} - V_{CPD}) \sin(2\pi f_{el} t) \tag{13.14}$$

$$F_{2f} = \frac{1}{4} C_z^{'} V_{AC}^2 \cos(4\pi f_{el} t) \tag{13.15}$$

In EFM, the first or second harmonic response is monitored typically without any application of a DC bias. To gain quantitative information on the V_{CPD} distribution on the surface, KPFM is used. According to (13.14), the compensation of the electrostatic interaction by setting $V_{DC} = V_{CPD}$ nullifies the amplitude at f_{el}. In KPFM, a feedback loop minimizes the first harmonic amplitude $A_f = G(f)F_f$ (where $G(f)$ is the frequency-dependent mechanical transfer function) by adjusting V_{DC} to measure V_{CPD} (closed-loop, or CL-KPFM operation). CL-KPFM is the standard operation mode for ambient conditions and available on almost every commercial AFM platform, however, the requirement for DC bias regulation causes catastrophic effects in aqueous solutions [45]. These problems are circumvented by open loop (OL) or dual harmonic (DH) KPFM. Here, the first and second harmonic amplitude response (A_f and A_{2f} to an alternating voltage are measured. Dividing A_f by A_{2f} and solving for V_{CPD} yields:

$$V_{CPD} = \frac{1}{4} V_{AC} \mathrm{X}_{12}(f) \frac{A_f}{A_{2f}} \tag{13.16}$$

$\mathrm{X}_{12}(f) = G(f)/G(2f)$ is a correction factor that takes into account the resonance enhancement (transfer gain) for the two frequencies. To ensure that $\mathrm{X}_{12}(f)$ is not changing during the course of a measurement, e.g., by strong tip-sample forces or changes in the damping, it is advisable to choose frequencies far away from the mechanical resonance frequency. The off-resonance detection inevitably results in a reduced signal-to-noise ratio. Recently, multi-frequency open loop approaches to KPFM using either band excitation [46, 47] or non-linear frequency mixing have been proposed [48, 49]. These on-resonance techniques are expected to have improved signal to noise, as well as avoiding the requirement for cantilever transfer function correction. So far, these approaches have only been demonstrated in air.

13.3 Applications of EFM in Liquid

Surface charges at the solid-liquid interface govern a myriad of important processes, which has ultimately driven the exploration of AFM-based measurements of the EDL structure. In this section, the use of AFM-based applications to measure

charge in liquid environments is discussed, starting from early force-distance or lift-mode measurements in different pH solutions and ionic concentrations, to more recent high resolution force-volume measurements for mapping the EDL structure. After that, we review in detail recent applications of EFM measurements in liquid. As shall be outlined in this section, the removal of the requirement for bias feedback regulation makes liquid EFM measurements a very promising approach.

13.3.1 Bias-Free Approaches

Early attempts to relate AFM force-distance curves to surface charges were a direct extension of surface forces apparatus studies [50, 51]. These measurements, performed as a function of salt concentration and pH and utilizing a colloidal sphere attached to an AFM cantilever, were found to be in agreement with Derjaguin, Landau, Verwey, and Overbeek (DLVO) theory [50, 51]. Butt used an analytical model to show that the electrostatic force measured by an AFM tip (i) increased with increasing surface charge density, (ii) decayed exponentially with distance from the surface, and (iii) could be reduced with increasing salt concentration [52]. These findings were verified experimentally shortly thereafter [53]. Several groups noted the importance of knowing the size and shape of the tip for localized, quantitative measurements [53–55] Distinguishing between various surface forces, e.g., electrostatic, hydration, van der Waals, present in an electrolyte solution has been discussed in several papers [53, 56, 57]. Butt, also showed that local surface charge densities of bacteriorhodopsin membranes could be measured in electrolyte solutions using force-curves with knowledge of the charge density of an alumina substrate which was used as a calibration standard [58]. Colloid probe measurements [50] have also proven useful for measurements of charge density and Debye length as a function of pH, electrolyte type, and concentration, finding agreement with the DLVO theory for large separations and in the low potential regime [50, 57, 58, 59, 60]

By extension, force-distance curves can be recorded in a sparse grid, or force-volume mode, providing a spectroscopic imaging mode. Force mapping in electrolyte solutions has been performed by several groups, notably Rotsch and Radmacher [61] and Heinz and Hoh [62]. Force-volume imaging allows a number of parameters including height, adhesion, electrostatic forces, and decay length (from exponential fit) to be mapped in 3D spatial co-ordinates [61]. Sotres and Baró showed that the approach can be used to resolve the EDL force of DNA [63] and plot force maps at different tip-sample distances [64]. Recently, fast force-volume modes have become standard on some commercial AFMs, enabling faster spectroscopic imaging of electrostatics in aqueous solutions [65]. Electrostatic force-volume imaging has also been implemented in liquid using FM-AFM [66, 67]. Umeda et al. [67] applied 3D FM-AFM force mapping to visualize the EDL

force of DNA in high molarity electrolyte (100 mM KCl), finding good agreement with calculations [67].

Several groups reported that contact mode AFM imaging was sensitive to electrostatic forces in aqueous solutions depending on the choice of imaging force [61, 68, 69, 70]. The idea of reducing electrostatic repulsion to enable low imaging force [52] is widely used to enable high-resolution contact mode imaging of soft biological samples, notably by Müller [71]. In fact, imaging a surface under different salt concentrations provides a route to distinguish electrostatic from purely topographic interactions. Heinz and Hoh demonstrated this approach using lipid bilayers and bacteriorhodopsin membranes, wherein the subtraction of topographs recorded in contact mode at different salt concentrations allowed an electrostatic surface map to be obtained [62]. Philippsen et al. used this approach to reveal the electrostatic potential of transmembrane channels with 1 nm lateral resolution [72].

In another approach, Johnson et al. showed that electrostatic force could be measured using a lift-mode technique wherein the first line scan, operated in intermittent contact mode, recorded topography and the static-mode lift scan measured electrostatic force [73]. These so-called charge density maps can then be quantified using numerical simulations [74, 75]. The technique was used to characterize DNA and lipid bilayers [73–75].

13.3.2 Applications Utilizing Constant Voltage

Application of a DC bias is a prerequisite for both CL-KPFM and electrochemical measurements. Raiteri and Butt investigated bias-dependent forces acting on a cantilever with a metal coating on one side in aqueous electrolyte. The measurements were performed in an electrochemical cell, in which current flow between cantilever and counter electrode and voltage drop between cantilever and a reference electrode were measured simultaneously with the forces acting on the cantilever. The cantilever response to voltage pulses was also recorded as a function of time, revealing relaxation times of dynamic processes [76]. The counter electrode was too far away from the cantilever $(d \gg \lambda_D)$ to explain the force in terms of an electrostatic interaction between the electrodes. The authors concluded that electrochemically-induced surface stress, i.e., the surface energy due to ion adsorption and the EDL, could explain the results [76]. In a similar implementation using a metal sample as the working electrode, an insulating tip, and reference and counter electrodes, Raiteri et al. investigated platinum and gold electrodes, reporting a bias-dependent topography of the Au(111) surface with a transition between $\sqrt{3} \times \sqrt{3}$ and $1x1$ surface reconstructions at –0.3 V relative to the standard hydrogen electrode [59]. Döppenschmidt and Butt used HOPG as the working electrode, finding agreement at negative potentials with Poisson-Boltzmann theory [77]. The same setup was used by Hillier et al. for force and electrochemical

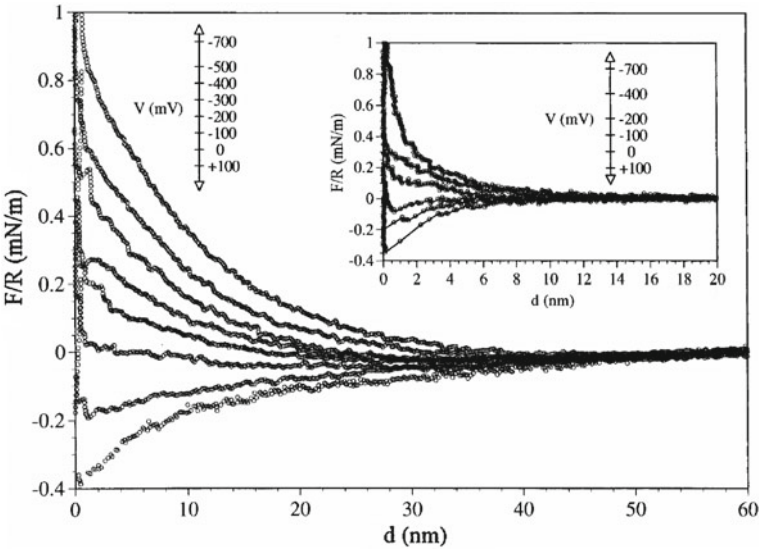

Fig. 13.5 Colloid probe measurement showing the force between a silica sphere and gold electrode in an aqueous solution of 10 mM (inset: 100 Mm) KCl as a function of the electrode potential (vs. saturated calomel electrode). Reproduced with permission [60]

measurements between a silica probe and silica or gold surfaces [60]. The silica-silica forces could be described by DLVO theory [60]. The force between silica and gold was measured as a function of potential applied to the gold electrode (Fig. 13.5) revealing that the electrostatic repulsion decreased as the bias increased from –700 to 100 mV versus saturated calomel electrode [60]. In addition, the 'potential of zero force' could be determined as a function of separation by sweeping the potential applied to the gold electrode (Fig. 13.6) [60]. This measurement procedure bears resemblance to open loop bias spectroscopy (OLBS), sometimes referred to as Kelvin probe force spectroscopy (KPFS), a useful method for CPD determination [45]. Hu et al. used semiconducting TiO_2 as the working electrode, allowing the role of electrode potential and adsorbed species on band bending and EDL formation to be investigated [78]. Raiteri et al. used an electrically connected gold substrate and gold sphere attached to an AFM cantilever as the working electrode in an electrochemical setup with counter and reference electrodes to measure and control the force between the two gold surfaces [79].

Force-volume imaging modes can also be implemented during the application of DC bias and in three-electrode electrochemical configuration [65]. Marlière and Dhahri used such an approach to map the charge distribution of bacteria in physiological environments [65].

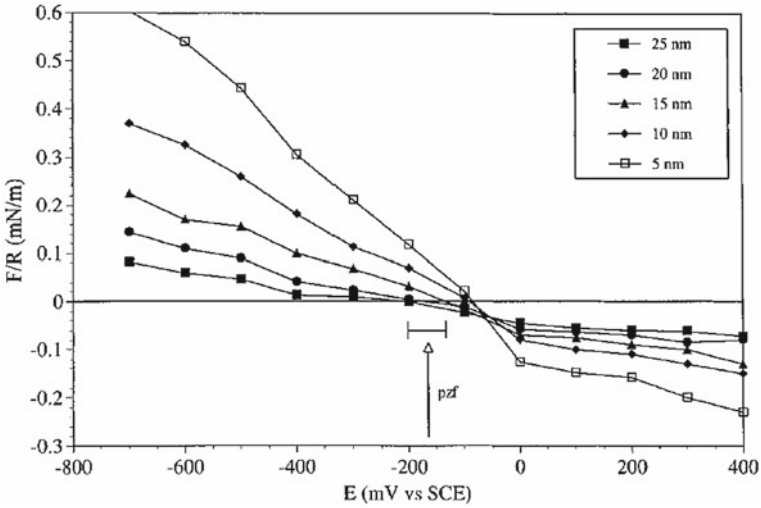

Fig. 13.6 Colloid probe measurement showing the electrode potential dependence of the force between a silica sphere and gold electrode in 10 mM KCl solution with increasing separations between 5 and 25 nm. The potential of zero force (pzf) is shown. Reproduced with permission [60]

13.3.3 Applications Utilizing Voltage Modulation

Voltage modulation further opens the door to measure dynamic, frequency-dependent electrostatic forces. The group of Simpson developed a technique called dielectrophoretic force microscopy that utilized a conductive cantilever to which an AC voltage was applied during alternating line scans [80–82]. In this manner, separate images of topography and topography combined with electric force were recorded. In this way, the dielectric force could be isolated and visualized, generally at high (~MHz) frequencies, as demonstrated on bacteria [80]. Dielectric spectra were also obtained by sweeping the frequency of the ac field to perform dielectrophoretic spectroscopy of individual mammalian red blood cells [82]. In another VM approach, Rodriguez et al. applied an AC voltage between interdigitated electrodes in water and measured the resulting dynamic torsion and deflection of the cantilever at the modulation frequency in lift mode [83].

Rodriguez et al. also performed a contact mode VM approach in liquid environments called piezoresponse force microscopy (PFM) [84]. PFM is similar to EFM in that an AC voltage is applied to the tip and the first harmonic response of the tip is recorded [85]. In the case of PFM, the response is generally related to surface deformations, whereas in EFM, the response is generally related to the electrostatic force on the tip and lever [86]. In a parallel to the early contact mode work showing that the electrostatic contribution to image contrast could be

influenced by choice of setpoint, [61, 68, 69, 70]. Rodriguez et al. showed that contrast in a liquid PFM experiment could be tuned between largely electromechanical origin to largely electrostatic origin by lowering the imaging force until the tip loses contact with the surface [84]. Rodriguez et al. further demonstrated solvent- and bias-dependent control over ferroelectric switching [87].

Electrostatic forces have also been used to actuate the cantilever in dynamic mode AFM [88–92]. Several approaches have been reported, including those that apply AC voltage between conducting cantilevers and substrates [88–90]. Some approaches have adopted bespoke cantilever holders for contacting one or more electrodes on the back of the cantilever [92], or between a metal coated liquid cell window and the reflective, conductive coating of a cantilever (Fig. 13.7, top) [93]. Zhang et al. used the latter to obtain lattice-resolved images of mica (Fig. 13.7, bottom), noting improvements obtained via application of a DC bias in addition to the AC voltage [93]. Umeda et al. [89] explored the frequency dependence of the capacitive actuation of a VM probe, as shown in Fig. 13.8. They observed a trend in the data which suggested that in the low frequency regime the response was dominated by a surface stress component [94]. The authors observed a transition frequency inherently linked to the dielectric properties of the solution [89]. By comparing different liquid media (KCl, acetronitrile, acetic acid, fluorocarbon liquid), the surface stress contribution became larger with increasing dielectric

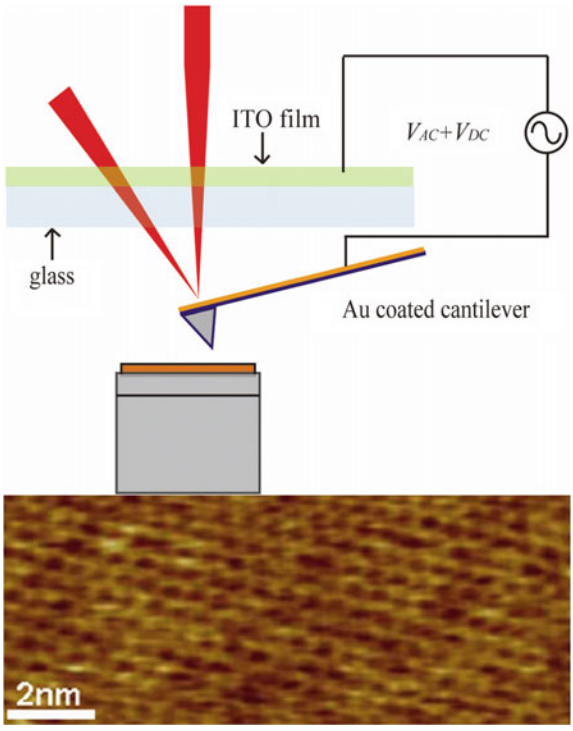

Fig. 13.7 (top) Schematic of electrostatic actuation of dynamic AFM. (bottom) High resolution image of mica obtained in 0.1 M KCl solution using the capacitive force driving method to drive the cantilever oscillation. Reproduced with permission [93]

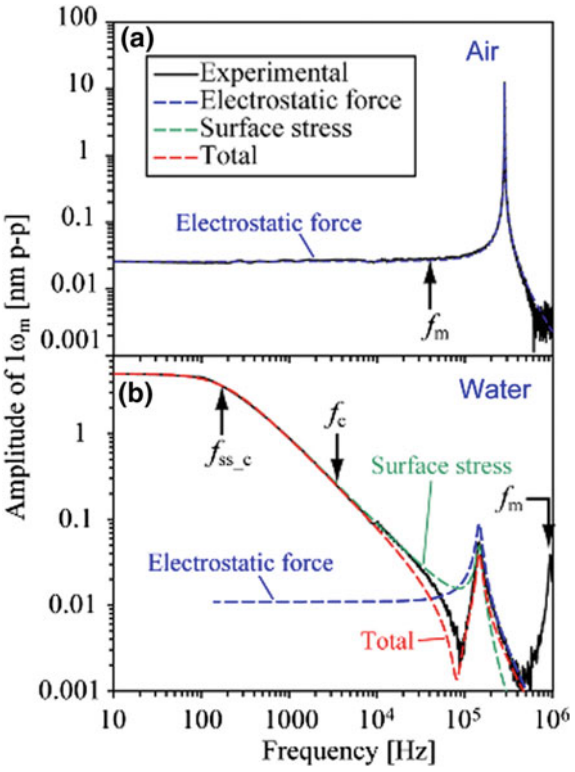

Fig. 13.8 Frequency response curves of the first harmonic amplitude as a function of frequency measured in **a** air and **b** deionized water with broken curves showing fits for the various force components considered. Reproduced with permission [94]

constant of the liquid medium. It is believed that operation well above this frequency can allow largely un-inhibited electrostatic actuation of the cantilever.

Recently, Marchand et al. [91] used an electrically driven approach to record non-contact images of self-assembled monolayers on gold (Fig. 13.9). In this implementation, the second harmonic response to the electrical drive was used for height control.

The group of Gomila has pioneered the use of EFM to quantitatively map dielectric constants of biomaterials such as viruses [95], DNA [96], bacteriorhodopsin [97], lipid bilayers [97], and bacteria [98, 99] in air. Measurements are made possible via numerical analysis and the group has extended their modeling in air [100] to liquid environments [101], allowing the dielectric constants of lipid bilayers to be measured in liquid (Fig. 13.10) [102]. In a series of papers from this group, the importance of the frequency dispersion of the electrostatic force in electrolytes of varying molarity were investigated.

Based on the work by Sounart et al. and Panchawagh et al. [103, 104], Gramse et al. approximated the critical frequency, f_c, for realizing liquid EFM using a simplified equivalent circuit model (Fig. 13.11) [101, 105]. The EDLs formed at the tip and sample (C_{EDL}) are treated as capacitors in series with the sample capacitance (C_{sample}) and solution resistance (R_{sol}). C_{EDL} is often assumed to be much higher

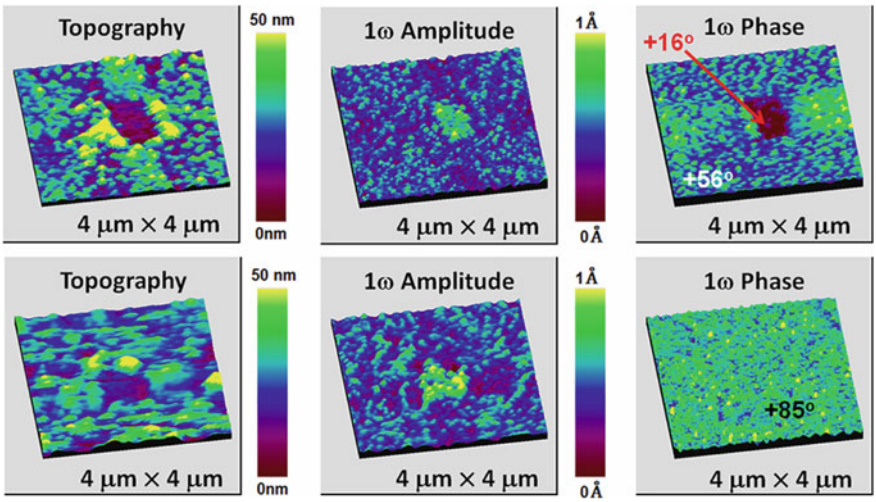

Fig. 13.9 Noncontact images of gold surfaces covered with self-assembled monolayers of Au-$SC_{11}H_{22}COOH$, top, and Au-$SC_{11}H_{22}NH_2$, bottom, measured using electrostatic actuation. Imaging was performed using the $2f$ amplitude for feedback control while monitoring the f amplitude and phase. Reproduced with permission [91]

than the capacitance of the passivation layers on the sample, C_{sample}, and can be neglected since the capacitances are in series, as shown in Fig. 13.11 [31]. Assuming a parallel plate model, the capacitive and resistive elements can be described per unit area as [103, 106]:

$$R_{sol} = \frac{z}{\sigma_{mol} c} \tag{13.17}$$

$$C_{sol} = \frac{\epsilon_0 \epsilon_{r,sol}}{z} \tag{13.18}$$

$$C_{sample} = \frac{\epsilon_0 \epsilon_{r,sample}}{z}, \tag{13.19}$$

where the conductivity of the solution is expressed as $\sigma_{sol} = \sigma_{mol} \cdot c$, with the molar conductivity σ_{mol} and the ion concentration c, z is the electrode separation, h the height of the samples dielectric layer, ε_0 is the permittivity of free space, and ε_r represents the relative solution or sample permittivity. As R_{sol} and C_{sol} are distance dependent, the complex geometry of the AFM probe (i.e., cantilever, cone, apex) will require more sophisticated circuit models including an infinitesimal number of coupled circuits (Fig. 13.11c). Gramse et al. performed measurements on Si/SiO_2 test structures as a function of frequency in a number of ionic concentrations (Fig. 13.12). In their amplitude modulated EFM configuration, they could show that a very high electrical carrier frequency (MHz) was needed to map spatial

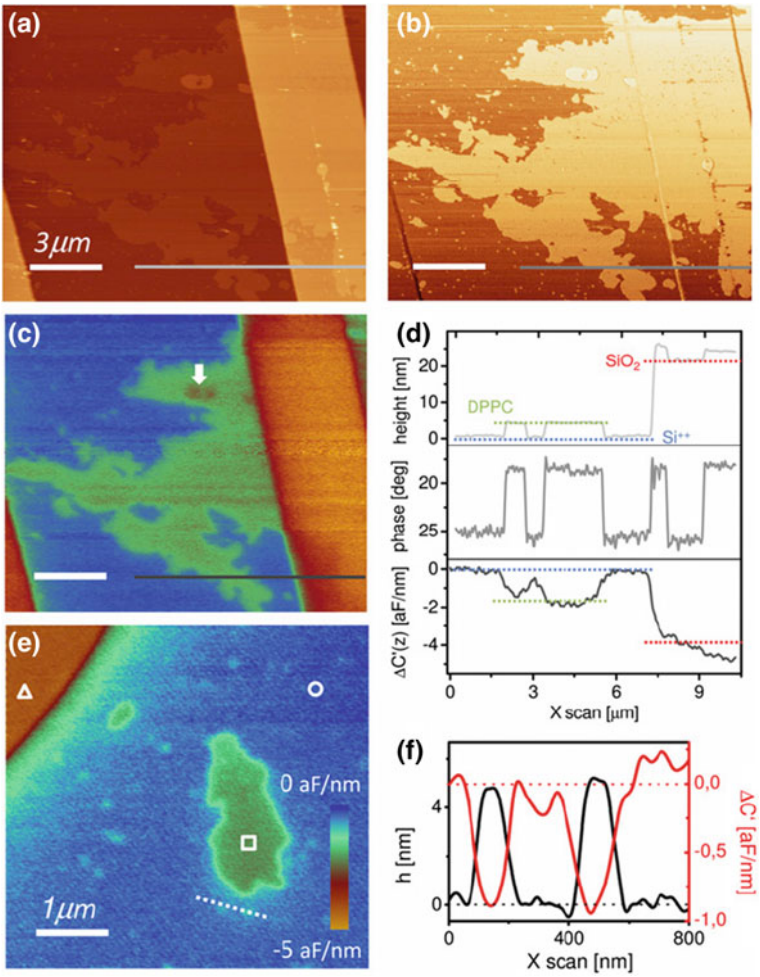

Fig. 13.10 **a** Topography, **b** phase, and **c** dielectric images of phospholipid (DPPC) patches adsorbed onto SiO_2 (z = 80 nm, f = 80 MHz and $V_0 = 0.25$ V amplitude. **d** Profiles of topography, phase and dielectric images. **e** Zoomed-in dielectric image of isolated lipid bilayer patches next to the SiO2 structure, acquired at z = 50 nm. **f** Topographic and dielectric profiles of two closely spaced ~100-nm bilayer patches (taken along the dashed light-gray line in panel e). Reproduced with permission [102]

variation in dielectric properties. The transition frequency, above which EFM operation needed to be performed, corresponded to:

$$f_c = \tau_{RC}^{-1} = \frac{1}{2\pi R_{sol} C_{eq}} = \frac{h\sigma_{sol}}{\pi \varepsilon_0 \varepsilon_d z} \tag{13.20}$$

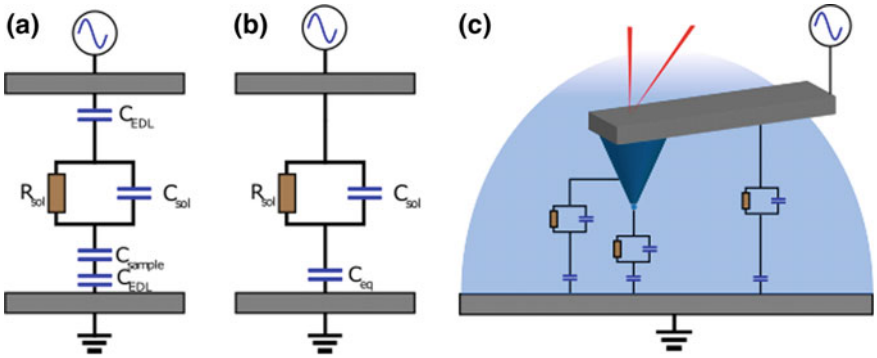

Fig. 13.11 **a** Equivalent circuit model of the tip-sample EDLs where C_{dl} is the EDL capacitance, C_{sample} is the sample capacitance, C_{sol} and R_{sol} are the solution capacitance and resistance, respectively. **b** Simplified equivalent circuit model where the EDL and sample capacitance are represented as an equivalent capacitance (C_{eq}). **c** Schematic of the complex tip sample geometry which can be represented as coupled circuit models as a result of the different length scales of the systems (i.e., R_{sol} and C_{sol} are distant dependent)

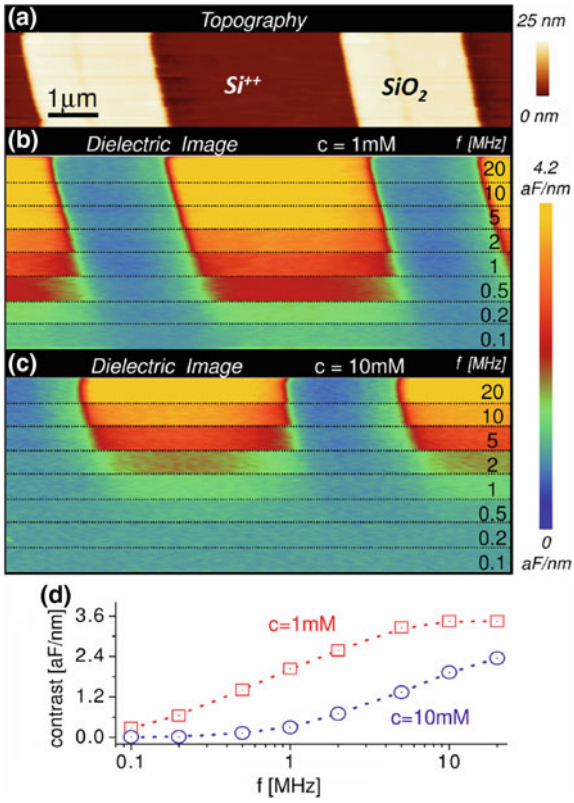

Fig. 13.12 **a** Topography and **b** and **c** dielectric contrast images of 20 nm thin and 2.5 μm wide Si/SiO_2 micro-stripes. Dielectric images were obtained at 100 nm separation in electrolyte having ion concentrations **b** c = 1 mM and **c** c = 10 mM. The applied frequency **f** was changed from 20 to 0.1 MHz to show how the image contrast depends on the frequency and finally disappears at low frequencies. **d** Dielectric contrast extracted from images **b** and **c** as a function of the applied frequency. Reproduced with permission [105]

where C_{eq} is the equivalent capacitance of the system. The electric force acting on a conductive probe in response to an applied AC voltage, $V(t) = V_0 \sin(\omega t)$, was approximated as;

$$[F_\omega(z,t)] = \frac{1}{4}\frac{\partial C_{sol}(z)}{\partial z}\frac{f/f_{eq}}{1+f^2(1/f_{eq}+1/f_{sol})^2}V_0^2 \tag{13.21}$$

Considering $\partial C_{sol}(z)/\partial z = -\varepsilon_0\varepsilon_r/z^2$ (per unit area), it is possible to explain the frequency dependence of the electrostatic force in electrolytes with different ion concentrations (Fig. 13.12d). The sigmoidal frequency dependence of the electrostatic force is in agreement with that found previously for the field of microelectromechanical systems [107]. Similar to the discussion regarding relaxation processes in Fig. 13.2b, the sigmoidal frequency dependence in Fig. 13.12d, which was previously reported for MEMS devices [103], can be split into three possible regions dominated by very different imaging mechanisms. Firstly, at low frequencies, $f \ll f_c$, where the excitation timescale is much larger than the response time of the ions in solution, the system will be in equilibrium with the EDL screening fully established, and hence no electrostatic force or actuation will be detected. At intermediate frequencies, $f \approx f_c$, the magnitude of actuation increases over a broad frequency range, suggesting the dynamic processes (ion migration and diffusion) will result in partial screening of the electrode and attenuation of the actuation is observed. At high frequencies, $f > f_c$, the polarity of the electric field changes at a rate faster than that of ionic response and thus electrostatic shielding can be avoided. Kumar et al. recorded VM force-distance curves to extract Stern potential and Debye length in electrolyte solutions [108]. The tip-sample capacitance model adopted in this work relies heavily on the Debye-Hückel linearization of the Poisson-Boltzmann equation, and hence is not expected to be valid for high molarity solutions (>100 mM) or for tip voltages above the thermal potential $\left(V_{tip} \gg \Psi_{th}\right)$.

The techniques discussed in this section deal largely with the measurement of electrostatic force resulting from surface charge, surface potential, EDL, etc. Often the origin of the force is elucidated by adjusting pH or ion concentration, fitting the distance dependence, or subtracting data recorded at different ion concentrations or separations. Quantification generally requires knowledge of the actual tip shape and in some cases of the surface charge and electric potential distribution, which typically necessitates some numerical analysis.

13.4 Applications of KPFM in Liquid

While KPFM has been widely used to quantitatively map surface potentials of nanostructures and molecular systems in ambient and ultra-high vacuum environments, for many systems at solid-liquid interfaces, in situ nanoscale electrical

measurements are required. In this section, we review such attempts at liquid KPFM, and discuss them in terms of their veracity, applicability, and reproducibility.

13.4.1 Macroscopic Kelvin Probe in Liquid

Quantitative surface potential measurements in liquid have been of interest to many research groups over several decades. Interestingly, attempts at extending the macroscopic Kelvin probe (KP) method from gaseous to liquid environments were first reported as early as 1968 [109]. Although studies are limited, a few groups attempted to test the performance of KP in a variety of solutions. Fort et al. [109]. performed a feasibility study of liquid KP noting that accurate and reliably measurements were only possible under a few polar liquids (toluene, bromo-benzene, bromo-decane) whereas difficulties were encountered in others (acetone, benzonitrile, decanol). The authors noted that KP measurements were not possible in partially conducting or non-polar liquids [109]. Several difficulties in realizing liquid KP were identified in these early studies [110], particularly related to parasitic and stray currents between the KP and sample electrodes due to the finite conductivity of the medium. Further complications arose from viscous damping of the KP due to liquid convection, EDL dynamics, and electrochemical reactions at the KP electrode. Bastide et al. [110]. demonstrated surface photovoltage of semiconductor surfaces immersed in liquids. In their approach, the probe was completely insulated from the liquid and measurements were performed through a glass slide to avoid the complications outlined above.

Clearly, if the macroscopic KP community had realized a simple methodology for the transition from gas to liquid operating conditions, such an approach would already be readily available. However, these results are very telling, and the findings are indicative of the complex range of electrostatic and electrochemical phenomena that occur at the solid-liquid interface.

13.4.2 Applications of Classical KPFM in Non-polar Liquid

The first major breakthrough in liquid KPFM was the implementation of classical KPFM in electrically insulating nonpolar solvents by Domanski et al. [111]. We denote the classical KPFM method as that described by Nonnemacher et al. which employs CL bias feedback to compensate the electrostatic interaction [25]. Domanski et al. studied the changes in work function of gold substrates upon hexadecanethiol chemisorption (Fig. 13.13) [111]. In this work, the authors demonstrated two routes to achieve a quantitative understanding of the adsorption process. In the first route, the tip was not present during the adsorption step and the work function of the tip was assumed to remain constant throughout, finding good agreement with UV photoelectron spectroscopy measurements in ultra-high

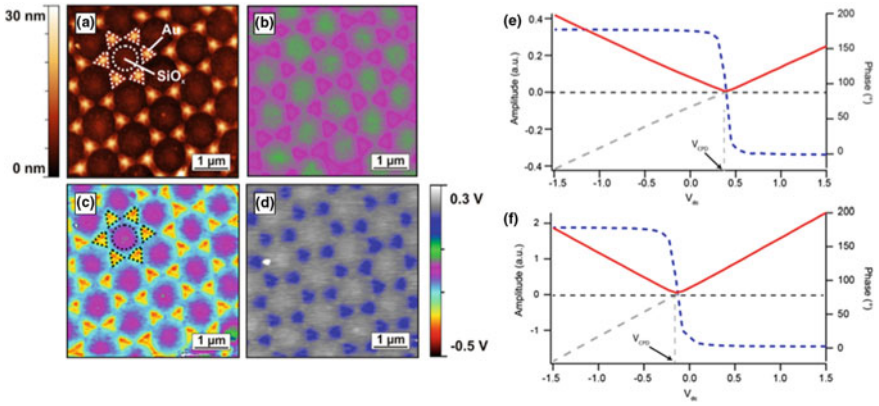

Fig. 13.13 **a** Topography image of a SiO_x/Au structure prepared by nanosphere lithography. KPFM images of the CPD measured in **b** Air and **c**, **d** decane **c** before and **d** after exposure to hexadecanethiol for 90 min. Reproduced with permission. [111] KPFS showing the oscillation amplitude (red line), phase (dashed blue line) and in-phase response (dashed grey line) in **e** ambient and **f** decane. KPFS was performed using a specified tip—sample separation of 200 nm, and voltage amplitude of 1 V with a frequency of 20 kHz applied to the tip

vacuum. In a second route, they used SiO_x/Au patterned substrates (Fig. 13.13), where the SiO_x was used as a reference to quantify changes in the gold work function upon thiol adsorption. Umeda et al. [94]. later reported surface potential measurements of a p-n patterned silicon sample imaged in fluorocarbon liquid. Note, although KP had been demonstrated macroscopically some 44 years previously, these two papers represented the first time such measurements could be performed with nanoscale spatial contrast.

The viability of KPFM in nonpolar solutions can be understood when one considers the open loop KPFM (or EFM) response, using KPFS, as shown in Fig. 13.13e, f [45]. The bias dependence of the electrostatic force can be measured by KPFS and compared to the theoretically expected curve. KPFS was performed over an electrochemically inert highly ordered pyrolytic graphite (HOPG) electrode in both ambient (Fig. 13.13e) and nonpolar (decane) solvent (Fig. 13.13f). The observed presence of a unique minimum is a prerequisite for the operation of CL-KPFM. The observed shift in CPD from air to decane, is likely a combination of the removal of the water layer from the tip and sample surfaces $\left(\Delta\Phi_{H_2O}\right)$ and the interaction between the decane molecules and electrode (tip and sample) surface modifying the permittivity. Assuming that the change in work function as a result of physisorption is similar for freshly cleaved HOPG as reported by Domanski et al. for gold [111], a similar value for $\Delta\Phi_{H_2O} = 0.18 \pm 0.01$ eV was obtained. This finding demonstrates the influence of the water layer in an ambient KPFM measurement, while also opening the possibility for well-controlled KPFM measurements in an insulating liquid.

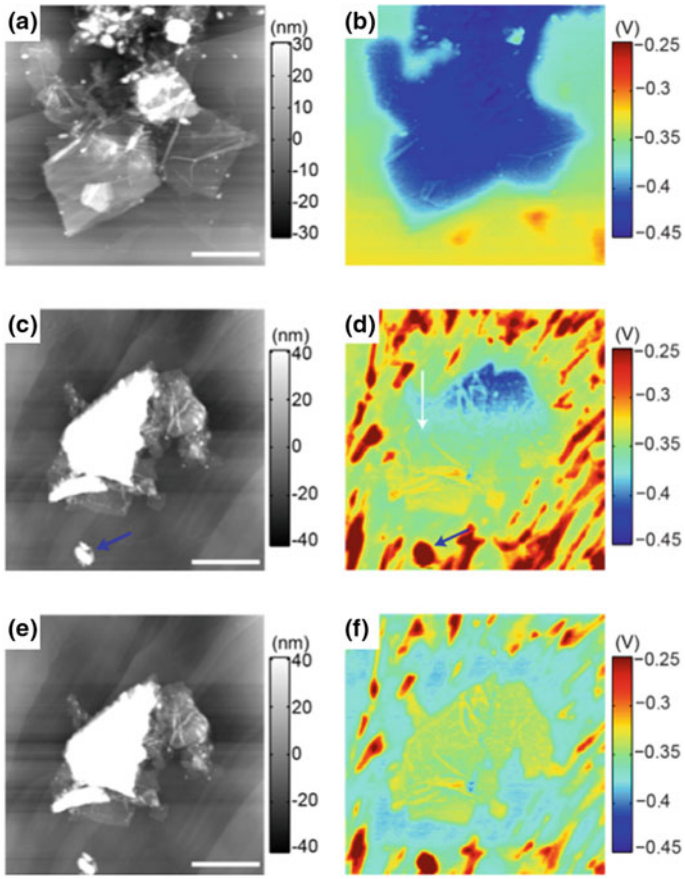

Fig. 13.14 KPFM imaging of graphene oxide in nonpolar liquid. Graphene oxide **a** topography and **b** CPD measured in ambient at a lift height of 50 nm with $V_{ac} = 2$ V with a frequency of 78.4 kHz. **c**, **e** Topography and **d**, **f** CPD measured **c**, **d** ~5 min and **e**, **f** ~80 min after immersion in decane collected at a lift height of 50 nm with $V_{ac} = 5$ V with a frequency of 38.4 kHz. White arrow in **d** indicates scan direction (scale bar = 5 μm). Graphene oxide (Cheap Tubes, Vermont) were diluted in isopropanol and deposited on HOPG before being imaged in decane. Reproduced with permission [112]

Collins et al. [112] demonstrated KPFM in liquid on few and single layer graphene oxide (Fig. 13.14). In ambient, the graphene oxide had a higher CPD value (–422 ± 5 mV) than the underlying HOPG surface (–330 ± 3 mV). Upon immersion in decane, the surface potential of the HOPG substrate became inhomogeneous, with surface potential domains becoming visible in the KPFM image. Furthermore, images taken immediately after immersion in decane demonstrated slow temporal changes in the measured CPD. Figure 13.14c, d was taken ~5 min

after immersion in decane with each image taking ~18 min to collect. The CPD of the graphene oxide drifted linearly by ~65 mV during the first image. The CPD of the underlying substrate, however, did not change significantly within this timeframe. The fact that the rate of change was material dependent suggests that a electrochemical process was taking place at the surface and not on the tip. Figure 13.14e, f shows a KPFM image collected ~80 min after immersion in decane. Within this timeframe, the charged domains reduced in size and the substrate CPD became more negative, while the graphene oxide remained at the potential reached during Fig. 13.14d. This example demonstrates the potential of KPFM for measuring dynamic chemical processes at the solid-liquid interfaces.

Clearly, operating classical KPFM in nonpolar solvents presents an opportunity to overcome problems associated with the conductivity of aqueous solutions, including the delocalization of the applied fields. Furthermore, the absence of mobile charges in nonpolar liquids leads to behavior matching that of a lossless dielectric, a fundamental assumption underlying KPFM operation [38, 45]. In this way, KPFM in nonpolar liquid, presents an opportunity to: (a) study surfaces in a controlled fashion in the absence of an inherent water layer, (b) reduce the imaging forces compared to ambient which can be important for soft materials, and (c) study multi-layered charge structures in nonpolar electrified interfaces, or electrochemical potentials of thin layers and surfactants [113–115]. However, for many energy and most biological applications, aqueous based solvents are most often used, making this approach unpractical.

13.4.3 Breakdown of Classical KPFM in Polar Liquid

Beyond non-polar liquids, several groups have been intensively exploring the possibility of using classical KPFM in polar liquids. Initially, this feasibility was tested by performing KPFS in various polar liquids and comparing with air [45]. Collins et al. noted that, in order to obtain meaningful materials and system properties using KPFM, (i) the electrostatic force must be constant with respect to time (i.e., equilibrium conditions with ~1 fs relaxation time for air), (ii) the first harmonic response must be linear with respect to the applied DC bias, and (iii) the measurement itself must not alter the measured surface potential [38].

Collins et al. further investigated the V_{dc} dependence of A_ω and $A2_\omega$ under increasing bias ranges on Au surfaces in deionized water, Fig. 13.15a, b [45]. Data sweeps were collected for a small (±200 mV), medium (±400 mV) and large (±800 mV) bias range, consecutively. The measurement resulted in complex responses including hysteretic behavior and the presence of multiple maxima and minima, matching previous reports by Raiteri et al. [76] and Umeda et al. [94]. The general shape and magnitude of the response was heavily dependent on sweep rate, suggesting an underlying temporal dependence of the response. Furthermore,

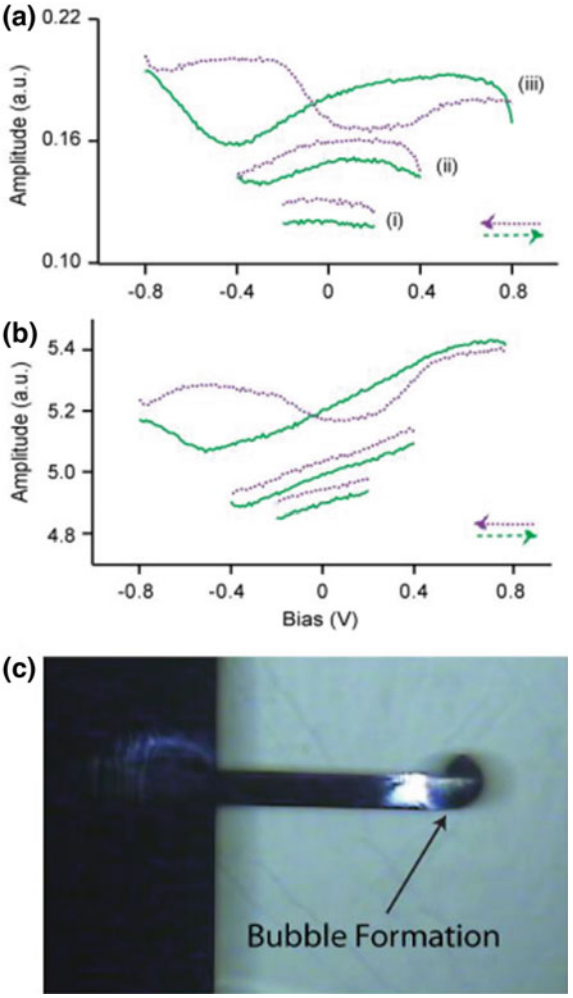

Fig. 13.15 **a** First and **b** second harmonic amplitude response recorded above an Au surface in the order of (i) small (±200 mV), (ii) medium (±400 mV), and (iii) large (±800 mV) bias ranges. Measurements were performed using a sweep rate of 100 mV/s in deionized water, while a 5 kHz signal with an amplitude of 0.5 V was applied to the probe. **c** Optical image of bubble formation at the tip in response to the application of 2 V (nominal cantilever length is 225 μm). Adapted from [45]

complex hysteretic behavior and presence of multiple maxima and minima was observed for larger (+800 mV) bias sweeps. These results demonstrate that in polar solvents, even under negligible ion concentrations (e.g., deionized water) the absence of a unique minimum in A_ω, and the presence of non-linear hysteresis and irreversible reactions at larger biases are fundamental barriers to the application of KPFM. The authors noted that when using bias sweeps larger than ~2 V, substantial changes in the AFM cantilever deflection signal occurred (not shown), often followed by visible bubble nucleation in the tip-sample gap (e.g., Fig. 13.15c). Attempts at implementing KPFM in conductive liquids will often result in similar, if not more catastrophic, bubble formation by virtue of the absence of a defined minimum, which results in the application of large DC biases by the feedback loop.

13.4.4 Applications of Open Loop-KPFM in Liquid

In recent years, significant work has been undertaken towards extending advanced open loop (i.e., feedback-free, see Sect. 13.2.2) forms of KPFM to liquid. The term "open loop" refers to a system which does not require feedback control; however, in this section we add the additional caveat of being free from DC bias application. Takeuchi et al. were the first to demonstrate an OL-KPFM imaging technique by mapping the CPD of semiconducting materials in ultra-high vacuum [116]. It used the response at the first and the second harmonic of the electrical excitation (see Sect. 13.2.2).

In general, the DH-KPFM approach garnered little attention until its potential was demonstrated for mapping surface potentials in aqueous solutions. Kobayashi et al. [117] were the first to demonstrate quantitative surface potential mapping in liquid using this approach, which they referred to as open loop electric potential (OLEP) microscopy, cp. also Chap. 3 in this book. In its first liquid implementation OLEP was operated in conjunction with FM-AFM [117] (later with AM-AFM [118]) as topographic feedback while the two electrical response signals were detected using lock-in amplifiers (Fig. 13.16). Measurements of A_f and A_{2f} as a function of AC voltage were used as a check on the veracity of (13.14) and (13.15). It was noted that at low frequencies (1 kHz), Fig. 13.16b, c, the dependence of both A_f and A_{2f} on V_{ac} deviated considerably from the governing equations. On the contrary, for higher drive frequency (30 kHz) A_f and A_{2f} demonstrated the expected linear and squared V_{ac} dependence, respectively. This was explained by the absence of spurious forces, such as bias induced surface stress or electrochemical reactions.

Using this approach, local variations in the potential distribution at a solid-liquid interface could be imaged in a weak electrolyte solution (<3 mM). A contrast between a dodecylamine thin film and the HOPG substrate in 1 mM NaCl solution was observed in the low frequency regime (1 kHz), where spurious forces can be expected to influence the measurement [117].

In a subsequent OLEP work, the surface potential contrast between latex beads with different charges and sizes was measured [118]. As shown in Fig. 13.17, OLEP operated at 30 kHz could be used to discern between particles terminated by amino and carboxyl groups. OLEP measured a 70 mV potential difference between the amino and carboxyl groups, showing reasonable agreement with a ~55 mV difference in zeta potential as measured by dynamic light scattering at a pH of 7. The authors also ruled out crosstalk between potential and topography channels by performing a similar measurement for latex beads having the same charge termination with different geometries [118]. These results indicate that, at low molarities, OLEP/DH-KPFM can be used for quantitative, or at least semi-quantitative potential measurements.

Collins et al. made a direct comparison between ambient and aqueous measurements using DH-KPFM by studying the influence of the imaging environment on the work function of graphene (Fig. 13.18) [119]. They found that the work function of the copper substrate changed upon immersion whilst the graphene

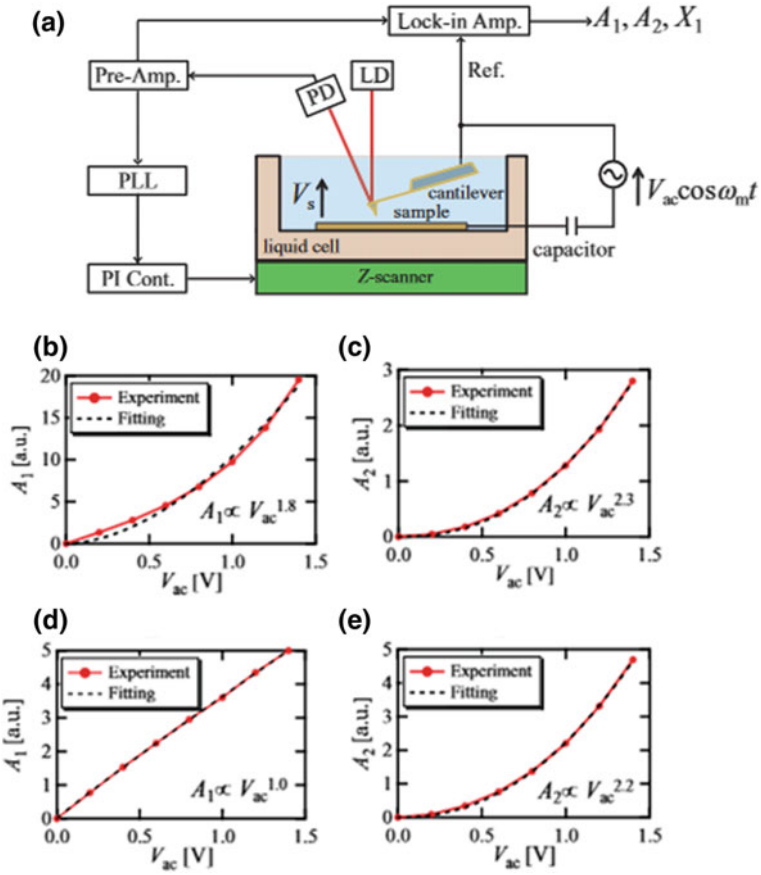

Fig. 13.16 Schematic showing the operation of DH-KPFM (or OLEP) in liquid. AC amplitude dependence of the first (A_f) (**b**, **d**) and second (A_{2f}) (**c**, **e**) harmonic amplitude measured with a drive frequency of (**a**, **b**) 1 kHz and (**d**, **e**) 30 kHz in 1 mM NaCl above a HOPG sample. Adapted with permission from [117]

surface remained unchanged, which could indicate that graphene was acting as an effective corrosion inhibitor for the copper substrate [119]. These results highlighted the potential of DH-KPFM for the quantitative investigation of the graphene-liquid interface, which may elucidate the role that sample fabrication, layer number, and defects have on the electrochemical behavior of graphene and other 2D materials and devices.

Part of the problem with achieving a high frequency excitation was the necessity to operate the electrical excitation well below the natural resonance frequency of the cantilever. Subsequently, Kobayashi et al. developed a similar method which they called dual frequency (DF) OLEP-EFM [120]. In this method, two AC voltages

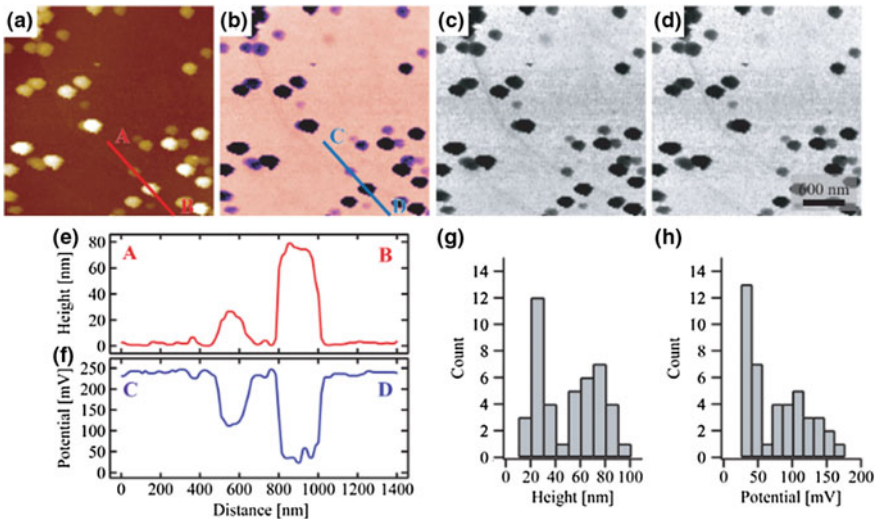

Fig. 13.17 **a** AFM topography **b** potential, **c** A_f and **d** A_{2f} images of latex beads in 1 mM NaCl solution (scan size 3 μm × 3 μm). **e** Height and potential profiles measured along line A–B in panel **a** and line C–D in panel **b** respectively. Histograms of the **g** height and **h** potential from **a** and **b**. Reproduced with permission [118]

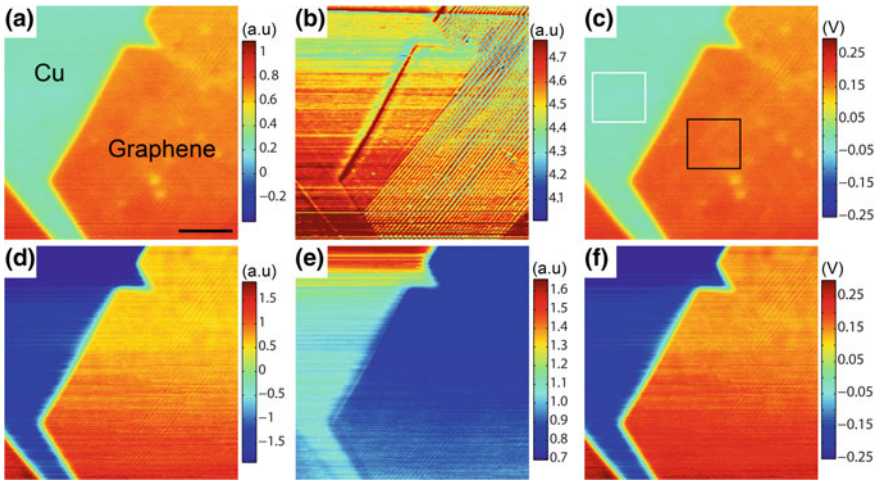

Fig. 13.18 DH-KPFM images of single layer graphene on copper foil in **a**–**c** air and **d**–**f** deionized water using a lift height of 50 nm (scale bar = 5 μm). (a, d) First harmonic mixed response $\left(A_f \cos\left(\varphi_f\right)\right)$ images and **b**, **e** A_{2f} images. **c**, **f** CPD Reproduced with permission [119]

having different frequencies are combined to produce mixing products, which are detected and used to calculate the electric potential. This mode has the advantage of high frequency modulation (twice as high as that in the conventional OLEP mode). They performed potential measurements of nanoparticles on a graphite surface in 1 mM and 10 mM NaCl solutions [120]. More recently, DF OLEP-EFM was used to investigate the nanoscale corrosion behavior of fine Cu wires and duplex stainless steel in situ [121]. Temporal variation in consecutive potential images exhibited nanoscale dynamics, thus allowing real-time identification of local corrosion sites even when surface topography remained largely unchanged (see Fig. 13.19). It is likely that such approaches will be useful for investigating reactions under surface oxide layers or highly corrosion-resistant materials.

In summary, open loop KPFM approaches have shown promise in recent years for quantitative electrochemical potential measurements on the nanoscale. These techniques avoid complications associated with DC bias induced surface stress and electrochemical reactions, which prohibit the operation of CL bias feedback in aqueous solutions. However, the frequency range and operation mechanisms are similar to CL-KPFM. To measure meaningful surface potential values, the system has to be operated in the quasistatic regime, i.e., at frequencies $f \gg f_c$, (13.20). Practically, however, it is very difficult to determine whether a given system of cantilever, sample, electrolyte, and excitation signal is operating in the quasistatic regime or not. This means that these approaches are currently limited to low ionic concentrations where ion dynamics can be suppressed.

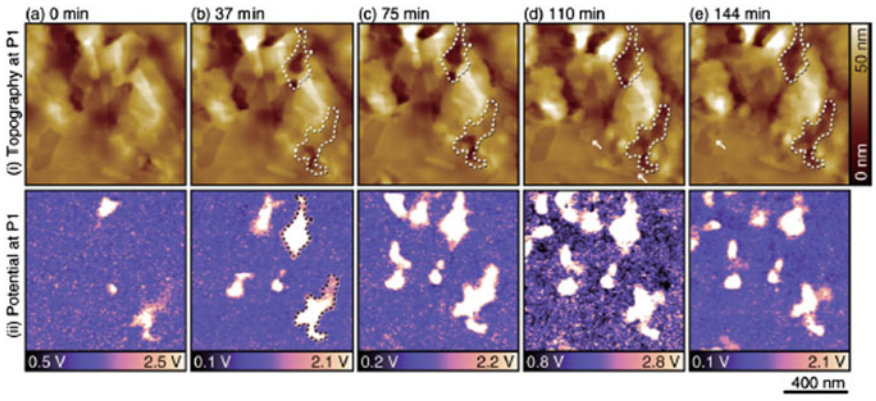

Fig. 13.19 Temporal variation in surface potential of corrosion sites on duplex steal using dual frequency OLEP-KPFM. Reproduced with permission [121]

13.5 Bias and Time Resolved Approaches

The examples that we presented so far have demonstrated that the existing KPFM-based techniques are not well equipped to deal with the complex ion dynamics and associated charge screening effects in response to the tip bias. When ion dynamics are present, these single frequency excitation approaches provide only a snapshot of the complex bias and time dynamics taking place between tip and sample. Hence, the vast majority of research efforts have focused at suppressing electrochemical processes and ion dynamics. For energy or biological applications, the requirement of a high concentration of mobile ions (»10 mM) makes avoiding ion dynamics, in the frequency space addressable by AFM (<10 MHz) unlikely. Under this limitation, the complexity of the electrochemical processes taking place between tip and sample requires the adoption of a multidimensional approach to capture the bias (V) and time (t) dependence of the response at each spatial (x, y) location on the sample. Furthermore, for many systems including batteries, supercapacitors, and membrane channels, local electrochemical dynamics govern the overall functionality. Thus, static potential measurements only provide a snapshot of the dynamics taking place.

13.5.1 Electrochemical Force Microscopy

Electrochemical force microscopy (EcFM) is a generalized force based approach for electrochemical measurements in liquids [38]. EcFM combines the force sensitivity of AFM with the ability to probe the bias- and time-dependence of electrochemical dynamics at the probe-sample junction and spatially across boundaries. In EcFM measurements, the tip is positioned a specified distance from the surface, while electrostatic and electrochemical processes in the probe sample junction are activated using a combination of single frequency AC voltages and DC bias waveforms, as shown in Fig. 13.20. Although in principle any DC bias waveform can be used, the approach has been demonstrated using a bipolar square waveform in which the magnitude of the bias pulses is increased linearly with time. The duration of these pulses is chosen to be short enough to suppress electrochemical reactions such that they do not result in irreversible changes in the system. To capture both charging and relaxation characteristics, the cantilever response is captured both during the bias application (bias-on state) and following the bias application (bias-off state). The data can be presented as an EcFM spectrum representing the voltage- and time-dependent response for a single location as shown in Fig. 13.20.

Collins et al. performed comparative single point measurements in air, non-polar solvents, and polar solvents, Fig. 13.21 [45]. As shown in Fig. 13.21a–f, EcFM response in both air and decane tracked the applied voltage precisely. Hence, the principles of KPFM, a linear bias dependence and time-invariant electrostatic

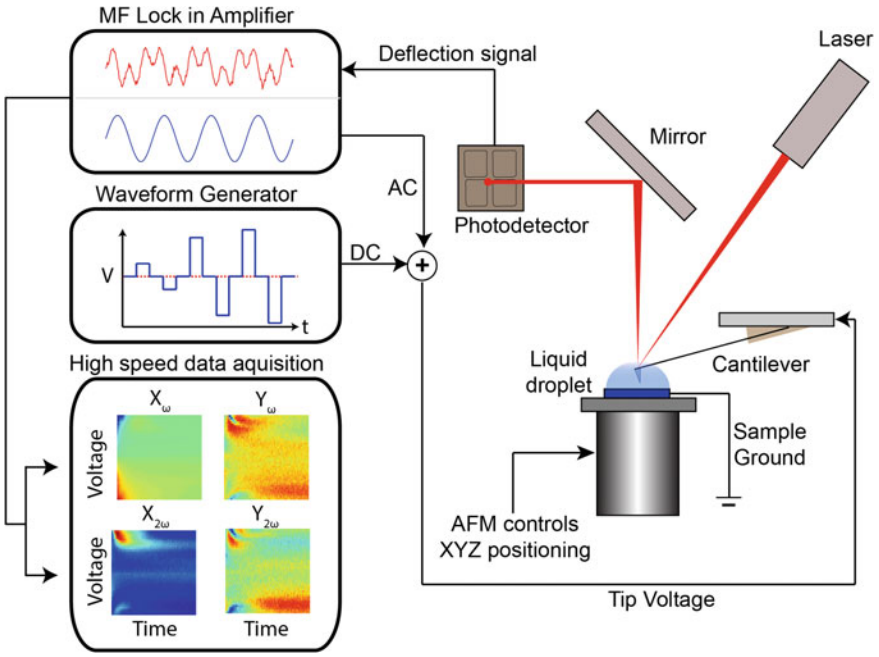

Fig. 13.20 Schematic of the experimental setup for EcFM

response, were satisfied. In deionized water, however, a very different response mechanism was observed. A large increase in the response was observed at the instant the bias pulse was applied, which relaxed within 5 ms to ~36% of the peak value (Fig. 13.21a, h). Similar information can be obtained from the bias-off state. For deionized water (Fig. 13.21i), transients were detected after the application of all bias pulses demonstrating that such measurements can be used to locally probe ionic relaxation dynamics. Collins et al. used a modified Poisson-Nernst-Planck equation to relate the relaxation time in water to ion diffusion controlled charge screening between cantilever and sample [38].

Additional to the temporal evolution, the EcFM data can be analyzed in terms of DC bias-dependent effects. Thereby, EcFM can be used to determine the CPD by linear fitting as is done in KPFS to find the bias at which the response is minimized (Fig. 13.22). Using the data recorded in decane, the CPD between tip and a gold electrode was determined for each time slice and a constant CPD of (85 ± 2) mV was observed (Fig. 13.22c). In ambient, the slope of the linear fit to the amplitude data gives a measure of the capacitance gradient, $C_Z^{'}$. In the presence of mobile ions, other bias- and time-dependent processes can occur, complicating physical interpretation. Nevertheless, changes in the amplitude slope provide information about relaxation dynamics. In decane, $C_Z^{'}$ changed only slightly during the measurement. In deionized water, the response was largely linear with applied bias for short

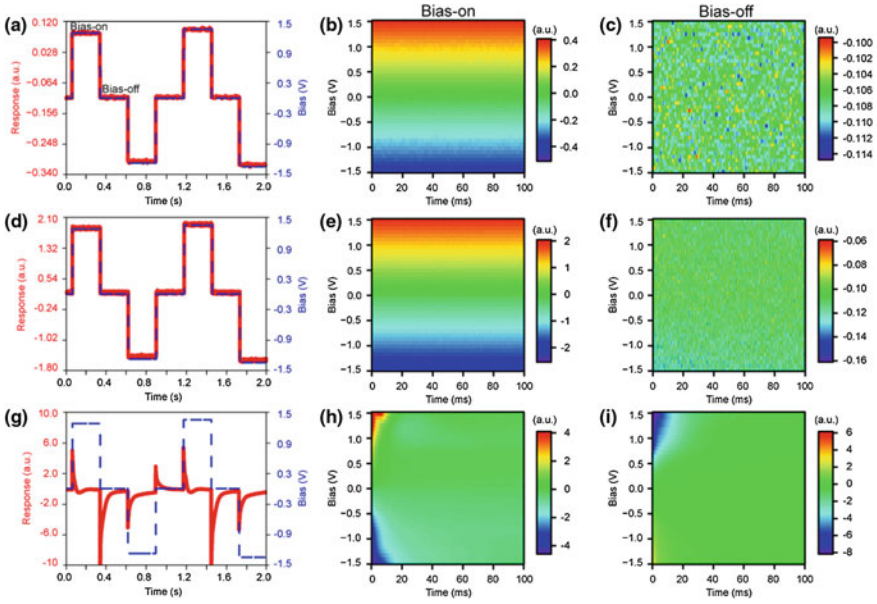

Fig. 13.21 Single point EcFM first harmonic response $\left(A_f \cos\left(\varphi_f\right)\right)$ captured in **a**, **b**, **c** air, **d**, **e**, **f** decane and **g**, **h**, **i** deionized water 200 nm from a grounded Au electrode. **a**, **d**, **g** Temporal response (solid red line) of the EcFM response to the applied DC bias waveform (dashed blue line). Full response spectra showing bias-on **b**, **e**, **h** and bias-off **c**, **f**, **i** states. Measurements were performed with V_{ac} = 0.5 V [25 kHz] applied to the probe. Reproduced with permission [45]

timescales (<10 ms) (Fig. 13.22b). However, gradual changes of the measured CPD (Fig. 13.22d) were observed, which varied by greater than 700 mV within the 100 ms duration of the bias pulse. The authors assigned these changes to the screening by the EDLs between probe and sample although at longer timescales above 10 ms, the zero-response crossing became ill defined and thus a reliable CPD measurement was no longer possible. However, the relaxation of $C_Z^{'}$, was well-described by a double exponent fit (blue line) having relaxation times of $\tau_1 = 4.2$ ms and $\tau_2 = 31.7$ ms which the authors related to charging of the EDL through a diffusion limited process. This time dependence in polar liquids, which is absent in air and nonpolar solvents, prohibits the implementation of KPFM in ionically-active liquids and highlights a general scheme for capturing dynamic effects when ion dynamics are present.

In solutions above 1 mM, Collins et al. noted the absence of a dynamic EcFM response at low biases (e.g., <250 mV in K_2SO^4 [38]). However, at larger biases, slow (>50 ms) non-linear processes were observed, which were too fast to be ascribed to screening or ion diffusion. The authors attributed these non-linearities to the onset of electrochemical reactions (region I of Fig. 13.2b). The absence of fast

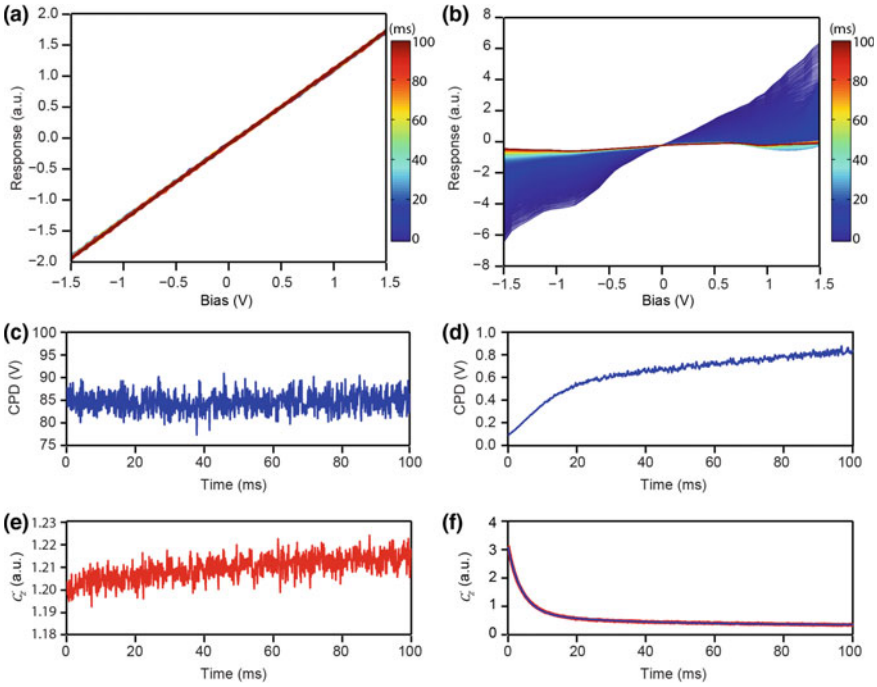

Fig. 13.22 EcFM measurements [bias-on] in **a**, **c**, **e** decane and **b**, **d**, **f** deionized water recorded 200 nm above a grounded Au electrode. **a**, **b** EcFM bias-resolved mixed response with time represented on the color scale. **c**, **d** The measured CPD and **e**, **f** C_Z'. Measurements were performed with $V_{ac} = 0.5$ V [25 kHz] applied to the probe. Reproduced with permission [45]

processes was explained by the slow lock-in detection speeds (100 μs–4 ms), which was slower than the expected screening processes in these solutions [38, 122].

Collins et al. further implemented EcFM in an imaging scheme as shown in Fig. 13.23 for a Au electrode deposited on a SiO_2 layer [38]. Here, 2D EcFM bias- and time-dependent spectroscopic response were recorded in a 30 × 30 grid across the electrodes (Fig. 13.23a), giving rise to a 4D data set (*x, y, V, t*). To demonstrate the spatial variability present in the data, the first and second harmonic EcFM amplitude response recorded 5 ms after the onset of the +1.5 V and −1.5 V bias pulses are plotted (Fig. 13.23c–f). Average cross sections for each image, from the region indicated in Fig. 13.23a, are shown in Fig. 13.23b. The observed spatial variation between Au and SiO_2 is present for all biases and times. For both first and second harmonics, the EcFM response shows a bias-polarity dependence for SiO_2 suggesting that the EcFM signal is localized and dependent on the material below the tip. In the absence of a full model to describe the multidimensional EcFM data (*x, y, V, t*), the analysis can be complicated, as it cannot be reduced to phenomenological fitting procedures with parameters having a known physical

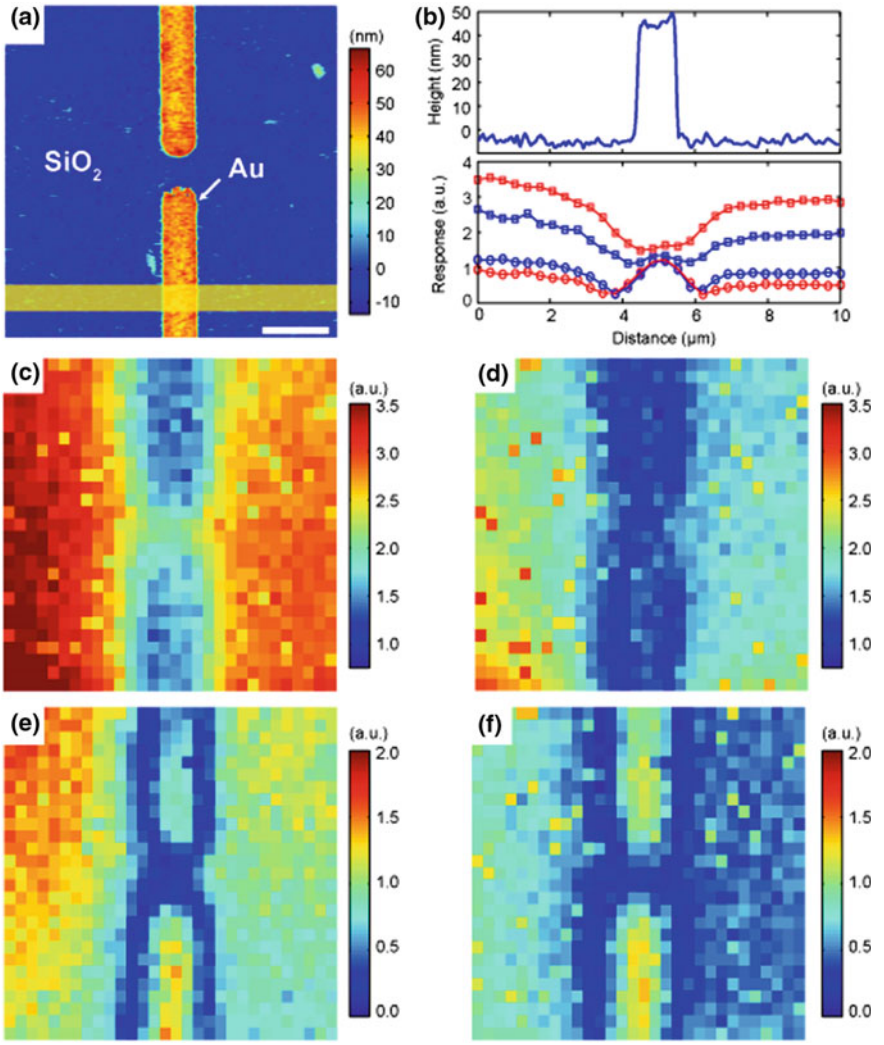

Fig. 13.23 **a** Topography image of Au electrodes on a SiO_2 substrate recorded using tapping mode AFM (scale bar = 2 μm, image size = 10 × 10 μm). **b** Average cross sectional EcFM response recorded 200 nm above the surface and determined from the area marked with a yellow box in **a** for A_f (squares) and A_{2f} (circles) EcFM response during the application of +1.5 V (red) and −1.5 V (blue) bias pulses. Spatial variability maps from a grid of 30 × 30 2D EcFM measurements of the **c**, **d** A_f and **e**, **f** A_{2f} harmonic EcFM amplitude response at 5 ms after the onset of the bias-on state for **c**, **e** +1.5 V and **d**, **f** −1.5 V, respectively. Measurements were performed with V_{ac} = 1 V [19 kHz] applied to the probe. Reproduced with permission [38]

relationship. One solution could be the use of multivariate statistical approaches for visualizing variability in the multidimensional response without relying on a priori physical models, as demonstrated recently by Collins et al. [45].

13.6 Conclusions and Outlook

VM AFM techniques are in a unique position to map the surface structure together with electronic, electrostatic, electrochemical, and electromechanical functionality on submicron to nanometer length scales. Indeed, EFM and KPFM have made enormous contributions to the fields of biology, physics, and materials sciences in the short time since their inception. While these techniques are traditionally operated at the solid-gas interface, their application to the solid-liquid interface would greatly expand the scope of their application, allowing investigation of many important electrochemical processes crucial for the development of next generation energy devices (e.g., supercapacitors, batteries) or understanding structure-function relationships of biological systems.

Throughout this chapter, we have reviewed attempts at achieving KPFM-based measurements in liquid, the majority of which have concentrated on suppressing the effect of ion dynamics and electrochemical reactions. It has been shown that classical KPFM can be performed in nonpolar solvents where problems associated with the finite conductivity of aqueous solutions is largely absent. Traditional closed loop KPFM, however, has not yet been demonstrated in polar liquids. For operation in polar liquids, alternative KPFM approaches (e.g., DH-KPFM) that require only the application of AC voltage have been developed. Such approaches negate problems associated with DC bias induced electrochemical reactions. While both DH-KPFM and EFM measurements have been shown to allow quantitative measurements of surface potential or dielectric permittivity, respectively, they break down at modest ion concentrations (in excess of a few mM) due to the requirement for operating in a quasistatic regime. Furthermore, a clear distinction between the quantitative quasistatic regime and a dynamic regime of operation, where charge screening and ion transport phenomena influence the result, is difficult to determine precisely. Within the frequency space addressable using AFM, it is unlikely that the measurements can be performed at sufficiently high frequencies to avoid ion dynamics altogether, and hence the broad applicability across all solutions is unlikely.

For studies in the presence of a modest concentration of ions (>10 mM) it is not always possible or desirable to avoid the influence of ion dynamics on VM AFM measurements. In the presence of mobile ions, AC voltages and/or DC biases applied between tip and sample will result in migration and diffusion of ions to the interface, as well as faradaic reactions involving electron transfer across the interface. Clearly, time- and bias-dependent processes will complicate the implementation of conventional VM AFM techniques and require more multidimensional measurement approaches. EcFM was developed to capture and visualize the voltage

and time characteristics of the forces acting on a VM probe. Unlike KPFM, EcFM contains valuable information, e.g., about the charge screening mechanisms as evidenced in the transient relaxation. However, only slow processes (e.g., ion diffusion, Faradaic reactions) can be detected at high molarities using EcFM, which is limited by the detection speed of the lock-in amplifier used. To effectively probe fast charge screening dynamics in higher molarity electrolytes, high speed detection ($< \mu s$) is required. Many of these bottlenecks can be overcome by the adoption of recently developed fast detection methods [43, 123, 124, 125]. Apart from slow detection rates (~0.5–4 ms in KPFM), another disadvantage of using lock-in amplifiers (or a phase locked loop) is that a lock-in intrinsically limits the detection to a small number of harmonics. Nevertheless, higher harmonics and frequency mixing/intermodulation products can be expected from the non-linear nature of the force in the presence of ionic motion (compare Sect. 13.2.1.3). In order to capture the full cantilever response in a VM AFM experiment, general acquisition mode KPFM [126–128] or intermodulation EFM [48], which allow capture of multiple harmonics simultaneously, should be explored.

In addition, improving the spatial resolution and confinement of the electric field will be crucial towards true molecular or atomic scale mapping of electrochemical processes. It is likely that this will require the incorporation of specialized probes. Bare conductive probes with metal coatings induce non-local electrochemical processes and conduct significant currents in liquid electrolytes. Consequently, probes that are insulated except at the tip apex are needed in order to localize the potential and minimize the effective probe area [129–131]. This requires the continued development of approaches for fabrication of electrochemically shielded conductive AFM probes.

Finally, liquid KPFM-based methods offer the capability to measure electrochemical potentials and their distribution on submicron scales, not merely the average values from a macroscopic electrochemical measurement. However, in the presence of mobile ions, EDL dynamics, and electrochemically reactive interfaces, it is unrealistic to expect meaningful information from single frequency approaches developed for the solid-liquid interface. This is primarily due to the fact that under such conditions the surface potential is ill-defined and inherently dynamic in nature. In the future, multidimensional KPFM approaches and analysis methods that link dynamic bias-dependent dynamic processes with local structure will become increasingly important.

The force experienced by the tip in a complex ionic electrolyte contains all the signatures of the local electronic, ionic, and relaxation dynamics. At the same time, in the absence of an a priori model that encapsulates the complex electric field at the AFM tip driving the ionic and charge dynamics, as well as possible reactions, we need analysis and visualization tools to separate the different phenomena. During the last few years, big data-driven scientific exploration tools have offered an opportunity to tackle and analyse large multidimensional datasets [132]. Adoption of such approaches, in combination with high performance computing, will enable meaningful exploration of systems in high molarity solutions.

Acknowledgements A portion of the research was conducted at and supported by the Center for Nanophase Materials Sciences, which is a DOE Office of Science User Facility (LC). BJR acknowledges support from Science Foundation Ireland (14/US/I3113) and the European Union's Horizon 2020 research and innovation programme under the Marie Skłodowska-Curie grant agreement No 644175.

References

1. Y. Li, G.A. Somorjai, Nano Lett. **10**, 2289 (2010)
2. G.A. Somorjai, Y. Li, *Introduction to Surface Chemistry and Catalysis* (John Wiley & Sons, New York, NY, 2010)
3. F. Mansfeld, J. Appl. Electrochem. **25**, 187 (1995)
4. H. Bhni, T. Suter, A. Schreyer, Electrochim. Acta **40**, 1361 (1995)
5. J.R. Miller, P. Simon, Science (80) **321**, 651 (2008)
6. D.S. Silvester, Analyst **136**, 4871 (2011)
7. T.G. Drummond, T.G. Drummond, M.G. Hill, M.G. Hill, J.K. Barton, J.K. Barton, Nat. Biotechnol. **21**, 1192 (2003)
8. M.J. Williamson, R.M. Tromp, P.M. Vereecken, R. Hull, F.M. Ross, Nat. Mater. **2**, 532 (2003)
9. H.A.O. Hill, Coord. Chem. Rev. **151**, 115 (1996)
10. A.J. Bard, L.R. Faulkner, *Electrochemical Methods: Fundamentals and Applications* (Wiley, New York, 2001)
11. P. Simon, Y. Gogotsi, Nat. Mater. **7**, 845 (2008)
12. M. Winter, R.J. Brodd, Chem. Rev. **104**, 4245 (2004)
13. P. Poizot, S. Laruelle, S. Grugeon, L. Dupont, J.-M. Tarascon, Nature **407**, 496 (2000)
14. D.E. Williams, C. Westcott, M. Fleischmann, J. Electrochem. Soc. **132**, 1796 (1985)
15. M. Park, X. Zhang, M. Chung, G.B. Less, A.M. Sastry, J. Power Sources **195**, 7904 (2010)
16. P. Balaya, Energy Environ. Sci. **1**, 645 (2008)
17. J.Y. Son, K. Kyhm, J.H. Cho, Appl. Phys. Lett. **89**, 92907 (2006)
18. S.V. Kalinin, D.A. Bonnell, Phys. Rev. B **63**, 125411 (2001)
19. S.A.L. Weber, H.-J.J. Butt, R. Berger, *Scanning Probe Microscopic Nanoscience Nanotechnology 3* (Springer, Berlin, 2013), pp. 551–573
20. E. Drolle, K. Hammond, W.F.D. Bennett, E. Lyman, M. Karttunen, Z. Leonenko, arXiv 1607.00057 (2016)
21. F. Hane, B. Moores, M. Amrein, Z. Leonenko, Ultramicroscopy **109**, 968 (2009)
22. Z. Leonenko, M. Rodenstein, J. Döhner, L.M. Eng, M. Amrein, Langmuir **22**, 10135 (2006)
23. C. Leung, D. Maradan, A. Kramer, S. Howorka, P. Mesquida, B.W. Hoogenboom, Appl. Phys. Lett. **97**, 203703 (2010)
24. A.K. Sinensky, A.M. Belcher, Nat. Nanotechnol. **2**, 653 (2007)
25. M. Nonnenmacher, M.P. O'Boyle, H.K. Wickramasinghe, M.P. O'Boyle, H.K. Wickramasinghe, Appl. Phys. Lett. **58**, 2921 (1991)
26. M.Z. Bazant, K. Thornton, A. Ajdari, Phys. Rev. E Stat. Nonlinear, Soft Mat. Phys. **70**, 1 (2004)
27. M.Z. Bazant, M.S. Kilic, B.D. Storey, A. Ajdari, New J. Phys. **11**, 2 (2009)
28. H. Helmholtz, Ann. Phys. Chem. **89**, 211 (1853)
29. G. Gouy, J. Phys. Theor. Appl. **9**, 457 (1910)
30. D.L. Chapman, Philos. Mag. Ser. **6**(25), 475 (1913)
31. M.Z. Bazant, K. Thornton, A. Ajdari, Phys. Rev. E Stat. Nonlin. Soft Matter Phys. **70**, 21506 (2004)
32. O.Z. Stern, Electrochemistry **30**, 508 (1924)
33. H.-J. Butt, K. Graf, M. Kappl, *Physics and Chemistry of Interfaces* (Wiley-VCH, 2006)

34. M.S. Kilic, M.Z. Bazant, A. Ajdari, Phys. Rev. E **75**, 21502 (2007)
35. M.S. Kilic, M.Z. Bazant, A. Ajdari, Phys. Rev. E **75**, 21503 (2007)
36. B.D. Storey, L.R. Edwards, M.S. Kilic, M.Z. Bazant, Phys. Rev. E **77**, 36317 (2008)
37. M.Z. Bazant, K. Thornton, A. Ajdari, **1** (2008)
38. L. Collins, S. Jesse, J.I. Kilpatrick, A. Tselev, O. Varenyk, M.B. Okatan, S.AL. Weber, A. Kumar, N. Balke, S.V Kalinin, B.J. Rodriguez, Nat. Commun. **5**, 3871 (2014)
39. M.Z. Bazant, M.S. Kilic, B.D. Storey, A. Ajdari, New J. Phys. **11**, 75016 (2009)
40. I. Borukhov, D. Andelman, H. Orland, Electrochim. Acta **46**, 221 (2000)
41. A.H. Boschitsch, P.V. Danilov, J. Comput. Chem. **33**, 1152 (2012)
42. R. Borgani, D. Forchheimer, J. Bergqvist, P.-A. Thorén, O. Inganäs, D.B. Haviland, Appl. Phys. Lett. **105**, 143113 (2014)
43. L. Collins, A. Belianinov, S. Somnath, B.J. Rodriguez, N. Balke, S.V. Kalinin, S. Jesse, Nanotechnology **27**, 105706 (2016)
44. L. Collins, A. Belianinov, R. Proksch, T. Zuo, Y. Zhang, P.K. Liaw, S.V. Kalinin, S. Jesse, Appl. Phys. Lett. **108**, 1 (2016)
45. L. Collins, S. Jesse, J.I. Kilpatrick, A. Tselev, M.B. Okatan, S.V. Kalinin, B.J. Rodriguez, Beilstein J. Nanotechnol. **6**, 201 (2015)
46. S. Guo, S. V. Kalinin, S. Jesse, Appl. Phys. Lett. **100**, (2012)
47. L. Collins, J.I. Kilpatrick, S. a L. Weber, A Tselev, I. V Vlassiouk, I.N. Ivanov, S. Jesse, S. V Kalinin, B.J. Rodriguez, Nanotechnology **24**, 475702 (2013)
48. R. Borgani, D. Forchheimer, J. Bergqvist, P.-A. Thorén, O. Inganäs, D.B. Haviland, Appl. Phys. Lett. **105**, 143113 (2014)
49. R. Borgani, L.K.H. Pallon, M.S. Hedenqvist, U.W. Gedde, D.B. Haviland, Nano Lett. **16**, 5934 (2016)
50. W. Ducker, T. Senden, R. Pashley, Nature **353**, 239 (1991)
51. W.A. Ducker, T.J. Senden, R.M. Pashley, Langmuir **8**, 1831 (1992)
52. H.J. Butt, Biophys. J. **60**, 777 (1991)
53. H.J. Butt, Biophys. J. **60**, 1438 (1991)
54. V.G. Levadny, M.L. Belaya, D.A. Pink, M.H. Jericho, Biophys. J. **70**, 1745 (1996)
55. R. Raiteri, S. Martinoia, M. Grattarola, Biosensors **11**, 1009 (1996)
56. A.L. Weisenhorn, P. Maivald, H.J. Butt, P.K. Hansma, Phys. Rev. B **45**, 11226 (1992)
57. H.J. Butt, M. Jaschke, W. Ducker, Bioelectrochemistry Bioenerg. **38**, 191 (1995)
58. H. Butt, Biophys. J. **63**, 578 (1992)
59. R. Raiteri, M. Grattarola, H.-J. Butt, J. Phys. Chem. **100**, 16700 (1996)
60. A.C. Hillier, S. Kim, A.J. Bard, J. Phys. Chem. **100**, 18808 (1996)
61. C. Rotsch, M. Radmacher, Langmuir **13**, 2825 (1997)
62. W. Heinz, J. Hoh, Biophys. J. **76**, 528 (1999)
63. J. Sotres, A.M. Baró, Appl. Phys. Lett. **93**, 103903 (2008)
64. J. Sotres, A.M. Baró, Biophys. J. **98**, 1995 (2010)
65. C. Marlière, S. Dhahri, Nanoscale **7**, 8843 (2015)
66. D. Ebeling, D. van den Ende, F. Mugele, Nanotechnology **22**, 305706 (2011)
67. K. Umeda, K. Kobayashi, N. Oyabu, K. Matsushige, H. Yamada, Nanotechnology **26**, 285103 (2015)
68. T.J. Senden, C.J. Drummond, P. Kekicheff, Langmuir **10**, 358 (1994)
69. S. Manne, J.P. Cleveland, H.E. Gaub, G.D. Stucky, P.K. Hansma, Langmuir **10**, 4409 (1994)
70. D.J. Müller, A. Engel, Biophys. J. **73**, 1633 (1997)
71. D.J. Müller, D. Fotiadis, S. Scheuring, S. a Müller, A. Engel, Biophys. J. **76**, 1101 (1999)
72. A. Philippsen, W. Im, A. Engel, T. Schirmer, B. Roux, D.J. Müller, Biophys. J. **82**, 1667 (2002)
73. A.S. Johnson, C.L. Nehl, M.G. Mason, J.H. Hafner, Langmuir **19**, 10007 (2003)
74. Y. Yang, K.M. Mayer, J.H. Hafner, Biophys. J. **92**, 1966 (2007)
75. Y. Yang, K.M. Mayer, N.S. Wickremasinghe, J.H. Hafner, Biophys. J. **95**, 5193 (2008)
76. R. Raiteri, H.J. Butt, J. Phys. Chem. **99**, 15728 (1995)

77. A. Döppenschmidt, H.J. Butt, Colloids Surfaces A Physicochem. Eng. Asp. **149**, 145 (1999)
78. K. Hu, F.-R.F. Fan, A.J. Bard, A.C. Hillier, J. Phys. Chem. B **101**, 8298 (1997)
79. R. Raiteri, M. Preuss, M. Grattarola, H.J. Butt, Colloids Surfaces A Physicochem. Eng. Asp. **136**, 191 (1998)
80. B.P. Lynch, A.M. Hilton, C.H. Doerge, G.J. Simpson, Langmuir **21**, 1436 (2005)
81. A.M. Hilton, B.P. Lynch, G.J. Simpson, Anal. Chem. **77**, 8008 (2005)
82. B.P. Lynch, A.M. Hilton, G.J. Simpson, Biophys. J. **91**, 2678 (2006)
83. B.J. Rodriguez, S. Jesse, K. Seal, A.P. Baddorf, S.V. Kalinin, J. Appl. Phys. **103**, 14306 (2008)
84. B.J. Rodriguez, S. Jesse, A.P. Baddorf, S.V. Kalinin, Phys. Rev. Lett. **96**, 237602 (2006)
85. D. Denning, J. Guyonnet, B.J. Rodriguez, Int. Mater. Rev. **61**, 46 (2016)
86. B.J. Rodriguez, S. V. Kalinin, *Springer Series Surface Science* (Springer, 2012), pp. 243–287
87. B.J. Rodriguez, S. Jesse, A.P. Baddorf, S.H. Kim, S.V. Kalinin, Phys. Rev. Lett. **98**, 247603 (2007)
88. K.I. Umeda, N. Oyabu, K. Kobayashi, Y. Hirata, K. Matsushige, H. Yamada, Appl. Phys. Express **3**, 20 (2010)
89. K.I. Umeda, K. Kobayashi, N. Oyabu, Y. Hirata, K. Matsushige, H. Yamada, J. Appl. Phys. **113**, (2013)
90. K.I. Umeda, K. Kobayashi, K. Matsushige, H. Yamada, Appl. Phys. Lett. **101**, 123112 (2012)
91. D.J. Marchand, E. Hsiao, S.H. Kim, Langmuir **29**, 6762 (2013)
92. C.J. Long, R.J. Cannara, Rev. Sci. Instrum. **86**, (2015)
93. J. Zhang, D.M. Czajkowsky, Y. Shen, J. Sun, C. Fan, J. Hu, Z. Shao, Appl. Phys. Lett. **102**, 73110 (2013)
94. K.I. Umeda, K. Kobayashi, N. Oyabu, Y. Hirata, K. Matsushige, H. Yamada, J. Appl. Phys. **116**, 134307 (2014)
95. L. Fumagalli, D. Esteban-Ferrer, A. Cuervo, J.L. Carrascosa, G. Gomila, Nat. Mater. **11**, 808 (2012)
96. A. Cuervo, P.D. Dans, J.L. Carrascosa, M. Orozco, G. Gomila, L. Fumagalli, Proc. Natl. Acad. Sci. **111**, E3624 (2014)
97. A. Dols-Perez, G. Gramse, A. Calò, G. Gomila, L. Fumagalli, Nanoscale **7**, 18327 (2015)
98. D. Esteban-Ferrer, M.A. Edwards, L. Fumagalli, A. Ju??rez, and G. Gomila, ACS Nano **8**, 9843 (2014)
99. M. Van Der Hofstadt, R. Fabregas, R. Millan-Solsona, A. Juarez, L. Fumagalli, G. Gomila, ACS Nano **10**, 11327 (2016)
100. G. Gomila, G. Gramse, L. Fumagalli, Nanotechnology **25**, 255702 (2014)
101. G. Gramse, M. Edwards, L. Fumagalli, G. Gomila, Nanotechnology **24**, 415709 (2013)
102. G. Gramse, A. Dols-Perez, M.A. Edwards, L. Fumagalli, G. Gomila, Biophys. J. **104**, 1257 (2013)
103. T.L. Sounart, T.A. Michalske, K.R. Zavadil, J. Microelectromech. Syst. **14**, 125 (2005)
104. H.V. Panchawagh, T.L. Sounart, R.L. Mahajan, J. Microelectrom. Syst. **18**, 1105 (2009)
105. G. Gramse, M.A. Edwards, L. Fumagalli, G. Gomila, Appl. Phys. Lett. **101**, 213108 (2012)
106. G. Gramse, M.A. Edwards, L. Fumagalli, G. Gomila, Nanotechnology **24**, 415709 (2013)
107. T.L. Sounart, T.A. Michalske, Transducers 2003—12th International Conference Solid-State Sensors, Actuators Microsystems, Digitalized Technical Paper vol. 1, p. 615 (2003)
108. B. Kumar, S.R. Crittenden, Nanotechnology **24**, 435701 (2013)
109. T. Fort, R. Wells, Surf. Sci. **12**, 46 (1968)
110. S. Bastide, D. Gal, D.C. Kronik, S. Bastide, D. Gal, D. Cahen, **4032**, (1999)
111. A.L. Domanski, E. Sengupta, K. Bley, M.B. Untch, S. A L. Weber, K. Landfester, C.K. Weiss, H.-J. Butt, R. Berger, Langmuir **28**, 13892 (2012)
112. L. Collins, J. Kilpatrick, S. V. Kalinin, B.J. Rodriguez (2017)
113. Q. Guo, V. Singh, S.H. Behrens, Langmuir **26**, 3203 (2010)
114. C.E. Espinosa, Q. Guo, V. Singh, S.H. Behrens, Langmuir **26**, 16941 (2010)

115. Q. Guo, J. Lee, V. Singh, S.H. Behrens, J. Colloid Interface Sci. **392**, 83 (2013)
116. O. Takeuchi, Y. Ohrai, S. Yoshida, H. Shigekawa, Jpn. J. Appl. Phys. **46**, 5626 (2007)
117. K. Naritaka, A. Hitoshi, F. Takeshi, Rev. Sci. Instrum. **81**, 123705 (4404)
118. N. Kobayashi, H. Asakawa, T. Fukuma, J. Appl. Phys. **110**, 44315 (2011)
119. L. Collins, J.I. Kilpatrick, I. V. Vlassiouk, A. Tselev, S.A.L. Weber, S. Jesse, S. V. Kalinin, B.J. Rodriguez, Appl. Phys. Lett. **104**, (2014)
120. N. Kobayashi, H. Asakawa, T. Fukuma, Rev. Sci. Instrum. **83**, 33709 (2012)
121. K. Honbo, S. Ogata, T. Kitagawa, T. Okamoto, N. Kobayashi, I. Sugimoto, S. Shima, A. Fukunaga, C. Takatoh, T. Fukuma, ACS Nano **10**, 2575 (2016)
122. L. Collins, S. Jesse, J.I. Kilpatrick, A. Tselev, M.B. Okatan, S.V. Kalinin, B.J. Rodriguez, Beilstein J. Nanotechnol. **6**, 201 (2015)
123. D.C. Coffey, D.S. Ginger, Nat. Mater. **5**, 735 (2006)
124. J. Murawski, T. Graupner, P. Milde, R. Raupach, U. Zerweck-Trogisch, L.M. Eng, J. Appl. Phys. **118**, 0 (2015)
125. J.L. Garrett, J.N. Munday, Nanotechnology **27**, 245705 (2016)
126. L. Collins, A. Belianinov, S. Somnath, N. Balke, S.V. Kalinin, S. Jesse, Sci. Rep. **6**, 30557 (2016)
127. L. Collins, A. Belianinov, R. Proksch, T. Zuo, Y. Zhang, P.K. Liaw, S.V. Kalinin, S. Jesse, Appl. Phys. Lett. **108**, 1 (2016)
128. L. Collins, M. Ahmadi, T. Wu, B. Hu, S.V. Kalinin, S. Jesse, ACS Nano **11**, 8717 (2017)
129. B.J. Rodriguez, S. Jesse, K. Seal, A.P. Baddorf, S.V. Kalinin, P.D. Rack, Appl. Phys. Lett. **91**, 93130 (2007)
130. J.H. Noh, M. Nikiforov, S. V. Kalinin, A. A. Vertegel, P.D. Rack, Nanotechnology **21**, 365302 (2010)
131. D. Ziegler, A. Klaassen, D. Bahri, D. Chmielewski, A. Nievergelt, F. Mugele, J.E. Sader, P. D. Ashby, in *2014* IEEE 27th International Conference of the Micro Electro Mechanical System (IEEE, 2014), pp. 128–131
132. S.V. Kalinin, E. Strelcov, A. Belianinov, S. Somnath, R.K. Vasudevan, E.J. Lingerfelt, R.K. Archibald, C. Chen, R. Proksch, N. Laanait, S. Jesse, ACS Nano **10**, 9068 (2016)

Part IV
Atomic Scale Experiments

Chapter 14
Kelvin Probe Force Microscopy with Atomic Resolution

Yan Jun Li, Haunfei Wen, Zong Min Ma, Lili Kou, Yoshitaka Naitoh and Yasuhiro Sugawara

Abstract The surface potential distribution measured using Kelvin probe force microscopy (KPFM) is influenced by the contact potential difference (CPD) between the tip and surface, the stray capacitance of the cantilever, and fixed monopole charges on the surface and tip. The interpretation of atomic-scale KPFM contrast studies has been controversial. Here, we investigate the contrast mechanism in KPFM with atomic resolution. First, the effect of stray capacitance on potential measurements is explored in the FM-, AM-, and heterodyne AM-KPFM modes. The distance dependence of the modulated electrostatic force in AM-KPFM is much weaker than that in FM- and heterodyne AM-KPFM, and the stray capacitance of the cantilever, which strongly affects potential measurements in AM-KPFM, is almost completely eliminated in FM- and heterodyne AM-KPFM. The very small local contact potential difference (LCPD) corrugation in AM-KPFM is attributed to an artefact induced by the topographic feedback. Next, an investigation of the LCPD on a TiO_2 (110)-1 $\times$ 1 surface and atom-dependent bias-distance spectroscopic mapping are performed. The LCPD of TiO_2 (110) is dominated not only by the permanent surface dipole between the tip apex atom and the surface, but also by the dipoles induced by the chemical interaction between the tip and sample. Finally, we propose a new multiple-image method for obtaining the frequency shift, tunneling

Y. J. Li · H. Wen · L. Kou · Y. Naitoh · Y. Sugawara (✉)
Department of Applied Physics, Graduate School of Engineering, Osaka University,
2-1 Yamada-oka, Suita, Osaka 565-0871, Japan
e-mail: sugawara@ap.eng.osaka-u.ac.jp

Y. J. Li
e-mail: liyanjun@ap.eng.osaka-u.ac.jp

H. Wen
e-mail: hfwen@ap.eng.osaka-u.ac.jp

Y. Naitoh
e-mail: naitoh@ap.eng.osaka-u.ac.jp

Y. J. Li · Z. M. Ma
National Key Laboratory for Electronic Measurement and Technology,
North University of China, No. 3, Xueyuan Road, Taiyuan 030051, Shan Xi, China
e-mail: mzmncit@nuc.edu.cn

S. Sadewasser and T. Glatzel (eds.), *Kelvin Probe Force Microscopy*,
Springer Series in Surface Sciences 65, https://doi.org/10.1007/978-3-319-75687-5_14

current, and LCPD images. For the first time, we obtain three images on a TiO_2(110) surface with atomic resolution at 78 K. The LCPD has a higher value on a defect site than on the nearby O rows because excess electrons caused by surface defects are delocalized on the nearby Ti rows. The multiple-image method can be used to investigate the charge transfer phenomena between nanoparticles and surface sites and to elucidate the mechanisms of catalytic reactions.

14.1 Introduction

Among the atomic-scale surface characterization techniques, atomic force microscopy (AFM) is a powerful tool for investigating surface properties and has been extended to the manipulation of atoms, enabling the creation of novel nanostructures, particularly on insulator surfaces [1–5]. Kelvin probe force microscopy (KPFM) and electrostatic force microscopy (EFM), which are based on AFM, have been widely used to measure surface potential distributions, charge transfer, electronic/electrical properties, and so forth. KPFM with atomic resolution has been applied to various surfaces, including conductive, semiconductive, and insulating surfaces, such as for imaging the charge distribution within a molecule [6–10].

The underlying principle of KPFM is that the contact potential difference (CPD) between the tip and the sample surface is detected from the shift in the resonance frequency or amplitude of the cantilever by applying an ac bias voltage. This modulates the electrostatic interaction force between the tip and the sample. A dc bias voltage is used to nullify the average electrical force related to the CPD.

In atomic-resolution KPFM, the CPD is specifically referred to as the local contact potential difference (LCPD) [11]. The surface potential distribution measured using KPFM is influenced by the CPD between the tip and the surface, the stray capacitance of a cantilever, fixed monopole charges and the dipole moment on surfaces and interfaces. The interpretation of the results of atomic-scale KPFM contrast studies has been controversial [12–15]. Here, we describe an investigation of the contrast mechanism in KPFM with atomic resolution. In Sect. 14.2, we investigate the effect of stray capacitance on measurements of the surface potential using KPFM. Section 14.3 describes the investigation of the surface potential distribution on a TiO_2 (110) 1×1 surface by KPFM and atom-dependent bias-distance spectroscopic mapping. In Sect. 14.4, we describe a new multiple-image method for obtaining the LCPD, frequency shift, and tunneling current on a TiO_2 (110) 1×1 surface with atomic resolution. We summarize our results in Sect. 14.5.

14.2 Stray Capacitance Effect in Kelvin Probe Force Microscopy

The measurement principle of KPFM can be applied in three major modes (see Chaps. 1 and 3 for detailed overviews): frequency modulation (FM-KPFM) [16], amplitude modulation (AM-KPFM) [17, 18], and heterodyne AM-KPFM [19]. In FM-KPFM, the electrostatic force is modulated by applying an ac bias voltage with frequency ω_m (that ranges in practice from 100 to 1000 Hz within the bandwidth of

the phase-locked loop (PLL)); the obtained ω_m component of the frequency shift Δf_m of the cantilever is detected to regulate the bias feedback. This method has high sensitivity to short-range interactions [20, 21], producing a high spatial resolution. In AM-KPFM, the electrostatic force is modulated by applying an ac bias voltage at the second resonance frequency ω_2 of the cantilever. The deflection of the cantilever at ω_2, A_2, is detected to regulate the bias feedback. This method can improve the sensitivity of potential measurements, but it also has high sensitivity to long-range interactions and a large stray capacitance effect between the sample surface and the tip [21, 22]. In heterodyne AM-KPFM, the heterodyne technique is combined with AM-KPFM: an ac electrostatic force of $\cos\omega_2 t$ is generated by mixing the cantilever oscillation at the first resonance ($A\cos\omega_1 t$) with the ac bias voltage $V_{AC}\cos(\omega_2 - \omega_1)t$. The cantilever deflection at ω_2, A_2, is detected to regulate the bias feedback. This method has been demonstrated to remove the effect of stray capacitance between a tip and a sample surface [19].

Here, we describe the effect of stray capacitance on potential measurements using KPFM. The stray capacitance effect was explored in the FM-, AM-, and heterodyne AM modes. We theoretically show that the distance dependence of the modulated electrostatic force in AM-KPFM is significantly weaker than in FM- and heterodyne AM-KPFM and that the stray capacitance of the cantilever is almost entirely eliminated in FM- and heterodyne AM-KPFM. It was experimentally confirmed that the CPD in AM-KPFM was significantly larger than that in FM- and heterodyne AM-KPFM owing to the effect of stray capacitance. We also compared the atomic-scale corrugations in the LCPD among the three modes on a Si(111)-7 × 7 surface, and it was found that the LCPD corrugation in AM-KPFM was significantly weaker than that in FM- and heterodyne AM-KPFM. The very weak LCPD corrugation in AM-KPFM was attributed to the artefact induced by the topographic feedback.

14.2.1 Theoretical Comparison of FM-, AM- and Heterodyne AM-KPFM

Figure 14.1a shows a schematic of the sample and the cantilever with a probe tip. The geometry of the cantilever with the tip can be described using the following three parameters: the surface area of the cantilever S, the height of the tip h, and the radius of curvature of the tip apex R. The cantilever-tip-sample capacitance (C) is modeled as the sum of the tip-sample capacitance without the cantilever (C_{tip}) and the cantilever-sample stray capacitance without the tip (C_{canti}), as shown in Fig. 14.1b, c. The detected electrostatic force $F_{el} = (1/2)(\partial C/\partial z)V^2$ is given by [23, 24]

$$F_{el} = -\frac{\pi\varepsilon_0 R^2}{z(z+R)}(V_{tip}+V_{bias})^2 - \frac{\varepsilon_0 S}{2(z+h)^2}(\langle V_{canti}\rangle + V_{bias})^2, \tag{14.1}$$

where z and ε_0 are the tip-sample distance and the dielectric constant in vacuum, respectively. V_{bias} and V_{tip} are the bias voltage and the CPD between the tip and the

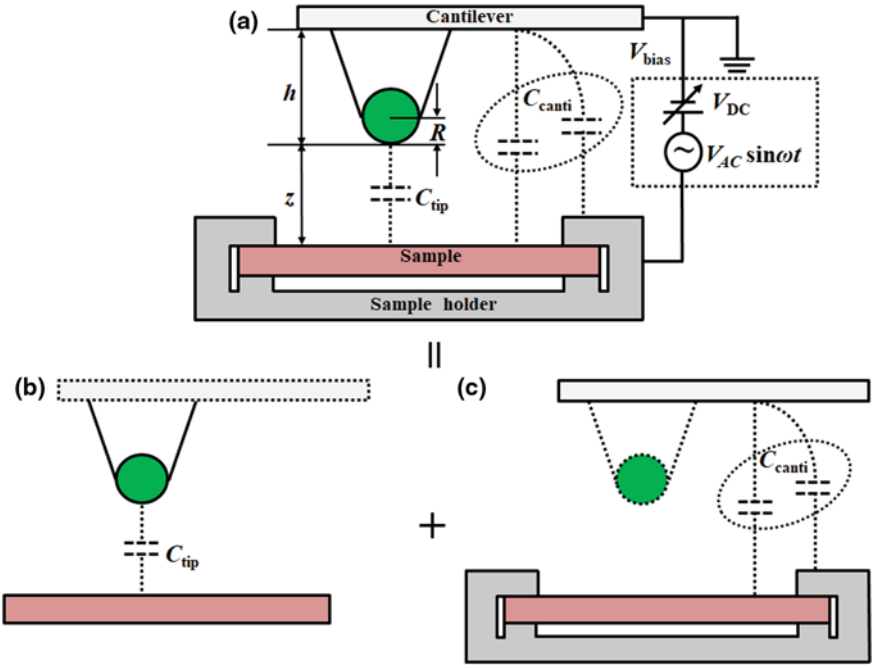

Fig. 14.1 **a** Schematic of a sample and a cantilever with a tip. Here, C_{tip} and C_{canti} are the tip-sample capacitance, **b** without the cantilever and the cantilever-sample stray capacitance, **c** without the tip, respectively. S, h, and R denote the cantilever surface area, the tip height, and the radius of curvature of the tip apex, respectively

sample, respectively. $\langle V_{canti} \rangle$ is the spatially averaged CPD between the cantilever and a macroscopic structure, such as the metal electrodes that hold the sample. When the tip is very close to the surface, $z + R \sim R$ and the tip-sample distance is given by $z(t) = z_{t0} + A\cos\omega_1 t$. Thus, (14.1) is rewritten as

$$F_{el} = -\frac{\pi\varepsilon_0 R}{z_{t0}}\left[1+\frac{A}{z_{t0}}\cos\omega_1 t\right]^{-1}(V_{tip}+V_{bias})^2 - \frac{\varepsilon_0 S}{2(z_{t0}+h)^2}\left[1+\frac{A}{z_{t0}+h}\cos\omega_1 t\right]^{-2}(\langle V_{canti}\rangle + V_{bias})^2, \tag{14.2}$$

where z_{t0} and ω_1 are the mean tip position and the first resonance frequency of the cantilever, respectively. When the amplitude of the oscillation is larger than the mean tip position, $A \ll z_{t0}$, using the Taylor series expansion, (14.2) is written as

$$F_{el} = -\frac{\pi\varepsilon_0 R}{z_{t0}}\left[1-\frac{A}{z_{t0}}\cos\omega_1 t\right](V_{tip}+V_{bias})^2 - \frac{\varepsilon_0 S}{2(z_{t0}+h)^2}\left[1-2\frac{A}{z_{t0}+h}\cos\omega_1 t\right](\langle V_{canti}\rangle + V_{bias})^2. \tag{14.3}$$

Thus, the electrostatic force can be expressed by (14.3).

14.2.1.1 FM-KPFM

Figure 14.2 shows a schematic of an FM-KPFM setup. When a bias voltage signal ($V_{\mathrm{bias}} = V_{\mathrm{DC}} + V_{\mathrm{AC}} \cos\omega_{\mathrm{m}}t$) is applied, a lock-in amplifier detects the ω_{m} component of the resultant frequency shift Δf_{m} of the cantilever. V_{DC} is applied to the surface of the sample to nullify the measured frequency shift, thereby enabling the measurement of V_{CPD}. Thus, the electrostatic force F_{FM} at frequency ω_{m} is given by

$$F_{\mathrm{FM}}(\omega_{\mathrm{m}}) \approx 2\left[\frac{\pi\varepsilon_0 RA}{z_{\mathrm{t0}}^2} + \frac{\varepsilon_0 SA}{(z_{\mathrm{t0}}+h)^3}\right][(1-\alpha_{\mathrm{FM}})V_{\mathrm{tip}} + \alpha_{\mathrm{FM}}\langle V_{\mathrm{canti}}\rangle + V_{\mathrm{DC}}]V_{\mathrm{AC}}\cos\omega_{\mathrm{m}}t, \tag{14.4}$$

where α_{FM} is given by

$$\alpha_{\mathrm{FM}} = \frac{\frac{\varepsilon_0 SA}{(z_{\mathrm{t0}}+h)^3}}{\frac{\pi\varepsilon_0 RA}{z_{\mathrm{t0}}^2} + \frac{\varepsilon_0 SA}{(z_{\mathrm{t0}}+h)^3}} = \left[1 + \frac{\pi R}{S}\frac{(z_{\mathrm{t0}}+h)^3}{z_{\mathrm{t0}}^2}\right]^{-1}, \tag{14.5}$$

where $(1 - \alpha_{\mathrm{FM}})$ and α_{FM} are the electrostatic force proportions due to the tip and the cantilever, respectively. From (14.4), the tip component of the electrostatic force $F_{\mathrm{FM}}(\omega_{\mathrm{m}})$ (the first term on the right-hand side) is proportional to $1/z_{\mathrm{t0}}^2$.

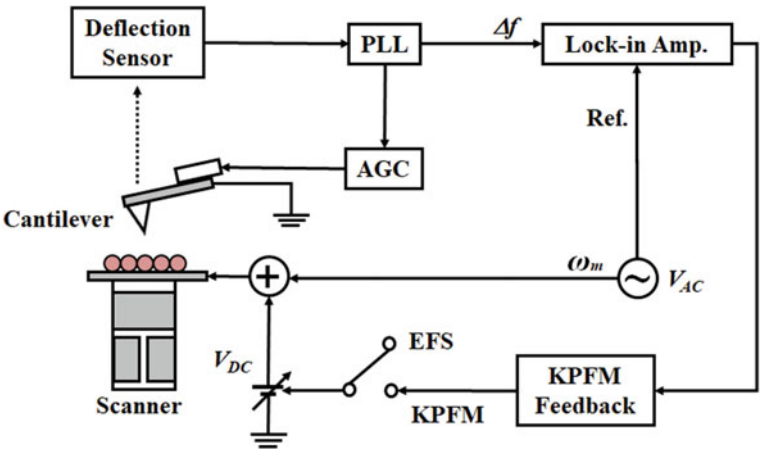

Fig. 14.2 Schematic of FM-KPFM. An ac bias voltage ($V_{\mathrm{AC}}\cos\omega_{\mathrm{m}}t$) is generated by an oscillator. A lock-in amplifier measures the ω_{m} component of the frequency shift Δf_{m}, which is used as a feedback signal in the potential measurement. The parts of the setup used for topographic measurement are omitted in this figure

This strong dependence on the distance indicates that FM-KPFM is sensitive to short-range interactions.

The variation in the frequency shift $\Delta f = -f_0/(2kA)F_{\mathrm{FM}}$ induced by a conservative electrostatic force [25, 26] at a frequency ω_{m} can be expressed as

$$\Delta f_{\mathrm{FM}}(\omega_{\mathrm{m}}) = -\frac{f_{01}}{k_1 A}\left[\frac{\pi\varepsilon_0 \mathrm{RA}}{\mathrm{z}_{\mathrm{t0}}^2} + \frac{\varepsilon_0 \mathrm{SA}}{(\mathrm{z}_{\mathrm{t0}}+\mathrm{h})^3}\right][(1-\alpha_{\mathrm{FM}})V_{\mathrm{tip}} + \alpha_{\mathrm{FM}}\langle V_{\mathrm{canti}}\rangle + V_{\mathrm{DC}}]V_{\mathrm{AC}}\cos\omega_{\mathrm{m}}t. \tag{14.6}$$

V_{CPD} between the tip and sample can be obtained by modifying V_{DC} such that $F_{\mathrm{FM}}(\omega_{\mathrm{m}}) = 0$:

$$V_{\mathrm{CPD}} = -V_{\mathrm{DC}} = -(1-\alpha_{\mathrm{FM}})V_{\mathrm{tip}} - \alpha_{\mathrm{FM}}\langle V_{\mathrm{canti}}\rangle. \tag{14.7}$$

Under the typical conditions shown in Table 14.1, $(1 - \alpha_{\mathrm{FM}}) = 99.3\%$ and $\alpha_{\mathrm{FM}} = 0.7\%$, indicating that the contribution of the cantilever to the electrostatic force at ω_{m} is negligible. Therefore, V_{CPD} between the tip and the sample is approximately given by

$$V_{\mathrm{CPD}} = -V_{\mathrm{tip}}. \tag{14.8}$$

14.2.1.2 AM-KPFM

Figure 14.3 shows a schematic of AM-KPFM. A bias voltage $V_{\mathrm{bias}} = V_{\mathrm{DC}} + V_{\mathrm{AC}}\cos\omega_2 t$ is applied and the cantilever deflection A_2 at frequency ω_2 is measured using a lock-in amplifier. V_{DC} is applied to the sample surface to nullify the measured amplitude, thus enabling the measurement of V_{CPD}. The electrostatic force at a frequency ω_2 is given by

$$F_{\mathrm{AM}}(\omega_2) \approx -\left[2\frac{\pi\varepsilon_0 R}{z_{\mathrm{t0}}} + \frac{\varepsilon_0 S}{(z_{\mathrm{t0}}+h)^2}\right][(1-\alpha_{\mathrm{AM}})V_{\mathrm{tip}} + \alpha_{\mathrm{AM}}\langle V_{\mathrm{canti}}\rangle + V_{\mathrm{DC}}]V_{\mathrm{AC}}\sin\omega_2 t, \tag{14.9}$$

where α_{AM} is given by

$$\alpha_{\mathrm{AM}} = \frac{\frac{\varepsilon_0 S}{(z_{\mathrm{t0}}+h)^2}}{2\frac{\pi\varepsilon_0 R}{z_{\mathrm{t0}}} + \frac{\varepsilon_0 S}{(z_{\mathrm{t0}}+h)^2}} = \left[1 + \frac{2\pi R}{S}\frac{(z_{\mathrm{t0}}+h)^2}{z_{\mathrm{t0}}}\right]^{-1}, \tag{14.10}$$

$(1 - \alpha_{\mathrm{AM}})$ and α_{AM} are the proportions of the electrostatic force provided by the tip and cantilever, respectively. Equation (14.9) shows that the tip component of the electrostatic force F_{AM} (the first term on the right-hand side) is proportional to $1/z_{\mathrm{t0}}$.

Table 14.1 Typical probe and measurement parameters in a KPFM/EFS simulation. Q_2, B, and n_{dc} are the quality factor of cantilever at second resonant frequency, bandwidth of deflection sensor, and noise density of deflection sensor, respectively

A (nm)	k_1 (N/m)	k_2 (N/m)	f_1 (kHz)	f_2 (kHz)	Q_2	z_{t0} (nm)	R (nm)	S (μm)	h (μm)	f_m (kHz)	V_{AC} (V)	B (Hz)	n_{ds} ($fm/\sqrt{Hz}$)
5	40	1568	300	300 × 6.27	30000	6	5	38 × 225	14	1	1	200	100

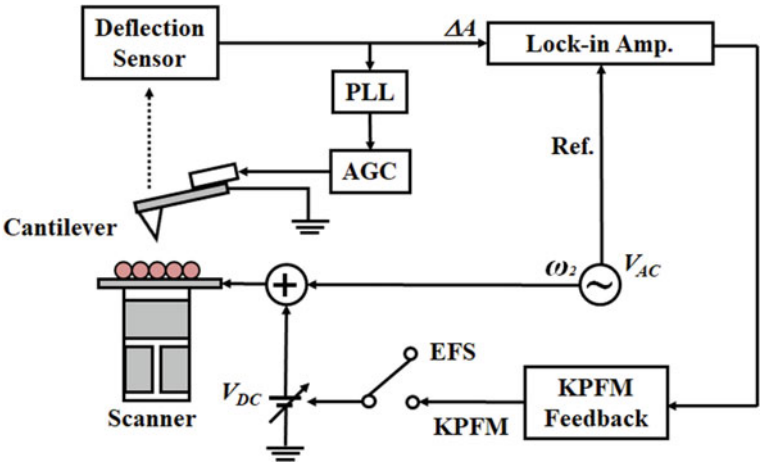

Fig. 14.3 Schematic of AM-KPFM. An ac bias voltage ($V_{AC}\cos\omega_2 t$) is generated by the oscillator. The ω_2 component of the cantilever deflection, which is used as a feedback signal in the potential measurement, is measured using a lock-in amplifier. The parts of the setup used for topographic measurement are omitted in this figure

This weak dependence on the distance implies that AM-KPFM is sensitive to long-range interactions.

In AM-KPFM, the amplitude variation $\Delta A = QF_{AM}/k$ induced by the electrostatic force [26] at frequency ω_2 is given by

$$\Delta A_{AM}(\omega_2) = -\frac{Q_2}{k_2}\left[2\frac{\pi\varepsilon_0 R}{z_{t0}} + \frac{\varepsilon_0 S}{(z_{t0}+h)^2}\right]\left[(1-\alpha_{AM})V_{tip} + \alpha_{AM}\langle V_{canti}\rangle + V_{DC}\right]V_{AC}\cos\omega_2 t, \tag{14.11}$$

where Q_2 and k_2 are the quality factor and the spring constant of the second resonance of the cantilever, respectively. V_{CPD} between the tip and sample is obtained by regulating V_{DC} such that $F_{AM}(\omega_2) = 0$:

$$V_{CPD} = -V_{DC} = -(1-\alpha_{AM})V_{tip} - \alpha_{AM}\langle V_{canti}\rangle. \tag{14.12}$$

Using the typical parameters shown in Table 14.1, it is shown that $(1 - \alpha_{AM}) = 10.7\%$ and $\alpha_{AM} = 89.3\%$, implying that the electrostatic force in AM-KPFM mainly originates from the cantilever contribution (V_{canti}) rather than the tip contribution (V_{tip}).

14.2.1.3 Heterodyne AM-KPFM

Figure 14.4 shows a schematic for heterodyne AM-KPFM. A bias voltage $V_{\text{bias}} = V_{\text{DC}} + V_{\text{AC}} \cos(\omega_2 - \omega_1)t$ is applied and the cantilever deflection A_2 at frequency ω_2 is measured using a lock-in amplifier; V_{DC} is applied to the sample surface to nullify the measured amplitude, thereby enabling the measurement of V_{CPD}. The electrostatic force at frequency ω_2 is given by

$$F_{\text{HAM}}(\omega_2) \approx \left[\frac{\pi\varepsilon_0 RA}{z_{\text{t0}}^2} + \frac{\varepsilon_0 SA}{(z_{\text{t0}}+h)^3}\right] \left[V_{\text{DC}} + (1-\alpha_{\text{HAM}})V_{\text{tip}} + \alpha_{\text{HAM}}\langle V_{\text{canti}}\rangle\right] V_{\text{AC}} \cos\omega_2 t, \tag{14.13}$$

where α_{HAM} is given by

$$\alpha_{\text{HAM}} = \frac{\frac{\varepsilon_0 SA}{(z_{\text{t0}}+h)^3}}{\frac{\pi\varepsilon_0 RA}{z_{\text{t0}}^2} + \frac{\varepsilon_0 SA}{(z_{\text{t0}}+h)^3}} = \left[1 + \frac{\pi R}{S}\frac{(z_{\text{t0}}+h)^3}{z_{\text{t0}}^2}\right]^{-1}, \tag{14.14}$$

$(1 - \alpha_{\text{HAM}})$ and α_{HAM} are the proportions of the electrostatic force provided by the tip and the cantilever, respectively. Equation (14.13) shows that the tip component of the electrostatic force F_{HAM} (the first term on the right-hand side) is proportional to $1/z_{\text{t0}}^2$. This strong dependence on the distance suggests that heterodyne AM-KPFM is sensitive to short-range interactions.

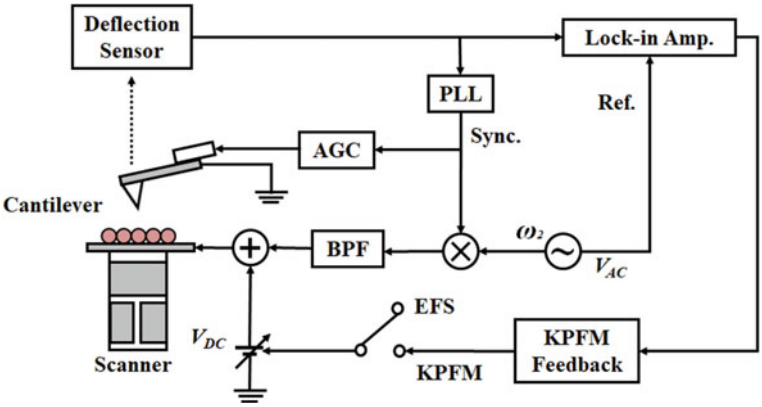

Fig. 14.4 Schematic of heterodyne AM-KPFM. An ac bias voltage ($V_{\text{AC}}\cos(\omega_2\text{-}\omega_1)t$) is generated by multiplying the oscillator signal ($\cos\omega_2 t$) by the PLL signal ($\cos\omega_1 t$), where the latter is synchronized with the first cantilever oscillation then band-pass-filtered (BPF). A lock-in amplifier measures the ω_2 component of the cantilever deflection, which is used as a feedback signal in the potential measurement. The parts of the setup used for topographic measurement are omitted in this figure

Table 14.2 Potential measurements in FM-, AM-, and heterodyne AM-KPFM

	Distance dependence	Electrostatic force proportions	
		Tip (%)	Cantilever (%)
FM-KPFM	$1/z^2$	99.3	0.7
AM-KPFM	$1/z$	10.7	89.3
Heterodyne AM-KPFM	$1/z^2$	99.3	0.7

The variation of the amplitude $\Delta A = QF_{\mathrm{HAM}}/k$ induced by the electrostatic force at frequency ω_2 is given by

$$\Delta A_{\mathrm{HAM}}(\omega_2) = \frac{Q_2}{k_2}\left[\frac{\pi\varepsilon_0 RA}{z_{t0}^2} + \frac{\varepsilon_0 SA}{(z_{t0}+h)^3}\right]\left[(1-\alpha_{\mathrm{HAM}})V_{\mathrm{tip}} + \alpha_{\mathrm{HAM}}\langle V_{\mathrm{canti}}\rangle + V_{\mathrm{DC}}\right]V_{\mathrm{AC}}\cos\omega_2 t. \tag{14.15}$$

V_{CPD} between the tip and sample can be obtained by regulating V_{DC} such that $F_{\mathrm{HAM}}(\omega_2) = 0$:

$$V_{\mathrm{CPD}} = -V_{\mathrm{DC}} = -(1-\alpha_{\mathrm{HAM}})V_{\mathrm{tip}} - \alpha_{\mathrm{HAM}}\langle V_{\mathrm{canti}}\rangle. \tag{14.16}$$

Using the typical parameters shown in Table 14.1, it is shown that $(1 - \alpha_{\mathrm{HAM}}) = 99.3\%$ and $\alpha_{\mathrm{HAM}} = 0.7\%$; thus, the contribution of the cantilever to the electrostatic force can be neglected in heterodyne AM-KPFM. Therefore, $V_{\mathrm{CPD}} \approx V_{\mathrm{tip}}$.

On the basis of the above theoretical analysis, Table 14.2 summarizes the distance dependence of the proportions of the modulated electrostatic force and the electrostatic force provided by the tip and cantilever in AM-, FM-, and heterodyne AM-KPFM. The results show that FM and/or heterodyne AM-KPFM should be used to obtain surface potential distributions with high spatial resolution. Experimental results reported later will confirm the effect of the cantilever on potential measurements in AM-KPFM.

14.2.2 Experimental Results of FM-, AM-, and Heterodyne AM-KPFM

14.2.2.1 Stray Capacitance Effect

Electrostatic force spectroscopy (EFS) (which gives the electrostatic force as a function of the bias voltage V_{DC}) [27] was performed to compare the effect of the stray capacitance in FM-, AM-, and heterodyne AM-KPFM. Figure 14.5 shows the experimental V_{DC}-dependence of the modulated electrostatic force on a Ge(001) surface (As-doped, 0.5–0.6 Ω cm). A commercial silicon cantilever (Nanosensors:

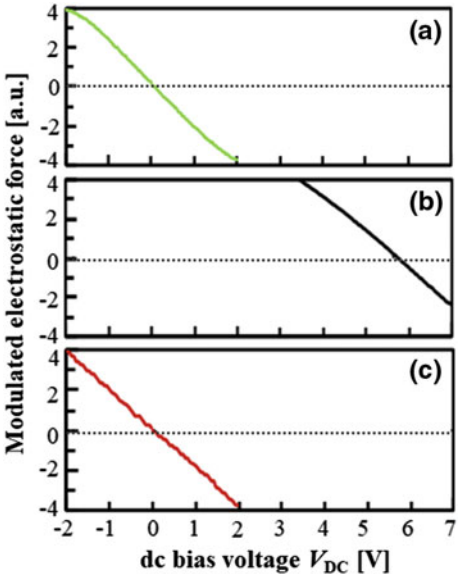

Fig. 14.5 Modulated electrostatic force between a W-coated cantilever and the sample surface in **a** FM-, **b** AM-, and **c** heterodyne AM-KPFM as a function of V_{DC}. The experimental parameters were $k_{1(2)} \approx 33$ (1294) N/m, $f_{1(2)} \approx 158(986)$ *k*Hz, $Q_{1(2)} \approx 10{,}000(4000)$, $\Delta f = -5.0$ Hz, $V_{AC} = 100$ mV, and $f_m = 500$ Hz in FM-KPFM

NCLR-W) was used as a force sensor with a spring constant k_1 of 33 N/m, a resonant frequency $f_1 = \omega_1/2\pi$ of 158 kHz, and a quality factor Q of 20,000. In this study, the tip-sample distance was fixed at $A = 4.0$ nm with $\Delta f = -5$ Hz and $V_{DC} = 0$ V, and EFS measurements were performed at $V_{AC} = 100$ mV. In Fig. 14.5a, c, V_{CPD} is 0.02 V for FM-KPFM and 0.06 V for heterodyne AM-KPFM, where AM-KPFM compensates the CPD between the tip and the sample surface. In Fig. 14.5b, V_{CPD} is 5.7 V in AM-KPFM, which is much larger than in FM- and heterodyne AM-KPFM. Because FM- and heterodyne AM-KPFM are highly sensitive to short-range interactions, as described above, and the V_{CPD} value in heterodyne AM-KPFM is almost the same as that in FM-KPFM, these results suggest that the effect of the stray capacitance from the cantilever, which has a serious effect in AM-KPFM, was almost completely eliminated in heterodyne AM-KPFM. The large increase in V_{CPD} in AM-KPFM is due to the spatially averaged CPD between the cantilever and the other macroscopic structures, such as the stray capacitance around the cantilever, the metal electrodes of the sample holder, and the insulating optical fiber.

14.2.2.2 Surface Potential Measurements

To further elucidate the stray capacitance effect in potential measurements, we obtained topographic and corresponding potential images on a Si(111)-7 × 7 surface (p-type, 0.03 Ω cm) using a single cantilever at room temperature. Figure 14.6a–d show topographic and potential images simultaneously obtained by FM-KPFM, Fig. 14.6b–e show those obtained by AM-KPFM, and Fig. 14.6c–f

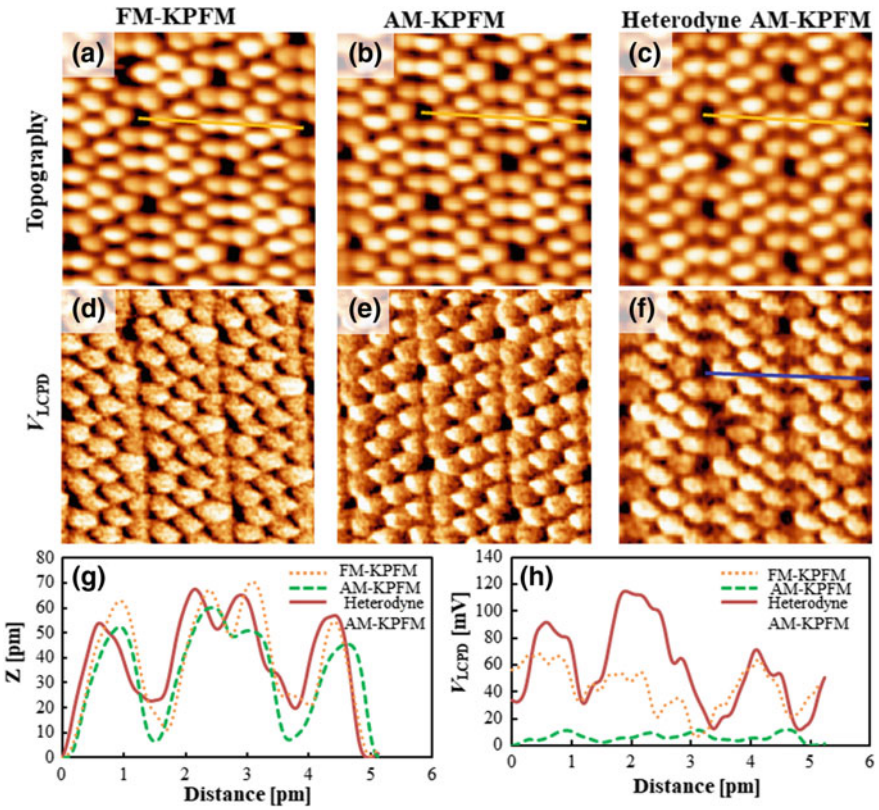

Fig. 14.6 **a** Topographic and **d** corresponding potential images simultaneously obtained by FM-KPFM on Si(111)-7 × 7. **b** Topographic and **e** potential images obtained by AM-KPFM. **c** Topographic and **f** potential images obtained by heterodyne AM-KPFM. **g** Topographic and **h** potential line profiles, where the dotted orange line, dotted green line, and red solid line respectively correspond to the FM-, AM-, and heterodyne AM-KPFM modes. (Frequency shifts of −16.5 Hz were used in FM- and heterodyne AM-KPFM, and a frequency shift of −6.5 Hz was used in AM-KPFM, scan area: 8 nm × 8 nm)

show those obtained by heterodyne AM-KPFM, respectively. Here, to simultaneously obtain the topographic and potential images at atomic resolution, the frequency shift Δf was set below −16.5 Hz in FM- and heterodyne AM-KPFM, and below −6.5 Hz in AM-KPFM. In other words, a potential image at atomic resolution could not be obtained from the weak tip-sample interactions in FM- and heterodyne AM-KPFM; although atomic resolution can be obtained even from the weak tip-sample interactions in AM-KPFM.

Next, we analyze the topographic and LCPD image contrasts. Figure 14.6g and h respectively show the topographic and potential line profiles. The dotted orange line, dotted green line, and red solid line correspond to the line profiles in FM-, AM-, and heterodyne AM-KPFM, respectively. The topographic line profiles exhibit similar

Table 14.3 Topographic and potential corrugations in FM-, AM- and heterodyne AM-KPFM

	ΔZ (pm)	$\Delta LCPD$ (mV)
FM-KPFM	65–70	70–75
AM-KPFM	50–60	10–15
Heterodyne AM-KPFM	55–70	80–110

topographic corrugations (Δz) for the three modes, although the potential line profile of the LCPD corrugations ($\Delta LCPD$) in AM-KPFM is much smaller than those in FM- and heterodyne AM-KPFM. The topographic corrugations Δz are estimated to be in the range of $\Delta z \approx 50$–70 pm for all the topographic images, and the LCPD corrugations $\Delta LCPD$ were estimated to be 10 mV for AM-KPFM and 70–110 mV for FM- and heterodyne AM-KPFM. The offsets of the CPDs are 230 mV, 430 mV and 530 mV, for FM-, AM- and heterodyne AM-KPFM, respectively. A summary of these values of Δz and $\Delta LCPD$ is given in Table 14.3. It can be concluded that the potential contrast in AM-KPFM was much weaker than that in FM- and heterodyne AM-KPFM. The question is, why was the potential contrast in AM-KPFM small and obtained even for a weak tip-sample interaction? It should be noted that: (1) V_{CPD} is given by the equation $V_{\mathrm{CPD}} = -(1-\alpha)\ V_{\mathrm{ti}} - \alpha \left\langle V_{\mathrm{canti}} \right\rangle$ (here, α represents α_{AM}, α_{FM}, and α_{HAM}, which are the proportions of the electrostatic force provided by the cantilevers). $\alpha = 89.3\%$ and $(1-\alpha) = 10.7\%$ mean that the electrostatic force is dominated by the cantilever ($\left\langle V_{\mathrm{canti}} \right\rangle$) for AM-KPFM, whereas $\alpha = 0.3\%$ and $(1-\alpha) = 99.7\%$ mean that the electrostatic force is dominated by the tip for FM- and heterodyne AM-KPFM. (2) The proportional change in the electrostatic force due to the cantilever ($\Delta\alpha$) with respect to the tip-sample distance (Δz_{t0}) in AM-KPFM is much larger than that in FM- and heterodyne AM-KPFM [28]. Hence, the potential change ($\Delta LCPD$) induced by Δz_{t0} is not negligible in AM-KPFM, whereas $\Delta LCPD$ induced by Δz_{t0} is negligible in FM- and heterodyne AM-KPFM. (3) As a result, changes in V_{CPD} are easily induced by Δz_{t0} in AM-KPFM, while such changes are difficult to induce in FM- and heterodyne AM-KPFM. Namely, the weak potential contrast in AM-KPFM is attributed to an artefact due to the change in the tip-sample distance (Δz_{t0}) induced by topographic feedback.

14.3 Surface Potential Measurement of TiO_2(110) by FM-KPFM

TiO_2 is one of the most attractive materials because of its wide applications such as photo-catalytic water splitting and the conversion of solar energy to electricity. The (110) facet is the most stable single-crystal surface of TiO_2 [29, 30], but nevertheless loses atoms in the preparation process. The TiO_2 (110)-1 × 1 surface is composed of alternating rows of fivefold-coordinated Ti (Ti_{5c}) atoms bridged by twofold-coordinated O (O_{2c}) atoms, and the surface charges are auto-compensated.

This surface loses atoms and reconstructs during surface sputtering and annealing at high temperature, introducing O atom vacancies and hydroxyl (OH) impurity defects into the surface. As a result, TiO_2 changes from an insulator into a semiconductor and is chemically active. The macroscale surface potential of TiO_2 (110) has been determined by KPFM [31]. However, V_{LCPD} for the defects on bare TiO_2 (110) surfaces has seldom been reported at the atomic scale by using KPFM. This is because KPFM requires a stable constant tip that is close enough to the surface and sensitive to the surface electronic charge density. AFM research on TiO_2 surfaces has revealed that the tip apex is easily changed, so distinctly different AFM contrasts have been measured [32–34]. The constantly changing tip apex in KPFM experiments has impeded the atomic-level surface potential measurement of TiO_2 (110). Thus, the origin of the V_{LCPD} of TiO_2 (110) is not yet fully understood. As described here, we investigated the surface potential distribution on a TiO_2 (110)-1 × 1 surface by KPFM and atom-dependent bias-distance spectroscopic mapping. The experimental results demonstrate that the local contact potential difference increases on twofold-coordinated oxygen sites, and decreases on OH defects and fivefold-coordinated Ti sites. We propose a qualitative model to explain the origin of the surface potential of TiO_2 (110).

14.3.1 Topography and Local Contact Potential Difference Image of TiO_2(110)

Figure 14.7 shows a ball model of the TiO_2 (110)-1 × 1 surface. Rows of O_{2c} atoms protrude above a plane of O_{3c}, Ti_{5c}, and Ti_{6c} atoms. O_{2c} species were removed during the sample preparation process and led to the formation of O_{2c} vacancies (O_v), which reacted with H_2O molecules from the residual vacuum and were converted to OH impurity defects [34]. The topography and V_{LCPD} images simultaneously recorded by FM-KPFM are shown in Fig. 14.8a and b, respectively. In both images, bright rows alternated with dark rows, and dark spots appeared on the bright rows; this contrast matches the titania 1 × 1 surface structure. The bright rows, dark rows, and dark spots are O_{2c} rows, Ti_{5c} rows, and defects, respectively, and the tip apex was terminated with a cation [34]. This contrast is the typical hole mode contrast [35–37], so the hole mode V_{LCPD} image is the first reported. In the line profile of the topography in Fig. 14.8c, the height difference between O_{2c} and Ti_{5c} is approximately 40 pm, and that between Ti_{5c} and OH is approximately 5 pm. These values are in accordance with the hole mode contrast line profile reported previously [32, 36]. In the line profile of V_{LCPD} in Fig. 14.8d, the difference between O_{2c} and Ti_{5c} is approximately 28 mV, and that between V_{LCPD} for Ti_{5c} and OH is approximately 27 mV. The minimum value in the V_{LCPD} line profile was assigned as zero.

To verify that the measured V_{LCPD} image is not an artifact and to examine the potential distribution in the z direction, we performed DC bias voltage and

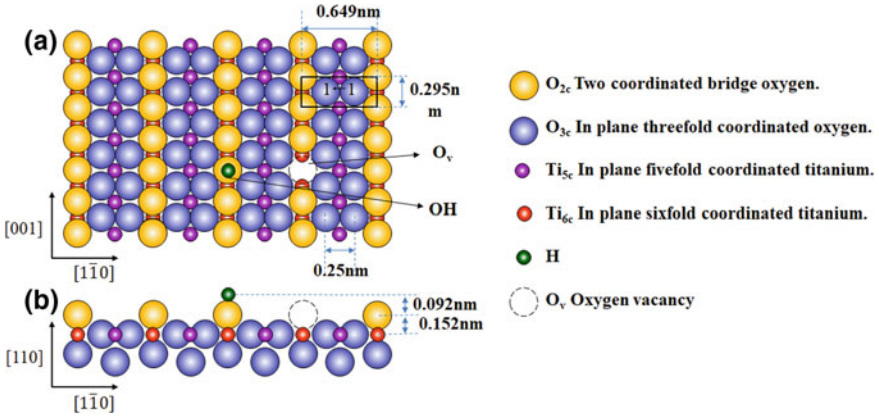

Fig. 14.7 **a** Top view and **b** side view of the ball model of the TiO_2(110) surface

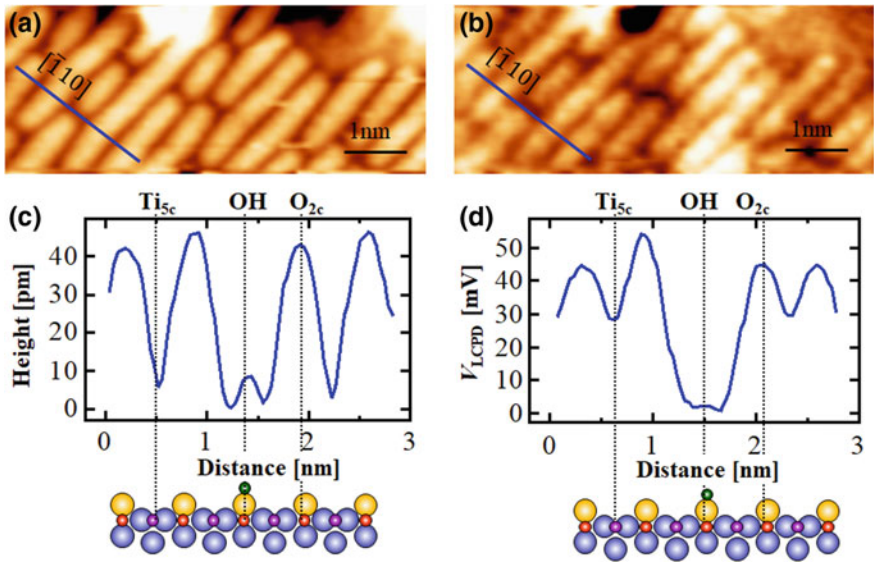

Fig. 14.8 **a** AFM topography and **b** V_{LCPD} image of TiO_2(110)-1 × 1 surface. Line profiles of **c** topography and **d** V_{LCPD} along blue lines in (**a**) and (**b**). $\Delta f = -9.3$ Hz, $A = 10$ nm, $f_0 = 160$ kHz, $f_{ac} = 640$ Hz, $V_{AC} = 0.68$ V. Image size: 8 × 3 nm^2

z-dependent Δf spectroscopic measurements over specific sites. Figure 14.9a, b illustrate the original Δf (V_{DC}, z) and $\Delta f'$ (V_{DC}, z) maps simultaneously measured over the O_{2c} atoms. Figure 14.9c–f show Δf (V_{DC}, z) and $\Delta f'$ (V_{DC}, z) over Ti_{5c} and Δf (V_{DC}, z) and $\Delta f'$ (V_{DC}, z) over OH, respectively. The minimum tip–sample distance over OH was assigned as the zero point. The Δf curves were adjusted to set points depending on the surface topography being measured. In the

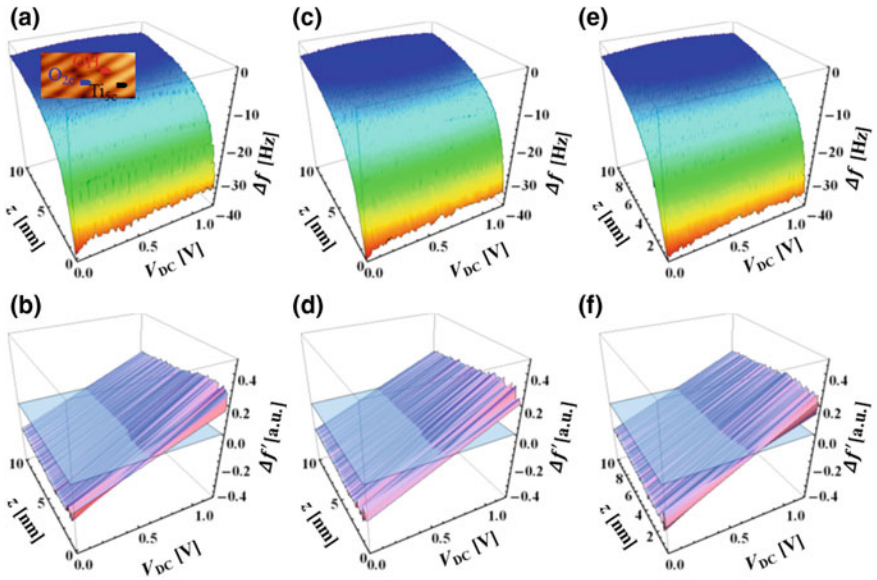

Fig. 14.9 **a** $\Delta f\,(V_{DC}, z)$ and **b** $\Delta f'\,(V_{DC}, z)$ spectroscopic maps over O_{2c}, indicated by the blue sign marked on the insert image. Bias voltage sweep range 0−1.1 V, z sweep range 0−1 nm. **c** $\Delta f\,(V_{DC}, z)$ and **d** $\Delta f'\,(V_{DC}, z)$ measured over Ti_{5c} indicated by the black sign, **e** $\Delta f\,(V_{DC}, z)$ and **f** $\Delta f'\,(V_{DC}, z)$ measured over OH indicated by the red sign

$\Delta f\,(V_{DC}, z)$ map, the vertical curve shows a $\Delta f\,(z)$ spectroscopic curve at a specific V_{DC}, whereas the lateral curve shows a $\Delta f\,(V_{DC})$ curve at a fixed z, which displays a parabolic dependence on V_{DC}. Similarly, in the $\Delta f'$ (z) map, the vertical curve shows the $\Delta f'$ (z) curve at a specific V_{DC}, and the lateral curve depicts $\Delta f'$ (V_{DC}) at a fixed z, which exhibits a linear dependence on V_{DC}. Each $\Delta f'$ (V_{DC}) curve was fitted by a line to extract the DC bias voltage when $\Delta f'$ $(V_{DC}) = 0$ (V_{LCPD}), which corresponds to the point with minimum electrostatic force and minimum Δf for each $\Delta f\,(V_{DC})$ curve.

Curves extracted from $\Delta f\,(V_{dc}, z)$ maps over the O_{2c}, Ti_{5c}, and OH are presented in Fig. 14.10. The $\Delta f\,(z)$ curves in Fig. 14.10a quantify Δf at the minimum electrostatic force at each tip–sample distance. Figure 14.10b shows the short-range force ($F_{SR}(z)$) calculated from $\Delta f\,(z)$ by subtracting the long-range force using the formulas in [38]. When $z > 4$ Å, the three atoms have the same constant short-range force. When $z < 4$ Å, the forces start to decrease and the short-range forces of O_{2c}, Ti_{5c}, and OH begin to diverge. The $V_{LCPD}(z)$ curves at the minimum electrostatic force at each tip–sample distance are depicted in Fig. 14.10c. The $V_{LCPD}(z)$ curves above the three atoms show a constant value in the long-range force region, and start to diverge when $z < 4$ Å. In the region of 2 Å $< z <$ 4 Å, V_{LCPD} of O_{2c} is the highest among the sites and increases slowly. In contrast, V_{LCPD} of Ti_{5c} and OH are relatively small and decrease slowly. At the start of the region of

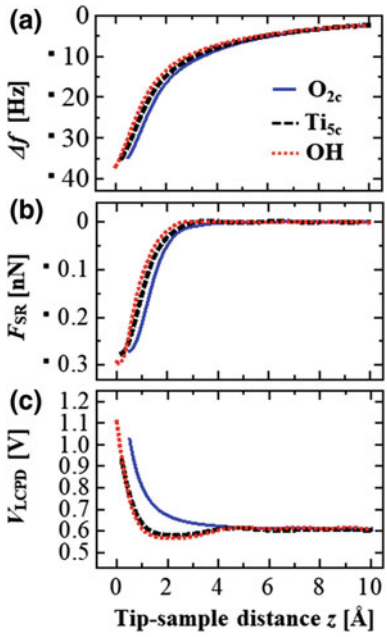

Fig. 14.10 **a** $\Delta f\,(z)$ curves extracted from $\Delta f\,(V_{DC}, z)$ maps at the minimum electrostatic force. The red dotted curve represents OH, black dashed curve represents Ti_{5c}, and blue curve represents O_{2c}. **b** $F_{SR}\,(z)$ calculated from $\Delta f\,(z)$. **c** $V_{LCPD}\,(z)$ spectroscopic curves extracted from $\Delta f\,(V_{DC}, z)$ as in (**a**)

the short-range force, the difference in V_{LCPD} between the three atoms is in accordance with the image of the V_{LCPD} contrast (Fig. 14.8b). Therefore, the V_{LCPD} image is not an artifact of the z topographic feedback. When $z < 2$ Å, V_{LCPD} spectroscopic curves measured over O_{2c}, Ti_{5c}, and OH increase clearly, while F_{SR} above the three atoms decreases sharply. The tendencies of the V_{LCPD} spectroscopic curves are different from those of the short-range force.

14.3.2 Model to Explain the Origin of the Surface Potential of TiO_2 (110)

In the hole mode, the tip apex was terminated with a cation, O_{2c} was partially negatively charged, and Ti_{5c} and OH were positively charged. Therefore, the original surface dipole and the positive dipole of the tip induced a dipole moment that contributed to the surface potential variation. In this case, the surface potential increased over O_{2c} and decreased over Ti_{5c} and OH. Their changes are in accordance with the V_{LCPD} spectroscopic curves in the region of 2 Å $< z <$ 4 Å.

TiO_2 is a typical metal oxide surface with a mixture of ionic and covalent bonding. We considered both the chemical and original surface charge effects of the TiO_2 surface. To qualitatively describe the chemical-interaction-induced surface potential variation, we used the Lennard–Jones potential V_{LJ}, which is described as

$$V_{LJ} = a\varepsilon\left[\left(\frac{r_m}{r}\right)^{12} - 2\left(\frac{r_m}{r}\right)^{6}\right], \tag{14.17}$$

where a is a variable, ε is the vacuum permittivity, r_m is the distance at which the potential reaches its minimum, and r is the distance between tip and sample surface particles. The potential produced by the chemical potential over a positive dipole is shown in Fig. 14.11a as a blue dotted line. The minimum chemical potential was observed at around 1 Å. To qualitatively describe the dipole-induced surface potential variation, we used the dipole interaction. On a TiO_2 (110) surface, for OH, H is a proton with a charge of +1, and the Mulliken charge of O under H is about −0.69. OH protrudes out of the surface and can be described as a permanent positive dipole [39]. The potential of the dipoles was approximated as

$$\phi(r) = \frac{qs}{4\pi\varepsilon_0}\left[\frac{1}{\sqrt{r^2 + (s/r)2 - rs\cos\theta}} - \frac{1}{\sqrt{r^2 + (s/r)2 + rs\cos\theta}}\right], \tag{14.18}$$

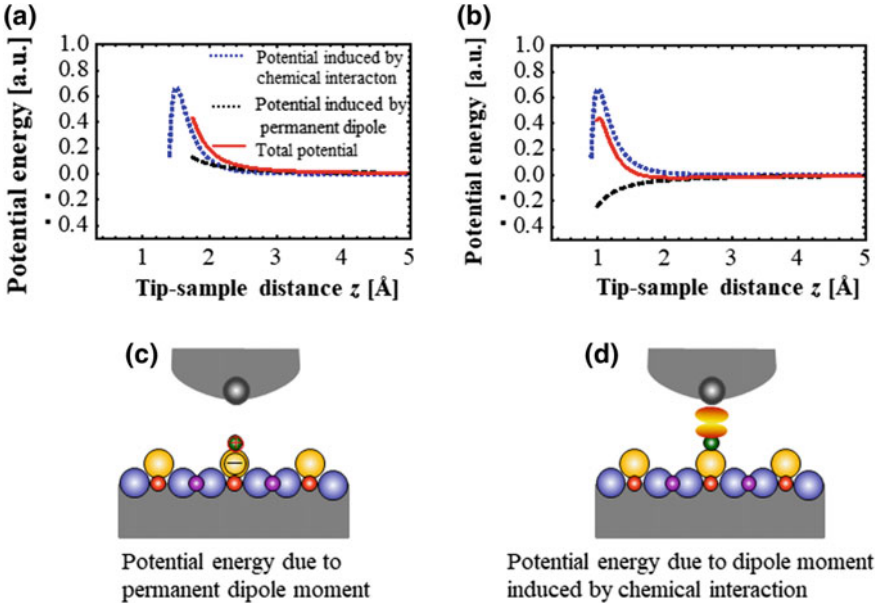

Fig. 14.11 Model for clarifying the surface potential. **a** Calculated potential for the negative dipole O_{2c}. The blue dotted, black dashed, and red solid line represent the potential induced by the chemical interaction, permanent dipole, and total potential, respectively. **b** Calculated potential for the positive dipole. **c** Schematic model for clarifying the potential energy due to a positive permanent dipole moment. **d** Schematic model for clarifying the potential energy due to a dipole moment induced by chemical interaction

where ϕ, q, s, and r represent the potential produced by the dipole, the charge of the dipole, the distance between the two atoms of the dipole, and the distance between the tip and midpoint of the dipole, respectively. θ is the angle between the axis along the dipole and the line along s; here, we assumed that θ is zero. The potential induced by the OH dipole is drawn as a black dashed line, as shown in Fig. 14.11a.

The total potential is the sum of the potential produced by the permanent dipole. The calculated total potential of OH is represented by a red solid line in Fig. 14.11a, which is nearly flat in the range of 1.5 Å $< z <$ 5 Å, and increases in the range of 1 Å $< z <$ 1.5 Å. The total potential of OH resembles the shape of the potential of OH in Fig. 14.10c. The zero point of the total potential is different from the measured potential of OH in the range of 2.5 Å $< z <$ 5 Å. This is because the measured potential includes the CPD effects, while in this calculation, the long-range CPD was not considered.

The Mulliken charge of O_{2c} is −0.60 [40], and O_{2c} protrudes out of the TiO_2 surface and forms a permanent negative dipole. Figure 14.11b shows the calculated potential of O_{2c}. The calculated total potential of O_{2c} is zero in the range of 2.5 Å $< z <$ 5 Å, slightly increases in the range of 1.5 Å $< z <$ 2.5 Å, and then sharply increases in the range of 1 Å $< z <$ 1.5 Å. The distance dependence of the calculated total potential of O_{2c} in Fig. 14.11b is similar to that of the O_{2c} potential in Fig. 14.10c. The absolute value of the dipole formed over OH is stronger than that over O_{2c}, which is inconsistent with previous results [41].

Our results are different from those of previous V_{LCPD} spectroscopic research on Si(111)-7 × 7 [5, 42], in which the V_{LCPD} curves of the adatoms showed similar tendencies, and the shapes of the V_{LCPD} curves and short-range force were similar. The surface potential of a Si(111)-7 × 7 surface is dominated by the tip–sample chemical interaction-induced charge redistribution. The chemical-force-induced charge redistribution affected the surface potential [2, 3]. Different from the Si surface, we suggest that the potential of the TiO_2 surface is composed of potential produced by the original permanent dipole (shown in Fig. 14.11c), the potential produced by the chemical interaction-induced dipole (shown in Fig. 14.11d), and the CPD.

Another reason for the discrepancy of our results with the reported ones may be that in this research, the tip apex was terminated by a cation, and the electrostatic interaction with the surface may cause the charge to redistribute. Because of this, the tip-induced electrostatic potential of the surface positive permanent dipole decreased and the tip-induced electrostatic potential of the negative permanent dipole increased. When the tip is terminated by an anion, the directions of the tip-induced electrostatic potential over these two surface polarity dipoles will reverse, and the measured total potential tendencies over OH and O_{2c} will be different from these results. Therefore, the measured surface potential of TiO_2 was also affected by the tip-apex polarity [33].

14.4 Simultaneous Measurement of Topography, Tunneling Current, and Surface Potential

The combination of AFM and scanning tunneling microscopy (STM) provides excellent opportunities for investigating atomic-scale physical properties such as the surface structure and density of states on Si(111) and TiO_2 surfaces [16, 17]. The simultaneous measurement of topography and tunneling current has also been performed by AFM/STM [18, 19], which can distinguish surface species by recording the tunneling current (I_t) during non-contact AFM (nc-AFM) imaging. The separation of single and double hydroxyls in an I_t image has also been reported, and the same features have been presented in an nc-AFM topographic image. Also, simultaneous measurement of the topography and CPD has been realized by AFM/KPFM [20, 21]. To simultaneously characterize the electronic structure and surface potential, it is important to obtain images of the frequency shift, tunneling current, and LCPD. Here, we describe a multiple-image method based on AFM/KPFM, where frequency shift, tunneling current, and LCPD images are obtained by measurement on a TiO_2(110) surface at 78 K.

14.4.1 Theory of FM-KPFM Without Bias Voltage Feedback

We discuss the theory of FM-KPFM without bias voltage feedback and derive equations for the relationship between the CPD and Δf. The electrostatic force F_{es} between the tip and sample surface is given by $F_{el} = (1/2)(dC/dz)V^2$, where C, z, and V are the capacitance of the cantilever-tip-sample, the tip-sample distance, and the tip-sample potential, respectively. Representing the tip apex as a spherical cap with radius of curvature R and the sample surface as an infinite plane [23], F_{el} is given by

$$F_{el} \cong -\frac{\pi\varepsilon_0 R^2}{z(z+R)}(V_{tip}+V_{bias})^2, \tag{14.19}$$

where V_{tip} represents V_{CPD}, and V_{bias} is the bias voltage applied between the tip and sample. When the tip is very close to the surface so that $z + R \sim R$, F_{es} can be approximated as [24]

$$F_{el} \cong -\frac{\pi\varepsilon_0 R}{z}(V_{tip}+V_{bias})^2, \tag{14.20}$$

where F_{es} is proportional to $1/z$ ($1/z^n$, $n = 1$). This approximation is not satisfied in ordinary FM-AFM; however, (14.20) is more intuitive than (14.19). For FM-AFM, z can be expressed as $z(t) = d + A + A\cos 2\pi f_0 t$, where d is the shortest distance

between the tip and sample, A is the oscillation amplitude, and f_0 is the resonance frequency of the cantilever. Δf can be calculated by integrating F_{es} over one oscillation period [43–45] as

$$\Delta f_{el} = \frac{f_0}{\sqrt{2\pi k A^{3/2}}} \int_0^{2A} \frac{F_{es}(z)}{\sqrt{z-d}} \frac{1-[(z-d)/A]}{\sqrt{1-[(z-d)/2A]}} \mathrm{d}(z-d), \tag{14.21}$$

where k is the spring constant of the cantilever. Substituting (14.20) into (14.21), Δf_{es} can be expressed as

$$\Delta f_{el} = -\frac{f_0 \pi \varepsilon_0 R}{kA^2} \left[\frac{d/A+1}{\sqrt{(d/A+1)^2-1}} - 1 \right] (V_{tip} + V_{bias})^2. \tag{14.22}$$

If the cantilever is oscillated with a large amplitude A that is much larger than the shortest tip-sample distance $d < A$, by expanding (14.22) as a Taylor series, Δf_{el} can be written as

$$\Delta f_{el} = -\frac{f_0 \pi \varepsilon_0 R}{\sqrt{2} k A^{3/2}} \frac{(V_{tip} + V_{bias})^2}{\sqrt{d}}, \tag{14.23}$$

where $V_{bias} = V_{dc} + V_{ac}\cos 2\pi f_m t$, where V_{dc} is the DC voltage. Therefore, $V_{tip} + V_{bias} = V_{dc} + V_{CPD} + V_{ac}\cos 2\pi f_m t$ and Δf_{es} is rewritten as

$$\Delta f_{el} = -\frac{f_0 \pi \varepsilon_0 R}{\sqrt{2d} k A^{3/2}} \left[(V_{dc} + V_{CPD})^2 + \frac{V_{ac}^2}{2} + 2(V_{dc} + V_{CPD}) V_{ac} \cos 2\pi f_m t - \frac{V_{ac}^2 \cos 4\pi f_m t}{2} \right]. \tag{14.24}$$

Equation (14.24) can be divided into three components:

$$\Delta f_{el\,(dc)} = -\frac{f_0 \pi \varepsilon_0 R}{\sqrt{2d} k A^{3/2}} \left[(V_{dc} + V_{CPD})^2 + \frac{V_{ac}^2}{2} \right], \tag{14.25}$$

$$\Delta f_m = -\frac{f_0 \pi \varepsilon_0 R}{\sqrt{2d} k A^{3/2}} 2(V_{dc} + V_{CPD}) V_{ac} \cos 2\pi f_m t, \tag{14.26}$$

$$\Delta f_{2m} = \frac{f_0 \pi \varepsilon_0 R}{\sqrt{2d} k A^{3/2}} \frac{V_{ac}^2}{2} \cos 4\pi f_m t. \tag{14.27}$$

Here, $\Delta f_{es(dc)}$, Δf_m, and Δf_{2m} represent the f_{dc}, f_m, and $2f_m$ components of Δf, respectively. V_{CPD} is calculated by dividing (14.26) by (14.27) and is given by

$$V_{\mathrm{CPD}} = -V_{\mathrm{dc}} - \mathrm{sgn}(\alpha_{\mathrm{m}})\frac{V_{\mathrm{ac}}}{4}\frac{|\Delta f_{\mathrm{m}}|}{|\Delta f_{2\mathrm{m}}|}, \tag{14.28}$$

where $\mathrm{sgn}(\alpha_{\mathrm{m}})$ is the sign of V_{CPD} and is determined by α_{m}, which is the phase difference between the V_{ac} bias voltage and Δf_{m}.

Note that the transfer function (T) of the PLL depends on the modulation frequencies f_{m} and $2f_{\mathrm{m}}$. This makes it necessary to calibrate the reduced gain, and V_{CPD} is expressed by

$$V_{\mathrm{CPD}} = -V_{\mathrm{dc}} - \mathrm{sgn}(\alpha_{\mathrm{m}})\frac{V_{\mathrm{ac}}}{4}\frac{|\Delta f_{\mathrm{m}}|}{|\Delta f_{2\mathrm{m}}|}\frac{T(f_{2\mathrm{m}})}{T(f_{\mathrm{m}})}. \tag{14.29}$$

In atomic-resolution FM-KPFM, the CPD is specifically referred to as the LCPD, namely, $V_{\mathrm{CPD}} = V_{\mathrm{LCPD}}$.

14.4.2 Experimental AFM/STM/KPFM System

Figure 14.12 shows the experimental setup of AFM/STM/KPFM used to simultaneously obtain multiple images of the frequency shift (Δf), tunneling current ($\langle I_{\mathrm{t}}\rangle$), and local contact potential difference (V_{LCPD}). In the AFM circuit, the cantilever was oscillated at its resonant frequency by automatic gain control (AGC) while maintaining a constant oscillation amplitude. The deflection of the cantilever was detected by an optical beam deflection system and fed into a phase-locked loop (PLL) circuit. A bias voltage $V_{\mathrm{BIAS}} = V_{\mathrm{DC}} + V_{\mathrm{AC}}\cos 2\pi f_{\mathrm{m}}t$ was applied between the tip and sample. The frequency shift (Δf) was measured using the PLL and divided into two circuits. One was used as the tip-sample interaction feedback signal in the first scan before performing the scan in the constant-height mode, and the other was fed into the lock-in amplifiers of the FM-KPFM system without bias voltage feedback. A band elimination filter (BEF) was used to eliminate the modulated signals to ensure stable feedback in the AFM circuit. V_{LCPD} was calculated from the f_{m} and $f_{2\mathrm{m}}$ components of the frequency shift, which were measured using two lock-in amplifiers. The tunneling current $\langle I_{\mathrm{t}}\rangle$ was recorded in a separate channel from the conductive tip while the bias voltage was applied to the sample. All the measurements performed in the multiple-signal imaging experiment were carried out in the constant-height mode to prevent crosstalk between the signals of the frequency shift and tunneling current. Experiments were performed using a laboratory-built nc-AFM apparatus equipped with an optical beam deflection (OBD) system under UHV (3×10^{-11} Torr) at a low temperature (78 K). The deflection noise density was estimated to be 9.8 fm/$\sqrt{\mathrm{Hz}}$, indicating the high sensitivity of the system [46].

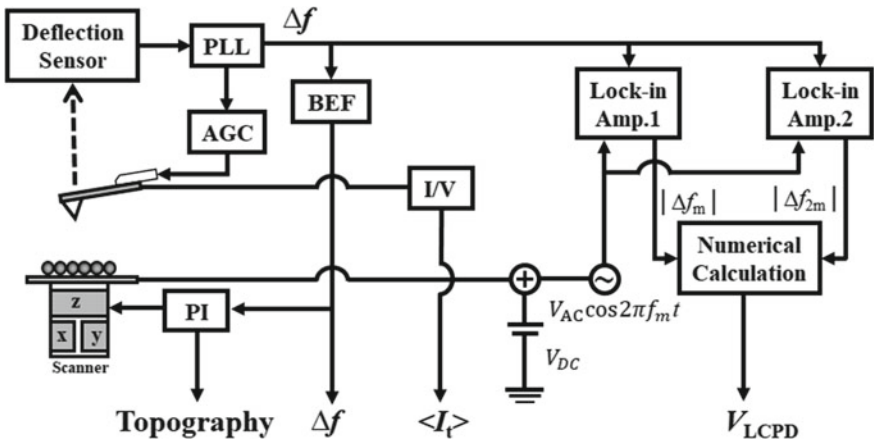

Fig. 14.12 Schematic diagram of AFM/STM/KPFM setup for simultaneously obtaining multiple images of the frequency shift (Δf), tunneling current ($\langle I_t \rangle$), and local contact potential difference (V_{LCPD})

14.4.3 Multiple Images with Atomic Resolution on a TiO_2(110) Surface

Figure 14.13 shows frequency shift ($|\Delta f|$), tunneling current ($|\langle I_t \rangle|$), and local contact potential difference (V_{LCPD}) images of a TiO_2(110)-(1 × 1) surface in the hole mode with atomic resolution and the corresponding line profiles. A commercial Ir-coated cantilever (Nanosensors SD-T10L100, $f_0 \sim 800$ kHz) was used as a sensor. In the $|\Delta f|$ image shown in Fig. 14.13a, an OH defect was observed as a dark spot (dark dotted circle) and a subsurface defect was also observed (blue dotted circle). In the $|\langle I_t \rangle|$ image (see Fig. 14.13b), the same contrast was obtained, and the subsurface defect was clearly detected. From the line profile, it was found that the tunneling probability at the O site was higher than that at the Ti site, in good agreement with previous studies by Schwarz et al., Enevoldsen et al., and Tanner et al. [27, 33, 47]. Note that the subsurface defect in the $|\langle I_t \rangle|$ image was observed as a dark feature, in contrast to other studies [27, 48]. We consider that this occurred for two reasons. First, it was probably due to the different tip-sample distances in our study and the previous studies. Second, the subsurface defects may have modified the electronic states near the Fermi level and decreased the tunneling probability of adjacent atoms. Our result is different from that in the other studies [27], in which it was reported that "subsurface defects decrease the barrier to tunneling". The subsurface defects may have modified the electronic states differently in the previous studies, in which the subsurface defect was assigned to a H atom. In the V_{LCPD} image (see Fig. 14.13c), the imaging contrast was the reverse of

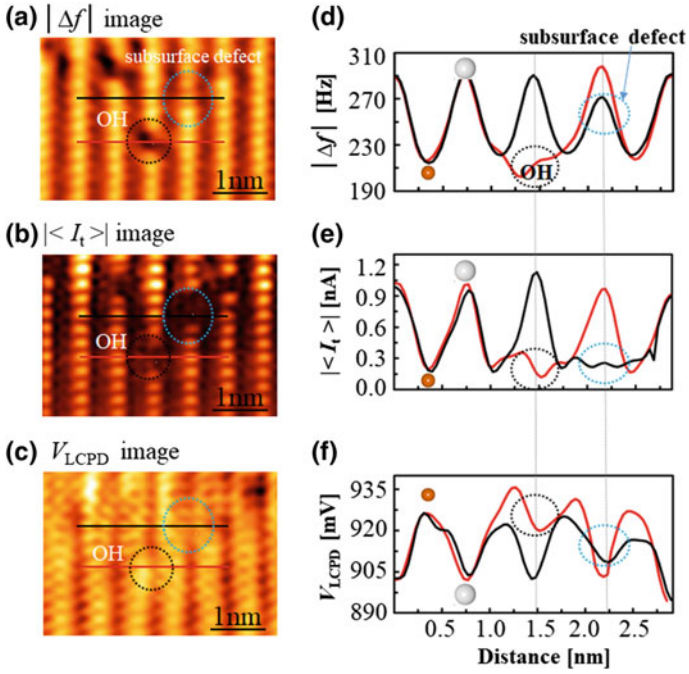

Fig. 14.13 Multiple images of TiO_2(110) surface with atomic resolution and corresponding line profiles obtained by AFM/KPFM. **a** Frequency shift ($|\Delta f|$) image, **b** tunneling current ($|\langle I_t \rangle|$) image, and **c** local contact potential difference (V_{LCPD}) image. **d**–**f** Line profiles across an OH defect on the surface and subsurface defect (along solid red line and solid black line in (**a**)–(**c**), respectively). ($f_0 = 812$ kHz, $Q = 23328$, $\Delta f = -299$ Hz, $V_{DC} = 1$ V, $V_{AC} = 1.5$ V, $A = 500$ pm, size: 4.3×3.05 nm^2)

that in the $|\Delta f|$ and $|\langle I_t \rangle|$ images, i.e., the OH defect and the rows of O and Ti atoms appeared as a bright spot and dark and bright rows, respectively. From the line profile, it was found that the relative value of V_{LCPD} between the Ti and O sites was approximately 30 mV, in good agreement with our previous study [49]. Excess electrons resulting from the surface defects were delocalized on the proximate Ti rows [50, 51], resulting in the higher value of V_{LCPD} on the defect sites than on the nearby O rows. Therefore, we have successfully imaged the frequency shift, tunneling current, and LCPD on a TiO_2(110) surface with atomic resolution for the first time. The multiple-image method is expected to help acquire significant results in surface physics and chemistry, and can also greatly assist in distinguishing different surface species and the site-dependent surface potential.

14.5 Conclusions

KPFM combined with AFM has been extensively used to measure potential distributions, charge transfer, and electronic/electrical properties on surfaces. The surface potential distribution measured using KPFM is influenced by the CPD between the tip and surface, the effect of stray capacitance of a cantilever, and fixed monopole charges on the surface and tip. The interpretation of atomic-scale KPFM contrast has been controversial. Here, we investigated the contrast mechanism in KPFM with atomic resolution.

The effect of the stray capacitance on potential measurements was explored in the FM-, AM-, and heterodyne AM-KPFM modes. The distance dependence of the modulated electrostatic force in AM-KPFM is much weaker than in FM- and heterodyne AM-KPFM, and the stray capacitance of the cantilever, which has a strong effect on potential measurements in AM-KPFM, was almost completely eliminated in FM- and heterodyne AM-KPFM. The LCPD corrugation in AM-KPFM was much smaller than that in FM- and heterodyne AM-KPFM at a low ac bias voltage, which was attributed to an artefact induced by the topographic feedback.

An investigation of the LCPD on a TiO_2 (110)-1 × 1 surface and atom-dependent bias-distance spectroscopic mapping were performed. The LCPD of TiO_2 (110) is dominated not only by the permanent surface dipole between the tip apex atom and the surface, but also by the dipoles induced by the chemical interaction between the tip and sample.

We proposed a new multiple-image method for obtaining frequency shift, tunneling current, and LCPD images. For the first time, we obtained three atomic-resolution images of a TiO_2(110) surface at 78 K. We found that the tunneling probability at an O site was higher than that at a Ti site for a small tip-sample distance. V_{LCPD} is higher on a defect site than on nearby O rows because excess electrons caused by surface defects are delocalized on the nearby Ti rows. The multiple-image method can be used to investigate the charge transfer between nanoparticles and surface sites and to elucidate the mechanisms of catalytic reactions.

Acknowledgements This work was supported by a Grant-in-Aid for Scientific Research from Japan Society for the Promotion of Science (JSPS) from the Ministry of Education, Culture, Sports, Science and Technology (MEXT) through MEXT/JSPS KAKENHI Grant Numbers JP16H06327, JP17H01061, and JP16H06504 for Scientific Research on Innovative Areas "Nano-Material Optical-Manipulation". This work was also supported by National Natural Foundation of China (Number 91336110) and China Scholarship Council (CSC).

References

1. G. Binnig, C.F. Quate, Ch. Gerber, Phys. Rev. Lett. **56**, 930 (1986)
2. R. García, R. Pérez, Surf. Sci. Rep. **47**, 197 (2002)
3. Y. Sugimoto, P. Pou, M. Abe, P. Jelinek, R. Pérez, S. Morita, Ó. Custance, Nature **446**, 64 (2007)
4. J. Bamidele, S.H. Lee, Y. Kinoshita, R. Turanský, Y. Naitoh, Y.J. Li, Y. Sugawara, I. Štich, L. Kantorovich, Nat. Commun. **5**, 4476 (2014)
5. Y. Naitoh, R. Turanský, J. Brndiar, Y.J. Li, I. Štich, Y. Sugawara, Nat. Phys. (2017) (Accepted for publication)
6. G.H. Enevoldsen, T. Glatzel, M.C. Chrisensen, J.V. Laurisen, F. Besenbacher, Phys. Rev. Lett. **100**, 236104 (2008)
7. S. Kawai, T. Glatzel, H. Hug, E. Meyer, Nanotechnology **21**, 245704 (2009)
8. L. Nony, F. Bocquet, C. Loppacher, T. Glatzel, Nanotechnology **20**, 264014 (2009)
9. M. Bieletzki, T. Hynninen, T.M. Soini, M. Pivetta, C.R. Henry, A.S. Foster, F. Esch, C. Barth, U. Heiz, Phys. Chem. Chem. Phys. **12**, 3203 (2010)
10. C. Barth, A.S. Foster, C.R. Henry, A.L. Shluger, Adv. Mater. **23**, 477 (2011)
11. K. Wandelt, Appl. Surf. Sci. **111**, 1 (1997)
12. L. Nony, F. Bocquet, C. Loppacher, Phys. Rev. B. **78**, 035410 (2008)
13. L. Nony, A.S. Foster, F. Bocquet, C. Loppacher, Phys. Rev. Lett. **103**, 036802 (2009)
14. S. Sadewasser, P. Jelinek, C.K. Fang, O. Custance, Y. Yamada, Y. Sugimoto, M. Abe, S. Morita, Phys. Rev. Lett. **103**, 266103 (2009)
15. M. Tsukada, A. Masago, M. Shimizu, J. Phys. Condens. Matter. **24**, 084002 (2012)
16. S. Kitamura, K. Kobayashi, H. Yamada, K. Matsushige, Appl. Surf. Sci. **157**, 222 (2000)
17. A. Kikukawa, S. Hosaka, R. Imura, Rev. Sci. Instrum. **67**, 1464 (1996)
18. T. Glatzel, S. Sadewasser, M.C. Lux-Sterner, Appl. Surf. Sci. **210**, 84 (2003)
19. Y. Sugawara, L. Kou, Z.M. Ma, T. Kamijo, Y. Naitoh, Y.J. Li, Appl. Phys. Lett. **100**, 223104 (2012)
20. S.A. Burke, J.M. LeDue, Y. Miyahara, J.M. Topple, S. Fostner, P. Grütter, Nanotechnology **20**, 264012 (2009)
21. D. Ziegler, J. Rychen, N. Naujoks, A. Stemmer, Nanotechnology **18**, 225505 (2007)
22. A. Sadeghi, A. Baratoff, S.A. Ghasemi, S. Goedecker, T. Glatzel, S. Kawai, E. Meyer, Phys. Rev. B. **86**, 075407 (2012)
23. S. Hudlet, M.S. Jeana, C. Guthmann, J. Berger, Eur. Phys. J. B. **2**, 5 (1998)
24. L. Olsson, N. Lin, V. Yakimov, R. Erlandsson, J. Appl. Phys. **84**, 4060 (1998)
25. B. Gotsmann, C. Seidel, B. Anczykowski, H. Fuchs, Phys. Rev. B. **60**, 11051 (1999)
26. T. Fukuma, K. Kobayashi, H. Yamada, K. Matsushige, Rev. Sci. Instrum. **75**, 4589 (2004)
27. M.Z. Baykara, H. Mönig, T.C. Schwendemann, Ö. Ünverdi, E.I. Altman, U.D. Schwarz, Appl. Phys. Lett. **108**, 071601 (2016)
28. Z.M. Ma, L. Kou, Y. Naitoh, Y.J. Li, Y. Sugawara, Nanotechnology **24**, 225701 (2013)
29. D.W. Goodman, J. Catal. **216**, 213 (2003)
30. U. Diebold, J. Lehman, T. Mahmoud, M. Kuhn, G. Leonardelli, W. Hebenstreit, M. Schmid, P. Varga, Surf. Sci. **411**, 137 (1998)
31. A. Sasahara, H. Uetsuka, H. Onishi, Surf. Sci. Lett. **529**, L245 (2003)
32. G.H. Enevoldsen, H.P. Pinto, A.S. Foster, M.C.R. Jensen, A. Kuhnle, M. Reichling, W.A. Hofer, J.V. Lauritsen, F. Besenbacher, Phys. Rev. B. **78**, 045416 (2008)
33. G.H. Enevoldsen, A.S. Foster, M.C. Christensen, J.V. Lauritsen, F. Besenbacher, Phys. Rev. B. **76**, 205415 (2007)
34. A. Yurtsever, Y. Sugimoto, M. Abe, S. Morita, Nanotechnology **21**, 165702 (2010)
35. K. Fukui, H. Onishi, Y. Iwasawa, Phys. Rev. Lett. **79**, 4202 (1997)
36. J.V. Lauritsen, A.S. Foster, G. Holesen, M.C. Christensen, A. Kuhnle, S. Helveg, J.R. Rostrup-Nielsen, B.S. Clausen, M. Reichling, F. Besenbacher, Nanotechnology **17**, 3436 (2006)

37. H.P. Pinto, G.H. Enevoldsen, F. Besenbacher, J.V. Lauritsen, A.S. Foster, Nanotechnology **20**, 264020 (2009)
38. J. Sader, S. Jarvis, Appl. Phys. Lett. **84**, 1801 (2004)
39. T. Minato et al., J. Chem. Phys. **130**, 124502 (2009)
40. A.T. Paxton, N.L. Thien, Phys. Rev. B. **57**, 1579 (1998)
41. A. Yurtsever, D. Fernandez-Torre, C. Gonzalez, P. Jelinek, P. Pou, Y. Sugimoto, M. Abe, R. Perez, S. Morita, Phys. Rev. B. **85**, 125416 (2012)
42. L. Kou, Z.M. Ma, Y.J. Li, Y. Naitoh, M. Komiyama, Y. Sugawara, Nanotechnology **26,** 195701 (2015)
43. F.J. Giessibl, Phys. Rev. B. **56**, 16010 (19977)
44. H. Holscher, U.D. Schwarz, R. Wiesendanger, Appl. Surf. Sci. **140**, 344 (1999)
45. F.J. Giessibl, H. Bielefeldt, Phys. Rev. B. **61**, 9968 (2000)
46. E. Arima, H.F. Wen, Y. Naitoh, Y.J. Li, Y. Sugawara, Rev. Sci. Instrum. **87**, 093113 (2016)
47. R.E. Tanner, M.R. Castell, G.A.D. Briggs, Surf. Sci. **412/413**, 672 (1998)
48. G.H. Enevoldsen, H.P. Pinto, A.S. Foster, M.C.R. Jensen, W.A. Hofer, B. Hammer, J.V. Lauritsen, F. Besenbacher, Phys. Rev. Lett. **102**, 136103 (2009)
49. L. Kou, Y.J. Li, T. Kamijyo, Y. Naitoh, Y. Sugawara, Nanotechnology **27**, 505704 (2016)
50. T. Minato, Y. Sainoo, Y. Kim, H.S. Kato, K.I. Aika, M. Kawai, J. Zhao, H. Petek, T. Huang, W. He, B. Wang, Z. Wang, Y. Zhao, J. Yang, J.G. Hou, J. Chem. Phys. **130**, 124502 (2009)
51. M. Setvin, C. Franchini, X. Hao, M. Schmid, A. Janotti, M. Kaltak, C.G. Van de Walle, G. Kresse, U. Diebold, Phys. Rev. Lett. **113**, 086402 (2014)

Chapter 15
The Electrostatic Field of CO Functionalized Metal Tips

Michael Ellner, Pablo Pou and Ruben Perez

Abstract This chapter conclusively shows that the electric field created by CO functionalized metal tips cannot be described by a single dipole. It is necessary to take into account both the positive dipole that describes the electric field created by the metal tip and the negative charge cloud strongly localized in front of the oxygen atom. We have incorporated this insight into a theoretical model that allows the efficient simulation of AFM measurements retaining a first-principles accuracy. Using this model, we have identified the contrast formation mechanisms for localized ionic defects (Cl vacancies on a metal–supported NaCl bilayer). The opposite sign and different spatial extension of the associated electric fields explain the rich contrast observed. While both terms compete to determine the contrast of uncompensated, extended defects like the Cl vacancy, atomic–scale resolution of the ionic lattice arises mainly from the CO electric field as the more extended field created by the metal apex averages out the contribution coming from those periodic and rapidly varying charge distributions. The insight gained from our analysis is used to address the apparent contradiction in the interpretation of previous experiments involving CO molecules either as a tip on a metallic apex probing ionic surfaces or as an adsorbate probed with a pure metallic tip.

15.1 Introduction

Frequency Modulation Atomic Force Microscopy (FM-AFM) has been recognized for a long time as one of the best tools for materials characterization at the atomic scale. This technique entered a new era with the use of metal tips decorated with CO molecules to visualize the internal structure of molecules with unprecedented resolution [1]. The contrast enhancement provided by these functionalized tips has made it possible to unveil the molecular structure of natural compounds [2] and small metallic

M. Ellner · P. Pou · R. Perez (✉)
SPM Theory & Nanomechanics Group, Departamento de Física Teórica de la Materia Condensada and Condensed Matter Physics Center (IFIMAC),
Universidad Autónoma de Madrid, 28049 Madrid, Spain
e-mail: ruben.perez@uam.es

S. Sadewasser and T. Glatzel (eds.), *Kelvin Probe Force Microscopy*,
Springer Series in Surface Sciences 65, https://doi.org/10.1007/978-3-319-75687-5_15

clusters [3], to follow the intermediate states of chemical reactions [4, 5], and, even, to visualize the subtle changes in charge density and bond length associated with the bond order of covalent bonds [6]. CO tips also act as a force–to–current transducer [7], achieving atomic resolution with Scanning Tunneling Hydrogen Microscopy [8] (STHM) and with Inelastic Electron Tunneling Spectroscopy [9] (IETS). CO tips also increase the resolution in Kelvin Probe Force Microscopy (KPFM) [10].

The high resolution achieved by the CO–terminated tips (CO tips) has been explained in terms of a strong Pauli repulsion between the closed-shell molecule acting as the probe and the electronic charge of the molecule probed [1, 11]. In addition, the associated tilting of the CO molecule [6, 12–14] amplifies the spatial variations of the charge density on the sample. Although Pauli repulsion plays a dominant role at very close distances, recent experiments on polar molecules [15–18], ionic samples [19] and metallic surfaces [3], consistently show that other interactions, in particular electrostatic (ES) forces, are also relevant to understand the complex observed contrast. The consensus ends here as the recent literature includes contradictory statements about the nature of the charge distribution of the CO molecule when acting as a tip or probed as an adsorbate. In the gas phase, CO has a total electric dipole of $\sim$0.12 D with its positive pole pointing to the oxygen. However, a CO tip dipole with its negative pole at the O atom (hereinafter called negative dipole) has been invoked by [19] to explain atomic corrugation in AFM measurements with a CO tip on an ionic copper nitride (Cu_2N) surface. The presence of a negative charge at the oxygen in CO tips is also supported by [16] in their analysis of AFM, STM and inelastic electron tunneling spectroscopy (IETS) images of Co phthalocyanines. Contrary to this, [20] explains the contrast formation of individual CO molecules adsorbed on different metal surfaces probed with a metal tip using a CO tip dipole with its positive pole at the O atom (as in the gas phase, hereinafter called positive dipole). The dipole orientation is not even consistent among studies of the CO molecule as an adsorbate, as [21] explain their measurements for CO on a Cu surface with the negative pole on the oxygen, just the opposite of the proposal reported in [20, 22] when studying the same system.

It is clear that further advances in high resolution imaging with CO tips call for a detailed characterization of the electronic charge distribution of metal-CO tips and its contribution to the AFM contrast. In this chapter, we face this challenge with a first–principles study of CO-decorated metal tips. We introduce a theoretical model, based on Density Functional Theory (DFT) calculations, that allows an efficient simulation of AFM images while retaining a first–principles accuracy. We validate our model with the analysis of experimental AFM measurements of Cl vacancies on a NaCl bilayer supported on a Cu(111) substrate. Our approach reproduces quantitatively the complex evolution of the contrast between the Na^+/Cl^- sites and the positive vacancy as a function of tip height. Based on these results, we conclude that the electrostatic field of a CO–metal tip can be represented by the sum of a dipole field that takes into account the positive charge accumulation at the metal apex due to the Smoluchowski effect [23], and the electrostatic field of an isolated CO molecule, that exhibits negative charge accumulation in front of the oxygen atom due to its lone pair. The interplay of these fields, with opposite sign in the near field and rather

different spatial extension, is the key to explain the contrast evolution observed in the AFM experiments on the Cl vacancies. Our analysis identifies the role played by the different tip–sample interactions as a function of the tip height and reconciles the apparently contradictory claims in the literature regarding the nature of the CO dipole.

The chapter is organized as follows. Firstly, we analize separately the electrostatic field created by a CO molecule (Sect. 15.2) and a metal tip (Sect. 15.3). DFT calculations provide the basis for the analysis of the CO-decorated metal tips presented in Sect. 15.4. The theoretical model to simulate high resolution (HR) AFM imaging with metal-CO tips is introduced in Sect. 15.5. Section 15.6 validates our model through the comparison with AFM measurements of Cl vacancies on a supported NaCl bilayer. Here, we discuss how to determine the dipole of the metal tips used in the experiment, illustrate the very different nature of the electrostatic contributions of the CO molecule and the metal tip, and show how their interplay gives rise to the complex AFM contrast observed. The chapter concludes with a detailed analysis of the inverse problem: the imaging of CO molecules adsorbed on metal substrates with metal tips. Our study reveals the limitations of previous models based on the assumption of a positive CO dipole and sheds new light on the interpretation of the AFM contrast in this classic surface science system.

15.2 The Dipole of CO Molecules in Gas Phase

In the gas phase, the carbon monoxide (CO) molecule has a total electric dipole of +0.12 D with its positive pole pointing towards the oxygen [24]. This is counterintuitive from an electronegativity point of view, however, because the CO triple bond contains one dative bond with both electrons stemming from the oxygen, the corresponding shift of electron density overcompensates the larger electronegativity of oxygen. The interplay between the oxygen lone pair and the overall positive dipole creates an electrostatic field with complex characteristics. To investigate this, we plot in Fig. 15.1a, d the z-component of the E–field of the molecule in gas phase as calculated with DFT (see Appendix A for details of the calculations) near the molecule and far from the molecule, and in Fig. 15.1b, e their respective profiles along the axial line that passes through the CO. Although the net dipole of the CO is positive, close to the molecule the O's lone pair dominates, resulting in an E–field that is repulsive towards electrons (represented by the red dome in Fig. 15.1a). It is only past 20 Å that the multipolar approximation becomes valid and the field, dominated by the positive dipole, inverts sign (see Fig. 15.1d, e for the far field). The question is whether such a dipole can be measured by AFM with a metallic tip. Supposing the metallic tip behaves as a positive dipole with a dipole moment $p = 1$ D, the ES force exerted by the CO can be computed as

$$F = -p\frac{dE_z}{dz}. \tag{15.1}$$

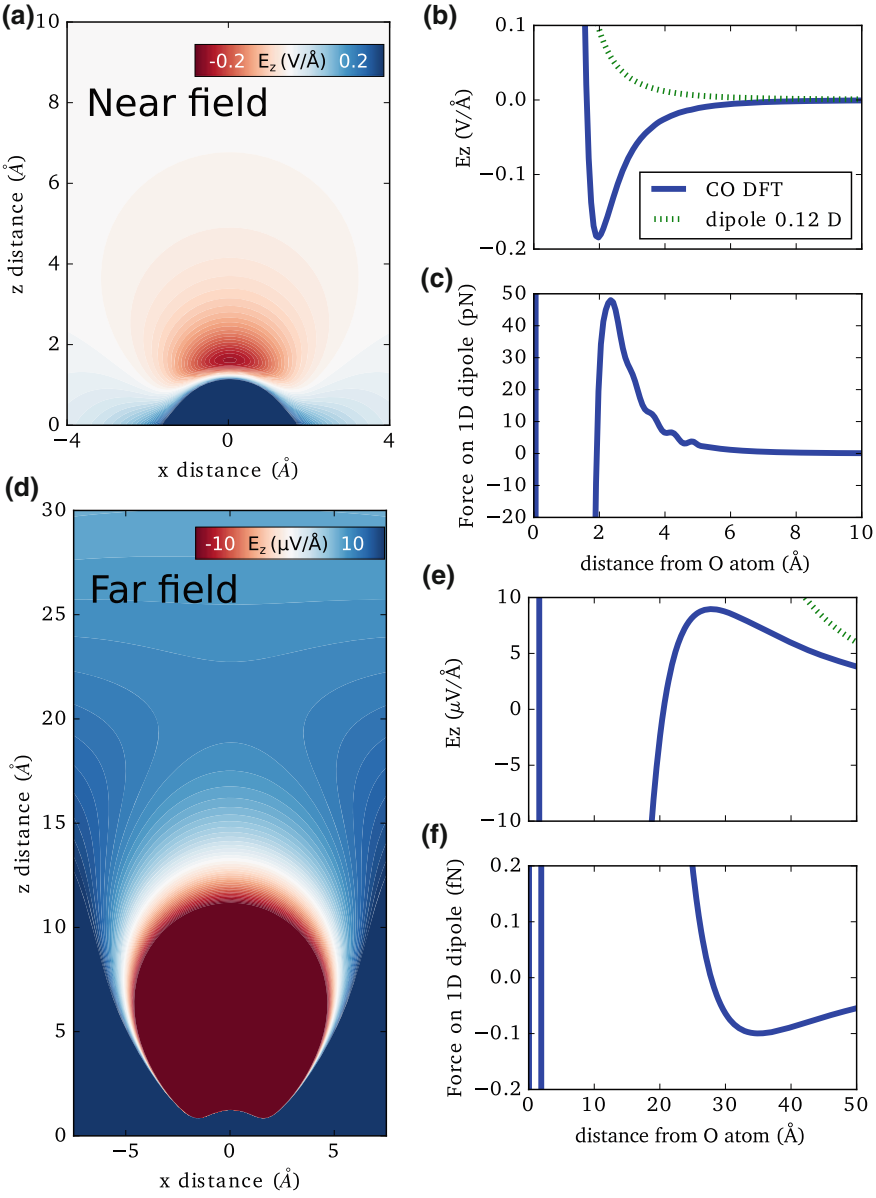

Fig. 15.1 z-component of the E-field of a CO molecule in gas phase near (**a**) and far (**d**) from the molecule. z-component of the E-field along the axial line of the CO near (**b**) and far (**e**) from the molecule. The ES force exerted by the CO molecule on a 1 D dipole near (**c**) and far (**f**) from the molecule. In all cases, the oxygen atom is placed at the origin $x, z = 0$ Å

As shown in Fig. 15.1f, the maximum force exerted after the inversion of the field (positive dipole behavior) is 0.1 fN. This magnitude of force is outside the experimental range of measurement of the AFM.

15.3 The Electric Field of Metallic Tips

In many instances, Si cantilevers or quartz sensors are coated with a metal through direct evaporation or controlled contact with the surface. If the resulting tip apex is sufficiently sharp, it can be used to image surfaces with atomic resolution [25]. The resolution of the AFM is further increased by functionalizing the metallic tip with a CO molecule [1]. In either case, an accurate characterization of the charge distribution of metallic tips is of utmost importance for the correct interpretation of the AFM images.

It has been recently shown that metallic tips have a positive dipole (partial positive charge at the tip apex) [22, 26–28]. In analogy to the surface dipole of adatoms, it can be explained by the smooth contour followed by the charge density that leaves an excess charge at the base of the protrusion and a lack of charge at the cusp [23]. In order to characterize the E–field created by metal tips, we have considered a Cu_{20} tip (see Fig. 15.2a) obtained by carving a 4-layer pyramid out of a Cu(111) slab. This is a realistic model tip as the pyramid exposes (111) faces that correspond to the more compact and more stable planes in an FCC structure.

Fig. 15.2b shows the z-component of the E-field of the tip as obtained with DFT (see Appendix A for details of the calculations). Indeed the charge density results in an ES potential that acts quantitatively as a positive dipole, both in the z and x-y directions. Furthermore, the strength of the dipole is larger than that of the surface dipole of the Cu(111) surface. However, the field cannot be quantitatively reproduced by that of a dipole for the full range of distances. Thus, we attempt to quantify the dipole for two different ranges of distances. This is done through a least-square fit to the analytical equation of a dipole along the axial symmetry line, assuming that the dipole is located at the position of the apex atom. Close to the apex (z =1–5 Å), the field can be reproduced by a large +3.5 D dipole centered at the tip apex (see Fig. 15.2c). This range of distance is relevant for interpreting NC-AFM images taken with metallic tips. Also, the result is consistent with previous works [22]. However, beyond $z = 5$ Å, the strength of the field decreases. At large distances, ($z = 6$–13 Å), the dipole decreases to 0.9 D (see Fig. 15.2d). A slightly better fit is obtained by relaxing the degree of freedom of the dipole origin. A dipole of 0.7 D centered 53 pm from the apex (away from the tip) best reproduces the field for intermediate distances. As we will see in the next section, this distance range is important for understanding the electrostatic interaction of metallic tips decorated with CO molecules.

Although the presence of a positive dipole for metallic tips is consistent with experimental observations, DFT seems to constantly underestimate the value of the dipole of metallic tips as compared to the dipoles needed to explain experimental

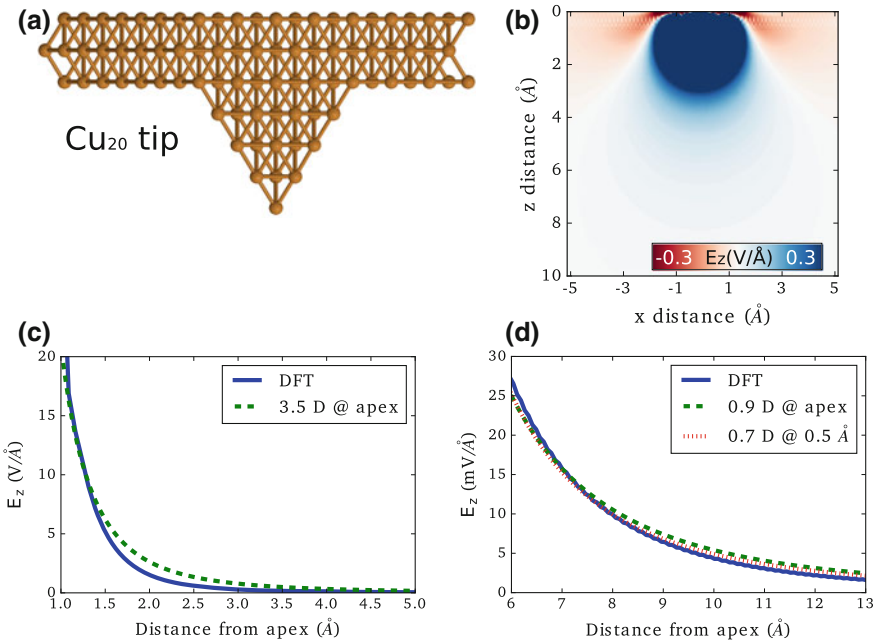

Fig. 15.2 Cu_{20} pyramid tip carved from a Cu(111) surface. **a** Ball–and-stick model. **b** Contour plot of the z-component of the E-field obtained from DFT calculations. The tip apex is centered at the origin $z = 0$ Å. **c** Comparison of the z-component of the E-field along the axial line from DFT and that of a +3.5 D dipole located at the apex atom. **d** Same as **c** for the intermediate distance range, considering both a +0.9 D dipole located at the apex atom, and a +0.7 D dipole centered ∼0.53 Å away from the tip apex that provides the best fit to the DFT results. Note that the z-component of the electric field for the +3.5 D dipole lies outside the scale in (**d**)

results [22, 26–29]. It can be argued that, since the metallic tip dipole originates from the Smoluchowski effect [23], it must increase as a function of the tip size (number of layers of the pyramidal cluster). DFT indeed reproduces this behavior: As shown in Fig. 15.3a, the dipole for a Cu tip carved from a Cu(111) surface, increases as a function of the number of layers, with the dipole/layer remaining constant. However, this increment in the size of the dipole moment is associated with the increase in the separation of the partial charges between the tip apex and the base of the cluster. In this case, it is no longer justified to assume that this dipole is located at the tip apex.

Alternatively, we propose to take the electric field created by metallic tips as the relevant physical magnitude. This quantity converges rapidly with the number of layers and can be well described fitting the value and the origin of an electric dipole, as discussed below. We have calculated with DFT the electric field of metallic tips as a function of the tip size. Figure 15.3b shows the z-component of the E-field along the symmetry line of Cu tips carved from a Cu(111) surfaces of size 2 through 7 layers. In contrast to the net dipole (Fig. 15.3a), there is no major change in the behavior of the field as a function of the tip size for tips larger than 4 layers. The small variations

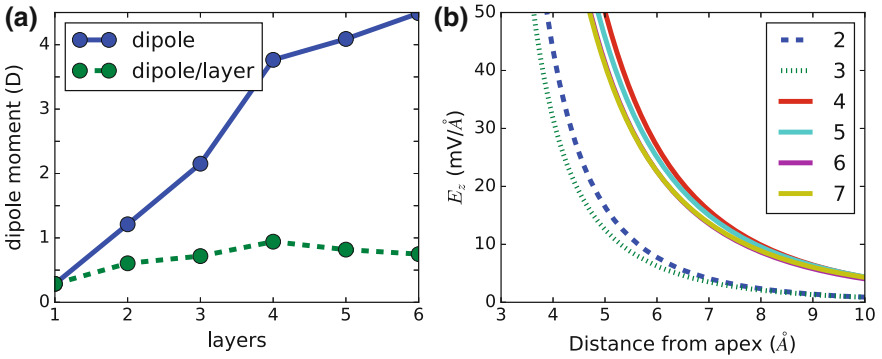

Fig. 15.3 **a** Total dipole moment as calculated from the charge density (solid blue line) and dipole moment per layer (dashed green line) for Cu tips obtained by carving a Cu(111) slab with different number of layers. **b** z-component of the E-field along the symmetry line of the Cu tips, showing that, contrary to the total dipole moment, past 4 layers there is no significant change in the E-field as a function of the number of layers

in the shape of the field for tips 4–7 can be attributed to the staking of the FCC[111] planes. The stark contrast between the pictures painted by the total dipole moment as calculated by integrating the charge density (Fig. 15.3a) and by examining the electric field (Fig. 15.3b) can be rationalized by a displacement of the origin of the dipole moment. If the dipole is increasing as a function of the tip size, then the origin of the dipole must be moving away from the apex and towards the inside of the pyramidal tip. It is worth noting that the behavior occurs on isolated clusters as well as on clusters attached to metal surfaces: The E-field is attractive towards electrons and there is no quantitative variation of the field as a function of the tip size.

In order to interpret AFM experiments and to construct models that simulate AFM images, one needs to go beyond a qualitative description of the potential of the tip. For the distance regime of interest for AFM (3–10 Å from the tip apex), the z-component of the E-field of the Cu_{20} metallic tip obtained from DFT (see Fig. 15.2) is reproduced by replacing the Cu tip by a dipole of 0.7 D centered 53 pm away from the tip apex. With a slightly worse overall fit, if the dipole is placed at the tip apex, the dipole value is reduced to $\approx$0.5 D. This result is consistent with previous works [28].

15.4 The Electric Field of Metal-CO Tips

The use of metal tips functionalized with CO molecules has allowed AFM to image surfaces and molecules with unprecedented resolution [1]. Although most images are taken at close tip-sample distance where the dominant interaction is Pauli repulsion, on polar molecules and ionic surfaces, the electrostatic interaction should play an important role on the contrast formation. Thus, the accurate characterization of metal-CO tips is important. In previous sections, we have examined separately the isolated

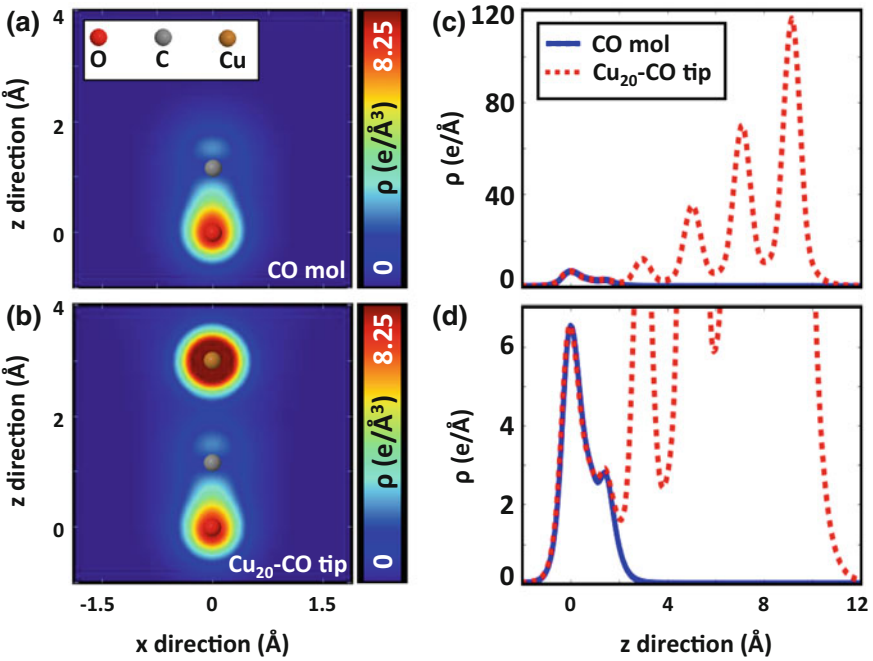

Fig. 15.4 Charge density of **a** an isolated CO molecule and **b** a Cu_{20}–CO tip on a plane passing through the last Cu atom and the CO molecule. **c** Integrated charge density (xy–average) along the axial line of the CO molecule and **d** a zoom of (**c**). The Cu atom of the tip apex, the C atom, and the O atom are located at z = 3 Å, z = 1.15 Å, and z = 0 Å respectively

CO molecule and metallic tips and found that they have opposite dipole behaviors at distances relevant for AFM imaging. We proceed now with the study of composite metal-CO tips in order to (1) find out how much does the metal-CO bonding affect the electrostatic behavior of both the CO molecule and the metal tip, and (2) get a qualitative description of the net E-field. As before, we will use the Cu_{20} tip as a model tip.

DFT calculations of Cu–CO tips show that the CO molecule bonds to the terminal Cu atom in an upright position with negligible structural changes (ionic relaxation) on the part of the CO molecule and the metal tip, and negligible charge transfer between the structures (see Appendix A for details of the calculations). In Fig. 15.4a, b the electronic charge density of a CO molecule and a Cu_{20}–CO tip are plotted. Around the CO molecule, the charge density is not affected by the presence of the metallic tip. This is seen more clearly in Fig. 15.4c, d where we plot the xy–plane averaged charge density of the CO molecule (solid blue lines) and Cu_{20}–CO tip (dashed red lines) around the axial symmetry line. Around the CO molecule, the charge densities are superimposed, thus confirming the absence of a significant charge redistribution between the CO and the metallic cluster. This result suggests that the electrostatic behavior of the compound Cu–CO tip is additive [30].

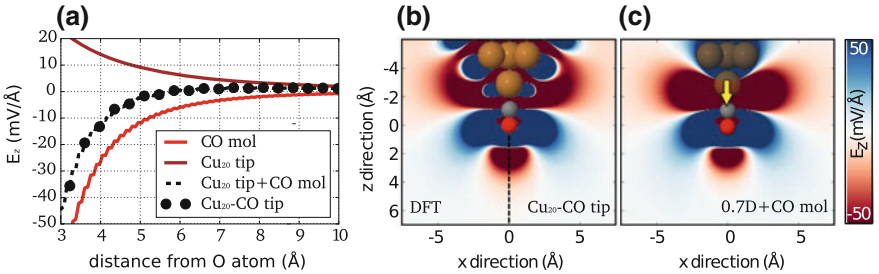

Fig. 15.5 **a** The z-component of the electric field (E_z) along the axial symmetry line of a CO molecule (red line), a Cu_{20} tip (brown line), the addition of both fields (dashed black line), and the field from the compound Cu_{20}–CO tip (black markers). Full 3D field of **b** a Cu_{20}–CO tip and **c** a 0.7 D dipole and a CO molecule

A further examination of the electrostatic behavior of the isolated CO molecule and the compound Cu_{20}–CO system confirms this. Figure 15.5 shows the z-component of the electric field (E_z) of a 4 layer (111)-oriented Cu tip (Cu_{20} tip) functionalized with a CO molecule. In Fig. 15.5a, the fields along the axial symmetry direction are plotted for the isolated CO molecule, the isolated metal tip, the sum of the isolated fields, and the field of a Cu_{20}–CO tip. Along the symmetry line, the sum of the isolated fields is practically identical to the one of the compound Cu_{20}–CO tip. As discussed in Sect. 15.3, the field of the metal tip can be replaced by that of a dipole. For distances relevant for AFM images with metal-CO tips ($z = 3-10$ Å from the O atom), we find, through a least-square fit along the axial line, that the field of the Cu tip can be substituted by a +0.7 D dipole centered 53 pm away from the outmost Cu atom. A 2D slice of the z-component of the fields of a Cu_{20}–CO tip and a 0.7 D dipole added to the field of a CO molecule are plotted in Fig. 15.5b, c. The comparison confirms the additivity of the molecule and metal tip contributions, showing that, in all three dimensions, the Cu–CO tip's E_z calculated with DFT shares the same quantitative and qualitative behavior as the 0.7 D + CO molecule's field.

A qualitative description of the metal-CO tip is helpful for interpreting AFM images. The electric field of the Cu–CO tip (Fig. 15.5b, c) retains the shape of the CO's electric field (Fig. 15.1) close to the apex. The electron cloud of the oxygen's lone pair creates a dome-shape electric field near the apex. The Cu tip reduces the strength and extent of the negative dome by surrounding it with a positive electric field. Although these results are for an isolated metallic cluster, there are no qualitative changes when a slab is attached to the base of the cluster.

15.5 A Theoretical Model to Simulate HR-AFM Imaging with Metal-CO Tips

In the preceding sections, we have characterized with DFT the electrostatic field of a metallic tip functionalized with a CO molecule. We have shown that while the metallic tip acts as a large positive dipole (partial positive charge at the tip apex), the CO introduces a dome with opposite sign that is repulsive towards electrons. As discussed in the introduction, previous works present contradictory explanations for the behavior of metal-CO tips. In order to solve this puzzle, we have to understand the interplay between the ES interaction of the extended positive dipole of the metallic tip and the localized repulsive dome of the CO molecule on the contrast formation of charged systems as probed by metal-CO tips.

In this section, we present the method that we have developed to calculate interaction-decomposed HR-AFM images with molecule decorated metal tips. It is based on DFT calculations and allows an efficient simulation of AFM images while retaining the first–principles accuracy needed to cover the whole distance range explored in the experiments, and to single out the different contributions to the total tip-sample interaction. In Sect. 15.5.1, we introduce the potential used to simulate images. It encompasses electrostatic, short-range, and vdW interactions and explicitly accounts for tip tilting effects. It is clearly necessary to validate experimentally our model. Section 15.5.2 motivates and describes the system that we have chosen for the theory–experiment comparison: a Cl vacancy on a NaCl(100) bilayer supported on a Cu(100) substrate [29]. Finally, in Sect. 15.5.3, we expand the discussion of the CO probe tilt by comparing AFM spectroscopies calculated with the model and with DFT.

15.5.1 Description of the Tip-Sample Interaction Potential

Our approach differs from previous theoretical models [12, 16] in two important aspects. We go beyond the simple dipole approximation for the CO probe and calculate the electrostatic energy by the interaction of the sample electrostatic potential (obtained from a DFT calculation) with the charge density of both the CO molecule (also calculated with DFT) and the metal tip apex (replaced by a positive dipole). While accounting for tip tilt, the full charge density of the CO molecule (on a real-space grid) is rotated. We also include a more accurate description of the short–range (SR) interaction, that is modeled as a sum of pair–wise Morse potentials with species–dependent (in this case Cl and Na) parameters fitted to reproduce our DFT force calculations. The vdW contribution is included with a semiempirical DFT–D3 approach [31], while the CO tilting is simulated by a spring [12] with a force constant of 0.24 N/m [18].

HR-AFM images obtained from CO functionalized metallic tips are simulated by minimizing the potential

$$V = V_{\text{tilt}} + V_{\text{vdW}} + V_{\text{SR}} + V_{\text{ES}} \tag{15.2}$$

for the probe position.

The CO tilting is defined through

$$V_{\text{tilt}} = \frac{1}{2}\kappa\delta^2\theta^2, \tag{15.3}$$

where $\delta = 302$ pm is the lever arm (distance from the outmost Cu atom of the tip to the O of the CO probe), $\kappa = 0.24$ N/m [18] is the spring constant, and θ is the tilt angle. Section 15.5.3 discusses the suitability of this model in terms of DFT calculations.

The van der Waals (vdW) interaction, not properly described by any of the exchange–correlation (XC) functionals commonly used in DFT simulations, can be included through any semi-empirical method as a correction to the DFT total energy. Specifically, here we use Grimme's DFT-D3 method [31]. The same correction is applied to the DFT energy used in the parametrization of the model. All the atoms from the sample, the CO probe, and the metal tip, modeled by a 20 atom Cu cluster, are included in the calculation. Although absolute vdW forces depend on the macroscopic part of the tip, the vdW contribution to the force contrast (the difference between forces on different sites) is well converged for this cluster size.

The short range (SR) contribution is approximated using a sum of pair-wise interactions between the CO probe and all of the Na(Cl) atoms in the sample. We have found that the best description for each of these interactions is obtained with a Morse potential,

$$V(r) = D_e((1 - e^{-a(r-r_e)})^2 - 1), \tag{15.4}$$

where D_e, a, r_e are the well depth, width of the potential, and equilibrium bond distances, respectively. Note that the Cu substrate is not included in the calculation of the SR interaction. Due to the short range nature of the Morse potentials, the exclusion of the Cu atoms is justified. The procedure used to parametrize the potential is described in Appendix B.

The electrostatic (ES) interaction is calculated from

$$V_{\text{ES}} = \int (\rho_{\text{CO}} + \rho_{\text{metal}})\Phi_{\text{sample}} d\mathbf{r}^3, \tag{15.5}$$

where ρ_{CO} and ρ_{metal} are the charge density of the CO probe and the Cu metal tip, and Φ_{sample} the electrostatic potential of the isolated surface (NaCl and substrate). The charge distribution and the electrostatic potential are calculated on a real-space grid (see Appendix A for details). The charge distribution of the Cu tip is simulated by two opposite localized charged Gaussian distributions (width at half-maximum of 10 pm) separated by 106 pm and centered 53 pm from the last Cu atom. It provide a net 1.5 D dipole. Notice the increase of the dipole size that simulates the metallic

tip as compared to the dipole strength predicted by DFT and discussed in Sect. 15.3. The increment will be justified in Sect. 15.6.3.

15.5.2 Cl Vacancy on a NaCl/Cu(100) Surface

In order to test the tip–sample interaction potential and the model tip described above, we have compared their predictions with an experimental NC-AFM study of a single Cl vacancy on a NaCl bilayer supported on a Cu(111) substrate probed by a Cu–CO tip [29]. This sample is ideal for this task because, in addition to the ionic lattice, there is a net positive charge at the vacancy site leading to three qualitatively different sites: Na cations (Na^+), Cl anions (Cl^-), and the net positively charged vacancy site [28, 32–34].

In our calculations, we have simulated this system with a single Cl vacancy on a NaCl bilayer supported on a 2-layer Cu(100) slab. We use a 6×6 surface unit cell and a large vacuum (33.7 Å $\times$ 33.7 Å $\times$ 48 Å) (see Fig. 15.6). We calculate the ionic structure with VASP [35], using the PBE XC functional supplemented by semi-empirical DFT-D3 van der Waals (vdW) interaction [31], a plane wave cutoff of 400 eV, a fine electronic convergence ($E_{\mathrm{SCF}} = 10^{-4}$ eV), a $3 \times 3 \times 1$ grid for the sampling of the Brillouin zone, and a force cutoff for ionic relaxations of 10^{-2} eV/Å.

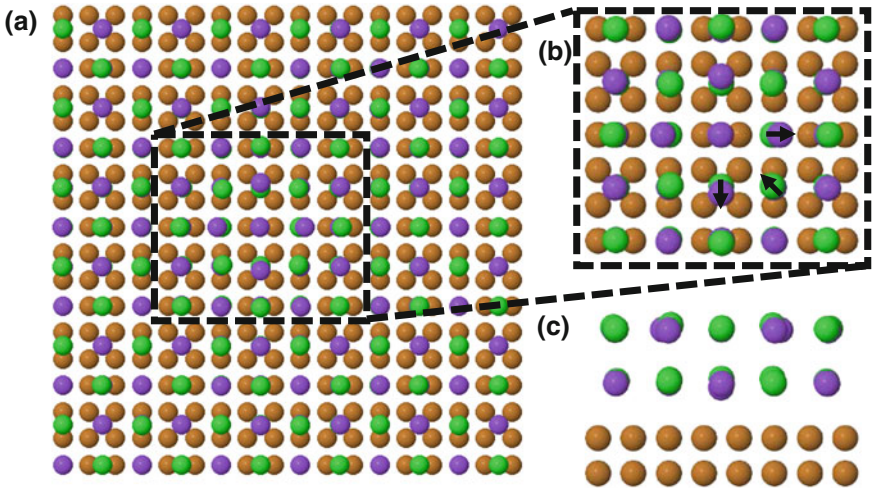

Fig. 15.6 **a** Cell used for the simulation of AFM images. The cell size is (33.7 $\times$ 33.7 $\times$ 48) Å^3. It includes a NaCl bilayer with a Cl vacancy (143 Cl atoms and 144 Na atoms), on 2 layers of Cu(100) (324 atoms). **b** Top and **c** lateral view of the atoms near the vacancy (area marked by dashed lines in the left panel). Na atoms adjacent to the vacancy relax away from the vacancy, while Cl atoms relax towards the vacancy. In addition, the Cl atoms shift away from the substrate

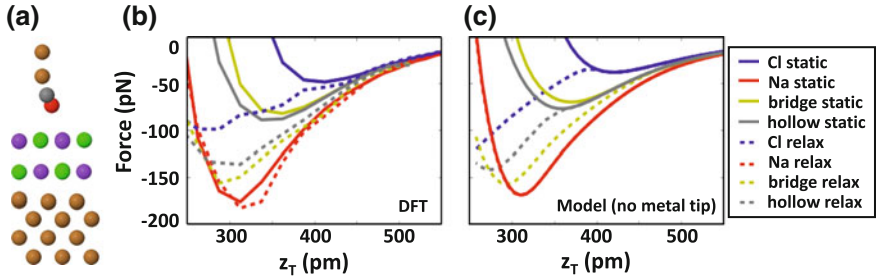

Fig. 15.7 **a** Lateral view of the DFT cell and the Cu_2–CO probe used in the tests for the description of the CO tilting. **b** Force curves with (dashed) and without (solid lines) CO tilting. The tip was moved in 25 pm intervals. **c** Forces computed with the model (only the CO probe was used as a tip)

The main structural difference introduced by the Cl vacancy with respect to the clean NaCl bilayer is that Na ions adjacent to the vacancy shift away from the vacancy approximately 30 pm, while the Cl ions shift towards the vacancy by 15 pm (Fig. 15.6b). In addition, the Cl ions adjacent to the vacancy also shift away from the substrate approximately 30 pm (see Fig. 15.6c).

15.5.3 CO Tilting: DFT Versus Model Calculations

In order to corroborate that the spring model with $\delta = 302$ pm and $\kappa = 0.24$ N/m treats the CO tilting correctly, we have carried out DFT force calculations of a clean NaCl bilayer on a 4-layer Cu(100) slab probed by a Cu_2–CO tip on a small cell. The Cu_2–CO tip is a Cu dimer with a CO molecule attached from the C atom. Figure 15.7a shows the NaCl/Cu(100) sample (7.95 Å × 7.95 Å unit cell) along with the tip. Figure 15.7b shows DFT force curves with (dash) and without (solid) relaxation of the CO probe. Figure 15.7c shows force curves calculated with the model on the sites mentioned above. The quantitative and qualitative behavior of the CO bending is well described by the model.

The arm length, $\delta = 302$ pm, used to describe the tilt of the CO molecule on the Cu tip is obtained from DFT calculations of a CO molecule adsorbed on a 4 layer (111)-oriented Cu tip (Cu_{20} tip). It is the length from the O atom to the outmost Cu atom. This arm length is well converged for this tip size. It is worth noting that the CO bond length calculated from DFT is 115 pm, thus the C-Cu adsorption length is 187 pm.

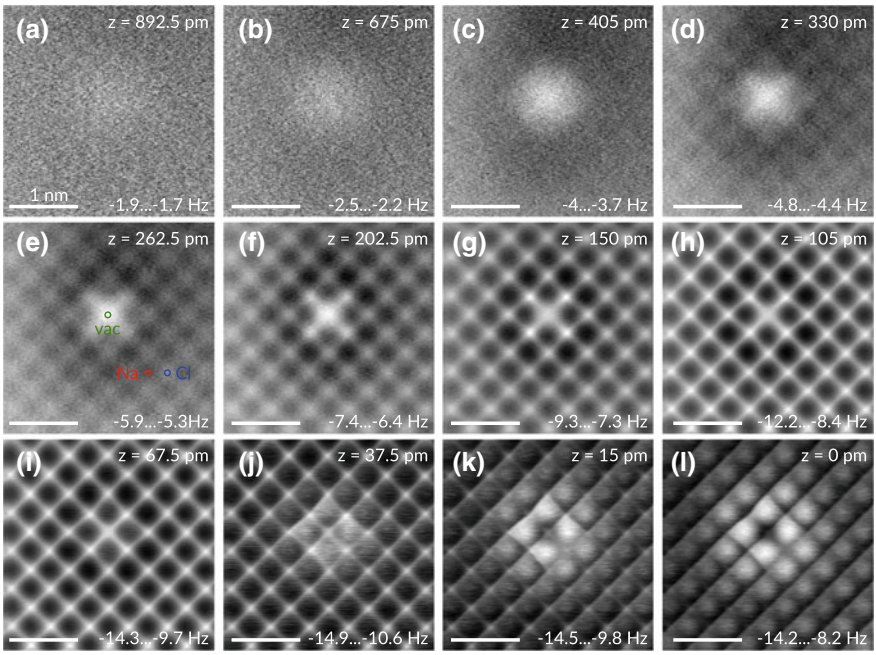

Fig. 15.8 Experimental constant-height AFM measurements of a Cl vacancy in bilayer NaCl on Cu(111) acquired with a CO tip. The tip height z, indicated in the top right, decreases from (**a**) to (**l**). $z = 0$ is defined as the distance at closest approach, corresponding to the data shown in (**l**). The frequency shift limits corresponding to black (more negative) and white are indicated in the bottom right of each panel. The positions of the vacancy site (vac, green), the Na site (Na, red), and the Cl site (Cl, blue) are indicated in panel (**e**). Scale bars correspond to 1 nm. Reprinted with permission from [29]. Copyright 2016 American Chemical Society

15.6 Experimental Validation of the Electric Field Created by a Metal-CO Tip: Cl Vacancy on a NaCl Bilayer

15.6.1 Experimental Results

We proceed to discuss experimental NC-AFM images of a Cl vacancy on a NaCl bilayer on Cu(111). The Cl vacancy can be unambiguously identified by atomically resolved STM [32, 33] and AFM images [34], by KPFM [28] and also by its characteristic features in Scanning Tunneling Spectroscopy (STS) [32]. In our case, images were gathered with a small amplitude AFM with a Cu–CO functionalized tip. The full details of the experimental setup and sample preparation are presented elsewhere [29].

Figure 15.8 shows the experimental AFM raw data of a Cl vacancy acquired with a CO tip as a function of tip-sample distance [29]. The distance was varied by nearly 0.9 nm, and the tip height corresponding to the closest approach defined

the reference height $z = 0$. From the data, four distinctly different distance regimes can be distinguished, each leading to specific contrast. For large tip heights ($z \sim$ 900−400 pm) (Fig. 15.8a–c), only the vacancy can be resolved as a faint and broad feature of less negative frequency shift. For $z \sim 400-200$ pm (Fig. 15.8d–f), atomic corrugation on the ionic lattice gradually emerges, with the Cl^- (Na^+) lattice sites leading to less (more) negative frequency shift. The vacancy site remains the feature of least negative frequency shift but the contrast compared to the surrounding Cl sites decreases with tip approach until it disappears at $z \sim 200$ pm. For smaller tip–sample distances, sharp bright ridges arise (Fig. 15.8g–j) connecting neighboring Cl sites and also the vacancy site with its four neighboring Cl sites. Finally, for tip heights below $z \sim 20$ pm, (Fig. 15.8k–l), the atomic contrast reverses, both on the ionic lattice and the vacancy. The vacancy becomes the darkest site (most negative frequency shift) while the Na sites are now the brightest features (least negative frequency shift), separated by a sharp, dark Cl grid.

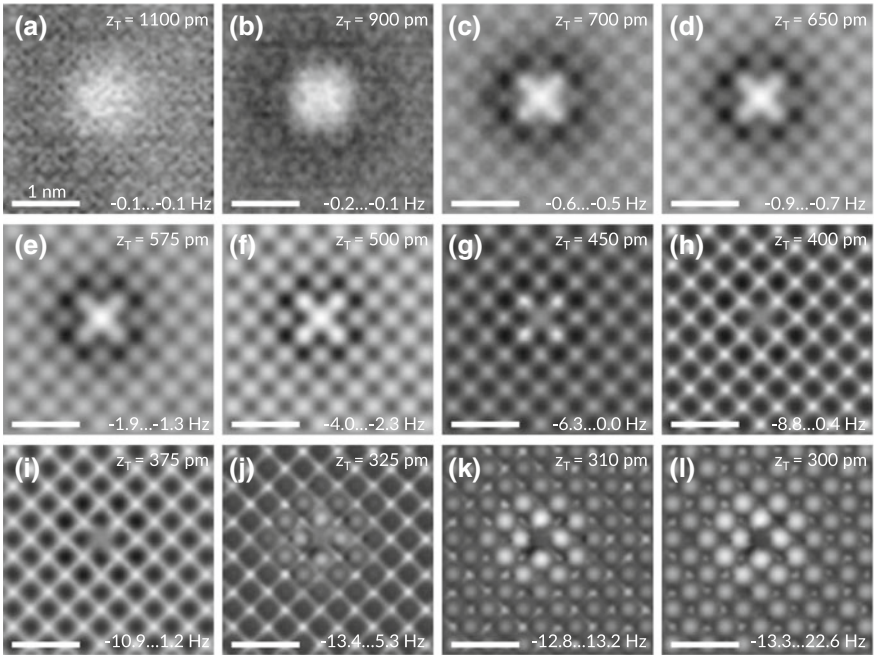

Fig. 15.9 Theoretical AFM images of a Cl vacancy in bilayer NaCl on Cu(100) using a CO probe and a 1.5 D dipole simulating a Cu tip. The tip height z_T, indicated in the top right, decreases from (**a**) to (**l**). The frequency shift limits corresponding to black (more negative) and white are indicated in the bottom right of each panel. Scale bars correspond to 1 nm. Reprinted with permission from [29]. Copyright 2016 American Chemical Society

15.6.2 Simulation Results

The method described in Sect. 15.5 was applied to a single Cl vacancy on a 6×6 surface unit cell (see Fig. 15.6) using a slab composed of a NaCl(100) bilayer and 2 Cu(100) layers and a large vacuum region (total cell size 33.7 Å $\times$ 33.7 Å $\times$ 49 Å) [29]. We model the CO functionalized Cu metallic tip by using the full charge density of the CO molecule and a 1.5 D dipole to simulate the metallic tip (in Sect. 15.6.3 we will explain the choice of the metallic tip dipole). Figure 15.9 shows calculated images for a range of tip heights z_T –defined as the distance of the O atom of the tip to the topmost atomic NaCl layer– corresponding to those in Fig. 15.8. We obtained excellent quantitative agreement with the experiment, reproducing the contrast at every site (vacancy, Na and Cl atoms close and far form the vacancy) and the contrast changes as a function of tip height. By comparison to the experiment, we can relate the experimental height scale z to the absolute tip-sample distances z_T with an offset of 300 pm: $z = z_T - 300$ pm.

Contrast changes with tip height arise from the variation of the relative weight of the short range (SR), electrostatic (ES), and vdW contributions to the total tip–sample interaction. Figure 15.10 illustrates the distance dependence of these contributions with frequency shift curves on the Na, Cl, and vacancy sites (marked in Fig. 15.10e), and 2D force maps at two characteristic tip–surface distances. The electrostatic force dominates the image contrast for tip heights z_T above 500 pm. Figure 15.10b shows that the electrostatic contribution to the frequency shift contrast (frequency shift differences among sites) remains larger than the SR one for tip heights larger than 450 pm. This change in the frequency shift contrast is responsible for the contrast change in the images observed at 500 pm in Fig. 15.9, as the frequency shift is proportional to the derivative of forces. The ES interaction is responsible for the bright (less attractive) broad feature associated with the positively charged vacancy at large tip heights, and for the atomic contrast that emerges in the medium tip height regime ($z_T \sim 700-500$ pm). In this distance range, the positive Na sites show a larger negative frequency shift (i.e. a more attractive interaction) than the negative Cl sites, while the positive vacancy site remains the least attractive site (Fig. 15.10b, d). Thus, the tip apparently exhibits the behavior of a negative dipole on Na/Cl, but that of a positive dipole on the vacancy site, highlighting the limitations of the common dipole approximation to describe the electric field created by the tip.

For small tip heights ($z_T < 500$ pm), the SR interaction becomes the most important contribution to the contrast due to the exponential growth of the Pauli repulsion above the Cl sites (Fig. 15.10b). This is best shown in Fig. 15.11 where 4 sets of force decomposed images as well as tip relaxation for probe-sample distances $z_T = 1000$, 650, 400, 375, and 300 pm are plotted. Forces are decomposed in terms of short-range, electrostatics, and van der Waals contributions. Images in the bottom row illustrate the tilting of the CO probe. The lines show trajectories of the O atom when the tip is scanned along a rectangular grid. At $z_T \sim 400-375$ pm, the CO molecule starts to tilt to avoid the high repulsion over the Cl anions, as shown by the difference between the static and relaxed curves in Fig. 15.10a, and the relaxation maps in

Fig. 15.11. Notice that, in this distance range, the Na/Cl contrast from the electrostatic contribution is much smaller compared to the SR. However, on the vacancy site, due to the small electron density, the Pauli repulsion is negligible and the electrostatic interaction remains dominant. Upon further approach, the CO probe increases its tilting toward the minima of the Potential Energy Surface (PES) (Fig. 15.11), and by doing so, the saddle line between two neighboring Cl ions (and the vacancy and its neighboring Cl ions) is sharpened [6, 12]. For the smallest tip heights explored ($z_T \sim$ 310–300 pm), the Na sites become brighter than the Cl sites (see Fig. 15.9). This contrast inversion is explained by the change of the slope of the force on the Na sites as it reaches its minimum at $z_T \sim$ 310 pm (see Fig. 15.10a). At this tip height,

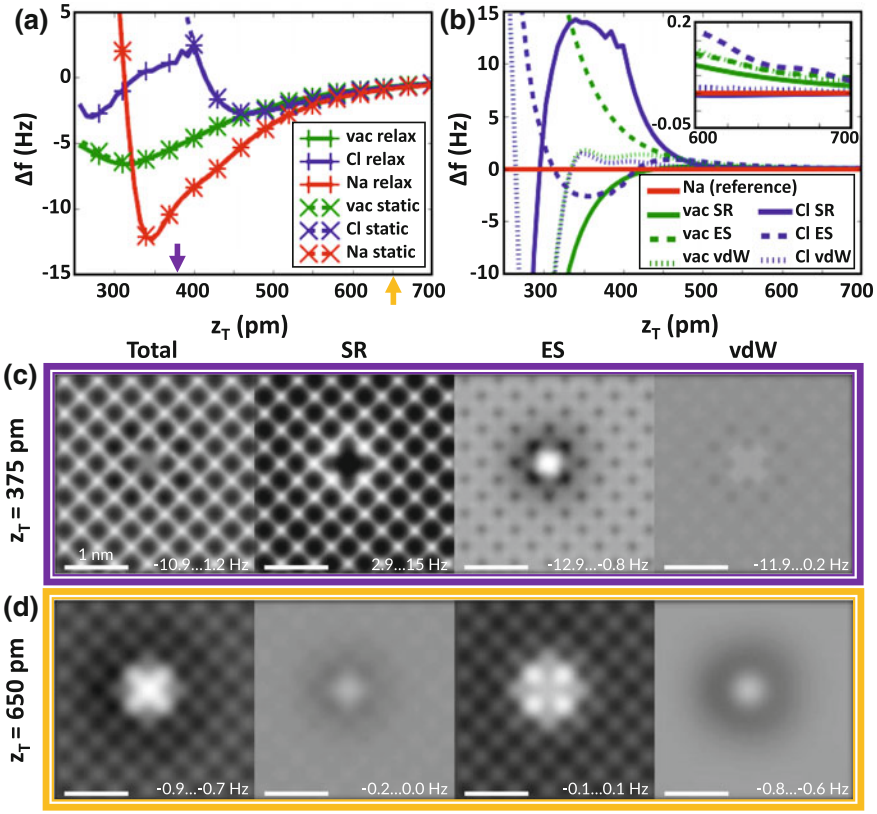

Fig. 15.10 **a** Total frequency shift with (solid) and without (dashed lines) relaxation of the CO probe for the vacancy (green), Cl (blue), and Na (red) sites. **b** Frequency shift decomposed spectroscopy for the above sites in terms of short range (solid), electrostatics (dashed), and van der Waals (dotted lines) interaction. Frequency shift decomposed images in terms of the above mentioned interactions for **c** $z_T = 375$ pm and **d** $z_T = 650$ pm. In order to highlight the influence of each contribution on the total frequency shift, the frequency shift limits are scaled to keep the frequency shift range in all contributions equal to the total frequency shift range

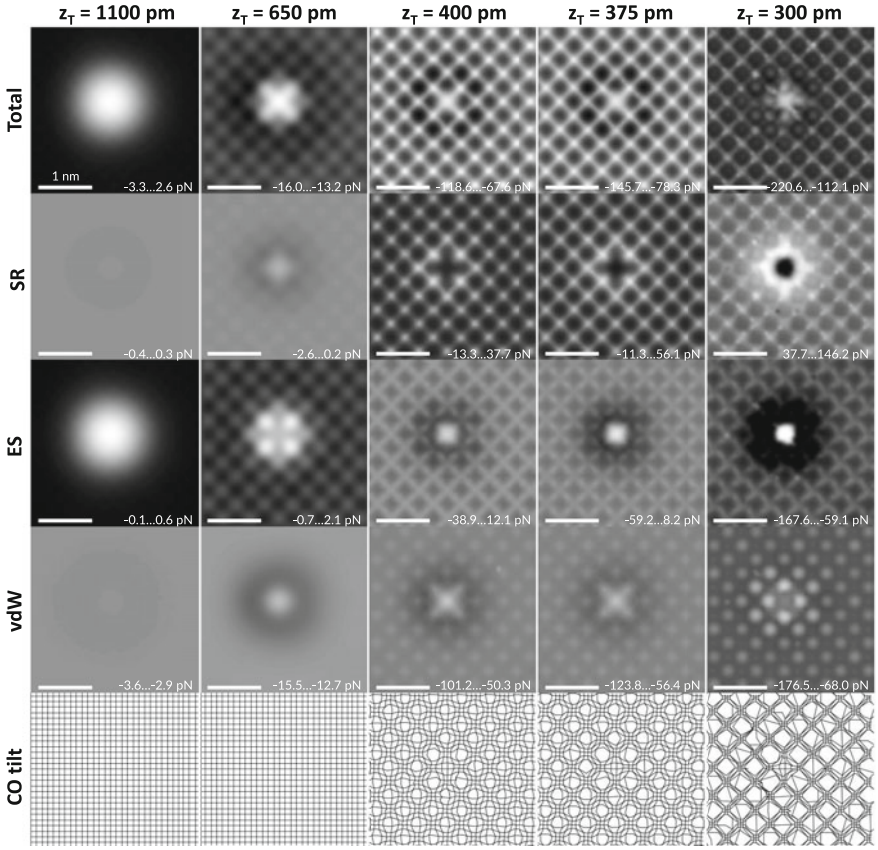

Fig. 15.11 Total force and force decomposed images in terms of short-range (SR), electrostatic (ES), and vdW interactions contributions for $z_T = 1000$, 650, 400, 375, and 300 pm. In order to highlight the influence of each contribution on the total force, the gray scale in all of the images corresponds to the variation range of the total force and the numbers at the bottom right of each image indicate the minimum and maximum values of the interaction. The bottom row represents the CO tilt. The lines show trajectories of the O atom when the tip is scanned along a rectangular grid (only half of the grid points used to construct the images are shown). Notice that the probe relaxes toward the Na site (low electronic density) and is more pronounced as the tip height distance decreases

the force still increases with decreasing tip height both on the Cl sites (due to the tip tilting towards the Na atoms) and on the vacancy (due to the small Pauli repulsion).

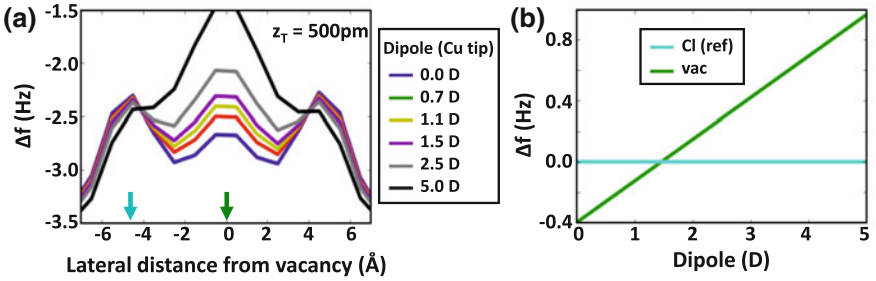

Fig. 15.12 **a** Constant-height profiles across the vacancy site using the CO probe and 0, 0.7, 1.1, 1.5, 2.5, and 5 D dipoles as a Cu tip. Profiles were calculated along the diagonal (following the X shape feature) at $z_T = 500$ pm. **b** Difference in frequency shift between the vacancy site and Cl ions adjacent to vacancy. A 1.5 D dipole is roughly the minimum dipole size needed to image these two sites with equal frequency shift

15.6.3 Determination of the Dipole that Describes the Metal Tip in the Experiment

In Sect. 15.3, we showed that replacing the Cu metal tip by a 0.7 D dipole is a good approximation for the E_z of Cu–CO tips calculated with DFT. However, for the Cl vacancy on the NaCl bilayer, such a small dipole underestimates the electrostatic tip-sample interaction and does not reproduce the experimental contrast of the vacancy at large probe-sample distances, where it appears brighter than the surrounding Cl sites (see Fig. 15.8a–e). This is true both for calculations performed with our model as well as for DFT force calculations of this surface probed by Cu–CO tips.

The choice of dipole size necessary to reproduce the experimental contrast is difficult. We have selected the smallest dipole needed to reproduce the contrast inversion near the vacancy around $z_T = 500$ pm (Fig. 15.8e–g). While the vacancy is brighter than the adjacent Cl sites in Fig. 15.8e, they are imaged with similar frequency shift in Fig. 15.8f, and, finally, the Cl ions become brighter in Fig. 15.8g. In order to pin-point the desired dipole strength, a constant height profile at $z_T = 500$ pm is computed in the vicinity of the vacancy and for different dipole sizes (Fig. 15.12a). The difference in frequency shift between the Cl site and vacancy site as a function of dipole can be extracted from the constant height simulation (Fig. 15.12b). The model reproduces the experimental observation described above with a dipole of roughly 1.5 D, approximately twice the value calculated from DFT. Note that, as described previously, the dipole is centered 53 pm away from the metal tip apex (in the direction of the surface) because it provides the best fit to the ES potential. In order to reproduce the experimental contrast with a dipole placed at the tip apex, a ≈ 2.0 D dipole would be needed.

Admittedly, larger dipoles seem to reproduce better the experimental contrast for large probe-sample distances ($z_T > 700$ pm). This is illustrated in Fig. 15.13 where AFM images for the far distance regime are simulated using different dipoles.

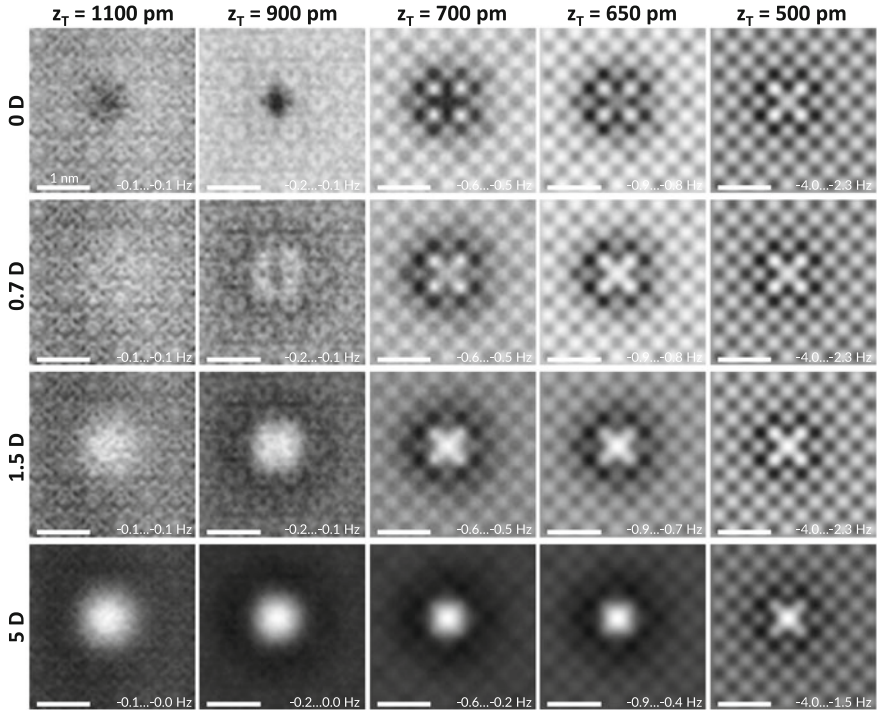

Fig. 15.13 Theoretical AFM images of a Cl vacancy in bilayer NaCl on Cu(100) using a CO probe and dipoles of 0, 0.7, 1.5, and 5 D acting as a Cu tip. The probe-sample distance, z_T, decreases from 1100 to 500 pm. The frequency shift limits corresponding to black (more negative) and white are indicated in the bottom right of each panel. Scale bars correspond to 1 nm

It is not clear if this discrepancy between the calculated and the effective dipole moment, which is necessary to reproduce the experiments, reflects the limitations of a pure, perfectly ordered Cu tip to represent the real metal tip structure, an incorrect description of the charge density around the vacancy by the PBE XC functional, or it arises from a failure in the description of other interactions.

15.6.4 Interplay Between CO and Metallic Tip Electrostatic Interactions

We are now in the position to discuss how the interplay of the electric field created separately by the CO and the positive dipole replacing the metal tip explains the observed contrast for the large and medium tip height regime ($z_T > 500$ pm). In consistence with literature, our DFT calculations predict that the total charge distribution of the isolated CO molecule shows a small dipole of 0.12 D, with its positive pole at

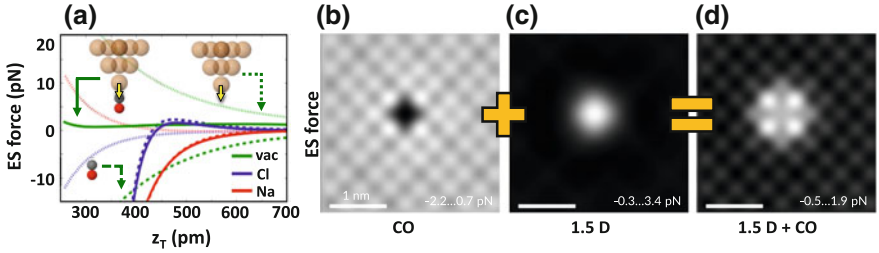

Fig. 15.14 **a** Electrostatic interaction of the isolated CO probe (dashed), a 1.5 D dipole simulating the metallic tip (dotted), and the CO- 1.5 D probe (solid lines) for the vacancy (green), Cl (blue), and Na (red lines) sites. Electrostatic interaction image using **b** isolated CO probe, **c** a 1.5 D dipole acting as a Cu tip, and **d** the composite CO + 1.5 D probe at $z_T = 650$ pm

the oxygen. However, as discussed in Sect. 15.2, the electric field of the molecule is quite complex and can only be replaced by the one created by this small dipole for very large tip–sample distances. For the closer distances relevant for AFM imaging, the field is ruled by the local charge distribution. Ahead of the oxygen atom, the electric field is effectively produced by a localized negatively charged cloud in front of this atom neutralized by a positive charge in the nucleus. This charge distribution arises from the asymmetry in the electronic charge density induced by the oxygen lone pair. In the near field, the resulting electric field resembles the one created by a negative dipole placed at the oxygen atom. Thus, the combined electrostatic field of the CO probe and the metal tip can be represented by two opposing dipoles.

The relevant question is, what role do these opposing dipoles play in the contrast formation? Fig. 15.14a shows the contribution to the electrostatic interaction of the Cu metal (1.5 D dipole), CO probe, and the compound 1.5 D-CO tip on the vacancy (green), Cl (blue), and Na (red) sites. The greatest difference between the electrostatic interactions of the CO probe and the compound 1.5 D-CO tip is obtained on the vacancy site (solid vs. dashed lines). At far distances, the 1.5 D dipole that simulates the metallic tip only probes electrostatically extended sites such as the vacancy. Furthermore, as discussed previously, at close probe-sample distances, the short range interaction is the dominant contribution on the contrast formation. Thus, the dipole only contributes to the contrast of the vacancy site with respect to the Cl/Na sites. On the contrary, the very localized electric field of the CO probe is the one responsible for the atomic resolution of the NaCl lattice. These conclusions are clearly illustrated in Fig. 15.14b–d that show images of the electrostatic interaction at $z_T = 650$ pm using the CO probe, a 1.5 D dipole, and the composite 1.5 D-CO probe.

Figure 15.15 provides an explanation for this behavior in terms of the lateral extension, 650 pm away from the probe, of the E_z of (a) the CO probe, and (b) the Cu apex (1.5 D dipole). The electric field of the metal apex extends over several lattice positions while the CO's is localized to a single atomic position. Effectively, the metal apex averages the periodic Cl^-/Na^+ charges. However, near the vacancy, the metal apex is able to probe the extended vacancy's net positive charge.

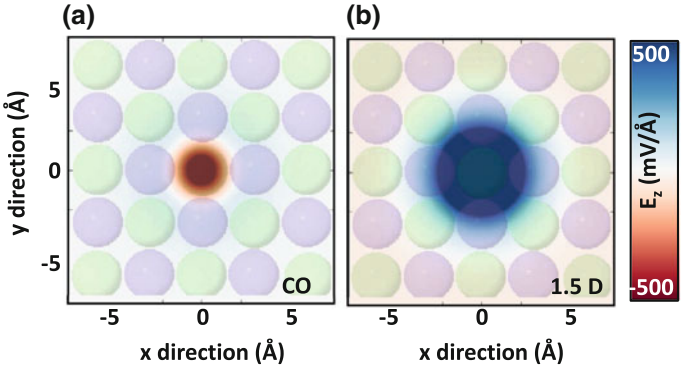

Fig. 15.15 Lateral distribution of the E_z of **a** the CO probe and **b** the 1.5 D dipole (that replaces the Cu tip charge distribution) in the NaCl top surface plane. The composite CO + 1.5 D probe is at $z_T = 650$ pm (as in Fig. 15.14). The atomic positions of the Cl vacancy on NaCl surface are superimposed. The electric field of the metal tip in (a) extends over several lattice sites and effectively averages out the opposite contributions of Na^+ and Cl^- ions to the electrostatic interactions. The field of the CO molecule in (b), confined to a single atomic position, is responsible for the atomic-scale lattice resolution

In summary, for the uncompensated positive charge of the vacancy, both dipoles contribute and compensate each other but the larger positive dipole dominates, leading to a repulsion above the vacancy site, already observable at large tip heights (Fig. 15.14). However, in the case of the atomic Na and Cl sites, the rather different spatial extension of the electric fields (see Fig. 15.15) leads to a completely different scenario. The dipole coming from the metal apex cannot resolve those sites because its field spreads out significantly at the sample surface, effectively averaging their opposite contribution. On the contrary, the smaller but rather localized electric field created by the CO molecule is crucial for explaining the observed atomic resolution.

15.6.5 Can a Single Dipole Mimic a CO Molecule on a Tip?

The main messages that should be extracted from the previous analysis is that the ES behavior of the metal-CO tips is complex. The metallic tip produces a field that is attractive towards electrons and can be modeled by a positive dipole (partial positive charge at the apex). On the other hand, the CO molecule has a net positive dipole but this is only relevant in the very far field where the dipolar approximation reproduces the electric field. Close to the O, the electric field is localized and repulsive towards electrons. The question we address now is, could a dipole quantitatively reproduce the HR-AFM images obtained using the 3D ES potential of the CO molecule?

For tip-sample distance relevant for AFM ($z < 1100$ pm as seen in Figs. 15.8 and 15.10), the electrostatic potential of the CO molecule is repulsive towards electrons. Thus we attempt to substitute the 3D potential of the CO molecule by the one

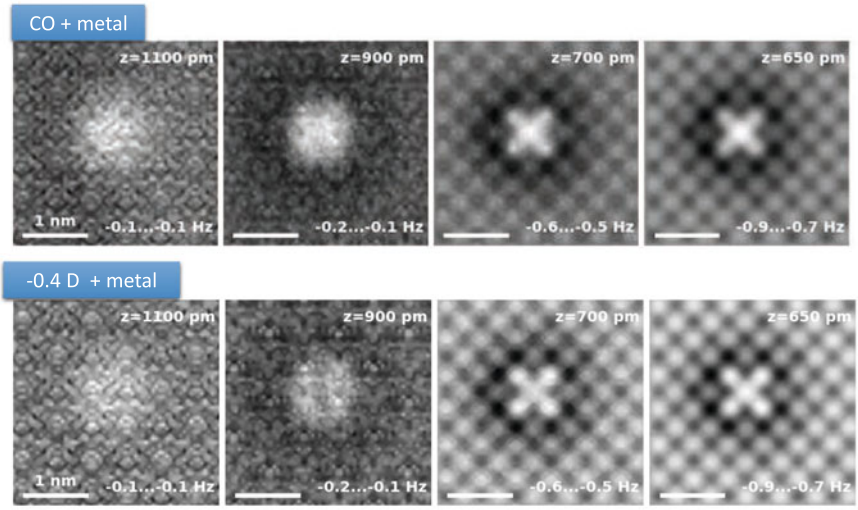

Fig. 15.16 Theoretical AFM images of a Cl vacancy in bilayer NaCl on Cu(100) using a CO probe and a 1.5 D dipole simulating a Cu tip. In the top row, the full CO charge distribution is used to model the CO part of the ES interaction and in the bottom row, the CO is replaced by a -0.4 D dipole. The frequency shift limits corresponding to black (more negative) and white are indicated in the bottom right of each panel. Scale bars correspond to 1 nm

produced by a negative dipole. For the distance range $z = 1100{-}650$ pm, we find that a dipole of -0.4 D quantitatively reproduces the AFM images calculated with the full 3D potential (see Fig. 15.16 for the comparison). For smaller distances the ES field of the CO molecule stops having a behavior that can be modeled by a dipole over a large enough range of distances. In addition, even for a qualitative description of AFM images, tilting effects and inhomogeneous sample charge distributions invalidate a dipole substitution. For this reason, we strongly discourage modeling the CO molecule by a single dipole, and, instead, favor the use of the whole charge density of the CO molecule.

15.7 AFM Imaging of the CO Molecule as an Adsorbate

Carbon monoxide surface adsorption has been a central point in the study of surface science. It has been widely studied with ensemble averaging techniques [36], as well as scanning probe techniques. For the NC-AFM, it is an especially important problem due to the use of the CO molecule for tip functionalization [1].

We have already characterized the electrostatic behavior of a metal-CO tip. The metallic tip acts as a positive dipole and, for distances relevant for AFM, the charge density of the CO is repulsive towards electrons. In principle, we would expect the CO

adsorbed on a metal surface to display the same behavior, and, thus, the interpretation of NC-AFM images taken with a metallic tip to be straightforward. However, the NC-AFM studies of the surface adsorption of the CO molecule found in the literature propose rather different interpretations. In most of the cases, the CO appears as an attractive feature [19, 30, 37–39], presumably due to the vdW interaction. Contrary to this, two studies have reported imaging the CO adsorption on Cu(111), NiO(001), and Mn/W(001) both in the attractive and repulsive regimes [20, 22]. In these studies, an attractive hump-like feature of 1 nm is observed for far tip-sample distances, while a repulsive donut-like feature appears at smaller distances.

There are two contradictory explanations for the contrast observed for the adsorbed CO in the repulsive regime using metallic tips. Schwarz et al. [20] propose a model in which the vdW interaction, modeled by a radially dependent attractive potential, competes with a repulsive dipole-dipole electrostatic interaction (which has both radial and angular dependence). This interaction arises from two antiparallel dipoles: the net positive dipole of the adsorbed CO molecule (+0.3 D for CO/Cu(111)), and the positive dipole of metallic tips (+1.5 D for Cu tips) [20, 22]. By assuming a larger interaction radius for the vdW interaction as compared to the interaction radius of the dipole-dipole interaction, a repulsive donut-like regime can be obtained with the model at a tip-sample distance (as measured by the tip apex and O atom separation) of >4.5 Å.

On a closer look, several issues arise with this model: (1) The contrast change is inverted. That is, the attractive hump-like feature is predicted for smaller tip-sample distances than the donut-like repulsive feature. (2) Both frequency shift and energy difference between the CO molecule and background substrate are more than an order of magnitude smaller than what is observed experimentally. (3) As we will see briefly, at $z > 4.5$ Å the electrostatic potential of the adsorbed CO on metal surfaces is repulsive towards electrons. The tip-sample distances at which the repulsive feature occurs are much larger than what is observed experimentally. When the CO is adsorbed on the Mn/W(001), the repulsive feature is imaged ≈2 Å higher than the minimum frequency shift of the substrate background [20]. Using an adsorption distance for the CO molecule of 2 Å the relative distance between the tip and the O atom is ≈2 Å.

We propose and alternative explanation based on the short-range repulsion due to the overlap of the tip and sample wave functions. We have carefully examined the electrostatic behavior of the sample with DFT calculations (see Appendix A for details). The first column of Fig. 15.17 shows the electric field with the molecule adsorbed on a top site at the distance predicted by DFT. In line with what we have shown for the Cu–CO tips, close to the CO, the field resembles the field of the isolated CO molecule. Above the O atom, it is repulsive towards electrons, even past 10 Å. As in the case of the isolated molecule, the overall dipole of the system is positive and indeed, at very far distances, there would be a contrast inversion of the field. The dipole actually increases with respect to the isolated molecule, from +0.1 D to +0.3 D. The increment was obtained by calculating the change in the work function of the sample

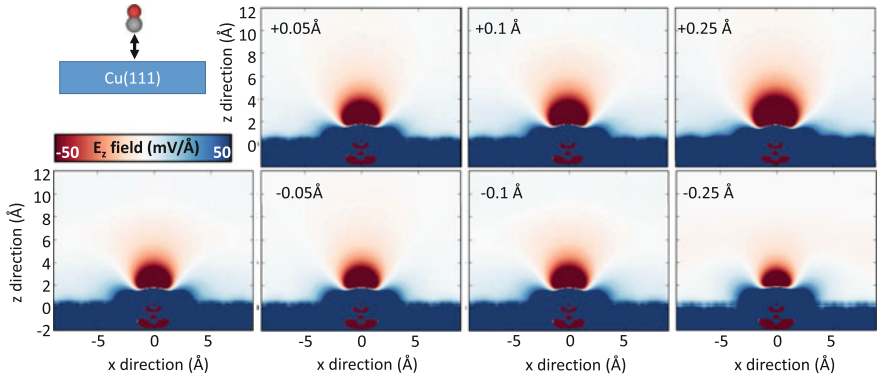

Fig. 15.17 z-component of E-field of CO on Cu(111) for various adsorption distances. On the first row the CO molecule is placed at the equilibrium adsorption distance. In the subsequent rows the molecule is displaced vertically

$$\text{dipole} = \frac{\epsilon_0 \text{Area} \Delta W}{e}. \tag{15.6}$$

It is worth noting that the CO/metal system is challenging for DFT. Experimental evidence clearly shows that the CO molecule adsorbs onto a Cu substrate on a top site [40]. However, DFT favors, even with the most sophisticated XC functionals, sites with a higher coordination. This classic problem, common to many FCC metals, has been traced back to the limitations of DFT in the description of the subtle energy differences among the triple, double, and single bond configurations of the CO molecule. In the particular case of Cu, DFT predicts the top site to be the stable adsorption configuration, but the energy difference between top and hollow adsorption sites is almost negligible.

Given the possible limitations of DFT, we have explored the robustness of the electrostatic properties of the system by varying the adsorption distance of the molecule. The panels in Fig. 15.17 display the electric field for different cases where the adsorption distance is varied in ± 0.05 Å increments. These results clearly show that there are no qualitative changes in the behavior of the electric field. Furthermore, the field is also robust against changes in the CO adsorption site (hollow and bridge).

From the analysis above, it is clear that the ES interaction between the CO/Cu(111) sample and a metallic tip is attractive for tip-sample distances below 10 Å. As discussed for the isolated CO molecule, there would be a contrast inversion for very large distances, but the resulting interaction is negligible and certainly not relevant to represent the experimental measurements. This leaves chemical repulsion as the only source for the repulsive features observed in the experiments. However, the repulsive features have only been observed in constant interaction maps, where the slopes of the frequency shift are always positive [20], and the Pauli repulsion led to very strong repulsive forces. Without ionic relaxations, the change of contrast between the hump-like attractive regime and the donut-like repulsive regime would

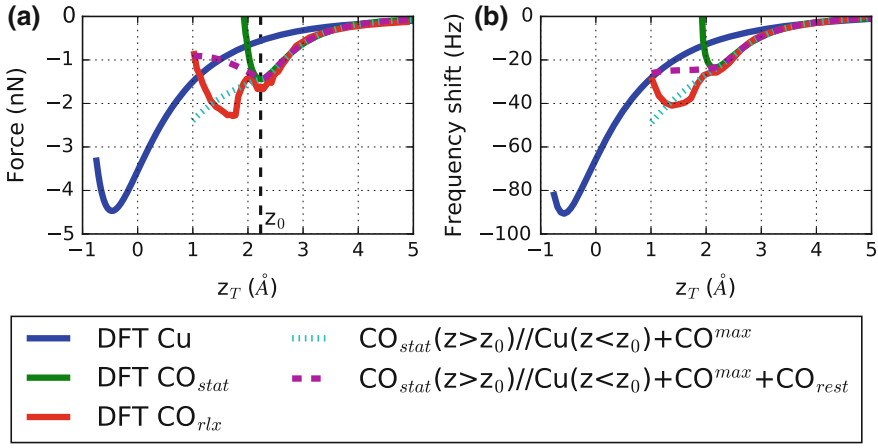

Fig. 15.18 Theoretical **a** force and **b** frequency shift versus distance plots of the adsorbed CO on Cu(111) surface as probed by a Cr_{14} tip. DFT calculations of a top site of the Cu(111) (blue lines), the adsorbed CO molecule in an upright position without relaxation (green lines), and the adsorbed CO molecule with ionic relaxation (red markers). Simulated AFM spectroscopies with (purple dashed lines) and without (cyan dotted lines) a CO tilt restoring force. The tip-sample distance corresponds to the height between the metal apex atom and the O atom with the CO in an upright position

occur at negative slopes. For this reason, ionic relaxation needs to be included in the explanation of the contrast formation.

In order to further understand the AFM contrast mechanism for the imaging of CO adsorbed on metallic surfaces with metallic tips, we have carried out DFT force vs distance calculations (see Appendix A for details of the calculations). As a model system, we use CO adsorption on a Cu(111) substrate as probed with a Cr_{14} tip (3 layer pyramid carved from a Cr(110) surface) that mimics the tip used in the experiments [20]. Figure 15.18a shows the force on top of a Cu atom (blue line) and the CO molecule in an upright position and without ionic relaxation (green line). The tip-sample distance (z_T) refers to the height between the tip apex and the O atom with the CO molecule in an upright position. The interaction on top of the CO molecule is attractive at large tip-sample distances and due to Pauli interaction becomes repulsive at smaller heights, with the minimum force occurring at $z_T = z_0 = 2.2$ Å. The interaction on top of a Cu atom has the same behavior but with the minimum force occurring at $z_T = -1.5$ Å (or 1.5 Å with respect to the Cu substrate). The distance between the minimum force roughly corresponds to the CO adsorption distance on the Cu substrate (3 Å from the O atom). Although the Cu site is overall more reactive (it has a minimum force of -4.4 nN compared to -1.4 nN for the CO site), the CO is more attractive for $z_T > 2.0$ Å. From this we can conclude that the change of contrast in AFM images occurs at most 2.5 Å from the maximum interaction (minimum force) measured at the background substrate. This is a key point that is supported by experimental findings [20] and yet not consistent with the dipole-dipole model described above.

A further corroboration is done by calculating the frequency shift. Figure 15.18b shows the frequency shift calculated using the large amplitude oscillation approximation,

$$\Delta f = \frac{f_0}{kA^{3/2}} \frac{1}{\sqrt{2\pi}} \int_0^\infty \frac{F_{ts}[d+z']}{\sqrt{z'}} dz', \tag{15.7}$$

with a typical experimental prefactor of the integral of -16.82 Hz/nN/Å$^{1/2}$. As in the force plot, the CO is more attractive (less negative frequency shift) for large tip-sample distances, and there is a contrast inversion at around 2 Å (this is approximately 2.5 Å from the minimum frequency shift of the substrate). Due to the exponential increment of the Pauli repulsion, the crossing between the CO and Cu frequency shift occurs after the CO's slope change (negative slope). As discussed before, in the experimental images the crossing is observed at positive slope frequency shifts. This can be accounted for by taking into account ionic relaxations. The CO, being fairly mobile on the substrate, has the ability to tilt or even hop between adsorption sites (top, hollow, bridge). This reduces the overlap of the molecule and apex wavefunctions and thus attenuates the repulsion. The adsorption of the CO atom on a Cu(111) surface is not a trivial problem. As stated before, DFT does not predict a sufficiently large barrier between the adsorption of the CO on a top site versus hollow site with the commonly used XC functionals. This makes difficult the interpretation of AFM calculations that include ionic relaxation; nonetheless, they are instructive. Red lines on Fig. 15.18a shows force versus distance DFT calculation on top of the CO molecule that include ionic relaxation. Up to the maximum interaction (z_0), the ionic relaxations are negligible and the forces are similar to the static ones. For smaller tip-sample distance, the CO molecule avoids the high repulsion caused by the proximity of the tip by two mechanisms. Close to z_0 the molecule starts to tilt and slightly increases the force, yet suppressing the exponential repulsion felt by the molecule fixed in the upright position. As the distance is further reduced, the molecule starts to shift to the hollow position causing a drop of force of 1 nN. Before the CO fully reaches the hollow position (the C atom remains closer to the original Cu atom than the neighboring ones), the CO starts to tilt again and the force increases non-exponentially. The shift towards the hollow site is a reversible process (upon tip retraction the CO returns to the top position), which makes the described dynamics experimentally plausible. Alternatively, a larger top/hollow barrier prolongs the initial CO tilt regime.

In order to fix the limitations of DFT, we have introduced a simple model to account for a large top/hollow barrier that enforces the CO to tilt upon tip approach. It is based on two suppositions: (1) through the CO tilt, the tip retains the maximum interaction with the CO (experienced at z_0) and only gains interaction through the substrate. (2) The tilt carries a penalization cost proportional to the tip-sample distance. The resulting interaction,

$$F[z] = \Theta(z - z_0)\mathrm{CO}_{\mathrm{stat}}[z] + \Theta(z_0 - z)\left[\mathrm{Cu}[z] + \mathrm{CO}_{\mathrm{max}} - k_{\mathrm{rest}}(z - z_0)\right], \tag{15.8}$$

is plotted in Fig. 15.18 as purple dashed lines (and cyan dotted lines without the restoring force). A spring constant of $k_{\text{rest}} = -1.5$ nN/Å was used in order to simulate the positive-slope-frequency-shift-crossing closest to z_0 (see Fig. 15.18b). The contrast inversion occurs at $z = 1$ Å, this is 1.5 Å away from the minimum frequency shift of the substrate. Also, 2 Å higher than the crossing ($z_T = 3$ Å), the contrast between the CO and the background is approximately 0.5 Å. This is also supported by experimental findings [20] and is inconsistent with the dipole-dipole model.

A final point of clarification. The above analysis was done on the model CO–Cu(111) system. Due to the large screening of metallic surfaces, we expect the analysis to be applicable to other metallic substrates. However, it may not apply to non-metallic substrates such as NiO [22], where ionic relaxations of the substrate and spin polarization play an important role in the chemisorption of the CO molecule and can induce relevant charge transfers resulting in a completely different electrostatic potential of the sample.

15.8 Conclusions

This chapter has explored the electric field created by CO functionalized metal tips. Our analysis conclusively shows that this field cannot be described by a single dipole. It is necessary to take into account both the positive dipole that describes the electric field created by the metal tip and the negative charge cloud strongly localized in front of the oxygen atom. We have incorporated this insight into a theoretical model that allows the efficient simulation of AFM measurements retaining a first-principles accuracy. Using this model, we have identified the contrast formation mechanisms for AFM images of localized ionic defects (Cl vacancies on a metal–supported NaCl bilayer) using CO-decorated metal tips. The electrostatic interaction dominates the contrast at large and medium tip–sample distances (>500 pm), while Pauli repulsion takes over at closer separations, where the CO probe tilts and highlights saddle lines as ridges. The opposite sign and different spatial extension of the associated electric fields explain the rich contrast observed. While both terms compete to determine the contrast of uncompensated, extended defects like the Cl vacancy, atomic–scale resolution of the ionic lattice arises mainly from the CO electric field as the more extended field created by the metal apex averages out the contribution coming from those periodic and rapidly varying charge distributions.

The insight gained from our analysis can be used to address the apparent contradiction in the interpretation of previous experiments involving CO molecules either as a tip on a metallic apex probing ionic surfaces [19] or as an adsorbate probed with a pure metallic tip [20]. Our results show that the electrostatic field of the CO tip is crucial to describe the AFM contrast on the atomic scale. We proved that the simplified description of the tip as a single dipole to explain the electrostatic interactions fails. We show that the contradictory assignment of the CO dipoles' direction in recent publications [19, 20] is related to this approximation and provide a consistent

interpretation for the images of CO adsorbates in the repulsive regime in terms of the Pauli repulsion.

We believe that our methodology for the calculation of AFM images including the detailed local charge distributions of the tip and sample obtained from first-principles calculations is the right tool to address two key open issues in high-resolution AFM: the origin of the intermolecular contrast observed in hydrogen-bonded and metal-coordinated systems, and the enhanced resolution in KPFM measurements with metal-CO tips.

A DFT Calculation Details

All density functional theory (DFT) calculations were carried out using the projector augmented wave (PAW) method as implemented in VASP [35]. We have used the PBE XC functional supplemented by semi-empirical DFT-D3 van der Waals (vdW) interaction [31], a plane wave cutoff of 400 eV, and fine electronic convergence ($E_{\mathrm{SCF}} = 10^{-4}$ eV) on all calculations. Furthermore,

- All volumetric data was calculated on an uniform mesh with 0.075 Å grid spacing with the dipole correction applied to the z-direction. For the electrostatic potentials, a uniform 1D filter in the z-direction was applied to the volumetric data in order to eliminate high frequency noise ($\lambda = 2$ grid points). The z-component of the E-fields shown in Sects. 15.2, 15.3, 15.4 and 15.7 was calculated from the gradient of the electrostatic potential.
- Calculations used to fit the model (Sect. 15.5) used a $3 \times 3 \times 1$ grid for sampling the Brillouin zone.
- Sect. 15.5.2 calculations used the Γ point for the sampling of the Brillouin zone and ionic relaxations were considered converged when forces were less than 10^{-2} eV/Å.
- Sect. 15.5.3 calculations used a $7 \times 7 \times 1$ grid for the sampling of the Brillouin zone and ionic relaxations were considered converged when forces were less than 10^{-2} eV/Å.

B Parametrization of the Short Range Interactions

In order to parametrize the Morse potentials of the SR interaction, we perform static DFT force calculations on a clean NaCl bilayer on a 4-layer Cu(100) slab probed by a CO molecule on a $2\sqrt{2} \times 2\sqrt{2}$ unit cell with a large vacuum (total cell size 15.9 Å $\times$ 15.9 Å $\times$ 42 Å) (see Fig. 15.19a, b). Calculations were carried out in VASP [35], using the PBE XC functional supplemented by semi-empirical DFT-D3 van der Waals (vdW) interaction [31], a plane wave cutoff of 400 eV, a fine electronic convergence ($E_{\mathrm{SCF}} = 10^{-4}$ eV), and a $7 \times 7 \times 1$ grid for the sampling of the Brillouin

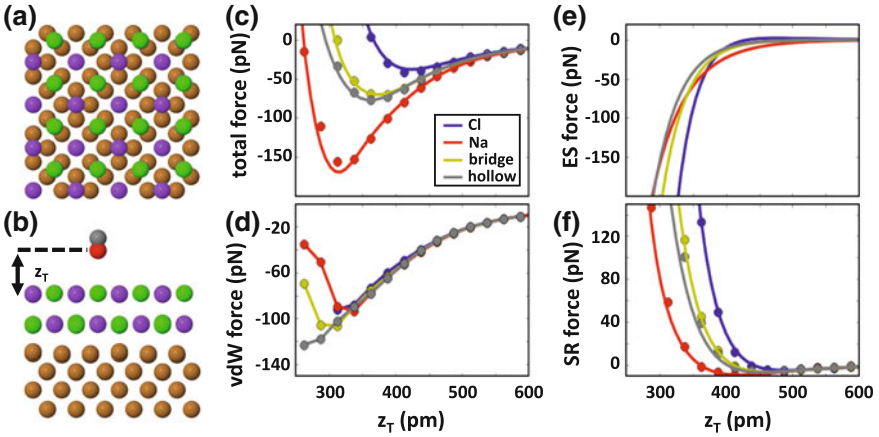

Fig. 15.19 **a** Front view of the relaxed clean NaCl/Cu(100) surface used in the DFT spectroscopy calculations. **b** Lateral view of the surface along with the CO probe. **c** Total, **d** vdW, **e** electrostatics (ES), and **f** short range (SR) forces for Cl (blue), Na (red), bridge (yellow) and hollow (gray) sites. Markers correspond to DFT data while the lines to calculations with the model. The Cl, Na, and bridge sites were used in the parametrization of the SR interaction, while the hollow site is calculated to show the ability of the model to reproduce the DFT results on any point of the surface

zone. Force curves were calculated with a 25 pm interval on 3 different sites: Cl, Na, and bridge (defined as the midpoint between a Na and Cl site). Figure 15.19c, d show the total and vdW forces obtained for those three sites (red, blue, and yellow markers correspond to the Cl, Na, and bridge sites in Fig. 15.19c, d. The electrostatic interaction is calculated, as in the model, from,

$$V_{\mathrm{ES}} = \int \rho_{\mathrm{CO}} \Phi_{\mathrm{sample}} d\mathbf{r}^3$$

(see Fig. 15.19e). Finally, the short range (SR) contribution (Fig. 15.19f) is obtained from

$$V_{\mathrm{SR}}^{\mathrm{DFT}} = V_{\mathrm{total}}^{\mathrm{DFT}} + V_{\mathrm{vdW}}^{\mathrm{DFT}} + V_{\mathrm{ES}}$$

and fitted, through a least-squares method, to a sum of Morse potentials,

$$V_{\mathrm{SR}} = \sum_{i=\mathrm{Na,Cl,ions}} D_e^i \left((1 - \exp\left[-a^i (|\mathbf{x} - \mathbf{x}^i| - r_e^i)\right])^2 - 1 \right),$$

where $|\mathbf{x} - \mathbf{x}^i|$ is the distance between the O atom in the CO probe and the corresponding ion, D_e^i (well depth), a^i (that controls the inverse of the width of the potential), and r_e^i (equilibrium bond distance) are the species dependent parameters determined by the fitting, and the sum extends to all the atoms of the ionic surface.

Table 15.1 Morse potential parameters fitted from DFT calculations. These parameters provide an excellent fit to the DFT force curves

	D_e (Ha)	a (Bohr^{-1})	r_e (Bohr)
Na–CO	8.15E – 15	1.62	12.82
Cl–CO	7.65E – 05	0.80	8.61

Results for the total, vdW, electrostatic, and short range forces on the 3 sites are plotted on Fig. 15.19c–f. Bullets correspond to the values obtained from DFT calculations and lines represent the results from the model. Note that the DFT-D3 theory is used to estimate the vdW interaction both in the DFT calculations and in the model; hence, markers and lines of Fig. 15.19d are identical. For the three sites, forces calculated with DFT and the model are in excellent agreement. Table 15.1 shows the fitted parameters.

In order to assess the transferability of our model to sites different from the ones included in the SR fitting, we have tested the predictions of the model for a new site: a hollow position (defined as the midpoint between two Cl atoms). Figure 15.19 shows the excellent agreement between the DFT calculations (grey markers) and the model (grey lines) on this site.

Acknowledgements We thank the financial support from AEI under project MAT2017-83273-R and from MINECO under projects MAT2014-54484-P and MDM-2014-0377. We thank Niko Pavliček, Bruno Schuler, Nikolaj Moll, Gerhard Meyer and Leo Gross for helpful discussions.

References

1. L. Gross, F. Mohn, N. Moll, P. Liljeroth, G. Meyer, The chemical structure of a molecule resolved by atomic force microscopy. Science **325**(5944), 1110–1114 (2009)
2. L. Gross, F. Mohn, N. Moll, G. Meyer, R. Ebel, W.M. Abdel-Mageed, M. Jaspars, Organic structure determination using atomic-resolution scanning probe microscopy. Nat. Chem. **2**(10), 821–825 (2010)
3. M. Emmrich, F. Huber, F. Pielmeier, J. Welker, T. Hofmann, M. Schneiderbauer, D. Meuer, S. Polesya, S. Mankovsky, D. Ködderitzsch, H. Ebert, F.J. Giessibl, Subatomic resolution force microscopy reveals internal structure and adsorption sites of small iron clusters. Science **348**(6232), 308–311 (2015)
4. D.G. de Oteyza, P. Gorman, Y.-C. Chen, S. Wickenburg, A. Riss, D.J. Mowbray, G. Etkin, Z. Pedramrazi, H.-Z. Tsai, A. Rubio, M.F. Crommie, F.R. Fischer, Direct imaging of covalent bond structure in single-molecule chemical reactions. Science **340**(6139), 1434–1437 (2013)
5. F. Albrecht, N. Pavliček, C. Herranz-Lancho, M. Ruben, J. Repp, Characterization of a surface reaction by means of atomic force microscopy. J. Am. Chem. Soc. **137**(23), 7424–7428 (2015)
6. L. Gross, F. Mohn, N. Moll, B. Schuler, A. Criado, E. Guitian, D. Pena, A. Gourdon, G. Meyer. Bond-order discrimination by atomic force microscopy. Science **337**(6100), 1326–1329 (2012)
7. C. Weiss, C. Wagner, C. Kleimann, M. Rohlfing, F.S. Tautz, R. Temirov, Imaging Pauli repulsion in scanning tunneling microscopy. Phys. Rev. Lett. **105**(8), 86103 (2010)

8. G. Kichin, C. Weiss, C. Wagner, F. Stefan Tautz, R. Temirov, Single molecule and single atom sensors for atomic resolution imaging of chemically complex surfaces. J. Am. Chem. Soc. **133**(42), 16847–16851 (2011)
9. C. Chiang, C. Xu, Z. Han, W. Ho, Real-space imaging of molecular structure and chemical bonding by single-molecule inelastic tunneling probe. Science **344**(6186), 885–888 (2014)
10. F. Mohn, L. Gross, N. Moll, G. Meyer, Imaging the charge distribution within a single molecule. Nat. Nanotechnol. **7**(4), 227–231 (2012)
11. N. Moll, L. Gross, F. Mohn, A. Curioni, G. Meyer, The mechanisms underlying the enhanced resolution of atomic force microscopy with functionalized tips. New J. Phys. **12**(12), 125020 (2010)
12. P. Hapala, G. Kichin, C. Wagner, F. Stefan Tautz, R. Temirov, P. Jelínek, Mechanism of high-resolution STM/AFM imaging with functionalized tips. Phys. Rev. B **90**(8), 85421 (2014)
13. M.P. Boneschanscher, S.K. Hämäläinen, P. Liljeroth, I. Swart, Sample corrugation affects the apparent bond lengths in atomic force microscopy. ACS Nano **8**(3), 3006–3014 (2014)
14. M. Neu, N. Moll, L. Gross, G. Meyer, F.J. Giessibl, J. Repp, Image correction for atomic force microscopy images with functionalized tips. Phys. Rev. B **89**(20), 205407 (2014)
15. N. Moll, B. Schuler, S. Kawai, X. Feng, L. Peng, A. Orita, J. Otera, A. Curioni, M. Neu, J. Repp, G. Meyer, L. Gross, Image distortions of a partially fluorinated hydrocarbon molecule in atomic force microscopy with carbon monoxide terminated tips. Nano Lett. **14**(11), 6127–6131 (2014)
16. P. Hapala, R. Temirov, F. Stefan Tautz, P. Jelínek, Origin of high-resolution IETS-STM images of organic molecules with functionalized tips. Phys. Rev. Lett. **113**(22), 226101 (2014)
17. F. Albrecht, J. Repp, M. Fleischmann, M. Scheer, M. Ondráček, P. Jelínek, Probing charges on the atomic scale by means of atomic force microscopy. Phys. Rev. Lett. **115**(7), 76101 (2015)
18. A.J. Weymouth, T. Hofmann, F.J. Giessibl, Quantifying molecular stiffness and interaction with lateral force microscopy. Science **343**(6175), 1120–1122 (2014)
19. M. Schneiderbauer, M. Emmrich, A.J. Weymouth, F.J. Giessibl, CO tip functionalization inverts atomic force microscopy contrast via short-range electrostatic forces. Phys. Rev. Lett. **112**(16), 166102 (2014)
20. A. Schwarz, A. Köhler, J. Grenz, R. Wiesendanger, A. Köhler, J. Grenz, R. Wiesendanger, Detecting the dipole moment of a single carbon monoxide molecule. Appl. Phys. Lett. **105**(1), 11606 (2014)
21. T. Hofmann, F. Pielmeier, F.J. Giessibl, Chemical and crystallographic characterization of the tip apex in scanning probe microscopy. Phys. Rev. Lett. **112**(6), 66101 (2014)
22. D.Z. Gao, J. Grenz, M.B. Watkins, F. Federici Canova, A. Schwarz, R. Wiesendanger, A.L. Shluger, Using metallic noncontact atomic force microscope tips for imaging insulators and polar molecules: tip characterization and imaging mechanisms. ACS Nano **8**(5), 5339–5351 (2014)
23. R. Smoluchowski, Anisotropy of the electronic work function of metals. Phys. Rev. **60**(9), 661–674 (1941)
24. G.E. Scuseria, M.D. Miller, F. Jensen, J. Geertsen, The dipole moment of carbon monoxide. J. Chem. Phys. **94**(10), 6660–6663 (1991)
25. B. de la Torre, M. Ellner, P. Pou, N. Nicoara, R. Pérez, J.M. Gómez-Rodríguez, Atomic-scale variations of the mechanical response of 2D materials detected by noncontact atomic force microscopy. Phys. Rev. Lett. **116**, 245502 (2016)
26. G. Teobaldi, K. Lämmle, T. Trevethan, M. Watkins, A. Schwarz, R. Wiesendanger, A.L. Shluger, Chemical resolution at ionic crystal surfaces using dynamic atomic force microscopy with metallic tips. Phys. Rev. Lett. **106**(21), 216102 (2011)
27. T. Trevethan, M. Watkins, A.L. Shluger, Models of the interaction of metal tips with insulating surfaces. Beilstein J. Nanotechnol. **3**, 329–335 (2012)
28. L. Gross, B. Schuler, F. Mohn, N. Moll, N. Pavliček, W. Steurer, I. Scivetti, K. Kotsis, M. Persson, G. Meyer, Investigating atomic contrast in atomic force microscopy and Kelvin probe force microscopy on ionic systems using functionalized tips. Phys. Rev. B **90**(15), 155455 (2014)

29. M. Ellner, N. Pavliček, P. Pou, B. Schuler, N. Moll, G. Meyer, L. Gross, R. Pérez, The electric field of CO tips and its relevance for atomic force microscopy. Nano Lett. **16**(3), 1974–1980 (2016)
30. Z. Sun, M.P. Boneschanscher, I. Swart, D. Vanmaekelbergh, P. Liljeroth, Quantitative atomic force microscopy with carbon monoxide terminated tips. Phys. Rev. Lett. **106**(4), 046104 (2011)
31. S. Grimme, J. Antony, S. Ehrlich, H. Krieg, A consistent and accurate ab initio parametrization of density functional dispersion correction (DFT-D) for the 94 elements H-Pu. J. Chem. Phys. **132**(15), 154104 (2010)
32. J. Repp, G. Meyer, S. Paavilainen, F.E. Olsson, M. Persson, Scanning tunneling spectroscopy of Cl vacancies in NaCl films: strong electron-phonon coupling in double-barrier tunneling junctions. Phys. Rev. Lett. **95**(22), 225503 (2005)
33. Z. Li, H.-Y. Tiffany Chen, K. Schouteden, K. Lauwaet, E. Janssens, C. Van Haesendonck, G. Pacchioni, P. Lievens, Lateral manipulation of atomic vacancies in ultrathin insulating films. ACS Nano **9**(5), 5318–5325 (2015)
34. B. Schuler, M. Persson, S. Paavilainen, N. Pavliček, L. Gross, G. Meyer, J. Repp, Effect of electron-phonon interaction on the formation of one-dimensional electronic states in coupled Cl vacancies. Phys. Rev. B **91**(23), 235443 (2015)
35. G. Kresse, J. Furthmüller, Efficiency of ab-initio total energy calculations for metals and semiconductors using a plane-wave basis set. Comput. Mater. Sci. **6**(1), 15–50 (1996)
36. J.T. Yates, Chemisorption on surfaces—an historical look at a representative adsorbate: carbon monoxide. Surf. Sci. **299**, 731–741 (1994)
37. J. Welker, F.J. Giessibl, Revealing the angular symmetry of chemical bonds by atomic force microscopy. Science **336**(6080), 444–449 (2012)
38. M. Ternes, C.P. Lutz, C.F. Hirjibehedin, F.J. Giessibl, A.J. Heinrich, The force needed to move an atom on a surface. Science **319**(5866), 1066–1069 (2008)
39. P. Deshlahra, J. Conway, E.E. Wolf, W.F. Schneider, Influence of dipole–dipole interactions on coverage-dependent adsorption: CO and NO on Pt(111). Langmuir **28**(22), 8408–8417 (2012)
40. A.J. Heinrich, C.P. Lutz, J.A. Gupta, D.M. Eigler, Molecule cascades. Science **298**(5597), 1381–1387 (2002)

Chapter 16
Imaging Charge Distribution Within Molecules by Scanning Probe Microscopy

Martin Ondráček, Prokop Hapala, Martin Švec and Pavel Jelínek

Abstract Charge distribution on surfaces and molecules plays an important role in many physical and chemical processes including catalytic reactions, adsorption, adhesion and charge transport. However, detailed mapping of the spatial charge distribution on atomic scale still remains a challenge, despite recent advances in the field of scanning probe microscopy. Consequently, we are witnessing extensive activity in search for a reliable and robust protocol to image the charge distribution. In this chapter, we will discuss different methods which provide information about charge distribution at atomic or submolecular scale, including Kelvin probe force microscopy, scanning quantum dot microscopy or high-resolution imaging with functionalized tips. We will briefly discuss the mechanism of each of the different methods as well as their advantages and drawbacks. Finally, we will provide a brief outlook and perspectives for further improvement of charge distribution mapping on the submolecular level.

16.1 Introduction

The development of modern society is now critically linked to information processing as well as energy storage and conversion technologies. One key factor for ensuring sustainable technological progress is the development of new technologies and materials. Tremendous progress has been achieved in the last decade in the search for novel materials at the nanometer scale with a large application potential. On-surface chemistry and molecular manipulation represents one of the most promising strategies for bottom-up fabrication of complex nanostructures and functional nanosystems. Large structures can be formed on a surface using molecular building-blocks not only by self-assembling due to weak intermolecular forces, but also by polymerization into covalently bonded networks [1]. Such covalently interconnected structures attain high structural integrity leading to steady conformations

M. Ondráček · P. Hapala · M. Švec · P. Jelínek (✉)
Institute of Physics of the Czech Academy of Sciences, Cukrovarnická 10,
Prague 6, Czech Republic
e-mail: jelinekp@fzu.cz

S. Sadewasser and T. Glatzel (eds.), *Kelvin Probe Force Microscopy*,
Springer Series in Surface Sciences 65, https://doi.org/10.1007/978-3-319-75687-5_16

and consequently exhibit high thermal stability and low degradation of the structural properties over time. On-surface chemistry has achieved a number of successes building covalent molecular nanostructures in that respect [2]. A second outstanding feature of covalent assemblies [3] is an efficient electron transport through the established bonds, which makes the networks suitable for molecular-electronics applications. Besides that, on-surface chemistry could promote to the formation of molecular species that cannot be formed otherwise (i.e. in solution chemistry). At the same time, our understanding of fundamental atomic-scale processes taking place on surface—including charge transfer among adsorbates and the substrate, stabilization of charge states, chemical reactions or intermolecular interactions—has substantially advanced too.

Nevertheless, the detailed understanding and control of material properties of real nanostructures, potentially suitable for fully functional nanodevices, remain difficult tasks with many challenges. The challenges involved are too complicated to be addressed directly in their full complexity. Therefore, the number of relevant parameters in the problems under consideration has to be reduced. Basic knowledge about the formation of new nanostructures and their emerging properties must be acquired by exploiting simple model systems. In this sense, our main approach is the usual one in surface science: the use of clean single crystal surfaces atomically controlled in ultra-high vacuum (UHV) environment. It represents an idealized system with respect to real technological applications, but it makes possible to explore fundamental reaction mechanisms of large organic molecules.

The SPM techniques have found wide applications in Nanotechnology and other research areas such as Surface Physics and Chemistry, Tribology, Molecular and Cell Biology etc. Possible applications of Scanning probe microscopy (SPM) techniques under UHV—the Scanning Tunneling Microscopy (STM) [4] and Atomic Force Microscopy (AFM) [5] go beyond just providing various kinds of information about the investigated sample at the atomic scale. Using both contact and non-contact modes of operation, SPM may also serve as an assembly tool for creating well-defined atomic-scale structures, which is a starting point for actually building nanotechnological devices. Recent progress in the SPM field brought the combination of STM and AFM techniques in one instrument using a modified tuning fork [6] or length extensional resonator sensors [7]. The atomic resolution and detailed information about spatial distribution of electronic states of nanostructures are routinely achieved by means of SPM in laboratories around the world nowadays. Despite these advances, several challenges still remain open. Besides single atom chemical identification [8] and spin resolution [9], precise determination of charge distribution at atomic scale is one of the biggest challenges in the SPM field nowadays.

The most frequently used technique, which has the potential to handle this task, is the Kelvin Probe Force Microscopy (KPFM) [10–12]. This technique is usually interpreted as measuring a work function difference between the microscope's tip and an investigated substrate. In principle, the work function Φ is a macroscopic quantity, which defines the energy required to take an electron from the Fermi level of the substrate and bring it to the vacuum level. This quantity is well defined for a bulk of material with a homogeneous surface, but its definition on an atomic and

molecular level becomes problematic. Therefore observation of sub-molecular contrast in the local contact potential difference (LCPD) [13–18]—the quantity measured in KPFM—stimulated a vivid debate about the origin of the contrast. Another stimulus came with the possibility to detect single-electron charge states in quantum dots [19] or single atoms [20] by means of KPFM. Later on, F. Mohn and his colleagues at IBM Research Zurich managed to map the distribution of the charge in a single molecule of naphthalocyanine deposited on sodium chloride [21].

The mapping procedure of molecular charges with the KPFM is experimentally a difficult task, with many interconnected obstacles—e.g. very long data acquisition times, tip stability issues, complex post-processing, etc. Moreover, such measurements typically yield only moderate spatial resolution. They are limited to moderate tip-molecule separations since results obtained at short distances suffer from various artifacts. However high resolution at the atomic or molecular level can nevertheless be reached only in this short distance regime. In order to attain sub-molecular resolution, the tip has to be brought so close to the probed surface or molecule that the electron densities of the tip and the sample overlap substantially. Under such conditions, the usual interpretations of KPFM in terms of work functions or local electric fields break down as the maps do not reflect the intra-molecular charge distribution any more. Therefore, there is a demand for new alternative approaches to mapping the electrostatic potential and charge distribution. The desired new approaches should overcome, or at least mitigate, some of the disadvantages of the KPFM technique. Much activity has been stimulated by the urge to address this demand, mainly in the field of non-contact AFM, the result of which has been not only better understanding of the KPFM technique itself but also working examples of suitable alternatives.

The aim of this chapter is to provide a brief overview of the history of atomically resolved KPFM. In particular, we will focus on possibilities to map out the electrostatic potential/field on single molecules. We will describe two alternative approaches to map the electrostatic field on surfaces. We will also mention the importance of the electrostatic forces for high-resolution images acquired with functionalized tips.

16.2 Atomic Resolution in Kelvin Probe Force Microscopy

KPFM [10] is an offshoot of non-contact AFM [22]. Early after its invention in 1991, its potential was recognized and it became a very active branch of the SPM family. As mentioned above, the KPFM technique measures variations of the contact potential difference (CPD), V_{CPD}, between a surface and the AFM probe, which may originate from a difference in their respective work functions. Figure 16.1 represents a simplified working principles of the KPFM method. The concept of KPFM consists of detecting the electrostatic force F_{el} that acts between the tip and the sample. The force F_{el} exhibits parabolic dependence on applied bias V under normal conditions:

$$F_{\mathrm{el}}(z, V) = \frac{1}{2}\frac{\partial C(z)}{\partial z}(V - V_{\mathrm{CPD}})^2, \tag{16.1}$$

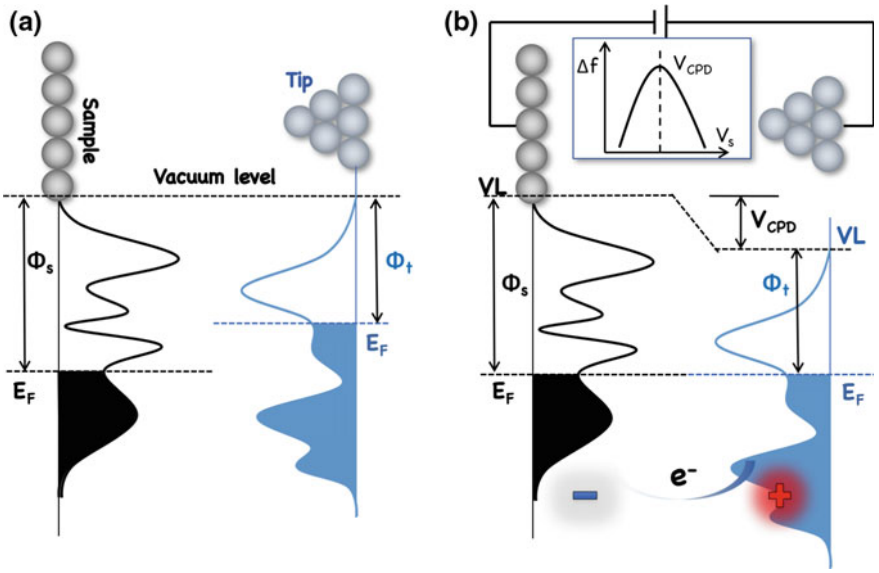

Fig. 16.1 Schematic view of principles of KPFM method. **a** The work function of sample, Φ_s, and tip, Φ_t, have different value and their electronic structure is aligned according to the vacuum level (VL). It means that the Fermi level (E_F) of tip and sample are not equal. **b** When probe and sample are brought into contact, the difference between work functions of sample Φ_s and tip Φ_t induces a flow of charge between the tip and the sample. This charge transfer gives rise to an additional dipole across the tunneling junction. Compensation of the field resulting from the dipole by an external bias allows one to determine the contact potential difference, V_{CPD}. There is a quadratic dependence of measured frequency shift Δf on applied bias V, with the parabola maximum at V_{CPD}

where C(z) is the capacitance and z is the distance between the tip and sample. According to the traditional macroscopic view, the extreme of the $F_{el}(V)$ function (the vertex of a parabola) is the point where bias voltage $V = V_{\mathrm{CPD}}$ applied between the tip and sample compensates the difference of work functions between the materials of these two electrodes. The work function of the tip Φ_t is usually unknown and may change from one experimental session to another. Consequently, the KPFM technique can only address relative spatial changes of surface work function across the studied sample. On the microscopic scale, the KPFM technique has been widely applied to characterize different surfaces, e.g. [15, 23]. However, one should keep in mind that, in general, any kind of electrostatic field can shift the force balance that determines V_{CPD}, not only the field associated with the difference of work functions. This is very important for inhomogeneous samples with defects as well as for molecules adsorbed on the substrate or on the tip. In such cases, the inherent static charge redistribution within both tip and sample creates local electrostatic fields, which shift the measured local contact potential difference (LCPD) on the atomic scale. The ensuing effect is hard to distinguish from variations of the work function.

Few years ago, several authors have reported atomically resolved LCPD images obtained on semiconductor [13, 14] and insulator [15, 16] surfaces. The mechanism of the atomic scale contrast in LCPD initiated a long-standing debate. To address the origin of the atomic contrast on ionic surfaces, Nony et al. [17] proposed an analytical model of the electrostatic force between the probe and a surface of an ionic crystal. The model is able to account for the atomic contrast observed in the LCPD in good agreement with KPFM experiments. The key ingredient of the model is the description of an induced polarization of classical point charges at the tip–surface interface due to the bias voltage modulation applied in KPFM experiments.

Nevertheless, this scenario using classical description of charges cannot be directly transferred to semiconductor surfaces, where a strong chemical bond between the tip and sample is typically established. Sadewasser et al. [18] carried out a combined experimental and theoretical study to address the origin of the atomic contrast in LCPD on semiconductor surfaces. The experiment revealed a strong variation of the Kelvin parabola and in particular of V_{CPD}, along the tip–sample distance on the Si(111)–7×7 surface. Moreover, complex data acquisition mapping the frequency shift as a function of tip-sample distance and applied bias allowed them to correlate the variation of LCPD with the short-range chemical force. Using theoretical simulations based on density functional theory (DFT) calculations, they attributed the contrast to a local variation of the surface dipole related to the formation of a chemical bond between an apex atom of the tip and a surface adatom. Figure 16.2 shows calculated induced electron densities (bond charges) in the tip-sample junction during the silicon tip approach towards a Si adatom on the Si(111)–7×7 surface. The bond charge gives rise to a local variation of the surface dipole, hence variation of the LCPD.

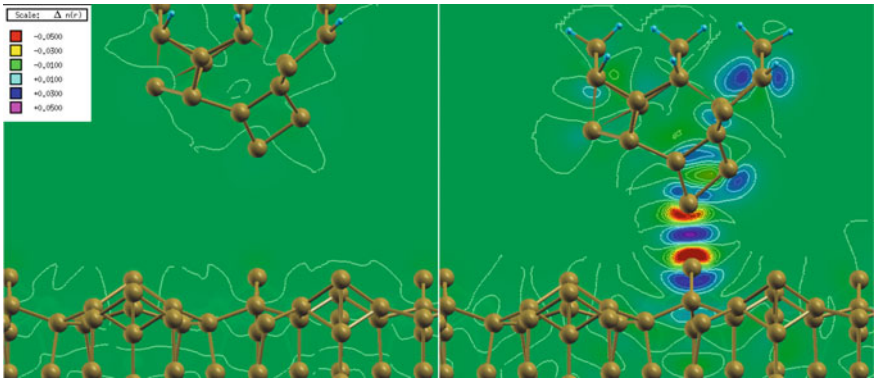

Fig. 16.2 Variation of bond charge between a Si tip and a Si adatom on the Si(111)–7×7 surface. Distribution of differential electron density induced in the tunneling junction due to formation of the covalent bond between Si atom on tip apex and Si adatom on the Si(111)–7×7 surface in (**a**) far distance on the onset of the covalent bond and **b** close tip-sample distance at the maximum of the chemical force [18]

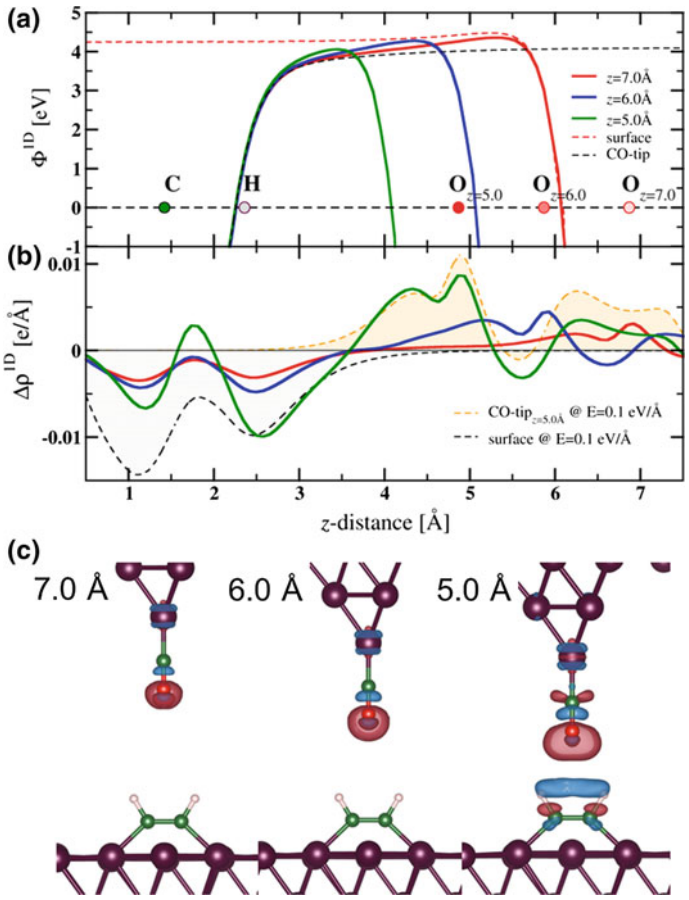

Fig. 16.3 Induced electron density in the tunneling junction during CO-tip tip approach towards a C_2H_2 molecule on Cu(111). **a** Calculated 1D plot of the tunneling barrier between CO-tip and C_2H_2 molecule on Cu(111) for different tip sample distances; **b** corresponding 1D-plot of induced electron density $\Delta\rho$ resulting from an enhanced electric field present in the tunneling junction; a reference induced electron density (dashed yellow line) created on the surface upon applying a homogenous electric filed of 0.1 eV/Å perpendicular to the surface [24]

Also in the case of two interacting molecules, a molecule of CO placed on the tip and an acetylene C_2H_2 deposited on Cu(111) surface, a substantial redistribution of electron density in the tunneling junction occurs [24]. According to theoretical DFT calculations, the electron density is induced upon tip approach in the junction as shown in Fig. 16.3. However it has a different spatial distribution than in the case of the Si adatom on the Si(111)-7×7, compare Figs. 16.2b and 16.3c. There is no covalent bond established between the CO and C_2H_2 molecules due to their low chemical reactivity. The lack of the covalent bond justifies the absence of the induced electron density in the middle part of the CO-C_2H_2 gap.

The induced electron density is a consequence of response to the local electric field in the junction caused by the existence of a finite dipole moment of the molecules forming the junction. Namely, the CO molecule attached on the tip apex increases the workfunction of Cu, whereas C_2H_2 decreases it. This charge transfer originates local electric field, which then enhances the electrical polarization of the molecules as they are approached to each other [24]. The presence of the local electric field in the junction will modify consequently the contact potential difference V_{CPD}. Thus, it is evident, that this effect has to be taken into account for the correct interpretation of KPFM measurements on organic molecules. These findings support the validity of the analytical model of Nony et al. [17] originally proposed for ionic surfaces.

Despite this insight, the quantitative agreement between KPFM experiments and theoretical analysis [25] is still missing. Moreover, the possibility to perform simultaneous AFM/STM measurements revealed that the tunneling current, flowing across the tunneling junction, may affect the surface potential and the resulting frequency shift signal. In particular, Weymouth et al. [26] found strong impact of the tunneling current on the measured force on samples with limited conductivity. This effect can strongly vary the Kelvin probe signal, thus hampering feasible experimental interpretation when the tunneling occurs.

16.2.1 Detection of Charge States

The KPFM technique has been also used to investigate single electron charging of quantum dots [19]. The capability to detect single electron charges with atomic scale resolution opened up completely new possibilities in studies of molecular electronics or organic photovoltaic cells. Moreover, the specific shape of Kelvin parabolas can provide further information about the dynamics of charge states, such as their lifetime. Namely, whenever charging and discharging rates are comparable to the oscillation frequency of the KPFM sensor, some correlation between the charge state and the phase of the tip oscillation will be present. Such correlation then gives rise to characteristic features in both basic channels provided by the AFM measurement, the frequency detuning as well as energy dissipation [27, 28]. Consequently, the deviations of the measured Kelvin curve from its ideal parabolic form allows one to extract some parameters that characterize the evolution of the charged system in time [29]. The KPFM technique has been successfully used to investigate single-electron charge switching of individual metal adatoms on top of an insulating film [20] and of molecules as well [30, 31]. These experiments demonstrated the ultimate spatial control of single electron charge states.

16.2.2 Mapping Charge Distribution Within Molecules

Knowledge of charge redistribution on single atoms or within a single molecule (i.e. intramolecular electrostatic field) deposited on a surface has fundamental importance in many research fields. The electrostatic field of a molecule has a notable influence on its other properties. In particular, the electrostatic properties may direct reactions of the molecule with other chemical species, e.g. by determining the active sites in the molecule at which the reaction will be initiated. No less important it is for understanding self-assembling processes of individual molecules into supramolecular complexes. As an other issue, the field affects the dynamics of electron-hole pairs, e.g. in photochemical or photoelectric processes. Detailed resolution of the charge distribution in the chemical bonds within a molecule significantly advances our current possibilities to study the charge transfer at the atomic and molecular level. For example, the detailed knowledge of the charge distribution on molecular level could help to design new drugs with optimal binding to biological receptors, molecular construction-sets which assemble into complex devices, information storage in atomic and molecular charge state or solar cells with more efficient charge separation.

Therefore, obtaining maps of the electrostatic field remains an important goal for scanning force microscopy, one which has not been yet fully attained. The tool that has been mostly used so far for this purpose is the Kelvin Probe Force Microscopy (KPFM). This techniques can in principle provide maps of the so-called local contact potential difference (LCPD) [32] with an atomic [20, 33] or molecular resolution [21, 34–36]. It has been demonstrated that the contrast in KPFM can be significantly improved by functionalizing the AFM probes [21, 37].

But while the KPFM signal may have a clear interpretation in terms of work-function variations over the coarser scales, it is sometimes far from clear how exactly the supposed LCPD signal relates to the relevant quantities such as the charge distribution or the electrostatic field [38]. Moreover, it was demonstrated that when the KPFM probe approaches very close to the detected object, various artifacts may spoil the LCPD signal [39]. Unfortunately, the same small distances that lead to the unwanted artifacts are necessary to achieve truly submolecular resolution in the LCPD maps. The problem is that the KPFM signal in this close proximity configuration arises from a non-trivial interplay between local electrostatic fields of the sample and also of the tip, the polarisability of both, the possible flow of tunneling current across the tip-sample junction, as well as any change in the geometry of the junction caused, for instance, by deflecting the functionalized apex of the probe by repulsive forces exerted on it by the sample. These issues prevent any accurate mapping of charge distribution in single molecules or molecule-sized structures using the classical KPFM setup.

Differential Kelvin Probe Force Spectroscopy

So far, the charge distribution was mostly studied by KPFM, which detects the changes in the local work function as discussed above. We have stressed that in order to get submolecular resolution, the probing tip has to be brought very close

to the investigated sample, which however introduces a number of undesired spurious effects on the measured LCPD. To solve this problem, a new measuring protocol that provides a way to remove the aforementioned artifacts was proposed. J. Repp et al. [39] introduced a new method, here referred to as the differential Kelvin probe force spectroscopy (KPFS). This method is based on the acquisition of 3D Δf-z spectroscopy taken at two different bias voltages. A difference of these two spectra is subsequently taken in order to extract the bias-dependent part of the frequency shift. One source of artifacts in the short-distance KPFM regime, often the dominant one unless the electron densities of the probe and the molecule overlap too much, is a bias-dependent deformation of both the tip termination and the molecule due to the effect of the strong electric field in the tip-molecule junction. Accordingly, the difference calculated from the two spectra is assumed to consist of two main components. One originates from the electrostatic force acting on the charge carried by the molecule due to the field of the tip, while the other component arises from the shifts of atomic positions caused by the effect of the electric field. The capability to achieve submolecular resolution of internal molecular charges was demonstrated on two very similar molecules, trimeric perfluoro-ortho-phenylene mercury ($F_{12}C_{18}Hg_3$) and its hydrogen derivative ($H_{12}C_{18}Hg_3$) with hydrogen atoms on peripheral benzene rings. Different electronegativity of hydrogen (H) as compared to fluorine (F) gives rise to different bond polarization between carbon and hydrogen atoms (C-H) on the one hand and carbon and fluorine (C-F) on the other, as shown in Fig. 16.4.

The acquired differential KPFS maps revealed molecular charge distribution with unprecedented resolution. What is more, the experimental maps show different

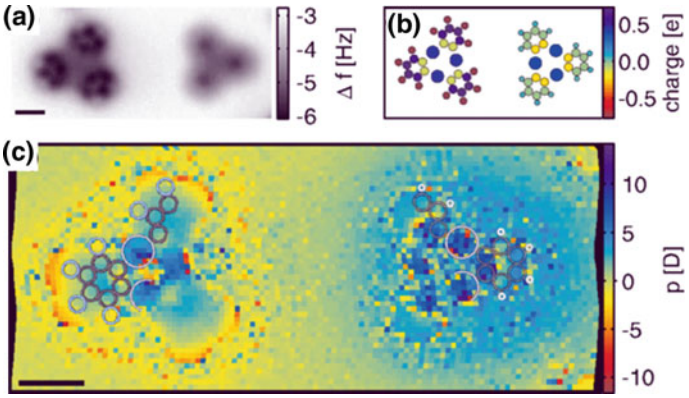

Fig. 16.4 Sub-molecular resolution of charge densities of molecules by means of the differential KPFS method. **a** Atomically resolved atomic force microscope image of molecules, trimeric perfluoro-ortho-phenylene mercury ($F_{12}C_{18}Hg_3$) and its hydrogen-terminated counterpart ($H_{12}C_{18}Hg_3$) on the surface of Cu(111). **b** The charge distribution simulated using quantum mechanical calculations. **c** Image of the sub-molecular charge distribution of the studied molecules obtained by the new differential KPFS method showing the different polarity of the chemical C-H and C-F bonds, respectively (adapted from [39])

polarity of C-F and C-H bonds in the two inspected molecules in good agreement with theoretical expectations. Namely, F atoms pull electrons from C atoms, giving the C-F bonds a strong polarity with the negative pole oriented towards the fluorine rim, while C-H bonds have a smaller polarity of the opposite sign. In this way, the differential KPFS pushed the limits of SPM to image molecular charges further, showing the possibility to observe the subtle charge differences that determine the polarity of chemical bonds within a molecule. On the other hand, the differential KPFS method still lacks any precise theoretical definition of the observable. Although the final maps obtained by this method were interpreted as maps of surface dipole density in the original paper [39], such interpretation relies on many simplifying assumptions and cannot be taken literally. Additionally, the acquisition procedure is not trivial and the method requires substantial time and data post-processing.

Scanning Quantum Dot Microscopy

C. Wagner and his colleagues proposed an alternative approach to overcome the inherent deficiencies of KPFM [40]. They employed a scanning probe with a single molecule located at the tip apex. Here, the molecule at the apex is exploited as a quantum dot for sensing the electrostatic fields on the scanned surface. Consequently, the authors named the new method the Scanning Quantum Dot Microscopy (SQDM). They acquired Kelvin parabolas $\Delta f(V)$ in the range of bias voltage where an electron can tunnel from the metallic tip onto the tip-decorating molecule (quantum dot), or vice versa. These events are reflected by characteristic instabilities (sharp spikes) observed on the Kelvin parabolas $\Delta f(V)$ at the corresponding bias voltages. The positions of the spikes correspond to energies of the frontier HOMO/LUMO molecular orbitals involved in the tunnelling process. The energies, at which the sharp spikes corresponding to charging/discharging events appear, are the main observables in SQDM. They provide information about the electrostatic interaction of the probe molecule on the tip and an inspected molecule on the surface. Thus, the basic idea of SQDM is to monitor a shift of the energy levels by the electrostatic potential of the target molecule or atom located on the sample surface. To do that, one has to acquire the Kelvin $\Delta f(V)$ curves across the scanned molecule at different distances, forming a multi-dimensional $\Delta f(V, x, y, z)$ data set. The electrostatic potential can be restored from the analysis of the data set tracking the energy shifts of frontier orbitals of the molecular probe. The SQDM method represents an elegant way of exploiting the so-called electrostatic gating, frequently used for quantum dots, to map out the electrostatic potential of a scanned surface as a function of tip position. Thanks to well defined charge states and clear theoretical interpretation, this method can be indeed quantitative. Nevertheless, the SQDM method possesses one severe disadvantage. It is a limited stability of the molecular probe at large bias voltages, which prevents scanning the surface at close tip-sample distances required for submolecular resolution. As a result, the SQDM method can be viewed as a far field method with only moderate spatial resolution compared to other SPM methods.

16.3 High-Resolution AFM/STM Imaging

Exceptional submolecular imaging of both electronic and atomic structures of individual molecules on surfaces is one of the most notable and exciting developments in the field of UHV SPM in the last years. Namely, R. Temirov et al. found that backfilling molecular hydrogen to the tunneling junction of a low-temperature STM microscope led to a functionalization of the apex of the scanning probe, which has greatly enhanced the spatial resolution in the STM images [41]. Afterwards, they demonstrated that a STM tip decorated by a range of atomic and molecular particles (Xe, CH_4, CO) allowed them to resolve chemical structures of large organic molecules deposited on metal surfaces [42]. This new technique became known as a scanning tunneling hydrogen microscopy (STHM). In a parallel effort, L. Gross et al. performed a high-resolution imaging of a pentacene molecule (i.e. visualization of chemical structure of the molecule including individual atomic and bond positions) by means of a frequency-modulated AFM [43]. The key was again a single CO molecule picked up on the tip from the substrate [44]. These days, we are witnessing a rapid development of high-resolution AFM/STM imaging with functionalized tips. For example, owing to the submolecular resolution of the technique, it was possible to identify individual intermediates and products of on-surface chemical reactions [45–49]. This capability provided completely new stimulus for on-surface chemistry.

The origin of high-resolution AFM images was originally attributed to the Pauli repulsion effect experienced by the functionalized tip apex as the tip comes very close to the sample [43, 50]. It is still debated, what are the limits of resolution achievable within this new technique or what other information can be extracted from it, apart from visualizing the bonds in the molecular structures [51]. Very soon after the pioneering results, it was discovered that the apparent bond lengths and angles are somewhat distorted [51, 52]. This was hampering the attempts to precisely determine where the atoms are exactly located within unknown structures and which are the true adsorption sites on surfaces. It has been extensively discussed that the image distortion is caused by lateral bending of the molecular probe decorating the tip apex, the bending being mostly driven by Pauli repulsion [51, 54, 55] at close tip-sample distances. However, the Pauli repulsion is not the only force which can cause the tip bend and thus the image being distorted. Whenever a functionalized probe particle possesses a charge, it will be moved by the electrostatic field of the inspected molecule, which is generated by its internal charge redistribution.

16.3.1 Impact of the Electrostatic Interaction on the High-Resolution AFM/STM Imaging

Generally, the imaging mechanism of high-resolution AFM/STM is a result of the attractive van der Waals (vdW), electrostatic and repulsive Pauli forces acting between the functionalized tip and the sample. Originally, only vdW and Pauli forces

were taken into account in its theoretical descriptions [43, 50, 54, 55]. Hence a question arises, what role plays the electrostatic force in the imaging mechanism? In general, the magnitude of the electrostatic force is dependent on the charge density distribution (polarity) at the frontier atom/molecule of the tip apex (the so called probe particle [55]) and the charge density distribution at the scanned surface. Detailed investigation of different cases revealed that the match of the AFM/STM simulations with experimental data can be substantially improved when the electrostatic force is accounted for [53, 56].

The impact of the electrostatic force on the high-resolution contrast can be clearly demonstrated on AFM images acquired on water tetramers deposited on a NaCl(001) surface [57]. Sharp lines in the Δf images emerge from branching of probe-particle trajectories over saddle points of the total tip-sample interaction potential at small tip-water separations, as discussed in [55]. In the case of non-planar and strongly polarized systems, such as the water clusters, the bending of the probe termination leads to even more intriguing and unintuitive results, which deserve detailed discussion. The total interaction potential between the functionalized tip and the water molecules adsorbed on the surface consists of Pauli repulsion, London dispersion and electrostatic interaction. A strongly polar character of water molecules gives rise to a pronounced electrostatic field above water complexes. The experimental evidence clearly shows distinct contrast of the water tetramer when it is resolved with CO or Cl-terminated tips. While a Cl-terminated tip has a strong negative monopole charge, the charge distribution of a CO tip is more complex. Thorough comparison between experimental results and simulations reveals that the best match is achieved for a weak quadrupole charge distribution with a negative lobe pointing in the direction of the surface. At small tip-sample distances, where the Pauli repulsion entirely dominates over the weak electrostatic interaction, a neutral tip model representing the CO tip also provides satisfactory agreement with experimental evidence [57].

Consequently, in the case of a CO tip, the image AFM contrast in close tip-sample distances can be fully understood with simulations including only Pauli repulsion and van der Walls interaction. A simulated Δf image with a neutral CO-like tip is shown in Fig. 16.5b, which agrees well with the experimental results (see Fig. 16.5a). Detailed analysis reveals that the sharp lines result from the Pauli repulsion and the consequent lateral relaxation of the CO at the apex of the tip. Such lines were also observed in the planar aromatic organic molecules. The sharp edges observed in AFM images should not be automatically related to the presence of interatomic bonds. Instead, they represent ridges of the potential energy landscape experienced by the functionalized probe [54, 55]. In particular, the sharp square, which coincides with the H-bonded loop, emerges from the deflection of the probe particle due to its repulsive interaction with four oxygen atoms of the water tetramer. In other words, the characteristic sharp lines appear between the protruding H atoms as a result of saddles and ridges in the repulsive Pauli interaction landscape. These saddles are also apparent on an isosurface of the total electron density of the water cluster shown in Fig. 16.5c. Such saddles in the potential energy landscape lead to branching of the probe particle trajectories, which are visualized in Fig. 16.5d.

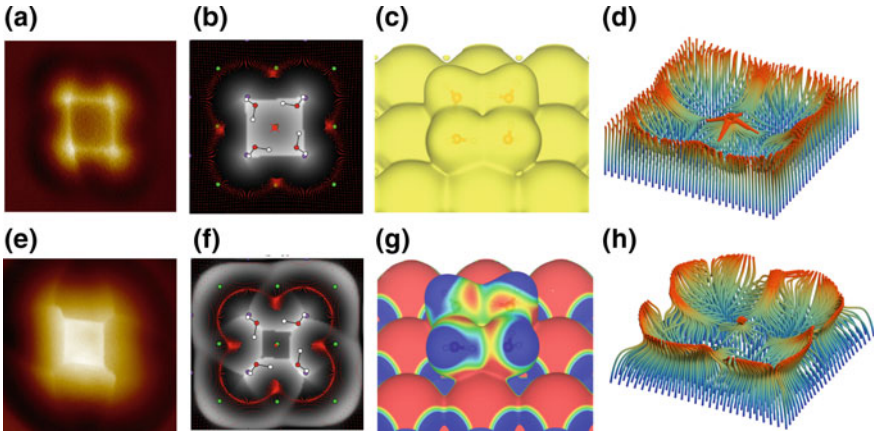

Fig. 16.5 High-resolution AFM images of water tetramer on a NaCl surface with CO and Cl tips and their relaxation. Experimental (**a**) and simulated (**b**) high-resolution AFM images acquired with a CO tip; **c** a calculated isosurface of the electron density of a water tetramer that corresponds to a constant level of Pauli repulsion; **d** calculated trajectories of the probe particle for the CO tip. Experimental (**e**) and simulated (**f**) high-resolution AFM images acquired with a Cl tip; **g** calculated electrostatic potential map of a water tetramer; **h** calculated trajectories of the probe particle for the Cl tip [57]

Contrary to the CO tip, the image contrast acquired with the Cl tip is strongly affected by the electrostatic field of the water cluster. This leads to very different features at small tip-sample distances, which can be also reproduced by AFM simulations using a negative monopole charge located on the probe particle (see Fig. 16.5f). Based on these simulations, we can rationalize the origin of two main differences that arise in comparison with the CO tip case: (i) the shrinking of the central square and (ii) appearance of additional chiral fork-like features at the periphery (see Fig. 16.5e, f). All these features can be ultimately tracked down to a map of electrostatic potential visualized in Fig. 16.5g overlaid on top of a contour of the total electron density (defining Pauli repulsion), along which the probe particle slides upon tip approaching. In the case of the Cl tip, the presence of the electrostatic field above the water tetramer makes the relaxation of the probe particle more complex. The probe particle (Cl ion) is repelled from the negatively charged center toward positively charged H atoms, but then it suddenly slips off due to the Pauli repulsion over protruding H atoms and the restoring spring force of the tip. This sudden slip-off leads to additional branching of the probe particle trajectories ultimately manifested as discontinuity of the Δf signal measured on opposite sides of the branching line, as one can see in Fig. 16.5h. Thus, it gives rise to the sharp chiral fork-like features visible in the AFM images observed experimentally; see Fig. 16.5e. We can conclude that the exact geometry of the sharp features is very sensitive to the delicate balance between electrostatic, Pauli repulsion and van der Waals forces. In the instance of the Cl tip, the electrostatic interaction plays the decisive role in the formation of the peculiar

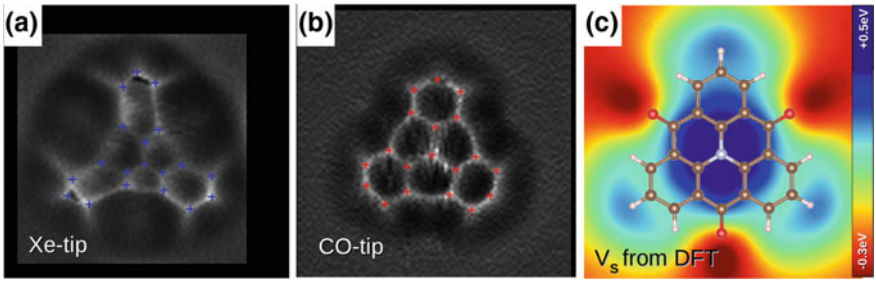

Fig. 16.6 Variation of the high-resolution AFM contrast of TOAT molecule acquired with different probes. **a** Constant height high-resolution AFM image acquired with a Xe tip; **b** Constant height high-resolution AFM image acquired with a CO tip; **c** Calculated Hartree potential above TOAT molecule obtained from DFT simulations. Adapted from [60]

submolecular contrast. Therefore the AFM images obtained with the Cl tip at small tip heights contain information about the electrostatic field.

In another experiment, van der Lit et al. investigated AFM images of a self-assembled monolayer of bis-(para-benzoic acid) acetylene molecules using Xe and CO-tip terminations [58]. The high-resolution AFM images show that brightness and contours of the edges vary according to the tip termination. Based on AFM simulations, they were able to establish that the electrostatic interaction between a functionalized tip and molecules on the surface determines the tip apex relaxations and consequently the observed AFM contrast. Thus, it is evident that the AFM contrast of polar molecules with strong inner charges can significantly change [59] with differently functionalized tips [60], even for one and the same molecule, as shown in Fig. 16.6. The importance of the electrostatic interaction in the AFM contrast was also discussed by Guo et al. [61] for π-conjugated molecules and Ellner et al. [62] for ionic surfaces.

16.3.2 Mapping Electrostatic Potential Using High-Resolution Imaging

From the discussion above, it is clear that the electrostatic field of the probed molecules may have substantial influence on a displacement of the probe particle and the resulting contrast. Consequently, the movement of the tip apex induces the variation of sharp edges seen in the high-resolution images, as shown in Fig. 16.7. This effect was used by Hapala et al. to introduce a new method [60], which enables mapping of the electrostatic field in the vicinity of the molecules of interest from high-resolution AFM/STM images.

The new method can determine the electrostatic field on a single molecule and their assemblies from distortions of high-resolution images acquired with scanning probes, see Fig. 16.7. For example, high-resolution AFM images of the

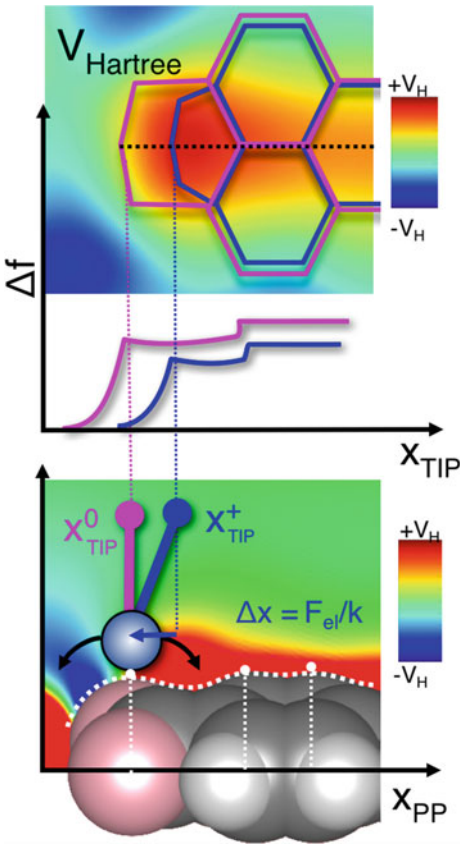

Fig. 16.7 Schematic picture demonstrating the effect of lateral bending of the probe particle on the position of the sharp edges in high-resolution AFM. (upper panel) Blue and pink lines represent different positions of the sharp edges observed in high-resolution images acquired with the probe particles experiencing different lateral (electrostatic) force. (lower panel) Side view of the lateral position of the probe particle x_{PP} with respect to the tip apex x_{TIP} experiencing a different lateral force at a saddle point. Background image renders the calculated Hartree potential of a scanned (PTCDA) molecule, the field of which induces the lateral bending Δx of the charged probe particle. Adapted from [60]

1,5,9-Trioxo-13-azatriangulene (TOAT) molecule acquired with Xe and CO-functionalized tips (see Fig. 16.6) show a different submolecular contrast. Due to the presence of a large molecular electrostatic field, the image distortion differs significantly for the two different functionalized tips. In general, the outermost atom/molecule of the probe is significantly moved during scanning by the molecule electrostatic field, in an analogy to the principle of a classical electroscope. Thus, the movement of the front atom on the probe causes distortions of the apparent positions of atoms and bonds in the images taken by means of the high-resolution AFM. The electrostatic field can be extracted by image-processing, in a similar way as the gravitational field is extracted from astronomical photographs of stars and galaxies distorted by Einstein gravitational lensing. In our situation, the image analysis is simpler thanks to a linear relation (Hooke's law) between the degree of the observed deformation (apparent displacement of the bifurcation edges in one of the images with respect to the other) and the electrostatic field. This allows us to obtain spatial distributions of the electrostatic field with sub-molecular resolution shown in Fig. 16.8.

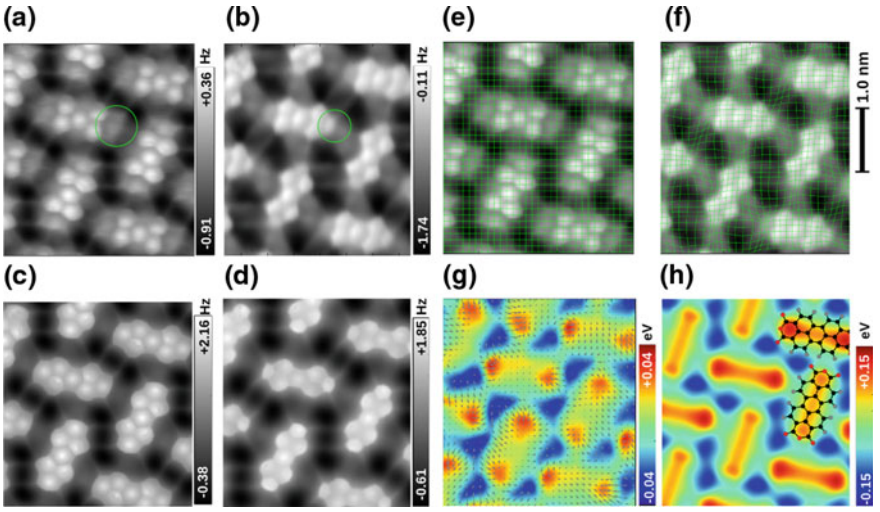

Fig. 16.8 Procedure to find the electrostatic field above a close-packed PTCDA layer. **a, b** Experimental high-resolution AFM images of a self-assembled monolayer of PTCDA deposited on Ag(111) obtained with two different Xe tips. **c** Simulated AFM image using an effective charge $Q = 0.0$ e and the effective lateral stiffness $k = 0.16$ Nm^{-1}. **d** Same as (**c**), but with $Q = +0.3$ e and $k = 0.20$ Nm^{-1}. **e, f** The experimental images superimposed with a deformation grid defined by comparing the corresponding sharp features between the two images in (**a**) and (**b**). **g** electrostatic potential calculated from the deformation field (grey arrows). **h** Calculated Hartree potential from DFT simulations 3.0 Å above the molecular layer. Adapted from [60]

The method consists of acquiring high-resolution AFM or STM images of the same molecular structure on the surface using two different tips with distinct charges. In principle, this can be accomplished by using two different functionalized tips, such as Xe and CO, or the same functionalized tip at two different applied biases. In the next step, the two images are aligned and the vertices corresponding to apparent positions of atoms in the high-resolution AFM images are identified; see blue and red crosses in Fig. 16.6a, b. In this particular case, symmetrization of the atomic positions by applying the $C3v$ symmetry of the molecule was enforced, with the purpose of eliminating the effects caused by a natural tip asymmetry [55]. In the next step, we use the displacement between the corresponding symmetrized vertices to generate a displacement vector field, employing the radial basis-function method of interpolation [60]. We should note that in the case of single molecules, the interpolation is not reliable in the featureless region far from the molecule due to a diminished atomic contrast. This fact limits the possibility to image the electrostatic potential around molecules standing alone on surfaces.

Importantly, it can be shown that the Pauli repulsion has negligible impact on the lateral position of the sharp edges (for details see discussion in Supplemental Material of [60]). Therefore, the deformation of the sharp edges in AFM/STM images is driven only by the electrostatic field and the van der Waals force components.

The van der Walls force field is attractive and thus homogeneously enlarges the image of the whole molecule. Under certain circumstances, the effect of vdW interaction can be neglected [60]. The electrostatic interaction can be both attractive and repulsive according to the electrostatic potential near the inspected molecule and according to the effective charge on the probe particle. As a consequence, the electrostatic interaction between the tip and the sample has a non-trivial impact on the image contrast.

The distortion-vector field we have extracted from the difference of two high-resolution images is proportional to the difference of electrostatic forces felt by the respective tip-terminating particles. Thus, the distortion vector field can be considered as a good approximation to the shape of the molecular electrostatic force field acting on the probe. To obtain quantitative analysis, one has to estimate lateral spring constant k and effective charge Q of the probes employed in the imaging. This can be achieved using an optimisation of input parameters k and Q to obtain the best match between simulated and experimental images, see Fig. 16.8a–d. For a more detailed description of the method see [60]. Alternatively, the scaling factor can be obtained by a calibration on a sample with known electrostatic field.

The method provides certain advantages over the KPFM method, mainly the substantial improvement of the spatial resolution of the electrostatic field, due to its applicability at intimate tip-sample contact. Moreover, the method enables us to acquire an additional information besides the map of the electrostatic field at the same time, namely to visualize the chemical (HR-AFM) or electronic (HR-STM) structure of the molecule under investigation. The main strategy of the method may also be utilised in the future for mapping other types of force fields (e.g. magnetic) around molecules. The definition of the observable is based on a solid theoretical background, which is crucial for an interpretation of the results. On the other hand, the method relies on detecting the sharp edges, a fact which poses some limits on its resolution outside of the regions where the single molecules reside.

In order to further improve the resolution of the method, it would be very helpful to find new atomic or molecular candidates for tip functionalization [37, 42], which would offer the possibility to control their electrostatic field. The two main factors for the wide popularity of CO or Xe tip functionalizations are (i) a reproducible and well described recipe for their preparation [44, 63, 64], and (ii) flexibility and structural stability of the atom/molecule on the metal tip apex. Nevertheless, control of the charge in such tips cannot be attained easily, as it may vary depending on atomistic details of its binding to the tip apex. Increased sensitivity to the charge could be achieved with tip functionalizations having a large internal charge or improved polarisability. Small molecules or functional groups that could be easily charged by an applied bias are among ideal candidates. Therefore, an extensive search is needed for new tip functionalizations with tunable charge/dipole/quadrupoles, easy polarisability and/or small redox potentials. Possible options are: hydroxyl groups, nitrogen oxides, isonitrile, nitrile, azide, quinones, or transition metal chelates. In a recent study, a ferrocene or nickelocene molecule was also suggested [65]. Finally, there is a need for a better understanding of the response of functionalized tips to changing bias voltage. In particular, we should be able to quantify their polarisability and any

actual redox charging. At the same time, we have to search for reliable and reproducible ways to place the functional groups on the tip apex.

16.4 Conclusions

We are witnesses of fast development of scanning probe techniques, which can resolve molecules with unprecedented spatial resolution providing detailed information about their chemical structure. Besides that, the KPFM method, the differential KPFS (bias-dependent atomic force spectroscopy) and the probe-particle method utilising functionalized tips are also sensitive to the electrostatic properties of the sample. Unfortunately, none of these approaches represents a robust and general method for the imaging of the electrostatic potential or field. Still, granted some reasonable simplifying assumptions, the methods may provide a lot of valuable (albeit perhaps only qualitative) information about charges of atoms or molecules or the polarity of chemical bonds. There is obviously room for further development. e.g. by finding better recipes for tip functionalization.

Acknowledgements We would like to thank to O. Krejčí, O. Stetsovych, J. Berger, J. Repp, F. Albrecht, I. Swart, L. Gross, Y. Yang, F.J. Giessibl and other colleagues for fruitful discussions. We acknowledge the support by GAČR, grant no. 17-24210Y. P.J. acknowledges the Praemium Academiae award from the Czech Academy of Sciences.

References

1. J.V. Barth, G. Costantini, K. Kern, Nature **437**, 671 (2005)
2. G. Franc, A. Gourdon, Phys. Chem. Chem. Phys. **13**, 14283 (2011)
3. L. Grill, M. Dyer, L. Lafferentz, M. Persson, M.V. Peters, S, Hecht. Nat. Nanotech. **2**, 687 (2007)
4. G. Binnig, H. Rohrer, Ch. Gerber, E. Weibel, Phys. Rev. Lett. **49**, 57 (1982)
5. G. Binnig, C.F. Quate, Ch. Gerber, Phys. Rev. Lett. **56**, 930 (1986)
6. F.J. Giessibl, App. Phys. Lett. **73**, 3956 (1998)
7. T. An, T. Eguchi, K. Akiyama, Y. Hasegawa, Appl. Phys. Lett. **87**, 133114 (2005)
8. Y. Sugimoto, P. Pou, M. Abe, P. Jelínek, R. Perez, S. Morita, O. Custance, Nature **446**, 64 (2007)
9. R. Wiesendanger, Rev. Mod. Phys. **81**, 1495 (2009)
10. M. Nonnenmacher, M.P.O. Boyle, H.K. Wickramasinghe, Appl. Phys. Lett. **58**, 2921 (1991)
11. J.M.R. Weaver, H.K. Wickramasinghe, J. Vac. Sci. Tech. B **9**, 1562 (1991)
12. S. Kitamura, M. Iwatsuki, Appl. Phys. Lett. **72**, 3154 (1998)
13. Y. Sugawara, T. Uchihashi, M. Abe, S. Morita, Appl. Surf. Sci. **140**, 371 (1999)
14. K. Okamoto, K. Yoshimoto, Y. Sugawara, S. Morita, Appl. Surf. Sci. **210**, 128 (2003)
15. G.H. Enevoldsen, T. Glatzel, M.C. Christensen, J.V. Lauritsen, F. Besenbacher, Phys. Rev. Lett. **100**, 236104 (2008)
16. F. Bocquet, L. Nony, Ch. Loppacher, T. Glatzel, Phys. Rev. B **78**, 035410 (2008)
17. L. Nony, A. Foster, F. Bocquet, C. Loppacher, Phys. Rev. Lett. **103**, 036802 (2009)
18. S. Sadewasser, P. Jelínek, C.-K. Fang, O. Custance, Y. Yamada, Y. Sugimoto, M. Abe, S. Morita, Phys. Rev. Lett. **103**, 266103 (2009)

19. R. Stomp, Y. Miyahara, S. Schaer, Q. Sun, H. Guo, P. Grütter, S. Studenikin, P. Poole, A. Sachrajda, Phys. Rev. Lett. **94**, 056802 (2005)
20. L. Gross, F. Mohn, P. Liljeroth, J. Repp, F.J. Giessibl, G. Meyer, Science **324**, 1428 (2009)
21. F. Mohn, L. Gross, N. Moll, G. Meyer, Nat. Nanotechnol. **7**, 227 (2012)
22. T.R. Albrecht, P. Grütter, D. Horne, D. Rugar, J. App. Phys. **69**, 668 (1991)
23. S. Sadewasser, M.Ch. Lux-Steiner, Phys. Rev. Lett. **91**, 266101 (2003)
24. M. Corso, M. Ondracek, Ch. Lotze, P. Hapala, K.J. Franke, P. Jelínek, J.I. Pascual, Phys. Rev. Lett. **115**, 136101 (2015)
25. A. Sadeghi, A. Baratoff, S.A. Ghasemi, S. Goedecker, T. Glatzel, S. Kawai, E. Meyer, Phys. Rev. B **86**, 075407 (2012)
26. A.J. Weymouth, T. Wutscher, J. Welker, T. Hofmann, F.J. Giessibl, Phys. Rev. Lett. **106**, 226801 (2011)
27. A. Roy-Gobeil, Y. Miyahara, P. Grütter, Nano Lett. **15**, 2324 (2015)
28. L. Cockins, Y. Miyahara, S.D. Bennett, A.A. Clerk, S. Studenikin, P. Poole, A. Sachrajda, P. Grutter, PNAS **107**, 9496 (2010)
29. M. Ondráček, P. Hapala, P. Jelínek, Nanotechnology **27**, 274005 (2016)
30. N. Kocić, P. Weiderer, S. Keller, S. Decurtins, S.-X. Liu, J. Repp, Nano Lett. **15**, 4406 (2015)
31. P. Rahe, R.P. Steele, C.C. Williams, Nano Lett. **16**, 911 (2016)
32. S. Sadewasser, Th. Glatzel, *Kelvin Probe Force Microscopy: Measuring and Compensating Electrostatic Forces* (Springer, Berlin, 2012)
33. L. Gross, B. Schuler, F. Mohn, N. Moll, N. Pavliček, W. Steurer, I. Scivetti, K. Kotsis, M. Persson, G. Meyer, Phys. Rev. B **90**, 155455 (2014)
34. B. Schuler, Sh. Liu, Y. Geng, S. Decurtins, G. Meyer, L. Gross, Nano Lett. **14**, 3342 (2014)
35. S. Kawai, A. Sadeghi, X. Feng, P. Lifen, R. Pawlak, Th. Glatzel, A. Willand, A. Orita, J. Otera, S. Goedecker, E. Meyer, ACS Nano **7**, 9098 (2013)
36. S.A. Burke et al., Nanotechnology **20**, 264012 (2009)
37. F. Mohn, B. Schuler, L. Gross, G. Meyer, App. Phys. Lett. **102**, 073109 (2013)
38. J.L. Neff, P. Rahe, Phys. Rev. B **91**, 085424 (2015)
39. F. Albrecht, J. Repp, M. Fleischmann, M. Scheer, M. Ondráček, P. Jelínek, Phys. Rev. Lett. **115**, 076101 (2015)
40. Ch. Wagner, M.F.B. Green, Ph. Leinen, Th. Deilmann, P. Krüger, M. Rohlfing, R. Temirov, F.S. Tautz, Phys. Rev. Lett. **115**, 026101 (2015)
41. R. Temirov, S. Soubatch, O. Neucheva, A.C. Lassise, F.S. Tautz, New J. Phys. **10**, 053012 (2008)
42. G. Kichin, Ch. Weiss, Ch. Wagner, F.S. Tautz, R. Temirov, J. Am. Chem. Soc. **133**, 16847 (2011)
43. L. Gross, F. Mohn, N. Moll, P. Liljeroth, G. Meyer, Science **325**, 1110 (2009)
44. L. Bartels, G. Meyer, K.H. Rieder, App. Phys. Lett. **71**, 213 (1997)
45. N. Kocić, X. Liu, S. Chen, S. Decurtins, O. Krejčí, P. Jelínek, J. Repp, Sh.-X. Liu, J. Am. Chem. Soc. **138**, 5585 (2016)
46. Th. Dienel, Sh. Kawai, H. Söde, X. Feng, K. Müllen, P. Ruffieux, R. Fasel, O. Gröning, Nano Lett. **15**, 5185 (2015)
47. Sh. Kawai, V. Haapasilta, B.D. Lindner, K. Tahara, P. Spijker, J.A. Buitendijk, R. Pawlak, T. Meier, Y. Tobe, A.S. Foster, E. Meyer, Nat. Comm. **7**, 12711 (2016)
48. O. Stetsovych, M. Švec, J. Vacek, J. Vacek-Chocholoušová, A. Jančařík, J. Rybáček, K. Kośmider, I.G. Stará, P. Jelínek, I. Starý, Nat. Chem. **9**, 213 (2017)
49. D.G. de Oteyza, P. Gorman, Y.Ch. Chen, S. Wickenburg, A. Riss, D.J. Mowbray, G. Etkin, Z. Pedramrazi, H.-Z. Tsai, A. Rubio, M.F. Crommie, F.R. Fischer, Science **340**, 1434 (2013)
50. N. Moll, L. Gross, F. Mohn, A. Curioni, G. Meyer, New J. Phys. **12**, 125020 (2010)
51. L. Gross, F. Mohn, N. Moll, B. Schuler, A. Criado, E. Guitian, D. Pena, A. Gourdon, G. Meyer, Science **337**, 1326 (2012)
52. M. Neu, N. Moll, L. Gross, G. Meyer, F.J. Giessibl, J. Repp, Phys. Rev. B **89**, 205407 (2014)
53. P. Hapala, R. Temirov, F.S. Tautz, P. Jelínek, Phys. Rev. Lett. **113**, 226101 (2014)

54. S.K. Hämäläinen, N. van der Heijden, J. van der Lit, S. den Hartog, P. Liljeroth, I. Swart, Phys. Rev. Lett. **113**, 186102 (2014)
55. P. Hapala, G. Kichin, Ch. Wagner, F.S. Tautz, R. Temirov, P. Jelínek, Phys. Rev. B **90**, 085421 (2014)
56. P. Hapala, M. Ondráček, O. Stetsovych, M. Švec, P. Jelínek, in *Noncontact Atomic Force Microscopy*, vol. 3, ed. by S. Morita, F.J. Giessibl, E. Meyer, R. Wiesendanger (Springer International Publishing, Berlin, 2015), p. 29
57. J. Peng, J. Guo, P. Hapala, D. Cao, M. Ondráček, B. Cheng, L. Xu, P. Jelínek, E. Wang, Y. Jiang, Nat. Comm. **9**, 122 (2018)
58. J. van der Lit, F. Di Cicco, P. Hapala, P. Jelínek, I. Swart, Phys. Rev. Lett. **116**, 096102 (2016)
59. N. Moll, B. Schuler, Sh. Kawai, F. Xu, L. Peng, A. Orita, J. Otera, A. Curioni, M. Neu, J. Repp, G. Meyer, L. Gross, Nano Lett. **14**, 6127 (2014)
60. P. Hapala, M. Švec, O. Stetsovych, N.J. van der Heijden, M. Ondráček, J. van der Lit, P. Mutombo, I. Swart, P. Jelínek, Nat. Commun. **7**, 11560 (2016)
61. Ch.-Sh. Guo, M.A. Van Hove, X. Ren, Y. Zhao, J. Phys. Chem. C **119**, 1483 (2015)
62. M. Ellner, N. Pavliček, P. Pou, B. Schuler, N. Moll, G. Meyer, L. Gross, R. Perez, Nano Lett. **16**, 1974 (2016)
63. D.M. Eigler, E.K. Schweizer, Nature **344**, 524 (1990)
64. A.J. Heinrich, C.P. Lutz, J.A. Gupta, D.M. Eigler, Science **298**, 1381 (2002)
65. M. Ormaza, N. Bachellier, M.N. Faraggi, B. Verlhac, P. Abufager, P. Ohresser, L. Joly, M. Romeo, F. Scheurer, M.-L. Bocquet, N. Lorente, L. Limot, Nano Lett. **17**, 1877 (2017)

Index

S. Sadewasser and T. Glatzel (eds.), *Kelvin Probe Force Microscopy*,
Springer Series in Surface Sciences 65, https://doi.org/10.1007/978-3-319-75687-5